Advances in Science, Technology & Innovation
IEREK Interdisciplinary Series for Sustainable Development

Soumia El Hani · Mohamad Essaaidi
Editors

Recent Advances in Electrical and Information Technologies for Sustainable Development

Proceedings of the 3rd International Conference on Electrical and Information Technologies—ICEIT 2017, Morocco

IEREK
RESEARCH & KNOWLEDGE ENRICHMENT

Springer

Advances in Science, Technology & Innovation

IEREK Interdisciplinary Series for Sustainable Development

Advances in Science, Technology & Innovation (ASTI) is a series of peer-reviewed books based on the best studies on emerging research that redefines existing disciplinary boundaries in science, technology and innovation (STI) in order to develop integrated concepts for sustainable development. The series is mainly based on the best research papers from various IEREK and other international conferences, and is intended to promote the creation and development of viable solutions for a sustainable future and a positive societal transformation with the help of integrated and innovative science-based approaches. Offering interdisciplinary coverage, the series presents innovative approaches and highlights how they can best support both the economic and sustainable development for the welfare of all societies. In particular, the series includes conceptual and empirical contributions from different interrelated fields of science, technology and innovation that focus on providing practical solutions to ensure food, water and energy security. It also presents new case studies offering concrete examples of how to resolve sustainable urbanization and environmental issues. The series is addressed to professionals in research and teaching, consultancies and industry, and government and international organizations. Published in collaboration with IEREK, the ASTI series will acquaint readers with essential new studies in STI for sustainable development.

More information about this series at http://www.springer.com/series/15883

Soumia El Hani • Mohamad Essaaidi
Editors

Recent Advances in Electrical and Information Technologies for Sustainable Development

Proceedings of the 3rd International Conference on Electrical and Information Technologies—ICEIT 2017, Morocco

Springer

Editors

Soumia El Hani
Electrical Engineering Department, ENSET Rabat
Mohammed V University
Rabat, Morocco

Mohamad Essaaidi
ENSIAS Rabat
Mohammed V University
Rabat, Morocco

ISSN 2522-8714 ISSN 2522-8722 (electronic)
Advances in Science, Technology & Innovation
IEREK Interdisciplinary Series for Sustainable Development
ISBN 978-3-030-05275-1 ISBN 978-3-030-05276-8 (eBook)
https://doi.org/10.1007/978-3-030-05276-8

Library of Congress Control Number: 2018964924

© Springer Nature Switzerland AG 2019
This work is subject to copyright. All rights are reserved by the Publisher, whether the whole or part of the material is concerned, specifically the rights of translation, reprinting, reuse of illustrations, recitation, broadcasting, reproduction on microfilms or in any other physical way, and transmission or information storage and retrieval, electronic adaptation, computer software, or by similar or dissimilar methodology now known or hereafter developed.
The use of general descriptive names, registered names, trademarks, service marks, etc. in this publication does not imply, even in the absence of a specific statement, that such names are exempt from the relevant protective laws and regulations and therefore free for general use.
The publisher, the authors and the editors are safe to assume that the advice and information in this book are believed to be true and accurate at the date of publication. Neither the publisher nor the authors or the editors give a warranty, express or implied, with respect to the material contained herein or for any errors or omissions that may have been made. The publisher remains neutral with regard to jurisdictional claims in published maps and institutional affiliations.

This Springer imprint is published by the registered company Springer Nature Switzerland AG
The registered company address is: Gewerbestrasse 11, 6330 Cham, Switzerland

Preface

Many emerging technologies like, green energy, smart grid, smart cities, greenhouse, mobile phones, Internet, Internet of Things, would not have been possible without electrical and information technologies. Furthermore, these technologies were instrumental for the technological revolution that has shaped modern societies, solved many of its development problems, and contributed to its economical unprecedented growth and social welfare.

This pervasive presence of electrical and information technologies in all aspects of engineering practice, from industrial engineering, to chemical, materials engineering, to the aerospace, and the emerging field of biomedical engineering, constitutes a real revolution that has characterized the second half of the twentieth century.

The book chapters given in this book are mainly the research outcomes and extended results of the best papers peer reviewed, accepted, and presented at the 3rd edition of the IEEE-International Conference on Electrical and Information Technologies, held in Rabat-Morocco on November 2017, IEEE-ICEIT'17.

This book, with two interrelated research domains, main objective is to illustrate a number of relevant applications of electrical and information technologies. It is dedicated to highlight new ideas and views by presenting ongoing challenges and responses in research. The contents may in turn inspire or validate new standards and practices in the professional field. The book could also be useful as a textbook for university students in electrical engineering at both undergraduate and postgraduate levels.

Rabat, Morocco

Soumia El Hani
Mohamad Essaaidi

Acknowledgements

Most of contributions, outcomes, and insights presented in this book were achieved through long-term teaching and research conducted by the authors and their research groups on the different topics on Electrical and Information Technologies. Our profound thanks go to the co-authors of the chapters in this book; it is a great pleasure to work with them.

This book would not have been possible without the perseverance, dedication, and hard work of the organizing and steering committees as well as Technical Program Committee members for ICEIT 2017, a special acknowledgment to them and to all eminent speakers and participants who have come from Morocco and other parts of the world.

The authors also would like to thank their colleagues from different countries: Dr. N. Bennis, Dr. J. Ortega, Dr. S. Guedira, Dr. M. Boulmalf, Dr. M. Tarbouchi, Dr. L. Azrar, Dr. E. Karatza, Dr. H. El Fadil, Dr. T. Sadiki, Dr. M. Bennani, Dr. A. Hasnaoui, Dr. A. Boutejdar, Dr. P. Maussion, Dr. M. Feddi, Dr. R. Ajhoune, Dr. Hakim Anouar Boudhir, Dr. A. Jilbab, Dr. B. Sareni, Dr. A. Naitali, Dr. Larbi Belarbi, Dr. N. Zidane, Dr. G. Mezzour, Dr. A. Abouloifa, Dr. M. Faquir, Dr. I. Benmiloud, Dr. J. El M'hamdi, Dr. R. El Gouri, Dr. H. Ouadi, and postgraduate students: I. Ouachtouk, I. Aboudrar and K. Dahi for their active role and continuous supports.

Last but not least, the editors take this opportunity to express their deepest gratitude to their family for all their patience and help during the preparation of this book.

Contents

Part I Power System and Electronics

Part II Control Systems

Part III Information Technology

Part IV Telecommunications and Vehicular Technologies

Part V Green Applications and Interdisciplinary Topics

Contributors

El Arbi Abdellaoui Alaoui EIGSI, Casablanca, Morocco
E3MI Team, Faculty of Sciences and Techniques at Errachidia, Department of Computer Science, University of Moulay Ismail, Meknès, Morocco

E. Abdelmounim Laboratory of Signal Analysis and Information Processing, Faculty of Science and Technology, Settat, Morocco

Abdellah Abouabdellah MOSIL, System Engineering Laboratory, ENSA, Ibn Tofail University, Kenitra, Morocco

Imad Aboudrar Energy Optimization, Diagnosis and Control, STIS Center ENSET, Mohammed V University, Rabat, Morocco

M. Aboulfatah Laboratory of Signal Analysis and Information Processing, Faculty of Science and Technology, Settat, Morocco

A. Abouloifa TI Lab, Faculty of Sciences Ben M'sik, Hassan II-Casablanca University, Casablanca, Morocco

Oluwaseun Simon Adekanle Laboratory of Signal Analysis and Information Processing, Faculty of Science and Technology, Settat, Morocco

Ahmed Aghmadi Energy Optimization, Diagnosis and Control, STIS Center ENSET, Mohammed V University, Rabat, Morocco

Said Agoujil E3MI Team, Faculty of Sciences and Techniques at Errachidia, Department of Computer Science, University of Moulay Ismail, Meknès, Morocco

Essadki Ahmed Mohammed V University, ENSIAS, Rabat, Morocco

Mounir Ait Kerroum LaRIT, Faculty of Sciences, Ibn Tofail University Kenitra, Kenitra, Morocco

Abdelmajid Akil Laboratory of Structural Engineering, Department of Electrical Engineering, Intelligent Systems and Electrical Energy, ENSAM, Hassan II University Casablanca, Casablanca, Morocco

Aumeur El Amrani LPSMS Laboratory, Faculty of Sciences and Technology, Errachidia, Morocco

C. Aouadi TI Lab, Faculty of Sciences Ben M'sik, Hassan II-Casablanca University, Casablanca, Morocco

M. Aourir TI Lab, Faculty of Sciences Ben M'sik, Hassan II-Casablanca University, Casablanca, Morocco

A. Baghdad Laboratory of Electronics Energy, Automatic & Data Processing (LEEA&TI) FST, Mohammedia University Hassan II of Casablanca, Mohammedia, Morocco

A. Ballouk Laboratory of Electronics Energy, Automatic & Data Processing (LEEA&TI) FST, Mohammedia University Hassan II of Casablanca, Mohammedia, Morocco

F. Z. Belhaj ESIT Team, LGS Laboratory ENSA, Ibn Tofail University, Kénitra, Morocco

Fatima Zahra Belhaj ESIT Team, LGS Laboratory ENSA, Ibn Tofail University, Kénitra, Morocco

Najib Bennis ENSET of Rabat, University Mohamed V of Rabat, Rabat, Morocco

El-Mahjoub Boufounas LPSMS Laboratory, Faculty of Sciences and Technology, Errachidia, Morocco

Mohammed Boulmalf UIR, Rabat, Morocco

T. Bouragba Engineering School of Industrial Systems (EIGSI Casablanca), Casablanca, Morocco

Abdelmajid Bybi Ecole Supérieure de Technologie de Salé, Materials Energy Acoustics Team (MEAT), Mohammed V University in Rabat, Salé, Morocco

K. Chigane Ecole Mohammadia d’Ingénieurs, Mohammed V University in Rabat, Rabat, Morocco

Khalid Chikh Energy and Electrical Systems Laboratory, Hassan II University ENSEM, Casablanca, Morocco
Interdisciplinary Laboratory of Science and Technology Research, Sultan Moulay Slimane University-EST, Béni Mellal, Morocco

P. Dherbécourt Normandy University, IUT, INSA Rouen, CNRS, Rouen, France

Hilal Drissi Ecole Supérieure de Technologie de Salé, Laboratoire d’Analyse des systèmes Traitement d’Information et du Management Intégré (LASTIMI), Mohammed V University in Rabat, Salé, Morocco

Hassan EL Fadil ESIT Team, LGS Laboratory ENSA, Ibn Tofail University, Kénitra, Morocco

Aziz El Afia Energy and Electrical Systems Laboratory, Hassan II University ENSEM, Casablanca, Morocco

Hassan El Fadil ESIT Team, LGS Laboratory ENSA, Ibn Tofail University, Kénitra, Morocco

M. El Hachimi Laboratory of Electronics Energy, Automatic & Data Processing (LEEA&TI) FST, Mohammedia University Hassan II of Casablanca, Mohammedia, Morocco

F. El Otmani TI Lab, Faculty of Sciences Ben M’sik, Hassan II-Casablanca University, Casablanca, Morocco

A. El Oualkadi LabTIC Laboratory, National School of Applied Science of Tangier, Abdelmalek Essaadi University, Tangier, Morocco

Yahia El Ouazzani LEAM, Faculty of Juridical, Economic and Social Sciences, Mohammed V University, Rabat, Morocco

Abdelhafid Elouardi SATIE, Digiteo Labs, Paris-Sud University, Paris Saclay University, Orsay, France

Mohamed Essaaidi ENSIAS, Rabat, Morocco

Youssef Fakhri LaRIT, Faculty of Sciences, Ibn Tofail University Kenitra, Kenitra, Morocco

Driss Filahi Enset of Rabat, University Mohammed V of Rabat, Rabat, Morocco

K. Gaouzi ESIT Team, LGS Laboratory ENSA, Ibn Tofail University, Kénitra, Morocco

Khawla Gaouzi ESIT Team, LGS Laboratory ENSA, Ibn Tofail University, Kénitra, Morocco

Mohammed Garoum Ecole Supérieure de Technologie de Salé, Materials Energy Acoustics Team (MEAT), Mohammed V University in Rabat, Salé, Morocco

Fouad Giri Laboratoire D'Automatique de Caen, Université de Caen, Bd Marechal Juin, Caen, France

M. Guisser Laboratory of Signal Analysis and Information Processing, Faculty of Science and Technology, Settat, Morocco

Sara Haddou Amar MOSIL, System Engineering Laboratory, ENSA, Ibn Tofail University, Kenitra, Morocco

Chalawane Haitam Mohammed V University, ENSIAS, Rabat, Morocco

Soumia El Hani Energy Optimization, Diagnosis and Control, STIS Center ENSET, Mohammed V University, Rabat, Morocco
Enset of Rabat, University Mohammed V of Rabat, Rabat, Morocco

A. Hassoune Laboratory of Energy & Electrical Systems (LESE), Superior National School of Electricity and Mechanical (ENSEM), Hassan II University of Casablanca, Casablanca, Morocco
Engineering School of Industrial Systems (EIGSI Casablanca), Casablanca, Morocco

Anne-Christine Hladky-Hennion Département ISEN, IEMN, UMR, CNRS 8520, Lille Cedex, France

Wissam Jenkal Laboratory of Systems Engineering and Information Technology (LiSTi), ENSA, Ibn Zohr University, Agadir, Morocco

E. Joubert Normandy University, IUT, INSA Rouen, CNRS, Rouen, France

W. Jouha Normandy University, IUT, INSA Rouen, CNRS, Rouen, France
LabTIC Laboratory, National School of Applied Science of Tangier, Abdelmalek Essaadi University, Tangier, Morocco

M. Khafallah Laboratory of Energy & Electrical Systems (LESE), Superior National School of Electricity and Mechanical (ENSEM), Hassan II University of Casablanca, Casablanca, Morocco

Mohamed Khafallah Energy and Electrical Systems Laboratory, Hassan II University ENSEM, Casablanca, Morocco

I. Lachkar RI Lab, ENSEM Casablanca, Hassan II-Casablanca University, Casablanca, Morocco

Mohammed Lahlimi LaRIT, Faculty of Sciences, Ibn Tofail University Kenitra, Kenitra, Morocco

Fatima Ez-zahra Lamzouri LPSMS Laboratory, Faculty of Sciences and Technology, Errachidia, Morocco

Rachid Latif Laboratory of Systems Engineering and Information Technology (LiSTi), ENSA, Ibn Zohr University, Agadir, Morocco

M. Masmoudi Normandy University, IUT, INSA Rouen, CNRS, Rouen, France

Hamza Mediouni Energy Optimization, Diagnosis and Control, STIS Center ENSET, Mohammed V University, Rabat, Morocco

Safa Mejhoudi Laboratory of Systems Engineering and Information Technology (LiSTi), ENSA, Ibn Zohr University, Agadir, Morocco

A. Mesbahi Laboratory of Energy & Electrical Systems (LESE), Superior National School of Electricity and Mechanical (ENSEM), Hassan II University of Casablanca, Casablanca, Morocco

Arbaoui Mohammed Mohammed V University, ENSIAS, Rabat, Morocco

Ayoub Moufid ENSET of Rabat, University Mohamed V of Rabat, Rabat, Morocco

Assia Naja ENSIAS, Rabat, Morocco
UIR, Rabat, Morocco

Ilias Ouachtouk Energy Optimization, Diagnosis and Control, STIS Center ENSET, Mohammed V University, Rabat, Morocco

Mustapha Ouadghiri Energy Optimization, Diagnosis and Control, STIS Center ENSET, Mohammed V University, Rabat, Morocco

M. Ouassaid Ecole Mohammadia d’Ingénieurs, Mohammed V University in Rabat, Rabat, Morocco

Nabila Rabbah Laboratory of Structural Engineering, Department of Electrical Engineering, Intelligent Systems and Electrical Energy, ENSAM, Hassan II University Casablanca, Casablanca, Morocco

Aziz Rachid ESIT Team, LGS Laboratory ENSA, Ibn Tofail University, Kénitra, Morocco

Fatima-Ezzahra Tahiri Energy and Electrical Systems Laboratory, Hassan II University ENSEM, Casablanca, Morocco

Abdelouahad Tahri ESIT Team, LGS Laboratory ENSA, Ibn Tofail University, Kénitra, Morocco

Nasser Tamou Mohammed V University, ENSIAS, Rabat, Morocco

Mourad Zegrari Laboratory of Structural Engineering, Department of Electrical Engineering, Intelligent Systems and Electrical Energy, ENSAM, Hassan II University Casablanca, Casablanca, Morocco

Hanane Zekkori E3MI Team, Faculty of Sciences and Techniques at Errachidia, Department of Computer Science, University of Moulay Ismail, Meknès, Morocco

Introduction

This proceedings book *Recent Advances in Electrical and Information Technologies for Sustainable Development* collects selected and extended version papers of the 2017 IEEE-International Conference on Electrical and Information Technologies (ICEIT'17). The topics focus on novel theories, latest research trends, methods and experimental results, and applications in the field of electrical and information technologies. The papers were selected from the hottest topic areas, such as power system and electronics, renewable energy, control systems, telecommunications and vehicular technologies.

The presented book gives the background to the main objective of the ICEIT'17 conference that is to bring together scientists, researchers, engineers, and practitioners interested in any one of a wide range of topics and aspects it covers which are focused on electrical and information technologies. Moreover, it also aims to provide real opportunities for expertise and knowledge sharing and dissemination among its participants.

Part I focuses on power system and electronics subject, such as applications of power semiconductor technology: devices, techniques and performance management, electric power generation, transmission and distribution, and power system analysis.

Part II discusses the control system and its applications, and different theoretical and practical methods are presented including robust and adaptive controls, modeling and identification, robotics, and control and intelligent systems.

Part III discovers information technology subject which involves information security, cloud computing distributed, web services, big data and intelligent business, energy-aware distributed system, signal and image processing, multimedia technology, and social media.

Part IV presents telecommunications and vehicular technologies subject, which covers power efficient telecommunication systems, wireless ad-hoc and sensor networks, cognitive radio, cooperative communications, radio resource management and optimization, information theory and coding systems, and vehicular communication systems.

Part V discusses the green applications and interdisciplinary topics which comprise intelligent and green technologies for transportation systems, smart building, smart house, smart campus, and smart city and green applications in health care, etc.

The rich variety of contributions appeals to a wide audience including scientists, researchers, engineers, students, and practitioners interested in any topics which are focused on electrical and information technologies.

The papers included in the book are shaped by the organizing board of the conference and authors of the papers.

Keywords

ICEIT • Electrical Engineering • Information Technologies •
Power System and Electronics • Control Systems • Telecommunications •
Vehicular Technologies • Green Applications

Part I

Power System and Electronics

One-Dimensional Electromechanical Equivalent Circuit for Piezoelectric Array Elements

Abdelmajid Bybi, Hilal Drissi, Mohammed Garoum, and Anne-Christine Hladky-Hennion

Abstract

In this chapter, we report a simple one-dimensional electromechanical method to model piezoelectric transducer array elements well known by slender bar elements. The method is inspired from Mason's simplified model, which is tested in the case of a piezoelectric plate and extended to a rectangular slender bar. The research work investigates the effects of the material parameters on the electroacoustic performances, i.e., on the electrical impedance and the displacement. First, it compares the performances of a piezoelectric plate obtained experimentally and those calculated from the equivalent circuit. Two approaches are tested: the first method consists of the determination of the circuit components from the manufacturer parameters and the second one deduces them from the measured electrical impedance. The second approach is then tested in the case of a piezoelectric rectangular slender bar similar to those constituting the medical imaging transducer arrays. In this case, the electrical impedance and the displacement obtained are very close to the measured ones, especially around the resonance frequency. The same approach will be used to study a complete transducer array, i.e., taking into account all the elements, the filling material, the matching layers, and the backing. This constitutes the objective of our future work.

Keywords

Piezoelectric transducer arrays • Electromechanical equivalent circuits • Mason's model • Piezoelectric slender bar

1 Introduction

The physical behavior of piezoelectric transducers and transducer arrays can be described by resolving the fundamental constitutive equations of piezoelectricity coupled with those of mechanics and electricity. However, depending on the geometry of the studied transducer and its boundary conditions, the problem can become very complicated to resolve analytically. Another option is to represent the transducer components, i.e., the piezoelectric material, the matching layers and the backing by electromechanical or electrical circuits, using the conventional analogies: voltage/force, current/speed, inductance/mass, etc. In this context, several models are proposed in the literature, for example, the KLM's (Krimholtz, Leedom and Matthaei) model (Royer and Dieulesaint 1999; Sherrit et al. 1999; Maréchal et al. 2007), the Redwood's model (Arnau 2008; Richard and Cobbold 2006) and the Mason's model (Royer and Dieulesaint 1999; Sherrit et al. 1999). All these models are generally limited to the one-dimensional behavior. Good results can be obtained by these models in the case of piezoelectric plates and Langevin transducers (Hernandez et al. 2010; Pérez et al. 2016). In the case of transducer arrays, the least understood aspect is the elementary transducer. This vibrating element is usually in the form of a rectangular piezoelectric slender bar where the dimension along the poling direction is determined by the chosen operating frequency. The length of the element is very large

---

A. Bybi (✉) · M. Garoum
Ecole Supérieure de Technologie de Salé, Materials Energy Acoustics Team (MEAT), Mohammed V University in Rabat, Avenue Le Prince Héritié, B.P.: 227 11000 Salé, Morocco
e-mail: abdelmajid_bybi@hotmail.fr

M. Garoum
e-mail: garoum1@yahoo.fr

H. Drissi
Ecole Supérieure de Technologie de Salé, Laboratoire d'Analyse des systèmes Traitement d'Information et du Management Intégré (LASTIMI), Mohammed V University in Rabat, Avenue Le Prince Héritié, B.P.: 227 11000 Salé, Morocco
e-mail: hilal.drissi@gmail.com

A.-C. Hladky-Hennion
Département ISEN, IEMN, UMR, CNRS 8520, Lille Cedex, France
e-mail: anne-christine.hladky@isen.fr

S. El Hani and M. Essaaidi (eds.), *Recent Advances in Electrical and Information Technologies for Sustainable Development*, Advances in Science, Technology & Innovation, https://doi.org/10.1007/978-3-030-05276-8_1

compared to the lateral dimensions, this allows considering a plane strain approximation. Consequently, two-dimensional electrical and numerical models are usually utilized in order to describe the physical behavior of this kind of elements (Hutchens and Morris 1985; Bybi 2012). Several authors used the KLM one-dimensional model to study the transducer array elements and they obtain satisfactory results (Zhang et al. 2012; Zhang 2011).

The aim of this work is to check the possibility of modeling the piezoelectric slender bar by one-dimensional electromechanical circuit inspired from the Mason's one. The first part is devoted to the description of a conventional piezoelectric transducer array and the presentation of the electromechanical circuit utilized to model the array elements. In the second part, a piezoelectric plate is modeled using LTspice simulation tool (http://www.linear.com/designtools/software/) and the results are compared to the ones obtained experimentally. The modeling method is then tested in the case of a rectangular slender bar to check its validity. In future work, this model will be tested in the case of a complete piezoelectric transducer array in order to study the crosstalk phenomenon and find solutions to this problem.

2 Electromechanical Equivalent Circuit for Piezoelectric Transducers

2.1 Piezoelectric Transducer Array

Linear and phased transducer arrays utilized in medical imaging and NDT applications are generally composed of N piezoelectric slender bar elements having a thickness T, a width W and a length L, spaced by a distance d and aligned as illustrated in Fig. 1. The elements are polarized in the x_3 (or z) direction and are bonded to each other by a nonconductive resin. The thickness T depends on the desired operating frequency, which is approximately equal to a half of the wavelength in the piezoelectric material (Royer and Dieulesaint 1999). In order to avoid the parasitic graing lobes, the spacing between the transducer array elements d (consequently the width W) must respect the Nyquist criterion $d < \lambda_w/2$ (λ_w wave length in the propagation medium: water in medical imaging) at the operating frequency (Wooh and Shi 1999; Huang et al. 2004). In order to obtain a dominant thickness mode, the ratio W/T must be less than or equal to 0.5 (Sato et al. 1979; Friedrich et al. 1990). Finally, the length L is usually taken much greater than T and W (approximately 10) (Hutchens and Morris 1985; Kim et al. 2006).

To improve the electroacoustic performances, each element of the array is also equipped with front and back matching layers in order to minimize the acoustical mismatching problem which creates a prolonged ringing after pulse excitation and thus decreases the transducer's frequency bandwidth. Generally, a conventional piezoelectric transducer having an acoustic impedance about 34 MRayls is matched to the impedance of the propagation medium about 1.5 MRayls (in the case of medical imaging applications) by one or two matching layers on its front face and one thick absorber layer (the backing) on its back face. The backing material should satisfy two main requirements. First, in order to widen the bandwidth of the transducer array by absorbing the radiated energy from the back face of the piezoelectric elements, it should have a high attenuation (about 50 dB at the operating frequency). Second, in order to guarantee a good coupling, it should have an acoustic impedance closely matched to that of the piezoelectric elements. The most commonly used material which satisfies these two requirements consist of an epoxy resin with high ultrasonic absorption filled with Tungsten powder which increases the density and therefore the acoustic impedance (Grewe et al. 1990). Finally, in order to reduce the electrical mismatching between the array elements and the transmission/reception electronics, an electrical matching circuit is also added to the individual array elements.

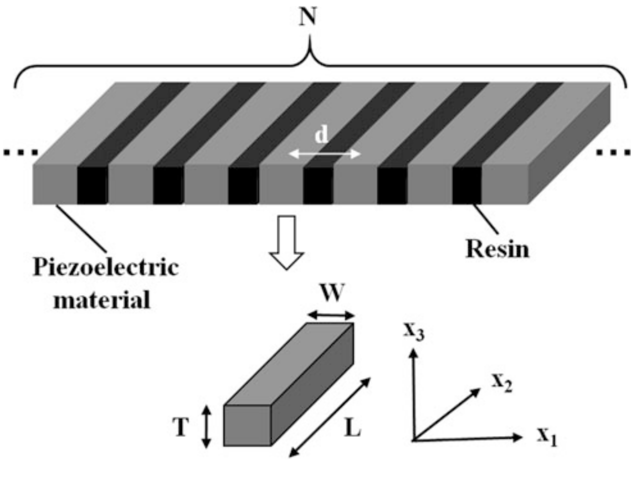

Fig. 1 Piezoelectric transducer array composed of N elements

In order to facilitate the fabrication of the transducer array and to check easily the validity of the equivalent electromechanical model, only the piezoelectric elements bounded to each other by an Epoxy resin are taken into account. Figure 2 shows an example of transducer arrays fabricated using the dice and fill technique (Savakus et al. 1981).

The manufactured array is composed of seven piezoelectric elements made of PZ27 ceramic characterized by the physical parameters given in Table 1 and having the following dimensions: T = 3.3 mm, W = 0.7 mm, L = 37 mm and d = 1.2 mm.

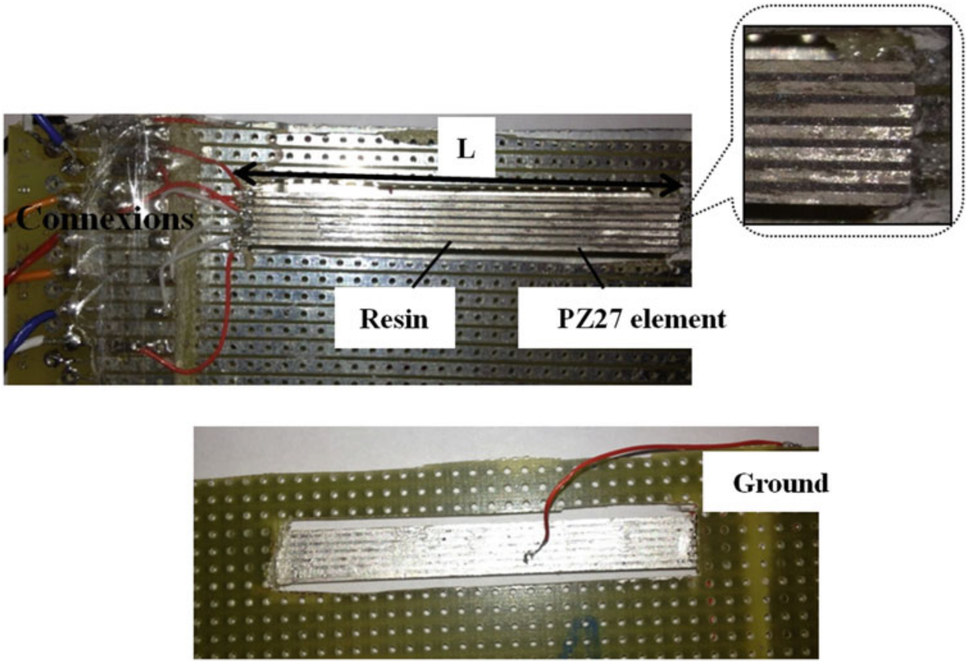

Fig. 2 Seven elements transducer array

Table 1 Ferroperm PZ27 parameters

Parameters	Value	Tolerance (%)
ρ (kg/m^3)	7700	±2.5
c_{33}^{D} (N/m^2)	144 * 10^9	±2.5
k_t	0.47	±5
e_{33} (C/m^2)	16	±5
ε_{33}^{S} (F/m)	8.1 * 10^{-9}	±10

2.2 Theory of Electromechanical Equivalent Circuits

In order to study the physical behavior of the ultrasonic piezoelectric transducers, several electromechanical models are proposed in the literature. All of them are deduced from the one-dimensional model equations and the electromechanical impedance matrix represented by a hexapole comprising an electrical port and two acoustic ports (Royer and Dieulesaint 1999). The most utilized models are the KLM's (Krimholtz, Leedom and Matthaei) model composed of a transmission line corresponding to the propagation phenomenon, in the center of which is connected an electric port that injects the current (Royer and Dieulesaint 1999; Sherrit et al. 1999; Maréchal et al. 2007) and the Mason's model using localized elements associated to an ideal electromechanical transformer converting the electrical energy to mechanical energy and vice versa (Royer and Dieulesaint 1999; Sherrit et al. 1999). For the sake of simplicity, we decided to use an equivalent circuit inspired from the Mason's one in order to model free piezoelectric transducers (Fig. 3) (Hernandez et al. 2010; Wilson 1988). As it will be seen later, the validity of this model is limited in the vicinity of the mechanical resonance frequency of the mode considered, i.e., the thickness mode in our case.

The circuit represented in Fig. 3 is composed of an electrical part (R_0, C_0) and a mechanical part (R_m, L_m, and C_m). The electrical quantities V and I are, respectively, the voltage applied across the transducer and the injected current. While v and F represent the vibration velocity and the force exerted on its surface. The elements R_m, L_m, and C_m correspond to a mass–spring system, for which R_m represents the mechanical dissipations, L_m the mass and C_m the compliance (flexibility) of the material. R_0 and C_0 represent the dielectric losses and the static capacitance of the piezoelectric material. The two parts are connected by a transformer converting the electrical energy to mechanical energy and vice versa and having a transformation ratio N. Because of its very large value (several MΩ), the resistor R_0 is generally neglected.

In order to determine the components of the circuit given in Fig. 3, i.e., C_0, C_m, L_m, R_m, and N, two methods are tested. The first approach consists in the determination of the components from the piezoelectric parameters and its

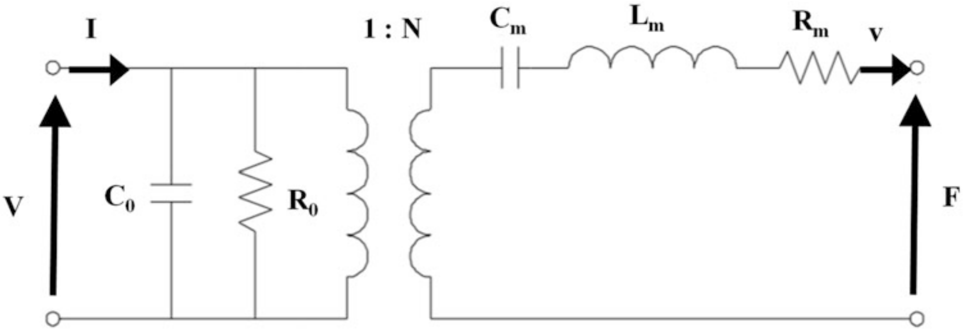

Fig. 3 Simplified Mason's model

dimensions. In this case, the following relations are used (Hernandez et al. 2010; Ferrari et al. 2001; Erhart et al. 2016):

$$C_0 = \frac{\varepsilon_{33}^S \ \mathrm{S}}{T} \tag{1}$$

$$L_m = \frac{\rho \, \mathrm{V}}{8} \tag{2}$$

$$C_m = \frac{1}{N^2} \frac{8 \, \mathrm{C}_0 \, k_t^2}{\pi^2 - 8 \, \mathrm{k}_t^2} \tag{3}$$

$$N = \frac{\mathrm{e}_{33} \, S}{T} \tag{4}$$

$$R_m = R_{res} N^2 \tag{5}$$

where T, V, and S correspond to the thickness of the piezoelectric material, its volume and the area of the electrodes. The symbols ρ, $\varepsilon_{33}^{\mathrm{S}}$, c_{33}^{D}, e_{33}, and k_t, are respectively the density, the clamped dielectric permittivity measured at constant strain S, the elastic stiffness measured in the x_3 (or z) direction at constant electric displacement field D, the piezoelectric constant in the x_3 direction and the electromechanical coupling coefficient. R_{res} corresponds to the resistance measured at the resonance frequency.

The second method is based on the calculation of the circuit parameters from the experimental electrical impedance by using the equations given below (Queirós et al. 2005):

$$C_0 = \sqrt{\frac{(Z_{\omega_s})^2(\omega_p^2 - \omega_s^2) + \sqrt{(2\omega_p^2 Z_{\omega_s} Z_{\omega_p})^2 +}\,(Z_{\omega_s})^4(\omega_p^2 - \omega_s^2)^2}{2(\omega_p^2 Z_{\omega_s} Z_{\omega_p})^2}} \tag{6}$$

$$R_m = \sqrt{\frac{(Z_{\omega_s})^2}{1 - (C_0 \omega_s Z_{\omega_s})^2}} \times N^2 \tag{7}$$

$$C_m = \frac{C_0 \left[\left(\frac{\omega_p}{\omega_s} \right)^2 - 1 \right]}{N^2} \tag{8}$$

$$L_m = \frac{1}{C_{\mathrm{m}} \omega_s^2} \tag{9}$$

where ω_s and ω_p correspond to the series resonant frequency and parallel resonant frequency (antiresonance), respectively. $Z_{\omega s}$ and $Z_{\omega p}$ represent the values of the measured impedance magnitude at ω_s and ω_p, respectively.

3 Modeling Results

3.1 Piezoelectric Plate

In order to check the validity of the equivalent model presented in Fig. 3, a simple structure corresponding to a Ferroperm piezoelectric plate with a thickness T = 1 mm, a width W = 25 mm and a length L = 50 mm is modeled using LTspice simulator (Fig. 4).

In this case, the thickness T is very small compared to the lateral dimensions W and T, this allows considering a one-dimensional thickness mode model. The circuit components C_0, N, R_1, C_1, and L_1 are calculated using the two methods described previously in Sect. 2. The first technique calculates them directly from PZ27 Ferroperm properties without taking into account the parameters tolerances (Table 1). The second method corresponds to the calculation of the components from the electrical impedance curve using the relations (6)–(9). The values obtained are given in Table 2.

Figure 5 compares the electrical impedance magnitude calculated using the values given in Table 2 with that measured using an impedance analyzer. First, it can be seen that the results provided by the equivalent circuit method and the measured one are very close. In all cases, a thickness resonant mode is observed. However, a frequency shift is obtained in the curve calculated from the material properties

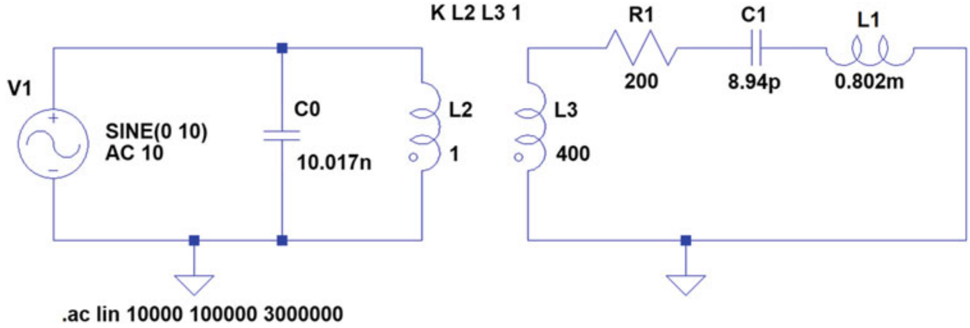

Fig. 4 LTspice model

Table 2 Circuit components calculated using two methods

Parameters	Ferroperm properties method	Impedance curve method
C_0 (nF)	10.12	10.02
N (N/V)	20	20
C_m (m/N)	$5.51 * 10^{-12}$	$8.94 * 10^{-12}$
L_m (kg)	0.0012	0.0008
R_m (kg/s)	198	200

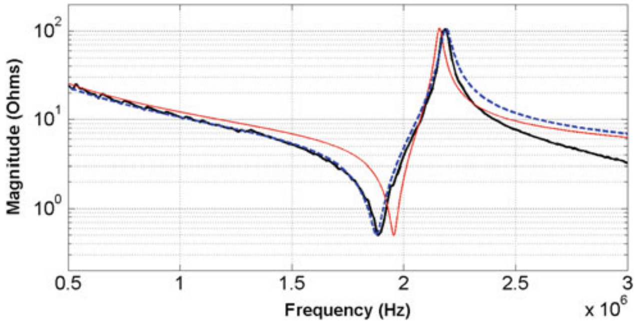

Fig. 5 Impedance magnitude: measured (solid thick line), calculated from Eqs. (6)–(9) (dashed thick line), calculated from PZ27 properties (solid thin line)

given by the manufacturer (solid thin line) compared to the measured one (solid thick line). The frequency shift is due to the materials tolerances, which are not taken into account. This indicates the importance of using an optimization algorithm for the determination of the piezoelectric material properties with more accuracy (Pérez et al. 2016; Queirós et al. 2005). Finally, a good result is obtained when the circuit components are determined using Eqs. (6)–(9). In this case, the calculated (dashed thick line) and the measured curve (solid thick line) are superposed. Nevertheless, beyond the electrical antiresonance frequency (maximum of impedance) corresponding also to the mechanical resonance frequency (maximum of displacement) the difference between the two curves increases. This difference is certainly due to the validity of the model in the vicinity of the thickness resonance frequency.

3.2 Piezoelectric Array Element

In the previous section, we have seen that the use of Eqs. (6)–(9) to determine the components of the equivalent circuit makes it possible to obtain results comparable to those measured. This method is therefore used to model a piezoelectric array element (a rectangular slender bar) made of PZ27 and having a thickness T = 3.3 mm, a width W = 0.7 mm and a length L = 37 mm. In this case, the width W is not greater than the thickness T as is the case for a plate. To better represent the structure behavior a two-dimensional model taking into account, the effects of the width W should be utilized. Nevertheless, previous research works indicated that for a ratio W/T less than or equal to 0.5 a dominant thickness mode is obtained (Sato et al. 1979; Friedrich et al. 1990). For this reason, we studied the possibility of extending the equivalent circuit model tested successfully in the case of a plate to the slender bar. The circuit components are $C_0 = 58.5$ pF; N = 0.141 N/V; $C_m = 1.49$ nm/N; $L_m = 82.82$ µkg and $R_m = 4.25$ kg/s.

Figure 6 compares the impedance magnitude and phase measured with that calculated by the equivalent circuit model. It is clearly seen that the results are very close. A small difference is observed out of the thickness resonance mode, i.e., for frequencies less than 400 kHz and more than 600 kHz. This is due to the limitation of the lumped equivalent circuit in the vicinity of the studied mode (thickness mode).

In Fig. 7, the displacement calculated by the model is compared to the one measured by a Laser Vibrometer (Polytec: head OFV-353 with OFV-3001 controller) at the radiation

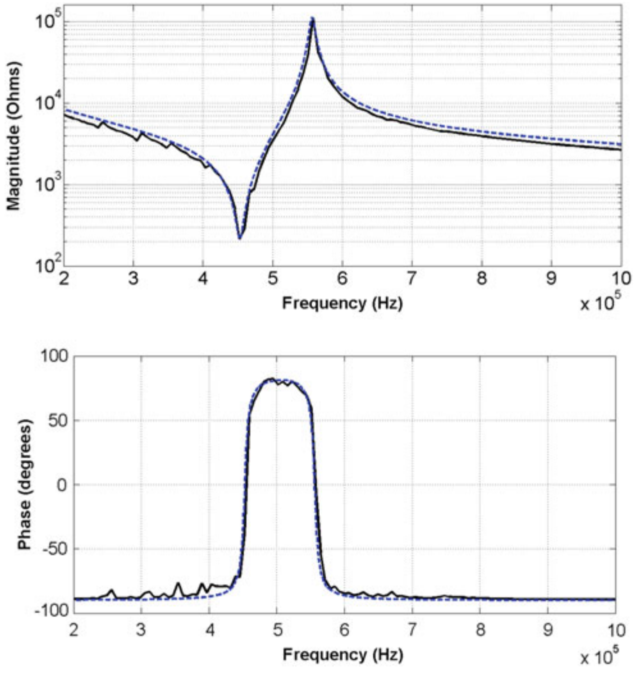

Fig. 6 Impedance magnitude and phase: measured (solid line) and calculated by the electromechanical model (dashed line)

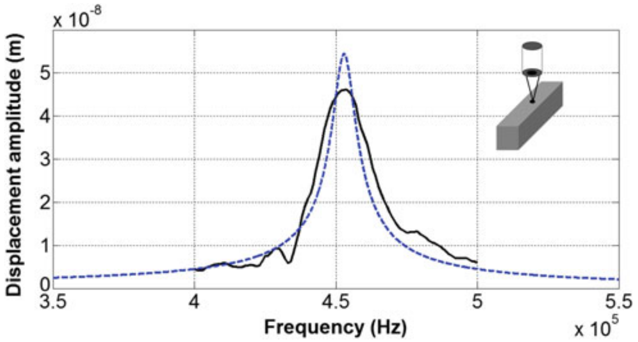

Fig. 7 Displacement amplitude: measured in the middle of the element (solid line) and calculated by the circuit model (dashed line)

surface of the element. The results obtained are globally similar: in the two cases, a maximum of displacement corresponding to a thickness vibration is obtained at the frequency 454 kHz. However, the simulated displacement curve (dashed line) is slightly narrow compared to the measured one (solid line), maybe because this corresponds to average values whereas the experimental one is a punctual measurement (in the middle of the radiation surface). This is also due to the assumptions of the model, i.e., one-dimensional model instead of two or three-dimensional models.

4 Conclusion

In this research work, two piezoelectric transducers are modeled by the use of one-dimensional electromechanical equivalent circuit inspired from the Mason's one. In order to study the influence of the material properties on the transducers performances and to check the validity of the method, two structures made of PZ27 ceramic are modeled: a plate and a rectangular slender bar. LTspice simulation tool is used to calculate the electrical impedance and displacement. The simulations indicate the importance of using an optimization algorithm for the determination of the piezoelectric material properties with more accuracy. The results also demonstrate the possibility to model the array elements by one-dimensional circuit especially in the vicinity of the resonance frequency. In future work, the circuit proposed will be tested in the case of a transducer array, i.e., taking into account all the elements and the resin, in order to study the crosstalk phenomenon and find solutions to this problem.

References

Arnau, A. (2008). *Piezoeletric transducers and appllications*. Springer Science & Business Media.

Bybi, A. (2012). Contribution à l'étude et à la correction de la diaphonie dans les réseaux de transducteurs piézoélectriques pour l'imagerie médicale. Dissertation, Université de Valenciennes et du Hainaut Cambrésis.

Cobbold, R. S. C. (2006). *Foundations of biomedical ultrasound*. Oxford University Press.

Erhart, J., Půlpán, P., & Pustka, M. (2016). *Piezoelectric ceramic resonators*. Springer.

Ferrari, V., Marioli, D., & Taroni, A. (2001). Theory, modeling and characterization of PZT-on-alumina resonant piezo-layers as acousticwave mass sensors. *Sensors and Actuators, A: Physical, 92*(1–3), 182–190. https://doi.org/10.1016/S0924-4247(01)00561-1.

Friedrich, W., Kaarmann, H., & Lerch, R. (1990). Finite element modeling of acoustic radiation from piezoelectric phased antennas. In *IEEE ultrasonics symposium*, Honolulu, HI (pp. 763–767).

Grewe, M. G., Gururaja, T. R., Shrout, T. R., & Newnham, R. E. (1990). Acoustic properties of particle/polymer composites for ultrasonic transducer backing applications. *IEEE Transactions on Ultrasonics, Ferroelectrics, and Frequency Control, 37*(6), 506–514. https://doi.org/10.1109/58.63106.

Hernandez, C., Bernard, Y., & Razek, A. (2010). Validation du modèle d'un transducteur de langevin piezoélectrique par schéma électrique equivalent. In *5ème colloque sur les Matériaux en Gérnie Electrique*, Montpellier.

Huang, J., Que, P. W., & Jin, J. H. (2004). A parametric study of beam steering for ultrasonic linear phased array transducer. *Russian Journal of Nondestructive Testing, 40*(4), 254–259. https://doi.org/10.1023/B:RUNT.0000043674.60035.0e.

Hutchens, C. G., & Morris, S. A. (1985). A two-dimensional equivalent circuit for the tall thin piezoelectric bar. In *IEEE ultrasonics symposium* (pp. 671–676). San Fransisco.

Kim, M., Kim, J., & Cao, W. (2006). Electromechanical coupling coefficient of an ultrasonic array element. *Journal of Applied Physics*, *99*(7), 074102-1-6. https://doi.org/10.1063/1.2180487.

LTspice Software. http://www.linear.com/designtools/software/.

Maréchal, P., Levassort, F., Tran-Huu-Hue, L. P., & Lethiecq, M. (2007). Lens-focused transducer modeling using an extended KLM model. *Ultrasonics, 46*(2), 155–167. https://doi.org/10.1016/j.ultras.2007.01.006.

Pérez, N., Buiochi, F., Brizzotti Andrade, M. A., & Adamowski, J. C. (2016). Numerical characterization of piezoceramics using resonance curves. *Materials*, *9*(2), 1–30. https://doi.org/10.3390/ma9020071.

Queirós, R., Girão, P. S., & Serra, A. C. (2005). Single-mode piezoelectric ultrasonic transducer equivalent circuit parameter calculations and optimization using experimental data. In *IMEKO TC4 symposium* (pp. 468–470).

Royer, D., & Dieulesaint, E. (1999). *Elastic waves in solids II: Generation, acousto-optic interaction, applications*. Springer Science & Business Media.

Sato, J., Kawabuchi, M., & Fukumoto, A. (1979). Dependance of electromechanical coupling coefficient on the width-to-thickness ratio plank-shaped piezoelectric transducers used for electronically scanned ultrasound diagnostic system. *Journal of the Acoustic Society of America, 66,* 1609–1611. https://doi.org/10.1121/1.383657.

Savakus, H. P., Klicker, K. A., & Newnham, R. E. (1981). PZT-epoxy piezoelectric transducers: A simplified fabrication procedure. *Materials Research Bulletin, 16*(6), 677–680. https://doi.org/10.1016/0025-5408(81)90267-1.

Sherrit, S., Leary, S. P., Dolgin, B., & Bar-Cohen, Y. (1999). Comparison of the Mason and KLM equivalent circuits for piezoelectric resonators in the thickness mode. In *IEEE ultrasonics symposium*, Lake Tahoe (pp. 921–926).

Wilson, O. B. (1988). *Introduction to theory and design of sonar transducers*. Los Altos: Peninsula Publication.

Wooh, S. C., & Shi, Y. (1999). A simulation study of the beam steering characteristics for linear phased arrays. *Journal of Nondestructive Evaluation*, *18*(2), 39–57. https://doi.org/10.1023/A:1022645204774.

Zhang, J. Y. (2011). Réseaux de transducteurs haute fréquence (100–300 MHz) à déphasage réalisés à partir des technologies MEMS. Dissertation, Université de Valenciennes et du Hainaut Cambrésis.

Zhang, J. Y., Xu, W. J., Carlier, J., Ji, X. M., Nongaillard, B., Queste, S., et al. (2012). Modelling and simulation of high-frequency (100 MHz) ultrasonic linear arrays based on single crystal LiNbO3. *Ultrasonics, 52*(1), 47–53. https://doi.org/10.1016/j.ultras.2011.06.009.

Abdelmajid Bybi was born in Nador, Morocco in 1983. He was awarded the Professional Master degree in Microelectronics Radiofrequency and Hyperfrequency from the Université des Sciences et Technologies de Lille in 2007 and the Research Master degree in Electronics, Instrumentation and Telecommunications from the Université de Valenciennes et du Hainaut Cambrésis in 2008. He was awarded Ph.D. in Electronics from the Université de Valenciennes et du Hainaut Cambrésis in 2012. He is currently Assistant Professor at Ecole Supérieure de Technologie de Salé (ESTS), Mohammed V University in Rabat. He is a member of the Material Energy Acoustics Team (MEAT) situated at the ESTS.

His research interests are

- the ultrasonic transducers and transducer arrays for medical imaging and NDT applications,
- acoustics applications, and
- electronics for biomedical applications.

Hilal Drissi is currently Professor at the Higher School of Technology of Salé (ESTS), Mohammed V University in Rabat, Morocco. He is a member of the Laboratoire d'Analyse des Systèmes, Traitement d'Information et du Management Intégré (LASTIMI) situated at the ESTS. He was awarded the Doctorate of State in Applied Science, Signal Processing from Ecole Mohammadia des Ingénieurs (EMI)—Rabat in 2000.

His main research interests are

- signal and image processing,
- cloud computing security and telecommunications, and
- ultrasonic transducers and electronics for biomedical applications.

Mohammed Garoum is currently Professor at the Higher School of Technology of Salé (ESTS), Mohammed V University in Rabat, Morocco since 1995. In 1991, he received his first Ph.D. in acoustics from the Ecole Central de Lyon France. In 1997, he was awarded his Second State Doctorate in Photoconductivity of semiconductor from the Institute of Sciences of Engineering and Scientific Development at Claude Bernard University Lyon I and Faculty of Sciences of Cadi Ayyad University, Marrakech. He has been Director of the Energy, Materials and Environment Laboratory and head of the acoustic team (2005–2017). He is the Founder and President of the Moroccan Society of Acoustics, since 2010 (Today affiliated to the ICA and EAA). He is also the Founder and Head of the "University Center for Research and Study in Acoustics and Thermal: Materials and Building" (CREAT) at the ESTS since 2015 and Head of the research group "Material Energy and Acoustics" (MEAT) since 2017. Pr M. GAROUM is Member of the National Commission for Thermal and Acoustic Standardization (more than 70 standards) and a consultant at the Technical German cooperation (GIZ) in training and building capacities in Building Energy Efficiency. He was and/or is still leader of some national and international cooperation projects (Moroccan, Spanish, French, German European and Tunisian) devoted to environmental acoustics, building and construction material acoustics, thermal characteristics of building and construction materials. His main research interests are

- materials and building energy efficiency,
- experimental characterization and simulation of thermo-physical and acoustical properties of building and construction materials,
- numerical inverse estimation of thermal and acoustical parameters using based gradient and global algorithms, and
- experimental characterization of environmental and industrial acoustics (Wind generators, road traffic, etc.).

Anne-Christine Hladky-Hennion was born in Lille, France in 1965. She was awarded the diploma of engineer (five-year engineering degree) of the Institut Superieur de l'Electronique et du Numérique in 1987 and Ph.D. in materials science from the Université des Sciences et Technologies de Lille in 1990. She is currently a principal scientist at the CNRS. Her main research interests are the study of phononic structures and acoustic metamaterials and particularly tunable piezoelectric metamaterials. She is a member of the French Acoustical Society (SFA) and of the IEEE Society.

An Extraction Method of SiC Power MOSFET Threshold Voltage

W. Jouha, A. El Oualkadi, P. Dherbécourt, E. Joubert, and M. Masmoudi

Abstract

Threshold voltage (V_{th}) is one of the most important electrical parameters in silicon carbide (SiC) metal-oxide-semiconductor field-effect transistors (MOSFETs) design, characterization, modeling, and simulation. The reduction of the threshold voltage increases the performance in terms of switching time for the power converter. The study of the evolution of V_{th} over time must be considered by the designers of the new generations of energy conversion systems. There are several existing methods for V_{th} extraction, and the aim of this chapter is to compare the commonly used MOSFET threshold voltage extraction methods and to propose a new method based on a physical approach. The extraction method proposed in this chapter is based on the static I–V measurements and the use of the Levenberg–Marquardt optimization algorithm. The implementation of the several extraction methods is tested and discussed by applying them to commercial components in order to evaluate their performance and validity in both the linear and saturation regions. The study is carried out for two generations of power SiC-MOSFETs of CREE constructor.

1 Introduction

Recently, silicon carbide MOSFETs are of great interest in high-power applications (energy conversion, automotive industry, and aeronautics). They replace the silicon components whose performances are limited in terms of voltage blocking capability, operation temperature, and switching frequency (Raynaud et al. 2010; Bjrk et al. 2011). Wide band gap components have interesting intrinsic properties, especially a high thermal conductivity. The SiC performance makes the SiC-MOSFETs a good competitor to traditional silicon MOSFETs and IGBTs (Zhao et al. 2007; Glaser et al. 2011). However, these new components require reliability studies and physical modeling to meet the integration requirements of energy conversion systems. The threshold voltage V_{th} is a fundamental parameter for MOSFET modeling and characterization. Its extraction requires precise values (Garcia Snchez et al. 2006). The tens of millivolts errors in the threshold voltage value can no longer be neglected in the modeling of the transistor behavior. The threshold voltage has an impact in the MOSFET performance in terms of the time and energy required for switching (Simonot et al. 2010).

In the literature, various methods have been developed and used to extract the threshold voltage (V_{th}) of a MOSFET (Wong et al. 1987; Tsuno et al. 1999; DieterSchroder 2006; Bazigos et al. 2011). In this chapter, a review of the commonly used MOSFET threshold voltage extraction methods is presented and discussed. The four largely used methods are tested on two generations SiC power MOSFETs of CREE constructor. Moreover, the chapter proposes a new procedure to extract the threshold voltage based on the Levenberg–Marquardt optimization algorithm using a physical approach. The results obtained with this proposed extraction method are compared to those obtained with other methods.

This chapter is organized as follows: Sect. 2 presents a description of the studied devices. Section 3 develops usual

W. Jouha (✉) · P. Dherbécourt · E. Joubert · M. Masmoudi
Normandy University, IUT, INSA Rouen, CNRS, GPM
UMR CNRS 6634, 76000 Rouen, France
e-mail: jouhaieea@gmail.com

P. Dherbécourt
e-mail: pascal.dherbecourt@univ-rouen.fr

E. Joubert
e-mail: eric.joubert@univ-rouen.fr

M. Masmoudi
e-mail: mohamed.masmoudi@univ-rouen.fr

W. Jouha · A. El Oualkadi
LabTIC Laboratory, National School of Applied Science of
Tangier, Abdelmalek Essaadi University, Tangier, Morocco
e-mail: eloualkadi@gmail.com

S. El Hani and M. Essaaidi (eds.), *Recent Advances in Electrical and Information Technologies for Sustainable Development*,
Advances in Science, Technology & Innovation, https://doi.org/10.1007/978-3-030-05276-8_2

threshold voltage definition for MOSFET transistors. Section 4 describes the proposed extraction procedure with four other V_{th} extraction procedures frequently used. Section 5 discusses and compares the obtained results by all these methods. Finally, the conclusion is given in Sect 6.

2 Description of the Studied Device

Two SiC-MOSFET samples for two generations of CREE constructor have been selected for this study: the second-generation SiC-MOSFET G2 (10 A, 1200 V) reference C2M0280120D and the third-generation SiC-MOSFET G3 (11 A, 900 V) reference C3M0280090D (Cree inc 2018a, b). The choice is based on the fact that both generations have close relative drain currents. Figure 1 shows the TO-247 package component and its electrical symbol.

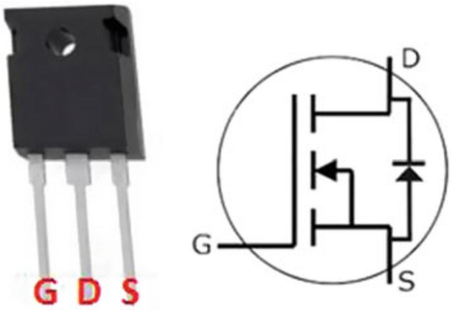

Fig. 1 The TO-247 package component (left) and its electrical symbol (right)

The constructor maintains the same planar structure for the two generations of n-channel enhancement MOSFETs. Figure 2 shows the physical structures of the two generations of SiC-MOSFETs. The performance is generally improved with the changes in the epitaxy thickness, pitch, and gate width. Indeed, the reduction in thickness of oxide for the third generation makes it possible to have a threshold voltage reduced compared to the second generation.

3 Threshold Voltage Definition

Conventionally, the threshold voltage is understood simply as the gate–source voltage (V_{gs}) at which significant drain current starts to flow, and physically the threshold voltage V_{th} is defined as the voltage applied to the metal electrode to enter the strong inversion domain of operation. When the semiconductor surface enters the strong inversion mode of operation, the surface potential (ψ_S) is equal to twice the bulk potential (ψ_B) (Ortiz-Conde et al. 1998; Baliga 2008). In this case, the V_{th} is given by

$$V_{th} = \frac{Q_S}{C_{ox}} + 2\psi_B \qquad (1)$$

where C_{ox} is the specific capacitance of the oxide, and Q_S represents the total charge in the semiconductor. The bulk potential (ψ_B) can related to the doping concentration (N_A) in the semiconductor and temperature T, and then the threshold voltage V_{th} is given by the following equation:

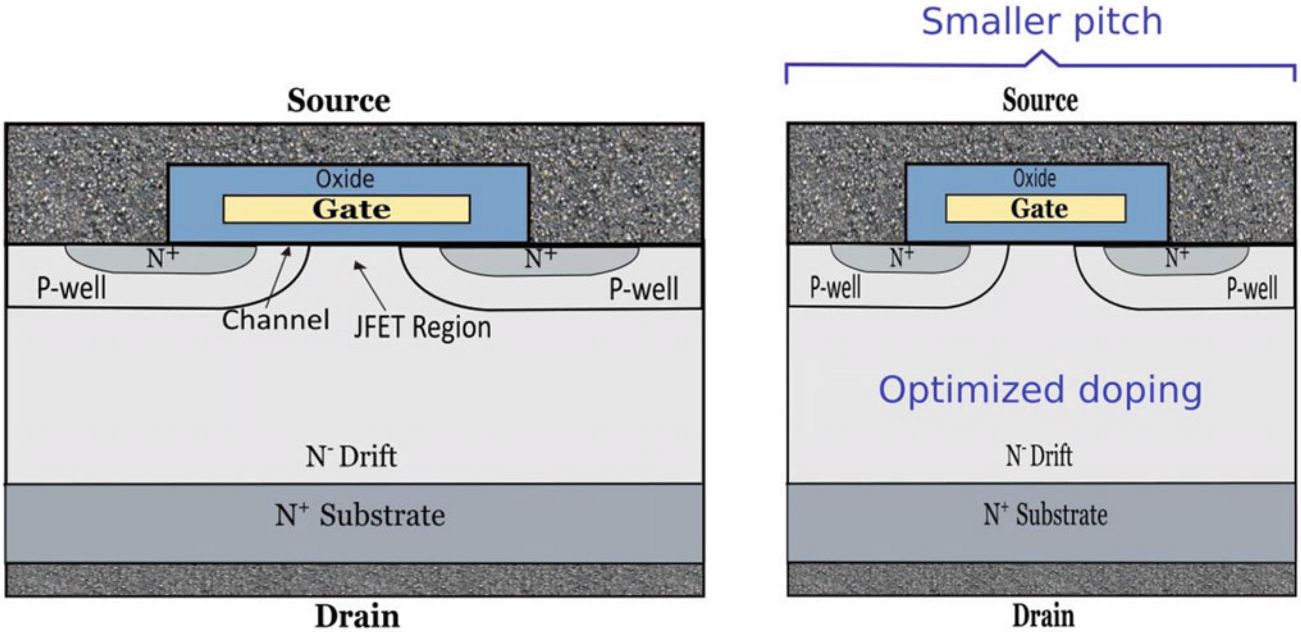

Fig. 2 MOSFET Structure of second generation (left) and third generation (right)

$$V_{th} = \frac{\sqrt{4\varepsilon_{SiC}kT_jN_A ln\left(\frac{N_A}{n_i}\right)}}{C_{ox}} + \frac{2kT_j}{q} ln\left(\frac{N_A}{n_i}\right) - \frac{Q_{ox}}{C_{ox}} \tag{2}$$

where ε_{SiC} is the relative permittivity of the semiconductor, n_i is the concentration of intrinsic carriers, k is the Boltzmann constant, and Q_{ox} presents the total effective charge in the oxide. This charge is composed by the mobile ion charge, the trapped oxide charge, the fixed oxide charge, and the interface state charge after taking into account the fact that these charges are distributed throughout the oxide. The value of the threshold voltage depends on some physical parameters which characterize the MOSFET structure such as the gate material, the thickness of oxide layer t_{ox}, substrate doping concentrations N_A, and the temperature. However, this definition of V_{th} is difficult to exploit because the Q_{ox} value and the physical parameters of the component need to be defined. Various studies show that the approximate definition of V_{th} is related to the extraction method. In the following section, we present various methods usually used to define and extract the threshold voltage value.

4 Extraction Methods of Threshold Voltage

Several definitions and methods have been developed to extract the threshold voltage (Booth et al. 1987; Tsuno et al. 1998; Dobrescu et al. 2000; Terada et al. 2001; Ortiz-Conde et al. 2002; Boucart and Ionescu 2008). They include the constant current method (CC), the linear extrapolation method (LE), g_m transconductance linear extrapolation method (GMLE), and transconductance change method (TC). In this chapter, these conventional methods are compared to a proposed method based on the current drain equation taking into account some physical parameters. For all procedures, the threshold voltage parameter is extracted directly from the static characterization (measured I–V curves) or from derived curves.

For this purpose, we have performed the I–V static characterizations using a pulsed bench presented in Fig. 3. This bench allows to avoid the self-heating of the device under test during the measurement duration by generating a pulse not exceeding 7 µs. The temperature stabilization of the device is assured by a Peltier module.

4.1 The Constant Current Method

The constant current method (CC) is extensively exploited in industry because of its simplicity (Ortiz-Conde et al. 2002). It defines V_{th} as the value of the voltage V_{gs} corresponding to the appearance of a significant drain current for a given V_{ds}. Some studies have been examined this current equal to $(W/L) \times 10^{-7}$, where W and L are the width and length of the channel, respectively (Terada et al. 2001). However, a recent study proposes that this current should depend on the voltage V_{ds} in order to obtain a coherent V_{th} value in the saturation zone (Bazigos et al. 2011). For our study, due to lack of the values of L and W, we calculate the voltage V_{th} for MOSFET with a similar way to the datasheets for $I_{ds} = 1.25$ mA (second generation), $I_{ds} = 1.2$ mA (third generation), at the output voltage $V_{ds} = 0.1$ V in linear regime, and $V_{ds} = 20$ V in the saturation regime. The results of the extraction of V_{th} by the CC method performed on second-generation device (G2) are shown in Fig. 4 for linear regime and Fig. 5 for saturation regime.

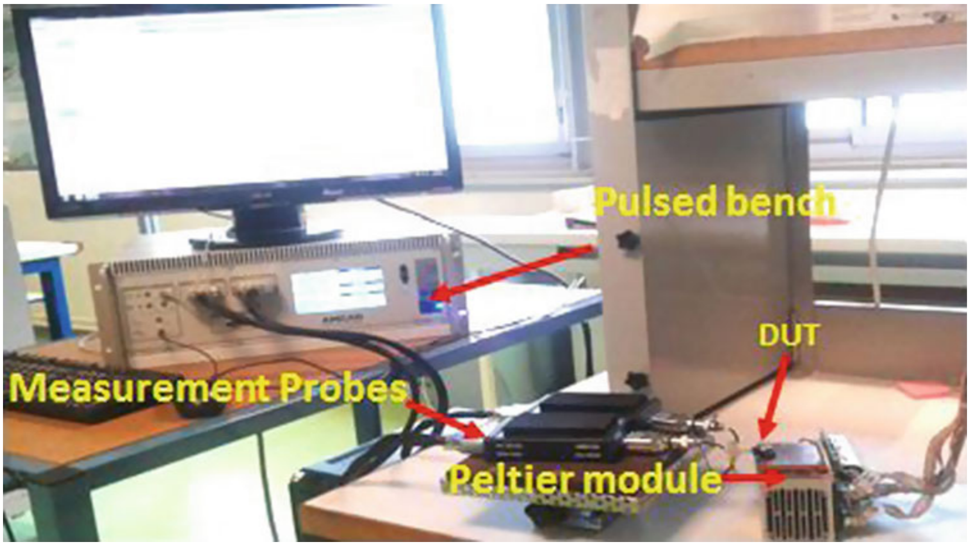

Fig. 3 The I–V static characterizations bench

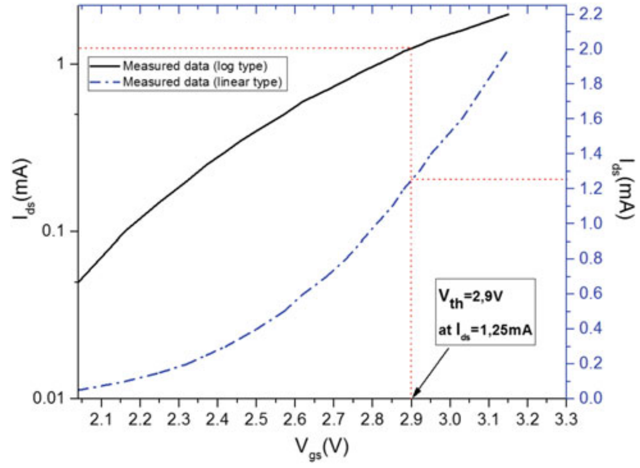

Fig. 4 Current constant method in the linear region ($V_{ds} = 0.1$ V) method implemented on the $I_{ds}V_{gs}$ measured for G2

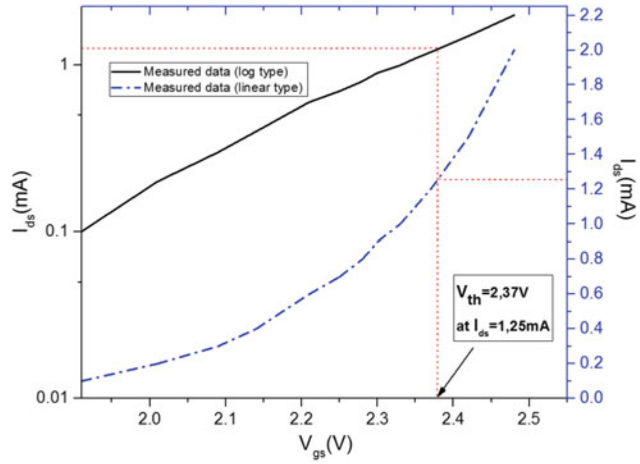

Fig. 5 Current constant method in the saturation region ($V_{ds} = 20$ V) method implemented on the $I_{ds}V_{gs}$ measured for G2

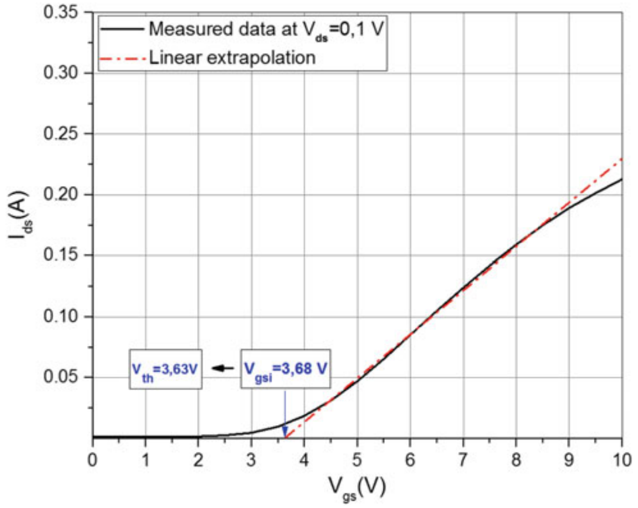

Fig. 6 Linear extrapolation method in the linear region implemented on the I_{ds}–V_{gs} characteristic for G2

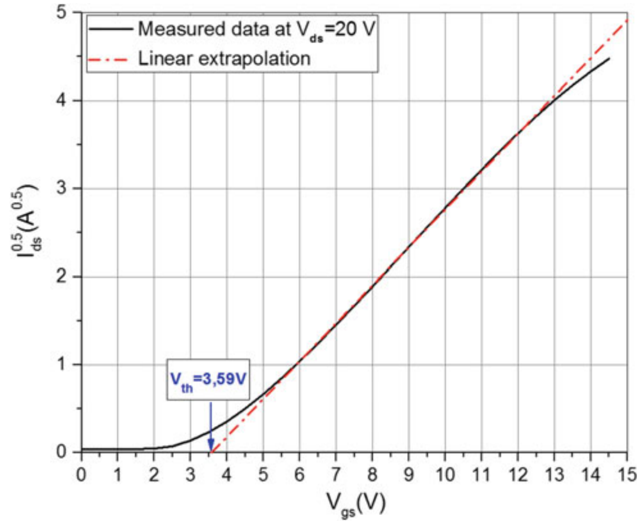

Fig. 7 Linear extrapolation method in the saturation region implemented on the $I_{ds}^{0.5}$–V_{gs} characteristics for G2

4.2 The Linear Extrapolation Method

The linear extrapolation method (LE) is most widely used. The threshold voltage is extracted directly from I–V characteristics curves. The drain current is measured as a function of the gate voltage at a low drain voltage to ensure operation in the linear MOSFET region (Dobrescu et al. 2000; DieterSchroder 2006). The threshold voltage is determined from the Vgs axis intercept ($I_{ds} = 0$) of the linear extrapolation of the I_{ds}–V_{gs} curve at its maximum first derivative (slope) point. The threshold voltage value is founded from the extrapolated or intercept gate voltage V_{gsi} by ($V_{th} = V_{gsi} - V_{ds}/2$). Figure 6 shows the extraction of V_{th} by this method using a component of the second generation in linear region.

The threshold voltage can also be determined in the MOSFET saturation regime, and we use similar method to that in the linear regime but with $I_{ds}^{0.5}$–V_{gs} characteristic curve at a high drain voltage ($V_{ds} > V_{gs} - V_{th}$) to assure operation of MOSFET in saturation region. Figure 6 shows the obtained results with this method using a second-generation device (Fig. 7).

4.3 The Transconductance g_m Linear Extrapolation Method

The transconductance g_m linear extrapolation method (GMLE) determines V_{th} from $g_m - V_{gs}$ characteristics curves. The V_{th} is defined by extrapolating the linearity of g_m, for small V_{gs} values, to the gate voltage where

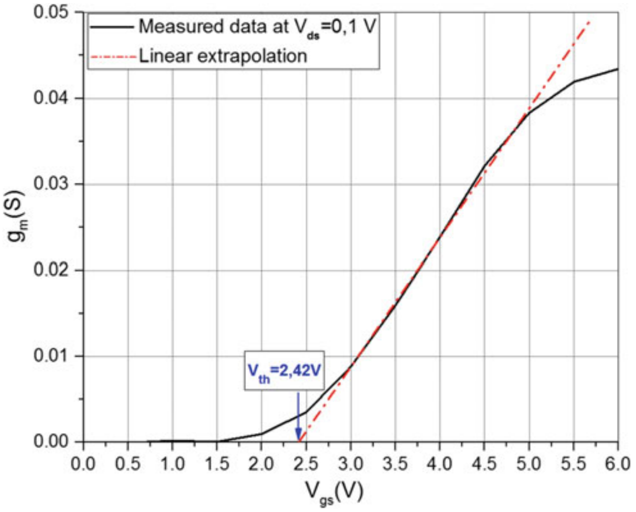

Fig. 8 g_m linear extrapolation method in the linear region implemented on the $g_m - V_{gs}$ characteristic for G2

transconductance g_m becomes equal to 0. Physically, this method uses the linear dependence of the effective carrier mobility μ_{eff} as a function of $(V_{gs} - V_{th})$. This mobility μ_{eff} is affected by the Coulomb scattering (Tsuno et al. 1998, 1999). Figure 8 shows the extraction of V_{th} based on GMLE method using a second-generation device.

In the saturation region, the same procedure is followed using $g_m^{0.5} - V_{gs}$ characteristics curves, with the measurements carried out under an output voltage included in the saturation region ($V_{ds} = 20\,\text{V}$). Figure 9 shows the extraction of V_{th} using GMLE method in saturation region.

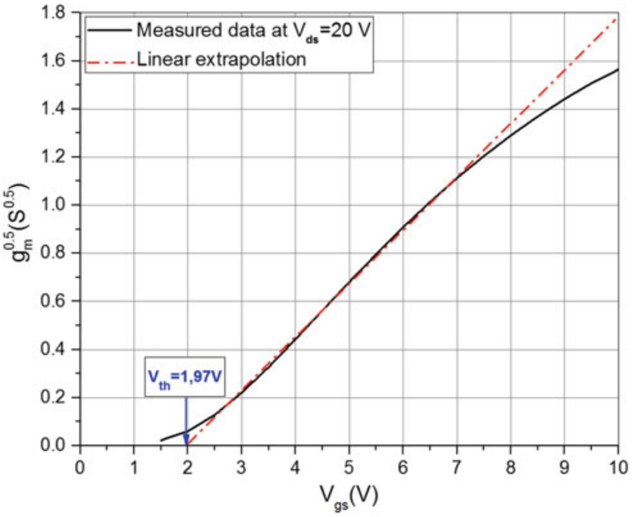

Fig. 9 g_m linear extrapolation method in the saturation region implemented on the $g_m^{0.5} - V_{gs}$ characteristic for G2

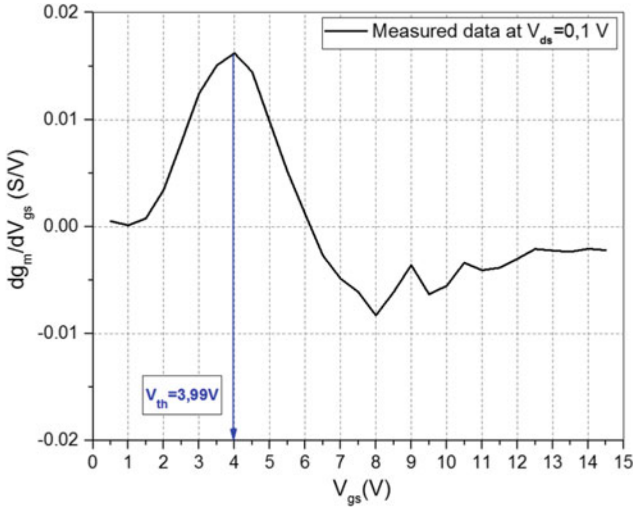

Fig. 10 Extraction of V_{th} in linear region using transconductance change method implemented on the $\frac{dg_m}{dV_{gs}} - V_{gs}$ characteristic for G2

4.4 The Transconductance Change Method

The transconductance change method (TC) uses the curve of the derivative of transconductance g_m versus V_{gs}. It determines V_{th} as the V_{gs} value at which the derivative of the transconductance is a maximum (Booth et al. 1987; Wong et al. 1987; Boucart and Ionescu 2008). Figure 10 shows the transconductance change method for extraction of V_{th} in linear region. However, Fig. 11 shows the extraction of V_{th} with the same method in saturation region implemented on the $\frac{dg_m^{0.5}}{dV_{gs}} - V_{gs}$ characteristic for the second-generation device.

4.5 New Procedure: The Optimization Levenberg–Marquardt Method

A common feature presented in the most V_{th} extraction methods based on the I_{ds}–V_{gs} input characteristics is the strong influence of the channel mobility degradation on the resulting value of the extracted V_{th}. In order to take into account this situation, we present a new extraction method called Optimization Levenberg–Marquardt method (OLM) (Jouha et al. 2017). Due to the definition of the drain current (Eq. 3) (McNutt et al. 2007), this method can be used in the saturation region ($V_{ds} = 20$ V).

$$I_{ds} = \frac{K_p (V_{gs} - V_{th})^2}{2(1 + \theta(V_{gs} - V_{th}))} \tag{3}$$

where θ is a parameter that takes into account the reduction of the mobility following the increase of a transverse electric field. Note that K_p is called the transconductance exprimed by (A/V^2). The term transconductance is abusively used in the literature, since there is a linear relationship between K_p and g_m according to the expression $(g_m = K_p \cdot V_{ds})$ (Baliga 2008).

The extraction of the threshold voltage is based on two steps: for the first one, we used Eq. 3 of the drain current in saturation region which takes into account the influence of the channel mobility degradation (θ parameter). For the

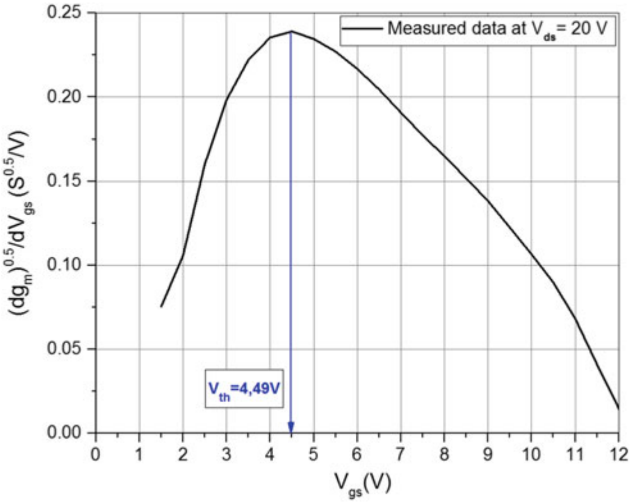

Fig. 11 Extraction of V_{th} in the saturation region using transconductance change method implemented on the $\frac{dg_m^{0.5}}{dV_{gs}} - V_{gs}$ characteristic for G2

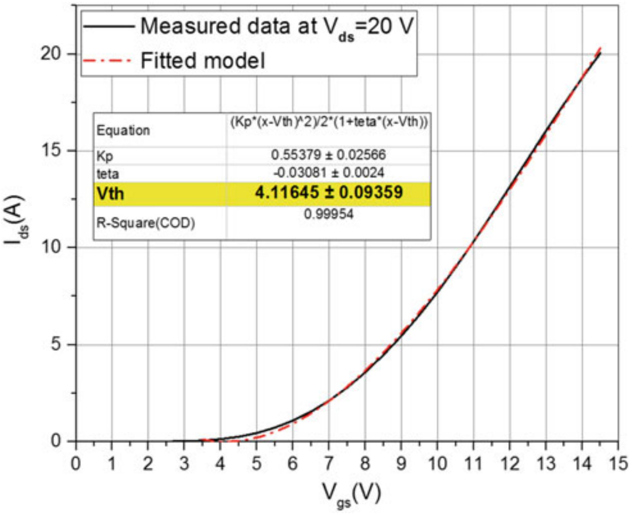

Fig. 13 Extraction of V_{th} in the saturation region using OLM method implemented on the I_{ds}–V_{gs} characteristic for G2

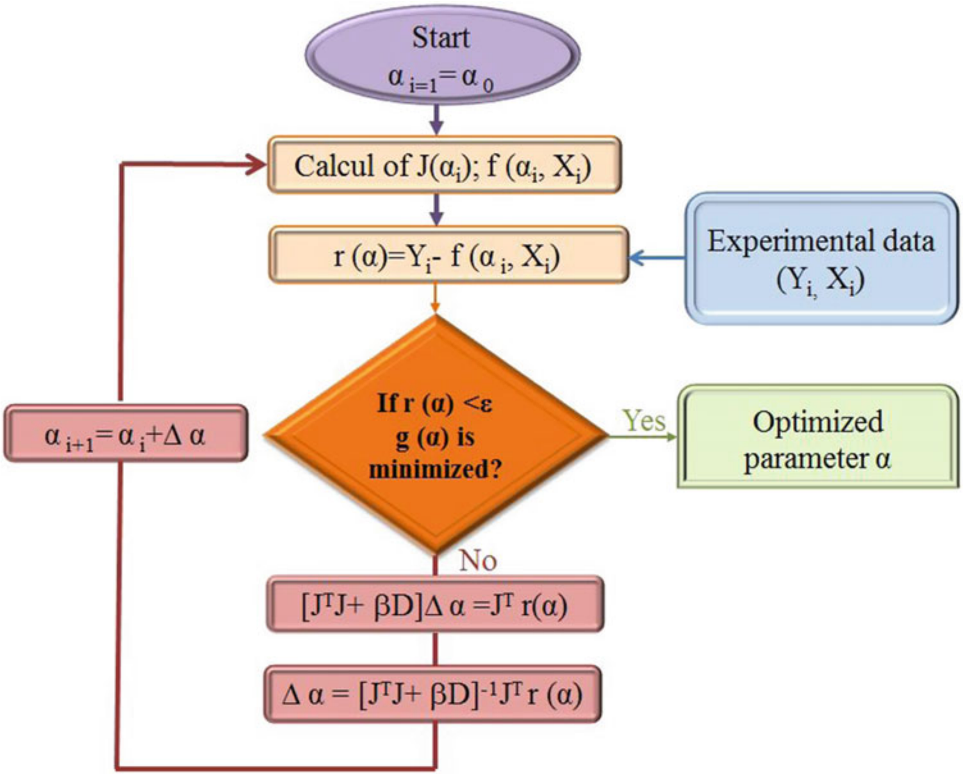

Fig. 12 Flowchart of the Levenberg–Marquardt algorithm

second step, we use the Levenberg–Marquardt (L-M) algorithm to optimize the parameters of Eq. 3 by fitting the curve of this equation with the measured I_{ds}–V_{gs} input curve. The Levenberg–Marquardt algorithm is developed by Levenberg and Marquardt (Levenberg 1944; Marquardt 1963). The flowchart of this algorithm is presented in Fig. 12.

It is an efficient iterative method for estimating nonlinear regression parameters of models. Consider the nonlinear model fit Y_i = f (α, X_i), where X_i (V_{gs} or Y_{ds}) and Y_i (I_{ds}) are the data extracted from the I–V measurements, α is a vector of dimension n that represents the parameters of the model (V_{th}, K_p, θ). The L-M method searches for (α_1, α_2, α_3, ..., α_n) which are the solutions of α (locally) minimizing g(α) defined by

$$g(\alpha) = \sum_{i=1}^{m} (Y_i - f(\alpha, X_i))^2 \tag{4}$$

The L-M algorithm finds the solution using

$$\alpha_{i+1} = \alpha_i - (J^T J + \beta D) J^T r(\alpha) \tag{5}$$

where r (α) = Y_i− f (α, X_i), J is the Jacobian matrix for f (α, X_i), J^T is the transposed matrix of J, β is a regularization parameter, and D is the identity matrix in which its dimension is equal to that of $J^T J$ to adjust the scales factors.

The principle of this extraction parameters method is illustrated in Fig. 13 using the second-generation device, showing a correct fitting of the model with the experimental measurement data.

We have previously validated this method in order to model the static MOSFET behavior for three generations of power MOSFET, obtaining a very satisfactory fitting of I–V curves. Moreover, this method is applicable for a temperature range from 0 to 135 °C, and it allows a complete extraction of other parameters values such as K_p and θ parameter on the whole temperature range.

5 Results and Discussions

The relative performance of the presented methods is compared under the same conditions by applying them to the measured characteristics of two test devices (G2 and G3). Tables 1 and 2 and Fig. 14 show the resulting threshold voltage values for these devices obtained from the presented extraction methods in two regions of operation (linear and saturation), and the proposed OLM method gives extracted values of the threshold voltage V_{th} in the saturation region.

Table 1 Threshold voltage values obtained from four extraction methods and the proposed method for the second generation of a power SiC-MOSFETs biased in the linear and saturation region

	Linear	Saturation (V)
CC	2.9 V	2.37
LE	3.63 V	3.59
GMLE	2.42 V	1.97
TC	3.99 V	4.49
OLM	NA	4.12

Table 2 Threshold voltage values obtained from four extraction methods and the proposed method for the third generation of a power SiC-MOSFETs biased in the linear and saturation region

	Linear	Saturation (V)
CC	2.79 V	2.04
LE	3.46 V	3.12
GMLE	2.30 V	1.75
TC	3.49 V	3.99
OLM	NA	3.37

Moreover, the value of the extracted threshold voltage depends on the used extraction method for two generations of devices. The obtained results are in agreement with those of the bibliography (Ortiz-Conde et al. 2002, 2013). The differences can be explained by the strong influence of the source and drain parasitic series resistances and the channel mobility degradation on the linearity of the I_{ds}–V_{gs} curve (Tsuno et al. 1999). However, the proposed method is very useful for an accurate evaluation of V_{th}, thanks to the excellent modeling of the output current I_{ds} in saturation region. It describes the dependence of I_{ds} to the mobility degradation, compared to other methods which are based only on the linearity of the curve versus gate–source voltage V_{gs}.

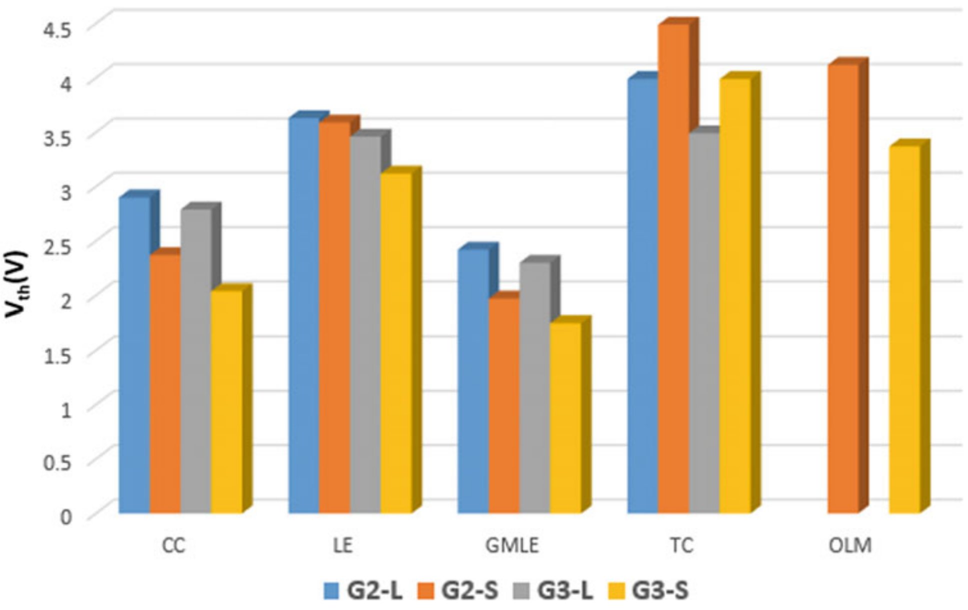

Fig. 14 Comparisons of threshold voltage values obtained for two generations of power SiC-MOSFETs (G2 & G3) biased in the linear (L) and saturation region (S)

6 Conclusion

In this chapter, we have presented, reviewed, and compared several extraction methods currently used to determine the threshold voltage value of SiC-MOSFETs from their drain current and transconductance g_m versus gate voltage characteristics measured either in linear and saturation operation regions. A new extraction method using physical approach is presented. This method is based on the measurements of input characteristics (I_{ds}–V_{gs}) and the optimization Levenberg–Marquardt algorithm. It is a very accurate method, thanks to the excellent modeling of the drain current in saturation operation regime of power transistor. The performance of the presented methods was compared under the same conditions by applying them to the measured characteristics of two SiC power MOSFETs generations.

The comparison of these V_{th} extraction methods shows that the proposed method is the only one that relies on the physical equations of the transistor that depends on the transconductance K_p and the channel mobility degradation μ_n. This makes the V_{th} extracted by the OLM method the best indicator for monitoring the transistor aging in operational conditions.

References

Baliga, B. J. (2008). *Fundamentals of power semiconductor devices*. US: Springer.

Bazigos, A., Bucher, M., Assenmacher, J., Decker, S., Grabinski, W., & Papananos, Y. (2011). An adjusted constant-current method to determine saturated and linear mode threshold voltage of MOSFETs. *IEEE Transactions on Electron Devices*, *58*(11), 3751–3758.

Bjrk, F., Treu, M., Hilsenbeck, J., Kutschak, M. A., Domes, D., & Rupp, R. (2011). *1200 V SiC JFET in cascode light configuration: Comparison versus Si and SiC based switches* (vol. 679–680, pp. 587–590).

Booth, R. V., White, M. H., Wong, H.-S., & Krutsick, T. J. (1987). The effect of channel implants on MOS transistor characterization. *IEEE Transactions on Electron Devices*, *34*(12), 2501–2509.

Boucart, K., & Ionescu, A. M. (2008). A new definition of threshold voltage in tunnel FETs. *Solid-State Electronics*, *52*(9), 1318–1323.

Cree inc. c2m0280120d sic mosfet datasheet. https://www.wolfspeed.com/media/downloads/171/C2M0280120D.pdf. Accessed April 11, 2018.

Cree inc. c3m0280090d sic mosfet datasheet. https://www.wolfspeed.com/media/downloads/825/C3M0280090D.pdf. Accessed April 11, 2018.

DieterSchroder, K. (2006). *Semiconductor material and device characterization* (3rd ed.). Hoboken, New Jersey: Wiley.

Dobrescu, L., Petrov, M., Dobrescu, D., & Ravariu, C. (2000). Threshold voltage extraction methods for MOS transistors. In *2000 International Semiconductor Conference. 23rd Edition. CAS 2000 Proceedings (Cat. No.00TH8486)* (Vol. 1, pp. 371–374).

Garcia Snchez, F. J., Ortiz-Conde, A., & Muci, J. (2006). Understanding threshold voltage in undoped-body MOSFETs: An appraisal of various criteria. *Microelectronics Reliability*, *46*(5), 731–742.

Glaser, J. S., Nasadoski, J. J., Losee, P. A., Kashyap, A. S., Matocha, K. S., Garrett, J. L., et al. (2011). Direct comparison of silicon and silicon carbide power transistors in high-frequency hard-switched applications. In *2011 Twenty-Sixth Annual IEEE Applied Power Electronics Conference and Exposition (APEC)* (pp. 1049–1056).

Jouha, W., Oualkadi, A. E., Dherbcourt, P., Joubert, E., & Masmoudi, M. (2017). A new extraction method of SiC power MOSFET threshold voltage using a physical approach. In *2017 International Conference on Electrical and Information Technologies (ICEIT)* (pp. 1–6).

Levenberg, K. (1944). A method for the solution of certain non-linear problems in least squares. *Quarterly of Applied Mathematics*, *2*, 164–168.

Marquardt, D. W. (1963). An algorithm for least-squares estimation of nonlinear parameters. *Journal of the Society for Industrial and Applied Mathematics*, *11*(2), 431–441.

McNutt, T. R., Hefner, A. R., Mantooth, H. A., Berning, D., & Ryu, S. H. (2007). Silicon carbide power MOSFET model and parameter extraction sequence. *IEEE Transactions on Power Electronics*, *22* (2), 353–363.

Ortiz-Conde, A., Garca-Snchez, F. J., Muci, J., Tern Barrios, A., Liou, J. J., & Ching-Sung, H. (2013). Revisiting MOSFET threshold voltage extraction methods. *Microelectronics Reliability*, *53*(1), 90–104.

Ortiz-Conde, A., Garciia Sanchez, F. J., Liou, J. J., Cerdeira, A., Estrada, M., & Yue, Y. (2002). A review of recent MOSFET threshold voltage extraction methods. *Microelectronics Reliability*, *42*(4), 583–596.

Ortiz-Conde, A., Rodrguez, J., Garca Sanchez, F. J., & Liou, J. J. (1998). An improved definition for modeling the threshold voltage of MOSFETs. *Solid-State Electronics*, *42*(9), 1743–1746.

Raynaud, C., Tournier, D., Morel, H., & Planson, D. (2010). Comparison of high voltage and high temperature performances of wide bandgap semiconductors for vertical power devices. *Diamond and Related Materials*, *19*(1), 1–6.

Simonot, T., Rouger, N., Nguyen, X. H., Crébier, J. C., Bourennane, A., Sanchez, J. L., et al. (2010). Tension de seuil réduite pour composants de puissance à grille: Intérêts et conséquences. *Électronique de Puissance du Futur* (p. 4). Saint-Nazaire, France.

Terada, K., Nishiyama, K., & Hatanaka, K.-I. (2001). Comparison of MOSFET-threshold-voltage extraction methods. *Solid-State Electronics*, *45*(1), 35–40.

Tsuno, M., Suga, M., Tanaka, M., Shibahara, K., Miura-Mattausch, M., & Hirose, M. (1998). *Reliable threshold voltage determination for sub-0.1 micron gate length MOSFETs* (pp. 111–116).

Tsuno, M., Suga, M., Tanaka, M., Shibahara, K., Miura-Mattausch, M., & Hirose, M. (1999). Physically-based threshold voltage determination for MOSFET's of all gate lengths. *IEEE Transactions on Electron Devices*, *46*(7), 1429–1434.

Wong, H. S., White, M. H., Krutsick, T. J., & Booth, R. V. (1987). Modeling of transconductance degradation and extraction of threshold voltage in thin oxide MOSFET's. *Solid-State Electronics*, *30*(9), 953–968.

Zhao, T., Wang, J., Huang, A. Q., & Agarwal, A. (2007). Comparisons of SiC MOSFET and Si IGBT based motor drive systems. *2007 IEEE Industry Applications Annual Meeting*, 331–335.

W. Jouha Ph.D. student in thesis co-supervision between Abdelmalek Essaadi University, National school of applied sciences of Tangier, Morocco and University of Rouen, GPM Laboratory, Rouen, France. In 2014, he graduated as an engineer in electronics and automatic systems from National school of applied sciences of Tangier, Morocco. His thesis research concerns the study and modeling of power SiC MOSFETs degradations subjected to thermal and electrical constraints.

Ahmed El Oualkadi (M'02) received Ph.D. degree in electronics from the University of Poitiers, France, in 2004. From 2000 to 2003, he was a research assistant in the Laboratoire d'Automatique et d'Informatique Industrielle—Ecole Supérieure d'Ingénieurs de Poitiers, Electronics & Electrostatics Research Unit, University of Poitiers, France. In 2004, he was an assistant professor at University Institute of Technology, Angoulême, France. In 2005, he joined the Université Catholique de Louvain, Microelectronics Laboratory, Louvain-la-Neuve, Belgium, as a research fellow where he worked on the analog and mixed design of low power high temperature circuits and systems, in SOI technology, for wireless communication. During this period, he has managed and participated in several European and regional projects in the areas of wireless communication and sensor networking. Currently, he is an associate professor in the Abdelmalek Essaadi University, National school of applied sciences of Tangier, Morocco. His main research interest is the analog IC, mixed-signal, RFIC and MMIC design for wireless communication and electronic circuit reliability.

Pascal Dherbécourt received a diploma degree and a Ph.D in physics of electronics of telecommunication in 2002. Between 1999 and 2008, he worked in the field of optical fibers telecommunications. In 2008, he joined the GPM Laboratory of University of Rouen and became co-founder and a member of Erdefi team (research team in reliability and failure analysis of electronic components). His main research interests are now reliability and failure analysis of high power microwave transistors for telecommunication and RADAR applications and switching power components. He is engaged in several national and international research projects. He participates in numerous research projects in collaboration with major companies. He is the author and co-author of more than sixty articles in international journals and congresses. At University of Rouen, he found a bachelor program in electronics in 2005, he also develops training programs for aeronautics and space business.

Eric Joubert (born in 1965) received an MSc degree in electrical engineering from ESIGELEC Rouen, France in 1988 and the PhD degree in electrical engineering from University of Rouen, France, in 1993. He first worked at LCIA/INSA de Rouen from 1993 to 1998 in cartographic polarisation analysis for 3D metrology. He joined LEMI/University of Rouen in 1998 and began works on polarization effects in high speed optical fibers. He is now working in GPM (Groupe Physique des Matériaux, UMR CNRS 6634) as associate professor. His major research interests also include polarization effects characterisation in optical system, optical metrology and microelectronic behaviour characterisation by electroluminescence analysis.

Mohamed MASMOUDI received the Ph.D. degree in materials science from the University of Rouen, France, in 1997. He joined LEMI / University of Rouen in 1998 and began work on the electrical characterization of semiconductors. He is now working in GPM (Groupe Physique des Matériaux, UMR CNRS 6634). He has carried out research on transistors and his current major research interests include microelectronic reliability on power transistors like silicon–carbide metal–oxide–semiconductor field-effect transistors (MOSFET SiC).

Flatness-Based Control of DC Machine-Serial Multicellular Power Converter Association

M. Aourir, A. Abouloifa, C. Aouadi, I. Lachkar, and F. El Otmani

Abstract

This chapter considers the control of serial multicellular power converter feeding DC motor. For this purpose, a new control strategy based on flatness approach is developed. The main aim consists on regulating the DC motor velocity to a desired level, keeping in mind the necessity of ensuring an equitable distribution of the supply voltage on the power switches of serial multicellular power converter. To this end, the regulation of the voltage at the terminals of the flying capacitors is necessary. The synthetized controller was verified by computer simulation using Matlab/SimPowerSystems, and the obtained results prove the effectiveness of the designed controller and show that the entire objectives are achieved.

Keywords

DC motor • Multicellular power converter • Speed regulation • Flying capacitor • Nonlinear control • Flatness approach • Routh–Hurwitz criteria

1 Introduction

The increased power-level needs in industrial applications, such as rail train, aeronautics, speed variation of electrical machines (Li n.d.), and renewable energies (Aouadi et al. 2017) are confronted by the technological limitation on the power semiconductors, and for these reasons, new topologies of energy conversion systems appeared, combining a high switching frequency, reduced voltage rate at the power semiconductors, reduced power losses and able to provide multilevel voltages. Among these systems, the serial multicellular power converter appeared at the beginning of the 1990s (Meynard et al. 2002), this structure consists on sharing an equitable distribution of the supply voltage on the power switches by regulating the voltage at the terminals of the flying capacitors to a special value related to the supply voltage. The advantages and the control complexity offered by this type of converter were lead automation engineers and researchers to focus on this system and the proposed some control approach and analysis such as passivity-based control (Cormerais et al. 2008) and backstepping (Aouadi et al. 2014) to benefit from the advantages of this type of power converter.

Several studies have been made on multicellular converters. Starting by the natural balancing obtained, in open loop, when the cell switches are controlled by an interleaved PWM with equal duty cycle and phase shifted by $2\pi/p$ (case of p cells) (Patin 2015). This open loop control strategy can provoke an instability if the converter has a prime number of cells (Bethoux and Barbot 2006). For the closed loop control, the hybrid modeling and switching design of multicellular converter are presented in Benmiloud et al. (2016) in order to regulate the voltage across flying capacitors and the current in the load of *RL* type. In Benmansour et al. (2007), Benmiloud and Benalia (2013), stability analysis and control based on hybrid theory were investigated for three cells serial multicellular power converter. Furthermore, Some solutions using active control and observation of floating capacitors were proposed in Gateau et al. (2002). In Djemaï et al. (2011), the authors addressed the speed control of DC machine feeding by the switched multicellular converter based on super-twisting algorithm.

This chapter presents the analysis, modeling and nonlinear control of DC motor-serial multicellular power converter association. The aim is to design a controller for realizing two main objectives, the first one is to regulate the velocity of DC motor to the desired reference signal, the second one consists on maintaining an equilibrate distribution of the

---

M. Aourir (✉) · A. Abouloifa · C. Aouadi · F. El Otmani
TI Lab, Faculty of Sciences Ben M'sik, Hassan II-Casablanca University, BP 7955 Casablanca, Morocco
e-mail: meriem.aourir-etu@etu.univh2c.ma

I. Lachkar
RI Lab, ENSEM Casablanca, Hassan II-Casablanca University, BP 7955 Casablanca, Morocco

S. El Hani and M. Essaaidi (eds.), *Recent Advances in Electrical and Information Technologies for Sustainable Development*,
Advances in Science, Technology & Innovation, https://doi.org/10.1007/978-3-030-05276-8_3

Table 1 Notation list

Ω	Speed machine
T_L	Load torque
J	Moment inertia of rotor
f	Viscous friction coefficient
k	Voltage constant
R, L	Armature resistance and inductance
$vc_{1,2}$	Voltage across capacitors
C	Capacity of condensers

supply voltage on the power switch devices by regulating the voltage across the flying capacitors namely vc_1 and vc_2. The whole system under study is described by the 4th average nonlinear model. Based on this model, the controller design is developed using the differential flatness approach.

This chapter is organized as follows: in Sect. 2 the multicellular power converter is described and modeled; Sect. 3 is dedicated to present the design of the flatness-based controller, while the simulation results are presented in Sect. 4, a conclusion and a reference list end the chapter.

To alleviate the paper presentation, a list of notations is given hereafter (Table 1).

2 Multicellular Power Converter Presentation and Modeling

The multicellular power converters are based on the association in series of the elementary commutation cells. Figure 1 illustrates the topology of a multicellular converter with three cells driving DC motor, wherein each cell is controlled by a binary signal taking value in set $\{0,\ 1\}$. It is necessary that the two switches of each cell operate in complementary way, it means, that only one switch is conducting at a given time. It is required to ensure a balanced distribution of the supply voltage to the various switches. In our case, each switch must support a voltage value equal to $ve/3$. This implies that the flying capacitor voltages must have the following values $vc_1 = ve/3$ and $vc_2 = 2ve/3$. It is among the objectives of the controller that will be presented in the next section.

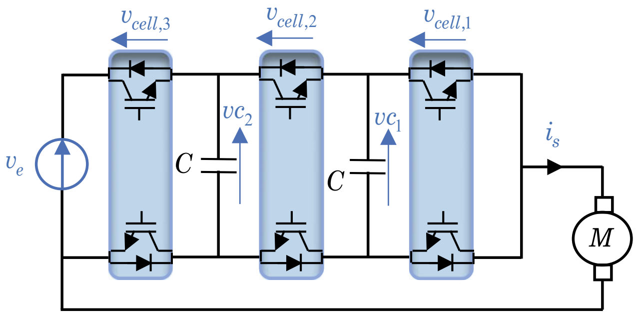

Fig. 1 Multicellular converter feeding DC motor

Applying Kirchhoff's laws to the above circuit, the model is then given in the following form:

$$C\frac{dvc_1}{dt} = (\mu_2 - \mu_1)\, i_s \tag{1a}$$

$$C\frac{dvc_2}{dt} = (\mu_3 - \mu_2)\, i_s \tag{1b}$$

$$J\frac{d\Omega}{dt} = k\, i_s - f\,\Omega - T_L \tag{1c}$$

$$L\frac{di_s}{dt} = (\mu_1 - \mu_2)\, v_{c1} + (\mu_2 - \mu_3)\, v_{c2} + \mu_3 v_e - R\, i_s - k\Omega \tag{1d}$$

where v_e is the input voltage, i_s denotes the output current, vc_1 and vc_2 represent the voltage across the flying capacitors and μ_1, μ_2 and μ_3 are the switching functions taking values in the discrete set $\{0,\ 1\}$.

Noting that the system under study can be seen as three subsystems: (i) subsystem (1a) describing the dynamic of the first flying capacitor voltage, (ii) subsystem (1b) which describing the dynamic of the second flying capacitor voltage, (iii) subsystem (1c, 1d) describing the dynamic of DC motor.

Equations (1a–1d) represent the instantaneous model of the multicellular power converter-DC machine association. This model cannot be used directly for the controller design due to the switched nature of the control inputs. Therefore, the control design for the above multicellular converter will be based upon the following average version of (1a–1d)

$$C\dot{x}_1 = (u_2 - u_1)\cdot x_4 \tag{2a}$$

$$C\dot{x}_2 = (u_3 - u_2)\cdot x_4 \tag{2b}$$

$$J\dot{x}_3 = k\cdot x_4 - f\cdot x_3 - T_L \tag{2c}$$

$$L\dot{x}_4 = (u_1 - u_2)x_1 + (u_2 - u_3)x_2 + u_3 v_e - Rx_4 - kx_3 \tag{2d}$$

Noting that this model is nonlinear owing to the product between the input control signals and state variables of the system (Table 2).

Table 2 State variables and control inputs

Variables	Definition
$x_i \quad (i = 1, 2)$	Average of $vc_i\,(i = 1, 2)$
x_3	Average of Ω
x_4	Average of i_S
$u_j \quad (j = 1, 2, 3)$	Average of $\mu_j \quad (j = 1, 2, 3)$

3 Controller Design

In this section, we will present the elaborated regulator based on the differential flatness; the choice of this technique of control refers to its usefulness in the situation where the generation of explicit trajectories is required. The control structure consists of two voltage loops which allow ensuring the good operation of multicellular converter and one loop for speed controller to regulate the velocity of DC motor.

3.1 Controller Objectives

There are two main objectives to achieve, the first one is to force the flying capacitors voltage vc_1 and vc_2 to track given reference signals $vc_{1,ref} = v_e/3$ and $vc_{2,ref} = 2v_e/3$, the second one is to regulate the speed of DC motor to the desired reference signal namely Ω_{ref}. The schematic diagram of the whole controlled system is shown in Fig. 2.

3.2 Flatness Review

In differential algebra, a system is viewed flat if a set of variables called flat outputs can be found such that all state variables and input components can be determined from these output components without integration (Fliess et al. 1995). Before showing the flatness properties of the considered system, we recall the definition of flat system with state x and input u defined by

$$\dot{x} = f(x, u) \quad x \in \Re^n,\ u \in \Re^m \tag{3}$$

The above system is said to be flat if there exists an output $y \in \Re^m$ (called flat output) such that $y = \varphi(x, u, \dot{u}, \ldots, u^r)$ where x and u can be written as independent functions of this flat output and its successive derivatives up to the q order for components of the state vector and $q + 1$ for components of the control vector:

$$x = \phi(y, \dot{y}, \ldots, y^q) \tag{4}$$

$$u = \Psi\left(y, \dot{y}, \ldots, u^{q+1}\right) \tag{5}$$

It is clear that the state and input variables can be expressed without integrating any differential equation, in terms of flat output and a finite number of its derivative.

3.3 Flatness Controller Design

3.3.1 Flatness Property

The first step of flatness approach is to define flat outputs which have the same dimension of input signals. In our case, we have the state variables $x = (x_1, x_2, x_3, x_4)^T \in \Re^4$ and input variables $u = (u_1, u_2, u_3)^T \in \Re^3$. Indeed, we have to define three flat outputs noted y_1, y_2, and y_3 as follows:

$$Y = I_3\, X \tag{6}$$

with $Y = (\,y_1 \quad y_2 \quad y_3\,)^T$, $X = (\,x_1 \quad x_2 \quad x_3\,)^T$ and I_3 is an identity matrix.

With this choice, we must check that the system under study is differentially flat. For this, we must verify that all state variables and input signals can be expressed in function of these flat outputs. In fact, it is easy to see that

$$x_j = y_j \quad \text{for } j = 1, 2, 3 \tag{7}$$

using (2c) and (6) we get the following form of the last state variable:

$$x_4 = \frac{1}{k}(J\dot{y}_3 + fy_3 + T_L) \tag{8}$$

Using (6) and (8), dynamics of (2a, 2b) can be written as

$$\dot{y}_1 = \frac{1}{Ck}\delta_1(J\dot{y}_3 + fy_3 + T_L) \tag{9}$$

$$\dot{y}_2 = \frac{1}{Ck}\delta_2(J\dot{y}_3 + fy_3 + T_L) \tag{10}$$

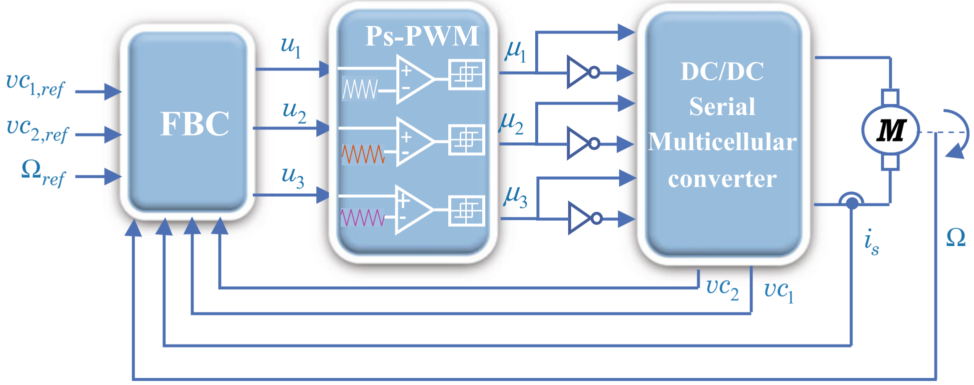

Fig. 2 Controlled system

with

$$\delta_1 = u_2 - u_1 \tag{11}$$

$$\delta_2 = u_3 - u_2 \tag{12}$$

This implied that

$$\delta_1 = \frac{C\dot{y}_1}{k}\left(J\dot{y}_3 + f y_3 + T_L\right) \tag{13}$$

$$\delta_2 = \frac{C\dot{y}_2}{k}\left(J\dot{y}_3 + f y_3 + T_L\right) \tag{14}$$

Using (2d) and (6), second time derivative of (2c) can be written as follows:

$$\ddot{y}_3 = \frac{1}{JL}\left(-k\delta_1 y_1 - k\delta_2 y_2 + k u_3 v_e - Rkx_4 - k^2 y_3 - Lf\,\dot{y}_3\right) \tag{15}$$

Using (13), (14) and solving the above equation with respect to u_3, one has

$$u_3 = \frac{L}{kv_e}\left(J\,\ddot{y}_3 - f\,\dot{y}_3\right) + \frac{Ck}{v_e}\frac{\dot{y}_1 y_1 + \dot{y}_2 y_2}{J\dot{y}_3 + f y_3 + T_L} + \frac{R\left(J\dot{y}_3 + f y_3 + T_L\right) + k^2 y_3}{k v_e} \tag{16}$$

Using (12), (14) and the above equation one has

$$u_2 = \frac{L}{kv_e}\left(J\ddot{y}_3 - f\dot{y}_3\right) + \frac{Ck}{v_e}\frac{y_1\dot{y}_1 + y_2\dot{y}_2 - v_e\dot{y}_2}{J\dot{y}_3 + f y_3 + T_L} + \frac{R\left(J\dot{y}_3 + f y_3 + T_L\right) + k^2 y_3}{k v_e} \tag{17}$$

At last, using (11), (13) and (17) we get

$$u_1 = \frac{L}{kv_e}\left(J\ddot{y}_3 - f\dot{y}_3\right) + \frac{Ck}{v_e}\frac{y_1\dot{y}_1 + y_2\dot{y}_2 - v_e\left(\dot{y}_2 + \dot{y}_1\right)}{J\dot{y}_3 + f y_3 + T_L} + \frac{R\left(J\dot{y}_3 + f y_3 + T_L\right) + k^2 y_3}{k v_e} \tag{18}$$

3.3.2 Trajectory Planning

The trajectory planning is a very important phase in flatness control design as it defines the evolution of all state and control variables, for this system, a first-order low-pass filter is applied to reference values $vc_{1,ref}$ and $vc_{2,ref}$, where a second-order type is applied to a reference value Ω_{ref}, to protect the system against fast and instantaneous changes of reference signals. Therefore, the reference trajectories can be described as

$$y_{j,p} = \frac{1}{1 + \tau s} vc_{j,ref} \quad (j = 1,\, 2) \tag{19}$$

$$y_{3,p} = \frac{1}{\left(1 + \tau_0 s\right)^2}\Omega_{ref} \tag{20}$$

where τ and τ_0 are real positive quantities to be given later.

3.3.3 Control Law Design

The proposed regulator must be designed in order to force the output vector $y = \left(y_1 \quad y_2 \quad y_3\right)^T$ to track its reference trajectory $y_p = \left(y_{1,p} \quad y_{2,p} \quad y_{3,p}\right)^T$ which is the filtered version of reference vector $y_{ref} = \left(vc_{1,ref} \quad vc_{2,ref} \quad \Omega_{ref}\right)^T$. The following state feedback controller is proposed:

$$\left(\dot{y}_{j,p} - \dot{y}_j\right) + a_j\left(y_{j,p} - y_j\right) = 0 \; (j = 1,\, 2) \tag{21}$$

$$\left(\ddot{y}_{3,p} - \ddot{y}_3\right) + a_4\left(\dot{y}_{3,p} - \dot{y}_3\right) + a_3\left(y_{3,p} - y_3\right) = 0 \tag{22}$$

According to the well-known Routh–Hurwitz criteria, the design parameters a_1, a_2, a_3 and a_4 are chosen to be real positive quantities in order to guarantee asymptotic stability of closed loop system. The actual control inputs namely $u = \left(u_1 \quad u_2 \quad u_3\right)^T$ can be calculated thanks to Eqs. (16), (17) and (18).

These control signals are used to generate the binary control signals (μ_1, μ_2, μ_3) of the multicellular converter through a phase shifted pulse width modulation generator. The schematic diagram of the whole system is shown in Fig. 3.

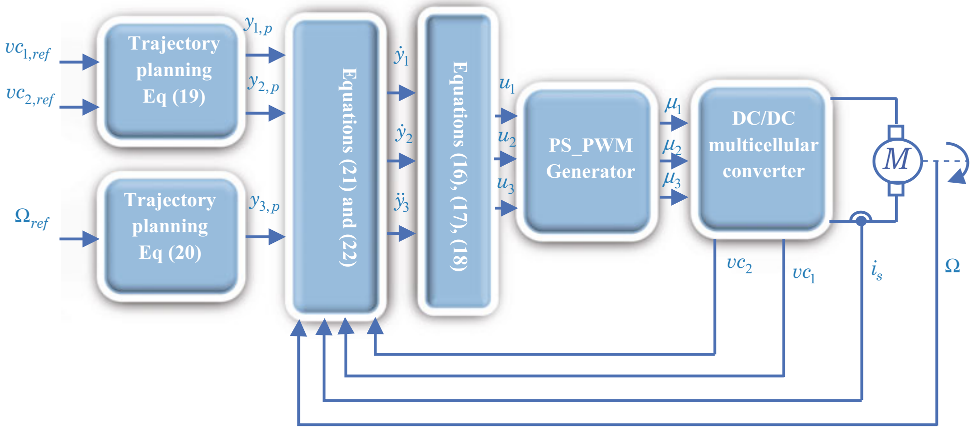

Fig. 3 Flatness regulator structure

Proposition 1 *Consider the system shown in* Fig. 1 *and described by its averaging model* (2a–2d) *with the control laws given by* (16), (17), (18), (21) *and* (22). *In the coordinates* $E = (e_1 \quad e_2 \quad e_3 \quad e_4)^T$, *the behavior of the closed loop system is described by the following dynamical equation:*

$$\dot{E} = \begin{pmatrix} A_1 & 0 \\ 0 & A_2 \end{pmatrix} E \tag{23}$$

with

$$A_1 = \begin{pmatrix} -a_0 & 0 \\ 0 & -a_1 \end{pmatrix} \text{ and } A_2 = \begin{pmatrix} 0 & 1 \\ -a_3 & -a_4 \end{pmatrix}$$

Noting that the system will be globally asymptotically stable if the matrix A_1 and A_2 are Hurwitz. Note that its eigenvalues are the roots of the following characteristic polynomials:

$$\pi_{A_1}(\lambda) = \lambda^2 + (a_1 + a_2)\lambda + a_1 a_2 \tag{24a}$$

$$\pi_{A_2}(\lambda) = \lambda^2 + a_4\lambda + a_3 \tag{24b}$$

To this end, applying for instance the well-known Routh's algebraic criteria, it follows that all zeros of the polynomial (24a, 24b) have negative real parts if the conditions (25) are fulfilled. That is, under these conditions, it turns out that the matrix A_1 and A_2 are actually Hurwitz.

$$a_1 a_2 > 0,\ a_1 + a_2 > 0,\ a_3 > 0 \text{ and } a_4 > 0 \tag{25}$$

4 Simulation Results

In this section, the controller that has been designed in the above section will be tested in the Matlab/SimPowerSystems environment with the following system and regulators characteristics (Table 3).

To illustrate the efficiency of the proposed controller, the simulation results are carried out in two trials to check the controller performances. In the first protocol, we have performed a step changes on the input voltage from 1500 to 1800 V at time 0.3 s. The obtained results are illustrated by Figs. 4, 5 and 6. Figures 4 and 5 show that the voltage references are achieved after a small transient time and with small ripples which does not exceed 2 V. Figure 6 shows that the tracking quality of the motor velocity is quite satisfactory in spite of this step changes. The second protocol consists of a step variation of the velocity reference at time 0.2 s (60–80 rad/s) and at time 0.4 s we applied a constant load torque (T_L = 40 Nm) to check the robustness of the proposed controller, the obtained results are presented in Figs. 7, 8, and 9. Figure 7 shows that the DC motor velocity tracks its reference with a good accuracy despite the effected variation with a fast transient time, as for the two last figures it is shown that the flying capacitors voltage kept unchanged in time but when we applied a load torque the voltage ripples are increased but kept quite small compared to 5% of the voltage value.

Table 3 System parameters

Subsystem	Parameters	Value
Input voltage	ve	1500 V
Converter	C	40 µF
	fd	10 kHz
Dc motor	L	0.028 mH
	R	2.581 Ω
	k	1.27
	J	0.1 Nm/rd/s^2
	f	10^{-6} Nm/rd/s
Speed regulator	a_3	3600 s^{-2}
	a_4	85 s^{-1}
	τ_0	10^{-2} s
Voltage regulator	a_1	300 s^{-1}
	a_2	300 s^{-1}
	τ	5.10^{-3} s

a. *input voltage variation*.

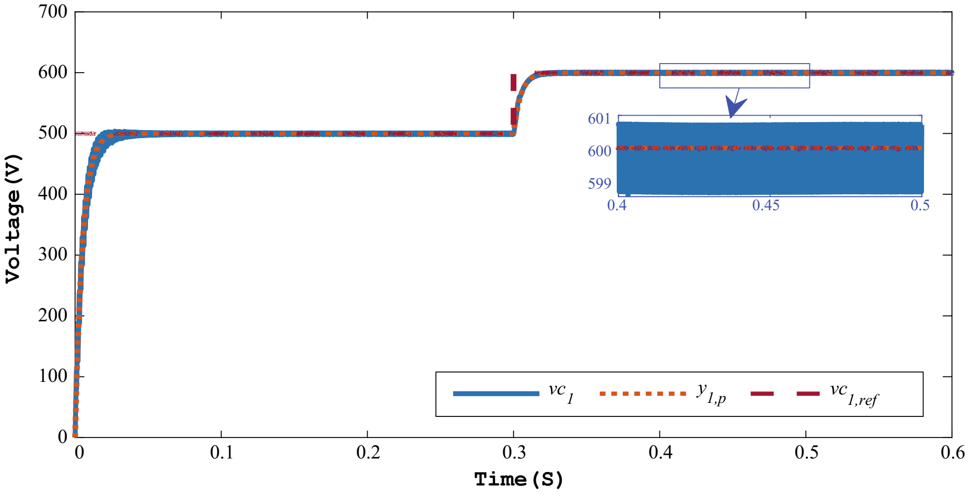

Fig. 4 Voltage across the first flying capacitor

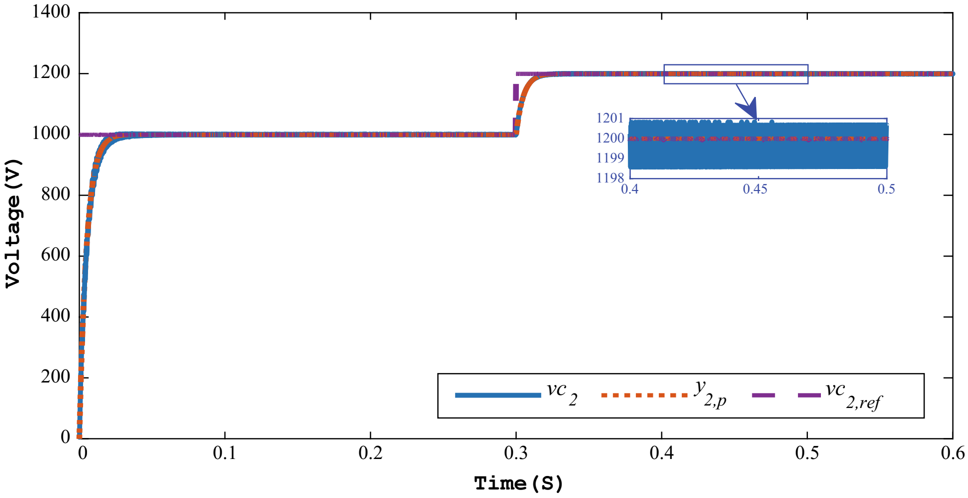

Fig. 5 Voltage across the second flying capacitor

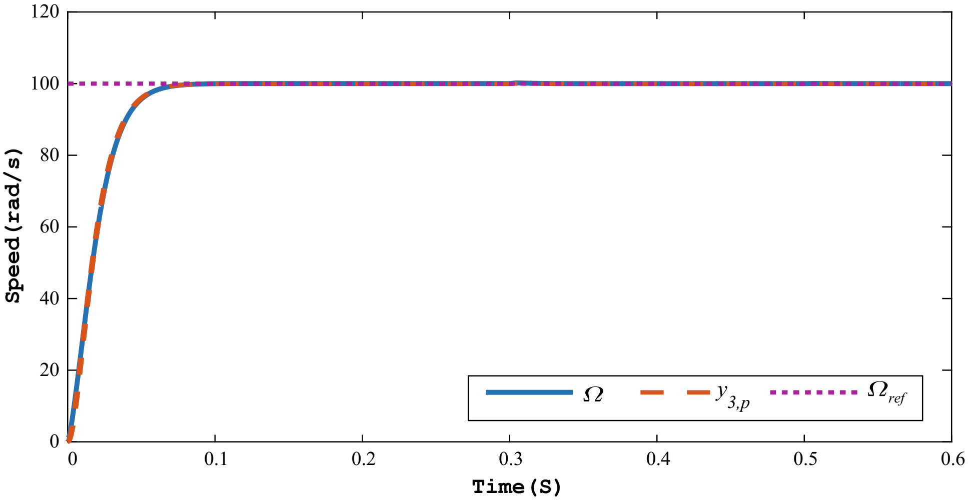

Fig. 6 DC motor velocity

b. *Angular speed variation and application of a load torque.*

Fig. 7 DC motor velocity

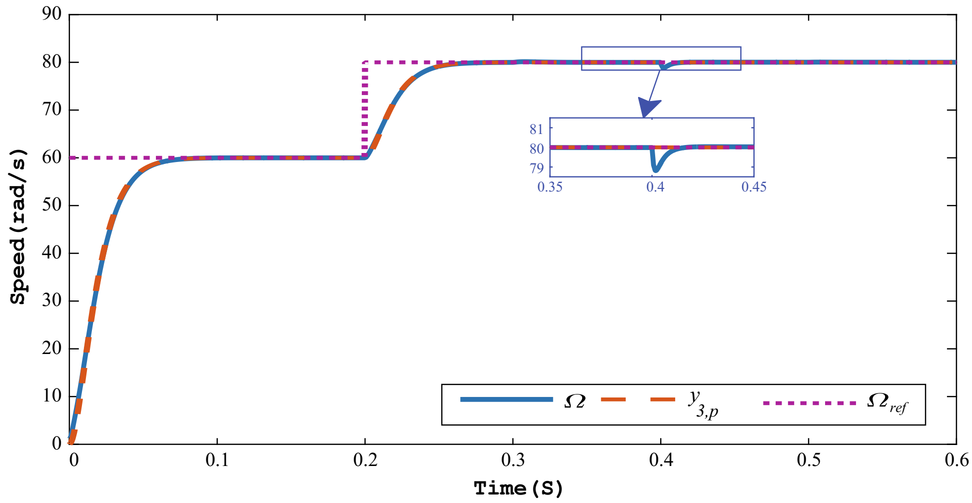

Fig. 8 Voltage across the first flying capacitor

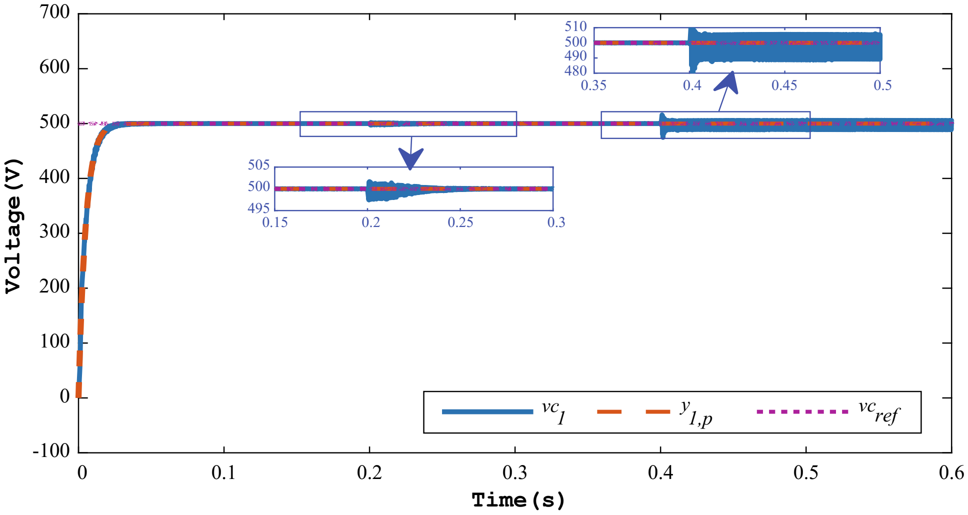

Fig. 9 Voltage across the second flying capacitor

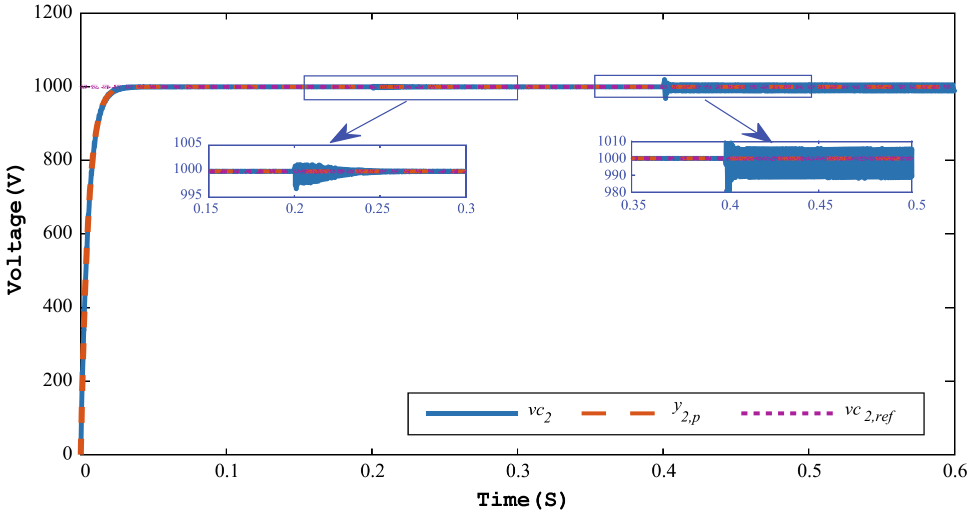

5 Conclusion

In this chapter, a new control approach is proposed for serial multicellular DC–DC power converter feeding a DC motor. At first, a modeling of the whole system is given, described by the fourth-order average nonlinear model, then the control laws are synthetized using the differential flatness approach. The developed controller has two main objectives to realize and guaranty the speed regulation and keeping the safe operation of the power converter by regulating the voltage at the flying capacitors terminals. The obtained results show that the entire objectives are achieved with a good accuracy and prove the effectiveness/robustness of the proposed controller.

References

Aouadi, C., Abouloifa, A., Aourir, M., Boussairi, Y., Hamdoun, A., & Lachkar, I. (2017). State-feedback nonlinear control of three-phase grid connected to the photovoltaic system. In *2017 IEEE International Conference on Environment and Electrical Engineering and 2017 IEEE Industrial and Commercial Power Systems Europe (EEEIC/I&CPS Europe)* (pp. 1–6). IEEE.

Aouadi, C., Abouloifa, A., Hamdoun, A., & Boussairi, Y. (2014). Backstepping based control of PV system connected to the grid. *International Journal of Computer & Information Technology, 3*.

Benmansour, K., Benalia, A., Djemaï, M., & de Leon, J. (2007). Hybrid control of a multicellular converter. *Nonlinear Analysis: Hybrid Systems, 1,* 16–29. https://doi.org/10.1016/j.nahs.2006.06.001.

Benmiloud, M., & Benalia, A. (2013). Hybrid control scheme for multicellular converter. In *2013 International Conference on Control, Decision and Information Technologies (CoDIT)* (pp. 476–482). IEEE.

Benmiloud, M., Benalia, A., Defoort, M., & Djemai, M. (2016). On the limit cycle stabilization of a DC/DC three-cell converter. *Control Engineering Practice, 49,* 29–41. https://doi.org/10.1016/j.conengprac.2016.01.010.

Bethoux, O., & Barbot, J.-P. (2006). Commande permettant le contrôle du convertisseur multicellulaire série à nombre non premier de cellules. In *Conférence Internationale Francophone En Automatique*.

Cormerais, H., Buisson, J., Richard, P. Y., & Morvan, C. (2008). Modelling and passivity based control of switched systems from bond graph formalism: Application to multicellular converters. *Journal of the Franklin Institute, 345,* 468–488. https://doi.org/10.1016/j.jfranklin.2008.01.001.

Djemaï, M., Busawon, K., Benmansour, K., & Marouf, A. (2011). High-order sliding mode control of a DC motor drive via a switched controlled multi-cellular converter. *International Journal of Systems Science, 42,* 1869–1882. https://doi.org/10.1080/00207721.2010.545492.

Fliess, M., Lévine, J., Martin, P., & Rouchon, P. (1995). Flatness and defect of non-linear systems: Introductory theory and examples. *International Journal of Control, 61,* 1327–1361.

Gateau, G., Fadel, M., Maussion, P., Bensaid, R., & Meynard, T. A. (2002). Multicell converters: Active control and observation of flying-capacitor voltages. *IEEE Transactions on Industrial Electronics, 49,* 998–1008. https://doi.org/10.1109/TIE.2002.803200.

Li, C. (n.d.). A modified neutral-point balancing space vector modulation for three-level neutral point clamped converters in high speed drives. *IEEE Transactions on Industrial Electronics, 13*.

Meynard, T. A., Foch, H., Thomas, P., Courault, J., Jakob, R., & Nahrstaedt, M. (2002). Multicell converters: Basic concepts and industry applications. *IEEE Transactions on Industrial Electronics, 49,* 955–964. https://doi.org/10.1109/TIE.2002.803174.

Patin, N. (2015). Introduction to multi-level converters. In *Power electronics applied to industrial systems and transports* (Vol. 2, pp. 193–213). Elsevier. https://doi.org/10.1016/B978-1-78548-001-0.50005-8.

Meriem Aourir received her degree in information processing in 2015 from the Faculty of Science Ben M'sik, Hassan II University. Since 2015, she has been preparing her Ph.D. in the field of automatic, renewable energy, multilevel power electronics at HASSAN II University, Casablanca, Morocco. The main topics of her research include renewable energy, nonlinear control, and hybrid control of multicell converters.

Abdelmajid Abouloifa received the Aggregation of Electrical Engineering from Normal High School, Rabat, Morocco, in 1999, and Ph.D. degree in control engineering from the University of Caen Basse-Normandie, Caen, France and from Mohammed V University, Rabat, Morocco in 2008. He is currently Professor at the Faculty of Sciences Ben M'Sik, HASSAN II UNIVERSITY of Casablanca, Morocco. His research interests include high-frequency power converter topologies, power-factor-correction techniques, power supplies, and nonlinear control.

Chaouqi Aouadi received his Ph.D. in automatic, electrotechnical and renewable energy, in 2018 from Faculty of Science Ben M'sik, Hassan II University, Morocco. He is received the MASTER degree in information processing from Faculty of Science Ben M'sik, Hassan II University, Casablanca, in 2013. His research interests include renewable energy, power-factor-correction techniques, and nonlinear control.

Ibtissam Lachkar received the graduate degree from the Normal High School of Technical Education, Rabat, Morocco, in 1995 and her degree of high depth studies from the Mohammedia School of Engineers, Rabat, in 2005. She received her Ph.D. from Mohammedia School of Engineers. Currently, she is an Assistant Professor at National School of Electricity and Mechanic.

Fadwa El Otmani received her degree in information processing in 2015 from the Faculty of Science Ben M'sik, Hassan II University. Since 2015, she has been preparing her Ph.D. in the field of automatic, renewable energy, power electronic converters at HASSAN II University, Casablanca, Morocco. The main topics of her research include renewable energy and nonlinear control techniques.

Design and Implementation of Different Control Strategies of Unit Power Factor Three-Phase PWM Rectifier for Output Voltage Regulation

Fatima-Ezzahra Tahiri, Khalid Chikh,
Mohamed Khafallah, and Aziz El Afia

Abstract

This chapter presents the analysis and design of different control strategies of unit power factor three-phase PWM rectifier: hysteresis current control, voltage-oriented control (VOC), and direct power control (DPC), in order to obtain high-performance DC bus voltage, lower input current harmonics, and higher unit power factor (UPF). The studied control strategies presented in this work are developed in MATLAB/Simulink environment and implemented in software of the DS1104 board. The simulation and experimental results demonstrate well the performance of the PWM rectifier control techniques.

Keywords

PWM rectifier • Hysteresis current control • VOC • DPC • UPF

1 Introduction

The development of the power electronics allowed realization of more powerful electric converters controlled that has an important role in the efficiency (Abdeldjalil and Messaoud 2015). The PWM rectifier has been increasingly employed for recent decades, owing to its advantages of high power factor, a low distortion line current with unity power factor for any load condition, and energy bidirectional transmission (Xiaohong et al. 2010; Xue and He 2013). Nowadays, it is widely used in the wind energy conversion system to maximize the extracted power from the wind as well as decoupling generator dynamics from the load.

This paper describes and compares three different control strategies of unit power factor rectifier: hysteresis current control, VOC, and DPC. The comparison is based on the ripples of output voltage, harmonics, wave shape of the input current, and load perturbations rejection. This chapter is organized as follows: modeling of PWM rectifier will be presented in Sect. 2. In Sect. 3, the control techniques for PWM rectifiers are discussed. Whereas in Sect. 4, the simulation and experimental results are presented and talked. Eventually, conclusion is presented in Sect. 5.

2 Modeling of PWM Rectifier (Tahiri et al. 2017)

The basic circuit of three-phase PWM rectifier is shown in Fig. 1.

The input voltage Ea, Eb, and Ec are three-phase sinusoidal voltages obtained from the grid. Ua, Ub, and Uc are the input voltages of the rectifier.

The continuous voltage can be expressed according to the switches (Sa, Sb, and Sc) state.

The compound voltages Uab, Ubc, and Uca are obtained from these relations (Abdeldjalil and Messaoud 2015; Harshada 2015):

$$\begin{cases} \mathrm{Uab} = \mathrm{Uao} + \mathrm{Uob} = \mathrm{Uao} - \mathrm{Ubo} \\ \mathrm{Ubc} = \mathrm{Ubo} + \mathrm{Uoc} = \mathrm{Ubo} - \mathrm{Uco} \\ \mathrm{Uca} = \mathrm{Uco} + \mathrm{Uoa} = \mathrm{Uco} - \mathrm{Uao} \end{cases} \tag{1}$$

"o" is the medium point which divides the input DC voltage and "n" is the index of the neutral point of the alternative side, then

$$\begin{cases} \mathrm{Uao} = \mathrm{Uan} + \mathrm{Uno} \\ \mathrm{Ubo} = \mathrm{Ubn} + \mathrm{Uno} \\ \mathrm{Uco} = \mathrm{Ucn} + \mathrm{Uno} \end{cases} \tag{2}$$

F.-E. Tahiri (✉) · K. Chikh · M. Khafallah · A. El Afia
Energy and Electrical Systems Laboratory, Hassan II University ENSEM, Casablanca, Morocco
e-mail: fatima-ezzahra.tahiri@ensem.ac.ma

K. Chikh
Interdisciplinary Laboratory of Science and Technology Research, Sultan Moulay Slimane University-EST, Béni Mellal, Morocco

S. El Hani and M. Essaaidi (eds.), *Recent Advances in Electrical and Information Technologies for Sustainable Development*,
Advances in Science, Technology & Innovation, https://doi.org/10.1007/978-3-030-05276-8_4

Fig. 1 Structure of three-phase voltage source PWM rectifier

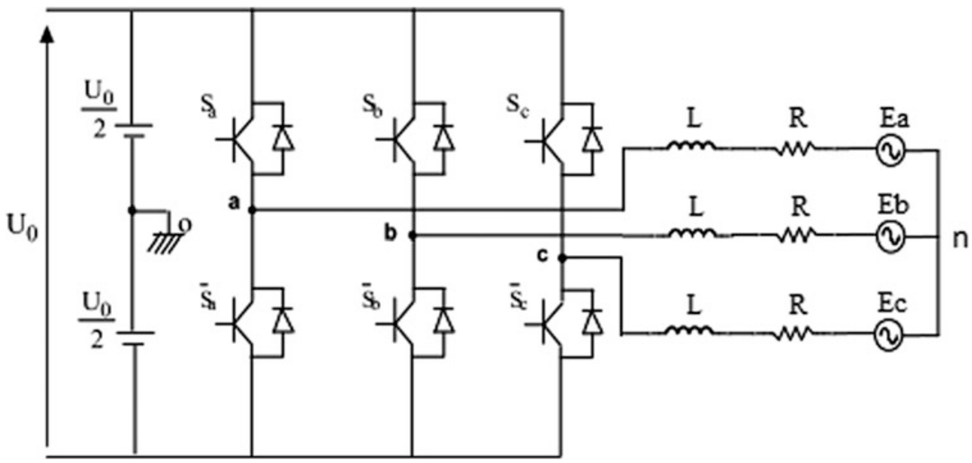

In the equilibrium condition:

$$\mathrm{Uan} + \mathrm{Uan} + \mathrm{Uan} = 0 \tag{3}$$

The substitution of (3) in (2) leads to

$$\mathrm{Uno} = \frac{1}{3}(\mathrm{Uao} + \mathrm{Ubo} + \mathrm{Uco}) \tag{4}$$

By replacing (4) in (2), we obtain

$$\begin{cases} \mathrm{Uan} = \frac{1}{3}(2\mathrm{Uao} - \mathrm{Ubo} - \mathrm{Uco}) \\ \mathrm{Ubn} = \frac{1}{3}(-\mathrm{Uao} + 2\mathrm{Ubo} - \mathrm{Uco}) \\ \mathrm{Ucn} = \frac{1}{3}(-\mathrm{Uao} - \mathrm{Ubo} + 2\mathrm{Uco}) \end{cases} \tag{5}$$

Then, the mathematical model of PWM rectifier in abc frame can be expressed as

$$\begin{cases} \mathrm{Uan} = \frac{\mathrm{Uo}}{3}(2\mathrm{Sa} - \mathrm{Sb} - \mathrm{Sc}) \\ \mathrm{Ubn} = \frac{\mathrm{Uo}}{3}(-\mathrm{Sa} + 2\mathrm{Sb} - \mathrm{Sc}) \\ \mathrm{Ucn} = \frac{\mathrm{Uo}}{3}(-\mathrm{Sa} - \mathrm{Sb} + 2\mathrm{Sc}) \end{cases} \tag{6}$$

$$\begin{cases} \mathrm{Uan} = \mathrm{Ea} - \mathrm{L}\frac{\mathrm{dIa}}{\mathrm{dt}} - \mathrm{R\ Ia} \\ \mathrm{Ubn} = \mathrm{Eb} - \mathrm{L}\frac{\mathrm{dIb}}{\mathrm{dt}} - \mathrm{R\ Ib} \\ \mathrm{Ucn} = \mathrm{Ec} - \mathrm{L}\frac{\mathrm{dIc}}{\mathrm{dt}} - \mathrm{R\ Ic} \end{cases} \tag{7}$$

$$\mathrm{C}\frac{\mathrm{dUo}}{\mathrm{dt}} = (\mathrm{Sa\ Ia} - \mathrm{Sb\ Ib} - \mathrm{Sc\ Ic}) - \mathrm{Ich} \tag{8}$$

where L and R are grid inductance and resistance, respectively, and C is the capacitor for filtering the DC voltage.

According to Park's transformation, the mathematical model of the rectifier in the two-phase synchronous rotation d-q coordinate can be defined as (Abdelmalek 2009; Hakan et al. 2016; Wei and Wang 2008)

$$\begin{cases} \mathrm{Ed} = \mathrm{L}\frac{\mathrm{dId}}{\mathrm{dt}} + \mathrm{R\ Id} - \mathrm{W\ L\ Iq} + \mathrm{Ud} \\ \mathrm{Ed} = \mathrm{L}\frac{\mathrm{dIq}}{\mathrm{dt}} + \mathrm{R\ Iq} + \mathrm{W\ L\ Id} + \mathrm{Uq} \\ \mathrm{C}\frac{\mathrm{dUo}}{\mathrm{dt}} = (\mathrm{Sd\ Id} + \mathrm{Sq\ Iq}) - \mathrm{Io} \end{cases} \tag{9}$$

where Id and Iq, respectively, represent active and reactive current components in d-q coordinate system, Sd and Sq represent switching functions in d-q coordinate system, Ud and Uq, respectively, represent active and reactive voltage sources in d-q coordinate system, and ω represent the synchronous rotation angular frequency.

Angle value (θ) required for above transformations can be found with phase-locked loop (PLL) or it can be obtained by using abc-αβ transformation.

3 Control Techniques for PWM Rectifier

3.1 Hysteresis Current Control

The hysteresis current control (shown in Fig. 2) requires a closed-loop control. The DC voltage Uo is measured and compared with a reference Uo_ref, the error signal obtained from this comparison is used to produce a waveform for current reference. The reference should be a sinusoidal waveform with the same frequency as the input voltage.

The control is carried out by measuring the instantaneous currents of the phases Ia, Ib, and Ic and forcing them to follow sinusoidal reference currents. The amplitude of the current reference is the output of a DC bus voltage regulator.

The sinusoidal waveform of the current reference is obtained by multiplying the reference current with a sine function, with the same frequency of the source, and with a

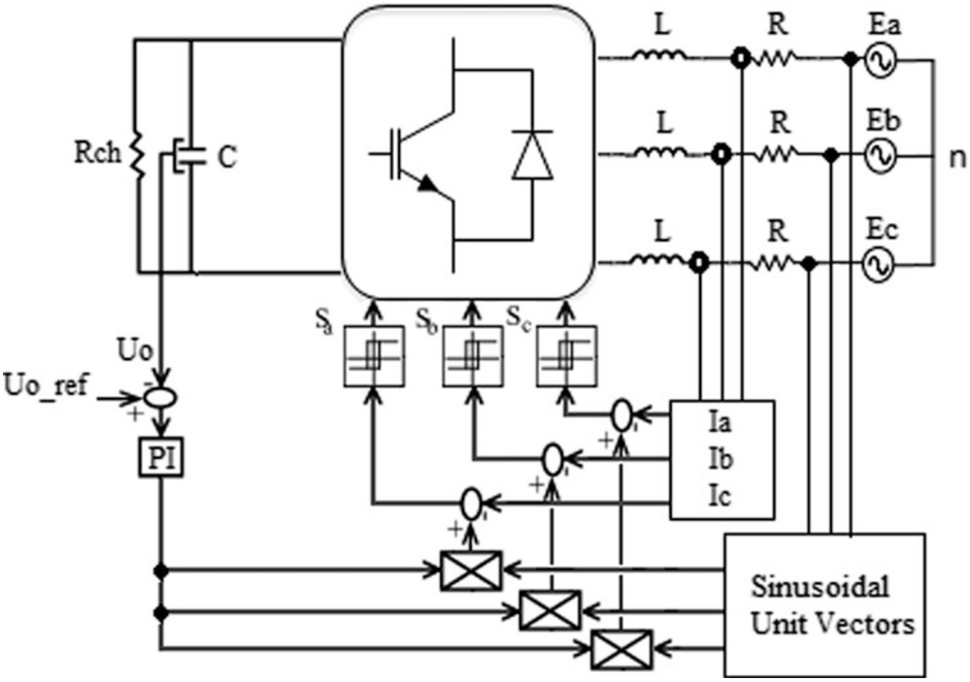

Fig. 2 Schematic diagram of the hysteresis current control

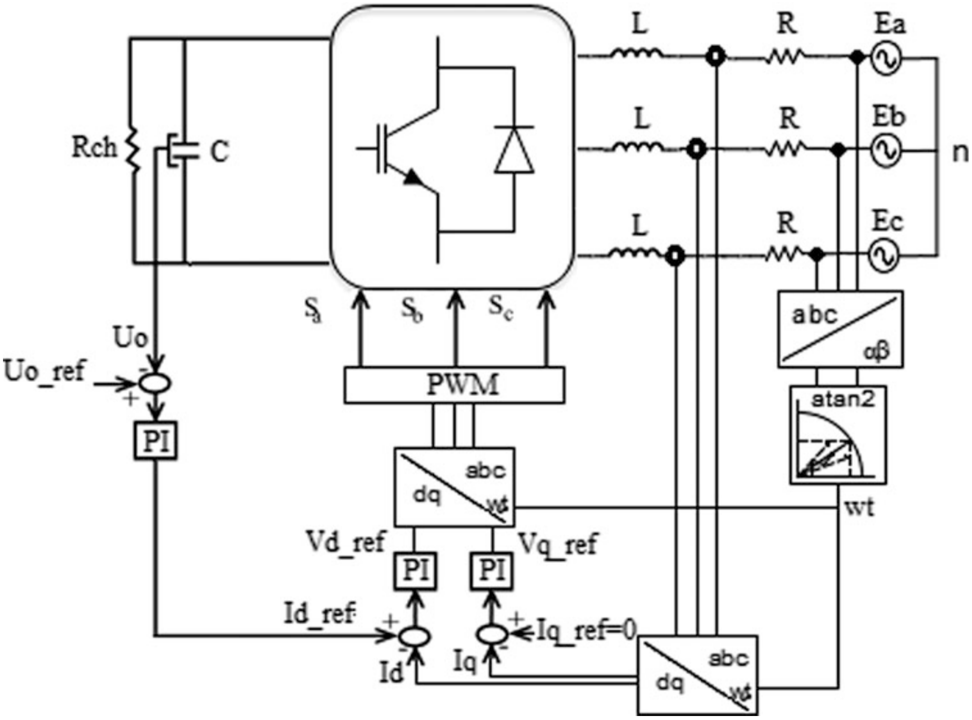

Fig. 3 Schematic diagram of the voltage-oriented control

desired phase shift angle. The reference must be synchronized with the power source. Once the reference has been created, the hysteresis PWM command is produced to switch the switches (Kendouli et al. 2011; Tiwari et al. 2003).

3.2 Voltage-Oriented Control (VOC) (Malinowski et al. 2003; Xue and He 2013)

The conventional control system uses closed-loop current control in a rotating reference frame. The voltage-oriented control (VOC) scheme is shown in Fig. 3.

A characteristic feature for this current controller is the processing of signals in two coordinate systems. The first is the stationary α-β and the second is the synchronously rotating d-q coordinate system. Thanks to this type of transformation, the control values are dc signals. An inverse transformation d-q/a-b-c is achieved on the output of the control system, and it gives the rectifier reference signals in rotating reference frame. For the coordinate transformations, the angle of the voltage vector is defined as

$$\gamma = \mathrm{actg}(V_\beta / V_\alpha) \qquad (10)$$

In voltage-oriented d-q coordinates, the ac line current vector is split into two rectangular components Id and Iq. The component Iq determines reactive power, whereas Id decides active power flow. Thus, the reactive and the active powers can be controlled independently. The unit power factor condition is met when the line current vector is aligned with the line voltage vector (Marian et al. 2002).

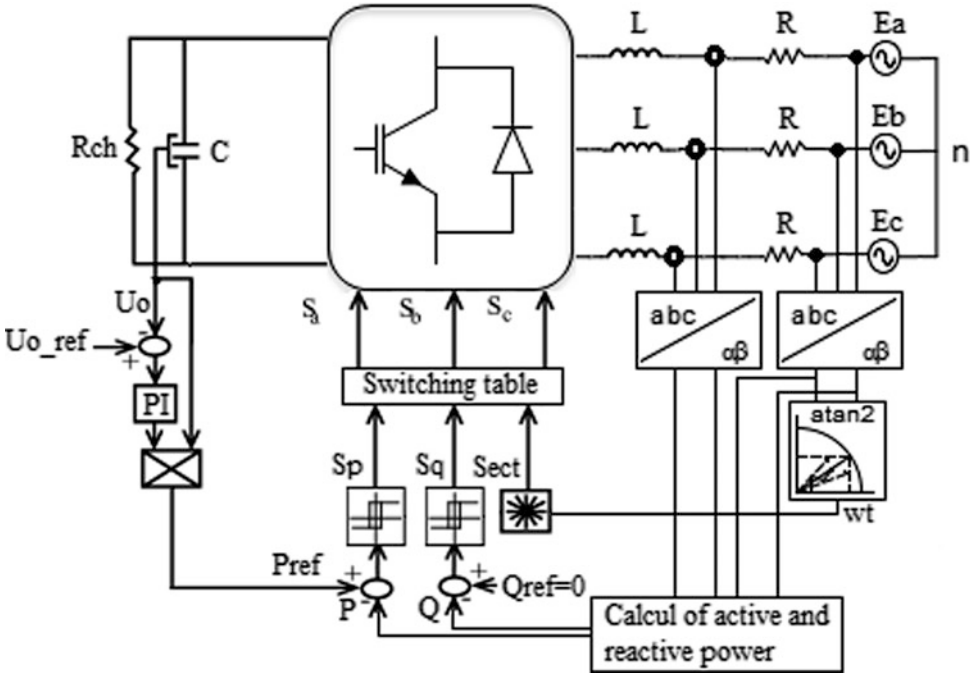

Fig. 4 Schematic diagram of the direct power control

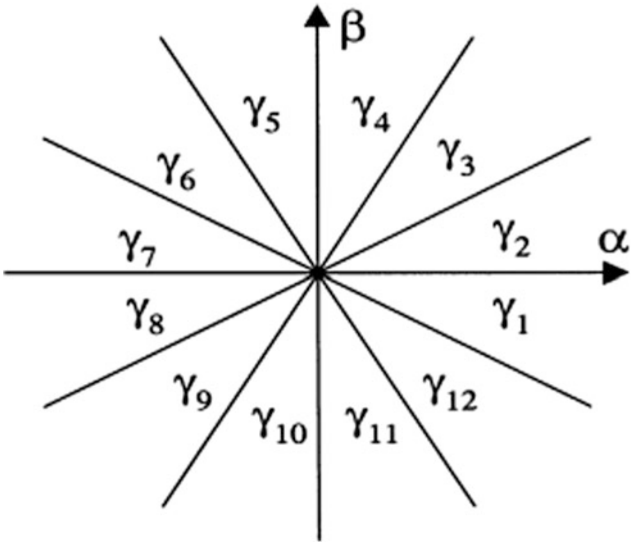

Fig. 5 Sector selection for DPC

3.3 Direct Power Control (DPC) (Abdelouahab et al. 2010; Ben Saïd et al. 2012; Djeriri 2014; Hassaoui et al. 2013; Minglian et al. 2011; Marian et al. 2002)

The direct power control is based on the control direct of the active and reactive powers. The block scheme of DPC is shown in Fig. 4.

The commands of reactive power Qref (set to zero for unity power factor) and active power Pref (delivered from the outer PI anti-windup DC voltage controller) are

Table 1 Applied switching states [Sa, Sb, Sc] according to sector and (Sp, Sq) binary function values (Ben Salem and Yahia 2014)

Sp	*Sq*	*γ1*	*γ2*	*γ3*	*γ4*	*γ5*	*γ6*	*γ7*	*γ8*	*γ9*	*γ10*	*γ11*	*γ12*
1	0	V6	V7	V1	V0	V2	V7	V3	V0	V4	V7	V5	V0
	1	V2	V7	V3	V0	V4	V7	V5	V0	V6	V7	V1	V0
0	0	V6	V1	V1	V2	V2	V3	V3	V4	V4	V5	V5	V6
	1	V1	V2	V2	V3	V3	V4	V4	V5	V5	V6	V6	V1

With: $V_0(000)$; $V_1(100)$; $V_2(110)$; $V_3(010)$; $V_4(011)$; $V_5(001)$; $V_6(101)$; $V_7(111)$

Table 2 Electrical parameters of power circuit and control coefficients

Line phase voltage	220 V
Line frequency	50 Hz
Line resistance	0.16 Ω
Line inductor	10 mH
Output filter capacitor	1100 μF
Switching frequency	2000 Hz
The controller gains	Kpv = 0.2105 Kiv = 2.0146 Kpi = 3.20 Kii = 51.20

compared with the calculated Q and P values, in reactive and active power hysteresis controllers, respectively.

The region of the voltage vector position is divided into 12 sectors, as shown in Fig. 5, and the sectors can be numerically expressed as

$$(n-2)\frac{\mathrm{Pi}}{6} \le \gamma_n < (n-1)\frac{\mathrm{Pi}}{6} \quad n = 1, 2, \ldots, 12 \tag{11}$$

The converter switching states are appropriately selected by a switching table (Table 1) based on the instantaneous errors between the commanded and estimated values of active and reactive powers (Sp and Sq) and the sector number.

4 Simulation and Experimental Results

The different control strategies have been simulated using Matlab/Simulink and tested experimentally in software of the DS1104 board, to verify the performance of the PWM rectifier during the variation of the output voltage reference and load. The chosen parameters are given in Table 2.

4.1 Simulation Results

See Figs. 6, 7, and 8.

4.2 Experimental Results

To verify and to confirm the simulation results, we realized a test bench shown in Fig. 9. An insulated gate bipolar

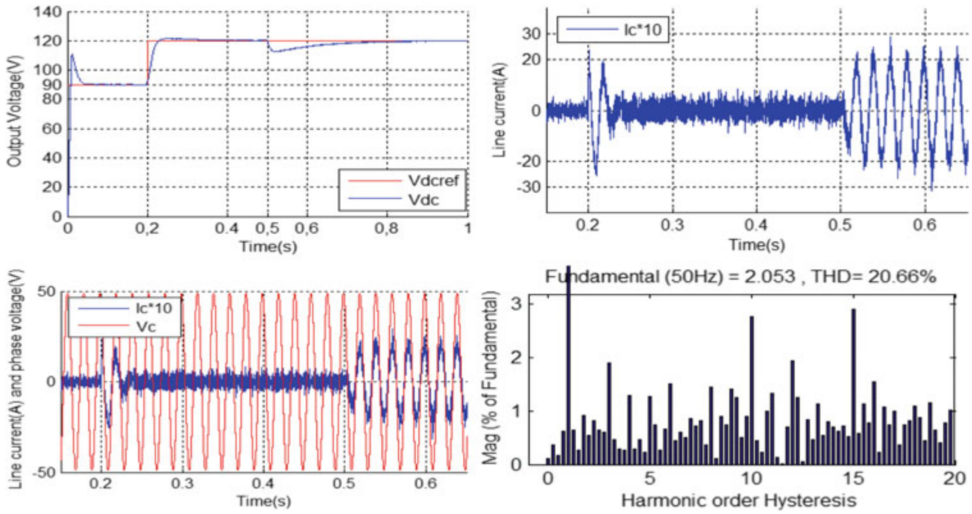

Fig. 6 Simulation results of the hysteresis control

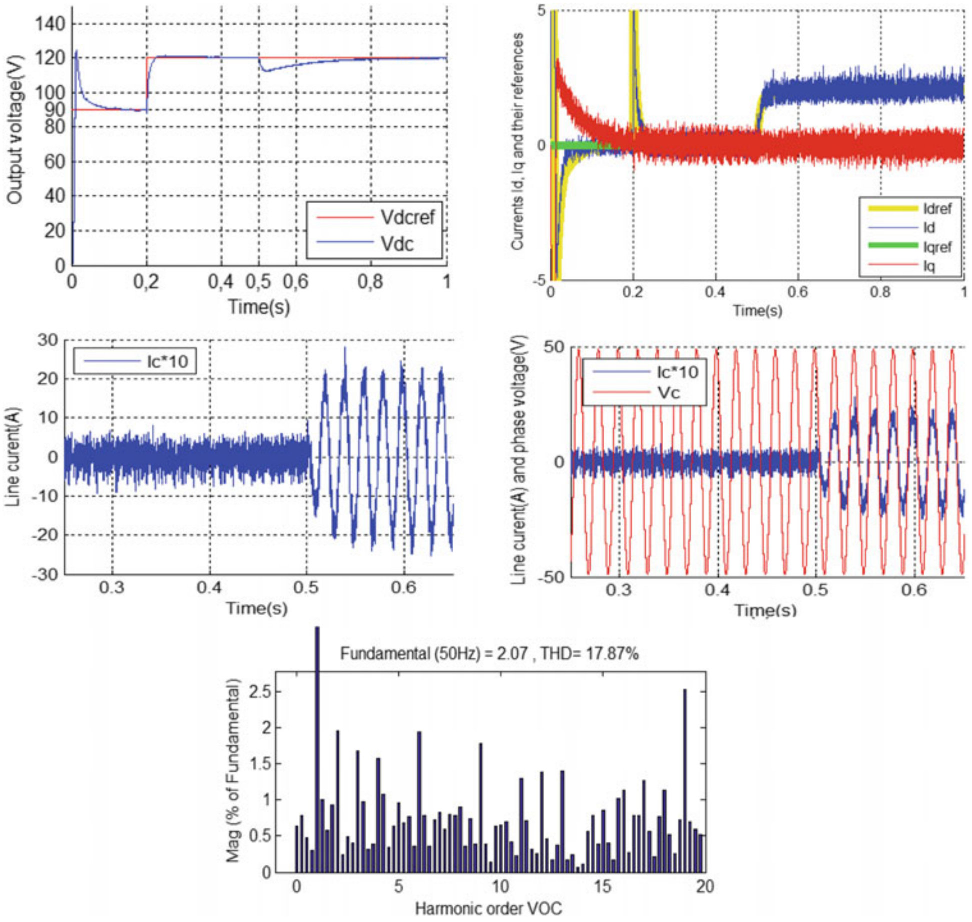

Fig. 7 Simulation results of the VOC

transistor (IGBT) rectifier is used to supply a DC resistive electrical load. A DS1104 digital signal processing (DSP) card is used to carry out the real-time algorithms, and this system is based on PowerPC 603e microprocessor (main processor) running at 250 MHz (CPU clock) on which the different control strategies were implemented and TMS320F240 DSP of Texas Instruments running at 20 MHz.

4.3 Interpreting Results

Figures 6, 7, 8, 10, and 11 give the simulation and experimental results of the hysteresis control, VOC, and DPC, respectively, during the variation of the reference voltage (90–120 V) and change of load resistance.

The simulation and experimental results for $0 < t < 8$ show the wavelength during the variation of the output voltage, which produces an increase, during a small time, in reference currents, while the voltage follows the reference and the line current is sinusoidal.

The simulation results for $4 < t < 5$ represent the robustness of the rectifier during the variation of a resistive load. The voltage follows the reference with a slight overtaking in the transitional regime. The line current is in phase with the line voltage, which results in a unity power factor.

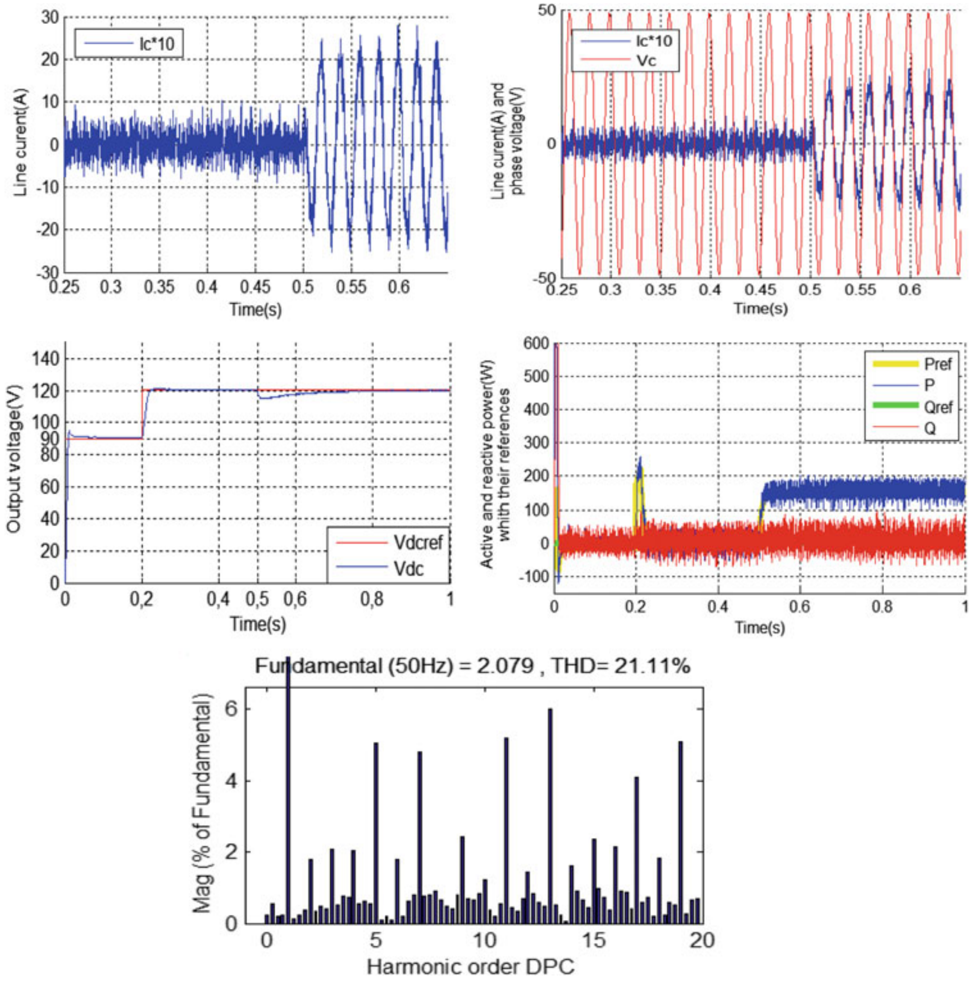

Fig. 8 Simulation results of the DPC

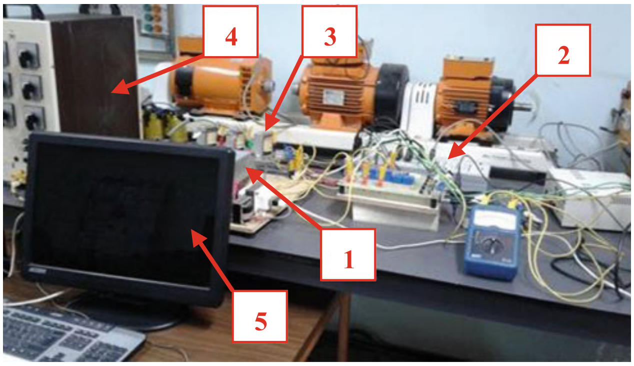

Fig. 9 Different parts of experimental test bench and its DSPACE system control. With: 1: PWM rectifier, 2: DSPACE I/O connectors, 3: interconnecting reactance, 5: resistive load, 6: PC monitors showing real-time implementation control algorithm

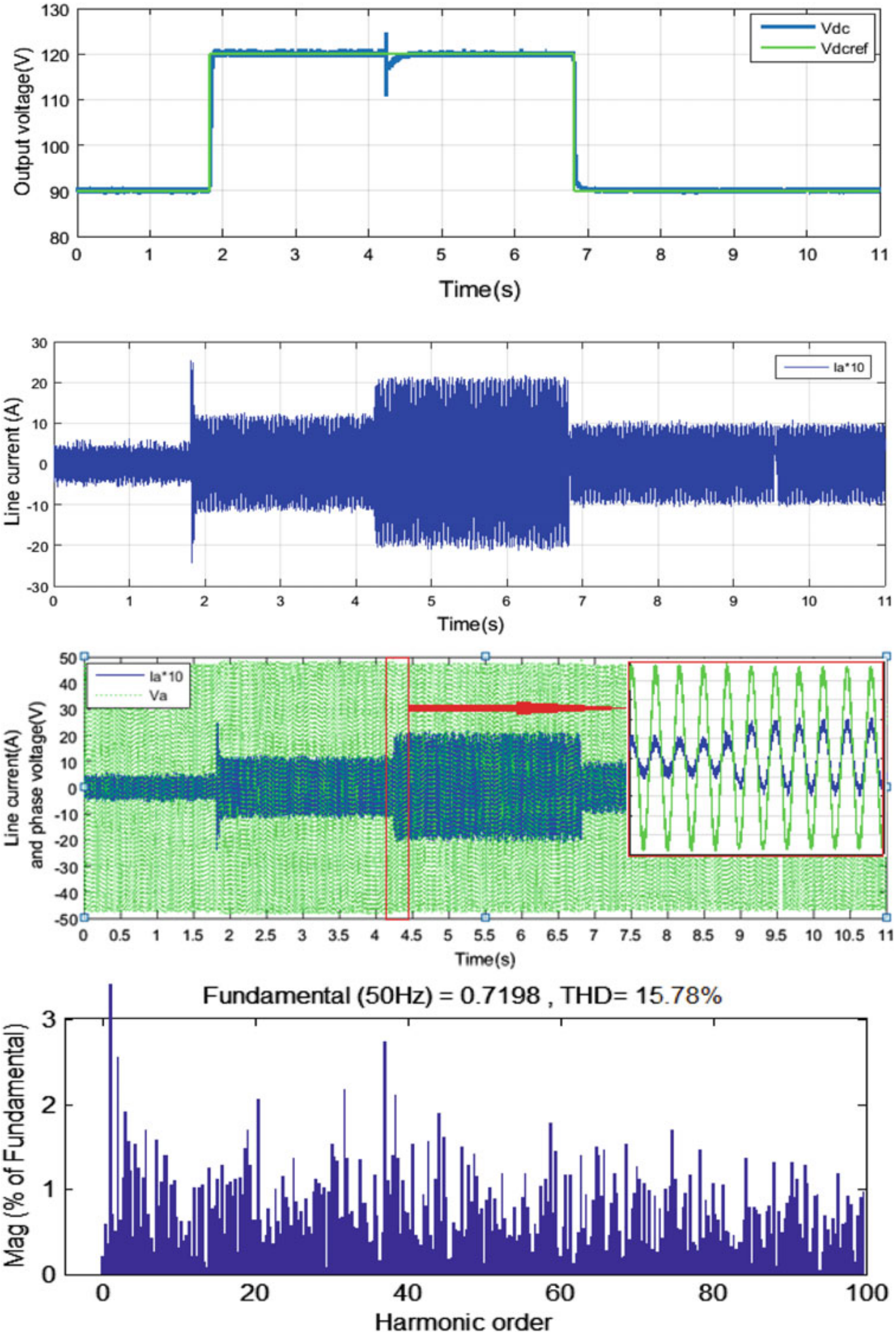

Fig. 10 Experimental results of the hysteresis control

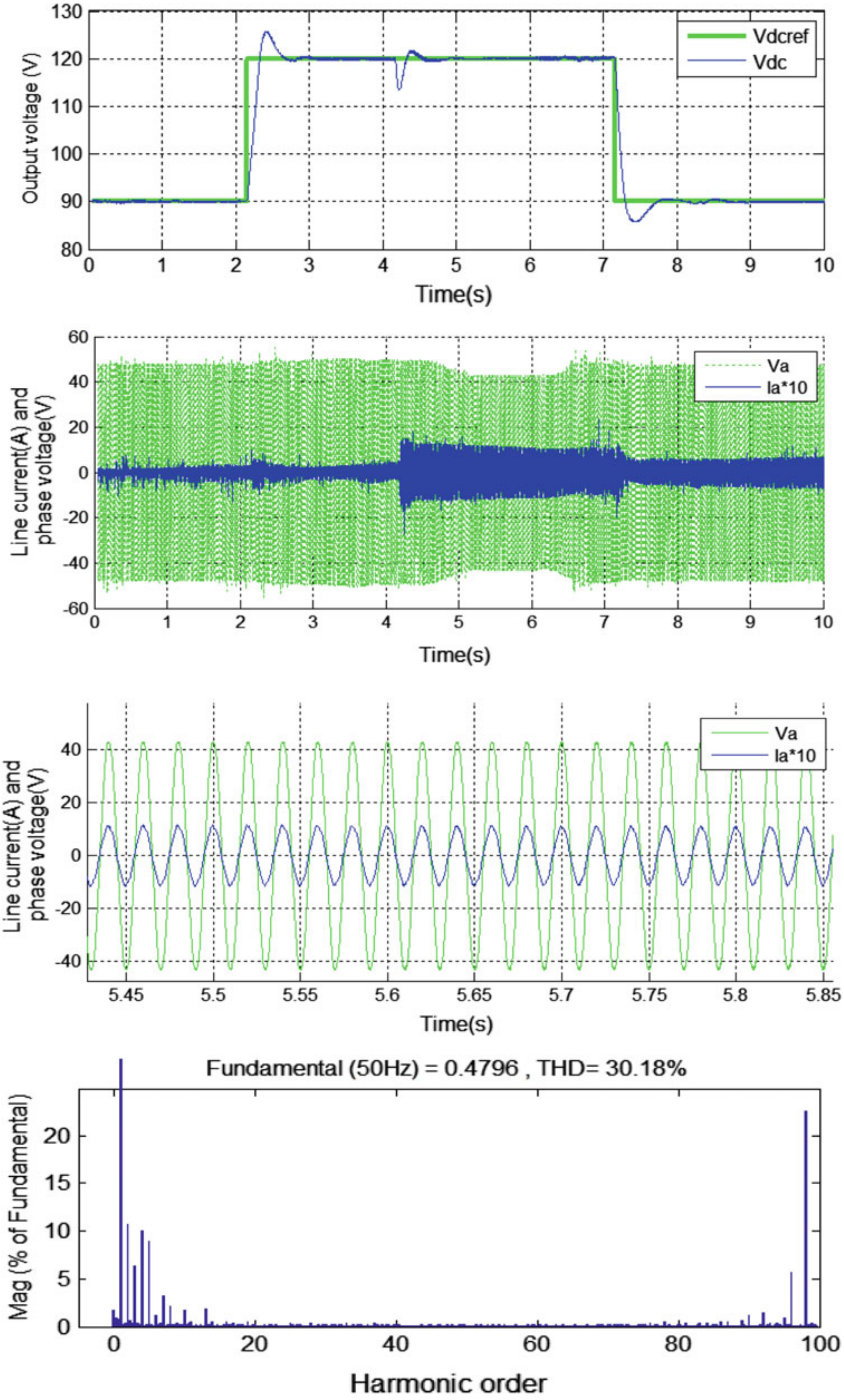
Fundamental (50Hz) = 0.4796 , THD= 30.18%

Fig. 11 Experimental results of the VOC control

5 Conclusion

In this chapter, a simulation study and experimental validation of different control strategies of unit power factor three-phase PWM rectifier were described.

The first method is hysteresis current control which has a series of advantages such as quick response, strong internal current limiting, and strong stability. But it presents some disadvantages, indeed, the hysteresis corrector produces a variable switching frequency, on the other hand, this method requires three or two current sensors, and three or two voltage sensors in addition to the DC bus voltage sensor, which makes the installation more expensive.

The second method is VOC strategy, which ensures fast dynamic response, good accuracy, and high static behavior via internal current control loops which use PI anti-windup correctors that properly eliminate static errors.

The third one is switching-table-based direct power control (DPC), where modulator and PI controllers of internal current control loops have been replaced by switching table and hysteresis controllers, respectively. However, high sampling frequency requirement and variable switching frequency make difficulties in hardware implementation.

FFT analysis of simulation and experimental results of these control strategies show that the VOC control has a better steady-state response than the others control strategies.

References

Abdeldjalil, D., & Messaoud, H. (2015). *Analysis of different converters used in wind energy conversion system*. IEEE. https://doi.org/10.1109/irsec.2014.7059815.

Abdelouahab, B., Jean-Paul, G., & Fateh, K. (2010). Predictive direct power control of three-phase pulse width modulation (PWM) rectifier using space-vector modulation (SVM). *IEEE Transactions on Power Electronics, 25*(1).

Ben Saïd, M., et al. (2012*). Full system on programmable chip solution for DPC control of three phase PWM boost rectifier*. IEEE. https://doi.org/10.1109/iecon.2012.6389408.

Ben Salem, K., & Yahia, K. (2014). *Modélisation et simulation d'un convertisseur AC/DC triphasé. Memory*. Université d'EL-Oued.

Boulahia, A. (2009). *Etude des Convertisseurs Statiques destinés à la Qualité de l'Energie Electrique. Memory.* University of Constantine.

Djeriri, Y., et al. (2014). A comparative study between field oriented control strategy and direct power control strategy for DFIG. *Journal of Electrical Engineering, 14*(2), 169–178.

Hakan, A., Fatih, K., Ahmet, G., Ceyhun, Y., & Mustafa, S. (2016). Improved control configuration of PWM rectifiers based on neuro-fuzzy controller. *SpringerPlus, 5,* 1142. https://doi.org/10.1186/s40064-016-2781-5.

Harshada, C. B. (2015). Review of control techniques of three phase boost type PWM rectifiers. *IJSR*, 2319–7064.

Hassaoui, N., Tlemcani, A., & Sebaa, K. (2013). *DPC and VFOC of PWM rectifier using fuzzy type-2*. IEEE. https://doi.org/10.1109/icosc.2013.6750829.

Kendouli, F., Nabti, K., Abed, K., & Benalla, H. (2011). Modélisation, simulation et contrôle d'une turbine éolienne à vitesse variable basée sur la génératrice asynchrone à double alimentation. *Revue des Energies Renouvelables, 14*(1), 109–120.

Ke-xin, W., & Shui-ming, W. (2008). *Modeling and simulation of three-phase voltage source PWM rectifier*. IEEE. https://doi.org/10.1109/icacte.2008.36.

Malinowski, M., Kazmierkowski, M. P., & Trzynadlowski, A. (2003). Review and comparative study of control techniques for three-phase PWM rectifiers. *Mathematics and Computers in Simulation, 63,* 349–361.

Marian, P., Krishnan, R., & Frede, B. (2002). *Control in power electronics selected problems*. Elsevier.

Minglian, Z., Ruiqiang, L., Enyong, H., Chunhua, X., & Xuefeng, Y. (2011). *Research on direct power control strategy*. IEEE. https://doi.org/10.1109/aimsec.2011.6010838.

Tahiri, F. E, Chikh, K., El Afia, A., Lamterkati, J., & Khafallah, M. (2017). *Simulation and experimental validation of VOC and hysteresis control strategies of unit power factor three-phase PWM rectifier*. IEEE. https://doi.org/10.1109/eitech.2017.8255238.

Tiwari A. N, Agawal, P., & Srivastava, S. P. (2003) Modified hysteresis controlled PWM rectifier. IEE *Proceedings - Electric Power Applications*, *150*(4).

Xiaohong, W., Xiaoming, P., Chunbo, Z., & Lianfang, T. (2010). *A power control strategy for PWM rectifier under unbalanced input voltage.* IEEE. https://doi.org/10.1109/apped.2010.8.

Xue, M., & He, M. (2013). Control of unit power factor PWM rectifier. *IJEPE, 5,* 121–124.

Fatima-Ezzahra Tahiri was born in Morocco in 1992. She received the engineer's degree in Electrical systems engineering from the National Higher School of Electricity and Mechanics (ENSEM) in 2014, Casablanca, Morocco. She prepares, currently, a Doctorate Thesis in energy and electrical systems laboratory at ENSEM.

Khalid Chikh was born in Morocco in 1982. He received the Master's degree in electrical engineering from the Faculty of Science Semlalia in 2007, Marrakech, Morocco; and the Ph.D. degree in electrical engineering in 2013 from the National Higher School of Electricity and Mechanics (ENSEM), Hassan II University, Casablanca, Morocco. Since February 2014, he has been with Sultan Moulay Slimane University-EST, Morocco, where he is currently professor at the Electrical Engineering Department. His current research interests are in the application of power electronics converters, motor drives, intelligent and digital control using the DSP implementations, renewable energy and energy storage.

Mohamed Khafallah was born in Morocco in 1964. He received B.Sc., M.Sc. and Doctorate degrees from Hassan II University, Casablanca II, in 1989, 1991 and 1995 respectively, all in Electrical Engineering. In 1995 he joined the Department of Electrical Engineering at the National Higher School of Electricity and Mechanics (ENSEM), Hassan II University, Casablanca. His current research interests are in the application of power electronics converts and motor drives.

Aziz El Afia received B.Sc., M. Sc. degrees from the University of Hassan II, Casablanca II in 1990, 1994 respectively and the Ph.D. degree in Electrical Engineering from The Higher National School of Electrical and Mechanical Engineering (ENSEM) of the University of Hassan II, Casablanca. Since 2011 he has been working as a Professor of Power Electronic at the Higher National School of Arts and Crafts of Casablanca (ENSAM). His current research interests are in power electronics converters and control of machines and drives for application from automotive to renewable energy.

Part II

Control Systems

A New Robust Control Based on Active Disturbance Rejection Controller for Speed Sensorless Induction Motor

Chalawane Haitam, Essadki Ahmed, Nasser Tamou,
and Arbaoui Mohammed

Abstract

This paper aims to present a new robust command called active disturbance rejection controller (ADRC) applied to the sensorless induction motor and introduces the problem of the parameters, which significantly deteriorate the performance of the control, this variation introduces an important role in the loss of dynamic performance in an undesirable coupling between flux and torque of the machine. This paper offers a new scheme for estimation of induction motor speed using αβ representation of the model in the stationary reference frame and measurements of accessible motor variables only (currents, voltages, and speed). A second-order of MRAS-based sliding mode estimator is designed for speed estimation. The proposed schemes are implemented using MATLAB simulation, which improve the system robustness against motor parameter variations and increase the performance of the speed loop controller.

Keywords

Induction motor • Active disturbance rejection control • Sliding mode model reference adaptive control observer • Indirect rotor-field-oriented control

1 Introduction

Speed sensorless indirect rotor-field-oriented control is the most used method to command the induction motor drive (Zhao et al. 2016), and was developed for the aim of decoupling the torque and the flux. This decoupling permits for a very fast response of torque. The principle of field-oriented control is to perform the dynamic model of the induction machine in the rotating reference with the rotor flux (Morey et al. 2016; Pu et al. 2016).

This work introduces a novel command called active disturbance rejection controller (ADRC) into the control of induction motors. The ADRC was introduced by Han in 1998 (Huang et al. 2004). The ADRC is a nonlinear controller for an unsettled system, it estimates and compensates the external disturbances and parameter changes, and accordingly the accurate model of the plant is not in demand. It means that the concept of ADRC is independent of the controlled system model and its parameters (Chakib et al. 2016). The major element of ADRC is the extended state observer (ESO), which is based on the approach of generalized functions and generalized derivatives. Using the extended state observer, the ADRC can achieve exact decoupling of induction motors. Afterward, the effect of external disturbances and parameter variations could then be estimated and compensated (Tan and Caifen 2016).

The work in Orr et al. 2016 presents three sliding mode MRAS speed estimators—these employ the rotor flux approach and are based on the motor equations in the stationary reference frame. One of the newness is that the signal fed into the adaptive model is a discontinuous (sliding mode) function. As a result of this, the system reacts very fast. The estimated speed is obtained by filtering this high-frequency switching signal, it has either high ripple or wide delay, its quality can be less than intended (Goyal et al. 2016).

The SM MRAS method implemented in this paper is an upgrade of the speed estimator in Comanescu 2016. A second-order sliding mode estimator design is used and it is

C. Haitam (✉) · E. Ahmed · N. Tamou · A. Mohammed
Mohammed V University, ENSIAS, Rabat, Morocco
e-mail: chalawanehaitam@gmail.com

E. Ahmed
e-mail: ahmed.essadki1@gmail.com

N. Tamou
e-mail: t.nasser@ensias.ma

A. Mohammed
e-mail: Mohammed.arbaoui@um5s.net.ma

S. El Hani and M. Essaaidi (eds.), *Recent Advances in Electrical and Information Technologies for Sustainable Development*,
Advances in Science, Technology & Innovation, https://doi.org/10.1007/978-3-030-05276-8_5

presented that this reduces the requirement for filtering. The resulting speed estimate is excellent and can be used directly in the control implementation (Comanescu and Xu 2016).

2 Induction Motor Model

The induction motor model in the stationary reference frame is presented in (1) and it consists of the equations of the currents and fluxes (Pantea et al. 2016).

$$\begin{cases} \dfrac{d\psi_\alpha}{dt} = -\eta\psi_\alpha - p\omega_r\psi_\beta + \eta M i_\alpha \\ \dfrac{d\psi_\beta}{dt} = p\omega_r\psi_\alpha - \eta\psi_\beta + \eta M i_\beta \\ \dfrac{di_\alpha}{dt} = \eta\beta\psi_\alpha + p\omega_r\beta\psi_\beta - \gamma i_\alpha + \dfrac{1}{\sigma L_s} v_\alpha \\ \dfrac{di_\beta}{dt} = -p\omega_r\beta\psi_\alpha + \eta\beta\psi_\beta - \gamma i_\beta + \dfrac{1}{\sigma L_s} v_\beta \end{cases} \tag{1}$$

The parameters of the induction motor are defined as presented in the following expressions:

$$\begin{cases} \sigma = 1 - \frac{M^2}{L_s L_r} \\ \beta = \frac{M}{\sigma L_s L_r} \\ \gamma = \frac{1}{\sigma L_s}\left(\frac{M^2}{L_r^2} R_r + R_s\right) \\ \eta = \frac{R_r}{L_r} \end{cases} \tag{2}$$

In a typical sensorless IRFOC implementation, the fluxes and speed require to be estimated. The fluxes are employed to calculate the field orientation angle of the IM, and the speed signal is required for feedback (Teja et al. 2016).

Indirect rotor-field-oriented control was developed for the aim of decoupling the flux and the torque (Chalawane et al. 2016). This decoupling permits for a good performance of torque. The principle of field-oriented control is to introduce the dynamic model of the induction machine in the rotating reference with the rotor flux (Figs. 1, 2).

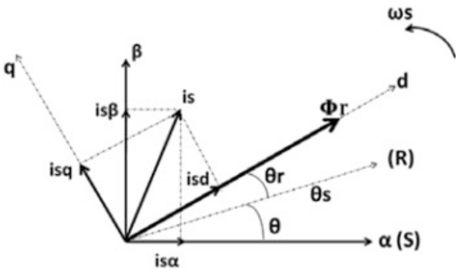

Fig. 1 Illustration of the rotor flux orientation

Nomenclature	
ω_r	Rotor speed
p	Number of pole pairs
η	Inverse of rotor time constant
M, L_s, L_r	Magnetizing, stator, and rotor inductances
R_s, R_r	Stator and rotor resistances
$x, \hat{x}$	Real and estimated values of x
i_α, i_β	Currents in stationary reference frame
v_α, v_β	Voltages in stationary reference frame
$\psi_{r\alpha}, \psi_{r\beta}$	Rotor fluxes in stationary reference frame
$\psi_{s\alpha}, \psi_{s\beta}$	Stator fluxes in stationary reference frame

3 ADRC Implementation for Stator Current Control

The active disturbance rejection control was introduced by Han (Huang et al. 2004), the design of ADRC is widely independent of the controlled system model and its parameters. Hence, this controller has the advantage of good

Fig. 2 Block diagram of IRFOC for induction motor

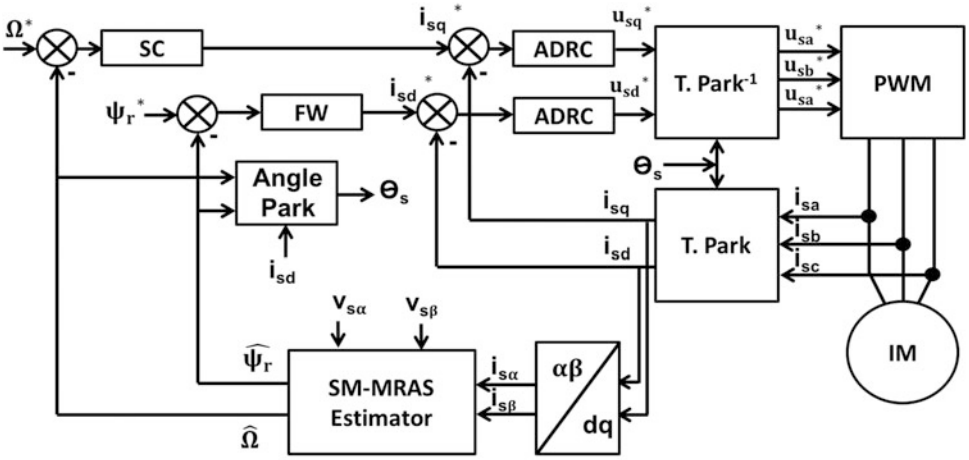

SC: Speed Controller **FW:** Field Weakening flexibility and robustness. The brief description of the ADRC is presented in the following expression (Patel and Zhao 2010; Alonge et al. 2017):

$$\ddot{y} = f(t, y, \dot{y}, w) + bu \tag{3}$$

with $x_3 = f$ as an augmented state, its state space form is

$$\begin{cases} \dot{x} = Ax + Bu + Eh \\ y = Cx \end{cases} \tag{4}$$

where u is input to be controlled, y is the output, and w is the disturbance.

$$A = [0\,1\,0;\ 0\,0\,1;\ 0\,0\,0], \quad B[0;\ b_0;\ 0], \quad C[1\,0\,0]$$
$$and\, h = f$$

Let $z_1, z_2,\ and\, z_3$ be the estimates of $y, \dot{y},\ and f$, respectively, the extended state observer corresponding to (4) can be presented as follows:

$$\begin{cases} \dot{z} = Az + Bu + L(y - \hat{y}) \\ \hat{y} = Cz \end{cases} \tag{5}$$

If the observer can track the system dynamic states fast enough, the error of the estimation can be ignored. This perfectly tuned observer leads to $z_3 \cong f$. Then, with the control law.

$$u = (u_0 - z_3)/b_0 \tag{6}$$

The plant given by (6) minimizes to a double integral plant $\ddot{y} = u_0$ that can be easily controlled with PD controller (Zhao et al. 2016),

$$u_0 = k_p(r - z_1) - k_p z_2 \tag{7}$$

where r is the reference input, k_p and k_d are the PD gains, respectively. Figure 3 gives the implementation information of the ADRC for i_{qs} with the ADRC controller. A similar controller can be applied to i_{ds}.

In this case, the stator currents are rearranged to be written in the form:

$$\frac{di_{sd}}{dt} = -\left(\frac{R_s}{\sigma L_s}\right) i_{sd} - \left(\frac{M}{\sigma L_r L_s}\right)\frac{d\psi_r}{dt} + \left(\frac{1}{\sigma L_s}\right) U_{sd} \tag{8}$$

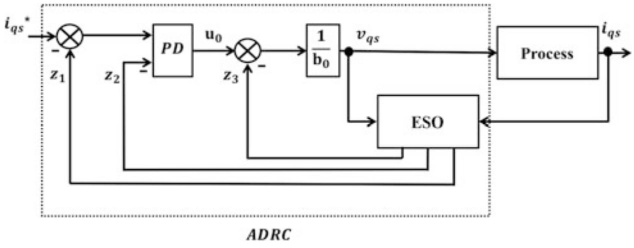

Fig. 3 Topology of ADRC controller

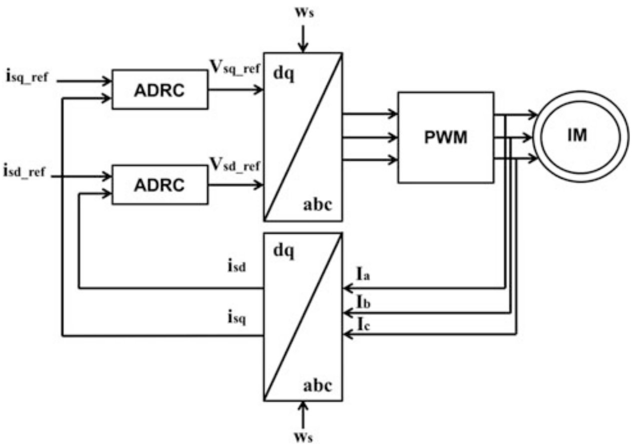

Fig. 4 Control system of stator currents using ADRC topology

$$\frac{di_{sq}}{dt} = -\left(\frac{R_s}{\sigma L_s}\right) i_{sq} - \left(\frac{\omega_s M}{\sigma L_r L_s}\right)\psi_r + \left(\frac{1}{\sigma L_s}\right) U_{sq} \tag{9}$$

In the canonical model of ADRC:

$$\begin{cases} \dfrac{di_{sd}}{dt} = f_d(i_{sd}, d, t) + b_0 u(t) \\ \dfrac{di_{sq}}{dt} = f_q(i_{sq}, d, t) + b_0 u(t) \end{cases} \tag{10}$$

or

$$\begin{cases} f_d = -\left(\dfrac{R_s}{\sigma L_s}\right) i_{sd} - \left(\dfrac{M}{\sigma L_r L_s}\right)\dfrac{d\psi_r}{dt} + \left(\dfrac{1}{\sigma L_s} - b_0\right) U_{sd} \\ u = U_{sd} \quad b_0 = \frac{1}{\sigma L_s} \end{cases} \tag{11}$$

$$\begin{cases} f_q = -\left(\dfrac{R_s}{\sigma L_s}\right) i_{sq} - \left(\dfrac{\omega_s M}{\sigma L_r L_s}\right)\psi_r + \left(\dfrac{1}{\sigma L_s} - b_0\right) U_{sq} \\ u = U_{sq} \quad b_0 = \frac{1}{\sigma L_s} \end{cases} \tag{12}$$

f_d and f_q are the total disturbances, respectively, affecting the stator currents i_{sd} and $i_{sq} \cdot u = U_{sd}$ and $u = U_{sq}$ are, respectively, the control inputs of the currents loops i_{sd} and $i_{sq} \cdot b_0$ which are the known part of the system parameters. By choosing an adequate response time, we can easily define the following parameters k_p, β_1 and β_2 of the ADRC controllers. Finally, the stator currents follow, respectively, their references i_{sd_ref} and i_{sq_ref} (Fig. 4).

4 Sliding Mode Observer for Fluxes and Speed

The adjustable model is designed using the rotor equations, and this observer estimates both the fluxes and the speed. The speed is a discontinuous (sliding mode) term, in the initial development, this is designed as a first-order SM term (Ahmed 2016; Zhao et al. 2014; Karlovský et al. 2016).

The equations of the observer are formed as follows:

$$\begin{cases} \dfrac{d\hat{\psi}_\alpha}{dt} = -\eta\hat{\psi}_\alpha - p\hat{\omega}_r\hat{\psi}_\beta + \eta M i_\alpha \\ \dfrac{d\hat{\psi}_\beta}{dt} = p\hat{\omega}_r\hat{\psi}_\alpha - \eta\hat{\psi}_\beta + \eta M i_\beta \end{cases} \tag{13}$$

$$\begin{cases} \hat{\omega}_r = M.sign(s) \\ s = \psi_\beta\hat{\psi}_\alpha - \psi_\alpha\hat{\psi}_\beta \end{cases} \tag{14}$$

The estimated speed $\hat{\omega}_r$ is discontinuous and is given by (14). Manifold s is constructed as a combination of the reference fluxes ψ_α,ψ_β and the estimated fluxes $\hat{\psi}_\alpha$, $\hat{\psi}_\beta$.

In sliding mode technique, the manifold s is differentiated, the result is presented in the following form:

$$\begin{aligned} \dot{s} = p\omega_r\left(\psi_\alpha\hat{\psi}_\alpha + \psi_\beta\hat{\psi}_\beta\right) + 2\eta\left(\psi_\alpha\hat{\psi}_\beta - \hat{\psi}_\alpha\psi_\beta\right) \\ + \eta M\left[\left(\hat{\psi}_\alpha - \psi_\alpha\right)i_\beta - \left(\hat{\psi}_\beta - \psi_\beta\right)i_\alpha\right] - p\left(\hat{\psi}_\alpha\psi_\alpha + \hat{\psi}_\beta\psi_\beta\right)\hat{\omega}_r \end{aligned} \tag{15}$$

The last term in (15) is very significant. With the assumption of that the adjustable model converges and $\hat{\psi}_\alpha \to \psi_\alpha$, $\hat{\psi}_\beta \to \psi_\beta$, the coefficient in front of $\hat{\omega}_r$ is completely different from zero and positive $p\left(\hat{\psi}_\alpha\psi_\alpha + \hat{\psi}_\beta\psi_\beta\right) = p\psi^2 > 0$. Thus, (15) can be rewritten as

$$\dot{s} = f - p\psi^2 M.sign(s) \tag{16}$$

Based on (16), if the design gain M is chosen high enough, the manifold s and its derivative $\dot{s}$ will have different signs; as a result of this, the manifold tends to zero and sliding mode introduces oneself. With $s = 0$, it can equally be assumed that $\dot{s} = 0$. The equivalent control of $\hat{\omega}_r$ represents the low-frequency component of the switching term $M.sign(s)$ (Utkin et al. 1999; Yan and Utkin 2002). This is

$$\omega_{r,eq} = \omega_r + \frac{\eta M\left[\left(\hat{\psi}_\alpha - \psi_\alpha\right)i_\beta - \left(\hat{\psi}_\beta - \psi_\beta\right)i_\alpha\right] + 2\eta\left(\hat{\psi}_\beta\psi_\alpha - \hat{\psi}_\alpha\psi_\beta\right)}{\hat{\psi}_\alpha\psi_\alpha + \hat{\psi}_\beta\psi_\beta} \tag{17}$$

If the adjustable model observer converges, the numerator of the second term shown in (17) is equal to zero. Thus, it is obvious that $\omega_{r,eq} \to \omega_r$. In a practical implementation, $\omega_{r,eq}$ is obtained by low-pass filtering the switching term $M.sign(s)$ and represents the estimated speed of the observer. However, while the first-order SM given by (14) is used, it is typical to obtain the estimated speed with important ripple; the use of weighty filtering is gainful but it deteriorates the transient of the estimated speed as increasing the delay.

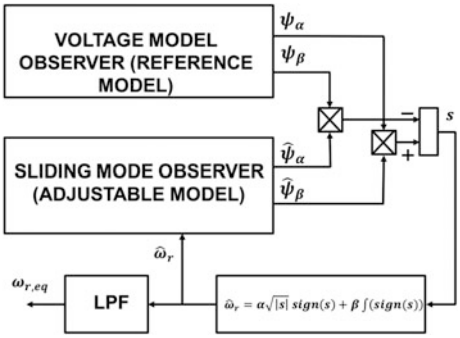

Fig. 5 Block diagram of the second-order SM MRAS observer

The quality of the estimated speed can be widely enhanced using the second-order sliding mode strategy. With this expression, the switching term $\hat{\omega}_r$ is redesigned as

$$\hat{\omega}_r = \alpha\sqrt{|s|}sign(s) + \beta\int(sign(s)) \tag{18}$$

In (10), α and β are constant design parameters and strictly positive:$\alpha > 0, \beta > 0$. Simulations will demonstrate that the obtained estimated speed from the second-order SM approach is of high quality, it is smooth, has low ripple, and it confirms closely the real speed (Zorgani et al. 2016).

Figure 5 shows a block diagram of the proposed second-order SM MRAS method (Fig. 6).

5 Simulation Results and Discussions

The theoretical schemes described in this work have been studied, simulated, and implemented in order to validate the control strategy and then evaluate the performance of the system. For the simulation results used in this paper, the parameter values of the system under study are summarized in Table 1. The system robustness, stability, and parameter sensitivity have been verified using computer simulation (Figs. 9, 10, and 12).

In order to verify the robustness of proposed active disturbance rejection controller, the simulation work has been accomplished by varying the stator and rotor resistances. As shown in the previous figures, it is obviously present that the proposed ADR controller is robust and efficient under disturbance variations and parameters.

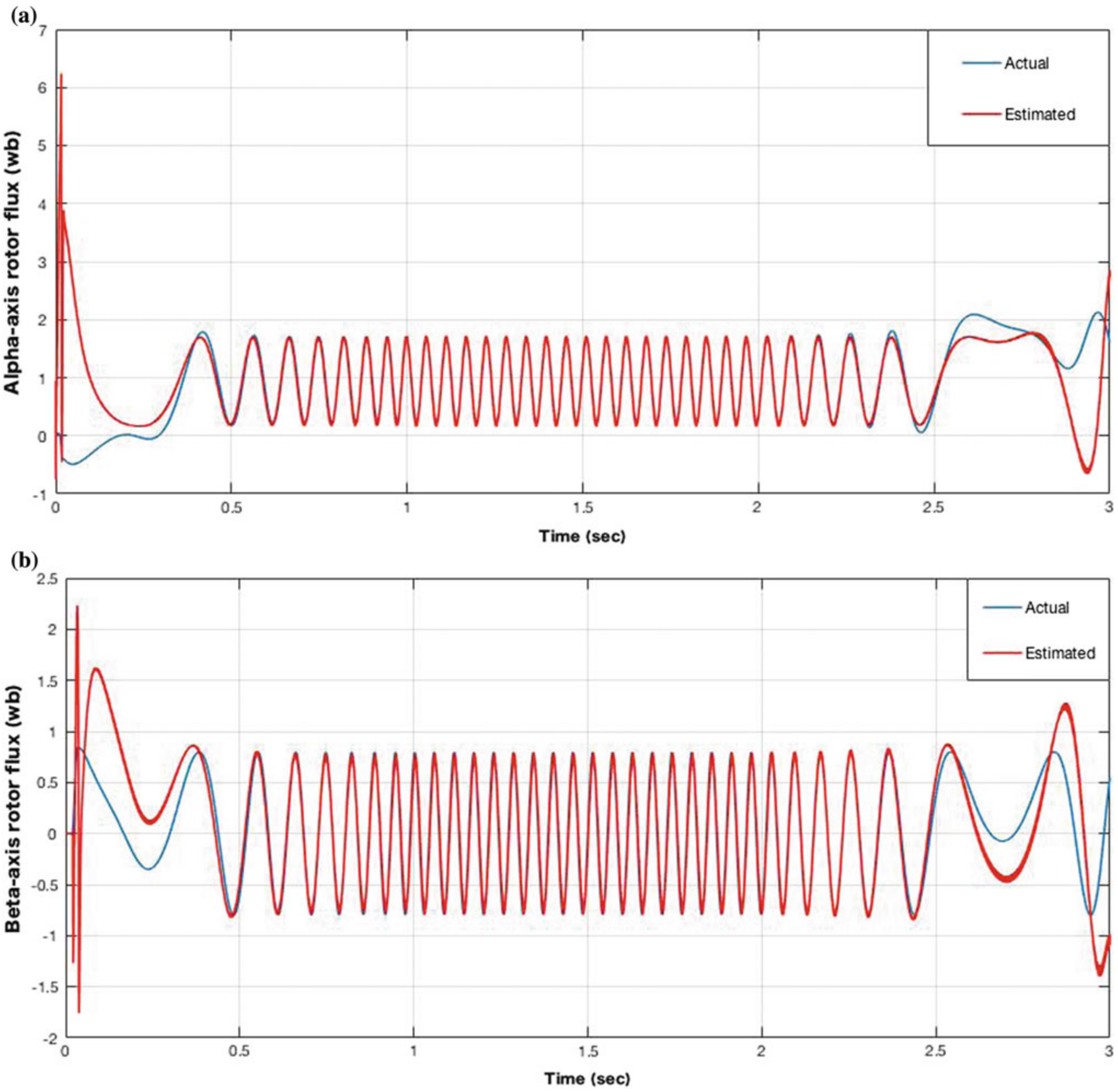

Fig. 6 Rotor fluxes estimation performance of SM MRAS **a** Alpha-axis rotor flux **b** Beta-axis rotor flux

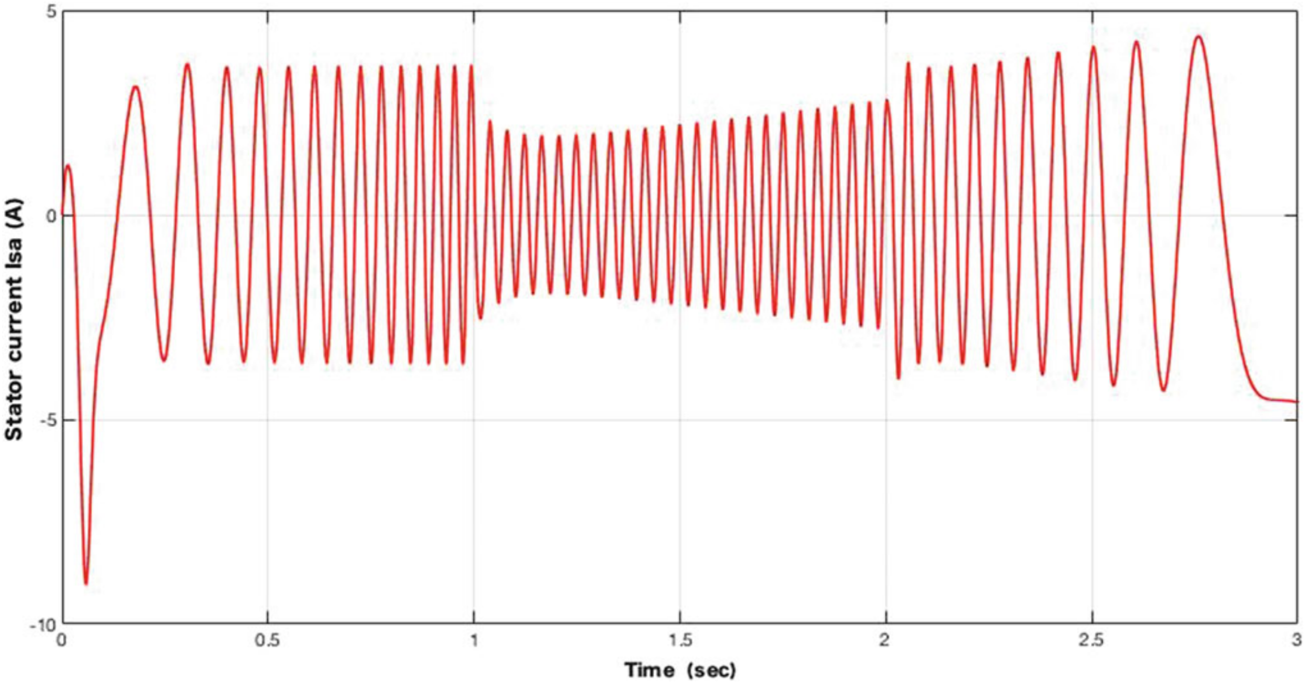

Fig. 7 Stator current Isa of IM using ADRC

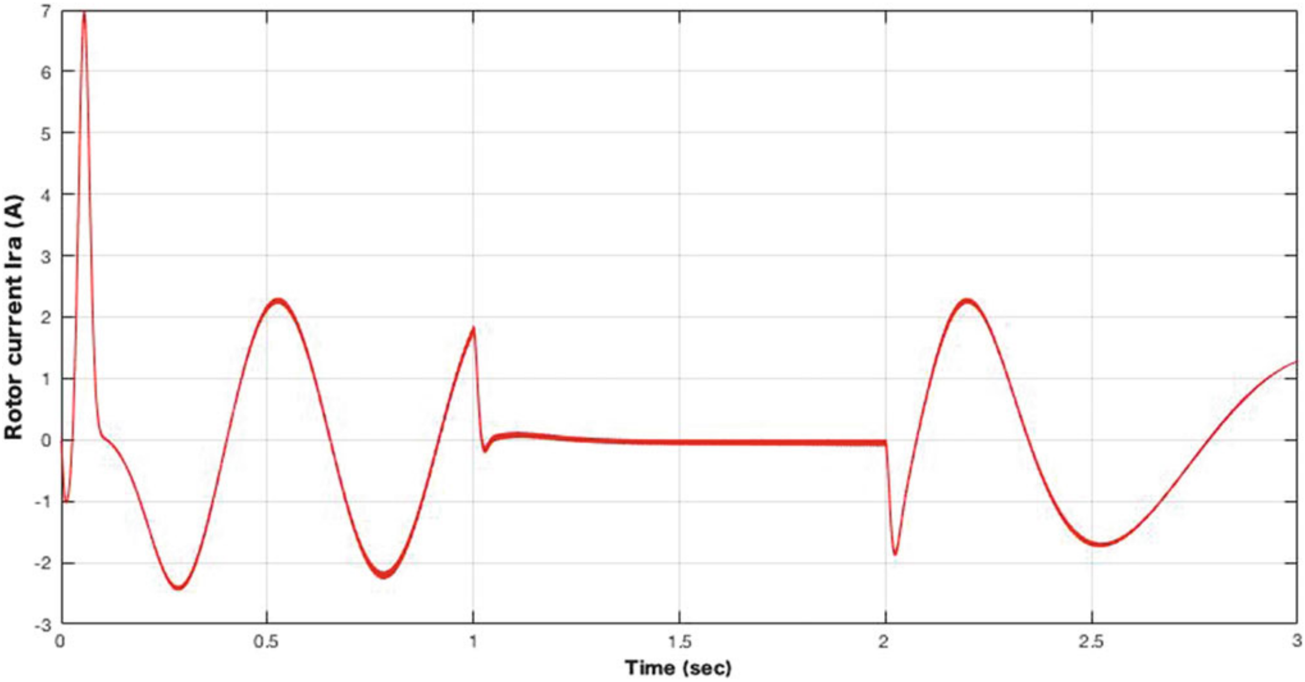

Fig. 8 Rotor current Ira of IM using ADRC

Table 1 Induction motor parameters

Symbol	Quantity	Numerical application
U	Power supply voltage	380 V
f	Current stator frequency	50 Hz
p	Number of pole pairs	2
Rs	Stator resistance	4.85 Ω
Rr	Rotor resistance	3.805 Ω
Ls	Inductance stator	0.274 H
Lr	Inductance rotor	0.274 H
M	Mutual inductance	0.258 H
J	Moment of inertia	0.031 kg.m^2

The speed reference steps up from 0 to 150 rad/s at 1 s, still constant at 150 rad/s until 2 s and steps down to −150 rad/s at 3 s. In Case I of Figs. 7 and 8 that show a sinusoidal state of the stator and rotor currents with a short and acceptable overshoot in the start-up. In Case II of Fig. 11, the actual speed follows the reference speed without overshoot that confirms it converges to the defined reference value.

At last, we can conclude that this control of ADRC is superior to the previous controls introduced in literature as PI, FLC, and NNs while they are not suitable to achieve the desired speed of IM drive without overshoot or steady-state error and not robust under the variation of load torque and parameters.

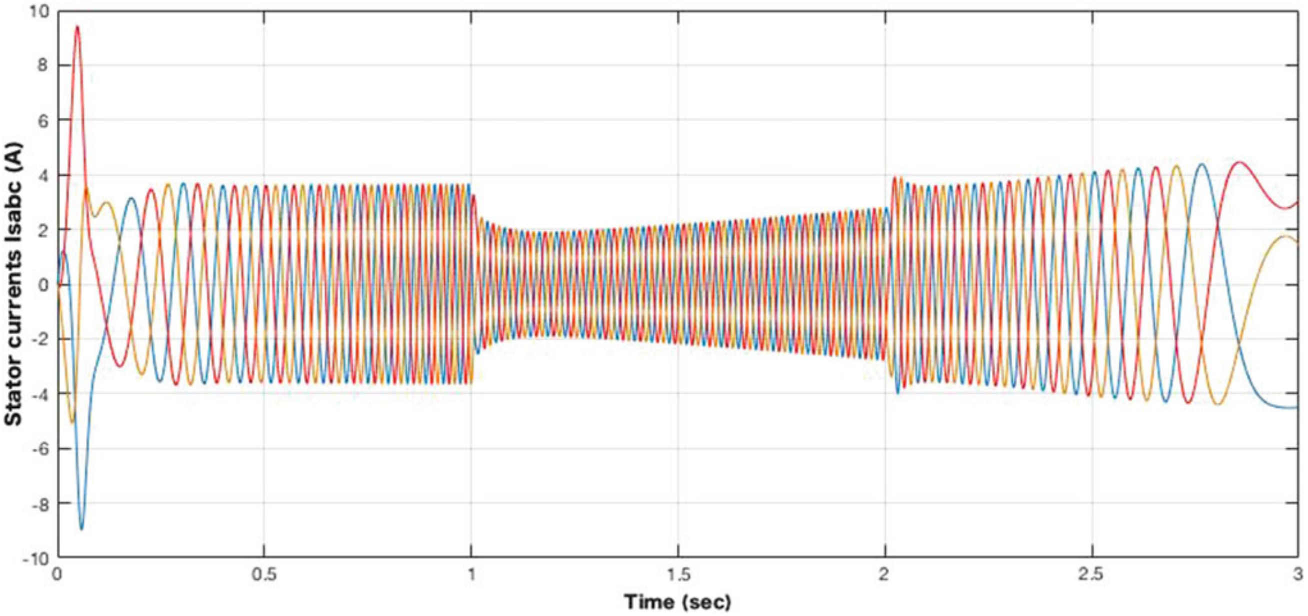

Fig. 9 Stator currents Isabc of IM using ADRC

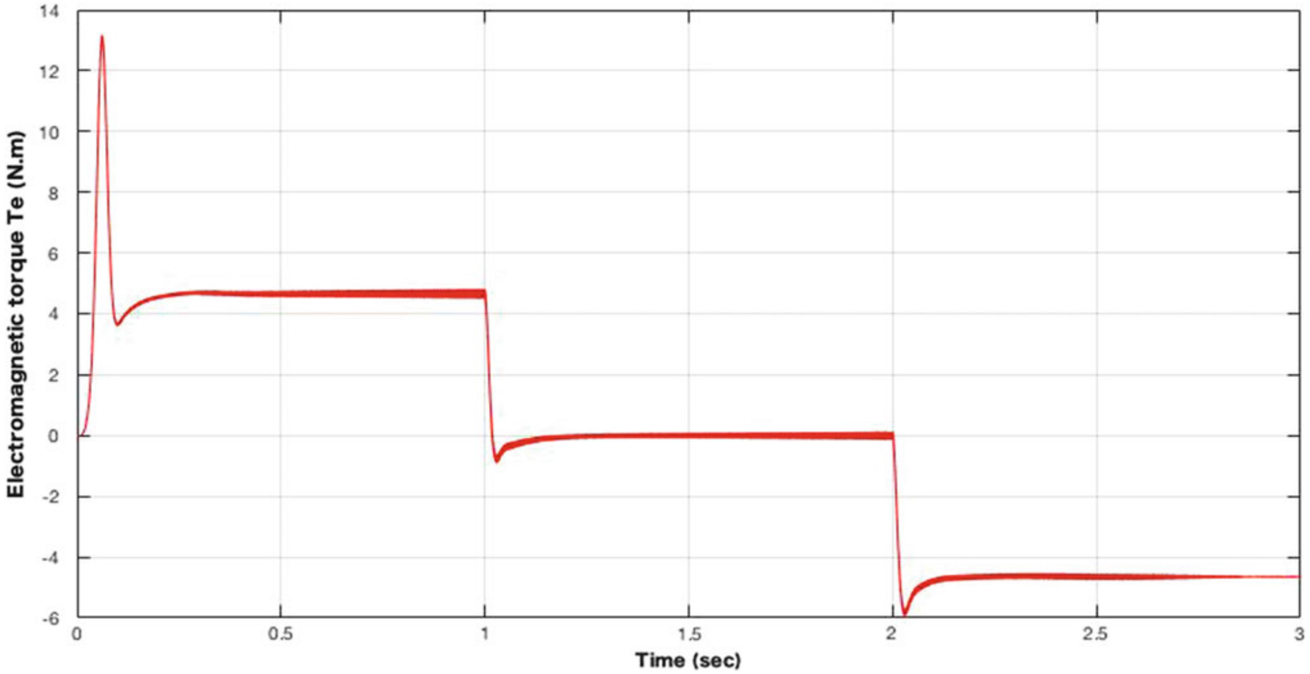

Fig. 10 Electromagnetic torque of IM using ADRC

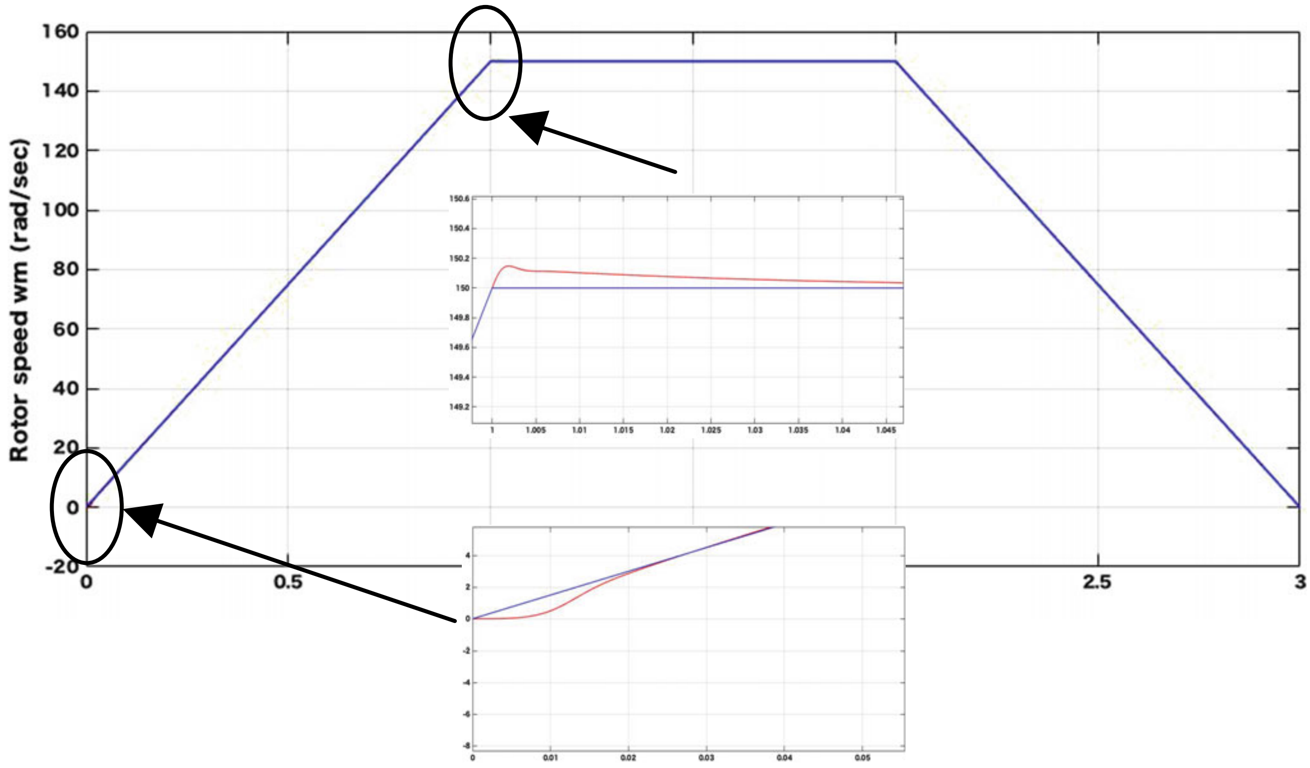

Fig. 11 Rotor speed of IM using ADRC

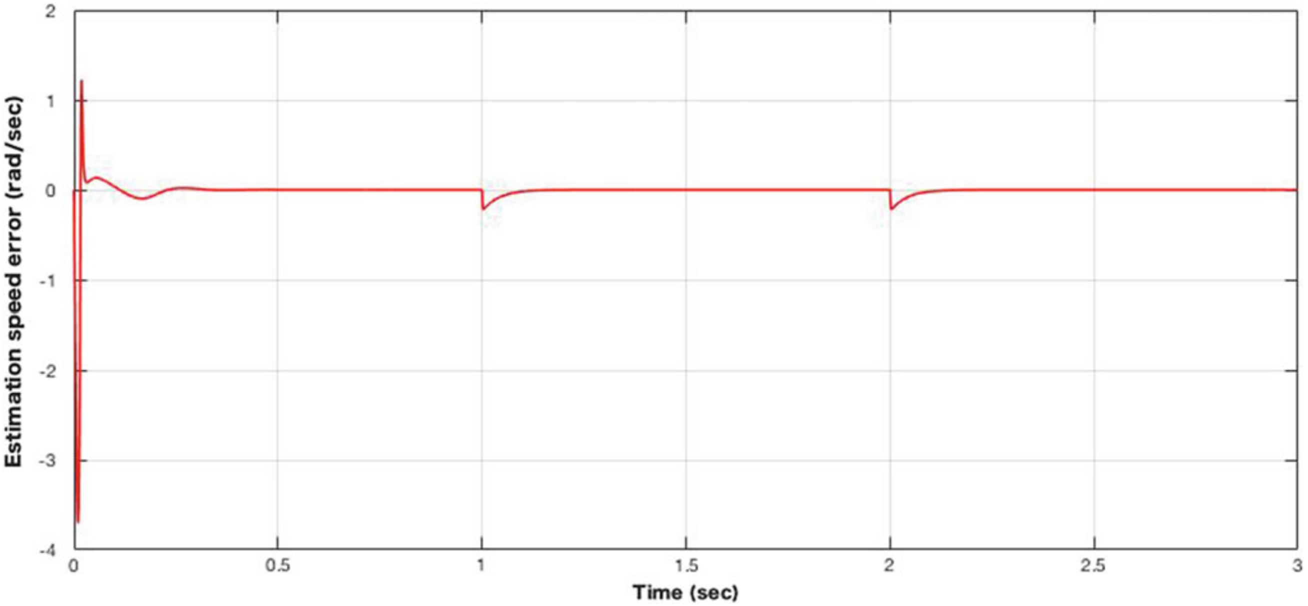

Fig. 12 Rotor speed error of IM using ADRC

6 Conclusion

This article introduces a new speed and flux estimation scheme for high-performance ADRC induction motor drives based on SM MRAS, this speed estimator gives the benefits of vector control without using any shaft encoder. In addition, the implementation of active disturbance rejection control has an advantage that it does not require knowledge of the controlled system model and its parameters as well as presents a high performance in term of various disturbances. The effectiveness and the robustness of the speed sensorless induction motor based on active disturbance rejection control under the variation of internal and external parameters are proven by simulated results using MATLAB/Simulink.

Appendix

ADRC controller parameters:
Stator current controller gain $k_{p-s} = 130$
Stator current parameter $b_{so} = 50$
Observation parameters of the loop current stator:
The direct current gains of stator

$$\beta_{1d} = 900;\ \beta_{2d} = 100$$

The quadrature current gains of stator

$$\beta_{1q} = 180;\ \beta_{2q} = 10^{-3}$$

References

Ahmed, A. H. O. (2016). Speed sensorless vector control of induction motors using rotor flux based model reference adaptive system. *Journal of Engineering and Computer Science*, *17*(1).

Alonge, F., et al. (2017). Robust active disturbance rejection control of induction motor systems based on additional sliding mode component. *IEEE Transactions on Industrial Electronics*.

Chakib, R., Cherkaoui, M., & Essadki, A. (2016). Inertial response used for a short term frequency control for DFIG wind turbine controlled by ADRC. *ARPN Journal of Engineering and Applied Sciences, 11*(5).

Chalawane, H., Essadki, A., & Nasser, T. (2016). MRAS and Luenberger observers using a SIFLC controller in adaptive mechanism based sensorless fuzzy logic control of induction motor. In *2016 International Conference on Electrical and Information Technologies (ICEIT)*. IEEE.

Comanescu, M. (2016). Design of a MRAS-based estimator for the speed and rotor time constant of the induction motor using sliding mode. In *2016 International Symposium on Power Electronics, Electrical Drives, Automation and Motion (SPEEDAM)*. IEEE.

Comanescu, M., & Xu, L. (2016). Sliding mode MRAS speed estimators for sensorless vector control of induction machine. *IEEE Transactions on Industrial Electronics, 53*(1), 146–153.

Goyal, V., Deolia, V. K., & Sharma, T. N. (2016). Neural network based sliding mode control for uncertain discrete-time nonlinear systems with time-varying delay. *International Journal of Computational Intelligence Research, 12*(2), 125–138.

Huang, H., Wu, L., Han, J., Feng, G., & Lin, Y. (2004). A new synthesis method for unit coordinated control system in thermal power plant-ADRC control scheme. In *International Conference on Power System Technology, PowerCon 2004* (Vol. 1, pp. 133–138). IEEE.

Karlovský, P., Linhart, R., & Lettl, J. (2016). Sensorless determination of induction motor drive speed using MRAS method. In *2016 8th International Conference on Electronics, Computers and Artificial Intelligence (ECAI)*. IEEE.

Morey, M. S., Virulkar, V. B., & Dhomane, G. A. (2016). MRAS based speed identification and online updating of rotor time constant for sensorless field oriented controlled induction motor. In *International Conference on Emerging Trends in Electrical Electronics & Sustainable Energy Systems (ICETEESES)*. IEEE.

Orr, J., Murray, B., & Comanescu, M. (2016). Design of a second-order sliding mode MRAS speed estimator for the induction motor drive. In *Power and Energy Conference at Illinois (PECI, 2016 IEEE)*. IEEE.

Pantea, A., et al. (2016). Six-phase induction machine model for electrical fault simulation using the circuit-oriented method. *IEEE Transactions on Industrial Electronics, 63*(1), 494–503.

Patel, D., & Zhao, L. (2010). Active disturbance rejection control of doubly-fed induction generator during voltage dip. In *Proceedings of ESA Annual Meeting on Electrostatics*.

Pu, W. C., et al. (2016) A study about estimator relation analysis based on sensorless rotor-field oriented vector control. In *2016 International Symposium on Computer, Consumer and Control (IS3C)*. IEEE.

Tan, W., & Caifen, F. (2016). Linear active disturbance-rejection control: Analysis and tuning via IMC. *IEEE Transactions on Industrial Electronics, 63*(4), 2350–2359.

Teja, B. R., & Mikkili, S. (2016). Deployment of Fuzzy based MRAS and IRFOC strategy with fast tracking for the sensorless speed control of SPIM. In *2016 IEEE 6th International Conference on Power Systems (ICPS)*. IEEE.

Utkin, V. I., Guldner, J. G., & Shi, J. (1999). *Sliding mode control in electromechanical systems*. New York: Taylor and Francis.

Yan, Z., & Utkin, V. I. (2002). Sliding mode observers for electric machines—An overview. In *The 28th Annual Conference of the Industrial Electronics Society* (Vol. 3, pp. 1842–1847). IECON.

Zhao, L., Huang, J., Liu, H., Li, B., & Kong, W. (2014). Second-order sliding-mode observer with online parameter identification for sensorless induction motor drives. *IEEE Transactions on Industrial Electronics, 61*(10), 5280–5289.

Zhao, L., et al. (2016). A parallel speed and rotor time constant identification scheme for indirect field oriented induction motor drives. *IEEE Transactions on Power Electronics, 31*(9), 6494–6503.

Zorgani, Y. A., Koubaa, Y., & Boussak, M. (2016). MRAS state estimator for speed sensorless ISFOC induction motor drives with Luenberger load torque estimation. *ISA Transactions, 61,* 308–317.

Haitam Chalawane received a Master degree in 2014 from High School of Technical Education ENSET, Mohammed V University, Rabat. He is currently working toward the Ph.D. degree in electrical engineering research at the electrical engineering department of ENSET. His major research interests are the advanced control techniques for electrical machines and drives.

Ahmed Essadki is currently a Professor and University Research Professor at the electrical engineering department of ENSET, Mohammed V University, Morocco. In 2000, he received his Ph.D. degree from Mohammadia Engineering School (EMI), (Morocco). From 1990 to 1993, he pursued his Master program at UQTR University, Quebec, Canada, respectively, all in electrical engineering. His current research interests include renewable energy, motor drives, and power system. He is a member of RGE Lab as research group leader.

Tamou Nasser is currently an Associate Professor at the communication networks department of National High School for Computer Science and Systems (ENSIAS), Mohammed V University, Morocco, since 2009. She received her Ph.D. degree in 2005 and her research MS degree, in 2000, respectively, all in electrical engineering from Mohammadia Engineering School (EMI), Morocco. Her research interests are renewable energy, motor drives, and power system, and she is a member of Al Jazari research group.

Mohammed Arbaoui received a Master degree in 2016 from High School of Technical Education ENSET, Mohammed V University, Rabat. He is currently working toward the Ph.D. degree in electrical engineering research at the electrical engineering department of ENSET. His major research interests are the primary frequency regulation by wind turbines and renewable energy research.

Optimal H^{∞} Control for a Variable-Speed Wind Turbine Using PSO Evolutionary Algorithm

Fatima Ez-zahra Lamzouri, El-Mahjoub Boufounas, and Aumeur El Amrani

Abstract

This paper presents an optimal tracking and robust controller for a variable-speed wind turbine (VSWT). The main objective of the controller is to optimize the energy captured from the wind at below rated power, and minimize the mechanical stress in the system. In order to guarantee the wind power capture optimization without any chattering behavior, this study proposes to combine the H^{∞} control with particle swarm o`ptimization (PSO) algorithm. The PSO technique with efficient global search is used to optimize the H^{∞} controller parameters simultaneously to control the system trajectories, which determines the system performance. The stability of the system using this controller is analyzed by Lyapunov theory. In present work, the simulation results of the proposed method (PSO-H^{∞}) are compared with the conventional sliding mode control (SMC). The comparison results reveal that the proposed controller is more effective in reducing the tracking error and chattering.

Keywords

Variable-speed wind turbine • Sliding mode control • Optimal H^{∞} control • Particle swarm optimization algorithm

1 Introduction

Nowadays, the exploitation of the wind energy for the electric power production is one of the great interests for research. Indeed, the intention concerns the use of this produced energy by aiming its best quality and reliability (Jena and Rajendran 2015; Herbert et al. 2007). Therefore, it is necessary to develop different tools for making the wind turbine (WT) systems more profitable (Asl and Yoon 2016). In general, there are two major types of wind turbines: the turbine with a fixed speed of the wind (FSWT) and that with variable-speed (VSWT) (Ofualagba and Ubeku 2008). In this study, we consider the case of variable speed, due to its great ability in the extraction of energy (Rajendran and Jena 2015). However, the variable-speed system is more complex and requires an effective control strategy. We can mainly distinguish two operating areas of the VSWT (i.e., below and above the rated wind speed). Below the nominal wind speed, the main objective of the controller is wind energy capture optimization; the torque control is used to maximize the power coefficient of wind turbine. Whereas, when wind speeds are above the rated wind speed, the control objective shifts from maximizing wind capture to regulating the power to its rated value; in this case, a pitch control can be used.

Sliding mode control emerges as an especially suitable option to deal with VSWT (Slotine 1984; Abdeddaim and Betka 2013; Boufounas et al. 2013; Kassem et al. 2013). This approach is one of the most important robust control approaches with respect to system dynamics and invariant to uncertainties. Nevertheless, when the uncertainties are large, it is essential to have a high discontinuous control gain which produces a higher amplitude of chattering. The H^{∞} controller is an effective approach for rejecting those uncertainties and external disturbances, ensuring stability and consistent performance (Yanga and Wang 2007; Nguang and Shi 2003). Yet, in the presence of large uncertainties, H^{∞} control approach produces oscillatory phenomenon due to the higher needed gain.

F. E. Lamzouri · E.-M. Boufounas (✉) · A. El Amrani
LPSMS Laboratory, Faculty of Sciences and Technology,
B.P. 509, Boutalamine, Errachidia, Morocco
e-mail: boufounass@yahoo.fr

F. E. Lamzouri
e-mail: lamzouri.fatimaezzahrae@gmail.com

A. El Amrani
e-mail: a.elamrani@fste.umi.ac.ma

S. El Hani and M. Essaaidi (eds.), *Recent Advances in Electrical and Information Technologies for Sustainable Development*,
Advances in Science, Technology & Innovation, https://doi.org/10.1007/978-3-030-05276-8_6

This paper presents a robust rotor speed tracking controller allowing VSWT to capture maximum wind energy. The designed method is a combination of H^{∞} controller and particle swarm optimization (PSO) technique (Jiang et al. 2017). This method was then selected to optimize the H^{∞} control gains simultaneously; these parameters control the system state trajectory which determines the system performance. In addition, the stability was shown by the Lyapunov theory and the effectiveness of the designed method was illustrated by the comparison with the conventional SMC controller. The simulation results are provided to demonstrate the performances of the proposed controller PSO-H^{∞}.

This study is organized as follows. The next section presents the system modeling. Section 3 shows the design of the proposed controller for power capture optimization. In Sect. 4, simulation results are provided to demonstrate the robust control performances of the proposed approach. Finally, Sect. 5 gives concluding remarks.

2 Wind Turbine Modeling

In this section, we are interested in the modeling of the mechanical part of the VSWT, which is presented by a two-mass model that is shown in Fig. 1. A VSWT is composed of an aeroturbine, a gearbox, and a generator. The aerodynamic power captured by the rotor is given as follows: (Boukhezzar and Siguerdidjane 2010):

$$P_a = \frac{1}{2}\rho\pi R^2 C_p(\lambda, \beta)v^3, \tag{1}$$

where C_p is the power coefficient, β is the pitch angle and the tip-speed ratio, λ, is given as follows:

$$\lambda = \frac{\omega_r R}{v} \tag{2}$$

with ω_r is the rotor speed, R is the rotor radius, ρ is the air density and v is the wind speed.

The power coefficient $C_p(\lambda, \beta)$ is a nonlinear function of λ and β (Wang et al. 2012)

$$C_p(\lambda, \beta) = C_1\left(\frac{C_2}{\lambda_i} - C_3\beta - C_4\right)\exp\left(-\frac{C_5}{\lambda_i}\right) + C_6\lambda, \tag{3}$$

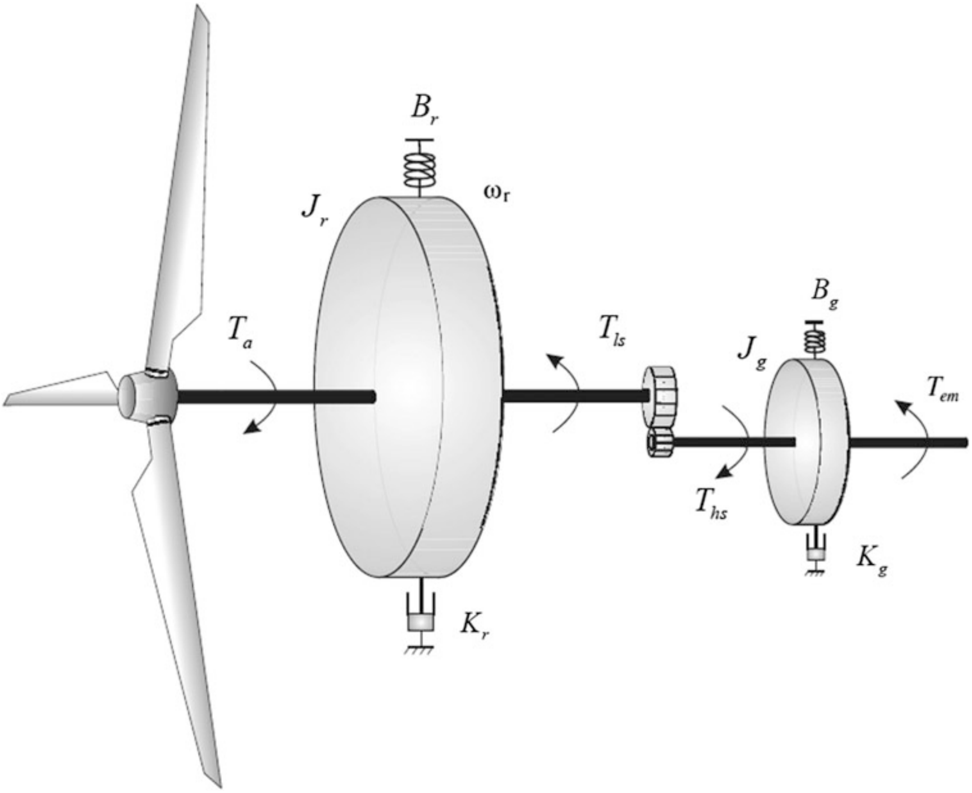

Fig. 1 Two-mass model of a wind turbine

where

$$\frac{1}{\lambda_i} = \frac{1}{\lambda + 0.08\beta} - \frac{0.035}{\beta^3 + 1} \tag{4}$$

with the parameters Ci are known constants without units.

By using the relationship

$$P_a = \omega_r T_a \tag{5}$$

The aerodynamic torque expression is given as

$$T_a = \frac{1}{2}\rho\pi R^3 \frac{C_p(\lambda,\beta)}{\lambda} v^2 \tag{6}$$

According to Fig. 1, the dynamics of the rotor is characterized by a differential equation of the first order

$$J_r\dot{\omega}_r = T_a - T_{ls} - K_r\omega_r \tag{7}$$

J_r and K_r are respectively the rotor inertia and the rotor external damping.

The low-speed shaft torque T_{ls} resulting effects of friction and torque generated by the differences between the rotor angular velocity ω_r and that of the output shaft ω_{ls}:

$$T_{ls} = B_r(\theta_r - \theta_{ls}) + K_{ls}(\omega_r - \omega_{ls}) \tag{8}$$

B_r and K_{ls} are respectively the shaft stiffness coefficient and the shaft damping coefficient.

The relationship between the high-speed shaft torque T_{hs} and the generator electromagnetic torque T_{em} is given by

$$J_g\dot{\omega}_g = T_{hs} - K_g\omega_g - T_{em} \tag{9}$$

J_g, ω_g and K_g are respectively the generator inertia, the generator speed and the generator friction coefficient.

Let us assume an ideal gearbox with transmission ratio n_g, we get

$$n_g = \frac{T_{ls}}{T_{hs}} = \frac{\omega_g}{\omega_{ls}} = \frac{\theta_g}{\theta_{ls}} \tag{10}$$

Replacing the time derivative of Tls from (8) and using (9) and (10) we get the following dynamic system model:

$$\begin{bmatrix} \dot{\omega}_r \\ \dot{\omega}_g \\ \dot{T}_{ls} \end{bmatrix} = \begin{bmatrix} a_{11} & a_{12} & a_{13} \\ a_{21} & a_{22} & a_{23} \\ a_{31} & a_{32} & a_{33} \end{bmatrix} \begin{bmatrix} \omega_r \\ \omega_g \\ T_{ls} \end{bmatrix} + \begin{bmatrix} b_{11} \\ b_{21} \\ b_{31} \end{bmatrix} T_a + \begin{bmatrix} b_{12} \\ b_{22} \\ b_{32} \end{bmatrix} T_{em}, \tag{11}$$

where

$$a_{11} = -\frac{K_r}{J_r}, a_{12} = 0, a_{13} = -\frac{1}{J_r}, a_{21} = 0, a_{22} = -\frac{K_g}{J_g}, a_{23} = \frac{1}{n_g J_g},$$
$$a_{31} = \left(B_{ls} - \frac{K_{ls}K_r}{J_r}\right), a_{32} = \frac{1}{n_g}\left(\frac{K_{ls}K_g}{J_g} - B_{ls}\right), a_{33} = -K_{ls}\left(\frac{J_r + n_g^2 J_g}{n_g^2 J_g J_r}\right),$$
$$b_{11} = \frac{1}{J_r}, b_{12} = 0, b_{21} = 0, b_{22} = -\frac{1}{J_g}, b_{31} = \frac{K_{ls}}{J_r},$$

For the model chosen in this study, C_p characteristic for different values of β is shown in Fig. 2, which indicates that, C_p is high for small values of β, and, there is a unique λ at which the turbine is most efficient.

The power coefficient curve $C_p(\lambda,\beta)$ has a unique maximum which corresponds to the optimal wind energy $(\beta = 0)$:

$$C_p(\lambda_{opt}, \beta_{opt}) = C_{popt} \tag{12}$$

Therefore, the rotor provides maximum aerodynamic power only to the tip-speed λ_{opt}:

$$\lambda_{opt} = \frac{\omega_{ropt}R}{v} \tag{13}$$

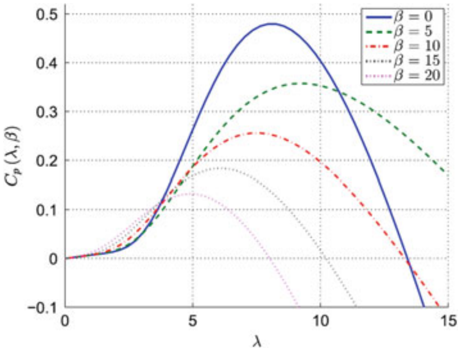

Fig. 2 Wind turbine power coefficient curve

In this work, the main controller objective is only to deal power capture optimization. To achieve the above objective, the variables λ and β must be maintained at their optimal values in order to ensure maximum value of C_p. Thus, the blade pitch angle is fixed at its optimal value β_{opt} $(\beta = 0)$. The tip-speed λ depends on both of the wind speed v and the rotor speed ω_r. As the wind speed is not a controllable input, the rotor speed ω_r must be adjusted by T_{em}, to track the optimal reference given by

$$y_r = \omega_{ropt} = \frac{\lambda_{opt}}{R} v \tag{14}$$

3 Controller Design for Power Capture Optimization

Let define $u = T_{em}$, $x_1 = \omega_r$ and $x_3 = \omega_g$. The system model described by (11) can be rewritten in the state space as follows:

$$\begin{cases} \dot{x}_1 = x_2 \\ \dot{x}_2 = f(x_1, x_2, x_3) + bu \\ \dot{x}_3 = a_{22}x_3 + \frac{a_{23}}{a_{13}}(x_2 - a_{11}x_1 - b_{11}T_a) + b_{22}u \\ y = x_1 \end{cases} \tag{15}$$

$u \in R$ and $y \in R$ are respectively the input and the output of the system. $b = a_{13}b_{32}$ and $f(x_1, x_2, x_3)$ is the nominal representation of the system.

3.1 H$^\infty$ Control Design

The H$^\infty$ control is one of the effective robust nonlinear control approaches, not only because it is easy to implement but also because it provides a property with respect to system dynamics and invariant to uncertainties (Yanga and Wang 2007).

In the following, the tracking error of the system is defined as

$$e(t) = \omega_r(t) - \omega_{ropt}(t) \tag{16}$$

We put w the sum of model uncertainties and the external disturbance, and the error vector is defined as:

$$\underline{E} = [e_1, e_2]^T = [e, \dot{e}]^T \in R^2 \tag{17}$$

The control objective is to force ω_r to follow a given bounded reference signal ω_{ropt}. The controller is then designed to impose an adaptive control algorithm so that the following asymptotically stable tracking.

$$e^{(2)} + k_1 e^{(1)} + k_0 e = 0 \tag{18}$$

is achieved while $w = 0$ (i.e., in the case of perfect model and free of external disturbance). While w appears, the following H∞ tracking performance is requested (Nguang and Shi 2003):

$$\int_0^\tau \underline{E}^T Q \underline{E} dt \le 2V(0) + \rho^2 \int_0^\tau w^2 dt \quad \tau \in [0\ \infty), \tag{19}$$

where V is the Lyapunov function, $Q = Q^T > 0, \rho \in R^+$ is the prescribed attenuation level and $w \in L_2[0, \tau]$. The real vector $k = [k_0, k_1]^T$ is chosen so that $h(s) = s^2 + k_1 s + k_0$ is a Hurwitz polynomial, where s is a complex variable.

Choose the H$^\infty$ compensator u_h as

$$u_h = \frac{1}{r}\underline{E}^T PB, \tag{20}$$

where P is the solution of the following Riccati equation:

$$A^T P + PA + Q - PB\left(\frac{2}{r} - \frac{1}{\rho^2}\right)B^T P = 0, \tag{21}$$

where r is a positive gain to be designed subject to $r < 2\rho^2$.

This control approach is very robust despite the model uncertainties and external disturbances. However, the major problem of this method is the choice of the gain r. The majority of the H$^\infty$ control parameters is adjusted by conventional or by manually methods, which are difficult and time-consuming. This paper introduces a technique which employs swarm intelligence for optimizing the gain of the proposed H$^\infty$ controller.

3.2 PSO Evolutionary Algorithm

PSO was originally proposed by Kennedy and Eberhart in 1995 (Jiang et al. 2017), and it is a type of derivative-free evolutionary search algorithms resulted by an intelligent and well-organized interaction between individual members in a group of birds or fish for example. This algorithm was planned to simulate the positioning and dynamic movements in biological swarms as they look for sources of food or keep away from adversaries.

In PSO, m particles fly through an n-dimensional search space. For each particle i, there are two vectors: the velocity vector $V_i = (v_{i1}, v_{i2}, \ldots, v_{in})$, and the position vector $X_i = (x_{i1}, x_{i2}, \ldots, x_{in})$. Similar to animals' swarms, the particles are updated according to their previous best position $P_i = (p_{i1}, p_{i2}, \ldots, p_{in})$ and the whole swarm's previous best position $P_g = (p_{g1}, p_{g2}, \ldots, p_{gn})$. This means that particle i adapts its velocity V_i and position X_i in each generation according to the equations below

$$v_{id}(t+1) = w \times v_{id}(t) + c_1 \times rand \times (p_{id} - x_{id}) + c_2 \times rand \times (p_{gd} - x_{id}) \quad (22)$$

$$x_{id}(t+1) = x_{id}(t) + v_{id}(t+1), \quad (23)$$

where, w is the inertial weight (JinXing 2013)

$$w = w(\max) - \frac{w(\max) - w(\min)}{MaxIteration} \times t \quad (24)$$

c_1 is the self-confidence factor

$$c_1 = c_1(\max) - \frac{c_1(\max) - c_1(\min)}{MaxIteration} \times t \quad (25)$$

and c_2 is the swarm confidence factor

$$c_2 = c_2(\max) + \frac{c_2(\max) - c_2(\min)}{MaxIteration} \times t \quad (26)$$

with $d = 1, 2, \ldots, n$; $w(\max)$, $w(\min)$ are the maximum and minimum values of w, MaxIteration is the maximum number of allowable iterations and t is the present iteration number.

The new velocity and position for each particle are calculated using the Eqs. (22) and (23) based on its velocity $v_{id}(t)$, best location P_{id} and the swarm's best location P_{gd}.

The objective function f to be minimized is chosen in this work as the Integral Square Error $(ISE) = \int e^2 dt$. This reflects the system time constant, which decides the performance of any nonlinear system.

The PSO algorithm tests the search space using m particles according to (22) and (23). Each particle i moves in search space and stores its best position p_{id} (k and r), then, it compares all positions to finally take out the chosen $k_{optimum}$ and $r_{optimum}$ which gives the minimum value of the fitness function f.

3.3 Proposed Optimal H$^{\infty}$ Controller

Theorem *Consider the system described by (15) in the presence of uncertainties and disturbances. If the system control is designed as*

$$u = \frac{1}{b}\left(-f(x_1, x_2, x_3) + y_r^{(2)} - k^T \underline{E} - u_h\right)$$

where $u_h = \frac{1}{r}\underline{E}^T PB$, with the parameter r is selected by PSO algorithm and $P = P^T \geq 0$ is the solution of the Riccati Eq. (21); then the H^{∞} tracking performance in (19) is achieved for a prescribed attenuation level ρ.

Proof We have:

$$x_1^{(2)} = f(x_1, x_2, x_3) + bu$$

and the equation of the control already proposed

$$u = \frac{1}{b}\left(-f(x_1, x_2, x_3) + y_r^{(2)} - k^T \underline{E} - u_h\right) \quad (27)$$

From (16) we have

$$e^{(2)} = f(x_1, x_2, x_3) + bu - y_r^{(2)}$$

Therefore

$$y_r^{(2)} = f(x_1, x_2, x_3) + bu - e^{(2)} \quad (28)$$

Substituting (28) into (27), then the output error dynamics may be expressed as

$$e^{(2)} = -k^T \underline{E} - u_h \quad (29)$$

The expression (29) can be represented by

$$\dot{\underline{E}} = A\underline{E} + B[-u_h], \quad (30)$$

where

$$A = \begin{pmatrix} 0 & 1 \\ -k_0 & -k_1 \end{pmatrix} B = \begin{pmatrix} 0 \\ 1 \end{pmatrix} \quad (31)$$

Consider the following Lyapunov function

$$V = \frac{1}{2}\underline{E}^T P \underline{E} \quad (32)$$

The time derivative of (32) may be expressed as

$$\dot{V} = \frac{1}{2}\dot{\underline{E}}^T P \underline{E} + \frac{1}{2}\underline{E}^T P \dot{\underline{E}} \quad (33)$$

Substituting (30) into (33), then the $\dot{V}$ can be written as

$$\dot{V} = \frac{1}{2}\underline{E}^T A^T P\underline{E} + \frac{1}{2}\underline{E}^T PA\underline{E} + \frac{1}{2}B^T P\underline{E}[-u_h] + \frac{1}{2}\underline{E}^T PB[-u_h], \tag{34}$$

where $\underline{E}^T PB = B^T P\underline{E}$, thus $\dot{V}$ can be written as

$$\dot{V} = \frac{1}{2}\underline{E}^T\left(A^T P + PA\right)\underline{E} + \underline{E}^T PB[-u_h] \tag{35}$$

Using (21) into (35) and replacing u_h by its expression, the $\dot{V}$ can be given as

$$\dot{V} = -\frac{1}{2}\underline{E}^T Q\underline{E} + \frac{\left(\underline{E}^T PB\right)^2}{r} - \frac{\left(\underline{E}^T PB\right)^2}{2\rho^2} - \frac{\left(\underline{E}^T PB\right)^2}{r} \tag{36}$$

Hence,

$$\dot{V} = -\frac{1}{2}\underline{E}^T Q\underline{E} - \frac{\left(\underline{E}^T PB\right)^2}{2\rho^2} \tag{37}$$

By choosing Q a positive symmetric matrix and $\rho \in R^+$ we have $\dot{V} < 0$. Therefore, the system controller is stable and the error will asymptotically converge to zero, i.e., a H$^\infty$ performance is achieved.

4 Simulation Results

In this part, simulation results are presented to demonstrate the effectiveness of the proposed controller, which are implemented using MATLAB Simulink. In order to make a comparison between the proposed and conventional control strategies, different simulations are considered for the case of the variable-speed fixed-pitch wind turbine. The characteristics of this turbine are presented below

$$R = 21.65\,\text{m}, \rho = 1.29\,\text{kg/m}^3, n_g = 43.165,$$
$$\lambda_{opt} = 8.09 \text{ at } \beta = 0,$$

$$J_r = 3.25 \times 10^5\,\text{kg m}^2, J_g = 34.4\,\text{kg m}^2,$$
$$K_{ls} = 9500\,\text{N m/rad/s},$$

$$B_{ls} = 2.691 \times 10^5\,\text{N m/rad}, K_r = 27.36\,\text{N m/rad/s},$$
$$K_g = 0.2\,\text{N m/rad/s},$$

$$C_1 = 0.5176, C_2 = 116, C_3 = 0.4, C_4 = 5, C_5 = 21,$$
$$C_6 = 0.0068.$$

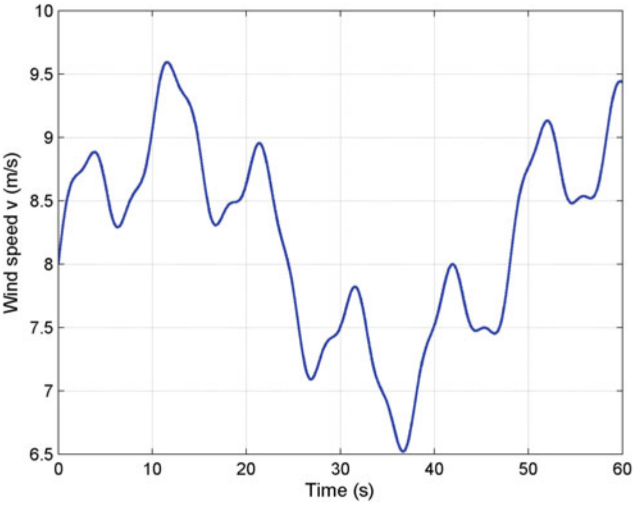

Fig. 3 Wind speed profile

All simulations are carried in the presence of a constant additive control input disturbance 1000 Nm in the electromagnetic torque and an additive measurement noise on ω_g, with a SNR of approximatively 20 dB.

The values of the control parameters are also presented as

$$k_0 = 1, k_1 = 2, Q = \begin{bmatrix} 0.001 & 0 \\ 0 & 0.001 \end{bmatrix}, \rho = 0.1, \gamma = 2,$$

The solution to Riccati equation for Q is $P = \begin{bmatrix} 0.0012 & 0.0002 \\ 0.0002 & 0.0002 \end{bmatrix}$

The parameters of the PSO algorithm are given as

$$w(\max) = 0.9, w(\min) = 0.4, c_1(\max) = 2, c_1(\min) = 0.1,$$
$$c_2(\max) = 2, c_2(\min) = 0.1, MaxIteration = 40, \text{swarm size} = 20.$$

In order to evaluate the performance of the proposed controller, a comparison between the proposed optimal H$^\infty$ control and conventional SMC controller is done. Figure 3 shows the actual wind profile applied to the turbine. The desired rotor speed and tracking response of the closed-loop system, applying the proposed PSO-H$^\infty$ and PSO-SMC controllers are illustrated in Fig. 4. Figure 5 presents a comparison of the corresponding control signals. The optimal and the actual aerodynamic power captured by the turbine are illustrated in Fig. 6. From these figures, it can be clearly seen that the best tracking performance is obtained without any chattering behavior when the proposed PSO-H$^\infty$ is applied. The optimized gains selected using PSO approach are $r_{optimum} = 0.0001$ and $k_{optimum} = 0.8000$.

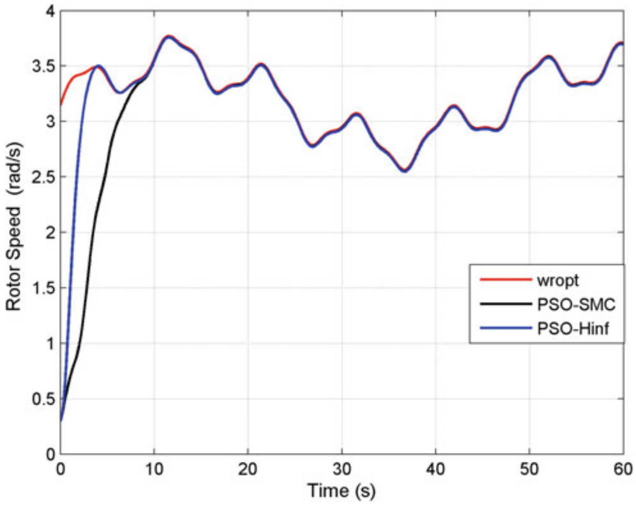

Fig. 4 Desired and actual rotor speed

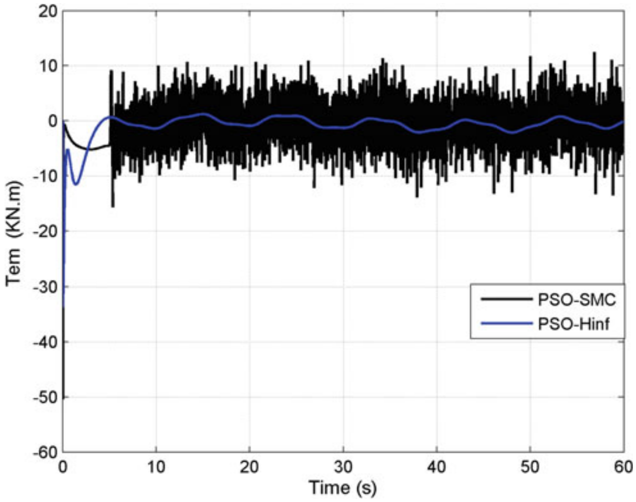

Fig. 5 Time evolution of applied torque

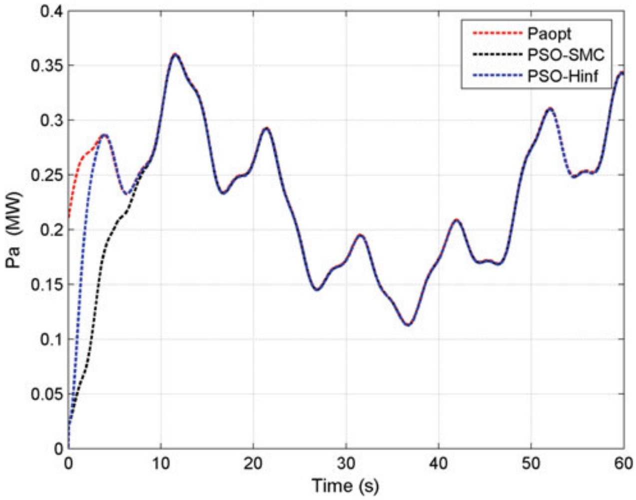

Fig. 6 Time evolution of the captured aerodynamic power

5 Conclusion

In this study, an optimal and robust controller for VSWT was introduced above rated power operating condition, in order to improve the energy captured from the wind. The technique consists of a combination of H^{∞} control with PSO technique. This approach is then selected to optimize the H^{∞} control gain. The comparison with the conventional PSO-SMC has been realized in the presence of uncertainties and external disturbances. The simulation results show that PSO-H^{∞} can provide a faster transient response without any chattering behavior compared to the conventional PSO-SMC, due to a low switching gain used by PSO-H^{∞}. Further studies would focus on other effective optimization methods, and extend our approach to the full wind energy system, including the electrical part.

References

Abdeddaim, S., & Betka, A. (2013). Optimal tracking and robust power control of the DFIG wind turbine. *International Journal of Electrical Power and Energy Systems, 49,* 234–242.

Asl, H. J., & Yoon, J. (2016). Power capture optimization of variable-speed wind turbines using an output feedback controller. *Renewable Energy, 86,* 517–525.

Boufounas, E., Boumhidi, J., Farhane, N., & Boumhidi, I. (2013). Neural network sliding mode controller for a variable speed wind turbine. *Control and Intelligent Systems, 41,* 251–258.

Boukhezzar, B., & Siguerdidjane, H. (2010). Comparison between linear and nonlinear control strategies for variable speed wind turbines. *Control Engineering Practice, 18,* 1357–1368.

Herbert, G. M. J., Iniyan, S., Sreevalsan, E., & Rajapandian, S. (2007). A review of wind energy technologies. *Renewable and Sustainable Energy Reviews, 11,* 1117–1145.

Jena, D., & Rajendran, S. (2015). A review of estimation of effective wind speed based on control of wind turbines. *Renewable and Sustainable Energy Reviews, 43,* 1046–1052.

Jiang, H., Wang, J., Wu, J., & Geng, W. (2017). Comparison of numerical methods and metaheuristic optimization algorithms for estimating parameters for wind energy potential assessment in low wind regions. *Renewable and Sustainable Energy Reviews, 69,* 1199–1217.

JinXing, C. (2013). Support vector regression based on optimal training subset and adaptive particle swarm optimization algorithm. *Applied Soft Computing, 13,* 3473–3481.

Kassem, A. M., Hasaneen, K. M., & Yousef, A. M. (2013). Dynamic modeling and robust power control of DFIG driven by wind turbine at finite grid. *Electric Power Systems Research, 44,* 375–382.

Nguang, S. K., & Shi, P. (2003). H∞ fuzzy output feedback control design for nonlinear systems: An LMI approach. *IEEE Transactions on Fuzzy Systems, 11,* 331–340.

Ofualagba, G., & Ubeku, E. U. (2008). Wind energy conversion system-wind turbine modelling. In *IEEE Power and Energy Society General Meeting—Conversion and Delivery of Electrical Energy in the 21st Century*.

Rajendran, S., & Jena, D. (2015). Validation of an integral sliding mode control for optimal control of a three blade variable speed variable pitch wind turbine. *Electrical Power and Energy Systems, 69,* 421–429.

Slotine, J. J. (1984). Sliding controller design for non-linear systems. *International Journal of Control, 40,* 421–434.

Wang, H. P., Pintea, A., Christov, N., Borne, P., & Popescu, D. (2012). Modelling and recursive power control of horizontal variable speed wind turbines. *Journal of Control Engineering and Applied Informatics, 14,* 33–41.

Yanga, Y. S., & Wang, X. F. (2007). Adaptive H∞ tracking control for a class of uncertain nonlinear systems using radial-basis-function neural networks. *Neurocomputing, 70,* 932–941.

Fatima Ez-zahra Lamzouri received his Engineering Degree from Moulay Ismail University of Meknes in 2016, she is currently pursuing the Ph.D. degree at Faculty of Sciences and Technology of Errachidia, Moulay Ismail University. His research interests include wind-photovoltaic hybrid power systems, nonlinear control, etc.

El-mahjoub Boufounas received his Ph.D. degree in Automatic Control and Computer Sciences from Sidi Mohamed ben Abdellah University of Fez, in 2015. He is now a professor of automatic at the Faculty of Sciences and Technology, Errachidia, Morocco. His research interests robust control, intelligent control, electrical power, energy systems, etc.

Aumeur El Amrani is a Professor at the Faculty of Sciences and Technology, Errachidia, Morocco. He received his Ph.D. degree in high-frequency electronics and optoelectronics, France in 2008. His current research areas concern organic photosensors, thermoelectric materials, and low-power photovoltaic systems engineering.

Nonlinear Control of the Web Winding System by Backstepping with Integral Action

Abdelmajid Akil, Mourad Zegrari, and Nabila Rabbah

Abstract

The Web Winding System (WWS) knows several constraints such as the thermal effects caused by the frictions, and the mechanical effects provoked by metal elongation, that generates dysfunctions due to the influence of the process conditions. A major objective in the web winding system control design is

- To obtain a precise thickness, with the best possible regularity when a sudden constraints occurs;
- To achieve stable rolling and ensure strip quality.

This work presents the conception of a new law of nonlinear control of the WWS. This is the backstepping method with introduction of integral actions. Furthermore, the simulation under the MATLAB/Simulink software allows the highlighting performance of the control strategy adopted.

Keywords

Web winding • Backstepping control • Lyapunov theorem • Integral action • Tracking error

1 Introduction

Cold rolling is generally reserved for flat products (sheet steel) by converting a hot-rolled product into a thin metal coil. The metal-based products are generally packaged in the form of coils. The production of these coils often requires several phases: unwinding, driving associated with processing or transformation of the belt and winding.

The Web Winding System (WWS) is described by its strongly nonlinear behavior. In all cases of rolling up or unfolding of a web material, the flatness difficulty arises.

Given the system complexity due to nonlinearity and the strong coupling between the web velocity and the web tension, many thickness control strategies have been proposed for the WWS control of the reversible cold rolling mill like a Control Lyapunov Function Approach (Rabbah et al. 2015a, b) and Compound control for speed and tension multivariable coupling system (Fang et al. 2015). Among these methods are the backstepping control introduced in Rabbah and Bensassi (2008) and Rabbah et al. (2015a, b) and the robust backstepping control introduced in Yang et al. (2013).

It is clear that the structure of the controller generated by in Rabbah and Bensassi (2008) and Rabbah et al. (2015a, b) is composed of a proportional action, to which is added a derivative action on the errors. The absence of integrator leads to the appearance of a constant static error not null (Benaskeur and Desbiens 2002). The problem solution is the design of a new backstepping control law.

This technique has an integral action. The aim is to regulate the web velocity and traction forces of the WWS and to understand the industrial problems that occur during rolling.

Our paper is organized as follows: Sect. 2 describes briefly the wws and its mathematical model. The objective of the proposed control and the design of the backstepping control law are presented in Sect. 3. Then, the simulation results are presented and interpreted in Sect. 6. The robustness study is presented in Sect. 5. A conclusion and some perspectives are cited in the last part of this work.

2 Web Winding System

2.1 WWS Description

Our study focuses on the WWS shown in Fig. 1. Reversible cold rolling mill is mainly composed of unwinding, main rolling mill, winding and guide rollers.

A. Akil (✉) · M. Zegrari · N. Rabbah
Laboratory of Structural Engineering, Department of Electrical Engineering, Intelligent Systems and Electrical Energy, ENSAM, Hassan II University Casablanca, Casablanca, Morocco
e-mail: abdelmajid.akil@gmail.com

S. El Hani and M. Essaaidi (eds.), *Recent Advances in Electrical and Information Technologies for Sustainable Development*, Advances in Science, Technology & Innovation, https://doi.org/10.1007/978-3-030-05276-8_7

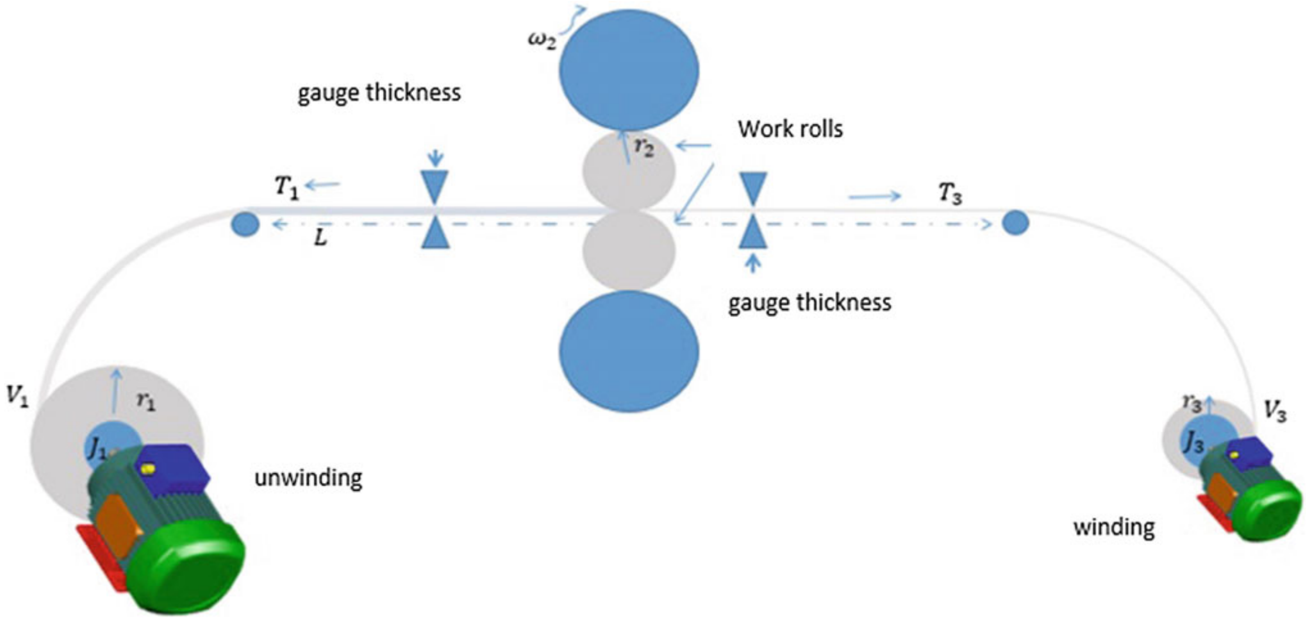

Fig. 1 Structure diagram of the reversible cold rolling mill

The variation of the exit strip flatness evolves because of the thermal dilation of the cylinders (He et al. 2003; Wang et al. 2010), but also due to the elasticity forces (Schmitz and Herman 1995).

Our goal is to maintain the strip thickness uniform in spite of the changing of the acting factors.

2.2 Mathematical Model of the WWS

Because of the complexity of the problem and the coupling of the system parameters, we use a mathematical model describing the set of physical processes by Rabbah and Bensassi (2007), Schmitz and Herman (1995) and Rabbah and Bensassi (2006)

$$\dot{T}_1 = -\frac{V_2}{L}\cdot T_1 + \frac{ES}{L}(V_2 - V_1)\,. \tag{1}$$

$$\dot{V}_1 = -\frac{1}{\tau_{em1}}\cdot V_1 + \frac{gr_1^2}{J_1}\cdot T_1 + \frac{r_1}{\tau_{em1}\cdot k_1}\cdot U_1 \tag{2}$$

with $\dot{J}_1 = 2\pi\rho l_a \dot{r}_1 r_1^3$ and $\dot{r}_1 = \frac{-h}{2\pi}\cdot\frac{V_1}{r_1}$

$$\dot{V}_2 = -\frac{1}{\tau_{em2}}\cdot V_2 + \frac{gr_2^2}{J_2}\cdot(T_3 - T_1) + \frac{r_2}{\tau_{em2}\cdot k_2}\cdot U_2 \tag{3}$$

$$\dot{T}_3 = -\frac{V_2}{L}\cdot T_3 + \frac{ES}{L}(V_3 - V_2)\,. \tag{4}$$

$$\dot{V}_3 = -\frac{1}{\tau_{em3}}\cdot V_3 - \frac{gr_3^2}{J_3}\cdot T_3 + \frac{r_3}{\tau_{em3}.k_3}\cdot U_3 \tag{5}$$

with $\dot{J}_3 = 2\pi\rho l_a \dot{r}_3 r_3^3$ and $\dot{r}_3 = \frac{h}{2\pi}\cdot\frac{V_3}{r_3}$.

These equations represent the complete dynamical model of a WWS. The controller can be designed based on this model. The different model parameters for reversible cold rolling mill are shown in Table 1.

Table 1 Model parameter for the web winding system

Parameter symbol	Parameter name
S	The transverse surface of the strip
R_1, R_2, R_3	Armature resistance of DC motor
L	Length strip length
E	Young modulus of the web
h_1	Input thickness of the strip
h_3	Output thickness of the strip
J_1, J_2, J_3	DC motor inertia
g	Intensity of gravity
k_1, k_2, k_3	Motor torque coefficient
τ_{em1}, τ_{em2}, τ_{em3}	The electromechanical time constant of the DC motor
r_1	The radius of unwinding
r_2	The radius of the work rolls
r_3	The radius of the winding
ρ	Density of the strip
T_1	Upstream tension
T_3	Downstream tension
V_1	Upstream linear velocity
V_2	Work roll velocity
V_3	Downstream linear velocity

The mathematical model consists of three subsystems: the first (sys1) consists of the state vector $[T_1, V_1]$ controlled by the voltage U_1, the second (sys2) a as a state vector $[V_2]$ is controlled by U_2 and the third subsystem (sys3) a as the state vector $[T_3, V_3]$ is controlled by the voltage U_3.

3 Synthesis of the Backstepping Control with Incorporation of an Integral Action

This part treats the control strategy of velocity and tensions by backstepping method with integral action (Benaskeur 2000; Larbaoui et al. 2014; Bellahcene et al. 2012).

The integral action has been explicitly introduced in this control model in order to reject all the step perturbations step type and of nonzero average.

The control problem considered consists in forcing the web velocities and the downstream/upstream web tensions to follow the reference signals given, noted respectively V_2^{ref}, T_1^{ref} and T_3^{ref}. This suggests the following errors:

$$\mathrm{e}_1 = \mathrm{T}_1^{\mathrm{ref}} - \mathrm{T}_1 + \mathrm{K}_{\mathrm{I1}} \int \left(\mathrm{T}_1^{\mathrm{ref}} - \mathrm{T}_1\right) \tag{6}$$

$$\mathrm{e}_2 = \mathrm{V}_2^{\mathrm{ref}} - \mathrm{V}_2 + \mathrm{K}_{\mathrm{I2}} \int \left(\mathrm{V}_2^{\mathrm{ref}} - \mathrm{V}_2\right) \tag{7}$$

$$\mathrm{e}_3 = \mathrm{T}_3^{\mathrm{ref}} - \mathrm{T}_3 + \mathrm{K}_{\mathrm{I3}} \int \left(\mathrm{T}_3^{\mathrm{ref}} - \mathrm{T}_3\right) \tag{8}$$

with $\mathrm{K}_{\mathrm{I1}} \int \left(\mathrm{T}_1^{\mathrm{ref}} - \mathrm{T}_1\right)$, $K_{I2} \int \left(V_2^{ref} - V_2\right)$ and $\mathrm{K}_{\mathrm{I3}} \int \left(\mathrm{T}_3^{\mathrm{ref}} - \mathrm{T}_3\right)$. Are integral actions added to the backstepping control where K_{I1}, K_{I2} and K_{I3} are real constants. Our objective is to ensure the convergence of the tracking error to zero in spite of uncertainties at each algorithm step.

The regulator synthesis will be done in two steps. In the first step, we will put the virtual controls and the stabilizing functions associated. In the second step, we determine the control laws able to ensure convergence towards zero of the difference between the virtual orders and the stabilizing functions associated.

Step 1: The dynamic of the tracking errors e_1, e_2 and e_3 are given by

$$\dot{e}_1 = \dot{T}_1^{ref} - \frac{ES}{L}(V_2 - V_1) + \frac{V_2}{L} T_1 + K_{I1}\left(T_1^{ref} - T_1\right) \tag{9}$$

$$\begin{aligned} \dot{e}_2 = \dot{V}_2^{ref} + \frac{gr_2^2}{J_2}(T_1 - T_3) + \frac{1}{\tau_{em2}} V_2 - \\ \frac{r_2}{\tau_{em2}.k_2} U_2 + K_{I2}\left(V_2^{ref} - V_2\right) \end{aligned} \tag{10}$$

$$\dot{\mathrm{e}}_3 = \dot{\mathrm{T}}_3^{\mathrm{ref}} - \frac{\mathrm{ES}}{\mathrm{L}}(\mathrm{V}_3 - \mathrm{V}_2) + \frac{\mathrm{V}_2}{\mathrm{L}} \mathrm{T}_3 + \mathrm{K}_{\mathrm{I3}}\left(\mathrm{T}_3^{\mathrm{ref}} - \mathrm{T}_3\right) \tag{11}$$

The tracking error e_2 tends asymptotically towards zero if; in this case, the virtual control is selected as follows:

$$\alpha_2 = \dot{V}_2^{ref} + \frac{gr_2^2}{J_2}(T_1 - T_3) + \frac{1}{\tau_{em2}} V_2 + K_{I2}\left(V_2^{ref} - V_2\right) \tag{12}$$

Thus, the dynamic error e_2 can be rewritten as follows:

$$\dot{e}_2 = \alpha_2 - \frac{r_2}{\tau_{em2} \cdot k_2} U_2 = -c_2 e_2 \tag{13}$$

The control U_2 is obtained as follows:

$$U_2 = \frac{\tau_{em2} \cdot k_2}{r_2}\left(\dot{V}_2^{ref} + \frac{gr_2^2}{J_2}(T_1 - T_3) + \frac{1}{\tau_{em2}} V_2 + K_{I2}\left(V_2^{ref} - V_2\right)\right) \tag{14}$$

The quantities $\frac{\mathrm{ES}}{\mathrm{L}}(\mathrm{V}_2 - \mathrm{V}_1)$ and $\frac{\mathrm{ES}}{\mathrm{L}}(\mathrm{V}_3 - \mathrm{V}_2)$ are posed like virtual control inputs for the system (9) and (11). It follows that the tracking errors e_1 and e_3 tend asymptotically towards zero if these virtual controls are selected such as

$$\frac{ES}{L}(V_2 - V_1) = \alpha_1 \text{ with } \alpha_1 = c_1 e_1 + \dot{T}_1^{ref} + \frac{V_2}{L} T_1 + K_{I1}\left(T_1^{ref} - T_1\right) \tag{15}$$

$$\frac{ES}{L}(V_3 - V_2) = \alpha_3 \text{ with } \alpha_3 = c_3 e_3 + \dot{T}_3^{ref} + \frac{V_2}{L} T_3 + K_{I3}\left(T_3^{ref} - T_3\right), \tag{16}$$

where c_1, c_2 and c_3 are the positive real constants unspecified. Indeed, we obtain: $\dot{e}_1 = -c_1 e_1$, $\dot{e}_2 = -c_2 e_2$ and $\dot{e}_3 = -c_3 e_3$.

The α_1, α_2 and α_3 quantities are called stabilizing functions. Then, the first Lyapunov candidate function is defined as

$$v_1 = \frac{1}{2}\left(e_1^2 + e_2^2 + e_3^2\right) \tag{17}$$

The derivative of the first Lyapunov function takes the form

$$\dot{v}_1 = -c_1 e_1^2 - c_2 e_2^2 - c_3 e_3^2 \tag{18}$$

Who shows the influence of the controlling parameters c_1, c_2 and c_3 on the convergence of the e_1, e_2 and e_3, errors.

For Eqs. (9) and (11), the found result supposes that $\frac{ES}{L}(V_2 - V_1)$ and $\frac{ES}{L}(V_3 - V_2)$ are effective controls. As such is not the case, we cannot impose the equalities (15) and (16) We will only try to tend these controls towards their ideal trajectories which are precisely the stabilizing functions α_1 and α_3. For this purpose, we introduce the errors

$$z_1 = \alpha_1 - \frac{ES}{L}(V_2 - V_1) + K_{I11} \int \left(\alpha_1 - \frac{ES}{L}(V_2 - V_1)\right) \tag{19}$$

$$z_3 = \alpha_3 - \frac{ES}{L}(V_3 - V_2) + K_{I33} \int \left(\alpha_3 - \frac{ES}{L}(V_3 - V_2)\right), \tag{20}$$

where K_{I11} and K_{I33} reals constants.

The dynamic of the e_1 and e_3 errors are expressed in function of z_1 and z_3 as follows:

$$\dot{e}_1 = -c_1 e_1 + z_1 \tag{21}$$

$$\dot{e}_3 = -c_3 e_3 + z_3 \tag{22}$$

The second step in the regulator synthesis consists in forcing all the $(\mathrm{e}_1; \mathrm{e}_2; \mathrm{e}_3; \mathrm{z}_1; \mathrm{z}_3)$ errors to converge towards zero with a suitable choice of the effective controls U_1, U_2 and U_3.

Step 2: The dynamic of the e_1 error is given by

$$\begin{aligned}\dot{z}_1 &= \dot{\alpha}_1 - \frac{ES}{L}\left(\dot{V}_2 - \dot{V}_1\right) + K_{I11}\left(\alpha_1 - \frac{ES}{L}(V_2 - V_1)\right)\\ &= c_1\dot{e}_1 + \ddot{T}_1^{ref} + \frac{\dot{V}_2}{L}T_1 + \frac{V_2}{L}\dot{T}_1 + K_{I1}\left(\dot{T}_1^{ref} - \dot{T}_1\right)\\ &\quad - \frac{ES}{L}\left(\dot{V}_2 - \dot{V}_1\right) + K_{I11}\left(\alpha_1 - \frac{ES}{L}(V_2 - V_1)\right)\end{aligned} \tag{23}$$

Taking into account (21), (1), (2), (3), (4) and (5), we obtain

$$\begin{aligned}\dot{z}_1 = {}& c_1(-c_1 e_1 + z_1) + \ddot{T}_1^{ref}\\ & + \frac{1}{L}T_1\left(-\frac{1}{\tau_{em2}}.V_2 + \frac{gr_2^2}{J_2}\cdot(T_3 - T_1) + \frac{r_2}{\tau_{em2}.k_2}\cdot U_2\right)\\ & + \frac{V_2}{L}\left(-\frac{V_2}{L}\cdot T_1 + \frac{ES}{L}(V_2 - V_1)\right)\\ & + K_{I1}\left(\dot{T}_1^{ref} - \frac{V_2}{L}\cdot T_1 + \frac{ES}{L}(V_2 - V_1)\right)\\ & - \frac{ES}{L}\left(\left(-\frac{1}{\tau_{em2}}.V_2 + \frac{gr_2^2}{J_2}\cdot(T_3 - T_1) + \frac{r_2}{\tau_{em2}\cdot k_2}\cdot U_2\right)\right.\\ & \left. - \left(\frac{1}{\tau_{em1}}\cdot V_1 + \frac{gr_1^2}{J_1}\cdot T_1 + \frac{r_1}{\tau_{em1}.k_1}\cdot U_1\right)\right)\\ & + K_{I11}\left(\alpha_1 - \frac{ES}{L}(V_2 - V_1)\right)\\ = {}& \gamma_1 + \frac{\mathrm{E.S.r_1}}{\mathrm{L}\ \cdot \tau_{\mathrm{em1}} \cdot \mathrm{k_1}} \cdot \mathrm{U_1}\end{aligned} \tag{24}$$

where γ_1 includes the measurable terms on the right of the first equality, that is to say

$$\begin{aligned}\gamma_1 = {}& c_1(-c_1 e_1 + z_1) + \ddot{T}_1^{ref}\\ & + \frac{1}{L}T_1\left(-\frac{1}{\tau_{em2}}\cdot V_2 + \frac{gr_2^2}{J_2}\cdot(T_3 - T_1)\right)\\ & - \frac{ES}{L}\left(\left(\frac{gr_2^2}{J_2}\cdot(T_3 - T_1) - \frac{gr_1^2}{J_1}\cdot T_1 + \frac{1}{\tau_{em1}}\cdot V_1 - \frac{1}{\tau_{em2}}\cdot V_2\right)\right)\\ & + \frac{V_2}{L}\left(-\frac{V_2}{L}\cdot T_1 + \frac{ES}{L}(V_2 - V_1)\right)\\ & + \mathrm{K_{I11}}\left(\alpha_1 - \frac{\mathrm{ES}}{\mathrm{L}}(\mathrm{V_2} - \mathrm{V_1})\right) + \mathrm{K_{I1}}\left(\dot{\mathrm{T}}_1^{\mathrm{ref}} - \left(-\frac{\mathrm{V_2}}{\mathrm{L}}\cdot \mathrm{T_1} + \frac{\mathrm{ES}}{\mathrm{L}}(\mathrm{V_2} - \mathrm{V_1})\right)\right)\\ & - \frac{\mathrm{r_2}}{\tau_{\mathrm{em2}}.\mathrm{k_2}}\left(\frac{\mathrm{ES} + \mathrm{T_1}}{\mathrm{L}}\right)\cdot \mathrm{U_2}\end{aligned} \tag{25}$$

In the same way, the dynamics of the e_3 error is

$$\dot{z}_3 = \dot{\alpha}_3 - \frac{ES}{L}\left(\dot{V}_3 - \dot{V}_2\right) + K_{I33}\left(\alpha_3 - \frac{ES}{L}(V_3 - V_2)\right) \tag{26}$$

While using (23), (1), (2), (3), (4) and (5), the preceding equation becomes

$$\begin{aligned}\dot{\mathrm{z}}_3 = {}& \mathrm{c_3}(-\mathrm{c_3 e_3} + \mathrm{z_3}) + \ddot{T}_3^{\mathrm{ref}}\\ & + \frac{1}{\mathrm{L}}\mathrm{T_3}\left(-\frac{1}{\tau_{\mathrm{em2}}}.\mathrm{V_2} + \frac{\mathrm{gr_2^2}}{\mathrm{J_2}}.(\mathrm{T_3} - \mathrm{T_1}) + \frac{\mathrm{r_2}}{\tau_{\mathrm{em2}}\ .\ \mathrm{k_2}}.\mathrm{U_2}\right)\\ & + \frac{\mathrm{V_2}}{\mathrm{L}}\left(-\frac{\mathrm{V_2}}{\mathrm{L}}\cdot \mathrm{T_3} + \frac{\mathrm{ES}}{\mathrm{L}}(\mathrm{V_3} - \mathrm{V_2})\right)\\ & + \mathrm{K_{I3}}(\dot{\mathrm{T}}_3^{\mathrm{ref}} - (-\frac{\mathrm{V_2}}{\mathrm{L}}\cdot \mathrm{T_3} + \frac{\mathrm{ES}}{\mathrm{L}}(\mathrm{V_3} - \mathrm{V_2})))\\ & - \frac{\mathrm{ES}}{\mathrm{L}}\left(\left(-\frac{1}{\tau_{\mathrm{em3}}}\cdot \mathrm{V_3} - \frac{\mathrm{gr_3^2}}{\mathrm{J_3}}\cdot \mathrm{T_3} + \frac{\mathrm{r_3}}{\tau_{\mathrm{em3}}\cdot \mathrm{k_3}}\cdot \mathrm{U_3} + \frac{1}{\tau_{\mathrm{em2}}}\cdot \mathrm{V_2(t)}\right.\right.\\ & \left.\left. + \frac{\mathrm{gr_2^2}}{\mathrm{J_2}}\cdot(\mathrm{T_1} - \mathrm{T_3}) - \frac{\mathrm{r_2}}{\tau_{\mathrm{em2}}\cdot \mathrm{k_2}}\cdot \mathrm{U_2}\right)\right)\\ & + \mathrm{K_{I33}}\left(\alpha_3 - \frac{\mathrm{ES}}{\mathrm{L}}(\mathrm{V_3} - \mathrm{V_2})\right)\\ = {}& \gamma_3 - \frac{\mathrm{E\cdot S\cdot r_3}}{\mathrm{L}\ \cdot \tau_{\mathrm{em3}}\cdot \mathrm{k_3}}\cdot \mathrm{U_3},\end{aligned} \tag{27}$$

where γ_3 includes the measurable terms on the right of the first equality, that is to say

$$\begin{aligned}\gamma_3 = {}& c_3(-c_3 e_3 + z_3) + \ddot{T}_3^{\mathrm{ref}}\\ & + \frac{1}{L}T_3\left(-\frac{1}{\tau_{em2}}\cdot V_2 + \frac{gr_2^2}{J_2}\cdot(T_3 - T_1)\right)\\ & + \frac{V_2}{L}\left(-\frac{V_2}{L}\cdot T_3 + \frac{ES}{L}(V_3 - V_2)\right)\\ & - \frac{ES}{L}\left(-\frac{1}{\tau_{em3}}\cdot V_3 - \frac{gr_3^2}{J_3}\cdot T_3 + \frac{1}{\tau_{em2}}\cdot V_2 + \frac{gr_2^2}{J_2}\cdot(T_1 - T_3)\right)\\ & + K_{I3}\left(\dot{T}_3^{ref} - \frac{V_2}{L}\cdot T_3 + \frac{ES}{L}(V_3 - V_2)\right)\\ & + K_{I33}\left(\alpha_3 - \frac{ES}{L}(V_3 - V_2)\right)\\ & - \frac{r_2}{\tau_{em2}\cdot k_2}\cdot\left(\frac{ES - T_3}{L}\right)U_2\end{aligned} \tag{28}$$

To study the stability of the system (13), (21), (22), (24) and (26), of state vector $(\mathrm{e}_1; \mathrm{e}_2; \mathrm{e}_3; \mathrm{z}_1; \mathrm{z}_3)$, we consider the Lyapunov candidate function increased

$$v_2 = v_1 + \frac{1}{2}\left(z_1^2 + z_3^2\right) \tag{29}$$

Its derivative with respect to time

$$\dot{v}_1 = e_1\dot{e}_1 + e_2\dot{e}_2 + e_3\dot{e}_3 + z_1\dot{z}_1 + z_3\dot{z}_3$$

Taking into account (13), (21), (22), (24) and (27), we obtain

$$\begin{aligned}\dot{v}_2 = & -c_1e_1^2 - c_2e_2^2 - c_3e_3^2 - d_1z_1^2 - d_3z_3^2\\ & + z_1\left(e_1 + d_1z_1 + \gamma_1 + \frac{ES}{L}\frac{r_1}{\tau_{em1}\cdot k_1}\cdot U_1\right)\\ & + z_3\left(e_3 + d_3z_3 + \gamma_3 - \frac{ES}{L}\frac{r_3}{\tau_{em3}\cdot k_3}\cdot U_3\right),\end{aligned}$$

where d_1 and d_3 are the positive real constants unspecified. The preceding equation suggests choosing the U_1, U_2 and U_3, controls such as

$$\begin{cases} e_1 + d_1z_1 + \gamma_1 + \frac{ES}{L}\frac{r_1}{\tau_{em1}\cdot k_1}\cdot U_1 = 0\\ e_3 + d_3z_3 + \gamma_3 - \frac{ES}{L}\frac{r_3}{\tau_{em3}\cdot k_3}\cdot U_3 = 0\end{cases}$$

We can deduce the three laws control, there forms are

$$\begin{cases} U_1 = -\frac{\tau_{em1}\cdot k_1.L}{ESr_1}(e_1 + d_1z_1 + \gamma_1)\\ U_2 = \frac{\tau_{em2}\cdot k_2}{r_2}\begin{pmatrix}\dot{V}_2^{ref} + \frac{gr_2^2}{J_2}(T_1 - T_3) + \frac{1}{\tau_{em2}}V_2\\ + K_{I2}\left(V_2^{ref} - V_2\right)\end{pmatrix}\\ U_3 = \frac{\tau_{em3}\cdot k_3\cdot L}{ESr_3}(e_3 + d_3z_3 + \gamma_3)\end{cases}$$

The derivative $\dot{v}_2$ becomes

$$\dot{v}_2 = -c_1e_1^2 - c_2e_2^2 - c_3e_3^2 - d_1z_1^2 - d_3z_3^2$$

It is a negative definite function of the vector $(e_1; e_2; e_3; z_1; z_3)$. It follows that the state vector system of the $(e_1; e_2; e_3; z_1; z_3)$ has a equilibrium point globally asymptotically stable on the position $(e_1; e_2; e_3; z_1; z_3) = (0; 0; 0; 0; 0; 0)$. That means in particular that the tracking errors (for the winding velocity and the upstream/downstream tensions) tend towards zero whatever the initial conditions.

4 Simulation and Results Discussion

In order to prove the advantage of the backstepping method with integral action, the simulations are carried out on a 1422 mm reversible cold rolling mill using actual industrial data in order to verify the performance of the regulator elaborated previously.

We have taken as references $T_1 = 100\,\text{N}$, $V_2 = 29$ m/s and $V_3 = 120\,\text{N}$.The values chosen for the regulator parameters of backstepping during simulations are $(c_1, c_2, c_3, d_1, d_1, K_{I1}, K_{I2}, K_{I3}, K_{I11}, K_{I33}) = (10^2, 10^2, 10^2, 10, 10; 10^2, 10^3, 10^2, 10^3, 10^3)$.

Figure 2 are noted an according to shape of the velocity perfectly follows its reference which is achieved very rapidly, with a very fast response at time 0.4 s.

The simulation results of our approach are shown in Fig. 3a (Upstream tension) and in fig. 3b (downstream

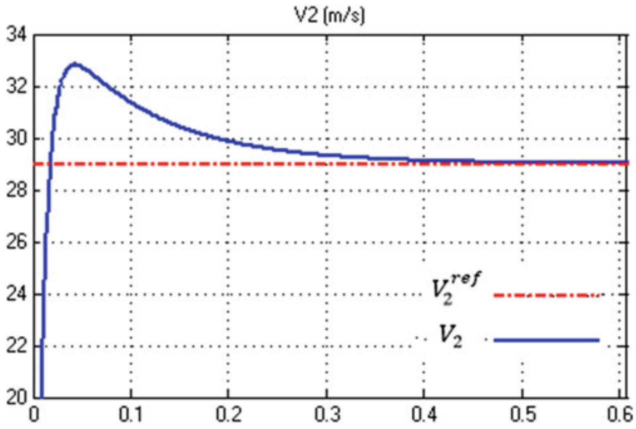

Fig. 2 Web velocity by backstepping control with integral action

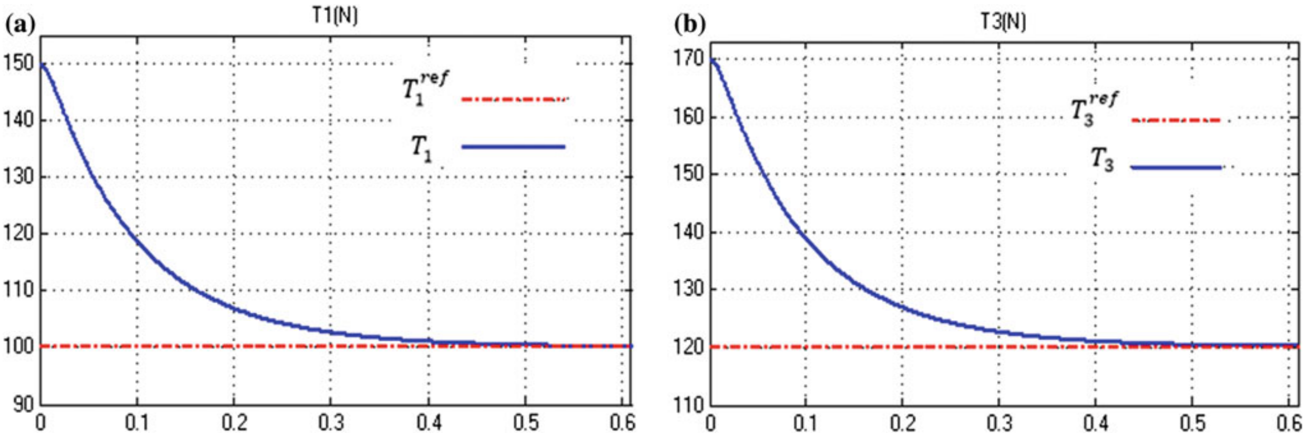

Fig. 3 Backstepping control with integral action of: **a** upstream tension, **b** downstream tension

tension). This figures show the comparison results of state trajectories and the corresponding reference signal. These results show that the continuation errors corresponding to the each parameter are cancelled after 0.5 s for the tensions.

The simulation results of backstepping method (Rabbah et al. 2015a, b) show the continuation errors corresponding to the each parameter are canceled after 30 s for the tensions $(T_1; T_3)$ and 15 s for the web velocity V_2.

The simulation results of ILQ design method (Zheng et al. 2015) show the continuation errors corresponding to the each parameter are canceled after 2 s for the tensions $(T_1; T_3)$ and 1, 5 s for the web velocity V_2.

Comparing between the backstepping method with integral action, ILQ design method and backstepping method, we find the simulation of backstepping method with integral action describe the good performance of the system in terms of trajectory tracking. The proposed control law shows that the output variables T_1, V_2 and T_3 have a faster tracking response with the backstepping control strategy with integral action.

5 Robustness Study

To ensure the good performance of the proposed control law, we have studied the robustness and efficiency of our approach on the WWS mathematical model of the by adding the perturbations to T_1, V_2 and T_3 (Fig. 4).

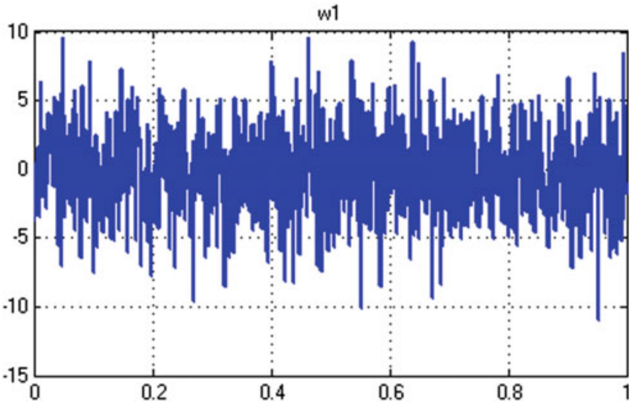

Fig. 4 Perturbation applied to T_1, V_2 and T_3

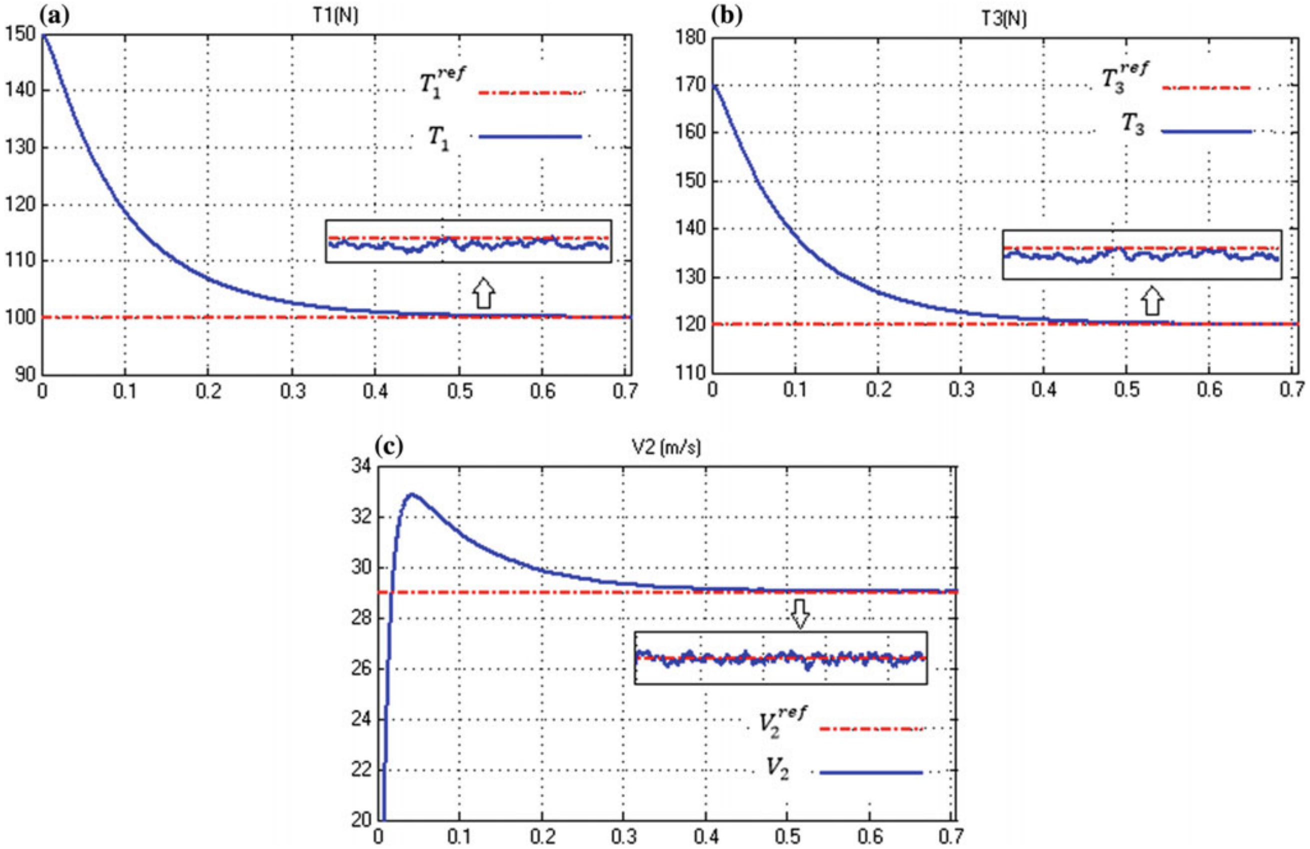

Fig. 5 Backstepping control with integral action with perturbation: **a** Tension downstream, **b** Tension upstream and **c** web velocity

The temporal responses of T_1, V_2 and T_3 following a perturbation are shown in Fig. 5.

Figure 5 gives an approximate indication of the of perturbations effects applied to T_1, V_2 and T_3. The results show that the system performs well in terms of trajectory tracking and rejection of perturbation.

The numerical simulations results of the backstepping control with integral action applied to the WWS with perturbation clearly show the rejection of the perturbation and the perfect tracking of the reference of the velocity V_2 and the tensions T_1 and T_3, confirming the good selection of the control coefficients of the nonlinear velocity controller and of the traction tensions. Consequently, these results are globally similar to those obtained with the backstepping control with non-perturbation integration.

6 Conclusion

In this work, we propose a nonlinear backstepping control by introducing an integral action to command the strip thickness by acting on the web velocity and the web tension of the WWS. This control, while preserving stability, eliminates residual errors, in the presence of perturbation with nonzero mean. By comparing the backstepping and backstepping control strategy with integration action, the results of the simulation show that the system retains the asymptotic monitoring performance of these parameters. The backstepping strategy with integration action has better performance and robustness stability.

In future work, we are planned to extend our studies using adaptive backstepping control and neural control to compare the results of two techniques.

References

Bellahcene, Z., Bouhamida, M., Benghanem, M., Laidani, A. (2012). La Commande Intégrale Backstepping Appliquée à un Hélicoptère à quatre hélices, in *2nd International Conference on Maintenance, Management, Logistics and Electrical Engineering*, ENSET Oran.

Benaskeur, A. R. (2000). Aspects de l'application du backstepping adaptatif à la commande décentralisée des systèmes non linéaires. Université Laval, Québec.

Benaskeur, A. R., & Desbiens, A. (2002). Backstepping-based adaptive PID control. *IEE Proceedings-Control Theory and Applications*, *149*(1), 54-59. https://doi.org/10.1049/ip-cta:20020100.

Fang, Y., Liu, L., Li, J., & Chang, R. (2015). Compound control for speed and tension multivariable coupling system of reversible cold strip mill. *Journal of Central South University, 22*(2), 529–538. https://doi.org/10.1007/s11771-015-2552-4.

He, J., Yu, S., & Zhong, J. (2003). Tension-speed decoupling control of temper mill for plate-strip steet. *Control and decision., 8,* 522–526.

Larbaoui, A., Belabbes, B., Meroufel, A., Tahour, A., Bouguenna, D. (2014). Backstepping control with integral action of PMSM integrated according to the MRAS Observer. *IOSR Journal of Electrical and Electronics Engineering* (IOSR–JEEE). *9*(4), 59–68.

Rabbah, N., Bensassi, B. (2007) Modelling and simulation of web winding system of a reversible rolling mill. *International Conference on Applied Simulation and Modelling (ASM2007)*. Palma de Mallorca- Spain, pp: 474–478.

Rabbah, N., & Bensassi, B. (2006). Modélisation et simulation d'un système de laminage à froid quarto réversible. Rencontre Nationale des Jeunes Chercheurs de Physique (RNJCP). Casablanca–Morocco.

Rabbah, N., & Bensassi, B. (2008). *The web winding system control by the backstepping method*. Briatico, Italy, The International Workshop on Modelling & Applied Simulation.

Rabbah, N., Machkour, N., & Zegrari, M. (2015). A Control Lyapunov Function Approach for Nonlinear Web Winding System. *International Journal of Innovative Research in Science, Engineering and Technology*, *4*(7), 5387–5393. https://doi.org/10.15680/ijirset.2015.0407046.

Rabbah, N., Machkour, N., Kheddiouiand, E., & Ait Elmahjoub, A. (2015b). Backstepping control of the web winding system. *International Journal Engineering and Technologie IJET-IJENS, 15*(06), 31–35.

Schmitz, A., & Herman, J. C. (1995). Modélisation du laminage à froid des aciers. Etude des aspects métallurgiques. Analyse par la méthode des tranches. CRM Faculté Polytechnique de Mons. pp. 37–43.

Wang, B., Dong, Y., & Zhao, K. (2010). Compound control for hydraulic flight motion simulator. *Chinese Journal of Aeronautics, 23*(2), 240–245. https://doi.org/10.1016/S1000-9361(09)60211-9.

Yang, X., Peng, K., Tong, C. (2013). *Robust backstepping control for cold rolling main drive system with nonlinear uncertainties*. Hindawi Publishing Corporation pp. 1–7. http://dx.doi.org/10.1155/2013/387890.

Zheng, G., Chao, X. L., & Yang, Z. (2015, July). Research on speed and tension multivariable system of reversible cold strip mill based on ILQ theory. In *International Conference on Machine Learning and Cybernetics* (pp: 110 − 115). https://doi.org/10.1109/icmlc.2015.7340907.

Abdelmajid Akil received the Master of Science and Technology degree in Automatic, Signal Processing and Industrial Computing from faculties of science and technology, Hassan University 1, Settat in 2012.

From 2010 to 2012, he was electrician industrial equipment within the society Moroccan food processing (MFPO), Berrechid, Morocco. Since 2013, he has been a Professor of mathematics at Ibn Rochd High School, Berrechid, Morocco.

He is currently pursuing the Ph.D. degree at the Department of Electrical Engineering, Laboratory of Structural Engineering, Intelligent Systems and Electrical Energy, National Higher School of Arts and Crafts (ENSAM), Hassan II University, Casablanca, MOROCCO. His research interests include the nonlinear control of dynamical systems as applied to metal rolling processes.

Mourad Zegrari is graduated from Higher Normal School of Technical Education (ENSET) of Rabat in 1994. He obtained The Ph.D. degree in Industrial control from Hassan II University of Casablanca in 2012, then the University habilitation in electrical engineering. Actually, He is professor and head of electrical engineering department of Ecole Nationale Supérieure d'Arts et Métiers (ENSAM) of Casablanca. The author is consultant for several industrial units and author for many modeling and industrial control works.

Nabila Rabbah is a state electric engineer from the ENSEM of Casablanca. She obtained her master degree in Industrial Automation from ENSEM-Casablanca, and then she received her Ph.D. degree in Automation and Industrial IT in 2008 from Hassan II University of Casablanca, Morocco. Since 2011, she is a professor in the department of electric engineering of the ENSAM-Casablanca. She is a coordinator of the research team "Modeling, Control and Embedded Systems". She contributes by numerous publications in the field of the command.

Rapid Model Predictive Controller for Artificial Pancreas

M. El Hachimi, A. Ballouk, and A. Baghdad

Abstract

Artificial Pancreas (AP) will help large diabetic patients to manage their disease. This paper presents a new Control Algorithm used in AP. This algorithm is based on a model predictive control and characterized by an acceleration of control law without producing overshoot. The method consists on the introduction of two penalization function in the cost function according to the system dynamic. Simulations under a realistic scenario in approved platform of simulation demonstrate the success of this method to obtain satisfactory control performances.

Keywords

Artificial pancreas • Control algorithm • Overshoot • Model predictive control • Cost function • System dynamic

Abbreviations

AP	artificial pancreas
MPC	model predictive control
T1DM	Type 1 diabetes mellitus
BG	blood glucose
z-MPC	zone-MPC
e-MPC	enhanced-MPC
CHO	carbohydrates
CGM	continuous glucose monitor
CSII	continuous subcutaneous insulin injection
FDA	Food and Drug Administration
TDI	total daily insulin
mg/dL	milligrams per deciliter N
pmol/min	picomoles per minute
UVA/Padova	Universities of Virginia/Padova

1 Introduction

Type 1 Diabetes Metabolism (T1DM) is a form of diabetes caused by an autoimmune destruction of beta cells in the pancreas, the body becomes incapable to produce enough insulin. The lack of insulin causes hyperglycemia with dangerous complications. Only external insulin injections can treat T1DM. Insulin is a hormone produced by beta cells of the pancreatic islets that promotes glucose absorption in body cells to produce energy.

An individual with type 1 diabetes is confronted to the long-term risks associated with hyperglycemia (vascular problems, retina diseases), and the short-term risk of hypoglycemia (drowsiness, coma). Individual must be diligent with frequent blood glucose meter (finger stick) tests, and insulin dosage adjustments (at mealtime and as “correction” boluses). For tight control of blood glucose an individual must be diligent, and constantly managing their disease. For that it is very desirable to develop an artificial pancreas system that automatically adjusts insulin infusion in response to glucose changes, thus reducing patient burden. The Artificial Pancreas (AP) is a system thought to automate the exogenous insulin supply and is composed of a subcutaneous glucose sensor, which allows Continuous Glucose Monitoring (CGM), a subcutaneous insulin pump, and a control algorithm. Figure 1 gives an overview of the Artificial Pancreas (Doyle et al. 2014).

Continuous time blood glucose measurement (CGM): CGM devices provides glucose readings in real time, it produces frequently sampled data sets (e.g., every 5–10 min) allowing them to serve as AP-enabling technology, CGM can also display trends and blood glucose rate of change and is capable to alert the patient about upcoming hyper- or hypoglycemia.

Pump injection: Insulin pumps allow automatic insulin delivery. There are several technologies that can perform this task: an intra-venous route, subcutaneous insulin infusion (SCII) or intra-peritoneal insulin delivery. Continuous

M. El Hachimi (✉) · A. Ballouk · A. Baghdad
Laboratory of Electronics Energy, Automatic & Data Processing (LEEA&TI) FST, Mohammedia University Hassan II of Casablanca, BP 14-20650 Mohammedia, Morocco
e-mail: contact.hachimi@gmail.com

S. El Hani and M. Essaaidi (eds.), *Recent Advances in Electrical and Information Technologies for Sustainable Development*,
Advances in Science, Technology & Innovation, https://doi.org/10.1007/978-3-030-05276-8_8

Fig. 1 An overview of the artificial pancreas system

subcutaneous insulin infusion (CSII) uses a portable electromechanical pump to mimic non diabetic insulin delivery as it infuses at preselected rates normally a slow basal rate with patient-activated boosts at mealtime.

Studies on the glucose monitor, insulin pump, and sensor have been successfully done and approved for medical use by Food and Drug Administration (FDA). However, the current artificial pancreas is still lacking in terms of the development of a control algorithm, which controls all the devices so as to make it an automated system, therefore, the closed-loop system progress is still at manual stage.

In general recent studies use two **Control Algorithms**; Proportional-Integral-Derivative (PID) and Model Predictive Control (MPC). **PID** has been used by Jacobs et al. (2014) to design a control algorithm that incorporates both fading memory proportional derivative controller (FMPD) and adaptive system for estimating changing sensitivity. Huyett et al. (2015) realize a fully implantable AP using intra-peritoneal (IP) insulin delivery and glucose sensing. Ly et al. (2016) determine the feasibility and efficacy of an automated PID with insulin feedback (PID-IFB) controller in overnight closed-loop (OCL) control of children and adolescents. Pinsker et al. (2016) compare MPC and PID control for the AP, and indicate that MPC performed particularly well.

The most used algorithm in glucose control is the MPC, which is based on prediction of glucose dynamics using a model of the patient metabolic system, this algorithm is suitable for reducing of time delays due to subcutaneous glucose sensing and insulin infusion. **MPC** has been used by Jacobs et al. (2015) to show how exercise can be automatically detected and use an exercise dosing adjustment algorithm. Del Favero et al. (2015) suggest in randomized 2-month study a modular model predictive control (MMPC) managed by a wearable system. Resalat et al. (2016) introduce a DH-MPC approach that can switch between dual hormone and single hormone. Doyle's group extends the MPC by defining a new cost function named zone MPC instead of a set-point target (Gondhalekar et al. 2015).

The purpose of this paper is to design a new control algorithm implemented in the Artificial Pancreas based on MPC. The principle of the new method is to introduce a new formulation of the cost function of MPC that gives a fast controller capable to reject rapidly the effect of meal intake and avoid hypoglycemia. The reminder of this paper is organized as follows: first, we provide a modelization phase in Sect. 2. Design of the controller will be presented in Sect. 3. Then we present the tuning controller procedure in Sect. 4. Section 5 Summaries simulation and discuss result of the controller implementation. Conclusions will be outlined in Sect. 3

2 Modelization

Multiple control-relevant models have been developed to design the control algorithms for AP, but the predictions of these models still not perfect. Furthermore, the asymmetry in the glycemic scale must also be taken into account, considering the rapid effect of hypoglycemia that occurs in a very small range of glycemia, and the long-term effects of hyperglycemia that are seen in a large range. This is especially inherent because of the dangerous effect of excess insulin, and the incapacity to remove insulin from the subject after delivery (Finan et al. 2010). ARX model is used in this work because of its simplicity and its capacity to guarantee good predictions. This model is identified from information available in the UVa/Padova simulator. The model is personalized using a priori patients' characteristics in order to limit the conservatism due to large inter-subject variability.

2.1 Insulin-Glucose Transfer Function

The plant is a discrete time and linear time-invariant (LTI) system using a sample-period Ts = 5 min. The model is linearized around a steady-state that has been reached by applying the basal rate specific to the subject U_{BASAL} U/h, and lead to a steady-state output ys = 110 mg/dL. The input of the plant is the administered insulin bolus U [U] delivered per sample-period, and the output of the model is the subject's blood glucose value Y [mg/dL].

The transfer function of the system is

$$\frac{y(z^{-1})}{u(z^{-1})} = \frac{1800\, F \cdot c}{u_{TDI}} \cdot \frac{z^{-3}}{\left(1 - p_1 Z^{-1}\right)\left(1 - p_2 Z^{-1}\right)^2} \tag{1}$$

With c: = −60 $(1 - p_1)(1 - p_2)^2$, F: = 1.5, $p_1 = 0.98$, $p_2 = 0.965$. U_{TDI} [U] is the subject specific total daily insulin amount.

2.2 State-Space Model

The transformation from the function transfer to the state-space model leads to the following system:

$$x_{i+1} = Ax_i + Bu_i \tag{2a}$$

$$y_i = Cx_i \tag{2b}$$

$$A := \begin{bmatrix} p_1 + 2p_2 & -p_1p_2 - p_2^2 & p_1p_2^2 \\ 1 & 0 & 0 \\ 0 & 1 & 0 \end{bmatrix} \in \mathbb{R}^{3\times 3}$$

$$B := \frac{1800\, F \cdot c}{u_{TDI}} \cdot [1\,0\,0]^T \in \mathbb{R}^3$$

$$C := [0\,0\,1] \in \mathbb{R}^{1\times 3}$$

Fc is a safety factor, it is unitless and it can be specific, but fixed in this paper to 1.5. $p_1 = 0.98$, $p_2 = 0.965$ are poles of the transfer function. U_{TDI} [U] is the subject specific total daily insulin amount, and the constant c is employed to set the correct gain, and for unit conversion $c := 1.47 \times 10^{-3}$.

2.3 State-Estimation

The Luenberger observer (a linear state estimator) is used to estimate the initial state for each iteration. The state estimator is implemented as

$$\hat{x}_{k+1} = A\hat{x}_k + BU'_k - L\left(Y'_k - \hat{Y}'_k\right) \tag{3}$$

$$\hat{Y}'_k = C\hat{x}_k \tag{4}$$

$$L = K^T \tag{5}$$

$$K = -(CPC^T + \hat{R})^{-1}CPA^T \tag{6}$$

$\hat{x}_k$ represents the estimated states of X_k and $\hat{Y}'_k$ represent the estimated BG Y_k, L is the observer gain. P satisfies the discrete algebraic Riccati equation

$$P = APA^T + \hat{Q} - APC^T(CPC^T + \hat{R})^{-1}CPA^T \tag{7}$$

where $\hat{Q} = 1$ and $\hat{R} = 1000$ are positive definite design parameters.

3 Control Design

3.1 Controller

A Control Algorithm is a software embedded in an external processor that receives information from the CGM and realizes a series of mathematical calculations. Based on these calculations, the controller sends recommendation to the infusion pump to inject the computed amount of insulin. The system is subject to important disturbances, like meal, stress, and exercises.

We choose to use the MPC because it presents many advantages in control of blood glucose first the use of constraints on the insulin delivery rate (and/or insulin on board) can be explicitly included in the control calculation; then the capacity to include the effect of meals, exercise. Further it can compensate the delay induced by the system by prediction of the evolution of the system. In MPC procedure a model is used to predict the effect of control moves on future outputs then an optimization is performed to compute the best set of current and control moves to reach an objective (Lee et al. 2016), the basic idea of MPC is shown in Fig. 2.

3.2 Cost Function

In order to enhance glucose control, the proposed approach use different scaling to glucose values above and below the targets. Above the target we design a quadratic penalty on glucose excursions, however for values below the target, the cost function is reshaped to apply an exponential penalty on glucose excursions. The exponential formulation means that glucose excursions near the target have a reasonably conservative, but nonzero, response to fluctuations around the target, while maintaining the ability to respond quickly to larger excursions.

The resulting enhanced-MPC (e-MPC) cost function J for which the MPC is optimized is defined as

$$\boldsymbol{J}'\left(\left\{\boldsymbol{U}^k\right\}_{j=0}^{\boldsymbol{Nu}-1}\right)=\sum_{j=1}^{\boldsymbol{Np}}\boldsymbol{Q}(\boldsymbol{k})\hat{\boldsymbol{Y}}(\boldsymbol{k})^2+\sum_{j=1}^{\boldsymbol{Np}}\exp\left(\boldsymbol{a}\breve{\boldsymbol{Y}}(\boldsymbol{k})\right) \\ +\boldsymbol{R}(\boldsymbol{k})\sum_{j=0}^{\boldsymbol{Nu}-1}\boldsymbol{U}(\boldsymbol{k})^2 \tag{8}$$

And subject to

$$\boldsymbol{x}_0 := \boldsymbol{x}_{\boldsymbol{i}} \tag{9a}$$

$$\boldsymbol{x}_{\boldsymbol{k}+1} := \boldsymbol{A}\boldsymbol{x}_{\boldsymbol{k}} + \boldsymbol{B}\boldsymbol{u}_{\boldsymbol{k}} \quad \forall \boldsymbol{k} \in \mathbb{Z}_0^{N_{p-1}} \tag{9b}$$

$$\boldsymbol{y}_{\boldsymbol{k}} := \boldsymbol{C}\boldsymbol{x}_{\boldsymbol{k}} \quad \forall \boldsymbol{k} \in \mathbb{Z}_0^{N_y} \tag{9c}$$

$$0 \le \boldsymbol{u}_{\boldsymbol{k}} + \boldsymbol{u}_{\boldsymbol{BASAL}}(\boldsymbol{i}+\boldsymbol{k}) \le \boldsymbol{u}_{\boldsymbol{max}} \quad \forall \boldsymbol{k} \in \mathbb{Z}_0^{N_{u-1}} \tag{9d}$$

$$\hat{\boldsymbol{Y}}_{\boldsymbol{k}} := \max(\boldsymbol{Y}_{\boldsymbol{k}}, 0) \quad \forall \boldsymbol{k} \in \mathbb{Z}_0^{N_y} \tag{9e}$$

$$\breve{\boldsymbol{Y}}_{\boldsymbol{k}} := \min(\boldsymbol{Y}_{\boldsymbol{k}}, 0) \quad \forall \boldsymbol{k} \in \mathbb{Z}_0^{N_y} \tag{9f}$$

where: $\mathbb{Z}_+$ is the set of positive integers. $\mathbb{Z}_a^b$ is the set of consecutive integers $\{a, \ldots, b\}$. $\boldsymbol{N_p} \epsilon \mathbb{Z}_+$ is the prediction horizon. $\boldsymbol{N_u} \ \epsilon \ \mathbb{Z}_1^{Np}$ is the control horizon. $\boldsymbol{u}, \boldsymbol{x}, \boldsymbol{y}$ are respectively the predicted input u, the state x and the glucose output y. $\boldsymbol{R} \ \epsilon \ \mathbb{R} > 0$ is the penalization of the control inputs, $\boldsymbol{Q} \ \epsilon \ \mathbb{R} > 0$ is the penalization of the system output. $\boldsymbol{a} = \mathbf{0.18}$ represents the exponential coefficient. Equations (9a)–(9c) predict the future state of the system. Equation (9d) represent input constraint. Equations (9e) and (9f) provide a positive and negative zone deviations to penalize in (8).

4 Tuning Procedure

4.1 Engineering Rules for Selecting Weights

The output weight (**Q**) provides additional degrees of freedom to solve the tuning problem. Small value of **Q** yield to a smooth output and large value yield to a faster output tracking. A correct setting of the input weight (**R**) helps to prevent both aggressive control and an oscillatory behavior of the controlled outputs. Moreover, increasing **R** can cause a sluggish control performance, and may produce unacceptable effects on the closed-loop system. Figure 3 presents a comparison between different control settings of **Q: R** ratio of MPC in response to a typical meal disturbance of 60-g CHO.

Seen the significantly impacts of this MPC parameters on the closed loop performance, a good tuning of this parameters will improve the set-point tracking and disturbance rejection.

Fig. 2 Basic concept of MPC

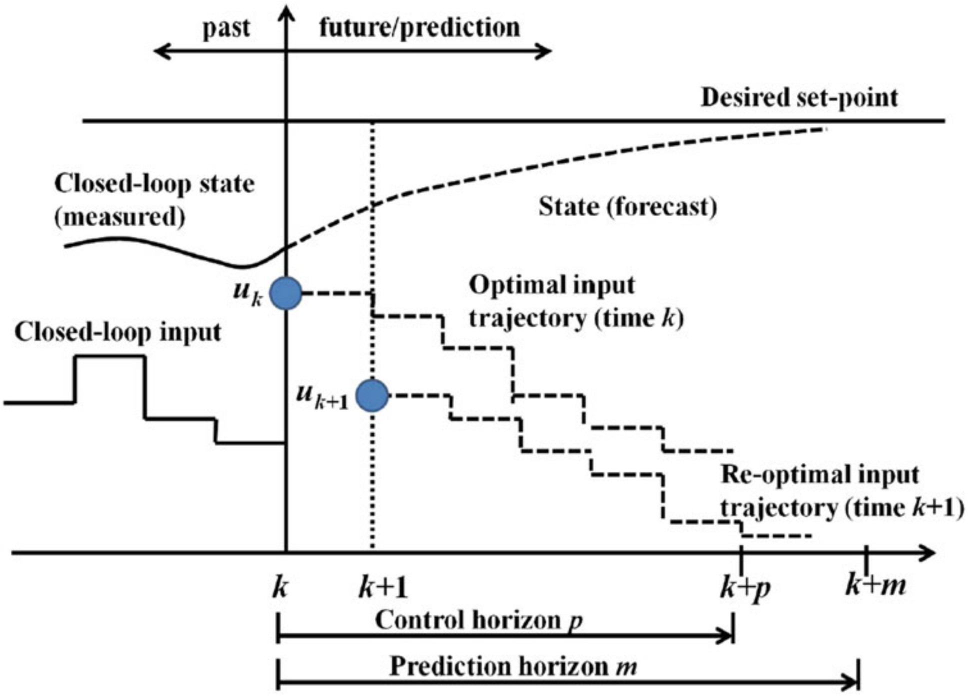

4.2 Penalization of the Cost Function

The proposed mechanism penalizes the output and the inputs based on weights that are function of the rate of change Q = Q(α1) and R = R(α1), respectively. These weights are used to scale the control variables. The introduction of this weights functions allows conservative controller to give an "extra kick" when the glucose trajectory is rising, but the mechanism does not actively allow the controller to "back off" when the trajectory is falling.

The glucose rate of change α1 is defined as follows:

$$\varphi_1 = \frac{3Y_I - 4Y_{I-1} + Y_{I-2}}{2\Delta t}, \tag{10}$$

where t is time, Δt is the time difference between two sample intervals, Y_i is the glucose measurement and the subscripts i − 1, i − 2 and i are the two previous and current samples. Figure 4 illustrates the variation of the output (a) and the Input (b) penalization. Equation (11) describes the adjusted output weight upon the rate of change. Equation (12) describes the variation of the input weight upon the rate of change.

$$Q = \begin{cases} Qmin & if\ \alpha 1 \le \alpha 1_{min} \\ \frac{H_2}{2}\cos\left(\frac{2\pi}{T_2}\cdot\alpha 1\right) + \frac{Qmax + Qmin}{2} & if\ \alpha 1_{min} < \alpha 1 < 0 \\ Qmax & if\ \alpha 1 \ge 0 \end{cases} \tag{11}$$

With: $\alpha 1_{max} = -1$, **Qmax = 1, Qmin = ε = 10^{-6}**, $\frac{T_2}{2} = -\alpha 1_{min}$, $H_2 = \frac{\mathbf{Qmax - Qmin}}{2}$.

$$R = \begin{cases} Rmax & if\ \alpha 1 \le 0 \\ \frac{H_1}{2}\cos\left(\frac{2\pi}{T_1}\cdot\alpha 1\right) + \frac{Rmax + Rmin}{2} & if\ 0 < \alpha 1 < \alpha 1_{max} \\ Rmin & if\ \alpha 1 \ge \alpha 1_{max} \end{cases} \tag{12}$$

With: $\alpha 1_{max} = \mathbf{1.75}$, **Rmax = 11000, Rmin = 14,** $\frac{\mathbf{T_1}}{\mathbf{2}} = \alpha 1_{max}$, $H_1 = \frac{\mathbf{Rmax - Rmin}}{2}$.

The resulting optimization problem is solved via a sequence of quadratic programming (QP) problems within a region specified by linear constraints and bounds. A suitable technical computing software (e.g., MATLAB "fmincon.m") is used to solve the optimization problem and the following hard constraints are implemented on the manipulated variables (I_D'): −basal ≦ I_D' ≦72 U/h; where the subject's basal rate (as set by the subject's physician) is expected to be in the range of 0.6–1.8 U/h.

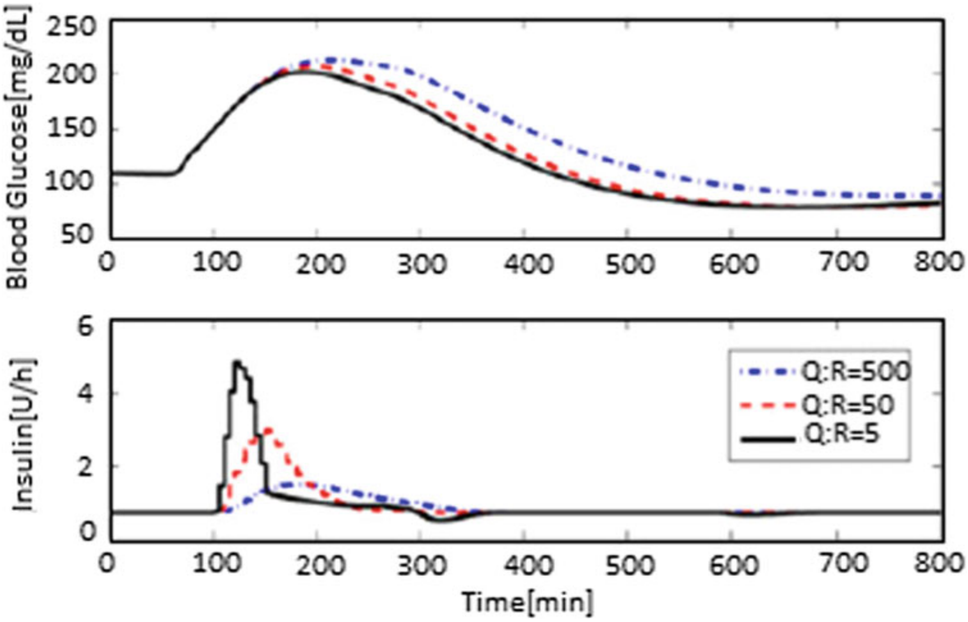

Fig. 3 Comparison of different control settings of Q: R

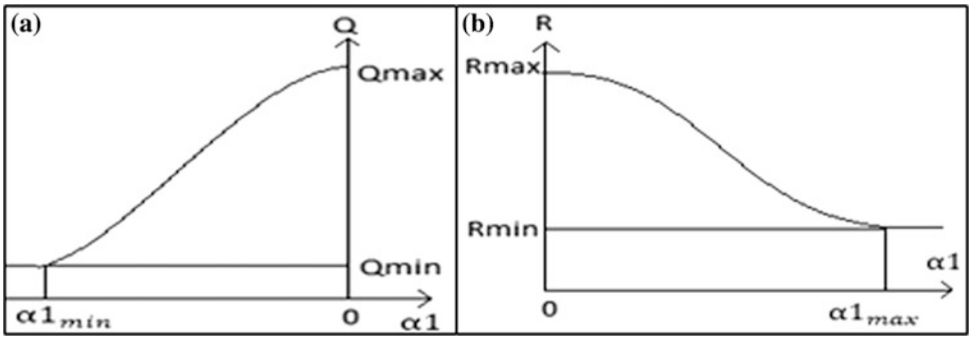

Fig. 4 Evolution of output (**a**) and input (**b**) penalization

4.3 Flowchart of the Proposed Controller

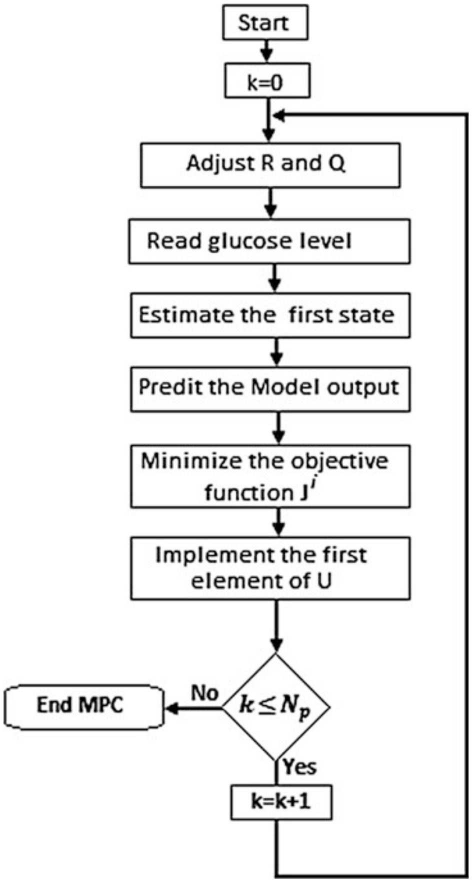

5 In Silico Artificial Pancreas Evaluation

5.1 Metabolic Simulator System

A simulation environment of the metabolic system for evaluation of AP has been developed at the University of Virginia and the University of Padova (Kovatchev et al. 2010). The UVa/Padova simulator was approved by the U.S. Food and Drug Administration (FDA) for verification of control algorithms used in AP before doing clinical trials on T1DM subjects, these trials are equivalent to animal tests. The simulator contains a set of different virtual patients with varying parameters, such as weight, age, gender, 30 in silico subjects of the commercial version (v3) of the UVa/Padova simulator are used in this study to evaluate the control performance of the new MPC strategy, this subjects are composed from 10 adults, 10 children, and 10 adolescents.

5.2 Protocol of Simulation

We compare in this work the enhanced-MPC (e-MPC) to the zone-MPC (z-MPC) that uses a symmetric and a fixed penalization of the cost function (Grosman et al. 2010). The two algorithms manage the blood glucose level of 30 virtual patients of the UVa/Padova simulator under 28 h of simulation. The simulations begun at 6:00 pm with two hours of open-loop until 8:00 pm when the feedback controller got turned on, after that the simulation run in closed-loop until 10:00 pm the following day. Every simulation included three meals during the day: Dinner 60 g carbohydrate (gCHO), breakfast 60 (gCHO), lungh 70 (gCHO) meals consumed at 8:00 pm, 08:30 am, and 1:30 pm, respectively.

5.3 In Silico Results

Figure 5 depicts the mean Blood Glucose and insulin delivery trajectories obtained in simulation for 30 in silico patients. The mean glucose value during the entire trial was 136.5 mg/dL for the e-MPC versus 141.3 mg/dL for the z-MPC. The time within the euglycemic range is 68.3% for e-MPC versus 61.5% for z-MPC. The mean glucose during the post prandial period after the unannounced meals was 171.2 mg/dL for e-MPC versus 183.4 mg/dL for z-MPC and the time taken to return to the 70–180 mg/dL safe glucose range were also improved with 215 min for e-MPC versus 230 min for z-MPC.

Results show that the use of e-MPC increases the time spent in target range (80 $\le$ glucose $\le$ 140 mg/dl), reduces

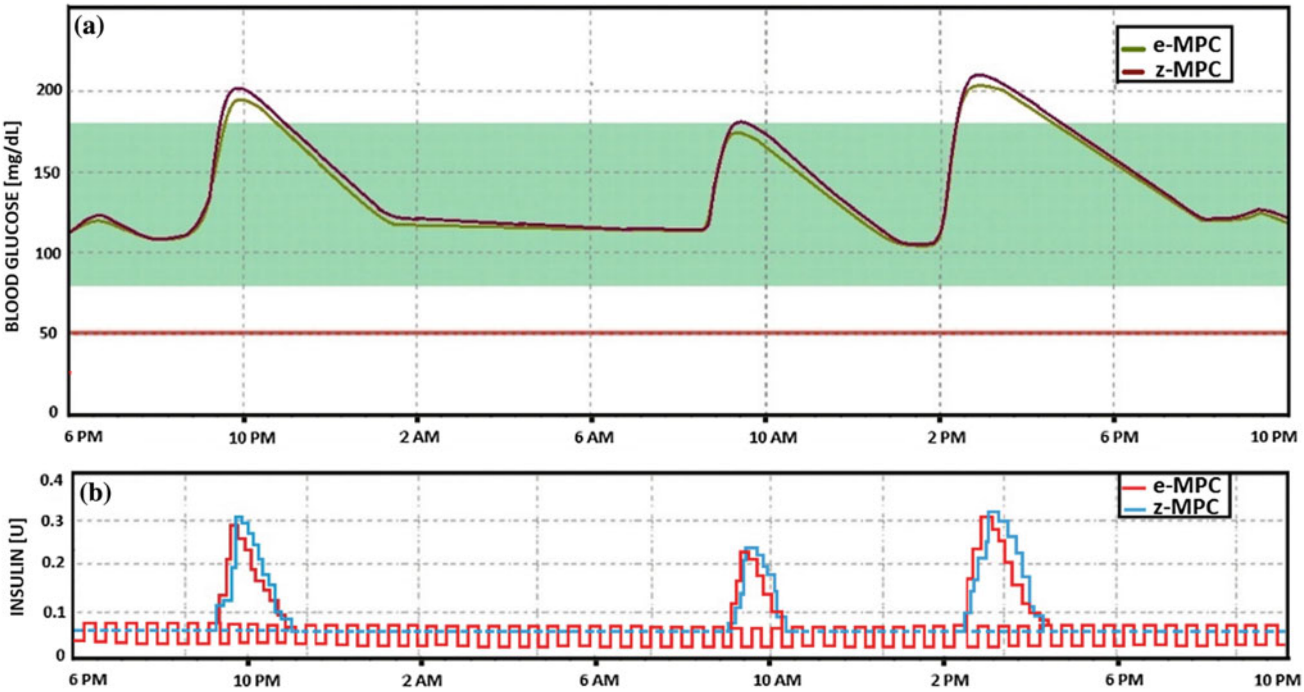

Fig. 5 Mean glucose (**a**) and insulin (**b**) traces of 30 in silico subjects controlled by the e-MPC and the z-MPC

the peak of glucose and minimizes the percentage of postprandial glucose levels above 200 mg/dl; furthermore, the acceleration of the command introduced by the e-MPC allows to reject rapidly the effect of disturbance, to avoid hypoglycemia and to minimize the amount of insulin injected.

6 Conclusion

This paper presents a new algorithm of control implemented in the Artificial Pancreas. In order to maintain reasonable responses to disturbance caused by meals, we introduce an enhanced MPC that uses an exponential scaling for movements below the target and a quadratic scaling for movement above the target. The proposed MPC was tuned with two inconstant weights sets to guarantee the desired performance. In silico trials under an approved platform of test demonstrate the Efficiency of the proposed method to overcome control challenges. Future study should focus more on physical activities and stress that are also included among the types of disturbances in blood glucose control.

Acknowledgements This work returns the framework of the research project SISA1 “Mini intelligent Power plant” began between research center SISA and our University. We are anxious to think the Hassan II University of Casablanca for the financing of this project.

References

Del Favero, S., Place, J., Kropff, J., Messori, M., Keith-Hynes, P., Visentin, R., et al. (2015). Multicenter outpatient dinner/overnight reduction of hypoglycemia and increased time of glucose in target with a wearable artificial pancreas using modular model predictive control in adults with type 1 diabetes. *Diabetes, Obesity & Metabolism, 17,* 468–476.

Doyle, F. J., Huyett, L. M., Lee, J. B., Zisser, H. C., & Dassau, E. (2014). Closed-loop artificial pancreas systems: engineering the algorithms. *Diabetes Care, 37,* 1191–1197. https://doi.org/10.2337/dc13-2108.

Finan, D. A., Jørgensen, J. B., Poulsen, N. K., Madsen, H. (2010). Robust model identification applied to type 1 diabetes. In *Proceedings of the American Control Conference*, Baltimore, MD, USA, pp. 2021–2026.

Gondhalekar, R., Dassau, E., Doyle, III F (2015). *Velocity-weighting to prevent controller-induced hypoglycemia in MPC of an artificial pancreas to treat T1DM*. American Control Conference Palmer House Hilton. Chicago, IL, USA, July 1–3.

Grosman, B., Dassau, E., Zisser, H. C., Jovanovic, L., & Doyle, F. J., III. (2010). Zone model predictive control: A strategy to minimize hyper- and hypoglycemic events. *Journal of Diabetes Science and Technology, 4,* 961–975.

Huyett, L. M., Dassau, E., Zisser, C., & Doyle, F. J. (2015). Design and evaluation of a robust PID controller for a fully implantable artificial pancreas. *Industrial & Engineering Chemistry Research, 54*(42), 10311–10321.

Jacobs, G., El Youssef, J., Castle, J., Bakhtiani, P., Branigan, D., Breen, M., Bauer, D., Preiser, N., Leonard, G., Stonex, T., Ward, W.K. (2014). Automated control of an adaptive bihormonal, dual-sensor artificial pancreas and evaluation during inpatient studies. *IEEE Transactions on Biomedical Engineering* Volume: 61, Issue: 10.

Jacobs, P. G., Resalat, N., & El Youssef, J. (2015). Incorporating an exercise detection, grading, and hormone dosing algorithm into the artificial pancreas using accelerometry and heart rate. *J Diabetes Sci Technol, 9*(6), 1175–1184.

Kovatchev, B. P., Cobelli, C., & Renard, E. (2010). Multinational study of subcutaneous model-predictive closed-loop control in type 1 diabetes mellitus: summary of the results. *Journal of Diabetes Science and Technology, 4,* 1374–1381.

Lee, J., Gondhalekar, R., Dassau, E., & Doyle, F. J., III. (2016). Shaping the MPC cost function for superior automated glucose control. *Industrial & Engineering Chemistry Research, 49*(7), 779–784.

Ly, T. T., Keenan, D. B., Roy, A., Han, J., Grosman, B., Cantwell, M., … & Buckingham, B. A. (2016). Automated overnight closed-loop control using a proportional-integral-derivative algorithm with insulin feedback in children and adolescents with type 1 diabetes at diabetes camp. *Diabetes Technology & Therapeutics*, *18*(6), 377–384.

Pinsker, J. E., LeeJ, B., Dassau, E., Seborg, D. E., Bradley, P. K., Gondhalekar, R., et al. (2016). Randomized crossover comparison of personalized MPC and PID control algorithms for the artificial pancreas. *Diabetes Care, 39,* 1135–1142.

Resalat, N., El Youssef, J., Reddy, R., & Jacobs, P. G. (2016) Design of a dual-hormone model predictive control for artificial pancreas with exercise model. In *38th Annual International Conference of the IEEE Engineering in Medicine and Biology Society (EMBC).*

Mohamed El Hachimi got a degree of Electrical Engineer from FSTM University Hassan II then he continues his study at the same Faculty to get a doctorate in control system and he is teaching Electricity and Electronic in FSTM.

Abdelhakim Ballouk is currently working as a professor in Faculty of sciences and technologies University Hassan II. His current research interests are on control system.

Abdennaceur Baghdad is currently working as a professor in Faculty of sciences and technologies University Hassan II. His current research interests are on telecommunications.

Observer-Based Adaptive Backstepping Control of Grid-Connected Wind Turbine Under Deep Grid Voltage Dip

Oluwaseun Simon Adekanle, M. Guisser, E. Abdelmounim, and M. Aboulfatah

Abstract

The stator windings of the DFIG are directly connected to the grid. This makes the DFIG susceptible to grid fault in form of short-circuit among the phases. The stator and rotor of the DFIG are electromagnetically coupled; therefore, the resulting stator current surge during low-voltage dips provokes inrush current at the delicate back-to-back converters and DC-link capacitor voltage swell. When rotor current and DC-link voltage increase above their admissible Save Operating Zone (SOZ), rotor converters are damaged and active–reactive power control is consequently lost even after the fault is cleared. In this paper, a robust nonlinear disturbance rejection controller, under the context of Lyapunov stability theory, is first employed to control the Rotor and Grid Side Power Converters under normal grid conditions. Then, an active crowbar and DC-link chopper are designed to be switched on at the detection of grid fault to serve as protection for the turbine. A comparative analysis under MATLAB/Simulink is carried out using the PI-controller (PIC) and Adaptive Backstepping Controller (ABC) for a 1.5 MW turbine.

Keywords

Adaptive Backstepping control • Doubly Fed Induction Generator • Fault ride through technique • High Gain observer

1 Introduction

For three major reasons, the DFIG has gained prominence among wind energy generators. First, the rotor converters can be rated to support only 25–30% of the total nominal power of the generator, thereby reducing the cost. Second, it can operate over a larger range of wind speed. This means energy can still be extracted even at low wind speed. Lastly, the rotor converters can be controlled to place the turbine system at an operating point where energy extraction is maximal through a technique called 'Maximum Power Point Tracking (MPPT)'.

Several orientation schemes have been engaged in the literature, like Stator Voltage Orientation (SVO) and Stator Flux Orientation (SFO) and have been combined successfully with the PIC (Pena et al. 1996; Srirattanawichaikul et al. 2016), Sliding Mode Controller (Ebrahimkhani 2016), Backstepping Controller (Cai et al. 2014), and Fuzzy Logic (Belmokhtar et al. 2014) to control the DFIG effectively but under stable grid conditions.

However, the DFIG is sensitive to grid disturbances and the occurrence of grid fault like grid voltage dip leads to stator current oscillations, pulsations in stator active and reactive power and electromagnetic torque oscillations (Mwasilu et al. 2012; Justo et al. 2015). Furthermore, the strong electromagnetic coupling between the stator and rotor easily propagates inrush rotor current to the delicate back-to-back converters. When this happens, there is DC-link voltage swell and rotor converters may be found operating outside their SOZ. The converters are consequently damaged and the power control is lost even after the fault is cleared.

Many Fault Ride through Techniques (FRT) to enable the DFIG tolerate grid fault have be proposed in the literature, which may be categorized into three groups: (1) integration of additional protection device, (2) installation of reactive power supplying devices like STATCOM and DVR (Shen et al. 2017) and (3) use of advanced control approach (Bu

O. S. Adekanle (✉) · M. Guisser · E. Abdelmounim
M. Aboulfatah
Laboratory of Signal Analysis and Information Processing, Faculty of Science and Technology, Settat, Morocco
e-mail: adekanlesimon@gmail.com

M. Guisser
e-mail: mguisser@gmail.com

E. Abdelmounim
e-mail: hassan.abdelmounim@hotmail.fr

M. Aboulfatah
e-mail: Aboulfatah_mo@hotmail.com

S. El Hani and M. Essaaidi (eds.), *Recent Advances in Electrical and Information Technologies for Sustainable Development*, Advances in Science, Technology & Innovation, https://doi.org/10.1007/978-3-030-05276-8_9

et al. 2013). The crowbar resistor is the most used protection device (Yang et al. 2016). It is a simple set of resistor bank connected in parallel with the rotor windings via an IGBT switch. The RSPC is disconnected from the rotor and the slip rings are switched to the crowbar resistors during fault. The crowbar can be integrated with other protection devices such as DC-chopper connected in parallel with DC-link capacitor to limit the capacitor overcharge and Series Dynamic Resistor (SDR) connected in series with rotor windings to reduce the current through the converters (Meenakshi 2013).

These FRT are often combined with the PIC. However, when grid fault occurs, the PIC cannot efficiently handle the current surge at the instant of fault occurrence and fault clearance because of the extremely nonlinear behaviour of the system under these conditions. The Sliding Mode Controller used in Saad et al. (2015) is robust but its performance is marred by high-frequency low oscillations called chattering.

The authors in Roy and Mahmud (2017) proved the Adaptive Backstepping Controller (ABC) to be robust against parameter variation, and system uncertainties. In this paper, the ABC is examined under external disturbances in the form of grid voltage dip. A High Gain Observer is designed to estimate the power generated at the rotor side of the machine and the power loss in the RSPC to render the control strategy more efficient and eliminate the influence of measurement noise introduced by sensors. The ABC is combined with the crowbar and DC-chopper without disconnecting the converters to enhance the FRT of the DFIG.

This paper is organized as follows: the next paragraph deals with system modelling. Then, the control technique is carefully elaborated, followed by simulation results and analysis. A short conclusion is presented at the end of the paper.

2 System Modelling

As described in Fig. 1, the overall grid-connected wind turbine comprises a Doubly Fed Induction Generator connected to utility grid directly via its stator and indirectly through its rotor with the intermediary of back-to-back converters.

2.1 Rotor-Side Converter Model

To achieve independent control of active and reactive power, the Stator Voltage Orientation elaborated in Srirattanawichaikul et al. (2016) is achieved using Phase Locked Loop (PLL) by aligning the d-axis of the reference frame to the stator voltage position. In (1) and (2), the derivatives of the *d*-*q* components of rotor current are expressed in function of rotor resistance R_r, stator flux linkage φ_{sq}, rotor currents (i_{rd}, i_{rq}), slip angular velocity ω_r, stator and rotor self-inductance L_s and L_r, mutual inductance L_m, stator angular velocity ω_s, and rotor speed ω_m.

$$\frac{di_{rd}}{dt} = \frac{v_{rd}}{\sigma L_r} - \frac{R_r i_{rd}}{\sigma L_r} + \omega_r i_{rq} + \frac{L_m \omega_r \varphi_{sq}}{\sigma L_r L_s} \tag{1}$$

$$\frac{di_{rq}}{dt} = \frac{v_{rq}}{\sigma L_r} - \frac{R_r i_{rq}}{\sigma L_r} - \omega_r i_{rd} \tag{2}$$

where $\sigma = 1 - \frac{L_m^2}{L_s L_r}$ and $\omega_r = \omega_s - p \cdot \omega_m$.

Power and electromagnetic torque equations can be given under Voltage-Oriented Control as (3) and (4), respectively. It can be observed from the equations that Electromagnetic Torque and stator Reactive Power can be controlled independently by controlling d-axis and q-axis currents

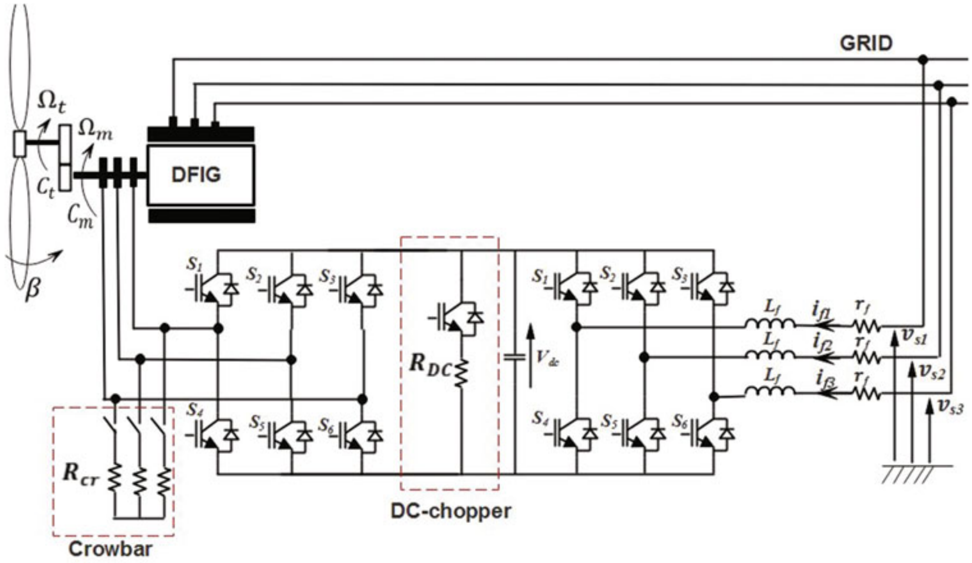

Fig. 1 Grid connected Doubly Fed induction generator setup

components independently. This is the notion of the decoupled control.

$$T_{em} = \frac{3}{2} p \frac{L_m}{L_s} \left(\varphi_{sq} i_{rd} \right) \tag{3}$$

$$\begin{cases} P_s = -\frac{3}{2} \frac{L_m}{L_s} v_{sd} i_{rd} \\ Q_s = -\frac{3}{2} \frac{v_{sd}}{L_s} \left(\varphi_{sq} - L_m i_{rq} \right) \end{cases} \tag{4}$$

2.2 Grid-Side Converter Model

Aligning the d-axis of the voltage vector to the synchronously rotating reference frame, the direct and quadrature components of the current passing through the filter can be expressed, in function of filter resistance R_f and inductance L_f, as in (5) and (6), respectively.

$$\frac{di_{fq}}{dt} = -\frac{R_f}{L_f} i_{fq} - \omega_s i_{fd} - \frac{v_{fq}}{L_f} \tag{5}$$

$$\frac{di_{fd}}{dt} = -\frac{R_f}{L_f} i_{fd} - \omega_s i_{fq} + \frac{v_{sd}}{L_f} - \frac{v_{fd}}{L_f} \tag{6}$$

The equations of active and reactive power exchanged between the grid and the filter are given in (7).

$$\begin{cases} P_f = \frac{3}{2} \left(v_{sd} i_{fd} \right) \\ Q_f = -\frac{3}{2} \left(v_{sd} i_{fq} \right) \end{cases} \tag{7}$$

The instantaneous voltage V_{dc} across the capacitor can be expressed in (8), where C is the capacitance of the DC-link capacitor and i_{ond} the RSPC DC-bus current. P_{l_filter} and P_{l_GSPC} which represent power loss in the filter and GSPC are neglected in the literature but will be considered in this work to render the controller robust against the perturbations they cause.

$$v_{dc} \frac{Cdv_{dc}}{dt} = \frac{3}{2} V_{sd} i_{fd} - P_{l\_filter} - P_{l\_GSPC} - v_{dc} \cdot i_{ond} \tag{8}$$

3 Control Strategy

The controller used is the Adaptive Backstepping Controller (ABC). It is designed to take uncertainties, observation error or modelling errors into consideration and subsequently suppress their effect on the system.

3.1 Rotor-Side Power Converter (RSPC) Control

The control objectives at the RSPC are to drive the turbine to track the maximum power point no matter the wind speed; and to ensure reactive power control. The MPPT technique used in this paper is the torque control explained in Gaillard (2010).

Variables θ_{fd} and θ_{fq} are added to (5) and (6) to model uncertainties in the system and presented in (9) and (10).

$$\frac{di_{fq}}{dt} = -\frac{R_f}{L_f} i_{fq} - \omega_s i_{fd} - \frac{v_{fq}}{L_f} + \theta_{fq} \tag{9}$$

$$\frac{di_{fd}}{dt} = -\frac{R_f}{L_f} i_{fd} + \omega_s i_{fq} + \frac{v_{sd}}{L_f} - \frac{v_{fd}}{L_f} + \theta_{fd} \tag{10}$$

Let Q_{ref} be the reference stator reactive power value. It is usually taken as zero to ensure unity power factor at the stator side of the generator but during grid faults, when the DFIG has to supply reactive power to the grid to assist in grid recovery, Q_{ref} is different from zero.

Because of the unpredictable availability of wind power, to efficiently maximize power harvesting, the electromagnetic torque of the generator must track its optimum reference value computed by the MPPT technique at every instance. Please note that to avoid explaining the controller synthesis twice, only the control of d-axis current component will be explained. Current references are calculated from Torque and Reactive Power references by using Eqs. (11) and (12).

$$i_{rqref} = \frac{2L_s Q_{ref}}{3 v_{sd} L_m} + \frac{\varphi_{sq}}{L_m} \tag{11}$$

$$i_{rdref} = \frac{2L_s T_{emref}}{3pL_m \varphi_{sq}} \tag{12}$$

The tracking error variable to be controlled and its time derivative are given in (13) and (14), respectively.

$$\varepsilon_{rd} = i_{rd} - i_{rd}^{*} \tag{13}$$

$$\dot{\varepsilon}_{rd} = \frac{v_{rd}}{\sigma L_r} - \frac{R_r i_{rd}}{\sigma L_r} + \omega_r i_{rq} + \frac{L_m \omega_r \varphi_{sq}}{\sigma L_r L_s} + \theta_{rd} \tag{14}$$

Lyapunov function is defined as

$$V_{rd}(\varepsilon_{rd}) = \frac{1}{2} \varepsilon_{rd}^2 + \frac{\overline{\theta}_{rd} \overline{\theta}_{rd}}{2m_1} \tag{15}$$

Fig. 2 Graphical description RSPC control scheme

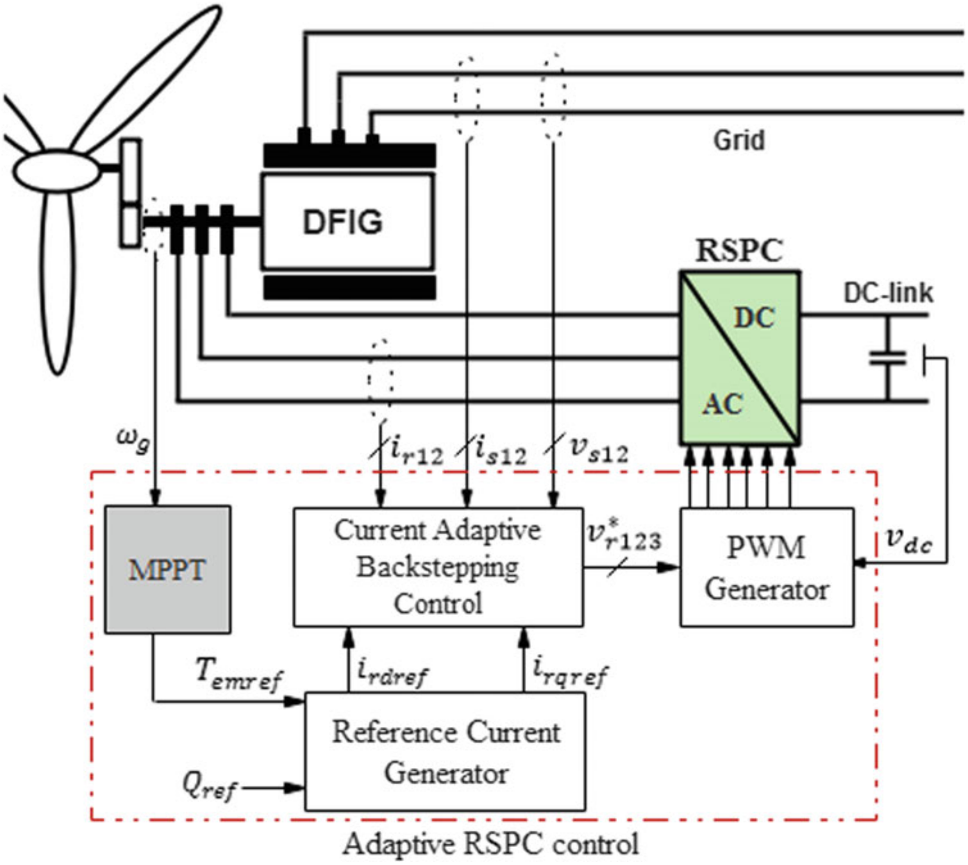

Since the Lyapunov function is positive, for the error to be stable and converge to zero, $\dot{V}_{rd}$ must be strictly negative. This consequently means that if the condition in (16) is satisfied, the d-axis rotor current stably tracks its reference variable.

$$\dot{V}_{rd} = \varepsilon_{rd}\overbrace{\left(\frac{v_{rd}}{\sigma L_r} - \frac{R_r i_{rd}}{\sigma L_r} + \omega_r i_{rq} + \frac{L_m \omega_r \varphi_{sq}}{\sigma L_r L_s} + \hat{\theta}_{rd}\right)}^{=-k_{rd}\varepsilon_{rd}} + \overline{\theta}_{rd}\overbrace{\left(\varepsilon_{rd} + \frac{\dot{\overline{\theta}}_{rd}}{m_1}\right)}^{=0} \tag{16}$$

The final controller output variable and the derivative of the uncertainty estimate are derived and expressed in (17) and (18), respectively.

$$v_{rd} = \sigma L_r\left(-k_{rd}\varepsilon_{rd} + \frac{R_r i_{rd}}{\sigma L_r} - \omega_r i_{rq} - \frac{L_m \omega_r \varphi_{sq}}{\sigma L_r L_s} - \hat{\theta}_{rd}\right) \tag{17}$$

$$\dot{\hat{\theta}}_{rd} = m_{rd}\varepsilon_{rd} \tag{18}$$

For the q-axis current control, the control output is given as

$$v_{rq} = \sigma L_r\left(-k_{rq}\varepsilon_{rq} + \frac{R_r i_{rq}}{\sigma L_r} + \omega_r i_{rd} - \hat{\theta}_{rq}\right) \tag{19}$$

$$\dot{\hat{\theta}}_{rq} = m_{rq}\varepsilon_{rq} \tag{20}$$

where K_{rd}, K_{rq}, m_{rd}, m_{rq} are control and adaptation parameters chosen strictly positive. Figure 2 gives a graphical description of this adaptive Backstepping Control of the DFIG wind turbine.

3.2 Grid-Side Power Converter (GSPC) Control

The objective of the Grid-Side Power Converter Control is to stabilize DC-link voltage and annul the reactive power in the RL filter. To be able to synthesize the control law immune to perturbation, the terms '$-P_{l\_filtre} - P_{l\_CPCR} - v_{dc}.i_{ond}$' representing power loss in the voltage Eq. (21) must be available. However, it is not readily available for measurement with the help of a sensor. We, therefore, propose the use of a High Gain observer to compute an estimation of these term in real time and in close loop with the controller. The use of an observer reduce the cost of the sensor and since observers act as filters, measurement noise is avoided. Equation (21) describes the dynamics of the voltage across the DC-link capacitor.

$$v_{dc}\frac{Cdv_{dc}}{dt} = \frac{3}{2}V_{sd}i_{fd} - P_{l\_filtre} - P_{l\_CPCR} - v_{dc}\cdot i_{ond} \tag{21}$$

For convenience, the following changes in variables have been made to (21).

$$\begin{aligned}\dot{z} = V_{dc}\frac{dv_{dc}}{dt}, z = \frac{V_{dc}^2}{2}, x_2\\ = -P_{l\_filtre} - P_{l\_CPCR} - v_{dc}\cdot i_{ond},\end{aligned}$$

The resulting equation representing the DC-link voltage is now (22), where x_2 represents the term to be observed.

$$\frac{dz}{dt} = \frac{3}{2C}v_{sd}i_{fd} + x_2 \tag{22}$$

Power Loss and Rotor Power Observer

In condensed form, (22) can be expressed as (23), where $X = [x_1\,x_2\,x_3]^T = [z\,x_2\,\dot{x}_2]^T$, $k = [1\,0\,0]$, $\varphi = [ai_{fd}\,0\,0]^T$, and $A = [0\,1\,0;\ 0\,0\,1;\ 0\,0\,0]$

$$\begin{cases}\dot{X} = AX + \varphi\\ y = kX\end{cases} \tag{23}$$

A High Gain Observer for the system described by (23) can be expressed as Adekanle et al. (2017)

$$\begin{cases}\dot{\hat{X}} = A\hat{X} + \hat{\varphi} - S^{-1}k^T\left(k\hat{X} - y\right)\\ \hat{y} = k\hat{X}\end{cases} \tag{24}$$

Where $\hat{X}$ and $\hat{y}$ are the vector estimates of X and y, respectively, the gain S can be determined using (25). If the observer gain θ is judiciously chosen, $\hat{X} = [\hat{x}_1\,\hat{x}_2\,\hat{x}_3]^T$ is an estimate of $X = [z\,x_2\,x_3]^T$, The resulting equation of the DC-voltage dynamics with all variables available that will be used for controller design is expressed as (26).

$$S_{i,j} = \frac{(-1)^{i+j}(i+j-2)!}{\theta^{i+j-1}(i-1)!(j-1)!} \tag{25}$$

$$1 \le i, j \le 3$$

$$\frac{d\hat{z}}{dt} = \frac{3}{2C}v_{sd}i_{fd} + \hat{x}_2 \tag{26}$$

To improve the convergence of the control variables and robustify the system against observation error and uncertainty, a term, θ, to model the unforeseen perturbation in the system is added to the voltage and current state-space equations of the GSC model as expressed in (27–29).

$$\frac{d\hat{z}}{dt} = \frac{3}{2C}v_{sd}i_{fd} + \hat{x}_2 + \theta_z \tag{27}$$

$$\frac{di_{fq}}{dt} = -\frac{R_f}{L_f}i_{fq} - \omega_s i_{fd} - \frac{v_{fq}}{L_f} + \theta_{fq} \tag{28}$$

$$\frac{di_{fd}}{dt} = -\frac{R_f}{L_f}i_{fd} + \omega_s i_{fq} + \frac{v_{sd}}{L_f} - \frac{v_{fd}}{L_f} + \theta_{fd} \tag{29}$$

DC-link Voltage and Filter Reactive Power Control

The control of the DC-link voltage to track V_{dcref} in close loop with the observer, which translates to controlling $\hat{z}$ to track $z_{ref} = V_{dcref}^2/2$, will be done in two steps. The first step computes current reference value from the control of DC-link voltage tracking error. The current reference value is then fed to the second step where an ABC is designed to drive the direct component of filter current to track the current reference.

Step 1: Equations (30) and (31) show DC-link voltage tracking error and its integral in terms of current and observer output.

$$\varepsilon_1 = \hat{z} - z_{ref} \tag{30}$$

$$\dot{\varepsilon}_z = \frac{3}{2C}v_{sd}i_{fd} + \hat{x}_2 + \theta_z \tag{31}$$

Lyapunov stability approach will be used to ensure the convergence and stability of the first error. The positive Lyapunov quadratic function shown in (32) is derived, and to ensure the stability of the error, the derivative of the function must be strictly negative, which means the equality in (33) must hold true.

$$V_z(\varepsilon_z) = \frac{1}{2}\varepsilon_z^2 + \frac{\bar{\theta}_z\dot{\bar{\theta}}_z}{m_z} \tag{32}$$

$$\dot{V}_z = \overbrace{\varepsilon_z\left(\frac{3}{2C}v_{sd}i_{fd} + \hat{x}_2 + \hat{\theta}_z\right)}^{-k_z\varepsilon_z^2} + \bar{\theta}_z\overbrace{\left(\varepsilon_z + \frac{\dot{\bar{\theta}}_z}{m_z}\right)}^{=0} \tag{33}$$

The virtual control output which is the current reference value for the next step and the derivative of the uncertainty are then deduced from the equality in (33) and expressed in (34) and (35), respectively.

$$i_{fd}^{*} = \alpha = \frac{2C}{3v_{sd}}\left(-k_z\varepsilon_z - \hat{x}_2 - \hat{\theta}_z\right) \tag{34}$$

$$\dot{\hat{\theta}}_z = m_z\varepsilon_z \tag{35}$$

Step 2: The second tracking error between the measured current and its reference value computed in step 1 can be defined as (36). Note that to avoid repetition of explanations, the equations for the design of d-axis current component controller is accompany the design equations at this step. Since the filter reactive power is controlled to track zero to achieve unity power factor, it translates to controlling q-axis current to track zero since there is direct proportionality between the two.

$$\begin{cases} \varepsilon_{fd} = i_{fd} - \alpha \\ \varepsilon_3 = i_{fq} - i_{fqref} \end{cases} \tag{36}$$

$$\begin{cases} \dot{\varepsilon}_{fd} = -\frac{R_f}{L_f} i_{fd} + \omega_s i_{fq} + \frac{v_{sd}}{L_f} - \frac{v_{fd}}{L_f} + \theta_{fd} - \dot{\alpha} \\ \dot{\varepsilon}_{fq} = -\frac{R_f}{L_f} i_{fq} - \omega_s i_{fd} - \frac{v_{fq}}{L_f} + \theta_{fq} \end{cases} \tag{37}$$

Lyapunov function and its derivative, taking into account the parameter modelling the uncertainty, are (38) and (39), respectively.

$$\begin{cases} V_{fd}\left(\varepsilon_{fd}\right) = V_z + \frac{1}{2}\varepsilon_{fd}^2 + \frac{1}{2}\frac{\bar{\theta}_{fd}^2}{m_{fd}} \\ V_{fq}\left(\varepsilon_{fq}\right) = \frac{1}{2}\varepsilon_{fq}^2 + \frac{1}{2}\frac{\bar{\theta}_{fq}^2}{m_{fq}} \end{cases} \tag{38}$$

$$\begin{cases} \dot{V}_{fd}\left(\varepsilon_z, \varepsilon_{fd}\right) = \dot{V}_z(\varepsilon_z) + \frac{1}{2}\varepsilon_{fd}\dot{\varepsilon}_{fd} + \frac{\bar{\theta}_{fd}\dot{\bar{\theta}}_{fd}}{m_{fd}} \\ \dot{V}_{fq}\left(\varepsilon_{fq}\right) = \frac{1}{2}\varepsilon_{fq}\dot{\varepsilon}_{fq} + \frac{\bar{\theta}_{fq}\dot{\bar{\theta}}_{fq}}{m_{fq}} \end{cases} \tag{39}$$

For the derivative of the positive Lyapunov function to be strictly negative, derivative of the estimate of the uncertainty and the final control variable are chosen and presented in (40) and (41), respectively.

$$\begin{cases} \dot{\hat{\theta}}_{fd} = m_{fd}\varepsilon_{fd} \\ \dot{\hat{\theta}}_{fq} = m_{fq}\varepsilon_{fq} \end{cases} \tag{40}$$

$$\begin{cases} v_{fd} = L_f\left(k_{fd}\varepsilon_{fd} + \frac{3}{2C}v_{sd}\varepsilon_z - \frac{R_f}{L_f}i_{fd} + \omega_s i_{fq} + \frac{v_{sd}}{L_f} + \hat{\theta}_{fd} - \dot{\alpha}\right) \\ v_{fq} = -L_f\left(-k_{fq}\varepsilon_{fq} + \frac{R_f i_{fq}}{L_f} + \omega i_{fd} - \hat{\theta}_{fq}\right) \end{cases} \tag{41}$$

These choices result in the derivatives of the defined Lyapunov function becoming strictly negative as expressed in (42) thereby guaranteeing the global stability of the tracking errors if $k_z, k_{fd}, k_{fq}, m_{fd}, m_{fq}$ are chosen strictly positive.

$$\begin{cases} \dot{V}_{fd}\left(\varepsilon_z, \varepsilon_{fd}\right) = -k_z\varepsilon_z^2 - k_{fd}\varepsilon_{fd}^2 \\ \dot{V}_{fq} = -k_{fq}\varepsilon_{fq}^2 \end{cases} \tag{42}$$

The Adaptive Backstepping Control of the Grid Side Power Converter is graphically summarized in Fig. 3.

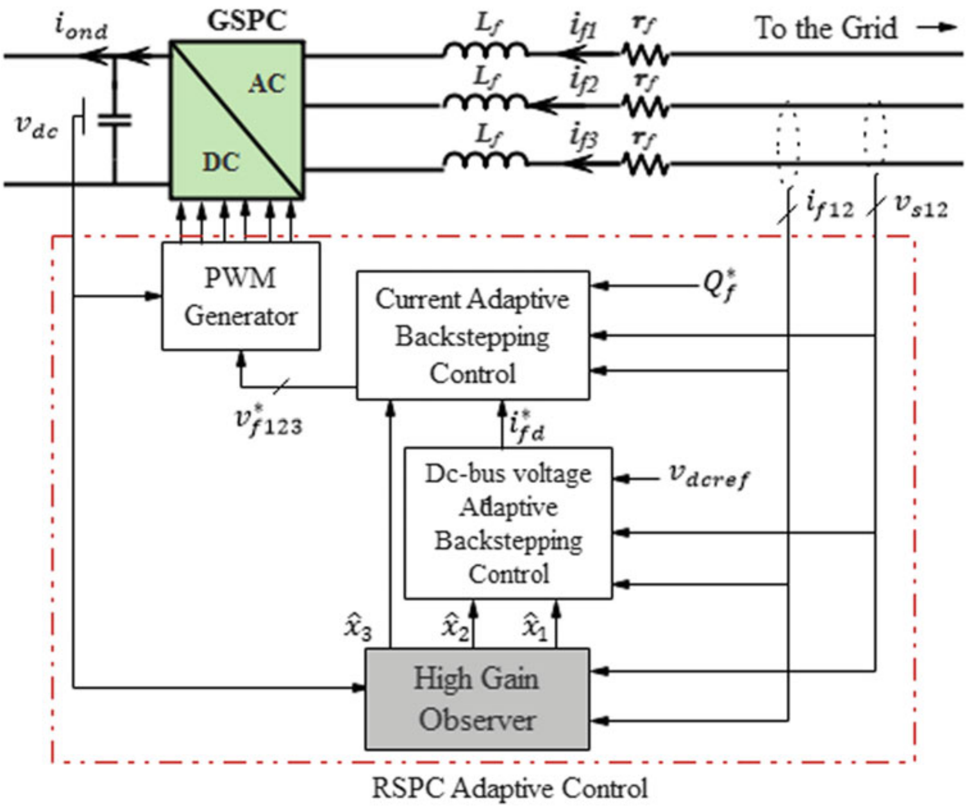

Fig. 3 ABC control of GSPC in close loop with the observer

4 Simulation Results

The detailed model of a 1.5 MW DFIG is simulated in MATLAB/Simulink environment. The descriptive diagrams of the control strategies for RSPC and GSPC are given in Figs. 2 and 3, respectively. The pole-zero cancellation technique is first used for PI-controller parameter tuning. The parameters are then optimized using MATLAB automatic tuning method. Simulation results under PI and ABC controllers will be given, compared and analyzed during low voltage dip with crowbar and DC chopper protection schemes activated.

The DFIG is considered able to ride through fault if it can limit the transient rotor current and the DC-link voltage within the Safe Operating Zone (SOZ) of the power converters and the DC-link capacitor respectively (Justo et al. 2015). The typical SOZ of DFIG is $V_{dc} \leq 135\%$ of V_{dc_nom} and 200% above the rated rotor current. This means that for the DFIG to effectively ride through grid fault, rotor current must be less than 2 p.u and DC-link voltage must be less than 1550 V.

4.1 Performance Under Grid Fault Without Protection Schemes Activated

This section of simulations demonstrates, under both PIC and ABC, DFIG response when it remains connected during grid voltage dip without any protection scheme. At 2 s simulation time, three-phase short-circuit grid fault is introduced, for 0.2 s, into the system. Symmetrical low voltage dip of over 90% of grid voltage is observed as shown in Fig. 4.

Figure 5 shows DC-link voltage under PI and Adaptive Backstepping controllers during the voltage dip. At the instance of fault occurrence, DC-link overcharge is observed under both controllers. While capacitor overcharge reaches 2200 V under the PI-controller, it is limited to 1900 V under the ABC controller. Though the ABC controller presents a better transient after fault clearance as response time is shorter, voltage surge under both controllers exceeds the SOZ of the DC-link capacitor.

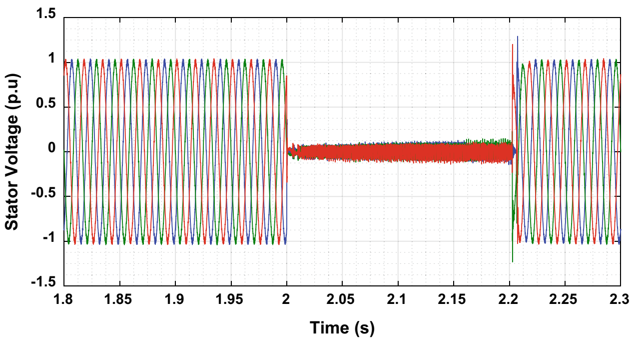

Fig. 4 Grid voltage under grid fault

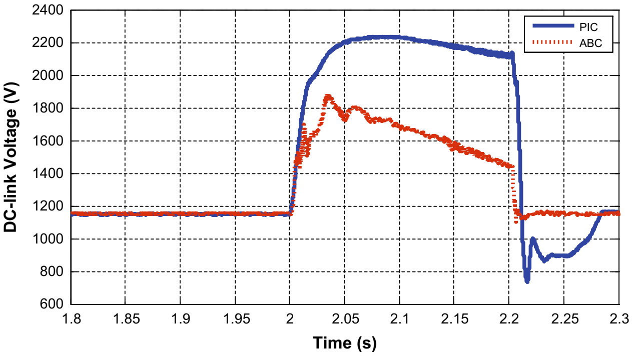

Fig. 5 DC-link voltage under grid fault

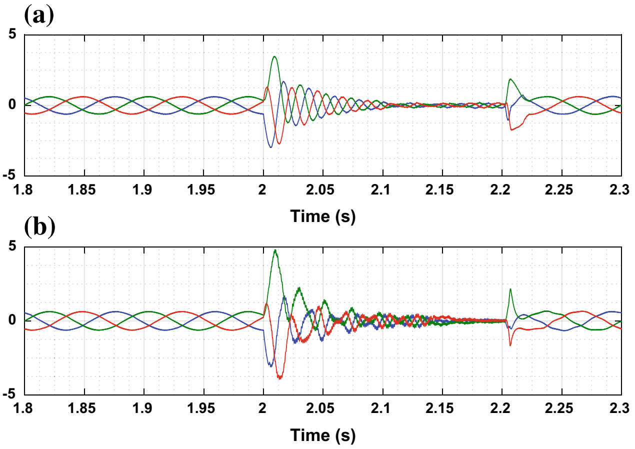

Fig. 6 Rotor current during grid fault using **a** PI-controller **b** ABC controller

Figure 6 shows rotor current response during fault under (a) PI-controller (b) ABC controller. Inrush rotor current occurred during the voltage dip and exceeds the SOZ of the rotor power converters under both control techniques at the instance of fault occurrence and fault clearance. In fact, under ABC controller, inrush current increases up to 500% of nominal rotor current while under the PI-controller the surge reaches 300%.

4.2 Performance Under Crowbar-Chopper Protection

The previous section shows the inability of the DFIG to ride through fault without extra protection schemes. In this section, an additional protection scheme called the ‘DC-chopper’ is combined with the crowbar to limit DC-link voltage swell and reduce rotor inrush current. The protection

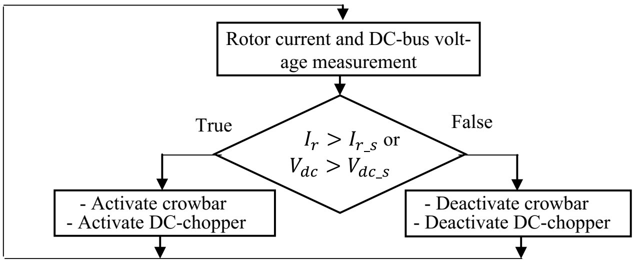

Fig. 7 Protection scheme management organigram

schemes are connected to the turbine system via IGBT switches as described in Fig. 1. Very large crowbar resistance value better attenuates rotor and stator current surge, reduces the reactive power absorbed by the DFIG during crowbar activation but causes high current surge and voltage stress on the rotor at the instance of activation and deactivation. Optimal crowbar resistance is determined using the formula derived in Yang et al. (2010) and expressed in (43).

$$R_{cr\_opt} = \frac{\sqrt{2}(V_{rmax}\omega_s L_s)}{\sqrt{\left(3.2V_s^2 - 2V_{rmax}^2\right)}} \tag{43}$$

The activation and deactivation algorithm of the protection schemes is schematized in Fig. 7. If DC-voltage or rotor current RMS value exceeds its predefined threshold value (V_{dc_s}, or I_{r_s}) activation signal is sent to the chopper and crowbar switches, power converters are not disconnected as the crowbar serves only to reduce the current between the rotor windings and the back-to-back converters. Normal operation is restarted when both DC-link voltage and rotor current RMS value are less than their threshold values, i.e., when the power converters are positioned back in their SOZ.

As shown in Fig. 8, DC-link voltage increases above it reference value of 1150 V at the instance of fault, which signifies that capacitor overcharge occurred. The overcharge exceeds the SOZ of the upper limit of 1550 V and reaches 1750 V when the DFIG is controlled using the PI-controller. The ABC controller under the same protection scheme, however, limits the voltage surge within the SOZ of the DC-link capacitor. Furthermore, the transient behaviour of the DC-voltage after fault clearance is improved by the ABC as a shorter settling time without overshoot is observed compared to the PI-controller performance.

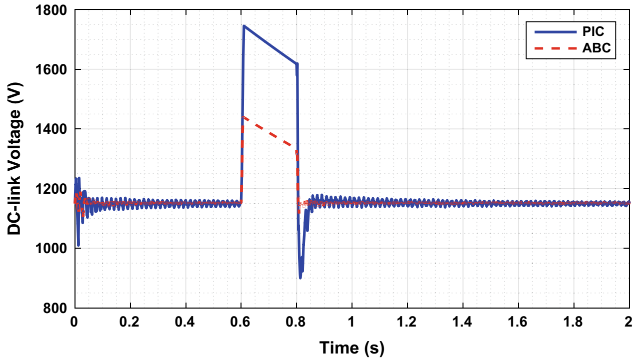

Fig. 8 DC-link voltage after

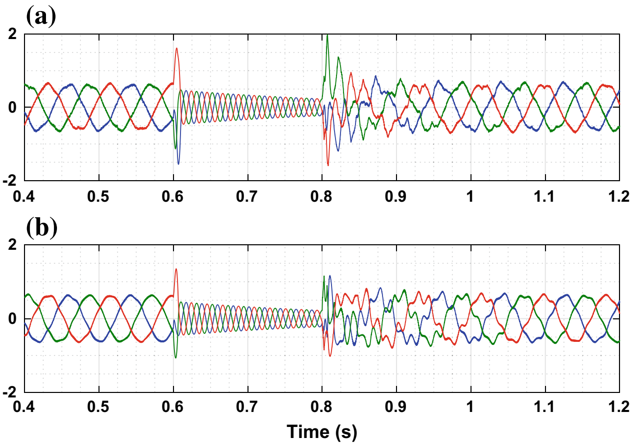

Fig. 9 Rotor current with protection scheme using **a** PI-controller **b** ABC

Table 1 Control parameters chosen for the observer-based adaptive control

k_z	k_{fd}	k_{fq}	m_{fd}	m_{fq}	K_{rd}	K_{rq}	m_{rd}	m_{rq}	θ
5	10	5	1	1	1	1	0.1	0.1	200

Figure 9 shows the rotor current dynamic under DC-chopper and crowbar protection during a fault. The RSPC is within its SOZ under both controllers but the ABC controller better improves the protection schemes than the PI-controller. Rotor current surge is limited to 1 p.u by the ABC controller both at the beginning and after the fault as shown in Fig. 9b while the PI-controller could only limit it to 2 p.u as presented in Fig. 9a.

The control and adaptation parameters are chosen as given in Table 1.

5 Conclusion

This paper deals with the optimization grid-connected DFIG wind turbine using Adaptive Backstepping controller in a closed loop with a High Gain Observer. At the RSPC of the back-to-back converter, robust Adaptive Backstepping Controller is synthesized to maximize the power captured from the wind and track reference stator reactive power. DC-link voltage and filter reactive power are controlled at the GSPC. High Gain Observer is employed to jointly estimate DC-bus current and power loss in RSPC and the output is fed to the DC-link voltage controller to reduce measurement noise and sensor dependence. Simulation results were given under grid voltage dip with DC chopper and crowbar protection schemes activated. Comparison between PI-controller and ABC performances is carried out. It is discovered that the ABC has better transient, faster tracking and can effectively prevent power converter damage in case of grid voltage dip up to 85%.

References

Adekanle, O., Guisser, M., Abdelmounim, E., & Aboulfatah, M. (2017). Integral backstepping controller combined with high gain observer for the optimization of grid-connected doubly-Fed induction generator. In *2017 International Conference on Wireless Technologies, Embedded and Intelligent Systems (WITS)*. IEEE (pp. 1–7).

Belmokhtar, K., Doumbia, M. L., & Agbossou, K. (2014). Novel fuzzy logic based sensorless maximum power point tracking strategy for wind turbine systems driven DFIG (doubly-Fed induction generator). *Energy, 76,* 679–693. https://doi.org/10.1016/j.energy.2014.08.066.

Bu, S. Q., Du, W., Wang, H. F., & Gao, S. (2013). Power angle control of grid-connected doubly fed induction generator wind turbines for fault ride-through. *IET Renewable Power Generation, 7,* 18–27. https://doi.org/10.1049/iet-rpg.2012.0130.

Cai, G., Liu, C., & Yang, D. (2014). Rotor current control for a doubly-Fed induction generator using a novel nonlinear robust control approach based on extended state observer-backstepping. *Transactions of the Institute of Measurement and Control, 37,* 494–504. https://doi.org/10.1177/0142331214543247.

Ebrahimkhani, S. (2016). Robust fractional order sliding mode control of doubly-Fed induction generator (DFIG)-based wind turbines. *ISA Transactions, 63,* 343–354. https://doi.org/10.1016/j.isatra.2016.03.003.

Gaillard, A. (2010). *Système éolien basé sur une MADA: contribution à l' étude de la qualité de l' énergie électrique et de la continuité de service*. Nancy-I: Henri Poincaré.

Justo, J. J., Mwasilu, F., & Jung, J.-W. (2015). Doubly-Fed induction generator based wind turbines: A comprehensive review of fault ride-through strategies. *Renewable and Sustainable Energy Reviews, 45,* 447–467. https://doi.org/10.1016/j.rser.2015.01.064.

Meenakshi R. (2013). Doubly fed induction generator for wind energy conversion system—A survey, 617–628.

Mwasilu, F., Jung, J.-W., Ro, K.-S., & Justo, J. J. (2012). Improvement of dynamic performance of doubly fed induction generator-based wind turbine power system under an unbalanced grid voltage condition. *IET Renewable Power Generation, 6,* 424–434. https://doi.org/10.1049/iet-rpg.2012.0110.

Pena, R., Clare, J. C., & Asher, G. M. (1996). Doubly Fed induction generator using back-to-back PWM converters and its application to variable-speed wind-energy generation. *IEE Proceedings—Electric Power Applications, 143,* 231. https://doi.org/10.1049/ip-epa:19960288.

Roy, T. K., & Mahmud, M. A. (2017). Active power control of three-phase grid-connected solar PV systems using a robust nonlinear adaptive backstepping approach. *Solar Energy, 153,* 64–76. https://doi.org/10.1016/j.solener.2017.04.044.

Saad, N. H., Sattar, A. A., & Mansour, A. E.-A. M. (2015). Low voltage ride through of doubly-Fed induction generator connected to the grid using sliding mode control strategy. *Renew Energy, 80,* 583–594. https://doi.org/10.1016/j.renene.2015.02.054.

Shen, Y., Zhang, B., Cui, T., et al. (2017). Novel control of DFIG with ESD to improve LVRT capability and to perform voltage support during grid faults. 2017 IEEE International Conference Energy Internet, 136–141. https://doi.org/10.1109/icei.2017.31.

Srirattanawichaikul, W., Premrudeepreechacharn, S., & Kumsuwan, Y. (2016). A comparative study of vector control strategies for rotor-side converter of DFIG wind energy systems.

Yang, J., Fletcher, J. E., & O'Reilly, J. (2010). A series-dynamic-resistor-based converter protection scheme for doubly-Fed induction generator during various fault conditions. *IEEE Transactions on Energy Conversion, 25,* 422–432. https://doi.org/10.1109/TEC.2009.2037970.

Yang, S., Zhou, T., Sun, D., et al. (2016). A SCR crowbar commutated with power converter for DFIG-based wind turbines. *International Journal of Electrical Power & Energy Systems, 81,* 87–103. https://doi.org/10.1016/j.ijepes.2016.01.039.

Oluwaseun Simon Adekanle was born in Ilutitun, Nigeria in 1988. In 2014, he obtained his master's degree in Automatic Control, Signal Processing and Industrial Computing from Hassan 1st University, where he is currently a Ph.D. student. His main research focus is on observer-based control of grid-connected Doubly Fed Induction Generator. He also has research interest ranging from signal processing to industrial application of Automatic Control. He is currently a student member of Laboratory of Signal Analysis and Information Processing (ASTI).

M'hammed Guisser received his Ph.D. in engineering science 'Automatic and Industrial Computing' in 2009 from the 'Higher National School of Electricity and Mechanics (ENSEM)', University Hassan II, Casablanca, Morocco.

His research interests include nonlinear control and state observer theory, robust and adaptive control, digital controller/observer and signal processing. He is involved in the applications of these techniques to the control of unmanned aerial vehicles UAV, robotic systems and control of renewable energy systems.

Currently, he is Assistant Professor in the Electrical Engineering Department of the 'Centre Régional des Métiers de l'Education et de la Formation' (CRMEF), Settat, Morocco, and researcher in Laboratory ASTI, FST, Settat, University Hassan I Morocco.

Elhassane Abdelmounim received his Ph.D. in applied Spectral analysis from Limoges University at science and technical Faculty, France in 1994.

In 1996, he joined, as Professor, applied physics department of science and technical faculty, Hassan 1st University, Settat, Morocco.

His current research interests include digital signal processing and machine learning.

He is currently coordinator of a Bachelor of Science in electrical engineering and researcher in 'ASTI' System Analysis and Information Technology Laboratory at science and technical faculty, Hassan 1st University, Settat, Morocco.

Mohammed Aboulfatah was born in Casablanca Morocco in 1967, he received his Ph.D. in Measures and Instrumentation from Bordeaux I University, France in 1994. From 1993 to 1995, he was associated professor at the Technological Institute of Bordeaux University. In 1996, he joined as permanent Professor, applied physics department of science and technical faculty, Hassan 1st University, Settat, Morocco.

He is currently head of Applied Physics department and coordinator of 'Automatic, Signal Processing and Industrial Computing' Master. His main research interests and experience include Instrumentation, Signal Processing, as a researcher member of ASTI Laboratory in Hassan 1st University.

Part III

Information Technology

Band Selection with Bhattacharyya Distance Based on the Gaussian Mixture Model for Hyperspectral Image Classification

Mohammed Lahlimi, Mounir Ait Kerroum, and Youssef Fakhri

Abstract

This paper investigates a new band selection approach with the Bhattacharyya distance based on the Gaussian Mixture Model (GMM) for Hyperspectral image classification. Our main motivation to model the Bhattacharyya distance using GMM is due to the fact that this tool is well known for capturing non-Gaussian statistic of multivariate data and that is less sensitive to estimation error problem than purely non-parametric models. To estimate the parameters of GMM, a Robust Expectation-Maximization (REM) algorithm is used. REM solves the shortcoming of the classical Expectation-Maximization (EM) algorithm by dynamically adapting the number of clusters to the data structure. The selected bands with the proposed approach are compared, in terms of classification accuracy, to the Bhattacharyya expressed in its parametric form and the Bhattacharyya modelled with GMM using the classical EM algorithm. The experiment was carried out on two real hyperspectral images, the Indiana Pines (92AV3C) sub-scene and the Kennedy Space Center (KSC) dataset, and the experimental results have demonstrated the effectiveness of our proposed method in terms of classification accuracy with fewer bands.

Keywords

Hyperspectral image • Remote sensing • Band selection • Bhattacharyya distance • Probability estimation • Gaussian mixture model • 92AV3C • KSC

1 Introduction

One of the main challenges in hyperspectral imaging is the Hughes phenomenon (Richards 2012; Shahshahani and Landgrebe 1994). Due to the increase of data dimensionality, not only common image processing algorithms show the incapacity to deal with high volume data sets (Jimenez and Landgrebe 1998), but also due to small sample size (Shahshahani and Landgrebe 1994) not having sufficient observation, a good estimate of the class parameters cannot be found, as consequence the classifier will not be properly trained (Richards 2012). Therefore, reducing the data dimensionality before the classification process is required. Among the two main approaches for dimensionality reduction, band selection is the preferred one in this study as the physical meaning of the data remains unchanged (Lee and Landgrebe 1993). Its main goal is to identify and choose only those bands that can contribute to or improve the classification task based on a chosen criterion (Webb 2003).

This study investigate a new band selection method using the Bhattacharyya distance based on The Gaussian Mixture Model (GMM), which utilize the simplest greedy search algorithm, the Sequential forward selection (SFS), as a search strategy (AitKerroum et al. 2010) since the low computational burden (Burrell et al. 2007) is its main advantage. This research needs to be conducted because in other studies (Le Bris et al. 2015; Simin et al. 2009; Jimenez and Landgrebe 1998), the required probability estimation to model the Bhattacharyya distance is often done under the assumption of the Normal Distribution. The biggest issue that we are dealing with, in remote sensing, is that the spectral response of hyperspectral image can be affected by many factors (Li et al. 2014). As consequence, using the single normal distribution assumption to describe the data is not sufficient. It is not flexible enough to capture the complex data structures encountered in real-world settings (Dundar and Landgrebe 2004). GMM, in the other hand, is a well-known tool that captures non-Gaussian statistic of

---

M. Lahlimi (✉) · M. Ait Kerroum · Y. Fakhri
LaRIT, Faculty of Sciences, Ibn Tofail University Kenitra, Kenitra, Morocco
e-mail: lahlimi.mohammed@gmail.com

M. Ait Kerroum
e-mail: maitkerroum@gmail.com

Y. Fakhri
e-mail: yousseffakhri@yahoo.fr

S. El Hani and M. Essaaidi (eds.), *Recent Advances in Electrical and Information Technologies for Sustainable Development*, Advances in Science, Technology & Innovation, https://doi.org/10.1007/978-3-030-05276-8_10

multivariate data (Li et al. 2014). GMM models the density as the sum of one or more weighted Gaussian component so it is usually less sensitive to estimation error problem than purely non-parametric models (Dundar and Landgrebe 2004).

The main challenge with GMM is the estimation of its parameters. In literature, the Expectation-Maximization (EM) algorithm (Martinez and Martinez 2007) is often used, however, the EM algorithm for Gaussian mixture models is quite sensitive to initial values (Yang et al. 2012) and the number of its components K needs to be given a priori. A good choice of the parameter K is quite important as it can directly affect the estimation of the covariance matrix. It is well known that when the ratio of the number of training samples to the number of band measurements is small, the estimates of the discriminant functions are not accurate (Shahshahani and Landgrebe 1994), and therefore we can easily end up with the "Hughes phenomenon" and the classification results may not be satisfactory. To overcome this shortcoming, a Robust Expectation-Maximization (REM) algorithm as defined in (Yang et al. 2012) is used, as it can automatically obtain an optimal number of clusters K.

In order to assess the effectiveness of the proposed approach, experiments were carried out on two real-world hyperspectral dataset. The Indiana Pines (92AV3C) scene (Baumgardner et al. 2015) firstly used by David Landgrebe and his students (Kuo and Landgrebe 2002; Jimenez and Landgrebe 1998). The Initial experiment was done on a four-class subset (Tadjudin and Landgrebe 2000; Camps-Valls and Bruzzone 2009) of this scene to lower the computation time and to have enough samples for a good probability estimation. The second hyperspectral scene is the Kennedy Space Center (KSC) (GIC 2015) also used in a quite number of studies (Wang and Wang 2015; Datta et al. 2014). The selected bands with the proposed approach are compared, in terms of classification accuracy by the Extreme Learning Machine (ELM) classifier (Huang et al. 2004, 2006), to the Bhattacharyya expressed in its parametric form and the Bhattacharyya modelled with GMM using the classical EM algorithm.

The remaining of this paper is organized as follows: Sect. 2 describes the band selection algorithm with the GMM-based Bhattacharyya distance. In Sect. 3, a brief description of Extreme Learning Machine (ELM) classifier is given. The experimental results with the proposed approach are presented in Sect. 4, while Sect. 5 contains the conclusion.

2 Band Selection Based on Bhattacharyya Distance

2.1 Search Strategy

Let $F = \{x_i\}_{i=1}^{d}$ be a set of d-dimensional band space with an output class ω. The aim, Fig. 1, is to find an optimal subset $S = \{x_i^{'}\}_{i=1}^{d}, S \subset F, d' \le d$ that keeps the maximum amount of discriminant information as possible while discarding any redundancy or irrelevant bands using the Bhattacharyya criterion as a similarity measurement. The simplest greedy search algorithm to explore the band space F is the Sequential Forward Selection (SFS). Its main advantage is that is relatively low in computational burden (Burrell et al. 2007) compared to the exhaustive evaluation of the band space F that involves $\binom{d'}{d}$ combinations.

The ideal greedy selection algorithm proposed (AitKerroum et al. 2010) to solve the problem can be described by the following procedures:

```
(1) Initialization: Set $F \leftarrow$ " initial set of $|F|$ input bands"
    and set $S \leftarrow$ "empty set".
(2) Computation of the cost-function with the output class:
    $\forall f \in F$, compute $J_b(\omega_i, \omega_j)$.
(3) Choice of the first band: find the band that maximizes
    $J_b(\omega_i, \omega_j)$, set $F \leftarrow F \setminus \{f_\omega\}$ and set $S \leftarrow \{f_\omega\}$.
(4) Greedy selection: repeat until $|S| = d'$.
    (a) Computation of the cost function with the output class:
        $\forall f \in F$, compute $J_b(\omega_i, \omega_j)$.
    (b) Selection of the next band: chose the band
        $f \in F$ that es $J_b(\omega_i, \omega_j)$, set $F \leftarrow F \setminus \{f_\omega\}$ and
        set $S \leftarrow S \cup \{f_\omega\}$.
(5) Output the set $S$ containing the selected bands.
```

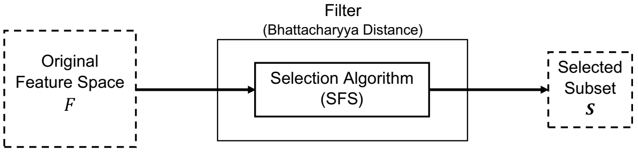

Fig. 1 Optimally use the Bhattacharyya distance for each combination in order to filter out poorly informative bands while keeping only the best ones

2.2 Bhattacharyya Distance

The Bhattacharyya is a probabilistic distance, covered in many texts on statistical pattern recognition (Theodoridis and Koutroumbas 2009; Webb 2003; Duda et al. 2000), measures the scatter degree of two classes (ω_1, ω_2). Between two distributions $p(x|\omega_1)$ and $p(x|\omega_2)$, this distance is given by

$$J_b(\omega_1, \omega_2) = -\log \int (p(x|\omega_1)p(x|\omega_2))^{\frac{1}{2}} dx \tag{1}$$

where $p(x|\omega_1)$ and $p(x|\omega_2)$ are, respectively, the prior conditional probability of the first and second class. In the multi-class problem, the Bhattacharyya is computed for every class pair (ω_i, ω_j) and the average class separability can be computed using the average Bhattacharyya

$$J = \sum_i \sum_j P(\omega_i) P(\omega_j) J_b(\omega_i, \omega_j) \tag{2}$$

The main challenge with the probabilistic distance is the requirement of an estimate of a probability density function. Under the assumption of the normal distributions with means μ_1, μ_2 and covariance matrices Σ_1, Σ_2, Eq. (1) can be simplified (Theodoridis and Koutroumbas 2009; Webb 2003) and expressed in its parametric form as

$$B = \frac{1}{4}(\mu_2 - \mu_1)^T \left|\frac{\Sigma_1 + \Sigma_2}{2}\right|^{-1} (\mu_2 - \mu_1) + \frac{1}{2} \log \frac{|\Sigma_1 + \Sigma_2|}{2\sqrt{|\Sigma_1||\Sigma_2|}} \tag{3}$$

2.3 Probability Estimation

In remote sensing, the spectral response of the hyperspectral image can be affected by many factors (Li et al. 2014). As consequence, using the single Normal distribution assumption to describe the data is not sufficient. It is not flexible enough to capture the complex data structures encountered in real-world settings (Dundar and Landgrebe 2004).

The reason why we are motivated to model the Bhattacharyya distance using the Gaussian Mixture Model (GMM) for hyperspectral data is due to the fact that GMM is a well-known tool that captures non-Gaussian statistic of multivariate data (Li et al. 2014). GMM models the density as the sum of one or more weighted Gaussian component. It combines much of the flexibility of the non-parametric methods with certain of the analytic advantages of parametric methods, it is usually less sensitive to estimation error problem than purely non-parametric models (Dundar and Landgrebe 2004).

For a GMM, a probability density function is written as the sum of K Gaussian components

$$p(x|\omega) = \sum_{k=1}^{K} \pi_k p(x|\mu_k, \Sigma_k) \tag{4}$$

where K the number of mixture component, π_k the mixing weight $\left(0 \le \pi_k \le 1, \sum_{k=1}^{K} \pi_k = 1\right)$ and $p(x|\mu_k, \Sigma_k)$ a d-dimensional Gaussian distribution

$$p(x|\mu_k, \Sigma_k) = \frac{1}{(2\pi)^{\frac{d}{2}} |\Sigma_k|^{\frac{1}{2}}} \exp\left[-\frac{1}{2}(x - \mu_k)^T \Sigma_k^{-1} (x - \mu_k)\right] \tag{5}$$

μ_k and Σ_k, are, respectively, the mean and the covariance matrix of the kth component.

2.4 Bhattacharyya Distances Based on GMM

From Eqs. (1) and (4), the Bhattacharyya based on GMM can be written as follows:

$$\begin{aligned} & J_b(\omega_i, \omega_j) \\ & = -\log \int \left(\left(\sum_{k=1}^{K_i} \pi_{i,k} p\left(x | \mu_{i,k}, \Sigma_{i,k}\right) \right) \left(\sum_{k=1}^{K_j} \pi_{j,k} p\left(x | \mu_{j,k}, \Sigma_{j,k}\right) \right) \right)^{\frac{1}{2}} dx \end{aligned} \tag{6}$$

To compute the cost-function J_b on the Ep. (6) a few parameters need to be estimated: π the mixing coefficient, μ the mean, Σ the covariance matrix and K the number of clusters. The estimation of those parameters is the main issue when using the GMM. By using the Expectation-Maximization (EM) algorithm (Duda et al. 2000), three of these parameters π, μ, Σ can be estimated, however, the EM algorithm for Gaussian mixture models is quite sensitive to initial values (Yang et al. 2012) and the number of its components K needs to be given a priori.

For the estimation of the covariance matrix, it is well known that small data sets usually cause "Hughes phenomenon" and singularity problems (Kuo and Landgrebe 2002) and by partitioning the already small set of data into multiple clusters and then estimating the cluster statistics, one ends up with an ill-conditioned mixture model (Dundar and Landgrebe 2002). Therefore, a good choice of the parameter K is quite important as it can directly affect the estimation of the covariance matrix. One way around this problem is the use of regularization techniques of sample covariance matrix such as "Leave One Out Covariance" (LOOC) estimator (Tadjudin and Landgrebe 2000) and the maximum entropy covariance selection (MECS) method (Thomaz et al. 2004).

To overcome the shortcoming of the classical EM approach, a Robust Expectation-Maximization (REM) algorithm as defined in (Yang et al. 2012) is used. REM was

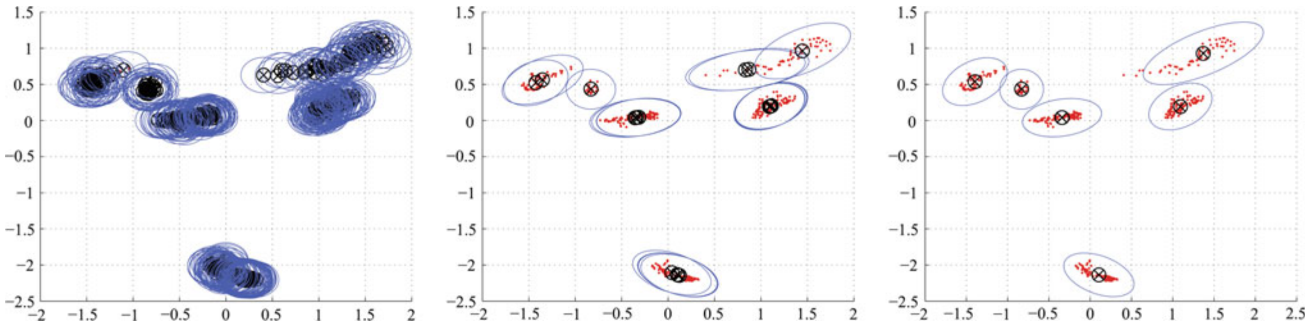

(a) Iteration 1 **(b) Iteration 10** **(c) Iteration 30**

Fig. 2 Example of the REM implementation **a**–**b** Initialization of the REM using all data points and then discarding the clusters that do not met required criteria; **c** the processes convergent to an optimum number of clusters k = 6 after 30 iterations

developed to solve the issue of the initialization of EM parameters by using all data points as initials to solve the problem, and when a cluster does not meet the required criteria it is discarded and the number of components K is decreased until achieving automatically an optimal number of clusters (Fig. 2). For more details about the algorithm see Yang et al. (2012).

3 Extreme Learning Machines

Extreme learning machines (ELM) is a simple and efficient learning algorithm for single-hidden layer feedforward neural networks (SLFNs), where the weights connecting inputs to hidden nodes are randomly assigned and never updated. It was first introduced by Huang et al. (2004, 2006) to overcome the slow learning speed and the poor generalization of the traditional machine learning algorithms. According to (Huang et al. 2004, 2006), ELM's learning speed can be thousands of times faster than traditional feedforward network learning algorithms like backpropagation (BP) algorithm while obtaining better generalization performance. The main qualities of this algorithm are (Huang et al. 2006):

- The learning speed of ELM is extremely fast.
- The better generalization performance than the gradient-based learning such as backpropagation.
- And it is much simpler and can solve problems like local minima.

From research conducted by Huang et al. (2004, 2006), ELM has proven its superiority in term of speed and good generalization over SVM and its variants. However, with the randomly generated input weights there will be a slight variation on the output value each time we repeat the same measurement. Therefore, the overall classification accuracy score using ELM will be, in our case, the average of several measurements.

4 Experimental Study

4.1 Dataset

92AV3C 4 class sub-scene: This scene was gathered by AVIRIS sensor on June 12, 1992, over the Indian Pines test site in Northwestern Indiana, first used by David Landgrebe and others (Kuo and Landgrebe 2002; Jimenez and Landgrebe 1998; Tadjudin and Landgrebe 2000; Camps-Valls and Bruzzone 2009). This sub-scene consists of pixels $[27-94] \times [31-116]$ for a size of 68×86. Further details are given in Table 1 (Fig. 3).

Kennedy Space Center: The dataset used in this experiment is acquired by AVIRIS sensor over the Kennedy Space Center (KSC) and it has been used in quite a number of studies (Wang and Wang 2015; Datta et al. 2014). For classification purposes, 13 classes representing the various land cover types that occur in this environment were defined for the site and 176 bands are used for the analysis after removing water absorption and low SNR bands (Fig. 4).

4.2 Experimental Setup

Hardware Setup: The proposed procedure presented in this work was tested in Matlab (R2014a), on a 64-bit PC with an i7 microprocessor (2.20 GHz) and 6 GB of RAM.

Classifier: To assess the proposed band selection approach performance, the dataset of each hyperspectral image was divided into two parts. The training and testing dataset were split into 50%/50% of pixels based on the provided ground truth map. The extreme learning machine classifier is used with 500 number of hidden neurons and the

Table 1 Data description of the Indian Pines 4 class sub-scene

	Class name	Total samples	Training samples	Test samples
1	Corn-notill	1008	505	503
2	Grass-trees	747	374	373
3	Soybean notill	737	367	370
4	Soybean-mintill	1947	973	974

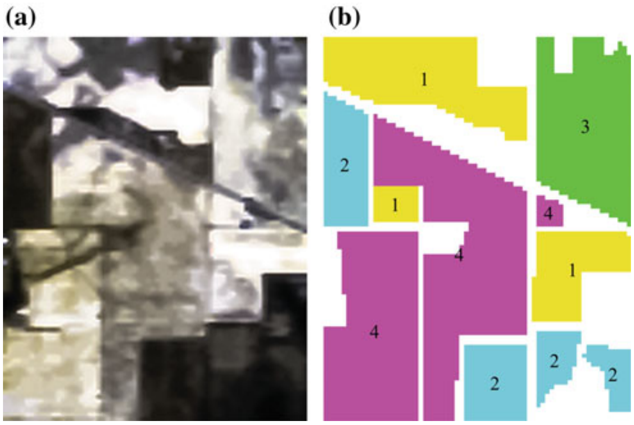

Fig. 3 **a** The Indian Pines 4 class sub-scene and **b** its Ground Truth Map

sigmoid for the activation function. The overall classification accuracy score with this classifier is the mean of 10 measurements.

4.3 Results and Discussions

In this work, the dimensionality of a hyperspectral image needs to be reduced by choosing the most informative bands that contribute to the classification process. As stated previously, to evaluate our bands, the Bhattacharyya distance as a similarity measurement is applied as stated in Sect. 2. In this section, we will try to see how well this probabilistic distance performs in the remote sensing context and how much the probability estimation can improve the band selection process and the overall classification accuracy.

4.3.1 Bhattacharyya Distance Assessment

The first experiment consists of evaluating the effectiveness of the Bhattacharyya distance using a sub-scene from the benchmark dataset Indian Pine. In order to see how this distance ranks the bands based on their class separability, we compute the cost-function J_b of the Eq. (6) for each band at the time. The higher the cost-function value on a band, the more classes can be separated and the better the classification score will be. Figure 5 illustrates the individual Bhattacharyya distance score of all the 220 bands, and as we can see, the section between 165 and 170 contain the highest J_b value. The first selected band with the highest score is 168. It has been reported in previous works (Tadjudin and Landgrebe 2000; Jimenez and Landgrebe 1998; Camps-Valls and Bruzzone 2009) that the bands 104–108, 150–163 and 220 in Indian Pine are the region of water absorption, therefore, they contain only noise and no useful information, which can clearly be seen in Figs. 5 and 6 using this criterion.

By continuing the selection processes, as we add the second chosen band $[168, 142]$, we can see as shown in Fig. 7, that with just the first two selected bands we were able to draw a decision boundary between the four classes of the Indian Pine sub-scene. The class with the number two corresponding to “Grass-tree” can already be separated from the rest with an overall ELM classification score of 78.14%. While the other classes are not completely separated yet. At the fifth dimension, the overall classification using ELM has reached 93.63%.

Fig. 4 **a** The Kennedy Space Center scene and **b** its Ground Truth Map

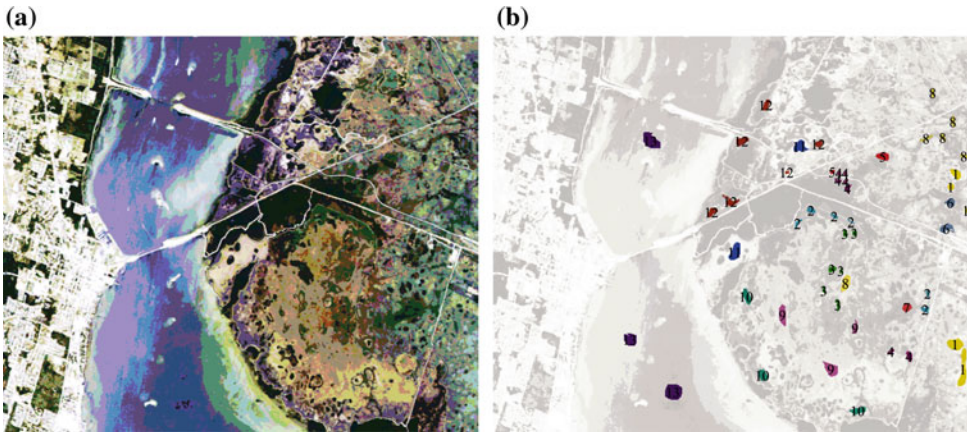

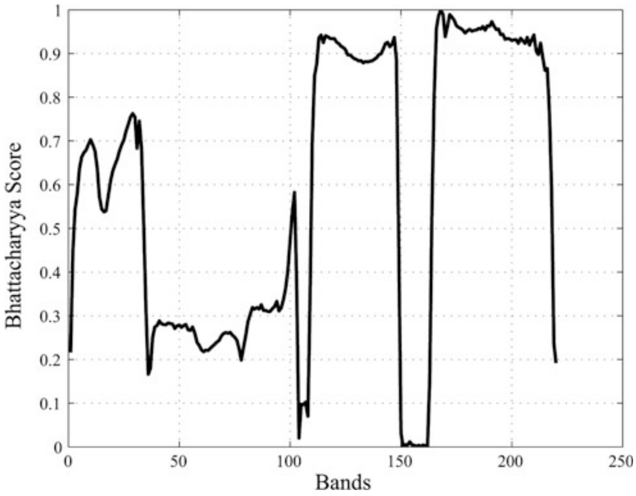

Fig. 5 The class separability score using the Bhattacharyya distance over each band of the Indian Pine subset

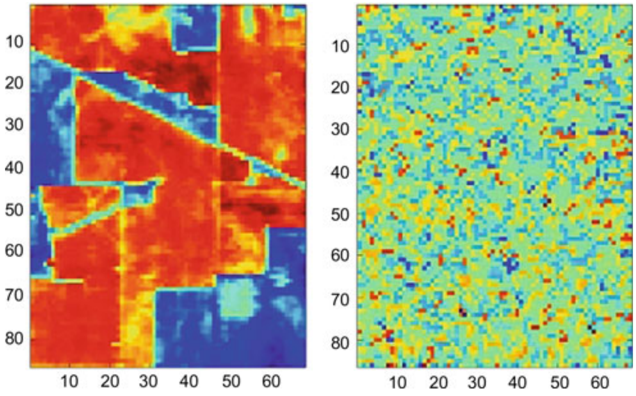

(a) band 168 **(b) band 153**

Fig. 6 **a** Is the first selected band 168 for 4 class 92AV3C subset, **b** is the band 153 one of the noisy band that got discarded by the selection algorithm

4.3.2 Probability Estimation

The band selection with the Bhattacharyya distance is performed on two hyperspectral dataset KSC and the portion of the 92AV3C scene. The probabilistic parameters in Bhattacharyya distance are estimated in three different ways. First, the mostly used, the Bhattacharyya in the parametric form is implemented. The second implementation is the GMM-based Bhattacharyya distance with the classical EM algorithm. For this model, the number of clusters K was set to 4 after a visual inspection since it must be defined a priori. The last approach is the proposed GMM using the REM algorithm. The selected bands using these three estimations are compared in Fig. 8 for the Indian Pine sub-scene and Fig. 9 for the Kennedy Search Center.

The first thing we can notice from these two figures is that the overall score of the selected band using Bhattacharyya distance in its parametric form is clearly lower than the ones using the GMM approach with EM and REM which was expected and do support our proposition of using Bhattacharyya based on GMM in this paper.

In Fig. 8, the selected band using the REM estimation shows better performances in terms of overall classification accuracy compared to GMM using the classical EM. At the fifth band, REM has reached 93.63% in the overall classification score leaving behind the other two approaches. In fact, for this dataset, we can reduce the data dimension from 220 bands to only 17 bands while losing only 1.13% in the overall classification by using REM compared to the overall score with all the 220 bands, in the meanwhile at the 17 dimensions we do lose in term of classification, 3.16% for the approach using the parametric form and 2.24% for the one using the GMM-EM. In order to cope with this difference, we need to go even higher in dimension, choosing more than 30 bands which is double what we get by using REM. We point out that when the number of selected bands

Fig. 7 **a** The decision boundary with the first two selected bands with Bhattacharyya based GMM-REM for the 4 class 92AV3C subset scene, **b** the probability estimation of each class

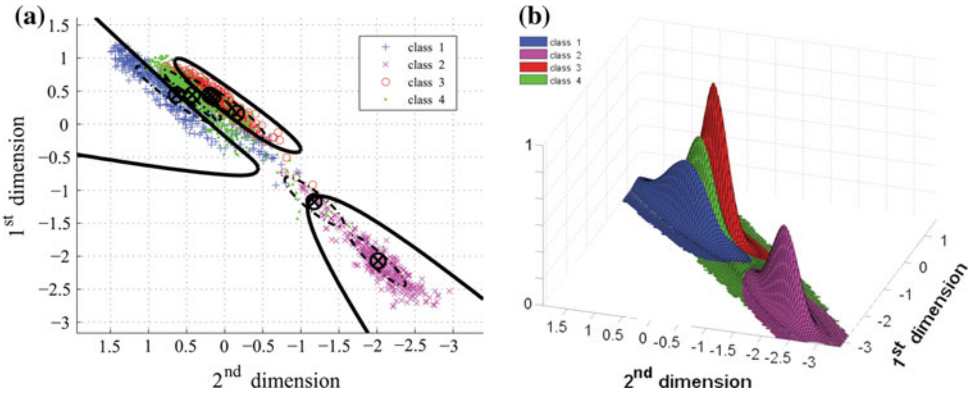

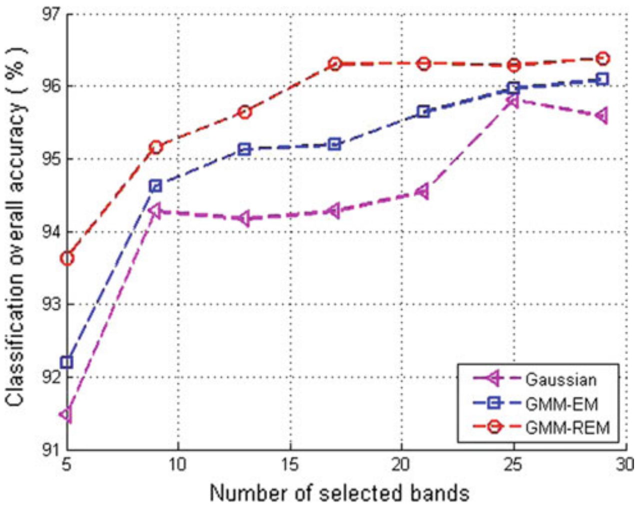

Fig. 8 Comparative performances of the selected bands using the ELM classifier for the studied sub-scene Indian Pines with 4 class

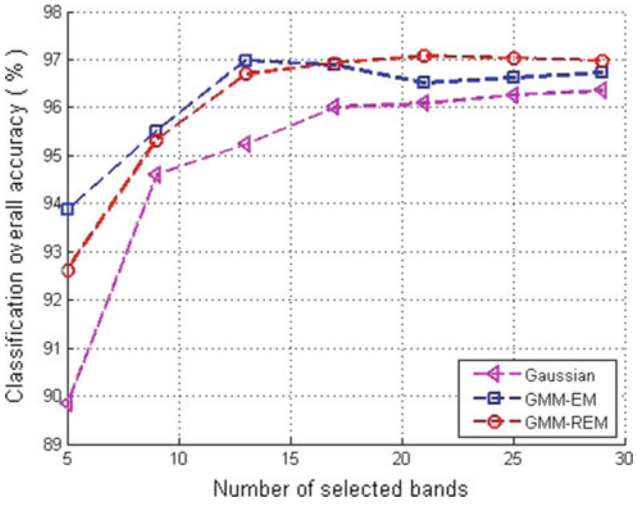

Fig. 9 Comparative performances of the selected bands using the ELM classifier for the studied scene of the Kennedy Search Center

is over 20 we start to witness the manifestation of the Hugh phenomenon; i.e. the number of samples is insufficient and the statistics are poor and no longer reliable.

Figure 9 corresponding to the Kennedy Search Center shows that the chosen band using GMM-EM is slightly better than REM in the beginning however REM do catch up at the band 15. For this dataset setting the number of clusters at 4 was relatively a good choice for the first 13 selected bands where it reaches its highest value before starting to decrease. After the 13 dimensions, we start to witness the manifestation of the "Hugh phenomenon". For this dataset, the number of observation was already small and by dividing it by 4 as we grow in dimension, the probability estimation needed to compute the Bhattacharyya distance is no longer reliable. Meanwhile, the GMM-REM curve is steadily increasing trying to avoid the curse of dimensionality while adapting dynamically the number of the cluster needed. We can also notice that, for this dataset, we can reduce the data dimension from 176 bands to only 10 bands with no loss in term of classification accuracy, in fact, we can also improve the classification process if we add in a few more bands.

5 Conclusion

This paper presented a new band selection algorithm with a GMM-based Bhattacharyya distance for hyperspectral image classification, using the sequential forward selection technique to reduce the data dimension.

Since the Normal distribution assumption needed to compute this criterion is not flexible enough to capture the complex data structures encountered in real-world settings, the Gaussian mixture model was used. GMM models the density as the sum of one or more weighted Gaussian component and it can capture non-Gaussian statistic of multivariate data. The EM algorithm is usually performed to get the GMM parameters, however, EM is sensitive to the initial values and the number of its components needs to be given a priori. Therefore, a GMM with a robust EM algorithm was introduced in this study to model the Bhattacharyya distance.

Our main contribution in this work is a new approach to give a robust estimation of Bhattacharyya distance using GMM and REM algorithm for hyperspectral band selection. The proposed approach compared to the classical methods is better according to the experiment results.

The initially performed experiment has shown the reliability of the proposed criterion as a similarity measure that can be used to choose the best bands from a given hyperspectral image dataset. And the experimental results, using a 92AV3C subset and KSC dataset, have demonstrated the effectiveness of our proposed method in terms of classification accuracy with fewer bands.

References

AitKerroum, M., Hammouch, A., & Aboutajdine, D. (2010). Textural feature selection by joint mutual information based on gaussian mixture model for multispectral image classification. *Pattern Recognition Letters, 31*(10), 1168–1174. https://doi.org/10.1016/j.patrec.2009.11.010.

Baumgardner, M. F., Biehl, L. L., & Landgrebe, D. A. (2015). 220 band aviris hyperspectral image data set: June 12, 1992 indian pine test site 3. https://doi.org/10.4231/r7rx991c, https://purr.purdue.edu/publications/1947/1.

Burrell, L., Smart, O., Georgoulas, G. K., Marsh, E., & Vachtsevanos, G. J. (2007). Evaluation of feature selection techniques for analysis of functional MRI and EEG. In *DMIN* (pp. 256–262).

Camps-Valls, G., & Bruzzone, L. (2009). *Kernel methods for remote sensing data analysis*. Wiley.

Datta, A., Ghosh, S., & Ghosh, A. (2014). Band elimination of hyperspectral imagery using partitioned band image correlation and capacitory discrimination. *International Journal of Remote Sensing, 35*(2), 554–577. https://doi.org/10.1080/01431161.2013.871392.

Duda, R. O., Hart, P. E., & Stork, D. G. (2000). *Pattern classification* (2nd ed.). New York, NY, USA: Wiley-Interscience.

Dundar, M. M., & Landgrebe, D. (2002). A model-based mixture-supervised classification approach in hyperspectral data analysis. *IEEE Transactions on Geoscience and Remote Sensing, 40* (12), 2692–2699. https://doi.org/10.1109/TGRS.2002.807010.

Dundar, M. M., & Landgrebe, D. A. (2004). Toward an optimal supervised classifier for the analysis of hyperspectral data. *IEEE Transactions on Geoscience and Remote Sensing, 42*(1), 271–277. https://doi.org/10.1109/TGRS.2003.817813.

GIC UdPV. (2015). Hyperspectral remote sensing scenes—kennedy space center (KSC). http://www.ehu.eus/ccwintco/index.php?title=Hyperspectral_Remote_Sensing_Scenes#Kennedy_Space_Center.28KSC.29.

Huang, G. B., Zhu, Q. Y., & Siew, C. K. (2004). Extreme learning machine: A new learning scheme of feedforward neural networks. In *2004 IEEE International Joint Conference on Neural Networks (IEEE Cat. No. 04CH37541)* (Vol. 2, pp. 985–990). https://doi.org/10.1109/ijcnn.2004.1380068.

Huang, G. B., Zhu, Q. Y., & Siew, C. K. (2006). Extreme learning machine: Theory and applications. *Neurocomputing, 70*(1), 489–501. https://doi.org/10.1016/j.neucom.2005.12.126.

Jimenez, L. O., & Landgrebe, D. A. (1998). Supervised classification in high-dimensional space: Geometrical, statistical, and asymptotical properties of multivariate data. *IEEE Transactions on Systems, Man, and Cybernetics, Part C (Applications and Reviews), 28*(1), 39–54. https://doi.org/10.1109/5326.661089.

Kuo, B. C., & Landgrebe, D. A. (2002). A robust classification procedure based on mixture classifiers and nonparametric weighted feature extraction. *IEEE Transactions on Geoscience and Remote Sensing, 40*(11), 2486–2494. https://doi.org/10.1109/TGRS.2002.805088.

Le Bris, A., Chehata, N., Briottet, X., & Paparoditis, N. (2015). Extraction of optimal spectral bands using hierarchical band merging out of hyperspectral data. *The International Archives of Photogrammetry, Remote Sensing and Spatial Information Sciences, 40*(3), 459.

Lee, C., & Landgrebe, D. A. (1993). Feature extraction based on decision boundaries. *IEEE Transactions on Pattern Analysis and Machine Intelligence, 15*(4), 388–400. https://doi.org/10.1109/34.206958.

Li, W., Prasad, S., & Fowler, J. E. (2014). Hyperspectral image classification using gaussian mixture models and markov random fields. *IEEE Geoscience and Remote Sensing Letters, 11*(1), 153–157. https://doi.org/10.1109/LGRS.2013.2250905.

Martinez, W., & Martinez, A. (2007). *Computational Statistics Handbook with MATLAB* (2nd ed.). Chapman & Hall/CRC Computer Science & Data Analysis: CRC Press.

Richards, J. (2012). *Remote sensing digital image analysis: An introduction*. Berlin: Springer. https://books.google.com/books?id=ETfwQnBMP4UC.

Shahshahani, B. M., & Landgrebe, D. A. (1994). The effect of unlabeled samples in reducing the small sample size problem and mitigating the hughes phenomenon. *IEEE Transactions on Geoscience and Remote Sensing, 32*(5), 1087–1095. https://doi.org/10.1109/36.312897.

Simin, C., Rongqun, Z., Wenling, C., & Hui, Y. (2009). Band selection of hyperspectral images based on bhattacharyya distance. *WSEAS Transactions on Information Science and Applications, 6*(7), 1165–1175.

Tadjudin, S., & Landgrebe, D. A. (2000). Robust parameter estimation for mixture model. *IEEE Transactions on Geoscience and Remote Sensing, 38*(1), 439–445. https://doi.org/10.1109/36.823939.

Theodoridis, S., & Koutroumbas, K. (2009). *Pattern recognition* (2nd ed.). Elsevier Science.

Thomaz, C. E., Gillies, D. F., & Feitosa, R. Q. (2004). A new covariance estimate for bayesian classifiers in biometric recognition. *IEEE Transactions on Circuits and Systems for Video Technology, 14*(2), 214–223. https://doi.org/10.1109/TCSVT.2003.821984.

Wang, S., & Wang, C. (2015). Research on dimension reduction method for hyperspectral remote sensing image based on global mixture coordination factor analysis. *The International Archives of Photogrammetry, Remote Sensing and Spatial Information Sciences, 40*(7), 159.

Webb, A. (2003). *Statistical pattern recognition* (2nd ed.). Wiley InterScience Electronic Collection, Wiley.

Yang, L., & Lin Yang, M. S., Lai, C. Y., & Lin, C. Y. (2012). A robust EM clustering algorithm for Gaussian mixture models. *Pattern Recognition, 45*(11), 3950–3961, https://doi.org/10.1016/j.patcog.2012.04.031.

Mohammed Lahlimi is a doctoral student at the Laboratory for Research in Computing and Telecommunications (LaRIT) in the Faculty of Sciences, Ibn Tofail University, Kenitra, Morocco. He received the State Engineer degree in Telecommunication and Networks from the National School of Applied Sciences of Fez (ENSAF), University Sidi Mohamed Ben Abdellah, Fez, Morocco, in 2013. His doctoral research is on remote sensing image processing and his work focuses on dimensionality reduction/band selection of hyperspectral imaging for classification purposes. His other research interests include pattern recognition and artificial intelligence.

Mounir Ait Kerroum received his Bachelor’s Degree (License és Sciences) in Electronic Physics in 1999 and his Master’s Degree (DESA) in Computer and Telecommunication from the Faculty of Sciences, University Mohammed V, Rabat, Morocco, in 2003.

He received his Ph.D. in 2010 from the University Mohammed V, Rabat, Morocco. He joined the National School Of business and Management of Kénitra, Ibn Tofail University, Morocco, as an Associate Professor in Mars 2010. Currently, he is the head of Network, telecommunications and artificial intelligence team at the Laboratory for Research in Computing and Telecommunications (LaRIT) in the Faculty of Sciences of Kenitra and associate Researcher at the Laboratory for Research in Computing and Telecommunications (LRIT) in the Faculty of Sciences of Rabat. His current research interests include pattern recognition, remote sensing image processing and artificial intelligence.

Youssef Fakhri received his Bachelor’s Degree (License és Sciences) in Electronic Physics in 2001 and his Master’s Degree (DESA) in Computer and Telecommunication from the Faculty of Sciences, University Mohammed V, Rabat, Morocco, in 2003 where he developed his Master’s Project at the ICI company, Morocco.

He received a Ph.D. in 2007 from the University Mohammed V - Agdal, Rabat, Morocco in collaboration with the Polytechnic University of Catalonia (UPC), Spain. He joined the Faculty of Sciences of Kénitra, Department of Computer Science and Mathematics, Ibn Tofail University, Morocco, as an Associate Professor in Mars 2009; he is the Laboratory head at LARIT, Associate Researcher at the Laboratory for Research in Computing and Telecommunications (LRIT) in the Faculty of Sciences of Rabat, and Member of Pole of Competences STIC Morocco. His current research interests include QoS in wireless communication, WSN, wireless.

Advanced Methods and Implementation Tools for Cardiac Signal Analysis

Safa Mejhoudi, Rachid Latif, Abdelhafid Elouardi and Wissam Jenkal

Abstract

The heart is considered as a muscular pump that propels the blood toward all the cells of the human body, this hollow muscle has an internal electrical activity that allows it to contract automatically. Measuring this activity, called ECG signal, is used to diagnose the heart disorders. So, in this chapter, we survey the current state-of-the-art methods of ECG processing which contain several steps such as preprocessing or denoising, feature extraction and then arrhythmias detection; and the technological solutions for real-time implementation on embedded architectures as CPU, GPU, or FPGA. Finally, we discuss drawbacks and limitations of the presented methods with concluding remarks and future challenges.

Keywords

ECG signal • Feature extraction • Algorithm • Real-time processing • Embedded architectures

1 Introduction

The heart is considered the most important organ of our body. It brings energy to the whole organism and controls the circulation of blood throughout the body. Understanding how it works was a meaningful field of study since many years ago. As technology develops, measured heartbeat signals can be further analyzed in order to know the health status of a person. This measured signal is called electrocardiogram (ECG) (Alberdi et al. 2016) and it takes waveforms which represent the electrical activity (Muthuswamy 2003) which in turn indicates the physiology and statistical features of the signal that change over time. Figure 1 shows the cardiac cycle with the associated waves of the ECG signal. It is mainly composed of five different waves that are P, Q, R, S, and T which reflect heart activity during a cardiac cycle (R-R interval). The Q, R, and S waves are treated as a single composite called QRS complex which describes the main heart activity.

Before the use of ECG signal to identify cardiac diseases, it must be analyzed at first. The analysis stage contains several steps, such as preprocessing and features extraction. In this chapter, we will shed light on these main axes, so we are going to present the various works recently published by the researchers as (Jenkal et al. 2015a, b; Giorgio 2016; Lim et al. 2015; Elhaj et al. 2016; Wenfeng et al. 2010) focusing on the proposed technological solutions using embedded architectures for the implementation of the algorithms either for ECG denoising, features extraction, or arrhythmias detection.

The rest of this chapter is organized as follows:

Section 2 will touch preprocessing technics that are devoted to denoise ECG signal from undesired artifacts. Section 3 will present some of the published works related to the detection of QRS complex as the most important feature in the ECG signal. Section 4 will be interested in works that propose solutions for the detection and identification of some heart diseases based on the preprocessing and QRS detection stages. Finally, a discussion and the conclusions of the chapter are given in Sects. 5 and 6, respectively.

2 ECG Preprocessing

When taking the signal from heart it gets mixed with different other signals such as power line interference, muscle activity, body movements, etc. And, the challenge is how to purify the signal from noises of different sources (Tracey and Miller 2012; Cao and Li 2010). During the preprocessing stage, the main objective is to filter the useful signals from

---

S. Mejhoudi (✉) · R. Latif · W. Jenkal
Laboratory of Systems Engineering and Information Technology (LiSTi), ENSA, Ibn Zohr University, Agadir, Morocco
e-mail: s.mejhoudi@gmail.com

A. Elouardi
SATIE, Digiteo Labs, Paris-Sud University, Paris Saclay University, Orsay, France

S. El Hani and M. Essaaidi (eds.), *Recent Advances in Electrical and Information Technologies for Sustainable Development*,
Advances in Science, Technology & Innovation, https://doi.org/10.1007/978-3-030-05276-8_11

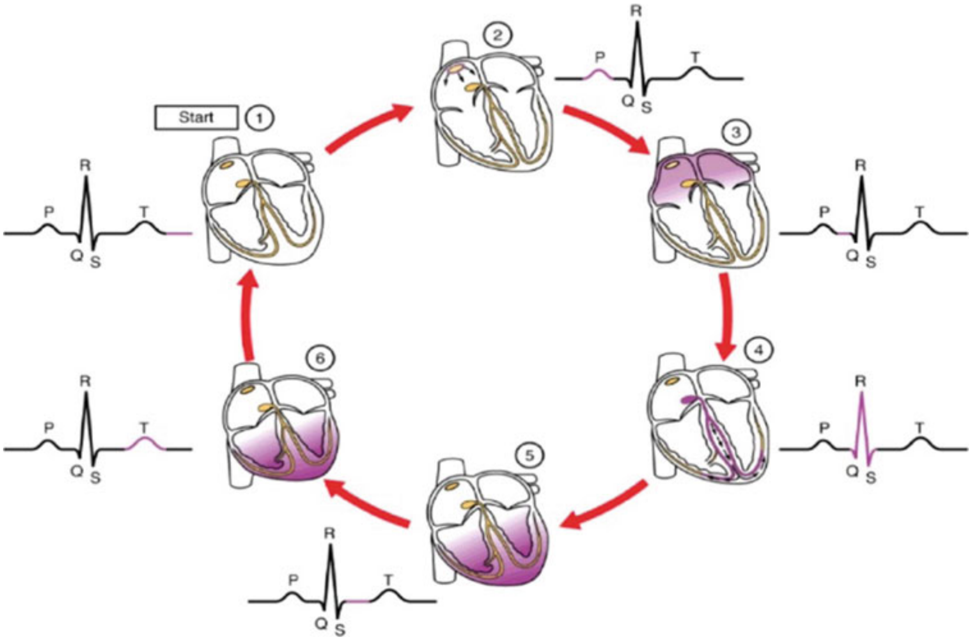

Fig. 1 Cardiac cycle with the associated waves of the ECG signal

unwanted noises. In electrocardiography, these noises are well identified but some of them have the particularity of overlapping with the spectral band of the ECG, which sometimes makes them difficult to remove.

2.1 Artifacts and Noise

Roughly speaking, ECG contaminants can be classified as (Wang et al. 2002; Clifford et al. 2006)

- **Power line interference**: a signal in the frequency of 50 or 60 Hz, and its bandwidth is below 1 Hz whose amplitude can obscure the morphological characteristics of ECG.
- **Baseline wander**: a low-frequency (0.15 up to 0.3 Hz) noise. This noise results from the patient respiration and produces a baseline shifting of the ECG signals.
- **Electrode contact noise**: it is the result of the bad contact between the electrode and the skin-inducing variations in the electrode–skin impedance, which adequately cuts off the measurement system from the subject.
- **Muscle contractions (electromyography noise)**: a high-frequency noise that results from muscles contraction.

However, these noises can be reduced by the existing algorithms and the wise use of hardware and experimental setup, we cannot remove them at all. For this reason, we must quantify the noise nature before choosing the appropriate algorithm adapted to the target architecture.

2.2 ECG Denoising Techniques

We will introduce in this part, some key methods mentioned in the literature and developed to remove artifacts that contaminate the ECG signal and their implementation on embedded architectures of different technologies as CPU, GPU, or FPGA.

Most of the works used adaptive filters or Finite/Infinite Impulse Response (FIR/IIR) filters by choosing a bandwidth relative to the useful information from the ECG signal (Laguna et al. 1992; Bhaskar and Uplane 2016).

Bhaskar and Uplane have proposed an algorithm based on the Finite Impulse Response (FIR) filter to remove high-frequency noise of muscles contraction (EMG), that have a frequency range of 1–10000 Hz and voltage levels of 0.1–10 mV related the patient movements (Gautam and Lee 2010). Low-pass FIR filters are designed using windowing method with a cutoff frequency of 100 Hz and a sampling frequency of 360 Hz (MIT-BIH database).

To implement his algorithm in FPGA architecture, Bhashkar used Distributed Arithmetic (DA) method which is a technique that improves the filter performance using Look Up Table (LUT), shift registers, and scaling accumulators instead of general-purpose multipliers, Fig. 2 (Sudhakar et al. 2012; Kumm et al. 2013).

The hardware implementation was done on Spartan 3E XC3S500e-4fg320 card of Xilinx, using Simulink Matlab version 7.4.0 (2007a) with the Xilinx system generator software version 10.1 which installs the Xilinx block set required for the hardware implementation in Matlab Simulink.

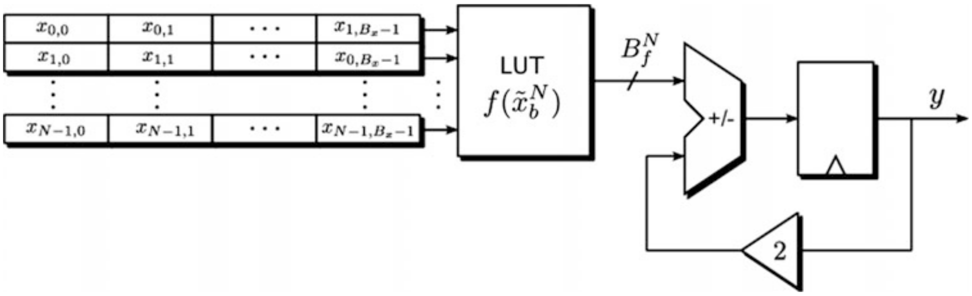

Fig. 2 Simple implementation of distributed arithmetic

In Aboutabikh and Aboukerdah (2015), the authors chose to apply an algorithm based on a single multiband digital filter (seven bands) of type FIR to filter an ECG signal affected by four types of interference signals, instead of using three digital filters LPF, HPF, and BSF with a filter order of 1500 and attenuation factor of 40 dB for various interference signals. This algorithm makes it possible to avoid the phase shift problems as well as the minimization of the computation time by removing different noises in the same time.

The method proposed by Aboutabikh is based on Direct Digital Frequency Synthesizers (DDFS), which are considered as a high-accuracy technique in frequency synthesizing domain designed to synthesize the ECG signal and various interference signals as it can be seen in Fig. 3.

The filter was implemented using a digital programmable device (Cyclone II EP2C70F896C6 FPGA), implemented on the education and development board: Altera DE2-70 Terasic.

A mean filter for ECG signal filtering can also be used like in Chouhan and Mehta (2007). In this technique, the average of the ECG signal is subtracted from the signal beforehand. Then a fifth-order polynomial is applied to obtain an estimate of the baseline which will then be subtracted from the ECG signal.

Since the ECG signal is a signal that contains several spectral components, it is also nonstationary and often affected by noise correlated to the signal, such as muscular artifacts. For this reason, multi-resolution analysis is proving to be a better tool for treatment. Thus, most recent work

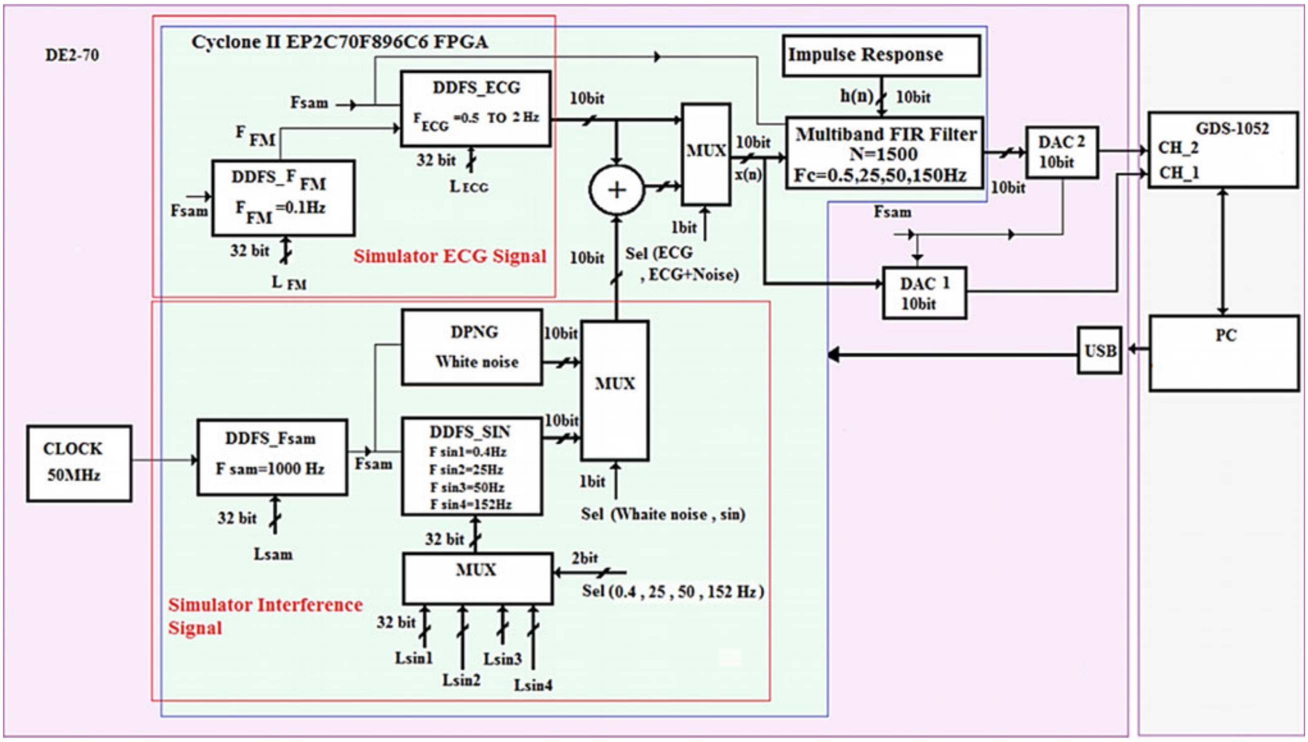

Fig. 3 The diagram block of the system

tends to use filtering based on DWT (Borries et al. 2005; Giorgio 2016; Jenkal et al. 2016). The DWT then transforms the signal under investigation into another representation which presents the information of the ECG signal in a more useful form, by the convolution of the signal with a function called “wavelet”. Indeed, the DWT is considered as a mathematical microscope that cuts the EC signal into frequency components at a resolution adapted to the scale.

For the DWT application, the Mallat algorithm is used, it provides then sufficient information for both the decomposition and the reconstruction of the original signal with a reduction in computation time and hardware resources for hardware implementation purposes (Mallat 2009). Thus, the structure of the Mallat algorithm is presented by Fig. 4, it consists of the computation of detail components d(n) and approximation components a(n) which are produced by high-pass FIR filters Hi_D(n) and low-pass FIR filters La_D (n), respectively. The reconstruction process is the reverse of the decomposition using low-pass La_R(n) and high-pass Hi_R(n) filters.

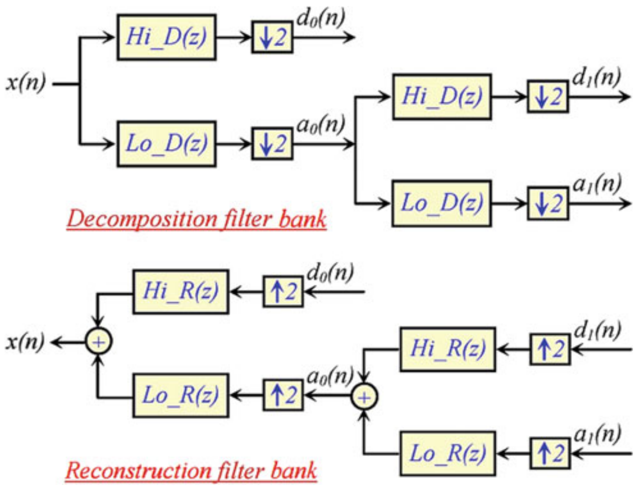

Fig. 4 Filter bank representation of DWT according to Mallat algorithm

As a general rule, the mother wavelet is chosen according to the similarity between the wavelet and the signal under investigation.

In El Mimouni and Karim (2014), the DWT is used to remove the Baseline Wander (BLW) noise from ECG signal. The Daubechies Wavelet is used as mother wavelet because it shows similarities with ECG signal. In this paper, the author presents an FPGA-based embedded system design which is developed with the Xilinx design tool, System Generator for DSP which is a plug-in to Simulink, the Simulink model of the proposed design is shown in Fig. 5 and it is implemented in the Digilent Nexys 3 board based on the Xilinx Spartan-6 XC6SLXI 6 FPGA device.

Jenkal has proposed a new technique called the adaptive dual threshold filter “ADTF” (Jenkal et al. 2018), it has been inspired from the dual threshold median method published by Gupta et al. (2015). It is a technique based on the median filter with an adaptive dual threshold for image denoising. That calculates three elements for each window of the ECG signal; the average of this window, the upper threshold and the lower threshold and the filtering operation consists in correcting the median value of the window using two thresholds, the block diagram of the ADTF is given by Fig. 6.

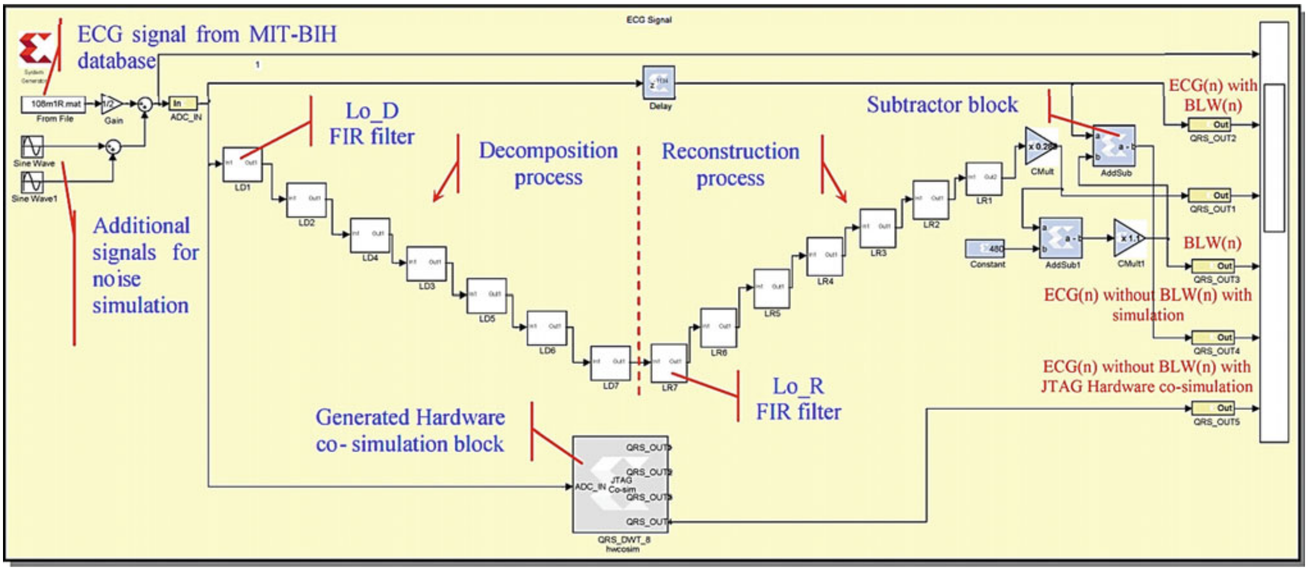

Fig. 5 Simulink model for BLW removal

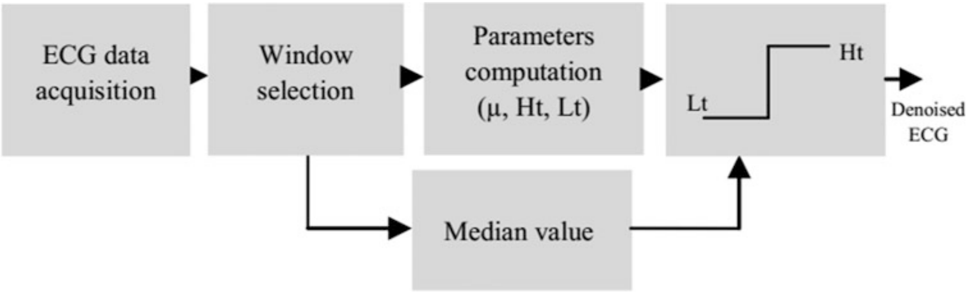

Fig. 6 Block diagram of the ADTF

The description of the algorithm is based on the VHDL language, and the implementation of the proposed architecture on different FPGA devices shows good results comparing it with the soft-ADTF.

One other of the most widely used techniques in the literature is the Empirical Mode Decomposition (EMD) method (Kabir and Shahnaz 2012; Blanco-Velasco et al. 2008). EMD decomposes the signal into a sum of Intrinsic Mode Functions (IMFs). An IMF is subtraction of lower and upper envelope by interpolation using local maxima and minima of the signal.

Shailesh et al. (2018) propose a methodology using Empirical Mode Decomposition (EMD) with Nonlocal Mean (NLM) framework using the differential standard deviation value to eliminate the noise from ECG signal. It consists of four stages that are R peak detection, differential standard deviation computation, EMD framework, and NLM framework.

The NLM method is also used by Cuomo et al. (2016) which its basic idea is to reconstruct the value of each sample point of the signal, by performing a weighted no local mean of all nearby values. The author proposed to implement his algorithm in Graphics Processing Unit (GPU) environment to exploit its computational power, instead of using standard CPU environments in order to overcome the high computational complexity of the NLM method and to guarantee real-time results. So the implementation is based on Compute Unified Device Architecture (CUDA) of NVIDIA.

The ECG signal denoising is just the first stage of the processing process, but it is essential to determine the fiducial points in the signal especially P, Q, R, S, and T. So an accurate diagnosis of the heart status of patients is based on the good suppression of the noises and artifacts which contaminate the signal and which can change its morphology.

3 Features Extraction

As it is already mentioned in this chapter, the ECG signal is composed of five different waves that are P, Q, R, S, and T. The QRS complex is considered as the most important parameter in an ECG signal, the detection of it is a golden tool for heart beat frequency computation and for heart diseases detection, so we will focus in this part on some works that are recently presented in this axis.

The QRS detection algorithm presented by Pan and Tompkins (1985) is the most widely used and frequently cited algorithm for the QRS complexes extraction from electrocardiograms. The PT algorithm is adapted by several researchers as in Hashim et al. (2016), where it is compared with the Derivative Based algorithms (DB) which are inspired from Balda et al. (1977).

Figure 7 shows the data flow diagram of PT algorithm which consists of band-pass filter frequency of 5–15 Hz, and differentiation to provide slope information for the peaks detection. The squaring stage is used to accentuate the R-peaks. The moving window integration gives a signal which includes information about both the QRS complex slope and width, and then adaptive threshold detection is applied.

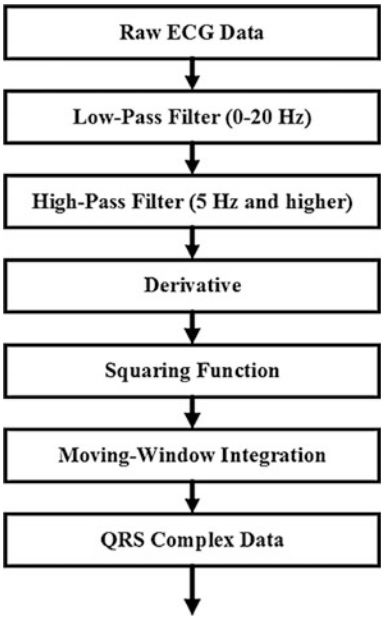

Fig. 7 Pan and Tompkins's Algorithm

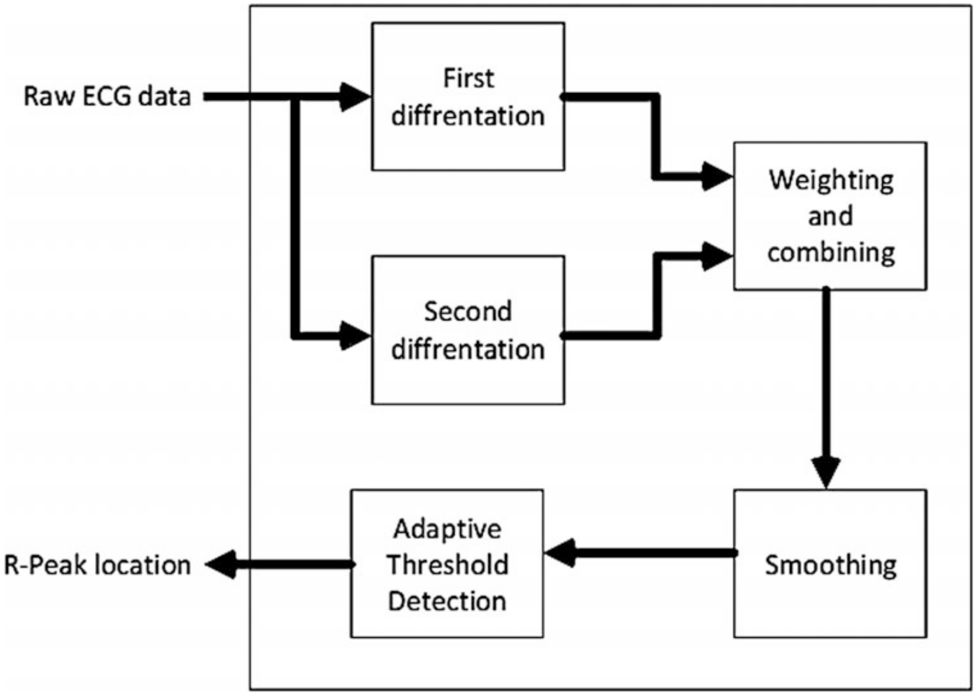

Fig. 8 Derivative Based algorithm

Figure 8 presents the data flow diagram of the DB algorithm which consists of a first and a second differentiation, weighting, and combination which aims to maximizing the difference of the QRS complex with other peaks, smoothing to avoid detection of false beat caused by the noise and then the adaptive threshold detection.

The two algorithms are implemented on a SoC embedded architecture, Altera's DE2-115 FPGA card, which hosts the Cyclone IV chip. It is designed using Altera Quartus II and Qsys EDA softwares. The NIOS II processor with full configuration plays the role of a system master controller and executes the ECG QRS complex detection algorithms.

In Sharma (2017), a novel technique for QRS detection is proposed which is the Weighted Total Variation (WTV) denoising. The use of weights permits attenuation not only of the noise, but also the in-band P- and T-waves.

The ECG signal is first passed through a band-pass filter to reduce the high-frequency muscular noise and the P- and T-amplitudes. Then, the filtered signal is differentiated in order to emphasize the QRS complexes which have a high slope and to reduce the amplitude of the P- and the T-waves. The third step is the WTV which denoises the signal by Total Variation (TV) minimization. The TV minimization is introduced for first time for edge-preserving image denoising in Rudin et al. (1992); it is, in discrete form, the summation of the absolute values of the first-order difference of the signal.

Sharma has implemented his method in MATLAB R2015b and executed it on an Intel Core i3 CPU@2.50 GHz with 4 GB RAM and 64-Bit Ubuntu 14.04 operating system.

4 Arrhythmia Detection

One of the most fields where ECG analysis is essential is the diagnosis of Cardiovascular Diseases (CVD.) As stated by the World Health Organization, CVDs are the major reason for deaths worldwide. And, as a result, the precise detection and classification of these diseases have been, since a long time, the center of interest of scientific researchers in biomedical domain. So, in this part, we are going to present some of dedicated algorithms to arrhythmia detection.

In Giorgio (2016), the DWT technique is applied for the real-time detection of the cardiac Ventricular Late Potentials (VLPs). The ECG is filtered in order to get an efficient VLPs detection then the algorithm finds the highest peak of the heartbeat energy and then counts the time interval to end the electrical activity for each heartbeat set at 50 μV as shown in Table 1.

The implementation and the verification of the algorithm functionality are done by Altera's DE2-115-Cyclone II board, most of blocks are designed directly using the Verilog HDL language with Quartus II. The results were

Table 1 VLP detection settings

Triggering value	Minimum value assumed for presence of electrical activity	Time required for a VLP presence warning
5000 μV	50 μV	70 ms

Table 2 Heart rate and RR interval for some heart arrhythmia

Heart Arrhythmias	Heart rate (BPM)	RR interval (S)
Normal Sinus Rhythm	60–100	0.60–1.0
Atrial Fibrillation	>350	Random
Atrial Tachycardia	160–240	0.25–0.375
Super Ventricular Tachycardia	140–240	–

displayed on the NiosII-Linux terminal and output files can be produced for the post-analysis on a host PC.

The authors in Kumari et al. (2015) use EMD method to facilitate the detection of different arrhythmias. So, after enhancement using EMD method, detection of R-peaks using threshold methodology, the detection of various cardiac arrhythmias is done easily by the RR intervals computation, we just need to know the heart rate of different arrhythmias as it is shown in Table 2.

This algorithm was implemented on the Xilinx Spartan 3E card using Verilog HDL. The results of the algorithm are given in terms of the accuracy to detect three arrhythmias: normal sinus rhythm (100%), supraventricular tachycardia (92.3%), and atrial fibrillation (92%).

5 Discussion

In this section, we will discuss the presented works in the previous sections. As few authors use the same evaluation scheme for tests, it is difficult to make a fair comparison between the methods, so we will try as it is possible to interpret the results of different works in terms of accuracy and reliability of the algorithm, its complexity, and therefore the computation time.

The preprocessing step is crucial in the analysis of ECG signals for different purposes. Therefore, some important techniques for ECG denoising are mentioned in this chapter. FIR filters seem to be a good solution for noise elimination, but it requires the well known of the noise frequency which is too difficult in some cases where the noise frequency is in the same bandwidth as the useful signal. The improvement of the filter specifications as in Aboutabikh and Aboukerdah (2015) increased a lot the order of the filter which makes the algorithm difficult to implement it on some architectures. In El Mimouni and Karim (2014), the DWT is used to remove the baseline wander “BLW” noise from ECG signal. In general, the DWT algorithm gives good results in ECG denoising, we have just to be careful in making the choice of the mother wavelet and the levels of decomposition. This method can give better results in terms of real-time processing if we try to implement it directly using HDL description instead of using Matlab and Simulink environments. The ADTF algorithm used in Jenkal et al. (2015a, b) gives satisfying results in denoising task; it presents less complexity compared with other methods, so it is easily designed for implementation in different FPGAs.

The PT and the DB algorithms used for QRS detection are compared in Hashim et al. (2016), in terms of accuracy. As a result, they give accuracies of 98.15% and 96.73%, respectively, so we can say that PT algorithm is more accurate than DB one. But, if we compare them in terms of computation time, the DB algorithm is fast than PT algorithm. The two algorithms require more optimization to perform real-time processing.

The DWT technique is used for real-time detection of cardiac VLPs (Giorgio 2016). In fact, the DWT is used to purify the signal and to facilitate the VLPs detection; the technique gives an average accuracy of 92%. Thus, we can say that the algorithm guarantees the detection of the presence of the VLPs but there is an uncertainty about their real number. A threshold methodology is applied after enhancement by EMD method in (Kumari et al. 2015) and it presents acceptable results in terms of accuracy detection of several cardiac arrhythmias, but this method has several drawbacks because of its algorithmic complexity produced by many mathematical calculations which increase the computation time.

According to this study, we can conclude that each algorithm has advantages and drawbacks. In order to have a reliable processing of the ECG signal, with the less algorithmic complexity and to guarantee a real-time processing of cardiac data, a hardware–software codesign is mandatory.

6 Conclusion

Recent studies on the ECG signal analysis are summarized in this chapter. Many techniques have been proposed to remove different noises in order to improve the original signals or to extract the useful information as the QRS complex on which arrhythmia detection is based.

The design and implementation of algorithms dedicated to cardiac signals processing, on embedded architectures based on GPU or FPGA become a big center of interest for researchers, with the intention of having an embedded system that is able to guarantee a precise and real-time diagnosis of cardiac status which can save many lives.

Acknowledgements This work is partially supported by the National Centre of Scientific and Technical Research of Morocco (CNRST). The authors also gratefully acknowledge the helpful comments and suggestions of the reviewers, which have improved the presentation.

References

Aboutabikh, K., & Aboukerdah, N. (2015). Design and implementation of a multiband digital filter using FPGA to extract the ECG signal in the presence of different interference signals. *Computers in Biology and Medicine, 62,* 1–13.

Alberdi, A., Aztiria, A., & Basarab, A. (2016). Towards an automatic early stress recognition system for office environments based on multimodal measurements: a review. *Journal of Biomedical Informatics, 59*(2016), 49–75.

Balda, R., Diller, G., Deardorff, E., Doue, J., & Hsieh, P. (1977). The HP ECG analysis program. In *Trends in Computer Processed Electrocardiograms* (pp. 197–205).

Bhaskar, P. C., & Uplane, M. D. (2016). High frequency electromyogram noise removal from electrocardiogram using FIR low pass filter based on FPGA. *Procedia Technology, 25,* 497–504.

Blanco-Velasco, M., Weng, B., & Barner, K. E. (2008). ECG signal denoising and baseline wander correction based on the empirical mode decomposition. *Computers in Biology and Medicine, 38,* 1–13. http://dx.doi.org/10.1016/j.compbiomed.2007.06.003.

Borries, R. F., Pierluissi, H. J., & Nazeran, H. (2005). Wavelet transform based ECG baseline drift removal for body surface potential mapping. In *Proceedings of the 27th Annual Conference on Engineering in Medicine and Biology, Shanghai* (pp. 3891–3894).

Cao, X., & Li, Z. (2010). Denoising of ECG signal based on a comprehensive framework. *International Conference on Multimedia Technology (ICMT), 1*(4), 29–31.

Chouhan, S., & Mehta, S. S. (2007). Total removal of baseline drift from ECG signal. In *Presented at International Conference on Computing: Theory and Applications, ICCTA'07*.

Clifford, G. D., Azuaje, F., & McSharry, P. E. (2006). *Advanced methods and tools for ECG data analysis*. Artech House Publishers.

Cuomo, S., De Michele, P., Galletti, A., & Marcellino, L. (2016). A GPU parallel algorithm for ECG signal denoising based on the NLM method. In *Proceedings of the IEEE 30th International Conference on Advanced Information Networking and Applications Workshops, WAINA* (pp. 35–39). http://dx.doi.org/10.1109/WAINA.2016.110.

El Hassan, E. L. M., & Karim, M. (2014). An FPGA-based implementation of a pre-processing stage for ECG signal analysis using DWT. 978-1-4799-4647-1/14/$31.00 ©2014. IEEE.

Elhaj, F. A., Naomie, S., Arief, R. H., Tan, T. S., & Taqwa, A. (2016). Arrhythmia recognition and classification using combined linear and nonlinear features of ECG signals. *Computer Methods and Programs in Biomedicine, 127,* 52–63.

Gautam, A., & Lee, H. J. (April–June 2010). ECG signal de-noising with asynchronous averaging and filtering algorithm. *International Journal of Healthcare Information Systems and Informatics, 5*(2), 30–36.

Giorgio, A. (2016). A new FPGA-based medical device for the real time prevention of the risk of arrhythmias. *International Journal of Applied Engineering Research, 11*(8), 6013–6017. ISSN 0973–4562.

Gupta, V., Chaurasia, V., & Shandilya, M. (2015). Random-valued impulse noise removal using adaptive dual threshold median filter. *Journal of Visual Communication and Image Representation, 26,* 296–304.

Hashim, M. A., Hau, Y. W., & Baktheri, R. (2016). Efficient QRS complex detection algorithm implementation on soc-based embedded system. *JurnalTeknologi (Sciences & Engineering), 78*(7–5), 49–58.

Jenkal, W., Latif, R., Toumanari, A., Dliou, A., & El B'charri, O. (2015a). An efficient method of ECG signals denoising based on an adaptive algorithm using mean filter and an adaptive dual threshold filter. *International Review on Computers and Software (IRECOS), 10*(11), 1089–1095.

Jenkal, W., Latif, R., Toumanari, A., Dliou, A., El B'charri, O., & Maoulainine F. M. R. (2015b). Efficient method of QRS complex extraction using a multilevel algorithm and an adaptive thresholding technique. In *Third World Conference on Complex Systems (WCCS)* (pp. 1–5). IEEE.

Jenkal, W., Latif, R., Toumanari, A., Dliou, A., El B'charri, O., &Maoulainine, F. M. R. (2016). An efficient algorithm of ECG signal denoising using the adaptive dual threshold filter and the discrete wavelet transform. *Biocybernetics and Biomedical Engineering, 36*(3), 499–508.

Jenkal, W., Latif, R., Toumanari, A., Elouardi, A., Hatim, A., & El Bcharri, O. (2018). Real-time hardware architecture of the adaptive dual threshold filter based ECG signal denoising. *Journal of Theoretical and Applied Information Technology*.

Kabir, M. A., & Shahnaz, C. (2012). Denoising of ECG signals based on noise reduction algorithms in EMD and wavelet domains. *Biomed Signal Process Control, 7,* 481–489. http://dx.doi.org/10.1016/j.bspc.2011.11.003.

Kumari, L. V. R., Padma, Y., Balaji, S. N., & Viswada, K. (2015). FPGA based arrhythmia detection. *Procedia Computer Science, 57,* 970–979.

Kumm, M., Möller, K., & Zipf, P. (2013). Reconfigurable FIR filter using distributed arithmetic on FPGAs. In *IEEE International Symposium on Circuits and Systems (ISCAS 2013)*. https://doi.org/10.1109/iscas.2013.6572277.

Laguna, P., Jane, R., & Caminal, P. (1992). Adaptive filtering of ECG baseline wander. In *Presented at Engineering in Medicine and Biology Society. Proceedings of the Annual International Conference of the IEEE* (Vol. 14).

Lim, H. W., Mohd Sani, M. S. A., Hashim, A., & Hau, Y. W. (2015). Throb: System-on-Chip based arrhythmia screener with self-interpretation. *International Journal of Electrical and Electronic Systems Research, (Special issue: Innovate Malaysia Design Conference), 8,* 30–36.

Mallat, S. (2009). *A wavelet tour of signal processing*. Academic Press.

Muthuswamy, J. (2003). Biomedical signal analysis. In *Standard handbook of biomedical engineering and design*. Tempe, Arizona: McGraw-Hill.

Pan, J., & Tompkins, W. J. (1985). A real-time QRS detection algorithm. *IEEE Transactions on Biomedical Engineering, 32,* 230–236.

Rudin, L. I., Osher, S., & Fatemi, E. (1992). Nonlinear total variation based noise removal algorithms. *Physica D: Nonlinear Phenomena, 60*(1), 259–268.

Shailesh, K., Damodar, P., & Sahu, P. K. (2018). Denoising of electrocardiogram (ECG) signal by using empirical mode decomposition (EMD) with non-local mean (NLM) technique. *Biocybernetics and Biomedical Engineering, 38,* 297–312.

Sharma, T., & Sharma, K. K. (2017). QRS complex detection in ECG signals using locally adaptive weighted total variation denoising. *Computers in Biology and Medicine, 87,* 187–199.

Sudhakar, V., Murthy, N. S., & Anjaneyulu, L. (2012). Area efficient pipelined architecture for realization of FIR filter using distributed arithmetic. In *International Conference on Industrial and Intelligent Information (ICIII 2012) IPCSIT* (Vol. 31). Singapore: IACSIT Press.

Tracey, B. H., & Miller, E. L. (2012). Nonlocal means denoising of ECG signals. *IEEE Transactions on Biomedical Engineering, 59*(9), 2383–2386.

Wang, H., Azuaje, F., & Black, N. (2002). Improving biomolecular pattern discovery and visualization with hybrid self-adaptive networks. *IEEE Transactions on Nanobioscience, 1*(4), 146–166.

Wenfeng, S., Daming, W., Weimin, X., Xin, Z., & Shizhong, Y. (2010). Parallelized computation for computer simulation of electrocardiograms using personal computers with multi-core CPU and general-purpose GPU. *Computer Methods and Programs in Biomedicine, 100,* 87–96.

Safa Mejhoudi She was born in Ouarzazate, Morocco on May 10, 1993. She received a Master degree in biomedical engineering in 2016 from Hassan 1st University, Faculty of Science and Technology, Settat, Morocco. She is currently a Ph.D. student within Laboratory of Systems Engineering and Information Technology (LISTI) at the National School of Applied Sciences, Ibn Zohr University, Agadir, Morocco. Her current research interests include signal processing, biomedical engineering, and embedded systems.

Rachid Latif He was born in Agadir, Morocco, on December 8, 1968. He received Ph.D. in signal processing in 2000 and the Habilitation degree in 2005, from Ibn Zohr University, Morocco. Currently, he is a full Professor in information technology with the Department of Industrial Engineering at the National School of Applied Sciences, Ibn Zohr University, Agadir, Morocco. His research interests include design and implementation of biomedical monitoring system, analysis of fetal cardiac signals, instrumentation of embedded systems, design of smart architectures for image and parallel programming models for heterogeneous architecture. Prof. Latif is the head of the Bio-Instrumentation and Systems Engineering research team (B2IS) and also the head of Master "Embedded Systems and Biomedical Engineering (SEIB)" and is a member of the Marocain Acoustical Society. In 2018 is appointed member and expert within the CNRST Morocco.

Abdelhafid Elouardi He received the M.S. degrees from Pierre & Marie Curie University, Paris, in 2001 and Ph.D. in Electronics from Paris-Sud University, Orsay, in 2005. He worked at Henri Poincar University, Nancy, as a researcher in 2005–2006. He is currently an Associate Professor at the Fundamental Electronics Institute, Paris-Sud University, Orsay, France. In Embedded Systems team of Autonomous Systems Department, his research interests include hardware–software codesign, evaluation and instrumentation of embedded systems, design of smart architectures for image and signal processing, simultaneous localization and mapping applications.

Wissam Jenkal He was born in Agadir, Morocco in 1991. He received the Master degree in automatic, signal processing, and industrial computer from the University of Hassan First, Faculty of Science and Technology, Settat, Morocco, in 2014. He received his Ph.D. on Signal Processing and Embedded Systems in 2018 in the Laboratory of Systems Engineering and Information Technology (LISTI) in the National School of Applied Sciences, Ibn Zohr University, Agadir, Morocco. His current research interests include biomedical engineering, embedded systems, and information technologies.

A Bi-criteria Distance Reduction Approach for Simple Plant Location Problem

Sara Haddou Amar, Abdellah Abouabdellah, and Yahia El Ouazzani

Abstract

Workspace location decision is considered as a complex problem that requires a detail evaluation and analysis approach. The determination process of a location position should be based on various factors and criteria in order to take into consideration all the requirements of the supply chain that are influencing the efficiency and the general performance of the workspace. The role of the workspace can be viewed differently according to the decision-maker preferences and the nature of business area. In this project, we propose an innovative resolution approach for the single workspace location problem in a polygonal area. Our objective is to locate the facility so as to minimize the total distance between the facility, the customers and the suppliers. Our bi-criteria approach is based on the consideration of the distance and the importance factor of each customer and supplier. We used the A-distance measurement and the aggregation methods to represent the real traveled distance as part of the mathematical modeling of the problem. The aim of the study is to determine the workspace location coordinates that put forward the economic, commercial, and ecological efficiency of the supply chain.

Keywords

Location problem • Decision support • Green modeling • Aggregation method • A-distance • Importance factor

1 Introduction

The workspace location is very important and a strategic decision involving several attributes. The location choice has a deep impact on the efficient and effective movement of items between the different elements of the supply chain: from raw material suppliers to processing facilities, component fabrication sites, finished goods assembly plants, distribution centers, warehouses, retailers, and customers (Demirel et al. 2010a, b). This variation of supply chain components and the nature of inter-relationships imply the consideration of various factors, criteria, and objectives in the location selection and determination. In addition to the supply chain requirements, decision-makers have different perspectives and expectations that should be introduced in the decision support methodologies and algorithms. In fact, according to Farahani et al. (2014), the primary objective in a typical hierarchical facility location problem is to determine the location in a multilevel network in a way to serve the customers at the lowest level of hierarchy: both efficiently (cost minimization objective) and effectively (service availability maximization objective).

Among supply chain studies, many papers on facility location problem have been published resulting in a board range of resolution methodologies (Dogan 2012). These different approaches are based on various objectives and criteria and also mathematical theories. In 2014, Letchford and Miller (2014) presented an aggressive reduction scheme for “Simple Plant location Problem”. The scheme involves four different reduction rules, along with lower and upper bounding procedures. It did turn out to be particularly effective for instances in which the facilities and clients correspond to points on the Euclidean plane. However, the “aggressive reduction” was introduced by Pisinger et al. (2007) for large-scale combinatorial optimization problems. The idea is to spend much time and effort in reducing the size of the instance, in the hope that the reduced instance will then be small enough to be solved by an exact algorithm.

S. Haddou Amar (✉) · A. Abouabdellah
MOSIL, System Engineering Laboratory, ENSA, Ibn Tofail University, Kenitra, Morocco
e-mail: sara.haddouamar@gmail.com

A. Abouabdellah
e-mail: a.abouabdellah2013@gmail.com

Y. El Ouazzani
LEAM, Faculty of Juridical, Economic and Social Sciences, Mohammed V University, Rabat, Morocco
e-mail: y.elouazzani@um5s.net.ma

S. El Hani and M. Essaaidi (eds.), *Recent Advances in Electrical and Information Technologies for Sustainable Development*,
Advances in Science, Technology & Innovation, https://doi.org/10.1007/978-3-030-05276-8_12

Unfortunately, the realistic approach and the exact geographical application to the proposed solution are difficult to conduct due to the various reductions in the solution development.

Rahmani and MirHassani (2014) used a genetic algorithm "Hybrid Evolutionary Firefly-Genetic Algorithm" to determine the facilities location and the movement of commodities with the aim of satisfying the customers' demands and minimizing the total cost. This resolution is similar to ant genetic system; the study did focus on the satisfaction of the demand regarding the handling cost and did prove a high level of efficiency regarding the considered objective, although the absence of the distribution factor in the development makes it vulnerable to fluctuation of costs, especially in transportation-based network.

Ana et al. (2014) proposed an approach with two-stage robust models and algorithms using p-median for facility location problem. The methodology is an application of a customized and enhanced of the column-and-constraint generation method including two practical issues: demand changes due to disruptions and facility capacities. The highlight of this proposal is the consideration of the demand changes which is a serious problem in a location analysis study but the lack of other importance factor makes the proposal limited.

Dantrakula et al. (2014) based their methodology on greedy algorithms: p-median algorithm and p-center algorithm. The purpose is to minimize the sum of the setup and transportation costs considered as a function of the number of opened facilities.

The simple plant location problem can be formulated differently according to the needs of the company and the location objectives. It is considered a multi-criteria decision-making problem due to the various attributes that should be considered in the resolution problem. In this project, we aim to determine a workspace location (coordinates $\mathrm{P}^* = (\mathrm{x}^*, \mathrm{y}^*)$) using a combined approach between the weighted average mathematical technique and the A-distance measurement. Our objective is to minimize the total traveled distance between the facility and both the suppliers and the customers. The remainder of this paper is organized as follows: Sect. 2 presents the problematic and introduces some definitions and formulations associated with A-distance. Section 3 concerns a detailed representation of the proposed approach and the steps of the methodology. Section 4 presents an application to workspace location selection problem in a polygonal area. The last section summarizes the findings and proposes suggestions for further research.

2 A-Distance and the Importance Index

2.1 Workspace Location Problem

In this project, we are interested in the determination of a workspace location. The problem consists of finding the optimal location coordinates $P^* = (y^*, x^*)$ that minimizes the total traveled distance between three components of the supply chain:

- The facility location (To be determined),
- The customer's locations, and
- The supplier's locations.

The optimization of total traveled distance translates our concerns regarding the economical, commercial, and environmental performance of the workspace and its supply chain.

Figure 1 displays our motivation behind the choice of the modeling objective:

The process of determination of the location $\mathrm{P}^* = (\mathrm{y}^*, \mathrm{x}^*)$ relies on three important components:

- The distance between the different locations,
- The importance weight of each customer, and
- The importance weight of each supplier.

The location decision depends on minimizing the distance regarding the importance of the destination in a way that the facility location should be relatively close to the most important suppliers and customers.

The developed approach is based on an improved weighted average methodology. The choice of weighted average helps to easily illustrate the distance and the locations' importance in the decision process.

We consider the A-distance to measure the approximated distance between two points. The following subsection presents the A-distance concept introduced by Widmayer et al. (1987).

Fig. 1 The modeling objective

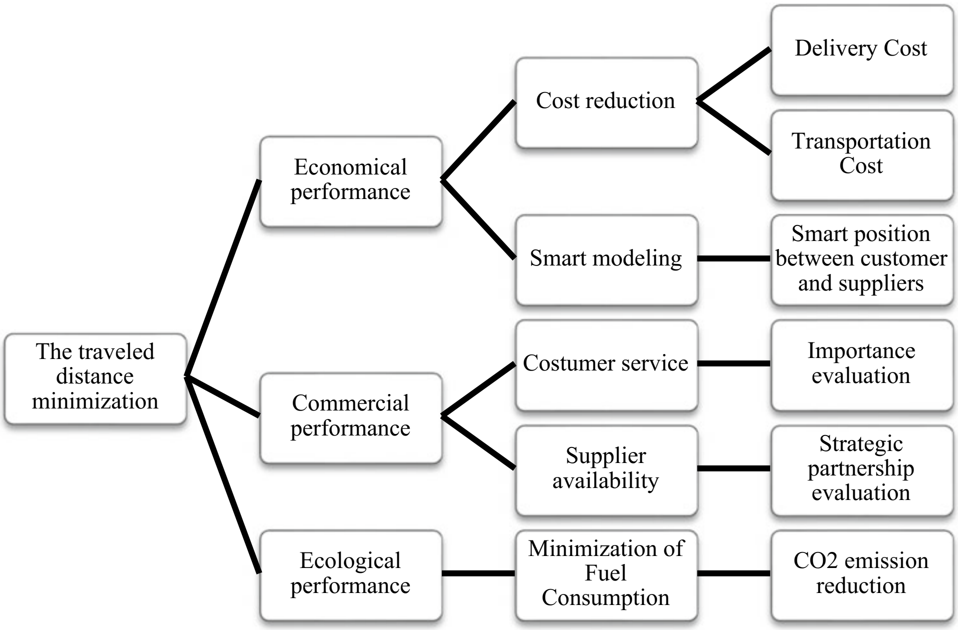

2.2 A-Distance: Mathematical Concept

We consider a polygonal study area “V” with a center noted “$O = (o_1, o_2)$”.

We consider the following:

C: The set of the customers, $C = \{C_1, C_2, \ldots, C_k\}$; $|C| = k$

F: The set of suppliers, $F = \{F_1, F_2, \ldots, F_l\}$; $|F| = l$

$C_i = (c_{i1}, c_{i2})$: The coordinates of the customer $C_i, \forall i \in [1 \cdot k]$

$F_i = (f_{i1}, f_{i2})$: The coordinates of the supplier $F_i, \forall i \in [1 \cdot l]$

If we can travel to any orientations, good approximation of distance between two points may be Euclidean distance. But the Euclidean way cannot be achieved in practice because of the existing of some barriers to travel (Matsutomi and Ishii 1998).

We consider “A” the set of allowed orientations.

$$A = \{\alpha_1, \alpha_2, \ldots, \alpha_r\};\ |A| = r.$$

The A-distance between the center “O” and a location “Ci” is the following:

$$\begin{aligned} d_A(O, C_i) = {} & M_1 |m_2(o_1 - o_2) - (c_{i1} - c_{i2})| \\ & + M_2 |m_1(o_1 - o_2) - (c_{i1} - c_{i2})| \end{aligned} \tag{1}$$

With

$$m_1 = \max(\tan\alpha_i, \tan\alpha_{i+1})\ \&\ m_2 = \min(\tan\alpha_i, \tan\alpha_{i+1})$$

$$M_1 = \frac{\sqrt{1 + m_1^2}}{m_1 - m_2}\ \&\ M_2 = \frac{\sqrt{1 + m_2^2}}{m_1 - m_2} \tag{2}$$

$$\alpha_i < \theta(O, C_i) < \alpha_{i+1}$$

Special case: if α_i or α_{i+1} are equal to $\frac{\pi}{2}$.

$$M_1 = \lim_{m_1 \to \infty} \frac{\sqrt{1 + m_1^2}}{m_1 - m_2} = 1 \text{ and } M_2 = \lim_{m_1 \to \infty} \frac{\sqrt{1 + m_2^2}}{m_1 - m_2} = 0$$

In consequence,

$$\lim_{m_1 \to \infty} M_2 m_1 = \lim_{m_1 \to \infty} \frac{m_1 \sqrt{1 + m_2^2}}{m_1 - m_2} = \sqrt{1 + m_2^2}$$

So

$$d_A(O, C_i) = |m_2(o_1 - o_2) - (c_{i1} - c_{i2})| + \sqrt{1 + m_2^2}(o_1 - o_2)$$

If $\alpha_i = 0$ and $\alpha_{i+1} = \frac{\pi}{2}$, $d_A(O, C_i) = |o_1 - o_2| + |c_{i1} - c_{i2}|$, since $m_2 = 0$, and it is very same as rectilinear distance.

The location decision process takes into consideration the importance factor of each customer and supplier.

We introduce in the next part the concept of importance index.

2.3 The Importance Index

The workspace location decision should take into consideration the importance of the customers and the suppliers (Demirel et al. 2010a). We propose in our approach to assign to each customer “Ci” and supplier “Fi” an importance weight that represents

- The expected average demands of the customer,
- The profitability,
- The lead time, and
- The responsiveness of the suppliers.

For the customers, the importance is measured by the amount of annual orders and turnover exchange.

We consider the set of customers $C = \{C_1, C_2, \ldots, C_k\}$; $|C| = k$.

M: The total annual average order of all customers

m_i: The annual average order of the customer $C_i, \forall i \in 1 \cdot k$

The importance weight of the customer C_i is

$$W_{C_i} = \frac{M - m_i}{M} \tag{3}$$

For the evaluation of the suppliers, the importance consists of the quality of the service and responsiveness.

We consider the set of suppliers $F = \{F_1, F_2, \ldots, F_l\}$; $|F| = l$.

The quality of the service of a supplier $F_i, \forall i \in 1 \cdot l$

$$Q_{F_i} = \frac{\mathrm{TAOF} - \mathrm{TAOP}}{\mathrm{TAOF}} \tag{4}$$

TAOF: Total annual orders fulfilled.

TAOP: Total annual orders prepared.

The responsiveness of a supplier is measured by

$$R_{F_i} = \mathrm{AATOP}$$

AATOP: The annual average time between order placement and its preparation.

Let consider

MQ: The average service qualities of all suppliers.

MR: The average responsiveness of all suppliers.

In consequences, the importance weight of the customer F_i is

$$W_{F_i} = \frac{MQ - Q_{F_i}}{MQ} + \frac{MR - R_{F_i}}{MR} \tag{5}$$

The proposed importance weights are developed especially for the purpose of the location determination. It is a combination of various metrics found in several studies, concerning customer's and supplier's evaluations. The proposed formulas are limited to this study and are not the subject of a profound research.

3 The Location Determination: The Developed Approach

The workspace location approach is based on the weighted average methodology. We take into consideration the location coordinates and the importance weight of the suppliers and the customers.

The objective is to minimize the total traveled distance. As shown in Sect. 2.1, the most optimal distance measurement between two points is the A-distance. It takes into consideration the barriers of the covered distances.

The weighted average methodology relies on location coordinates based on the Euclidian distance as shown in the following equation:

Let consider two points $P_1 = (a_1, b_1)$, $P_2 = (a_2, b_2)$ and their weights w_1 and w_2. The location of the third point $P_3 = (a_3, b_3)$ using the weighted average is

$$a_3 = \frac{\sum_{i=1}^{2} a_i \times w_i}{\sum_{i=1}^{2} w_i} \text{ and } b_3 = \frac{\sum_{i=1}^{2} b_i \times w_i}{\sum_{i=1}^{2} w_i} \tag{6}$$

The coordinates a_1, b_1, a_2, and b_2 are measured using the Euclidian distance (see Fig. 2).

In order to apply the weighted average methodology using A-distance, we should define fictitious coordinates that

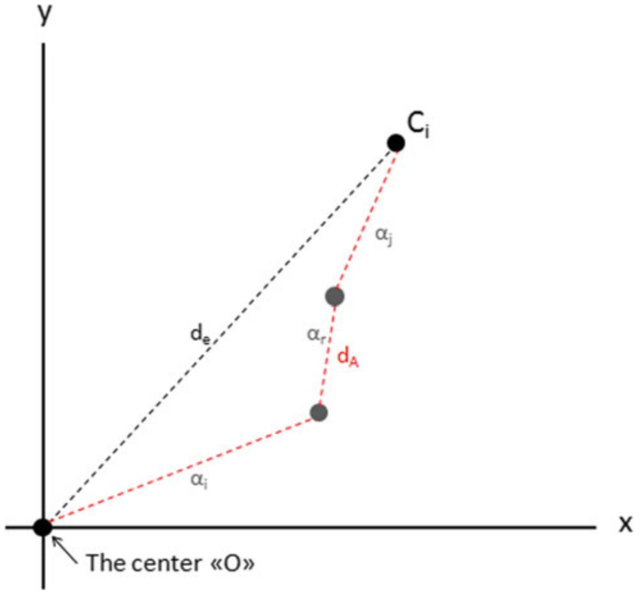

Fig. 2 Rrepresentation of the Euclidean distance and A-distance

represent the A-distance value. In fact, the A-distance between two points $P_1 = (a_1, b_1)$ and $P_2 = (a_2, b_2)$ is bigger than the Euclidian distance (see Fig. 3).

$$d_A(P_1, P_2) \geq d_E(P_1, P_2) \quad (7)$$

In our case, we need to represent the distance between the center "O" and the set of customers and suppliers. We define the fictitious coordinates of the customer $C_i, \forall i \in 1.k$ by (Fig. 4)

$$c^*_{i1} = c_{i1} + \mathrm{diff}_{A\leftrightarrow E}(C_i) \text{ and } c^*_{i2} = c_{i2} + \mathrm{diff}_{A\leftrightarrow E}(C_i) \quad (8)$$

For the supplier $F_i, \forall i \in [\![1 \cdot l]\!]$

$$f^*_{i1} = f_{i1} + \mathrm{diff}_{A\leftrightarrow E}(F_i) \text{ and } f^*_{i2} = c_{i2} + \mathrm{diff}_{A\leftrightarrow E}(F_i) \quad (9)$$

$$f^*_{i1} = f_{i1} + \mathrm{diff}_{A\leftrightarrow E}(F_i) \text{ and } f^*_{i2} = c_{i2} + \mathrm{diff}_{A\leftrightarrow E}(F_i) \quad (10)$$

$$\begin{aligned}\mathrm{diff}_{A\leftrightarrow E}(C_i) = d_A(O, C_i) - d_e(O, C_i) \text{ and } \mathrm{diff}_{A\leftrightarrow E}(F_i)\\ = d_A(O, F_i) - d_e(O, F_i)\end{aligned} \quad (11)$$

The workspace location $P^* = (x^*, y^*)$ using the A-distance weighted average is the following:

$$x^* = \frac{\sum_{i=0}^{k}(c^*_{i1} \times W_{C_i}) + \sum_{i=0}^{l}(f^*_{i1} \times W_{F_i})}{\sum_{i=0}^{k} W_{C_i} + \sum_{i=0}^{l} W_{F_i}} \quad (12)$$

$$y^* = \frac{\sum_{i=0}^{k}(c^*_{i2} \times W_{C_i}) + \sum_{i=0}^{l}(f^*_{i2} \times W_{F_i})}{\sum_{i=0}^{k} W_{C_i} + \sum_{i=0}^{l} W_{F_i}} \quad (13)$$

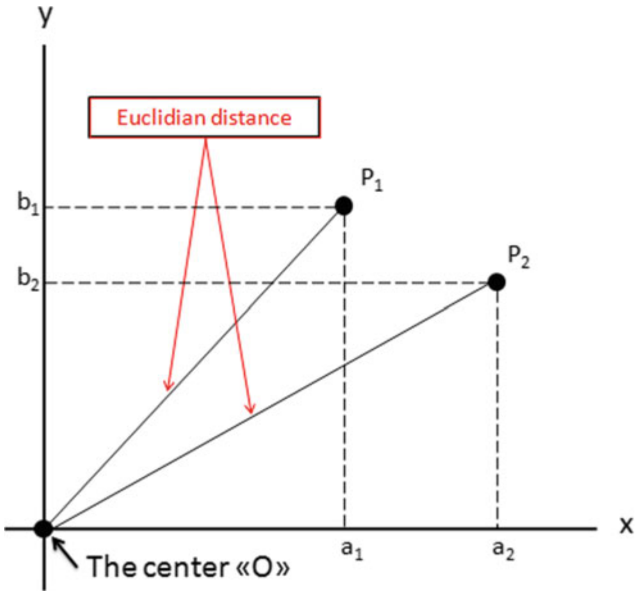

Fig. 3 The coordinates and Euclidian distance

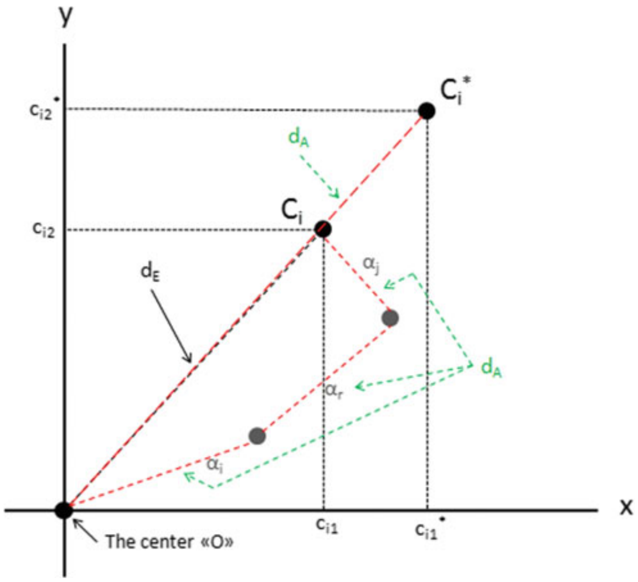

Fig. 4 The representation of the fictitious coordinates

4 Case Study: The Location of an Industrial Workspace

The application case study concerns the study of an industrial workspace location.

The management experts did choose the most important customers and suppliers to the new industrial facility. They reduced the study into nine customers and six suppliers located in six different cities.

We used GPS location coordinates to define the distances. Tables 1 and 2 show the initial data for the application case study.

The center "O" chosen by the experts is Table 3.

As mentioned, the coordinates of the new industrial workspace are the following (Table 4):

$$x^* = \frac{\sum_{i=0}^{9}(c^*_{i1} \times W_{C_i}) + \sum_{i=0}^{6}(f^*_{i1} \times W_{F_i})}{\sum_{i=0}^{9} W_{C_i} + \sum_{i=0}^{6} W_{F_i}} \quad (14)$$

$$y^* = \frac{\sum_{i=0}^{9}(c^*_{i2} \times W_{C_i}) + \sum_{i=0}^{6}(f^*_{i2} \times W_{F_i})}{\sum_{i=0}^{9} W_{C_i} + \sum_{i=0}^{6} W_{F_i}} \quad (15)$$

The proposed methodology is an improvement of the weighted average technique for facility location problem (FLP). The use of the A-distance enables the decision-maker to consider and represent the real traveled distance between two points. In consequence, the measurement of the new facility location coordinates reflects the real weighted distance.

The methodology provides a realistic approach for the facility layout approach regarding the modeling and resolution objectives.

Table 1 Customer's coordinates

Customer C_i	Weight W_{c_i}	The coordinates		d_e	d_A	Fictitious coordinates	
		c_{i1}	c_{i2}			c^*_{i1}	c^*_{i2}
C_1	0.847	3.971	3.150	1.42	55	8.047	7.226
C_2	0.898	3.895	4.445	1.28	20	22.608	23.158
C_3	0.837	4.018	4.992	1.51	40	42.501	43.475
C_4	0.949	4.254	3.410	1.43	36	38.817	37.974
C_5	0.903	0.427	0.401	1.16	67	66.264	66.238
C_6	0.880	1.629	2.018	1.22	23	23.403	23.792
C_7	0.880	5.759	4.166	1.97	35	38.786	37.193
C_8	0.887	3.683	2.615	1.57	67	8.804	7.735
C_9	0.887	4.681	8.099	3.61	90	91.071	94.489

Table 2 Supplier's coordinates

Supplier F_i	Weight W_{F_i}	The coordinates		d_e	d_A	Fictitious coordinates	
		f_{i1}	f_{i2}			f^*_{i1}	f^*_{i2}
F_1	1.604	0.427	0.410	1.163	67	66.264	66.238
F_2	1.577	1.629	2.018	1.226	23	23.403	23.792
F_3	1.489	5.797	4.166	1.972	35	38.786	37.193
F_4	1.707	3.683	2.615	1.579	67	8.804	7.735
F_5	1.856	4.018	4.992	1.516	40	42.501	43.475
F_6	1.763	3.971	3.150	1.423	55	8.047	7.226

Table 3 The center

The center	The coordinates	
O	3.537	2.410

Note The coordinates are extracted from the GPS coordinates; a small change is applied to facilitate the measurements and the calculation of the fictitious coordinates and the location of the workspace

Table 4 The new location

The new location coordinates	
X*	34.022
Y*	33.884

Our approach is based on the calculation of fictitious coordinates, this new technique is related to the center "O", and the measurements of the $\left(c^*_{i1}, c^*_{i2}\right)$ and $\left(f^*_{i1}, f^*_{i2}\right)$ are strictly attached to the choice of the center "O". Therefore, the center should be carefully chosen in order to minimize the distances. The most optimal center is a crossroads or a converging point to have a larger "A" set with the maximum available orientations "α_i".

5 Conclusion

Facility location is a very complex but an important decision; the choice of a location is very difficult to make given the variety of the criteria involved in the decision process (Amar Abouabdellah 2015, 2016a, b). Several methodologies can be adopted to create a resolution approach for the location problem, among those cited in the literature: genetic algorithms, mathematical programming, selection-based algorithms, and comparison techniques. The utility of each one of these methodologies depends on the formulation of the problem and the preferences of the decision-makers.

In this case, the problematic location of the new facility lies in the determination of the coordinates of the location regarding various attributes:

- The location of the suppliers;
- The location of the customers (current and potential ones);
- The importance factor of the suppliers; and
- The importance factor of the customers (existing and potential ones).

The importance factors are measured according to a multitude of performance factors such as annual average order, quality of the service, and responsiveness.

We proposed a new improved methodology based on the weighted average technique and the A-distance. The objective is to represent the real traveled distance between two points using the A-distance instead of the Euclidian distance.

The reason behind this choice is to take into consideration the geographical restrictions of the urban spaces and the characteristics of routes and delivery paths.

We introduced the measurement of fictitious coordinates to represent the difference between the Euclidian distance and A-distance. For future research enhancement, we propose to improve the resolution technique by considering the time delivery factor and bottling points in order to optimize the location of the new facility regarding distance and time. We can also include the Voronoï diagram to easily represent the active region.

References

Amar, S. H., & Abouabdellah, A. (2015) Analysis of workshop location with Lagrange interpolation. In *The 45th International Conference on Computers & Industrial Engineering. CIE45, Metz-France*, 28–30 October 2015. https://doi.org/10.1109/eitech.2017.8255295.

Amar, S. H., & Abouabdellah, A. (2016a). Facility layout planning problem: Effectiveness and reliability evaluation system layout designs. In *2016 International Conference on System Reliability and Science (ICSRS 2016)*, Paris-France, November 2016. https://doi.org/10.1109/icsrs.2016.7815848.

Amar, S. H., & Abouabdellah, A. (2016b). A combined approach for workspace location selection decision problem: A linguistic-mathematical modeling methodology. *International Journal of Applied Engineering Research, 11*(5), 3726–3730. ISSN 0973-4562.

Ana, Y., Zenga, B., Zhangb, Y., & Zhaoa, L. (2014). Reliable p-median facility location problem: Two-stage robust models and algorithms. *Transportation Research Part B: Methodological, 64,* 54–72.

Dantrakula, S., Likasiria, C., & Pongvuthithumb, R. (2014). Applied p-median and p-center algorithms for facility location problems. *Expert Systems with Applications, 41*(8), 3596–3604. https://doi.org/10.1016/j.eswa.2013.11.046.

Demirel, T., Demirel, N. Ç., Kahraman, C. (2010a). Multi-criteria warehouse location selection using Choquet integral. *Expert Systems with Applications, 37*(5), 3943–3952. https://doi.org/10.1016/j.eswa.2009.11.022.

Demirel, T., Demirel, N. Ç., Kahraman, C. (2010b). Multi-criteria warehouse location selection using Choquet integral. *Expert Systems with Applications, 37,* 3943–3952. https://doi.org/10.1016/j.eswa.2009.11.022.

Dogan, I. (2012). Analysis of facility location model using Bayesian networks. *Expert Systems with Applications,39,* 1092–1104. https://doi.org/10.1016/j.eswa.2011.07.109.

Farahani, R. Z., Hekmatfar, M., Fahimnia, B., & Kazemzadeh, N. (2014). Hierarchical facility location problem: Models, classifications, techniques, and applications. *Computers & Industrial Engineering, 68,* 104–117. https://doi.org/10.1016/j.cie.2013.12.005.

Letchford, A. N., & Miller, S. J. (2014). An aggressive reduction scheme for the simple plant location problem. *European Journal of Operational Research, 234*(3), 674–682. https://doi.org/10.1016/j.ejor.2013.10.020.

Matsutomi, T., & Ishii, H. (1998). Minimax location problem with a-distance. *Journal of the Operations Research Society of Japan, 41* (2), 181–195. https://doi.org/10.15807/jorsj.41.181.

Pisinger, W. D., Rasmussen, A. B., & Sandvik, R. (2007). Solution of large quadratic knapsack problems through aggressive reduction. *INFORMS Journal on Computing, 19*(2), 280–290. https://doi.org/10.1287/ijoc.1050.0172.

Rahmani, A., & MirHassani, S.A. (2014). A hybrid firefly-genetic algorithm for the capacitated facility location problem. *Information Sciences, 283,* 70–78. https://doi.org/10.1016/j.ins.2014.06.002.

Widmayer, P., Wu, Y. F., & Wong, C. K. (1987). On some distance problems in fixed orientations. *SIAM Journal on Computing,16,* 728–746. https://doi.org/10.1137/0216049.

Xu, D.-L., et al. (2012). *Prioritization method in the fuzzy analytic network process by fuzzy preferences programming method*. World Academy of Science, Engineering and Technology.

Sara Haddou Amar is a Doctor-Engineer and a Researcher. She graduated from Ibn Tofail University (Department of Mathematics). She has published various papers and participated in national and international conferences. Her major publications include studies on decision-making, multi-criteria analysis studies, location and facility layout decision process, monitoring, and evaluation. Her current main research perspectives are artificial intelligence and automation of the decision process, renewable energy (optimization, production, and transmission networks), and sustainable development.

Abdellah Abouabdellah is a Research Professor at the National School of Applied Sciences of Kénitra (Ecole Nationale des Sciences Appliquées de Kénitra, ENSA), Ibn Tofail University. He holds also the position of the Head of Industrial and Logistics department. His research interests include the conception of industrial workspaces, decision-making, hospital and pharmaceutical logistics, and ERP implementation.

Yahia El Ouazzani holds a Ph.D. in mathematics from Paris XI-Orsay University, majoring in partial differential equations and scientific computation. He is currently a Research Professor at Mohamed V University, Rabat, Morocco. His research interests include partial differential equations, numerical analysis, logistics, and optimization.

Part IV

Telecommunications and Vehicular Technologies

Lyapunov-Based Control of Single-Phase AC–DC Power Converter for BEV Charger

Aziz Rachid, Hassan EL Fadil, F. Z. Belhaj, K. Gaouzi, and Fouad Giri

Abstract

In this paper, we consider the problem of controlling single-phase ac–dc power converter for battery electric vehicle (BEV) charger. The control objectives are threefold: (i) unitary power factor (UPF) in grid side, (ii) tight regulation of dc-bus voltage to its constant reference in dc side, and (iii) asymptotic stability of the closed-loop system. Based on the nonlinear model of the studied system, a nonlinear controller is designed using Lyapunov approach. In order to validate the effectiveness of the proposed nonlinear controller, several numerical simulations are performed using the MATLAB/Simulink software.

Keywords

Ac–dc power converter • BEV charger • Unitary power factor • Nonlinear control • Lyapunov approach

1 Introduction

Nowadays, battery electric vehicles (BEVs) can be an alternative to the classical vehicle with thermal engine. Indeed, the BEVs can provide an ideal solution to reduce the environmental impact of transports and reduce energy dependency because they have low energy consumption and zero local emissions (Hegazy et al. 2013).

On the other hand, the batteries of these vehicles can store a considerable amount of electrical energy, which can be exploited to regulate and stabilize the power grid. This interactivity between vehicles and the power grid, called vehicle-to-grid (V2G), should be one of the key technologies in the future of smart grids (Monteiro et al. 2013). The term V2G refers to the concept where BEVs provide energy services while connected to the power grid. According to common practice, this term V2G implicitly includes both power flows: Grid-to-vehicle (G2V) called charging mode and vehicle-to-grid (V2G) called discharging mode (cf. Fig. 1) (Broneske and Wozabal 2017).

However, to ensure these two operating modes (G2V and V2G), the BEV must establish a bidirectional connection with the power grid. This functionality will allow them to inject energy into the power grid in addition to allowing battery charging (Zgheib et al. 2016). Such a connection will be established via a BEV charger, which is a key component for BEV.

Typically, a BEV charger includes two converters: an input power factor correction (PFC) ac–dc stage that converts input ac voltage to an intermediate dc voltage while reducing the input current harmonics injected to the grid, followed by a dc–dc converter that steps up or down the intermediate dc-bus voltage as required by the battery. Generally, these converters operate only in charging mode (G2V). They are unidirectional. Therefore, to enable V2G functionality, the converters must be bidirectional (Rachid

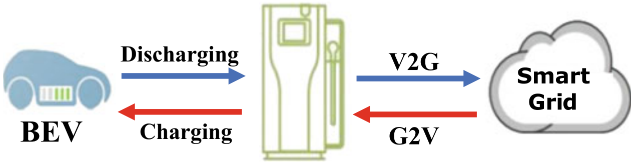

Fig. 1 Energy flow during G2V and V2G operating modes

A. Rachid (✉) · H. EL Fadil · F. Z. Belhaj · K. Gaouzi
ESIT Team, LGS Laboratory ENSA, Ibn Tofail University,
14000 Kénitra, Morocco
e-mail: rachidaziz03@gmail.com

H. EL Fadil
e-mail: elfadilhassan@yahoo.fr

F. Z. Belhaj
e-mail: fz.blhj@gmail.com

K. Gaouzi
e-mail: khawla.gaouzi@gmail.com

F. Giri
Laboratoire D'Automatique de Caen, Université de Caen,
Bd Marechal Juin, B.P 8156, 14032 Caen, France
e-mail: giri@greyc.ensicaen.fr

S. El Hani and M. Essaaidi (eds.), *Recent Advances in Electrical and Information Technologies for Sustainable Development*,
Advances in Science, Technology & Innovation, https://doi.org/10.1007/978-3-030-05276-8_13

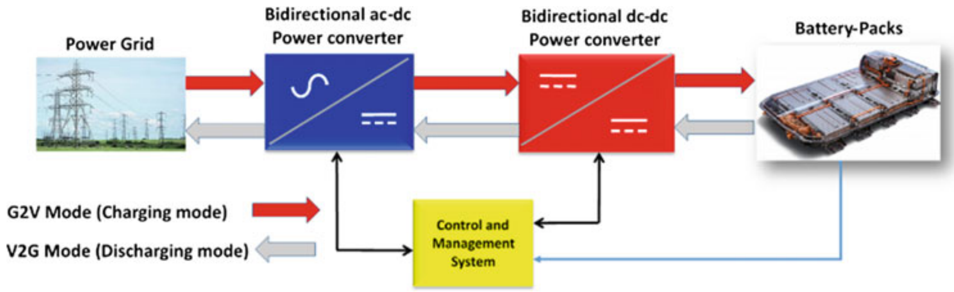

Fig. 2 Block diagram of bidirectional battery charger

et al. 2017). A functional diagram of such bidirectional battery charger is illustrated in Fig. 2 (Rachid et al. 2018).

In the G2V operation mode, the bidirectional ac–dc power converter operates as a boost rectifier with a unitary PFC and the bidirectional dc–dc power converter operates in the buck mode. In the V2G operation mode, the bidirectional ac–dc power converter operates as an inverter with the possibility to control the injected reactive power in the grid while the bidirectional dc–dc power converter operates in the boost mode (Rachid et al. 2017).

In this work, the problem of controlling single-phase ac–dc power converter during the G2V operating mode (charging mode) is dealt with. In this mode, the studied power converter operates as a boost PFC rectifier. After a nonlinear modeling of the studied system, a nonlinear controller is designed using Lyapunov approach.

The rest of the paper is organized as follows: in Sect. 2, the boost PFC ac–dc power converter is described and modeled; Sect. 3 is devoted to design a nonlinear Lyapunov-based controller; in Sect. 4, the controller performances are illustrated by several numerical simulations. A conclusion and references list end the paper.

2 System Overview and Modeling

2.1 System Overview

The electrical circuit of the studied system is illustrated in Fig. 3. It consists of full-bridge bidirectional ac–dc power converter (Chavan and Thorat 2016; Kisacikoglu et al. 2015; Monteiro et al. 2012; Pan and Zhang 2016; Tashakor et al. 2017; Verma et al. 2011; Yilmaz and Krein 2013; Zeng et al. 2013). It includes a filtering inductance L, four switches $(K_1, K_2, K_3 \text{ and } K_4)$, and a dc-bus voltage filtering capacitor C. This converter is supplied by a single-phase power grid and operates as a boost rectifier. According to Fig. 2, the current i_{dc} represents the input current of the dc–dc power converter.

The converter should be adequately controlled in order to ensure the following two objectives: unitary power factor (UPF) in grid side and dc-bus voltage regulation in dc side. To this end, an accurate model of the studied system must first be developed. This will be presented in the next subsection.

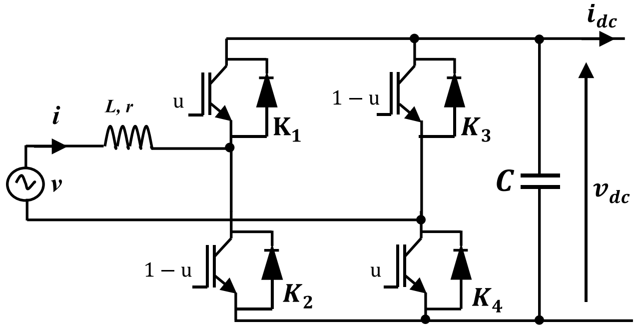

Fig. 3 Electric schema of the ac–dc power converter

2.2 System Modeling

We consider a full-bridge boost rectifier illustrated in Fig. 3, which consists of two arms. Each arm is made up of two switches which must operate in complementary way. The switching signal u is generated by a PWM circuit and takes values in the finite set $\{0, 1\}$ (El Fadil and Giri 2012a; Karagiannis et al. 2003).

Using Kirchhoff's laws and taking into account that u can take the binary values 1 or 0, the instantaneous model of the studied system is given by the following equations (Rachid et al. 2017)

$$\begin{cases} L\frac{di}{dt} = -ri - (2u-1)v_{dc} + v \\ C\frac{dv_{dc}}{dt} = (2u-1)i - i_{dc} \end{cases} \tag{1}$$

where v is the power grid voltage and i_{dc} is the input current of the dc–dc power converter.

For control design purpose, it is more convenient to consider the following averaged model, obtained by averaging the model (1) over one switching period (Krein et al. 1990).

$$\begin{cases} \dot{x}_1 = -\frac{r}{L}x_1 - \frac{(2\mu-1)}{L}x_2 + \frac{v}{L} \\ \dot{x}_2 = \frac{(2\mu-1)}{C}x_1 - \frac{i_{dc}}{C} \end{cases} \tag{2}$$

where x_1 and x_2 denote the average grid current $\bar{i}$ and the average dc–bus voltage $\bar{v}_{dc}$, respectively. The control input for the model (2) is the function µ (average value of u), called duty ratio function.

3 Controller Design

In this section, the controller design of the ac–dc power converter will be performed in order to ensure two objectives. The first objective is to achieve a unitary power factor (UPF) in ac side, which means that the power grid current $i(t)$ must be sinusoidal and in phase with the power grid voltage $v(t)$. The second objective is a perfect regulation of the dc-bus voltage.

The model illustrated by Eq. (2) shows clearly that the studied system is nonlinear. Therefore, a Lyapunov-based approach is adopted in this work (El Fadil et al. 2012, 2014; Freeman and Kokotović 1996; Khalil 2013; Tahri et al. 2014, 2016).

Let us first define the following tracking errors

$$\begin{cases} e_1 = x_1 - x_1^* \\ e_2 = x_2 - x_2^* \end{cases} \tag{3}$$

where x_1^* and x_2^* denote the references of the state variables x_1 and x_2, respectively.

Recall that the control objective is to regulate the dc-bus voltage x_2 to its desired constant value V_{dcref} and to enforce the input current x_1 to be sinusoidal and in phase with the AC power grid voltage $v(t)$. Then, the reference signals are chosen as follows

$$\begin{cases} x_1^* = \alpha v(t) \\ x_2^* = V_{dcref} \end{cases} \tag{4}$$

where α is any real positive parameter (although transient time variation is allowed).

The control objective is to enforce the two errors to vanish. To this end, the following Lyapunov function candidate is proposed:

$$V = \frac{1}{2}e_1^2 + \frac{1}{2}e_2^2 \tag{5}$$

It is clear that this function is a positive definite and radially unbounded function. Its time derivative is

$$\dot{V} = \dot{e}_1 e_1 + \dot{e}_2 e_2 \tag{6}$$

For asymptotic stability of the equilibrium $(e_1, e_2) = (0, 0)$, one can seek that $\dot{V}$ must be negative definite. It is obvious that this goal is reached if the derivatives of the two errors defined by (6) are chosen as follows:

$$\begin{cases} \dot{e}_1 = -c_1 e_1 \\ \dot{e}_2 = -c_2 e_2 \end{cases} \tag{7}$$

where c_1 and c_2 are positive design parameters.

Indeed, with this choice, the derivative (6) becomes

$$\dot{V} = -c_1 e_1^2 - c_2 e_2^2 \tag{8}$$

which shows that the equilibrium (0, 0) is globally asymptotically stable and, in turn, gives $\lim_{t\to\infty} e_1 = 0$ and $\lim_{t\to\infty} e_2 = 0$. The vanishing of the two errors clearly ensures the UPF and the dc-bus voltage regulation.

It follows, using (3) and (7), that

$$\begin{cases} \dot{x}_1 = -c_1 e_1 + \dot{x}_1^* \\ \dot{x}_2 = -c_2 e_2 + \dot{x}_2^* \end{cases} \tag{9}$$

By combining the first equations of (2) and (9), the control law μ can be obtained as follows:

$$\mu = \frac{1}{2} + \frac{L}{2x_2}\left(-\frac{r}{L}x_1 + c_1 e_1 + \frac{v}{L} - \dot{x}_1^*\right) \tag{10}$$

The objective now is to determine the parameter α involved in (4). Considering that $\dot{x}_2^* = \dot{V}_{dcref} = 0$ and combining the second equations of (2) and (9), one obtains

$$(2\mu - 1)x_1 = -c_2 e_2 C + \bar{i}_{dc} \tag{11}$$

By applying the power conservation principle, also called power in equal to power out (PIPO) (El Fadil and Giri 2012b; Tahri et al. 2014) to the power converter, one gets

$$v x_1 = (2\mu - 1)x_1 x_2 \tag{12}$$

which gives, using (3), (4), and (11),

$$\alpha v^2 + v e_1 = (-c_2 e_2 C + \bar{i}_{dc})x_2 \tag{13}$$

The left-hand term of (13) shows a double singularity, which can be eliminated by neglecting the term in $v(t)$ compared to that in $v^2(t)$ and then dividing by the averaged value of $v^2(t)$ instead of its instantaneous value. The parameter α is then obtained as follows:

$$\alpha = \frac{x_2}{V^2}(-c_2 e_2 C + \bar{i}_{dc}) \tag{14}$$

The next section is devoted to the validation of the proposed controller performances using simulation.

4 Simulation Results

In order to validate the proposed nonlinear controller performances, several numerical simulations are performed using the MATLAB/Simulink software. The system

Table 1 System parameters

Parameter	Value
Grid RMS voltage V	230 V
Grid frequency f	50 Hz
Filtering inductor L	5 mH
Inductor ESR r	0, 1 Ω
Switching frequency F_S	15 kHz
DC-bus capacitor C	2000 µF
DC-bus voltage V_{dcref}	400 V
Design parameter c_1	10 000
Design parameter c_2	10

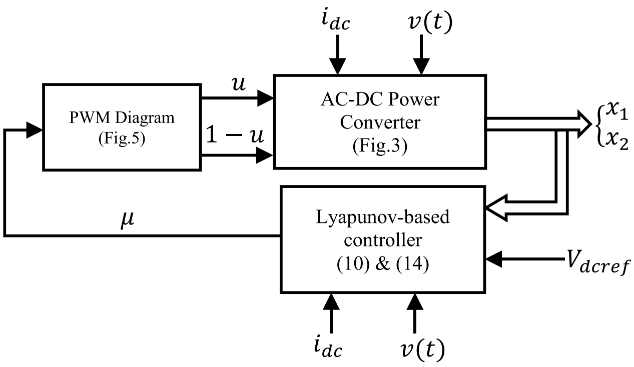

Fig. 4 Simulation bench of the ac–dc power converter

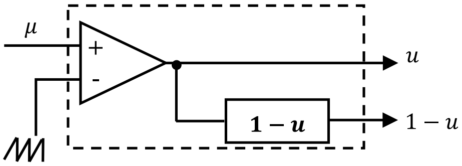

Fig. 5 PWM diagram

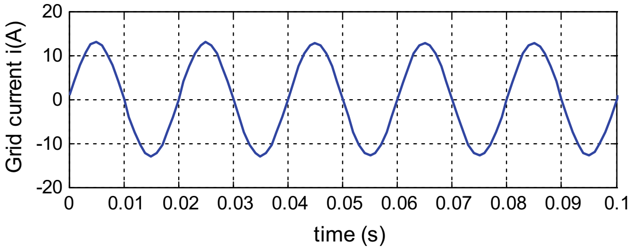

Fig. 6 Grid current $i(t)$

parameters are listed in Table 1. The simulation bench is shown in Fig. 4 and the PWM diagram is given in Fig. 5.

Figures 6, 7, 8, 9, and 10 illustrate the performances of the proposed nonlinear controller in the presence of a constant reference signal $V_{dcref} = 400\,\text{V}$ and a constant load current $i_{dc} = 5\text{A}$.

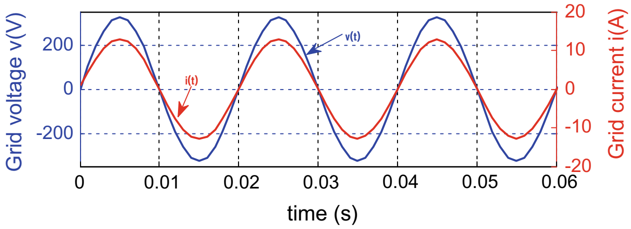

Fig. 7 Grid voltage $v(t)$ and grid current $i(t)$

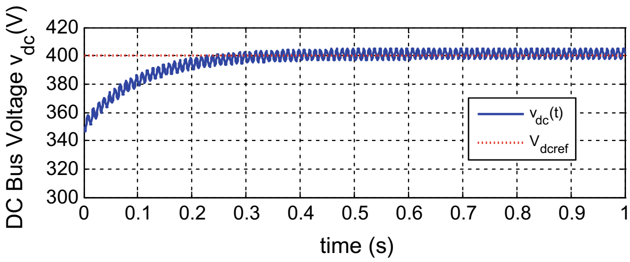

Fig. 8 Dc-bus voltage v_{dc}

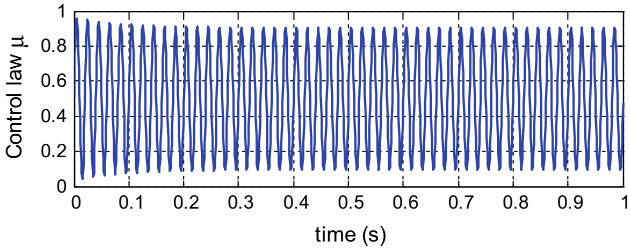

Fig. 9 Control law µ

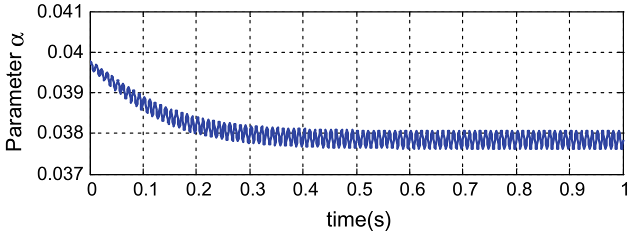

Fig. 10 Parameter α

All figures show clearly that the control objectives are achieved: UPF in grid side and a dc-bus voltage regulation in dc side. Indeed, Fig. 6 shows that the input current $i(t)$ is sinusoidal, and Fig. 7 illustrates that $i(t)$ and the power grid voltage $v(t)$ are in phase. On the other hand, Fig. 8 shows that the dc-bus voltage v_{dc} tracks perfectly its constant reference V_{dcref}. Finally, Figs. 9 and 10 show the control law µ and the parameter α, respectively.

In order to confirm the robustness of the proposed nonlinear controller, a variation of the load current i_{dc} is performed. The corresponding profile is shown in Fig. 11.

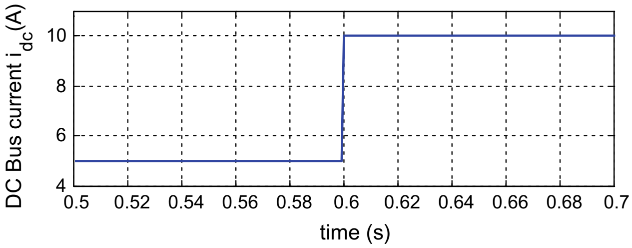

Fig. 11 Dc-bus current i_{dc} profile

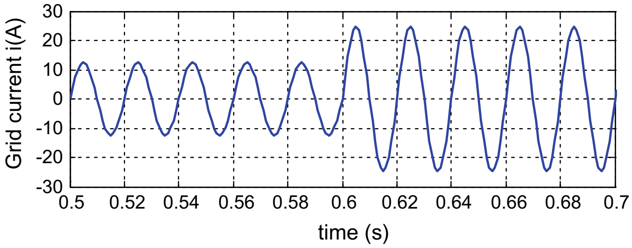

Fig. 12 Grid current $i(t)$ in the presence of load current i_{dc} step changes

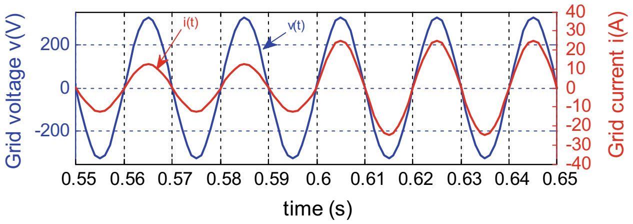

Fig. 13 Grid voltage $v(t)$ and current $i(t)$, in the presence of load current i_{dc} step changes

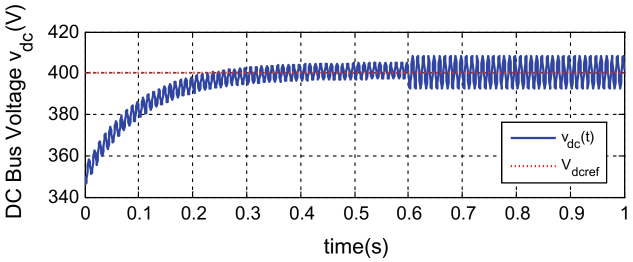

Fig. 14 Dc-bus voltage v_{dc} in the presence of load current i_{dc} step changes

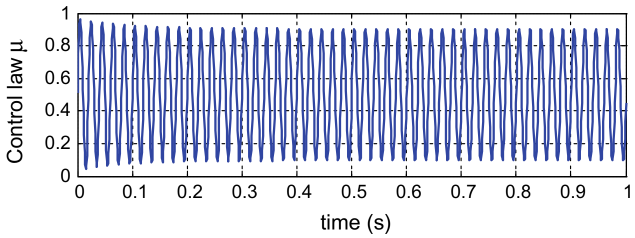

Fig. 15 Control law μ in presence of load current i_{dc} step changes

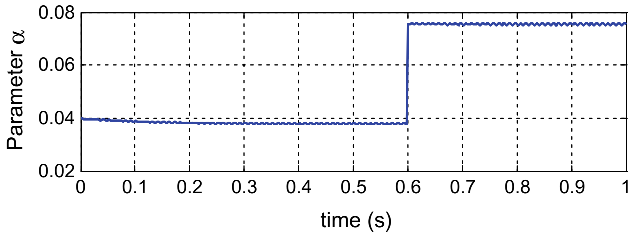

Fig. 16 Parameter α in the presence of load current i_{dc} step changes

Figures 12, 13, 14, 15 illustrate the controller behavior in the presence of the current i_{dc} changes.

Figure 12 shows clearly that the input current $i(t)$ is still sinusoidal, whereas at time 0.6 s its amplitude has doubled due to the variation of the current i_{dc}. Figure 13 illustrates that the power grid current $i(t)$ and the power grid voltage $v(t)$ are still in phase despite the variation of the load current i_{dc}. Figure 14 shows that the dc-bus voltage tracks perfectly its constant reference, while the value of its ripples has doubled. Figure 15 illustrates the obtained control law μ. Finally, Fig. 16 shows that the parameter α varies according to the variations of the load current i_{dc}.

5 Conclusion

In this paper, a single-phase ac–dc power converter aiming its integration in BEV charger with V2X functionality was presented. With this characteristic, the BEV will be able to deliver back a part of the stored energy in the batteries to the power grid, aiming to contribute to mitigate power quality problems.

The studied system consists of a full-bridge operated as boost PFC rectifier. The control objectives are to ensure a unitary power factor in ac side and enforce the dc-bus voltage to track its constant reference. After a nonlinear modeling of the ac–dc power converter, a nonlinear controller is designed. To do this, a Lyapunov-based controller is elaborated. It is shown, using numerical simulations, that the proposed nonlinear controller achieves the control objectives. As future work, the ac–dc power converter will be controlled as a PFC inverter in order to ensure a V2G operating mode.

Acknowledgements The authors gratefully acknowledge the support of the Moroccan Ministry of Higher Education (MESRSFC) and the CNRST under grant number PPR/2015/36.

References

Broneske, G., & Wozabal, D. (2017). How do contract parameters influence the economics of vehicle-to-grid? *Manufacturing & Service Operations Management, 19,* 150–164. https://doi.org/10.1287/msom.2016.0601.

Chavan, R. R., & Thorat, A. R. (2016). Modified PWM technique for bidirectional AC/DC converter to reduce switching loss with fuzzy logic control for grid tied microgrid system. In *2016 International Conference on Computation of Power, Energy Information and Communication (ICCPEIC)* (pp. 392–397). IEEE.

El Fadil, H., & Giri, F. (2012a). MPPT and unity power factor achievement in grid-connected PV system using nonlinear control. *IFAC Proceedings, 45*, 363–368.

El Fadil, H., & Giri, F. (2012b). Sliding mode control of fuel cell and supercapacitor hybrid energy storage system. In *Proceeding of the IFAC Symposium on Power Plants and Power Systems Control (PPPSC'12), IFAC Proceedings Volumes* (pp. 669–674). Toulouse, France: Elsivier. https://doi.org/10.3182/20120902-4-FR-2032.00117.

El Fadil, H., Giri, F., & Guerrero, J. (2012). Lyapunov based control of hybrid energy storage system in electric vehicles. In *Proceeding of the American Control Conference (ACC)* (pp. 5005–5010). Montréal, Canada: IEEE. https://doi.org/10.1109/ACC.2012.6314673.

El Fadil, H., Giri, F., Guerrero, J. M., & Tahri, A. (2014). Modeling and nonlinear control of a fuel cell/supercapacitor hybrid energy storage system for electric vehicles. *IEEE Transactions on Vehicular Technology, 63,* 3011–3018. https://doi.org/10.1109/TVT.2014.2323181.

Freeman, R. A., & Kokotović, P. (1996). *Robust nonlinear control design*. Boston, MA: Birkhäuser Boston. https://doi.org/10.1007/978-0-8176-4759-9.

Hegazy, O., Van Mierlo, J., Barrero, R., Lataire, P., Omar, N., & Coosemans, T. (2013). A comparative study of different control strategies of on-board battery chargers for battery electric vehicles. In *2013 8th International Conference and Exhibition on Ecological Vehicles and Renewable Energies (EVER)* (pp. 1–6). IEEE.

Karagiannis, D., Mendes, E., Astolfi, A., & Ortega, R. (2003). An experimental comparison of several PWM controllers for a single-phase AC-DC converter. *IEEE Transactions on Control Systems Technology, 11,* 940–947. https://doi.org/10.1109/TCST.2003.815549.

Khalil, H., 2013. Nonlinear Systems. Pearson Education, Limited.

Kisacikoglu, M. C., Kesler, M., & Tolbert, L. M. (2015). Single-phase on-board bidirectional PEV charger for V2G reactive power operation. *IEEE Transactions on Smart Grid, 6,* 767–775. https://doi.org/10.1109/TSG.2014.2360685.

Krein, P. T., Bentsman, J., Bass, R. M., & Lesieutre, B. L. (1990). On the use of averaging for the analysis of power electronic systems. *IEEE Transactions on Power Electronics, 5,* 182–190.

Monteiro, V., Ferreira, J. C., Meléndez, A. A. N., & Afonso, J. L. (2013). Electric vehicles on-board battery charger for the future smart grids. In *Doctoral Conference on Computing, Electrical and Industrial Systems*. Springer, pp. 351–358.

Monteiro, V., Gonalves, H., Ferreira, J. C., & Afonso, J. L. (2012). Batteries charging systems for electric and plug-in hybrid electric vehicles. In J. Carmo (Ed.), *New advances in vehicular technology and automotive engineering*. InTech. https://doi.org/10.5772/45791.

Pan, L., & Zhang, C. (2016). An integrated multifunctional bidirectional AC/DC and DC/DC converter for electric vehicles applications. Energies, *9,* 493. https://doi.org/10.3390/en9070493.

Rachid, A., El Fadil, H., Belhaj, F. Z., Gaouzi, K., & Giri, F. (2017). Lyapunov-based control of single-phase AC-DC power converter for BEV charger. In *Proceeding of the 3rd International Conference on Electrical and Information Technologies (ICEIT'2017).* Rabat, Morocco: IEEE. https://doi.org/10.1109/EITech.2017.8255296.

Rachid, A., El Fadil, H., Gaouzi, & K., Belhaj, F. Z. (2017). Output feedback control of bidirectional dc-dc power converter for BEV charger. In *Proceeding of the 4th International Conference on Automation, Control Engineering and Computer Science (ACECS), Proceedings Engineering and Technology (PET)* (pp. 46–51). Tangier, Morocco: IPCO.

Rachid, A., El Fadil, H., & Giri, F. (2018). Dual stage CC-CV charge method for controlling dc-dc power converter in BEV charger. In *Proceeding of the 19th IEEE Mediterranean Electrotechnical Conference IEEE MELECON'18* (pp. 74–79). Marrakesh, Morocco: IEEE.

Tahri, A., El Fadil, H., Giri, F., & Chaoui, F. -Z. (2016). nonlinear adaptive control of a hybrid fuel cell power system for electric vehicles—A Lyapunov stability based approach: Lyapunov based adaptive controller for electric vehicle hybrid power system. *Asian Journal of Control, 18*, 166–177. https://doi.org/10.1002/asjc.1231.

Tahri, A., El Fadil, H., Giri, F., & Chaoui, F. -Z. (2014). Nonlinear control and observation of a boost converter associated with a fuel-cell source in presence of model uncertainty. In *Proceeding of the 19th IFAC World Congress, IFAC Proceedings Volumes* (pp. 575–580). Cape Town, South Africa: Elsivier. https://doi.org/10.3182/20140824-6-ZA-1003.00537.

Tahri, A., El Fadil, H., Guerrero, J. M., Giri, F., & Chaoui, F. Z. (2014). Modeling and nonlinear control of electric power stage in hybrid electric vehicle. In *Proceedings of the 2014 IEEE Multi-Conference on Systems and Control (MSC)* (pp. 641–646). Aalborg University, Denmark: IEEE. https://doi.org/10.1109/CCA.2014.6981412.

Tashakor, N., Farjah, E., & Ghanbari, T. (2017). A bidirectional battery charger with modular integrated charge equalization circuit. *IEEE Transactions on Power Electronics, 32*, 2133–2145. https://doi.org/10.1109/TPEL.2016.2569541.

Verma, A. K., Singh, B., & Shahani, D. T. (2011). Grid to vehicle and vehicle to grid energy transfer using single-phase bidirectional AC-DC converter and bidirectional DC-DC converter. In *2011 International Conference on Energy, Automation, and Signal (ICEAS)* (pp. 1–5). IEEE.

Yilmaz, M., & Krein, P. T. (2013). Review of battery charger topologies, charging power levels, and infrastructure for plug-in electric and hybrid vehicles. *IEEE Transactions on Power Electronics, 28,* 2151–2169. https://doi.org/10.1109/TPEL.2012.2212917.

Zeng, Z., Yang, H., Zhao, R., & Cheng, C. (2013). Topologies and control strategies of multi-functional grid-connected inverters for power quality enhancement: A comprehensive review. *Renewable and Sustainable Energy Reviews, 24,* 223–270. https://doi.org/10.1016/j.rser.2013.03.033.

Zgheib, R., Al-Haddad, K., & Kamwa, I. (2016). V2G, G2V and active filter operation of a bidirectional battery charger for electric vehicles (pp. 1260–1265). IEEE. https://doi.org/10.1109/ICIT.2016.7474935.

Aziz Rachid received the B.S. in Electrotechnics, the Aggregation degree in Electrical Engineering, the M.S. in Electrical Engineering from the Higher School of Technical teaching (ENSET), Mohammed V University, Rabat, Morocco, in 1991, 1997, and 2016, respectively. From 1991 to 1997, he was an Electrical Engineering Professor in technical school, Agadir, Morocco. Since 1997, he has been an Associate Professor in BTS department in technical school Al Farabi, Salé, Morocco. Since 2004, he is a Cisco Instructor and he is teaching computer networks. He is currently pursuing the Ph.D. in Electrical Engineering at LGS laboratory, Ibn Tofail University, Kénitra, Morocco. His main research area includes electric vehicles, V2X technology, and nonlinear control of power converters. He has co-authored several journals and conference papers on these topics.

Hassan EL Fadil was born in Maghnia, Alnif, Morocco in 1970. He received the B.S. in Electronics, the Agrégation degree in Electrical Engineering, the M.S. in Automatic Control, and the Ph.D. in Automatic Control from Mohammadia School of Engineers, Mohammed V University, Rabat, Morocco, in 1994, 1999, 2003, and 2008, respectively.

Since 2011, he has been a successful Assistant Professor and Habilitated Professor in the National School of Applied Sciences, Ibn Tofail University, Kénitra, Morocco. He is currently with the LGS Laboratory, and his research interest includes nonlinear and adaptive control, power converters and electric motors control, renewable energy, distributed energy resources, smart grid, and electric vehicles. He has published over 70 journals/conference papers.

Fatima Zahrae Belhaj was born in Kenitra, Morocco in 1991. She received an electrical engineering degree from the National School of Applied Sciences, Mohammed Premier University, Oujda, in 2014.

She is currently pursuing the Ph.D. in the optimization of the energy of an electrical system combining a fuel cell and a super-capacitor used in electric vehicles, in the LGS Laboratory in the National School of Applied Sciences, Ibn Tofail University, Kénitra, under the supervision of Prof. H. El Fadil. Her research interests include optimization and nonlinear control systems of energy in electric vehicles. She is author or co-author of several papers on these topics.

Khawla Gaouzi was born in 1992. She received electrical engineering degree from the National School of Applied Sciences, Ibn Tofail University, Kénitra, in 2015.

Since 2016, she is preparing her Ph.D. in the nonlinear control of power converters, in the LGS Laboratory in ENSA Kenitra, under the supervision of Prof. H. El Fadil. Her research focuses on nonlinear and sampled data system, power converter control, and adaptive observer of nonlinear system. She is author or co-author of several conference papers.

Fouad Giri received a Ph.D. from the Institut National Polytechnique of Grenoble, France, in 1988 and is now Distinguished Professor at the University of Caen Basse-Normandie, Caen, France. He is currently serving as the General Chair of the IFAC Int. Workshops ALCOSP 2013 and PSYCO 2013. He is the Vice-Chair of the IFAC TC “Adaptive and Learning Systems” and is holding membership positions in the IFAC TCs on “Modelling, Identification and Signal Processing” and “Power Plants and Power Systems”, and the IEEE CSS TC “System Identification and Adaptive Control”. He is Associate Editor of the IFAC Journal Control Engineering Practice, of the IEEE Transactions on Control Systems Technology and of the Editorial Board of IEEE CSS conferences. His research interests include Nonlinear System Identification, Adaptive Nonlinear Control, Constrained Control, and control applications to Power Converters, Electric Machines, and Power Systems. He has supervised 20 Ph.D.s and has co-authored three books and over 250 journals and conference papers on these topics.

Optimization Techniques for DC Bus Voltage Balancing in a PV Grid System Based EVs Charging Station

A. Hassoune, M. Khafallah, A. Mesbahi, and T. Bouragba

Abstract

This work presents a smart algorithm to optimize energy in electric vehicles charging station while treating various constraints, i.e., the instability of renewable energy sources and the potential limited power provided by the grid. The PV array is recognized as one of the efficient energy sources to feed the charging station system; it is directly tied into a voltage DC bus, and thus the lithium–ion battery is implemented in this platform to complete the power flow of each potential charging scenario. In this research, a management algorithm is set to take into account the fluctuant power state of both, the DC and the AC bus. Besides, the algorithm handles also the state of charge of the storage battery of the charging station via two kinds of control, i.e., MPPT algorithm and PI control.

Keywords

Electric vehicle • Charging station • DC–DC converter • Maximum power point tracking • Battery storage buffer • Incremental conductance algorithm • Voltage loop control

1 Introduction

The reduction of greenhouse gases into the atmosphere is a common challenge. According to the Environmental Protection Agency (EPA), the transportation sector participates about 14% of total global greenhouse gas emissions (GHGEs); this rate includes fossil fuels burned for road, rail, air, and marine range. A global warming is mostly caused by these sorts of harmful environmental issues. Due to the continuous depletion in petroleum fuel, the shift from gas/oil based ordinary vehicle to electric vehicle becomes an urgent priority. Furthermore, the renewable energy sources are on the rise due to the progress of the global market; the PV generation has increased on a large rate mostly in the Europe and US, with the largest plant estimated at 60 MW at Olmedilla in Spain (Lenardic et al. 2010). New opportunities have been appeared for interface with the smart grid concept that includes the PV system with the grid utility.

Recently, researchers and industrial companies made the integration of renewable energy sources (RESs) for charging EVs more sophisticated and performant (Grahn and Söder 2011); the PV source is considered as the best alternative among all RES due to its efficiency property and its convenient investment cost. However, the charging station (CS) effectiveness is tested through many perspectives as the high rate of instantaneous power delivered at the EV and durability of services. The electricity network contribution is also combined in this platform as a backup plan when the solar energy is unable to get the PV standalone system on. Further, the implementation of the hybrid energy sources contained the PV system, electricity network, and the storage battery in one pattern must take into consideration some concerns, which are mainly related to the inefficiency and the instability of the PV power and the extra burden caused by loads on the grid (Bhatt et al. 2011).

Time to full charge for EVs is recognized as the inconvenient constraint in the charging mode; besides, EV is often charged at nighttime instead of day which causes a problem

A. Hassoune (✉) · M. Khafallah · A. Mesbahi
Laboratory of Energy & Electrical Systems (LESE),
Superior National School of Electricity and Mechanical (ENSEM),
Hassan II University of Casablanca, 20470 Casablanca, Morocco
e-mail: a.hassoune@IEEE.org

M. Khafallah
e-mail: m.khafallah@gmail.com

A. Mesbahi
e-mail: abdelouahed.mesbahi@gmail.com

A. Hassoune · T. Bouragba
Engineering School of Industrial Systems (EIGSI Casablanca),
20103 Casablanca, Morocco
e-mail: tarik.bouragba@eigsica.ma

S. El Hani and M. Essaaidi (eds.), *Recent Advances in Electrical and Information Technologies for Sustainable Development*,
Advances in Science, Technology & Innovation, https://doi.org/10.1007/978-3-030-05276-8_14

of overloading the distribution transformers (DT), and especially an AC load is basically connected to the DT. The National Household Travel Survey confirms that EVs are parked in workplaces for at least 5 h (Sera et al. 2006). Moreover, the installation of higher power rating transformers may still the best solving choice. The charging station performance is enhanced using smart optimization algorithms. Hence, the power flow will follow the direct guidelines provided by the energy management unit (EMU) of the CS. On the other hand, acquisition data is established in the EMU in order to implement the optimal power to match the applied charging operation from plugged in EVs. Furthermore, the proposed architecture is based on a change in DC bus voltage, and observing how the EMU reacts to maintain the continuity of service for the CS. Despite the overloading drawback of the grid and the PV power fluctuations, the unit would create an alternative solution; otherwise, the battery storage buffer (BSB) is presented as an ultimate way for charging EVs when AC load is given high priority to use the utility.

The major goal of any power system is to achieve a balance between demand and supply at any point of time especially during peak hours (Bhatti et al. 2016), where a huge demand is appeared. Due to the fact that EV users are tended to feed their batteries taking into account two constraints, i.e., a short delay of plugged time and a convenient charging cost, there are three modes of charging an EV battery through energy conversion devices. The converters offer a large scale of power due to the accurate control system, each rated power matches a specific charging mode, which are described as follows: Mode-1: Slow charging (used for domestic, long-time EV parking), Mode-2: Quick charging (used for private, public location), and Mode-3: Fast charging (used for public location) (Mouli et al. 2016).

2 Description of the EVCS Architecture

The combination of the photovoltaic grid system (PVGS) in the electric vehicle charging station (EVCS) is related to numerous factors that affect the CS yield (Sumathi et al. 2015). The impact of external inputs is considered important to complete the architecture, as the use of meteorological data, geographical position, and the daily rated power of the CS (Torreglosa et al. 2016). However, this work describes the main structure using Matlab/Simulink software, and the adopted technique is based on simulating separately each block of the general pattern that represents the EVCS. The proposed charging station diagram is illustrated in Fig. 1. PV array, EVs, and BSB are tied to DC bus; the diagram contains two forms of bus, i.e., DC and AC.

The PV system is connected with DC bus via DC/DC boost converter controlled by an MPPT algorithm that extracts maximum power from PV. The BSB is tied to the DC bus via bidirectional converter; it adapts low voltage of the battery to the bus voltage. Buck converters are used to charge EVs only through multiple charging modes connected parallel to PV/BSB. Each charging point contains a human control panel (HCP) to insert information as the state of charge (SOC) of the battery, duration time to load, the battery capacity, and the power required to attend the applied SOC. Another specification is taken into account the

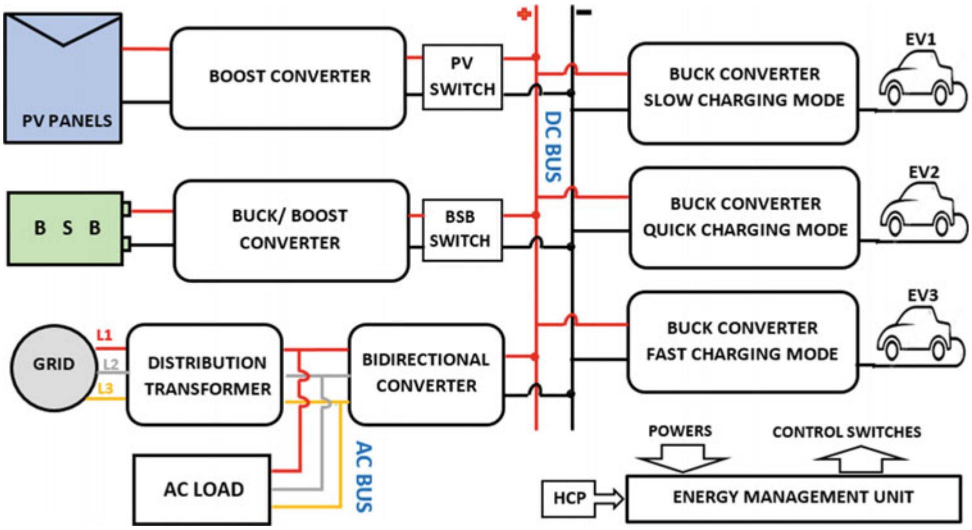

Fig. 1 Detailed scheme of three charging scenarios in EVsCS

company name/model of the vehicle to adapt properly the adequate operation mode and determine the priority level to load when power is limited in the CS. The EMU performance as shown in the EVCS diagram is tested via many standards (Jinrui et al. 2006), for instance, extraction of maximum power from the panel which requires the appropriate algorithm; the switch between the various modes of operation is also considered the main purpose of the controller (Forrisi et al. 2016).

The reference of DC bus voltage has been chosen, taking into consideration the switch operation between energy sources and/or BSB and the calculated power demand using the extracted data from HCP (Kamal et al. 2016).

2.1 DC Bus Voltage

The power flow generated and consumed by the group gathered PV, EVs, and BSB is operated at the DC bus level, where fluctuations in the voltage value are made to control more difficult. However, the SOC of the batteries (BSB, EV battery) may still the basic factor to decide the power flow direction. Figure 2 shows that the upstream part of the CS contains PV, EVs, and BSB, and the downstream part includes grid utility and its AC load.

The P_{UPS} regroups the global power delivered by the upstream side, while the AC load and the distribution transformer of the grid are constituted the downstream part. The equation linked the two diagrams is expressed in (1):

$$P_{DCB} = P_{UPS} - P_{DNS} \tag{1}$$

The stored power of the DC bus is expressed as follows:

$$P_{DCB} = CV_{DCB}\frac{dV_{DCB}}{dt} \tag{2}$$

Variations in power are related mainly to the PV system, the power demand from EVs, and the AC load. The interaction between all the blocs is described by (3):

$$P_{DCB} = P_{PV} + P_{BCB} + P_{Grid} - P_{EV} - P_{ACL} \tag{3}$$

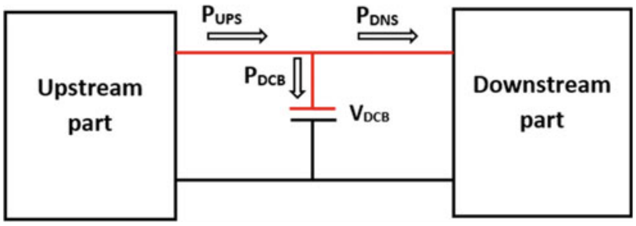

Fig. 2 Block diagram of different blocks of CS for EV

The energy management block is required to obtain the best compromise between the two types of load, i.e., EVs batteries and AC loads; besides, the used approach proposes priorities for charging numerous EVs parked in the same time with various scales of power of each vehicle.

2.2 AC Bus Voltage

In the proposed system, grid has a limited power due to the extra burden caused by additional AC loads, despite the installation of high-power transformers, a power management of the AC bus is paramount especially in peak hours where the CS is under strong demand. However, the power flow created at the AC bus is described as follows:

$$P_{ACB} = P_{Grid} - P_{ACL} \tag{4}$$

where P_{ACB} is the exchange of power between the DT and the AC loads.

2.3 Battery of the CS

The lithium–ion battery technology has become widely used in the most efficient storage system that required specific characteristics, for instance, fast charging, less self-discharge, working under wider operating temperature range, and accepts higher recharge rate (Andre et al. 2011). The adopted battery is charged from two energy sources, i.e., PV supply via DC/DC boost converter and grid via AC/DC converter, a reason to be controlled wisely in order to conserve its quality in even extreme conditions (Naumann et al. 2015); as a result, a long lifetime is warranted (Antonio et al. 2015). Furthermore, the characteristics of the battery are

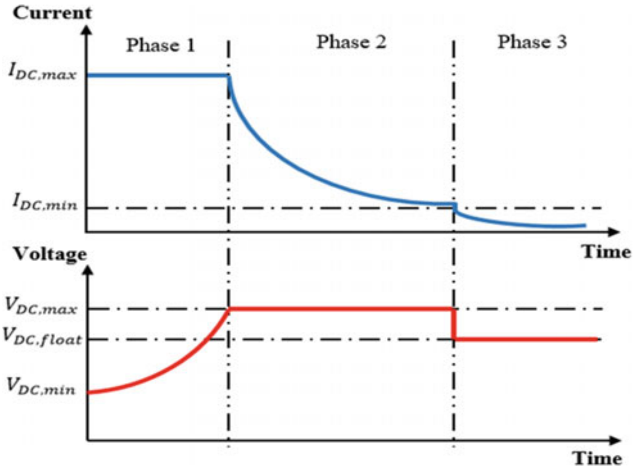

Fig. 3 BSB charging phases

described via three different phases depicted in Fig. 3. Each phase has been handled using one of two kinds of control, i.e., MPPT algorithm and voltage current loop control.

Due to the safety margin of the DC bus voltage, the BSB first phase is controlled with MPPT algorithm. This margin is limited to the allowed minimum V_{DCmin} and the overload maximum V_{DCmax} (Hassoune et al. 2017); the DC bus current is fixed to the maximum I_{DCmax} to avoid overheating and overstrain phenomena. Once V_{DC} achieves V_{DCmax}, the battery would be operated in the second phase where the EMU is switching off the MPPT algorithm and adjusting the voltage control to the V_{DCmax}. Nevertheless, the value of I_{DC} is kept increasing until it falls under I_{DCmin} where the third phase is reached, and in response the CU rehabilitates the control voltage to a reduced value V_{Ref}; this reference voltage is able to avoid the deep self-discharge of the battery by generating a very small charging current (López et al. 2016).

2.4 Energy Management Unit of the CS

The EMU major goal is to transfer the power flow from the two stream parts and control the switches; various dynamic inputs are made the management algorithm more complex. Yet, the extraction of maximum power from the PV system is considered the first assignment of the unit by generating a variable duty cycle for the DC–DC boost converter; besides, a voltage loop control is also integrated using the I_{DC} and the V_{DC} feedback. However, the maximum current delivered by the electrical grid is determined by taking into account the power consumed by the AC loads and the limited rated current of the distribution transformer (Siva Chaitanya Kumar 2014). A battery management system is included and activated when the BSB is fully charged or at under deep of discharge (DoD) situation; generally, in the terms of ensuring a long lifetime for the batteries, their depth of discharge rates are chosen with a margin of 15–85% (Vitols 2015). To apply all these requirements, Fig. 4 illustrates the voltage and the current control of charging the BSB under fluctuant state of DC bus.

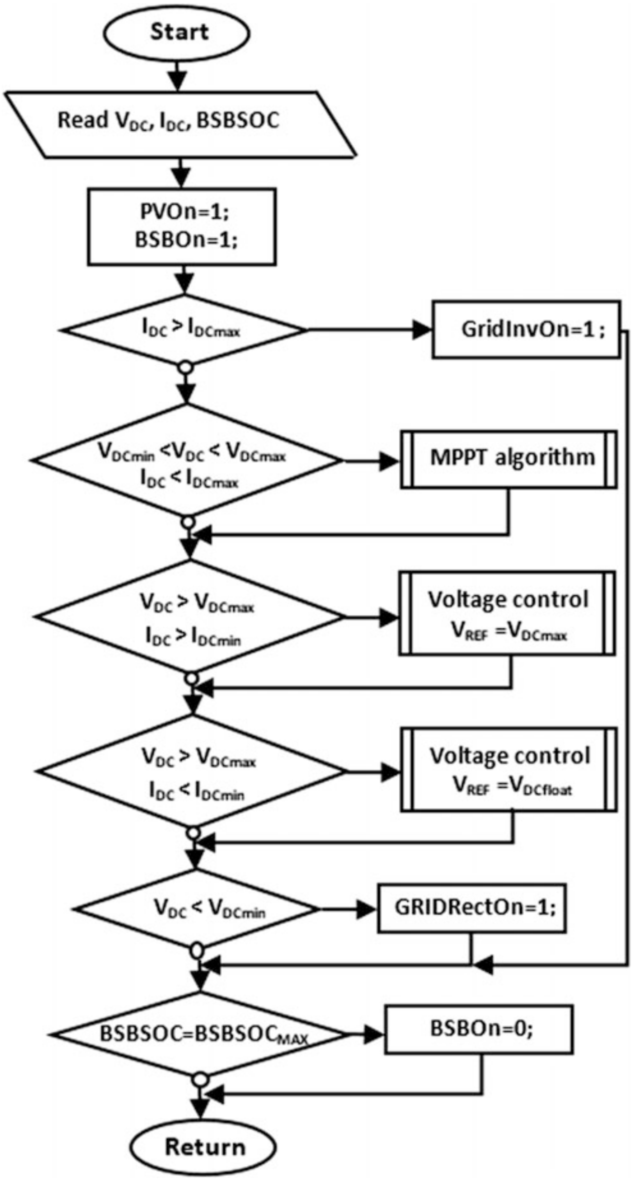

Fig. 5 Flowchart of the energy management approach

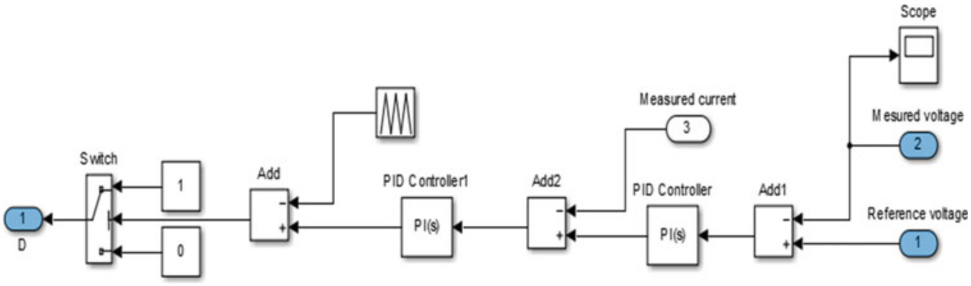

Fig. 4 Control loop block of voltage and current

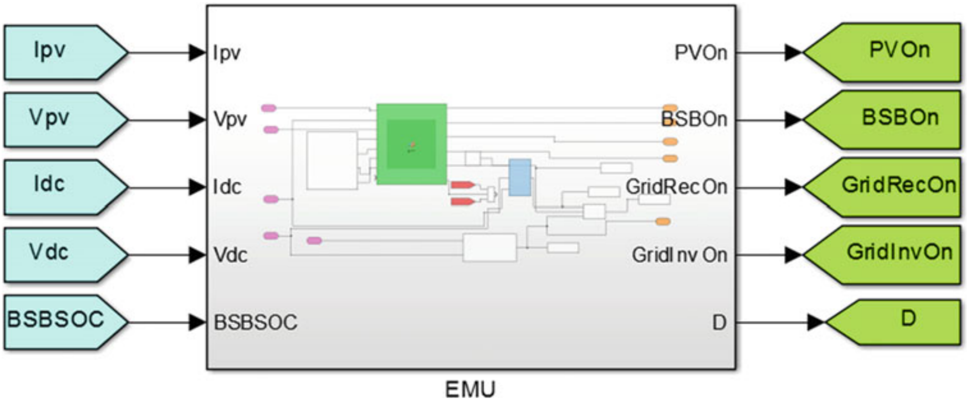

Fig. 6 Energy management unit of the PVGS

The flowchart of Fig. 5 describes the proposed strategy of energy management at the DC bus; the algorithm requires the knowledge of BSB settings as the maximum average of VDC and IDC. However, the current and voltage of the charging points, the DC bus state, and SOC of the BSB are responsible to set the power flow direction. The electricity network is controlled via two switches as the case of GridRecOn for a rectifying mode (Grid to CS), and the injection of extra power is secured by the GridInvOn switch (CS to Grid) (Hassoune et al. 2018). Moreover, the storage battery is equipped with a management system to isolate it when a full charge is attended; at this case, a BSBOn switch is set to maintain a long lifetime. Call program of the MPPT algorithm is implemented in ordinary cases, when the output voltage is across the limited voltage of the BSB; then, the EMU will switch to the voltage control method to preserve the battery characteristics.

The use of Matlab/Simulink provides the simplest illustration of the energy management strategy, and it uses multiple statistic and dynamic parameters in an efficient pattern (Nouaiti et al. 2017). Furthermore, the PV current and voltage are considered as inputs for the controller unit that generates the appropriate duty cycle for the boost converter. The DC bus characteristics and the SOC of the batteries are the keys of the proposed strategy. Following the management approach above, Fig. 6 shows the detailed EMU interface, where PVOn, BSBOn, GridRecOn, and GridInvOn are all power switches.

3 Simulation Results

The validation test of the proposed topology is designed through a PV system prototype that contains two panels mounted in series delivered 480 Wp. The MPPT algorithm and the voltage–current control loop are implemented in the DC/DC boost converter following the flowchart designations of the power flow. Moreover, the DC bus voltage is adapted

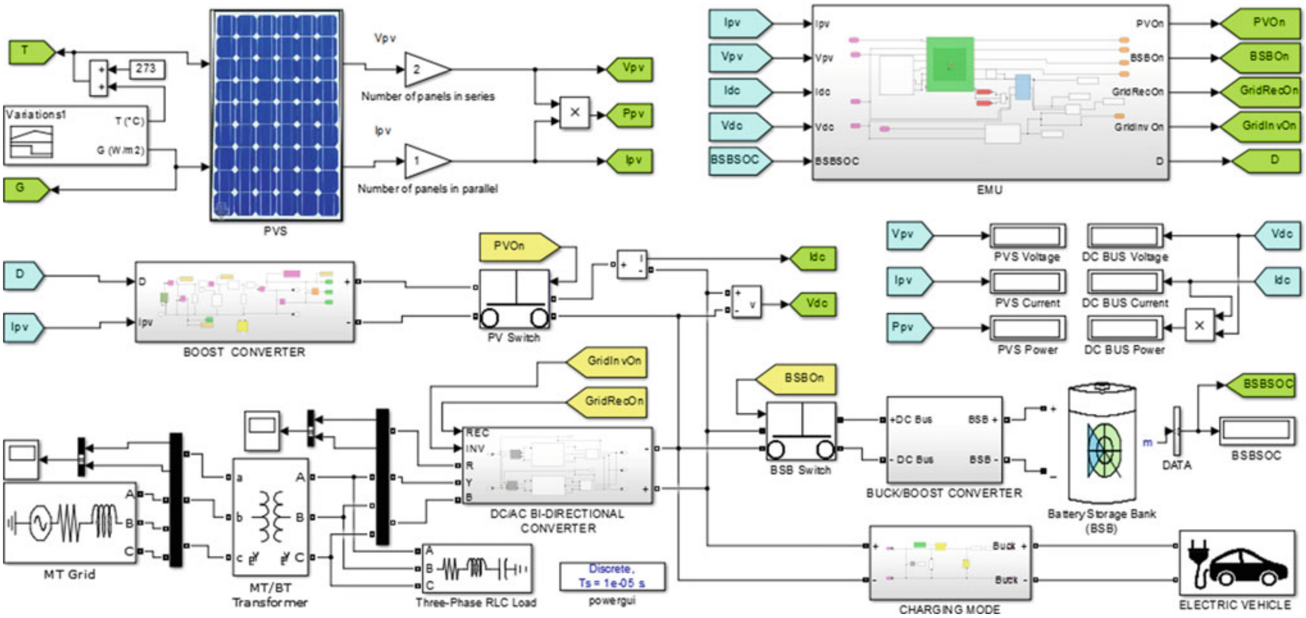

Fig. 7 PV-Grid system of the CS in Matlab/Simulink

Table 1 Electrical characteristics ISF-240 at 25 °C, 1 kW/m^2

Maximum power (P_{max})	240 W
Maximum power voltage (V_{mpp})	30,3 V
Maximum power current (I_{mpp})	7,91 A
Open circuit voltage (V_{oc})	37,1 V
Short circuit current (I_{sc})	8,46 A
Voltage temperature coefficient (K_v)	−0,323%/K
Current temperature coefficient (K_i)	0,042%/K

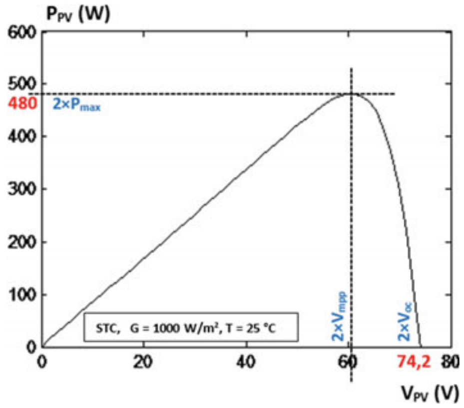

Fig. 8 Simulated P_{PV}–V_{PV} curve of ISF-240 PV (1 kW/m^2, 25 °C)

at 400 V, and the BSB settings are 48 V/8.3 Ah. The battery is tied to the DC bus through a bidirectional buck/boost converter. The distribution transformer is also combined with the use of a bidirectional ac/dc converter. Figure 7 expresses the adopted diagram including the power and the control part; the EMU controls the SOC of the batteries, manages the fluctuation of power at the DC bus level, and operates each switch of the PVGS.

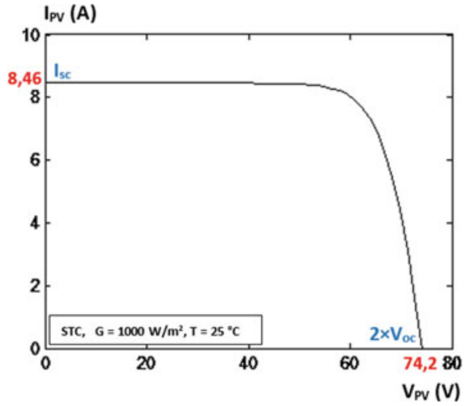

Fig. 9 Simulated I_{PV}–V_{PV} curve of ISF-240 PV (1 kW/m^2, 25 °C)

In order to get credible results, Table 1 illustrates the accompanied settings of the adopted panel delivered 240 W, contained 60 cells in 6 × 10 configuration.

After designing the photovoltaic model, a verification step is required for the previous task; ISF-240 panel is exanimated under standard test conditions (STC) which are typical values of cell temperature and irradiance 25 °C, 1000 W/m^2. Simulation results of the PV generator are shown in Fig. 8 and Fig. 9 which represent the I–V characteristics and the P–V characteristics, respectively.

The next significant step is the PV array working with MPPT algorithm in order to generate the maximum available power from a low sun irradiance. To optimize energy and preserve a lifetime warranty of the storage unit, a voltage control loop is also included in the control of the boost converter scheme. However, Fig. 10 depicts a climatic scenario implemented in the PVGS, which illustrates a concrete case of climatic conditions.

The DC bus voltage and the PV voltage are shown in Fig. 11. As can be seen, the boost converter raises the PV

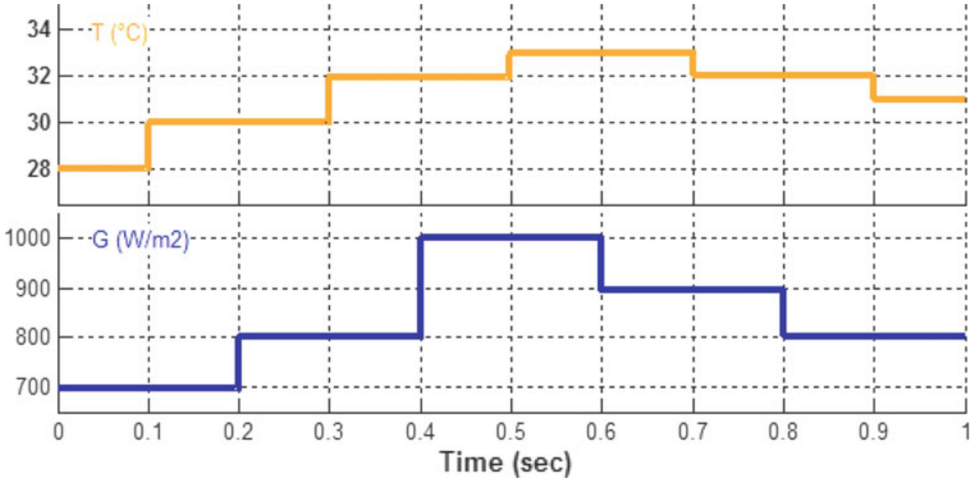

Fig. 10 Meteorological scenario of solar irradiation and temperature

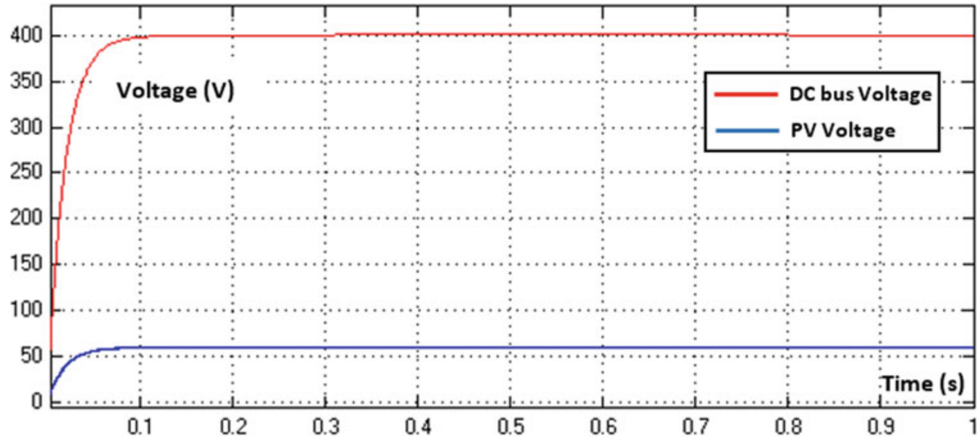

Fig. 11 DC bus voltage of the system versus time

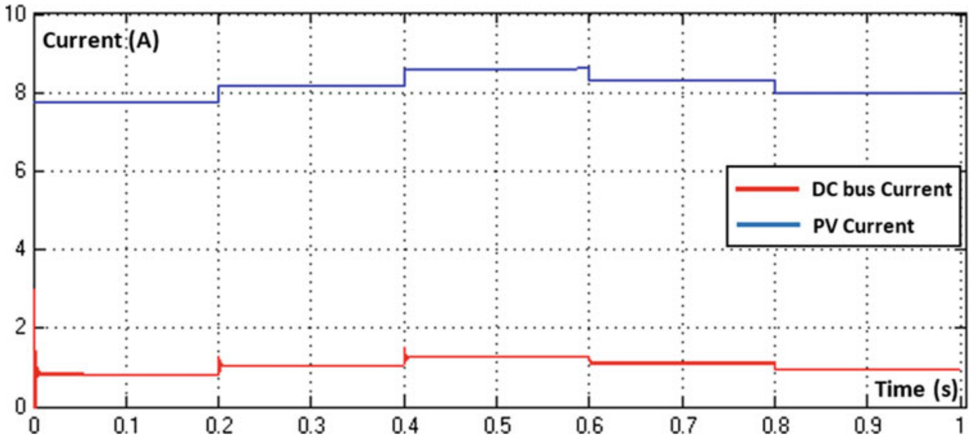

Fig. 12 DC bus current of the system versus time

voltage to a specific voltage margin (400–405 V), where the EMU operates under different modes, for instance, PV standalone mode and the bidirectional power flow of the CS with utility grid. The system reaches the steady state in short delay due to the PI controller; at t = 0.03 s, there is a large perturbation in voltage from the two margins of voltage.

To show the right performance of the EMU for DC bus voltage, the results obtained from switching between two kinds of control strategy of the boost converter have been plotted. Figure 12 shows the input and the output current of the converter.

The EMU controls the DC/DC boost with MPPT algorithm, until the converter output voltage reaches the VDCmax; after that, the voltage and current loops take control of the conversion system of the PV array. The current curve matched exactly the variation of the created climatic scenario. Figure 13 shows the variations of power from charging the BSB through the PV system including the grid reaction.

By means of proper switching, all the sources can be isolated from each other in order to achieve the required results. In the meanwhile, ideal switches and diodes are made the mode of operation possible to implement with high level of accuracy. It is assumed that the downstream part of the proposed diagram presents another daily load of the system such as the AC load linked with the DT.

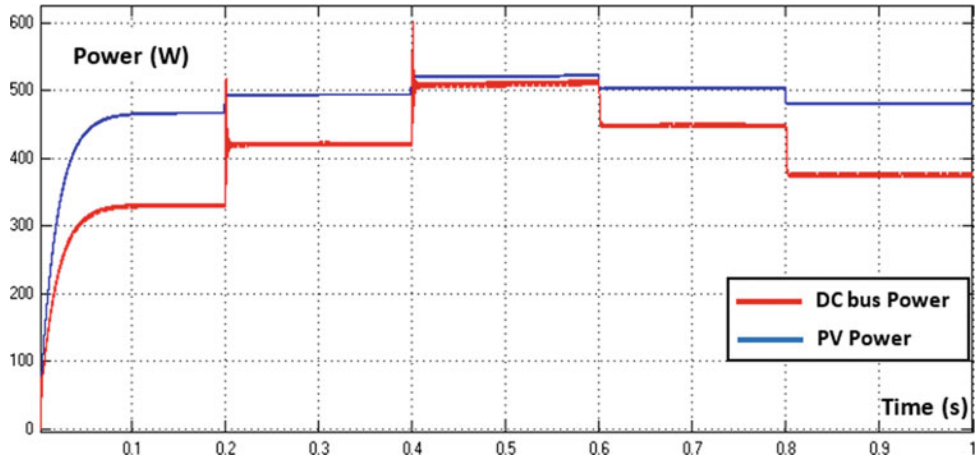

Fig. 13 Charging station DC power versus time

4 Conclusion

This work presents a smart topology to load a lithium–ion battery in EVCS through multiple optimization algorithms. In this regard, the efficiency of the system is tested using modes of operation, which have been validated by simulation results. Moreover, the reaction of the battery is stable even under higher recharge rate. In fact, this case is based on database of a project with full specifications, e.g., the meteorological data to emulate the PV array; simulation interpretation shows repeated reactions to the input climatic scenario as the temperature and the irradiance. This methodology aimed to establish a balance between the three different sources of energy including the contribution of the grid; besides, the technical purpose is to test the validity of the EVCS topology through various charging scenarios to feed an EV battery.

References

Andre, D., Meiler, M., Steiner, K., Walz, H., Soczka-Guth, T., & Sauer, D. U. (2011). Characterization of high-power lithium-ion batteries by electrochemical impedance spectroscopy. II: Modelling. *Journal of Power Sources, 196*(12), 5349–5356.

Antonio, D., Di, B., & Bocci, E. (2015). Energy analysis of a real grid connected lithium battery energy storage system. *Energy Procedia, 75,* 1881–1887.

Bhatt, R., Ieee, S. M., Chowdhury, B., & Ieee, S. M. (2011). Grid frequency and voltage support using PV systems with energy storage. In *Proceedings of IEEE Conference of North American Power Symposium* (pp. 1–6).

Bhatti, A. R., Salam, Z., Aziz, M. J. B. A., Yee, K. P., & Ashique, R. H. (2016). Electric vehicles charging using photovoltaic: status and technological review. *Renewable and Sustainable Energy Reviews, 54,* 34–47.

Forrisi, I., Martin, J., Nahid-mobarakeh, B., Pierfederici, S., Petrone, G., & Spagnuolo, G. (2016). A new approach for DC bus voltage balancing in a solar electric vehicle charging station. In *Proceedings of IEEE Transportation Electrification Conference and Expo* (pp. 1–5).

Grahn, P., & Söder, L. (2011). The customer perspective of the electric vehicles role on the electricity market. In *Proceedings of 8th International Conference on the European Energy Market* (pp. 141–148).

Hassoune, A., Khafallah, M., Mesbahi, A., & Breuil, D. (2017). Electrical design of a photovoltaic-grid system for electric vehicles charging station. In *14th International Multi-Conference on Systems, Signals & Devices* (pp. 228–233).

Hassoune, A., Khafallah, M., Mesbahi, A., & Bouragba, T. (2018). Power management strategies of electric vehicle charging station based grid tied PV-battery system. *International Journal of Renewable Energy Research, 8*(2), 851–860.

Jinrui, N., Fengchun, S., & Qinglian, R. (2006). A study of energy management system of electric vehicles. In *Proceedings of IEEE Vehicle Power and Propulsion Conference*

Kamal, T., Nadarajah, M., Hassan, S. Z., Li, H., Mehmood, F., & Hussain, I. (2016). Optimal scheduling of PHEVs in a PV based charging station. In *Proceedings of IEEE Transportation Electrification Conference and Expo* (pp. 1–6).

Lenardic, D. (2010). *Large scale photovoltaic power plants*. Retrieved June 06, 2010 from http://www.pvresources.com/en/top50pv.php.

López, J., Jr, S. I. S., Donoso, P. F., Morais, L. M. F., Cortizo, P. C., & Severo, M. A. (2016). Digital control strategy for a buck converter operating as a battery charger for stand-alone photovoltaic systems. *Solar Energy, 140,* 171–187.

Mouli, G. R. C., Bauer, P., & Zeman, M. (2016). System design for a solar powered electric vehicle charging station for workplaces. *Applied Energy, 168,* 434–443.

Naumann, M., Karl, R. C., Truong, C. N., Jossen, A., & Hesse, H. C. (2015). Lithium-ion battery cost analysis in PV-household application. *Energy Procedia, 73,* 37–47.

Nouaiti, A., Saad, A., Mesbahi, A., & Khafallah, M. (2017). Control strategies of a single phase switched capacitor nine-level inverter for PV system applications. *International Journal of Renewable Energy Research, 7*(4), 2017–2031.

Sera, D., Kerekes, T., Teodorescu, R., & Blaabjerg, F. (2006). Improved environmental conditions. In *Proceedings of 12th International Power Electronics and Motion Control Conference* (pp. 1614–1619).

Siva Chaitanya Kumar, K. P. L. (2014). Matlab/Simulink based modelling and simulation of residential grid connected solar photovoltaic system. *International Jouranl of Engineering Research & Technology*, *3*(3).

Sumathi, S., Ashok Kumar, L., & Surekha, P. (2015). *Solar PV and wind energy conversion systems.* ISBN 978-3-319-14940-0, 978-3-319-14941-7.

Torreglosa, J. P., García-Triviño, P., Fernández-Ramirez, L. M., & Jurado, F. (2016). Decentralized energy management strategy based on predictive controllers for a medium voltage direct current photovoltaic electric vehicle charging station. *Energy Conversion and Management, 108,* 1–13.

Vitols, K. (2015). Lithium ion battery parameter evaluation for battery management system. In *International Scientific conference on Power and Electrical Engineering of Riga Technical university* (7–10).

Abdelilah Hassoune was born in Settat, Morocco in 1993. He received the bachelors in Mathematical Sciences in 2010, and the Technical University degree in Electrical Engineering and Computer Science from the National High School of Technical Education, Mohammedia, Morocco, in 2012, the masters from the Multidisciplinary Faculty of the Hassan I University, Khouribga, Morocco, in 2013, and the Electrical Engineer diploma in Embedded Systems and Numerical Control from the National School of Applied Sciences Khouribga, Morocco, 2015.

He joined the Hassan II University of Casablanca, ENSEM, Morocco, in 2015 as a Ph.D. candidate at the Laboratory of Energy & Electrical Systems. His research interests include electric vehicles charging station with several publications in highly indexed journals.

He is a member of IEEE community with access to the world's largest technical professional organization dedicated to advancing technology for the benefit of humanity.

Mohamed Khafallah is now a Professor tutor in the Department of Electrical Engineering at the Superior National School of Electricity and Mechanical (ENSEM), Hassan II University of Casablanca, Morocco. His main research interests include the application of power electronics converts and motor drives.

He has published a lot of research papers in international journals, conference proceedings as well as chapters of books.

Abdelouahed Mesbahi received the M.A. from ENSET, Rabat, Morocco in 1990 and the DEA diploma in information processing in 1997 from Hassan II University, Faculty of sciences Ben M'sik Casablanca, Morocco. He obtained the Ph. D. in Engineering Sciences from Hassan II University, ENSEM Casablanca, Morocco in 2013.

Until 2013, he was a Teacher in Electrical Engineering department at ENSET Mohammedia Morocco. Actually, he acts as Assistant Professor in Electrical Engineering department at ENSEM, Casablanca, Morocco. His research in Energy and Electrical Systems Laboratory (LESE) is focused on sensorless control and advanced command applied to electrical machines and control of renewable energy systems. He is also an associate research member of SSDIA Laboratory based in Hassan II University ENSET, Mohammedia, Morocco.

Tarik Bouragba is the Associate Professor in the Department of Physics in EIGSICA engineering school of industrial system, Casablanca, Morocco. He completed his M.Sc and Ph.D. in Physics from Blaise Pascal University, Clermont-Ferrand, France. He worked as Replication Process Manager for 3 years at Nemotek Technologies SA, Rabat, Morocco and he contributes actively on a press release "Nemotek Debuts First Wafer-Level 720p HD Camera Module". He had participated in many national and international workshops, seminars, and conferences. He has 3 years of experience in material research and 3 years in teaching. His area of research includes material science and nanotechnology for cell application. His ongoing activities are focusing on renewable energies.

Study of the Performance of the DRHT and TSP in Delay Tolerant Networks

El Arbi Abdellaoui Alaoui, Hanane Zekkori, and Said Agoujil

Abstract

In Delay-Tolerant Networks (DTN), routing is a very challenging task due to their peculiar characteristics. Among various routing schemes, we find routing schemes based on clustering in order to improve the performances of this networks. In this work, we provide a DTN Routing Hierarchical Topology (DRHT) which incorporates three fundamental concepts: ferries messages, ferries routes, and clusters. The intra-cluster routing is managed by the cluster head, while the intercluster routing is managed by the ferries messages. This approach allows us to improve the performances of DTN networks. The simulations results have shown that our solution to the DRHT proves to be effective and adequate in the context of the DTN networks when compared to the other existing approaches.

Keywords

Delay-tolerant networks (DTN) • DRHT • TSP • Message ferry • Hierarchy routing

1 Introduction

In recent years, Delay-Tolerant Network (DTN) has emerged as one of the most promising evolutions of ad hoc networks, and are designed to operate without the need for infrastructure support. This network is characterized by an intermittent connectivity, an asymmetric flow, a high error rate, a long or variable delivery delay, extensive networks, and a high mobility of nodes. These factors provide a irregular connectivity, therefore, the delivery delay and the delivery rate are degraded in a considerable way (Abdellaoui Alaoui et al. 2015; Azzuhri et al. 2003). Hence the importance of thinking about designing a suitable topology for this type of network.

This work aims at dealing with the problematic data routing process. Many parameters are taken into the account to save network resources. The scheme of routing should deal with the increasing number of participants and their mobility, in order to provide a regular connectivity in a disconnected network.

The key idea behind our proposed approach is that we can optimize the delivery delay and delivery rate, particularly in the large-scale DTN networks. All this through the use of an adequate and structured topology to make the entire network related. Using this approach will allow us to optimize message delivery delays, energy consumption, buffer occupancy, bandwidth requirements, and throughput, moreover, this topology is necessary especially in large- scale networks. This approach is called DTN Routing Hierarchical Topology (DRHT).

Our proposed approach DRHT was the subject of some of our published works (Abdellaoui Alaoui et al. 2016a, b, c, e, f; Abdellaoui Alaoui and Nassiri 2016). Moreover, this paper complements our research and strengthens our proposed approach, by making a comparison with other routing approaches particularly the TSP. In addition, in this works (Abdellaoui Alaoui et al. 2016a, b, c, e, f; Abdellaoui Alaoui and Nassiri 2016), we have been content to test the network performances with only two metrics without comparison with other routing approaches, something that is not sufficient to evaluate the network performances.

E. A. Abdellaoui Alaoui (✉)
EIGSI, 282 Route of the Oasis, Mâarif, 20140 Casablanca, Morocco
e-mail: abdellaoui.e@gmail.com

E. A. Abdellaoui Alaoui · H. Zekkori · S. Agoujil
E3MI Team, Faculty of Sciences and Techniques at Errachidia, Department of Computer Science, University of Moulay Ismail, Meknès, Morocco
e-mail: hananzekkori06@gmail.com

S. Agoujil
e-mail: agoujil@gmail.com

S. El Hani and M. Essaaidi (eds.), *Recent Advances in Electrical and Information Technologies for Sustainable Development*,
Advances in Science, Technology & Innovation, https://doi.org/10.1007/978-3-030-05276-8_15

The rest of this paper is structured as follows: We describe our system model and problem statement. In Sect. 3, we explain the concept of the DTN routing hierarchical topology (DRHT). In Sect. 4, we study the probability of delivery for a bundle with specific TTL and we define the average duration of inter-contact. In Sect. 5, we introduce the configuration of the simulation. The illustrative simulation results are explored used our approach DRHT compared to Traveling Salesman Problem (TSP) route (Shah and Soni 2014; Sugihara and Gupta 2008) in Sect. and finally, some remarks and conclusions are offered in Sect. 7.

2 System Model and Problem Statement

We start this section by presenting our network model used in this paper. After, we provide the list of symbols used in this paper in Table 1 and some hypotheses used in this work, followed by the description of our problem statement and finally, we present the function objective.

2.1 Network Model

In our study, we consider a DTN network with a clustered architecture composed of N mobile nodes. The network is divided into groups called clusters, and each cluster is managed by a cluster head. Remember that two nodes in the network can exchange data only if they join the reciprocal range of communication, and we consider this as a sequence of “contact” between the two nodes in the network DTN (we talk about a contact because the existence of an end-to-end path in a DTN network is available only on a temporary period). Let the interval of pairwise inter-contact between the nodes n_i and n_j denotes the time duration from the instant when the nodes leave the communication range of each other until the next instant when they join it. In order to achieve the improvement of the DTN network performance in the existing analytical results, we appeal to the same model of mobility, in which the interval of pairwise meeting fills the exponential distribution with the same rate λ. In the literature, this model of mobility has been greatly used since it represents a reasonable approximation of the inter-contact interval in a considerable number of DTN networks (Zhu et al. 2010).

2.2 Notations

For the rest of this work, the following notation is used (Table 1):

Table 1 List of symbols

Notation	Definition
N	Total number of nodes of the shared network
C_k	Cluster of the network
N_k	Number of nodes in each area, with: $N = \sum_{k=1}^{K} N_k$
F	Message Ferry
n_i	Node i in the network
v	Speed of the ferry
P	Ferry route
$\|P\|$	Length of a ferry route
l_{ij}^{P}	Distance between the node n_i and n_j
$t_{w_{ij}}$	Time of wait to n_i before being transmitted to the ferry
$t_{c_{ij}}$	Time of carrying to the ferry before being delivered to n_j
d_{ij}^{P}	Average delay to transmit a message of n_i to n_j
μ_i	Message size $(1 \leqslant i \leqslant M)$

2.3 Hypotheses

The notion of ferry routes is discussed in Zhao and Ammar (2003), according to two hypotheses:

- The nodes are fixed and their positions are known for the ferry;
- The data traffic between two nodes can be estimated before the construction of the ferry route.

These two assumptions cannot be verified in DTN networks given the characteristics of this type of network. Therefore, we must modify and adapt them to DTN environments. Thus, we will consider the following two hypotheses:

- (H1): All nodes have the same transmission range;
- (H2): Each region of the network is considered as a cluster;
- (H3): Nodes move randomly inside and outside clusters;
- (H4): Traffic in the network is unpredictable;
- (H5): Range length of each cluster is strictly lower than the ferry route length;
- (H6): The contact between any two clusters C_k and $C_{k'}$ follows an exponential distribution of the parameter $\lambda = \lambda_{kk'} = \lambda_{k'k}$.

2.4 Problem Statement

Delay-Tolerant Networks (DTN) is characterized by intermittent and sporadic communication opportunities between

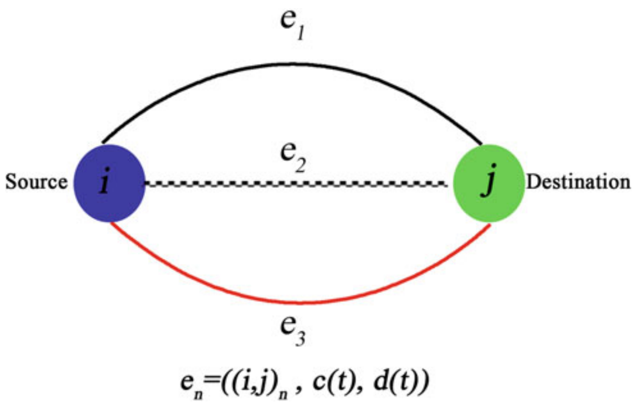

Fig. 1 Characteristics of a contact in a DTN network

nodes. Thus, a contact between the source node and the destination node may only exist for a brief and unpredictable delay, thereby leading to network partition. In order to make the transmission of data possible in DTN, recent researchers often extend the "store-and-forward" mechanism used in DTNs to "store-carry-forward" mechanism (Chuah et al. 2006). Since, each node in DTN can store messages in buffer during the unavailability of forwarding opportunity toward the destination, until the presence of this opportunity. Thus, in a DTN network, we no longer talk about physical link whose characteristics are known in advance, but rather of contact. Figure 1 describes the characteristics of a contact:

According to this Fig. 1, we can identify the following facts:

- Between two nodes, there may be one or several contacts $(e_1, e_2, \ldots, e_n)$
- A contact is characterized on the one hand by a capacity $c(t)$ which varies during the duration of its availability $d(t)$ and on the other hand by the two nodes that it interconnects (i, j).

In recent years, DTN networks have gained a very large popularity of the research community. In addition, DTN networks are currently involved in several applications. The development of routing scheme for DTN networks is generally a difficult task due to the intermittent connectivity about the network topology.

DTN networks are currently a very active research theme because they are used in many applications. The optimization of the delivery rate during an adequate delivery delay is a major constraint because this type of networks is characterized by an intermittent connection. Furthermore, DTN networks are usually used to transmit information in hostile or inaccessible environments. This problematic concerns all network levels; from the physical layer until the application layer.

In order to improve the DTN network performance and to make it related, we must ensure the connectivity between different clusters. This requires the determination of the positions to which the ferries must move, which will increase the number of nodes covered by these ferries. Thus, the movement of ferries will ensure the connectivity of the DTN network.

2.5 Function Objective

Let us to consider the ferry route P, the objective function of the average delivery delay can be written as

$$\Delta_d = \frac{\sum_{1 \leqslant i,j \leqslant N} b_{ij} d_{ij}^P}{\sum_{1 \leqslant i,j \leqslant N} b_{ij}} \tag{1}$$

The problem of the ferry route is presented in Zhao et al. (2005). The authors in Zhao et al. (2005) are used the ferry routes according to two hypotheses: first, the nodes are fixed and their position is known, and second, the average traffic b_{ij} between the node n_i and the node n_j can be estimated before calculating the route.

However, according to the hypothesis (H4), we can not determine in advance the parameter b_{ij} in the context of DTN networks, because ferries are considered dynamic in our approach. Thus, the Eq. 1 can be rewritten as

$$\Delta_{DRHT} = \frac{\sum_{i=1}^{M} \mu_i d_{ij}^P}{\sum_{i=1}^{M} \mu_i} \tag{2}$$

where M number of messages and μ_i denotes the message size $(1 \leqslant i \leqslant M)$.

3 DTN Routing Hierarchical Topology (DRHT)

This section describes our approach of routing in DTN networks. We are interested in the segmentation of nodes in a partitioned network in several clusters (areas). In the case of the DTN networks, that constitutes the general framework of our work, we define the network and its components: the partitioned areas and the design of the ferries routes connecting them.

3.1 Description of the Construction DRHT

In this sous-section, we describe our approach the DRHT, which has for objective to improve the performance of DTN networks. The design of the DRHT is based on three fundamental concepts: the clustering, ferries messages, and

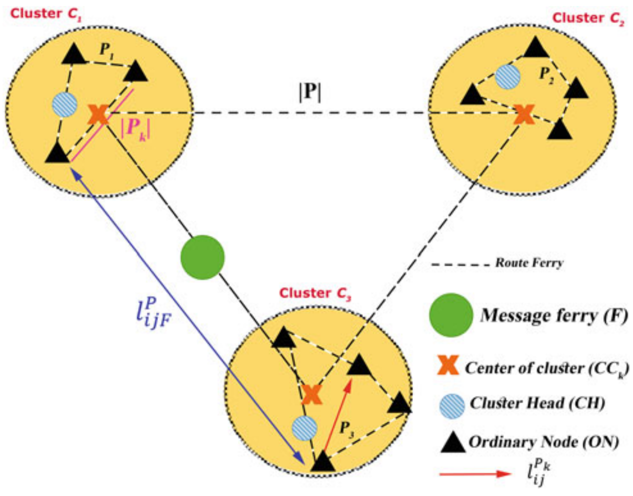

Fig. 2 Diagram of the DRHT

ferries routes. The dominant character in the DRHT is the number of ferries crossing the dissemination paths in order to ensure the connectivity between clusters. This topology is represented by the diagram in Fig. 2. In addition, each cluster is identified by three categories of nodes (Abdellaoui Alaoui et al. 2016a, f, c, b):

1. The Cluster Heads (CHs) are dominant nodes. The cluster head is the leader of the cluster;
2. The Centers of the cluster (CC_k) are exchange points at which the messages can exchange data between the different CHs via the ferries within each cluster;
3. The ordinary nodes (NO) are not dominant nodes.

Considering a DTN network is represented by a graph of N nodes and consisting of K clusters, where each cluster is mastered by a leading node called Cluster Head (CH). For simplicity, we limit the movement of a CH in a circular area. The center of a cluster C_k is represented by a geometric point, denoted as CC_k.

DRHT approach consists mainly of five phases:

1. The network partitioning;
2. The choice of the broadcaster node;
3. The scope and density of clusters;
4. The calculation of the ferry route. For each cluster, ferry route can be calculated by the algorithm proposed in Zhao et al. (2004), Zhang and Fei (2007);
5. The calculation of the global ferry route. Along the direction of the route P, the global ferry route can be obtained by connecting the CH position of each cluster.

3.2 Routing Phases in the DRHT

We consider a node n_i intending to send a message to a node n_j. In order to be able to exchange data efficiently between these two nodes, the routing in the DRHT consists of two phases, namely intra-cluster and intercluster.

Intra-cluster routing phase If $\{n_i, n_j\} \in C_k$, i.e., the two nodes are in the same cluster C_k. Thus, the two nodes have a high probability of contact and it occurs a direct transmission of data. In addition, it should be emphasized the role of the CH in the transmission of data during this phase.

Intercluster routing phase If $n_i \in C_k$ and $n_j \in C_{k'}$, i.e., the two nodes are in different clusters. Thus, the two nodes have a low probability of contact and communication between them becomes difficult. In order to increase the chances of contact, the ferries messages are involved. Indeed, if a ferry stops at the point CC_k, it is able to communicate with the CH of the cluster C_k. This contact between the ferry and the CH allows the transmission of data to the ferry so that this latter can deliver them to the CH of the cluster $C_{k'}$ at the point $CC_{k'}$. Consequently, the ferries make the whole of the network connected.

3.3 Analysis of Delivery Delay in the DRHT

In this section, we analyze the delivery delay introduced by the DRHT based on the works (Zhao and Ammar 2003; Zhao et al. 2004). Let n_i and n_j be two nodes located in different positions. The communication between the two nodes requires the intervention of the ferry F, which ensures the transmission of the message generated at the node n_i and its delivery to the node destination n_j. The analysis of the delivery delay of the generated message is presented in the following:

- The pause time of the message at n_i before being transmitted to F is

$$t_{w_{ij}} = \frac{|P|}{2v} \tag{3}$$

- The transport time of the ferry from n_i to n_j is

$$t_{c_{ij}} = \frac{l^P_{ij}}{v} \tag{4}$$

- The delay between generating the message in the node n_i and delivering it to the node n_j is

$$d^P_{ij} = t_{w_{ij}} + t_{c_{ij}}$$

$$\Rightarrow d_{ij}^{P} = \frac{|P|}{2v} + \frac{l_{ij}^{P}}{v} \tag{5}$$

When nodes n_i and n_j are in the same cluster C_k According to the above Eqs. (3)–(5), we calculate the delivery delay of a single ferry as follows:

$$d_{ij_F}^{P} = \frac{|P|}{2v} + \frac{l_{ij_F}^{P}}{v} \tag{6}$$

In the DRHT, let P_k be the ferry route of the cluster C_k and let $l_{ij}^{P_k}$ be the distance separating the node n_i and the node n_j in the route P_k. The delivery delay of the DRHT $d_{ij}^{P_k}$ is

$$d_{ij}^{P_k} = \frac{|P_k|}{2v} + \frac{l_{ij}^{P_k}}{v} \tag{7}$$

According to the Eqs. (6) and (7), we observe that $d_{ij}^{P_k} < d_{ij_F}^{P}$ since $|P_k| < |P|$ and $l_{ij}^{P_k} < l_{ij_F}^{P}$. This signify that the delivery delay of the DRHT is less than that of a single ferry when the n_i and n_j nodes belong to different clusters.

When nodes n_i and n_j are situated in different clusters C_k and $C_{k'}$ The delivery delay of the DRHT is divided to three phases; according to the Fig. 2:

- The delivery delay $d_{ij}^{P_1}$ in the cluster C_1:

$$d_{ij}^{P_1} = \frac{|P_1|}{2v} + \frac{l_{ij}^{P_1}}{v} \tag{8}$$

- The delivery delay $d_{ij}^{P_{CC_1}}$ is the pause time of the ferry at the cluster C_1 added to the carrying time of the ferry to the point CC_1 before delivering the message to the cluster C_2:

$$d_{ij}^{P_{CC_1}} = \frac{|P_{CC_1}|}{2v} + \frac{l_{ij}^{P_{CC_1}}}{v} \tag{9}$$

- The delivery delay $d_{ij}^{P_2}$ in the cluster C_2:

$$d_{ij}^{P_2} = \frac{|P_2|}{2v} + \frac{l_{ij}^{P_2}}{v} \tag{10}$$

Based on the above Eqs. (8)–(10), the total duration of the message transmission is $d_{ij}^{P_{all}} = d_{ij}^{P_1} + d_{ij}^{P_{CC_1}} + d_{ij}^{P_2}$ and we can write:

$$\begin{aligned} &\frac{|P_1|}{2v} + \frac{l_{ij}^{P_1}}{v} + \frac{|P_{CC_1}|}{2v} + \frac{l_{ij}^{P_{CC_1}}}{v} + \frac{|P_2|}{2v} + \frac{l_{ij}^{P_2}}{v} \\ &= \frac{(|P_1| + |P_{CC_1}| + |P_2|)}{2v} + \frac{l_{ij}^{P_1} + l_{ij}^{P_{CC_1}} + l_{ij}^{P_2}}{v} \end{aligned} \tag{11}$$

From Fig. 2, we observe that $|P_1| + |P_{CC_1}| + |P_2| < |P|$ and $l_{ij}^{P_1} + l_{ij}^{P_{CC_1}} + l_{ij}^{P_2} < l_{ij_F}^{P}$. Thus, when the node n_i and the node n_j belong to different clusters, the delivery delay of the DRHT is lower than that of a single ferry.

4 Modeling

In this section, we give a modeling of the delivery rate, the average duration of inter-contact and the delivery delay.

4.1 Probability of Successful Delivery

The contact between nodes follows an exponential distribution (Abdellaoui Alaoui et al. 2016d). Three performance evaluation metrics are considered, namely delivery rate of bundles, delivery delay, and buffer memory occupation. Let us consider τ_n the time of inter-contact between the nth and the $(n+1)$th bundle. The delivery probability of the bundle before the TTL expiry is given by the following formula (Abdellaoui Alaoui et al. 2016d):

$$P_r(T_n \le t_{TTL}) = 1 - e^{(-\lambda t_{TTL})} \tag{12}$$

4.2 Average Duration of Inter-contact

In this part, we analyze the message forwarding time in the DRHT and the time required before that two nodes can be in contact. That is the length of time during which the two nodes are mutually neighbors. The duration of contact is the delay between the end of a contact and the start of the next. We use stochastic formulas in order to calculate the inter-contact intensity λ and analyze the average duration of inter-contact between two nodes n_i and n_j. We suppose that the intensity of inter-contact λ and the average duration of inter-contact follow an exponential law, The average duration of the inter-contact is given by the following formula (Abdellaoui Alaoui et al. 2016d):

$$E(D) = \frac{1}{\lambda} \tag{13}$$

When an inter-contact time is short, the two related that nodes n_i et n_j meet themselves quite often. In other words, if two nodes n_i and n_j have a short inter-contact time, this means that we can wait for the next contact to send data. For long inter-contact time, we have to rely on some other supports (the *F* messages) in order to transfer data instead of unreasonably waiting and definitively losing data after the expiry of the *TTL* especially in large-scale networks.The number of these contacts and the distribution of the contact durations are two main factors helping in the determination of opportunist networks capacity. They give an overview of the quantity of data that can be transferred in each contact opportunity.

5 Simulation

In order to evaluate the performance of our approach the DRHT and to compare it to the TSP, we have designed and integrated both approaches under the simulator Opportunistic Network Environment (ONE) Keränen et al. (2009). The simulations that we have carried out are based on a model of synthetic mobility: the Random Waypoint. During the implementation of our simulations, we collect and store the different performance metrics of the DTN network (that we will detail in the next section) in order to perform in-depth analyses and interpretations. We consider the different inputs and outputs that are relevant to evaluate our routing approach. Table 2 summarizes the main configuration parameters for the simulation environment.

5.1 Metrics Performance

A DTN routing approach is judged better than another according to its own effectiveness. Given that our solution the DRHT has as objective to improve the performance of DTN networks, we have chosen to present the five following metrics (Abdellaoui Alaoui et al. 2015, 2016c):

- Delivery probability;
- Overhead ratio;
- Average latency;
- Average duration of inter-contact;
- Delivery delay.

Table 2 Parameters of simulation

Parametre	Value
Total simulation time	12 h
Deployment space size	$4500 \times 3400\,\mathrm{m}^2$
Routing protocol	Spray and Wait and Maxprop
Node buffer size	5 M
No of nodes	10, 20, 30, …, 100
Interface transmit speed	2 Mbps
Interface transmit range	10 m
Message *TTL*	60 min
Node movement speed	Min = 0.5 m/s Max = 1.5 m/s
Message creation rate	One message per 25–35 s
Message size	50–150 KB

6 Results and Discussion

In the simulated environment, we focused on comparing the performance in terms of the one metric: the average duration of inter-contact.

6.1 Delivery Rate

Figure 3 illustrate the bundles delivery rate in the TSP and DRHT approaches, and this for the three DTN routing protocols; depending on the density of the network, we notice that when the nodes density is low (10), the TSP and DRHT approaches present a low delivery rate of bundles. Indeed, the low density of nodes causes a weak connectivity of the network, consequently, the protocols cannot achieve certain destinations; especially, if the TTL of bundles expires. When the density of nodes is moderate (20–25), a significant rate of delivered bundles is noted for the two approaches. In fact, we notice that this delivery rate is very high in the DRHT, and can surpass 90% of delivered bundles, compared with around 35% in the TSP. However, with

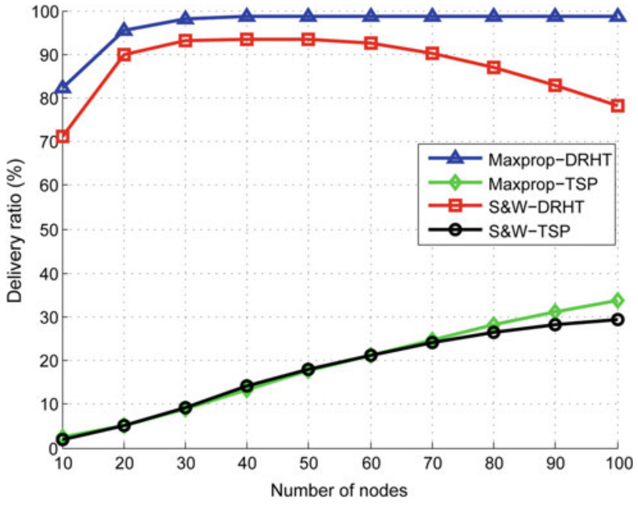

Fig. 3 Delivery rate by nodes density

the increase in the nodes density, we observe in the DRHT, a decline in the delivery rate following the high rate, particularly for Spray and Wait protocol. The Maxprop protocol maintains constant delivery rate values for an increased density (100). This is explained by the fact that the protocol Spray and Wait have a high traffic of control at a high density of nodes, then each node is obliged to transfer more traffic of control. Therefore, this traffic is responsible for a high collision rate and by disturbing the data traffic can increase the loss of bundles. However, the Maxprop protocol has a low traffic of control and maintains a constant delivery rate at a high density of nodes. Thus, in comparison with TSP, the DRHT provides a significant delivery rate (90%) and this with the three DTN protocols.

6.2 Average Latency

Figure 4 represents the average latency measured regarding the scenario adopted according to the nodes density. Two major factors intervene in measures of the average latency: the length of paths and the time spent in waiting queues. At first sight, for the TSP, we note that the average latency increases exponentially as the number of nodes increases. The TSP is the most affected by the traffic of control (overhead) and produces the highest latency. Indeed, it is because the bundle must wait more and more in the memory buffer before being delivered to a destination or deleted if its TTL is expired. However, for the DRHT, the increase in density reduces the average length of taken routes and therefore the average latency should decrease. This perception is observed in the case of a medium density (between 12 and 45 nodes). However, the second factor, which is the time spent in waiting queues, starts to dominate from 50 nodes of density. Its impact is clearly observed for high density of nodes. Indeed, at high density, each node must forward more traffic of control. Because the traffic of control is a priority, it will influence the delivery rate and cause small delays passed in waiting queues. This explains the small decrease in average latency observed in the second part of the curves in Fig. 4. In sum, due to its routing mechanism, the DRHT represents the most resistant approach to the effects of the increase in density and gives the best performances in terms of average latency, which allows it to minimize the delivery delay between the source and the destination.

6.3 Overhead Ratio

Figure 5 represents the results of our scenario for the DRHT and the TSP. It shows the overhead generated by both routing approaches, according to the number of nodes in the network. At first sight, we note that the overhead increases gradually as the number of nodes increases, for both routing approaches. When the density is weak (four nodes per cluster), the network is not related enough, and consequently, it is difficult to find intermediate nodes to deliver bundles in the network. Those reasons explain the observed reduction in overhead for both routing approaches between 5 and 10 nodes of density. Over 10 nodes of density, the network being related, we see that the overhead increases when the density does, this for both routing approaches. Therefore, an increase in density means an increase in replicated bundles in the network. That is why; we always look for algorithms that minimize the value of overhead ratio despite the increase in nodes' density. In fact, the DRHT with its routing mechanism, generates the most optimal overhead in particular with Spray and Wait protocol, and this by considering the delivery rate.

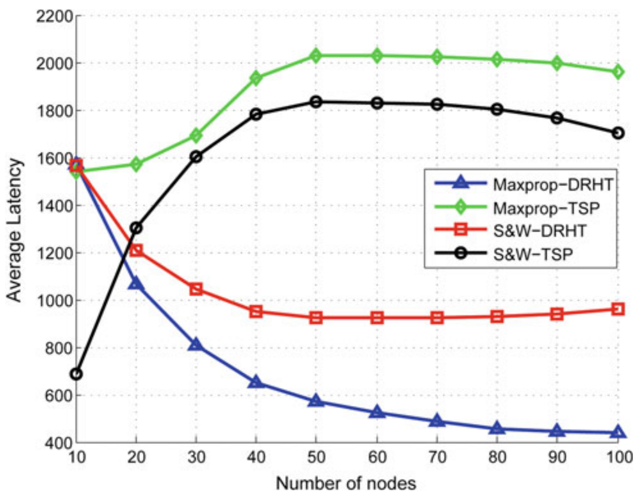

Fig. 4 Average Latency by nodes density

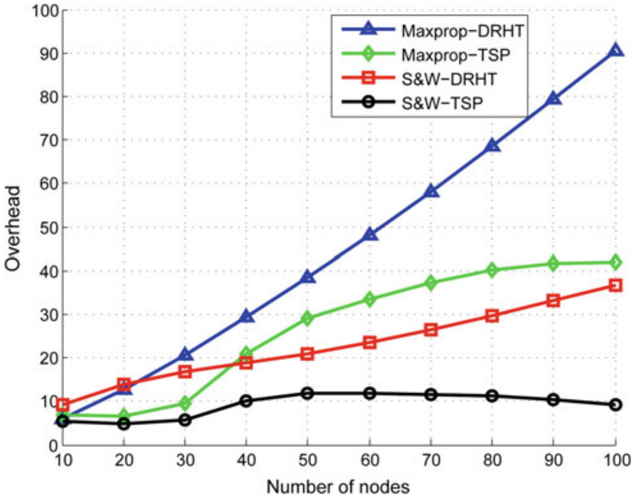

Fig. 5 Overhead in function of nodes' density

6.4 Average Duration of Inter-contact

In Figs. 6 and 7, we notice that for all DTN protocols, the average duration of inter-contact is long when the nodes density is weak, this is due to the great distances between nodes. When the density of nodes is increasing, we observe a reduction in the average duration of the inter-contact of the three protocols. This is due to the average degree of nodes becoming important and as a result, the end-to-end time is reduced. When the density of nodes becomes high, we observe that the average duration of inter-contact increases again for the Spray and Wait protocol that can be explained by the generation, at a high nodes density, of a considerable traffic of control by increasing the collision rate and disturbing data traffic, and then the average duration of inter-contact. However, the Maxprop protocol maintains effectively a quasi-constant average duration of inter-contact compared to the other DTN protocols. Thus, the Maxprop protocol is the most efficient in terms of optimization of the delivery delay between the source and the destination.

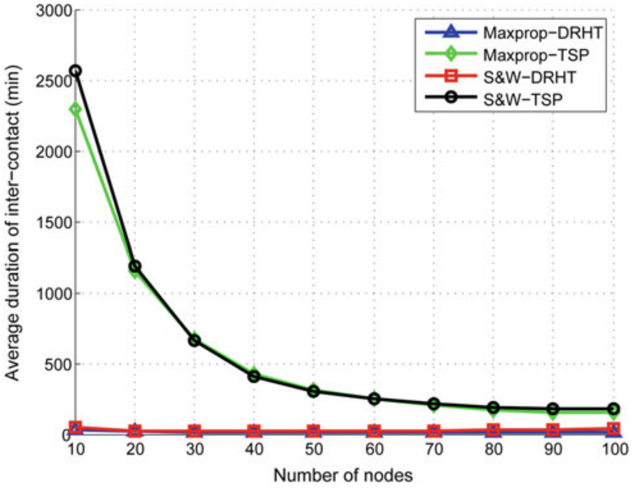

Fig. 6 Average duration of inter-contact in DRHT and TSP

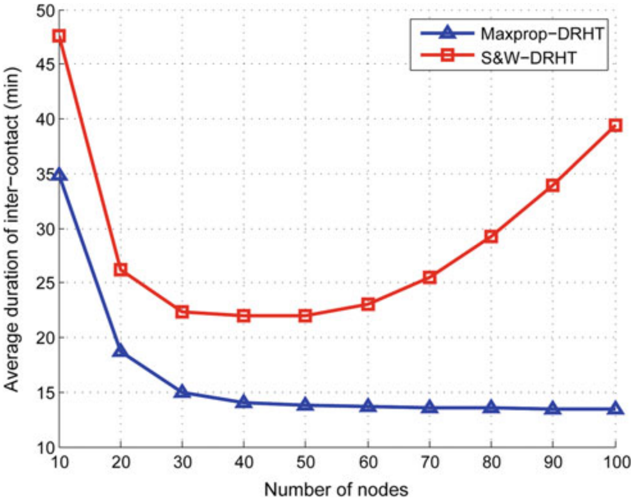

Fig. 7 Zoom on the average duration of inter-contact in the DRHT

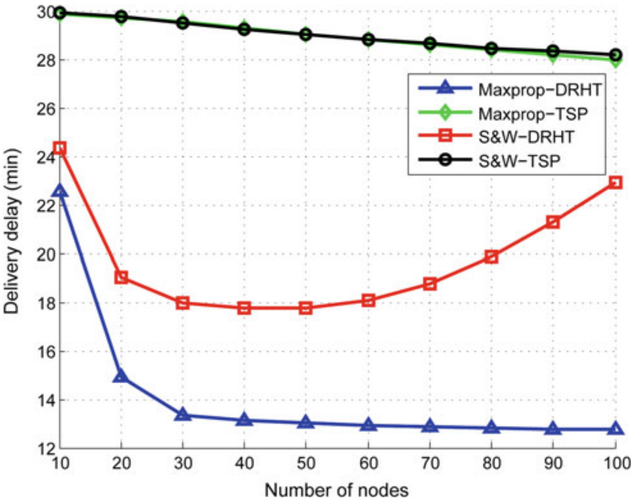

Fig. 8 Delivery delay by nodes density

6.5 Delivery Delay

Figure 8 represents the delivery delay of data from the source until the final destination in function of the number of nodes. We observe a normal behavior of the delivery delay which decreases with the increase in the density of nodes, this is explained by the increase in the average degree of the nodes whether for the DRHT or the TSP. Furthermore, and from this Fig. 8, we also observe that the DRHT approach offers a considerable optimization of the delivery delay compared to the TSP. Finally, we note that the Maxprop protocol offers the shortest delivery delay in both approaches

7 Conclusion

In this paper, we proposed a DTN Routing Hierarchical Topology (DRHT). The DRHT is based on the integration of three fundamental concepts: ferries messages, ferries routes, and clustering. The superposition of these three concepts allows us to improve the DTN routing performance in the case of large-scale networks. In effect, DRHT uses ferries messages in order to make the entire network connected. Thus, we have shown that the DRHT is the most effective approach in terms of the delivery rate and the delivery delay. The simulations results have shown that the DRHT is more performing and efficient compared to the TSP approach.

A perspective of our future research is the study of the optimal circulation of ferries in the DRHT, in order to save more energy and extend the network lifetime.

References

Abdellaoui Alaoui, E. A., Agoujil, S., Hajar, M., & Qaraai, Y. (2015). The performance of DTN routing protocols: A comparative study. *WSEAS Transactions on Communications, 14,* 121–130.

Abdellaoui Alaoui, E. A., & Nassiri, K. (2016). Maximizing the delivery rate for DTN networks. In *Third International Afro-European Conference for Industrial Advancement*. Springer.

Abdellaoui Alaoui, E. A., Agoujil, S., Hajar, M., & Qaraai, Y. (2016a). DTN network: Optimal cluster head in DTN routing hierarchical topology (DRHT). In *Advances in ubiquitous networking* (Vol. 2). Springer.

Abdellaoui Alaoui, E. A., Agoujil, S., Hajar, M., & Qaraai, Y. (2016b) Improving the delivery rate of data with: DTN routing hierarchical topology (DRHT). *International Journal of Communications, 10,* 95–101.

Abdellaoui Alaoui, E. A., Agoujil, S., Hajar, M., & Qaraai, Y. (2016c). Optimal cluster head in DTN routing hierarchical topology (DRHT). In *International Journal of Communication Networks and Information Security (IJCNIS), 8*(2), 101–111.

Abdellaoui Alaoui, E. A., Agoujil, S., & Hajar, M. (2016d). Stochastic modeling and analysis of DTN networks. In *Proceedings of The 2nd International Conference on Information Technology for Organizations Development (IT4OD)* (pp. 1–6), March 30–April 1st 2016. IEEE.

Abdellaoui Alaoui, E. A., Agoujil, S., Hajar, M., & Qaraai, Y. (2016e). Improving the data delivery using DTN routing hierarchical topology (DRHT). In *The International Conference on Wireless Networks and Mobile Communications (WINCOM'16)*, Fez, Morocco, 26–29 Oct 2016. IEEE.

Abdellaoui Alaoui, E. A., Agoujil, S., Hajar, M., & Qaraai, Y. (2016f). Improving the delivery rate of data with: DTN routing hierarchical topology (DRHT). In *Proceedings of The First International Conference of High Innovation in Computer Science (ICHICS 2016)* (pp. 121–124).

Azzuhri, S. R., Ahmad, H., Portmann, M., Ahmedy, I. & Pathak, R. (2003). An efficient hybrid MANET-DTN routing scheme for OLSR. In *Wireless Personal Communications*, 23 April 2016, Karlsruhe, Germany (pp. 27–34). ACM. https://doi.org/10.1007/s11277-016-3323-8.

Burgess, J., Gallagher, B., Jensen, D., & Levine, B. N. (April 2006). MaxProp: Routing for vehicle-based disruption-tolerant networks. In *Proceedings of 25th IEEE International Conference on Computer Communications*, Barcelona, Spain (pp. 1–11).

Cerf, V., Burleigh, S., Hooke, A., et al. (April 2007) Delay-tolerant networking architecture. In *RFC 4838*.

Chuah, M. C., Yang, P., Davison, B. D., & Cheng, L. (2006). Store-and-forward performance in a DTN. In *IEEE 63rd Vehicular Technology Conference, Melbourne, Vic, VTC 2006-Spring* (Vol. 1, pp. 187–191), 7–10 May 2006.

Fall, K. (2003). A delay-tolerant network architecture for challenged internets. In *Proceedings of the 2003 Conference on Applications, Technologies, Architectures, and Protocols for Computer Communications*, Karlsruhe, Germany (pp. 27–34). ACM.

Gavalas, D., Pantziou, G., Konstantopoulos, C., & Mamalis, B. (2006). Clustering of mobile ad hoc networks: An adaptive broadcast period approach. In *2006 IEEE International Conference on Communications* (pp. 4034–4039).

Huang, M., Chen, S., Zhu, Y., Xu, B., & Wang, Y. (2011). Topology control for time-evolving and predictable delay-tolerant networks. In *2011 IEEE 8th International Conference on Mobile Adhoc and Sensor Systems (MASS)*, Valencia, Spain (pp. 82–91).

Ip, Y. K., Lau, W. C., & Yue, O. C. (2007). Forwarding and replication strategies for DTN with resource constraints. In *2007 65th Vehicular Technology Conference, VTC2007-Spring* (pp. 1260–1264), 22–25 April 2007. IEEE.

Keränen, A., Ott, J., & Kärkkäinen, T. (2009) The ONE simulator for DTN protocol evaluation. In *SIMUTools'09: Proceedings of the 2nd International Conference on Simulation Tools and Techniques, ICST*, New York, NY, USA. Article No. 55.

Lai, Y., Chen, Z., Wu, W., & Ma, T. (2014). Comput: Multiple-resolution content sharing in mobile opportunistic networks. *Wireless Communications and Mobile*.

Maia, S., Silva, E., & Guardieiro, P. (2014). A new optimization strategy proposal for multi-copy forwarding in energy constrained DTNs. *IEEE Communications Letters*, *18*, 1623–1626.

Mangrulkar, R. S., & Atique, M. (Mar 2012). Performance evaluation of delay tolerant routing protocol by variation in buffer size. In *2012 International Conference on IEEE Advances in Engineering, Science and Management (ICAESM)* (pp. 509–513), 30–31 March 2012.

Mundur, P., Lee, S., & Seligman, M. (2011). Routing in intermittent networks using storage domains. *Wireless Communications and Mobile Computing,* 1213–1225.

Sammou, E., & Abdali, A. (2011). Routing in delay tolerant networks (DTN). *International Journal of Communications, Network and System Sciences, 4,* 53–58.

Shah, K. S., & Soni, U. H. (2014). Travelling salesman problem (TSP) for vehicle route optimization in MANETs using ABC algorithm. *International Journal for Research in Applied Science and Engineering Techhnology (IJRASET), 2,* 459–468.

Spyropoulos, T., Psounis, K., & Raghavendra, C. (2005). Spray and wait: An efficient routing scheme for intermittently connected mobile networks. In *Proceedings of the 2005 ACM SIGCOMM Workshop on Delay-Tolerant Networking*. ACM.

Sugihara, R., & Gupta, R. (2008). Improving the data delivery latency in sensor networks with controlled mobility. In *DCOSS 2008*. LNCS (Vol. 5067, pp. 386–399). Springer.

Sugihara, R., & Gupta, R. (2010). Speed control and scheduling of data mules in sensor networks. *ACM Transactions on Sensor Networks,* 1–29.

Vahdat, A., & Becker, D. (April 2000). *Epidemic Routing for Partially Connected Ad Hoc Networks*. Technical Report CS-200006. Duke University, Durham.

Zhang, Z., & Fei, Z. (2007). Route design for multiple ferries in delay tolerant networks. In *IEEE Wireless Communications and Networking Conference (WCNC)* (pp. 3460–3465).

Zhao, W., & Ammar, M. (2003). Message ferrying: Proactive routing in highly-partitioned wireless ad hoc networks. In *Proceedings of the Ninth IEEE Workshop on Future Trends of Distributed Computing Systems (FTDCS'03)*, Washington, DC, USA (pp. 308–314).

Zhao, W., Ammar, M., & Zegara, E. (2004). A message ferrying approach for data delivery in sparse mobile ad hoc networks. In *ACM MobiHoc*.

Zhao, W., Ammar, M., & Zegara, E. (2005). Controlling the mobility of multiple data transport ferries in a delay-tolerant network. In *IEEE INFOCOM* (pp. 1407–1418).

Zhao, W., Chen, Y., Zegura, E., Ammar, M., Corner, M., & Levine, B. (2006). Capacity enhancement using throwboxes in DTNs. In

International Conference on Mobile Adhoc and Sensor Systems (MASS) (pp. 31–40). IEEE.

Zhu, H., Fu, L., Xue, G., Zhu, Y., Li, M., & Ni, L. M. (2010). Recognizing exponential inter-contact time in VANETs. In *Proceedings of the 29th Conference on Information Communications (INFOCOM)* (pp. 101–105). IEEE.

El Arbi Abdellaoui Alaoui received PhD degree in Computer Science in 2017 from the Faculty of Sciences and Technology, Errachidia, University of Moulay Ismaïl, Meknès, Morocco. Prior to this, he received Master's degree in Telecommunication in 2013 from the National School of Applied Sciences, University of Sidi Mohamed Ben Abdallah, Fès, Morocco. He is currently a Research Professor at EIGSI Engineering School, Casablanca, Morocco. His research interests include mainly wireless networking, ad hoc networking, DTN networks, game theory, Internet of Things (IoT), smart cities, and optimization.

Hanane Zekkori received the B.Sc. in Computer Sciences from the University of Moulay Ismail, Faculty of Sciences and Techniques (FSTE), Errachidia, Morocco, in 2012, and M.Sc. degree in network and computer system from the University of Hassan 1st, Faculty of Sciences and Techniques (FSTS), Settat, Morocco, in 2014. Currently, she is working toward her Ph.D. at FSTE. Her current research interests include, delay tolerant network (DTN), mobile routing and security of DTN.

Said Agoujil received his Ph.D. and M.S. degrees in mathemat from Faculty of Sciences and Technology Marrakech (FSTM) in 2008, Morocco. He is currentlya professor hablity in Department of Computer Science, Faculty of Sciences and Technology Errachidia FSTE). His current research interests include : numerical analysis, wireless network, linear algebera, speech coding.

Application of Artificial Intelligence Techniques on Double-Squirrel Cage Induction Motor for an Electric Vehicle Motorization

Hamza Mediouni, Soumia El Hani, Ilias Ouachtouk,
Mustapha Ouadghiri, and Imad Aboudrar

Abstract

Electric Vehicles (EVs) are complex electromechanical systems described by nonlinear models and therefore, their control design and analysis is not an easy task. Double-Squirrel Cage Induction Motor (DSCIM) has the advantages of driving complex loads which require high starting torque and low starting current. This paper presents a speed control comparison between the PI controller and the advanced techniques of control based on the Artificial Neural Networks (ANN) and Fuzzy Logic (FL) in order to be applied for an electric vehicle motorization. The simulation results are numerically validated by using the MATLAB/Simulink universe; they highlight the robustness properties of the different control strategies based on field-oriented control technique.

Keywords

Electric vehicles (EVs) • Double-squirrel cage induction motor (DSCIM) • Artificial neural networks (ANN) • Fuzzy logic (FL) • Robustness properties

1 Introduction

In the near future, Electric Vehicles (EV s) seems to become an attractive solution in the field of transportation, due to environment reasons, namely the zero emissions, the low-noise disturbance, and the high-energy utilization [1, 2].

Electric Vehicle (EV) is a complex electromechanical system that contains basic power devices: the electric storage system (ESS) consisting of Lithium-Ion (Li-ion) batteries technology, the fully controlled power electronic devices, used as interface between the different parts and connected with the Electric Storage System (ESS) by a DC–DC converter, and the main component of Electric Vehicles (EV s) power devices is the electric motor which is used for system propulsion [1].

Double-squirrel cage induction motors are commonly used for driving loads by replacing the simple cage induction motor due to the advantages of high starting torque and efficient steady-state operation, they are widely used in many applications such as compressor pumps, reciprocating pumps, large refrigerators, crushers, boring mills, textile machinery, cranes, punches and lathes, etc. [3–5].

The dynamics of the complete EV system are described by a nonlinear model. As a result, the torque on the car wheels, the internal battery voltage, the DC converter duty ratio, and the velocity developed by the car are parameters that have to be controlled. In this work, we will be concentrated on the control of the car velocity developed by the electric motor. Several EV control strategies have been recently reported, and we can find those based on the knowledge of the machine parameters, therefore, we speak about classic controllers (PI, PID …) [3]. These controllers seem attractive but they suffer from many problems: the influence of internal parameters such as the rotor time constant and incorrect flux measurement or estimation at low speeds, the sensitivity to external disturbances, the presence of a mechanical sensor, and many other problems. As a consequence, the application of Artificial Intelligence Techniques was the suited solution to face these obstacles [3]. This paper represents a comparative study between the PI controller and the controllers based on the Artificial Intelligence such as Fuzzy Logic and the Artificial Neural Network applied on DSCIM for an EV motorization.

H. Mediouni (✉) · S. E. Hani · I. Ouachtouk · M. Ouadghiri
I. Aboudrar
Energy Optimization, Diagnosis and Control, STIS Center
ENSET, Mohammed V University, Rabat, Morocco
e-mail: Hamzamediouni16@gmail.com

S. E. Hani
e-mail: s.elhani@um5s.net.ma

S. El Hani and M. Essaaidi (eds.), *Recent Advances in Electrical and Information Technologies for Sustainable Development*,
Advances in Science, Technology & Innovation, https://doi.org/10.1007/978-3-030-05276-8_16

2 Double-Squirrel Cage Induction Machine Model

The mathematical model of a DSCIM is formed in a manner which closely parallels the derivation of the d, q model of a single-cage induction machine. Owing to the addition of the second cage, the rotor is now described with four differential equations in the common d, q frame of reference Fig. 1. By adopting the well-known assumptions of the generalized theory of electrical machines, the DSCIM can be described with the following set of equations in an arbitrary frame of reference [3, 6]:

The electrical system equations for DSCIM are given as

- Voltage equations:

$$\begin{cases} V_{ds} = R_s I_{ds} + \dfrac{d\varphi_{ds}}{dt} - w_s \varphi_{qs} \\ V_{qs} = R_s I_{qs} + \dfrac{d\varphi_{qs}}{dt} + w_s \varphi_{ds} \end{cases} \tag{1}$$

$$\begin{cases} 0 = R_{r1} I_{dr1} + \dfrac{d\varphi_{dr1}}{dt} - (w_s - w_r)\varphi_{qr1} + R_c(I_{dr1} + I_{dr2}) \\ 0 = R_{r1} I_{qr1} + \dfrac{d\varphi_{qr1}}{dt} + (w_s - w_r)\varphi_{dr1} + R_c(I_{qr1} + I_{qr2}) \\ 0 = R_{r2} I_{dr2} + \dfrac{d\varphi_{dr2}}{dt} - (w_s - w_r)\varphi_{qr2} + R_c(I_{dr1} + I_{dr2}) \\ 0 = R_{r2} I_{qr2} + \dfrac{d\varphi_{qr2}}{dt} + (w_s - w_r)\varphi_{dr2} + R_c(I_{qr1} + I_{qr2}) \end{cases} \tag{2}$$

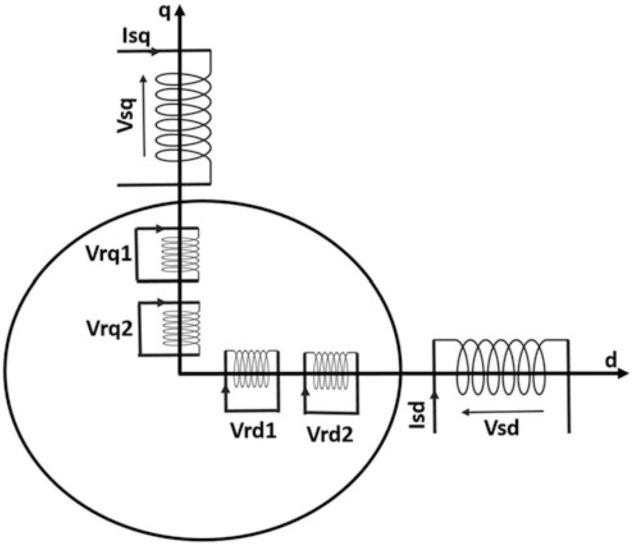

Fig. 1 DSCIM model using the park transformation in the f reference frame (d, q)

- Flux equations:

$$\begin{cases} \varphi_{ds} = L_s I_{ds} + L_m(I_{dr1} + I_{dr2}) \\ \varphi_{qs} = L_s I_{qs} + L_m(I_{qr1} + I_{qr2}) \end{cases} \tag{3}$$

$$\begin{cases} \varphi_{dr1} = L_{r1} I_{dr1} + L_m I_{ds} + L_{12} I_{dr2} \\ \varphi_{qr1} = L_{r1} I_{qr1} + L_m I_{qs} + L_{12} I_{qr2} \\ \varphi_{dr2} = L_{r2} I_{dr2} + L_m I_{ds} + L_{12} I_{dr1} \\ \varphi_{qr2} = L_{r2} I_{qr2} + L_m I_{qs} + L_{12} I_{qr1} \end{cases} \tag{4}$$

- Torque Expressions:

$$T_e - T_l = (J \cdot dw_r/d_t + kw_r)/P \tag{5}$$

$$T_e = PL_m\left[(I_{dr1} + I_{dr2}) I_{qs} - (I_{qr1} + I_{qr2}) I_{ds}\right] \tag{6}$$

where V, I, and φ denote voltage, current, and flux linkage, respectively, and indices “s” and “r” stand for stator and rotor. Indices 1 and 2 distinguish between the two rotor windings. Inductance L12 is defined as L12 = Lm + Lmr and symbols Lmr and Rc, stand for mutual leakage inductance between the two rotor windings and common end-ring resistance between the two cages in a DSCIM (this resistance does not exist in a deep-bar machine and will be set to zero). P is the number of pole pairs, electrical speed of rotation is “w”, T stands for torque, and J is the inertia coefficient.

3 Indirect Vector Control by Orientation of Rotor Flux

3.1 Principle and Strategy of the Indirect Vector Control

The underlying principle of vector control is to remove the internal coupling of the machine and return it to a linear control similar to that of a continuous current machine with a separated excitation [3, 7]. Depending on the design philosophy and the type of induction machine, there can be many different approaches to synthesize the machine currents to provide fast decoupling control.

With those conditions:

$$\begin{cases} \varphi_{dr} = \varphi_{dr1} + \varphi_{dr2} \\ 0 = \varphi_{qr1} + \varphi_{qr2} \end{cases} \tag{7}$$

$$\varphi_{qr1} = 0 \quad \text{and} \quad \varphi_{qr2} = 0 \tag{8}$$

We obtain for $R_c = 0$ the following equations:

$$\begin{cases} 0 = R_{r1}\, I_{dr1} + \frac{d\varphi_{dr1}}{dt} \\ 0 = R_{r1}\, I_{qr1} + (w_s - w_r)\, \varphi_{dr1} \\ 0 = R_{r2}\, I_{dr2} + \frac{d\varphi_{dr2}}{dt} \\ 0 = R_{r2}\, I_{qr2} + (w_s - w_r)\, \varphi_{dr2} \end{cases} \tag{9}$$

$$\begin{cases} I_{qr1} = \dfrac{I_{qs}(L_m - L_m L_2)}{L_{r1} \cdot L_{r2} - L_m^2} \\ I_{qr2} = \dfrac{I_{qs}(L_m - L_m L_1)}{L_{r1} \cdot L_{r2} - L_m^2} \end{cases} \tag{10}$$

$$(w_s - w_r)^* = \frac{L_m\, {I^*}_{qs} \,.\, [(L_{r2} - L_m)\, R_{r1} + (L_{r1} - L_m)\, R_{r2}]}{(L_{r1}\, L_{r2} - {L^2}_m) \,.\, \varphi_r^*} \tag{11}$$

$$T_e^* = \frac{3}{8} \cdot P \cdot L_m \frac{(L_{r2}\, L_{r1} - L_m^2)}{(L_{r1} + L_{r2} - 2L_m)} \cdot I_{qs}^* \cdot \varphi_e^* \tag{12}$$

3.2 Synthesis and Speed Regulator Calculation

The electromagnetic torque and the rotation speed are linked by the Eq. (5). Figure 2 shows the speed loop control:

where Kp and Ki represent, respectively, the proportional and integral gain.

The PI controller transfer function is

$$C(p) = K_p + \frac{K_i}{p} \tag{13}$$

The transfer function in the open loop is given by

$$H_{OL} = (K_p + \frac{k_i}{p}) \cdot \frac{1}{J \cdot p + k} \tag{14}$$

The transfer function in the closed loop is given by

$$H_{CL}(p) = \frac{(1 + \frac{K_p}{k_i} p) \cdot \frac{k_i}{J}}{p^2 + (\frac{K_p + k}{J})p + \frac{k_i}{J}} \tag{15}$$

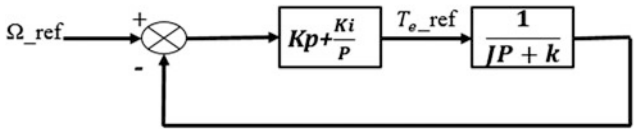

Fig. 2 Speed loop control

By comparing this equation with the general shape of transfer function of second order and after identifying, we obtain

$$\mathrm{Kp} = 0.8\,\mathrm{kg\,m^2/s\ and\ Ki} = 0.024\,\mathrm{kg\,m^2/s^2}$$

4 Control of DSCIM Using the Fuzzy Logic Controller

A fuzzy controller can be designed to emulate human deductive thinking, in the sense that the treated variables are not logical in the sense of binary logic, but linguistic variables [3]. Moreover, these linguistic variables are processed using rules that refer to certain knowledge of the system behavior. To design a Fuzzy Logic Controller, it starts first by selecting the input/output variables. The speed error reference value and its time variation have been selected as the inputs and the torque time variation as the output [3, 7]. In the design of a fuzzy logic controller, five membership functions were used for both error and change of error. Membership functions were constructed to represent the input and output value. The fuzzy logic controller consists of three stages: fuzzification, control rules evaluation, and defuzzification. The universe of discourse is divided into five overlapping fuzzy sets: Negative Large (NL), Negative Small (NS), Zero (ZE), Positive Small (PS), and Positive Large (PL). For the choice of the membership functions form, the symmetric triangular one has been chosen for all the membership functions with the exception of the extreme ends of each function whose trapezoidal form is used. The inference method based on the input fuzzy sets, uses appropriate IF-THEN rules in the knowledge base to imply the final output fuzzy sets [3, 7]. The inference matrix of the fuzzy controller is given in Table 1.

When the fuzzy outputs are computed, they must be transformed into numerical values. This study is based on the method of the center of gravity.

5 Control of DSCIM Using the Artificial Neural Network

5.1 The Basic Principle of Neural Networks

Artificial Neural Networks (ANNs) are computing systems whose structures are inspired by a simplified model of the human brain. By adjusting the values of the connections (or weights) between the elements (neurons) [3], we can train a neural network for a specific task. The training of the neural network depends on the network architecture and the nature of the problem studied, during the training phase, the input

Table 1 Inference matrix of the fuzzy controller

E	ΔE				
	NL	NS	ZE	PS	PL
NL	NL	NL	NL	NS	ZE
NS	NL	NL	NS	ZE	ZE
ZE	NL	NS	ZE	PS	PL
PS	ZE	ZE	PS	PS	PL
PL	ZE	ZE	PL	PL	PL

vector, and target output are given and the output of the neural network is compared with the target output [3, 8]. The general principle of learning algorithms is based on the minimization of a cost function, which can be defined as the quadratic of the differences between the outputs of the network and the target values [8], as it is shown on the Fig. 3. Artificial Neural Network technique is based on a learning defined as changing the synaptic weights of each interconnection in the network to update it, until the target error is reached. Generally, the back propagation method is used for adjusting the neural network weights during the training phase the neural network weights.

5.2 Neural Controller Applied on DSCIM

The MATLAB Neural Network toolbox is used to control the DSCIM given its ease of use and the results and performances that present. The proposed block used in this study consists of two neural networks: A Neural Identifier, which models the dynamics of the system, and a Neural Controller. The task of Neural Identifier is to model the dynamics of the system. For that, the Nonlinear Auto-Regressive Moving Average (NARMA) model is used. The NARMA model is an input–output representation of a nonlinear system in which a two-layer feed-forward network is used as the identifier [7, 9, 10]. After identifying the model of the system to monitor, it comes the turn of the Neural Controller, it is a feed-forward time-delay neural network and it consists of one hidden layer with eight neurons and an output layer. The training of the Neural Controller is done using the output of the Neural Identifier. After training the Neural Controller, the identifier could be taken off the system and the Neural Controller starts feeding the system with the appropriate signal [9].

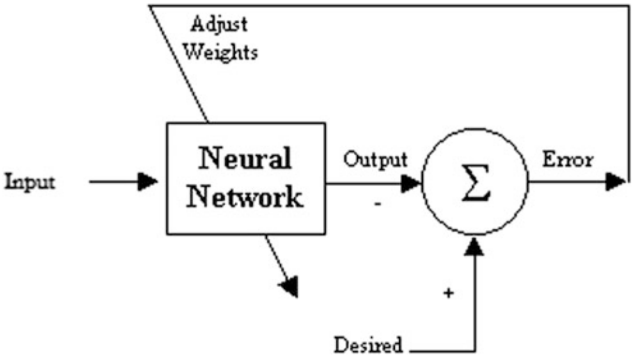

Fig. 3 Learning principle of neural networks

6 Simulation Results

Simulations were carried out using the software MATLAB/Simulink for a simulation time T = 1 s. The motor under investigation is 7.5 KW, 380-V, and 50 Hz, four poles, and three-phase double-squirrel cage induction motor.

6.1 DSCIM Associated with a Three-Phase Sinusoidal Supply

See Figs. 7, 8, and 9.

6.2 DSCIM Associated with the Speed Chain Control

See Figs. 10, 11, 12, and 13.

7 Results Interpretation and Discussion

The simulation results are performed for a simulation time T = 1 s.

The figures presented in Sect. 6.1 show the speed, torque, and stator currents of the DSCIM associated with a three-phase sinusoidal supply with and no load torque. From the Figs. 4, 5, and 6, we noticed that the electromagnetic torque and the stator currents tend toward a value close to zero after the transient regime and the rotation speed tends to the nominal value which is (w = 314 rad/s) (Figs. 7, 8, and 9).

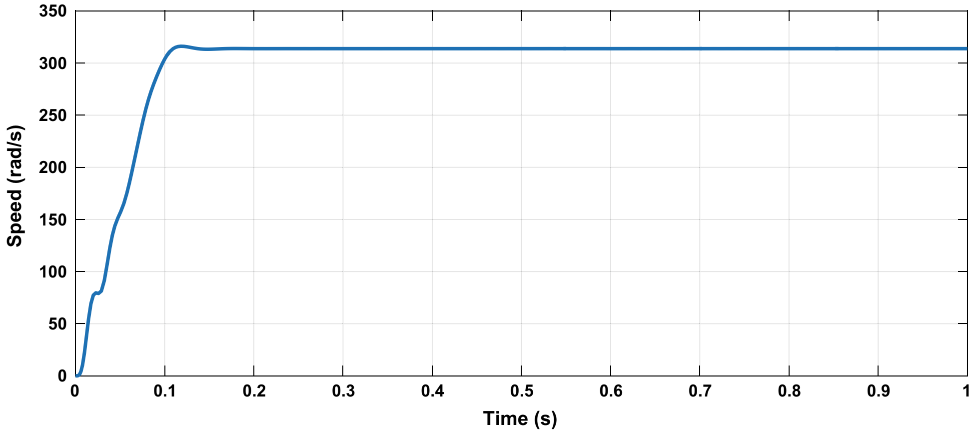

Fig. 4 Speed of DSCIM with no load

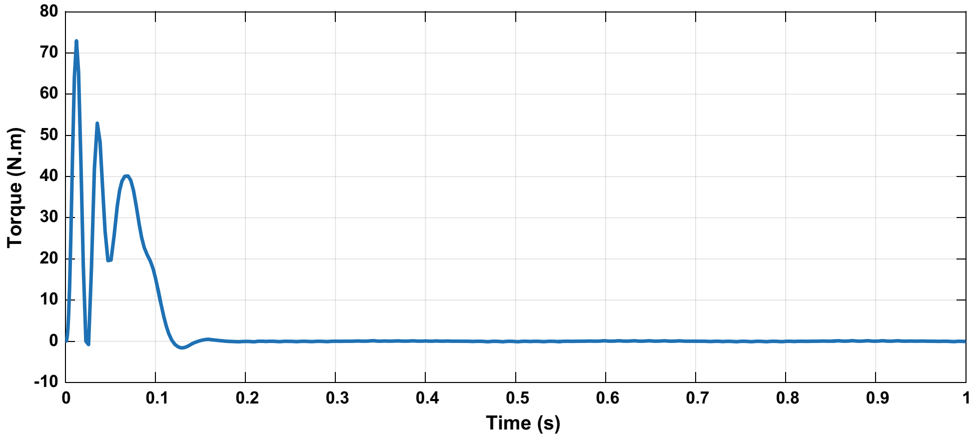

Fig. 5 Torque of DSCIM with no load

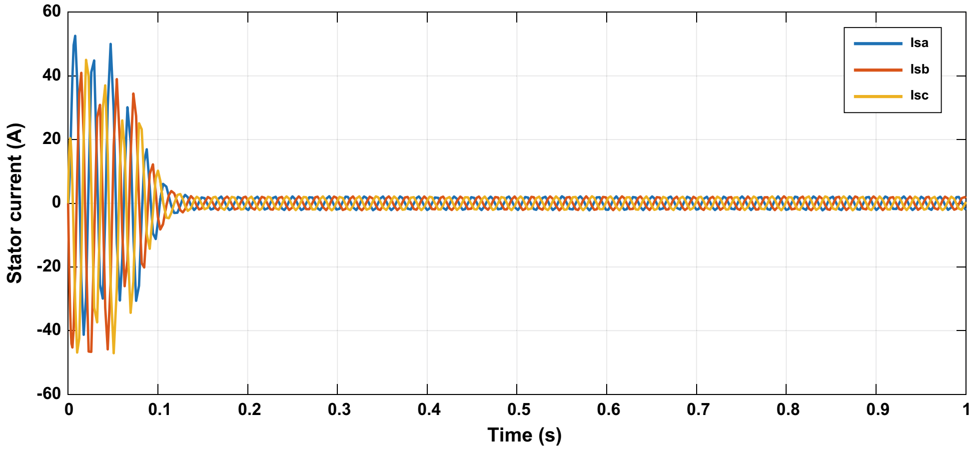

Fig. 6 Stator currents of DSCIM with no load

After applying a fixed load Tr = 20 N m applied at t = 0.4 s, the speed and the stator currents change direction and the electromagnetic torque follows the fixed load value.

Section 6.2 shows the response of the system following a trapezoidal set point while the machine is controlled by the PI, Fuzzy Controller, and the Neural controller.

Figures 10, 11, 12, and 13 show the rotation speed of the machine during the parametric variation and rotation inversion at t = 0.5 s. In Fig. 12, the rotor resistance was increased to 50% over the nominal value whereas in the Fig. 13, the moment of inertia was up to 50% over the nominal value.

Fig. 7 Speed of DSCIM with Tr = 20 N m applied at t = 0.4 s

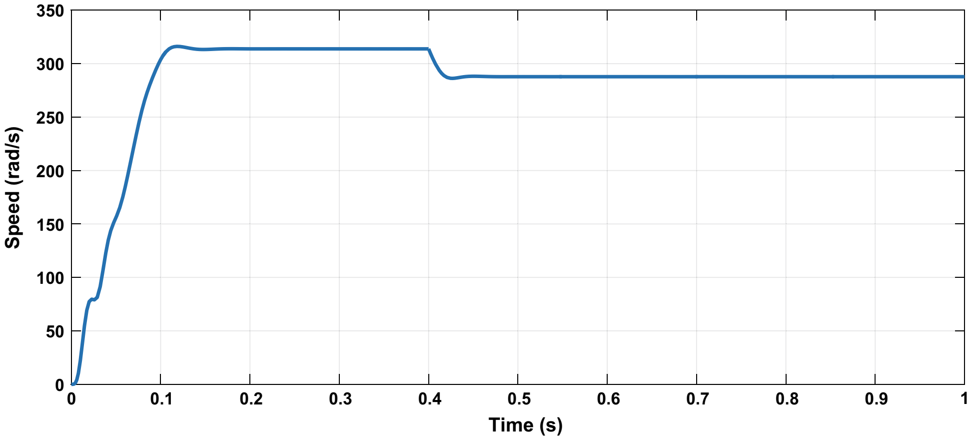

Fig. 8 Torque of DSCIM with Tr = 20 N m applied at t = 0.4 s

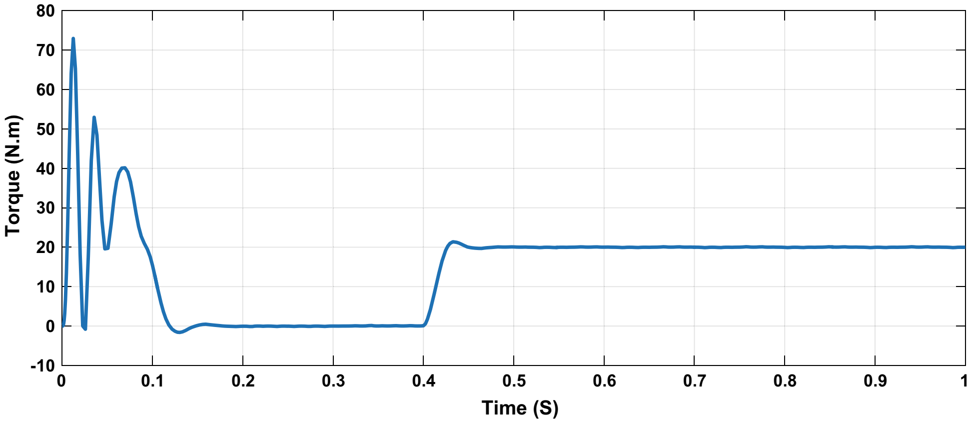

Fig. 9 Stator currents of DSCIM with Tr = 20 N m applied at t = 0.4 s

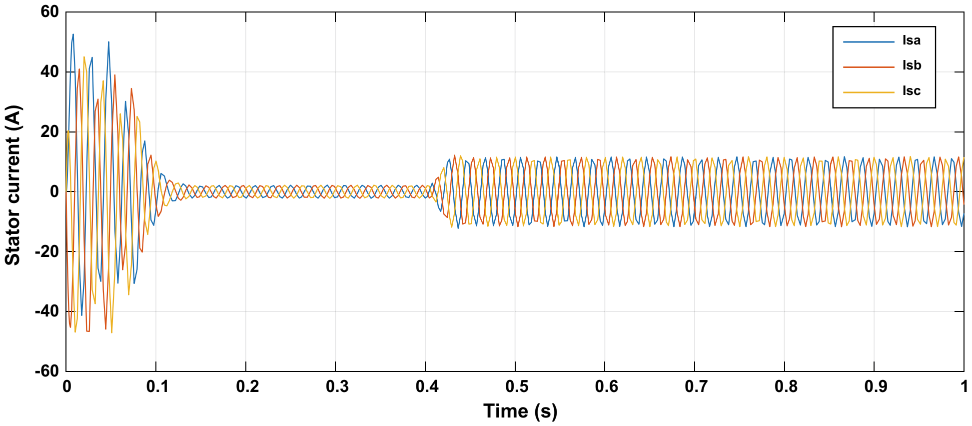

From the simulation results, we notice that the speed of the machine follows its reference and remains stable at the desired value even during the application of the fixed load torque. With a reversal of the direction of rotation, and with the application of a parametric variation for the rotor resistance (+50%) and for the moment of inertia (+50%), the response speed of the machine changes direction and well maintained at the desired value.

From the simulation results, we can say that the Neural controller present good performances in comparison with the PI controller and the Fuzzy controller when the machine is affected by the internal and external disturbances and it remains the fastest during a set point changing and it presents a high accuracy during acceleration and deceleration, and a less sensitivity to uncertainties disturbances.

Fig. 10 Speed of DSCIM with no load by the three controllers

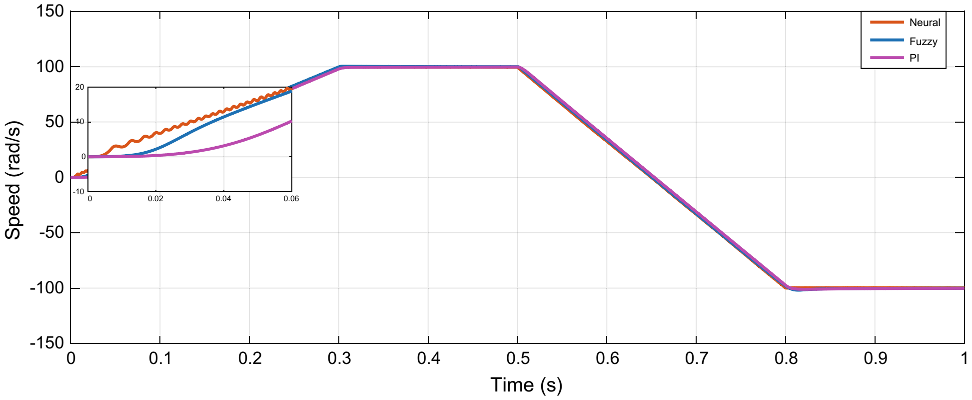

Fig. 11 Speed of DSCIM by the three controllers with Tr = 20 N m applied at t = 0.4 s

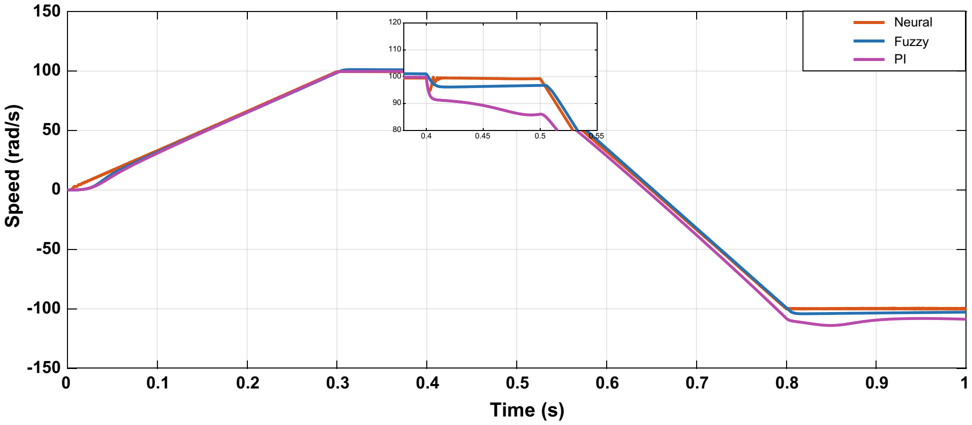

Fig. 12 Speed of DSCIM by the three controllers with Rr = 1.5 * Rrn

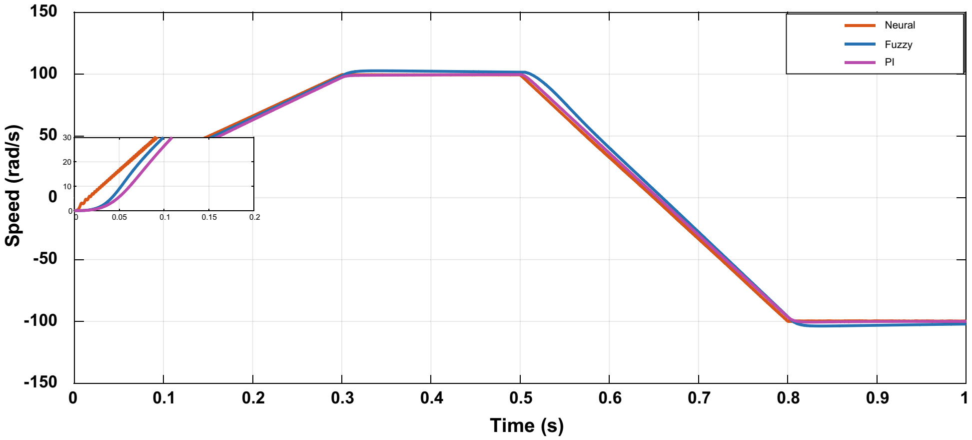

Fig. 13 Speed of DSCIM by the three controllers with J = 1.5 * Jn

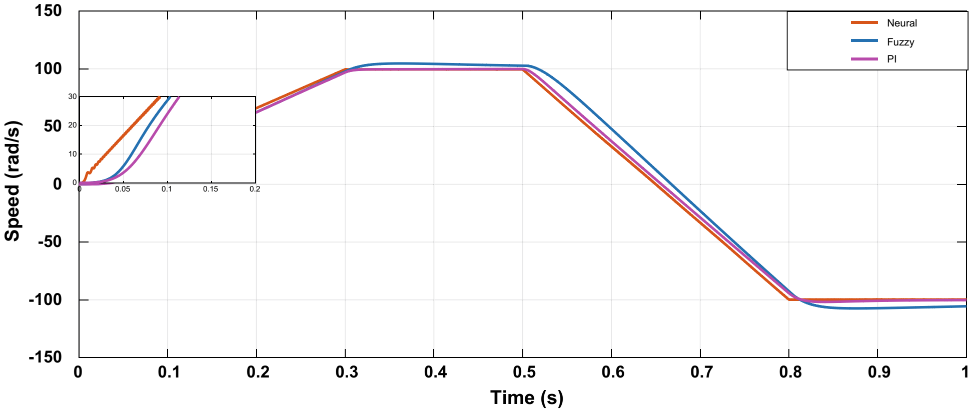

8 Conclusion

The Double-squirrel cage induction motor is a nonlinear system affected by parameters variation and unknown disturbances. The work was done in the form of a comparative study between the PI, Fuzzy, and the neural controller; it reveals the motivation to realize researches in the field of control by artificial intelligence techniques.

It is concluded that the neural controller had good performances face to parametric variations and to unknown disturbances comparing to the two other controllers. For that, it can be applied for the electric vehicle motorization based on Double-Squirrel Cage Induction Motor.

References

1. Makrygiorgou, J. J., & Alexandridis, A. T. (2017). Fuzzy logic control of electric vehicles: Design and analysis concepts. In: *2017 twelfth international conference on ecological vehicles and renewable energies (EVER)* (pp. 1–6). IEEE.
2. Arancibia, A., & Strunz, K. (March 2012). Modeling of an electric vehicle charging station for fast dc charging. In: *The IEEE proceedings on* industrial *electronics vehicle conference (IEVC)* (pp. 1–6).
3. Mediouni, H., El hani, S., & Ouachtouk, I. et al. (2017). Artificial neural networks applied on double squirrel cage induction motor for an electric vehicle motorisation. In: *2017 international conference on electrical and information technologies (ICEIT)* (pp. 1–6). IEEE.
4. Antonino-Daviu, J., Riera-Guasp, M., Pons-Llinares, J., Park, J., Lee, S. B., Yoo, J., et al. (2012). Detection of broken outer-cage bars for double-cage induction motors under the startup transient. *IEEE Transactions on Industry Applications, 48*(5), 1539–1548.
5. Gritli, Y., Lee, S. B., Filippetti, F., & Zarri, L. (2014). Advanced diagnosis of outer cage damage in double-squirrel-cage induction motors under time-varying conditions based on wavelet analysis. *IEEE Transactions on Industry Applications, 50*(3), 1791–1800.
6. Levi, E. (1997). General method of magnetising flux saturation modelling in d–q axis models of double-cage induction machines. *IEE Proceedings-Electric Power Applications, 144*(2), 101–109.
7. Menghal, P. M., & Laxmi, A. J. (Sept 2013). Application of artificial intelligence controller for dynamic simulation of induction motor drives. *Asian Power Electronics Journal, 7*(1).
8. Chan, T. F., & Shi, K. (2011). *Applied intelligent control of induction motor drives* (1st edn.). IEEE Willey Press.
9. Menghal, P. M., & Laxmi, A. J. (Sept 2013). Application of artificial intelligence controller for dynamic simulation of induction motor drives. *Asian Power Electronics Journal, 7*(1).
10. Khammar, F., Debbache, N. E. (2016). Application of artificial intelligence techniques for the control of the asynchronous machine. *Journal of Electrical and Computer Engineering*, Article ID 8052027, Algeria.

Hamza Mediouni was born in Khourigba, Morocco, in 1993. He received the M.S. degree in electrical engineering in 2016 from the Mohammed V University in Rabat, Morocco. Where he is currently working toward the Ph.D. degree in the Department of Electrical Engineering. Since 2017, his research interests are related to electrical machines, drives control, energy optimization, smart grid, and vehicle to grid systems.

Soumia El Hani Prof. Dr. IEEE Senior Member, received Engineering Degree in 1992 from Higher school of Mines-Rabat. She received the "Doctorat en Science" degree and the "Habilitation Universitaire" degree in Electrical Engineering, Automatic with honors, respectively, in 2003 and 2006 from Mohammed V University, "Ecole Mohammadia d'Ingénieurs" Morocco. Her research interests are in the area of Robust Control, Monitoring, and Diagnosis of Electromechanical Systems. She in charge of the research team "Energy Optimization, Diagnosis and control" EODIC, research Center in "Sciences et Technologies de l'Ingénieur et de la Santé". She is the author of several publications in the field of electrical engineering, including robust control systems, diagnosis, and control systems of Renewable Energy conversion.

She is the cofounder and the General Chair of the International Conference on Electrical and Information Technologies since 2015. She is the Scientific Committees member of IRSEC (Morocco), IEMDC 2017 Miami, ICSGCE since 2014 Malaysia. Soumia El Hani is a member of the Organizing and the Scientific Committees of several international conferences dealing with topics related to Renewable Energy, Electrical Machines and Drives. Professor Soumia El Hani is member of IEEE Power & Energy Society). Soumia El Hani is an Effective Member of the Moroccan SoroptimistAssociation and Founding Member and chair of the association 'l'Association Marocaine de la Recherche et de l'Ingénierie en Sciences et Technologies (AMARIST)".

She was the editor of the ICEIT2017 Proceedings, the coeditor of the ICEIT2016, ICEIT 2015 Proceedings. She is the author and coauthor of more than 50 papers which appeared in refereed specialized journals and symposia. She is the author of book chapters.

Moreover, she has supervised Ph.D. and Masters Theses dealing with different research topics concerned with her research interests. She has been the principal investigator and the project manager for research projects.

Ilias Ouachtouk was born in Foum Zguid-Tata, Morocco, in 1991. He received his M.S. degree in Electrical Engineering from the Mohammed V University in Rabat, Morocco, in 2014. Where he is currently working toward the Ph.D. degree in the Department of Electrical Engineering. Since 2015, his research interests include modeling and diagnosis of electrical drives, in particular, synchronous and asynchronous motors.

Imad Aboudrar was born in Chtouka Ait Baha-Agadir, Morocco, in 1993. He received the M.S. degree in electrical engineering in 2016 from the Mohammed V University in Rabat, Morocco. Where he is currently working toward the Ph.D. degree in the Department of Electrical Engineering. Since 2017, His research interests are related to control and management of a hybrid photovoltaic system.

Generic Client–Server Interfaces for Real-Time Remote Automatic Control Laboratory

Driss Filahi, Najib Bennis, and Soumia El Hani

Abstract

This paper constitutes a contribution in Distance Education field's (E-Learning), more precisely to the Distance Training by practical activities of the laboratory (E-Lab). Indeed, the majority of distance training platforms offer theoretical courses and a few practical activities which are essential in training theoretical Science and Technology. In this work, we propose a generic and open hardware/software architecture which permits remote access to a laboratory's equipment. We detail the implementation and the use of two user-friendly graphical interfaces using Internet/Intranet network and TCP/IP communication protocol. These interfaces designed in MATLAB environment, work both in intranet and internet network. It allows to a learner a real-time control and supervision to carry out all the practical activity according to a pedagogical scenario elaborated by the trainer. The functioning of these interfaces is illustrated by educational sessions articulated on the **P**roportional–**I**ntegral–**D**erivative (**PID**) regulation and the **G**eneralized **P**redictive **C**ontrol (**GPC**) of the temperature control system. The challenge is to elaborate a remote practical activity taking into the pedagogical effectiveness is accomplished in the proposed solution. The remote training platform equipped by a specific hardware and software, allows to achieve traditional laboratory experimentations.

Keywords

E-learning • E-lab • Matlab • Client/server architecture • TCP/IP • Automatic control • Supervision • PID • GPC

1 Introduction

Recently, enormous changes have been experienced in technological systems of information processing and communication commonly called Information and Communications Technology (ICT). In fact, since the appearance of ICT, there has been a revolution in the field of education and distance learning. Information and Communications Technology in Education (ICTE) covers the numerical tools and materials that can be used in teaching. They include a set of hardware and software designed and is used for remote practical activities (Petre et al. 2010). The first e-learning platforms provide theoretical training via the Internet through interactive courses. Remote lab is a Software/Material environment that lets students to experiment on devices from a remote location. Practical training, has not totally answered yet despite numerous platforms (Mucheta 2011). This last point can be seen as a real handicap in many fields, particularly in science and technology, where practical activities are crucial for technical education.

The development of the remote test bench highlights different advantages provided by the e-Lab concept:

- Avoid the duplicity of the laboratory's material, especially when they are expansive.
- Avoid to move experimental equipment from a laboratory to another;
- As soon as the distance learning session is open, the experimental situation should be simplified according to the learner's ability to progress at his own capacity.
- Avoid to expose the learner to corporal damages in the case of a false maneuver since he operates at a distance;

D. Filahi · N. Bennis (✉) · S. E. Hani
Enset of Rabat, University Mohammed V of Rabat, Rabat, Morocco
e-mail: n.bennisi@um5s.net.ma

D. Filahi
e-mail: driss.filahi@um5s.net.ma

S. E. Hani
e-mail: s.elhani@um5s.net.ma

S. El Hani and M. Essaaidi (eds.), *Recent Advances in Electrical and Information Technologies for Sustainable Development*, Advances in Science, Technology & Innovation, https://doi.org/10.1007/978-3-030-05276-8_17

- Provide the learner the ability to archive directly experimentation results done on his computer. The analysis of these results can be performed later;
- If experimentation activity is sufficiently complex, the learner has a freedom of investigation, which is very rarely granted to him during the traditional activities in the laboratory. So, he can by himself consider an experimental organization like to proceed by trial test or to repeat many similar attempts as long as he has access to the remote laboratory.

A remote laboratory of experimentation for both the trainer and the learner is no longer to be demonstrated today. There is a variety of educational activities in the field of distance education, but they are few to offer online training platforms that are incorporating practical activities. In (Petre et al. 2010), the projects are aimed at modeling a practical work remotely by developing an operational prototype that is developed in LabVIEW. These projects involve the remote control of simple electronic measuring instruments. The authors in (Larroque and Luthon 2016; Iftode and Fosalau 2013; Luthon and Larroque 2014) have proposed practical experiments to characterize remote electronic circuits based on a client/server architecture. The main limitation of these previous works does not really allow real-time control and observations since retrieval of the experimental results is achieved later. Remote control and remote manipulation in real-time and synchronization of communication between the server and the client is currently a challenge and a benefit for remote experimentation platforms. While remote virtual laboratories often use the LabVIEW software (Iftode and Fosalau 2013; Abu-Aisheh and Farahmand 2010; Bisoyi and Pati 2013; Tepelea et al. 2011) for supervision and instrumentation, there are also others based on MATLAB software (Suzana Uran and Karel Jezernik 2008; Abu-Aisheh and Farahmand 2010). Although the use of MATLAB seems rather rare in comparison with LabVIEW, it still holds a promise when it comes to the practical work of automatic and signal processing requiring a consistent numerical computing volume.

Our work is a contribution to the development of experimental tools for remote practical training. To provide a generic platform virtual laboratory type that will result in two graphical interfaces for remote manipulation in automatic discipline, we focus on the underlying following issues:

- How to achieve remote practical activities with pedagogical effectiveness?
- What is the communication protocol that guarantees a reliable transmission without losing any information between the client (Learner) and the server (Former)?
- How fully exploit the potential of numerical computing in real-time using Matlab software?
- How this solution applied to automatic field can be extended as easily as possible to others disciplines in the scientific and technical field?

The present work answers to these questions. We have organized the presentation of this paper in several sections. The overall architecture of the developed interfaces is introduced in Sect. 2. Section 3 is devoted to their software implementation. The E-PIDMAT and E-GPCMAT graphical interfaces resulting from the general architecture are detailed in Sect. 4. In this same section, a pedagogical scenario is described for carrying out a remote practical activity. Finally, in Sect. 5, we give some conclusions about the feasibility of our promising contribution in the e-learning field involving practical activities.

2 Software and Hardware Architecture Client/Server

To meet the above objectives, we have developed two prototypes for remote control laboratory on automatic field. These prototypes are based on the development of two Human–Machine Interfaces (HMI) developed in MATLAB

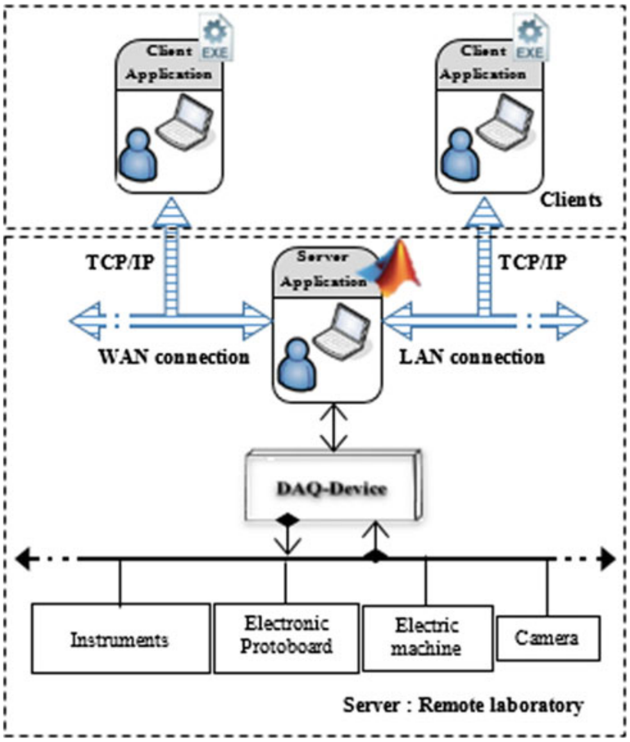

Fig. 1 General architecture of the client/server remote laboratory

environment. The software/hardware architecture is shown in Fig. 1. This is a Client/Server architecture type.

The server and client are connected to this architecture via the Intranet (LAN)/Internet (WAN) network using TCP/IP protocol (Larroque and Luthon 2016; Garcia-Zubia and Alves 2011). In this architecture, the server ensures real-time receipt of orders from the client controls the instrumentations and returns the results to the client. This one performs the experimentation using graphical interfaces. The functionalities of these interfaces will be described in more detail in Sect. 4. More details are given in (Driss Filahi et al. 2017).

2.1 Implementation and Supervision Software

The software tool chosen for the development of remote experimentation prototypes is MATLAB (The MathWorks, Inc., www.mathworks.com). This choice is dictated by the fact that MATLAB has a great computational capacity to deal with problems related to Automatic control field. Thanks to "Graphical User Interface—GUI" tool of MATLAB, it was possible to design a friendly Human–Machine Interfaces ensuring to a learner an easy remote supervision of material's laboratory and to a server the monitoring of all the requested tasks. The graphical interfaces E-PIDMAT and E-GPCMAT applications are developed using MATLAB software and Graphical User Interface.

Integration of Toolbox (Instrument Control Toolbox) allows communication between computers and devices by the availability of several protocols such as TCP/IP, UDP, and VISA, in our case, the TCP/IP protocol will be used to ensure Client/Server communication.

It should be noted that the E-PIDMAT and E-GPCMAT graphical interfaces will be generated by executable files that have been previously provided to the client. The idea is to exploit for this purpose the "Matlab Compiler" tool that allows for sharing applications such as an executable or a library. These interfaces are designed so that they are operated on the cient computer without MATLAB software will be installed and no prerequisite is requested to the learner. Indeed, it is a pedagogical intention that the learner focuses on the objectives of the practical activities related to the automatic control problem, rather than on Matlab software itself. These executable files are available individually to users or downloaded from an e-learning platform.

2.2 TCP/IP Protocol in Matlab

The TCP/IP protocol for communication between remote computers is implemented in MATLAB environment. It ensures the transmission and reception of various types of data through Internet/Intranet. The main reason for choosing this communication model is the reliability it provides for the exchange of data between the client application and the server application.

The first task of the client and the server applications is to establish a communication channel via the Internet/Intranet network using the TCP/IP protocol.

In order to guarantee practical remote in real-time situation, transmission and reception of data between the server and the client will be clocked sequentially with a timeout equal to 1 µs. MATLAB offers only the possibility of exchanging information between two remote computers, making it necessary to formulate a specific procedure for communication timing between the client and the server, without loss of exchanged information. The proposed procedure also ensures an exchange of real-time data, which gives a more realistic dimension to manipulation like as in the traditional case. Figure 2 shows the organization of the sending and reception of a data packet. Each packet includes three parts: digital data, binary data, and empty buffers. The digital data contains the different information to transmit, such as the set point, the command, the measurement or information about them (vector size for example). The binary data contain end-of-task verification information to ensure synchronization so that the destination computer correctly receives the transmitted data. The empty buffer sections separate the sent data. The MATLAB **strsplit** command points to the empty packets of the data packet, which finally lets to reconstruct the originally sent information.

In this procedure, some packets of information received by either the server or the client may be empty. As a

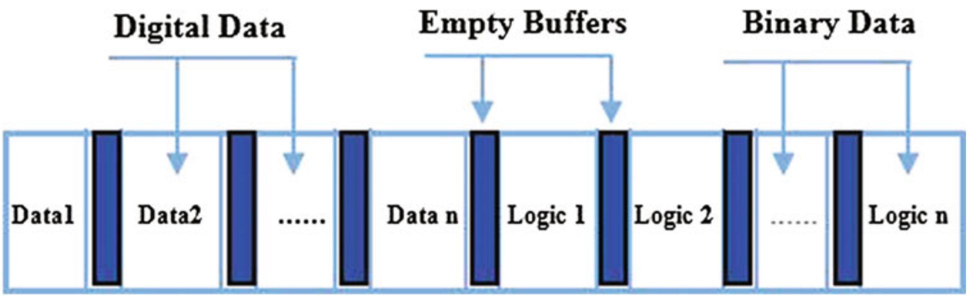

Fig. 2 Synoptic diagram of the packet sent at each sampling step

solution, we have implemented an algorithm that is executed at each sampling step whose purpose is to precede any information emitted by its size. This allows the receiver of the information (client or server) know the total size of the sent data.

2.3 Experimental and Instrumentation Equipment

Our architecture is based on the availability of a DAQ device and an accessible process through its electrical input/output. The example of equipment that is used to carry out remotely the practical activities is shown in Fig. 3:

The experimental test bench consists mainly of the following elements:

- An accessible laboratory process through its inputs/outputs. Here, a temperature control process.
- A DAQ device for the acquisition of measurement signals from the continuous process and the sending of commands to it. This card must be imperatively exploitable in the MATLAB environment. In our case, we used a card with several analogs and digital inputs/outputs connected to the computer server via the USB port.

It should be mentioned that in the general architecture, the principle of the server process communication system is independent of the nature of the used card. Likewise, this architecture is independent of the nature of the process to be controlled because it is assumed to have been accessible by its input/output. The temperature control process that is used here can be replaced by any another process as illustrated in Fig. 4.

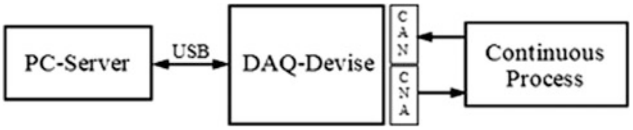

Fig. 4 Server and the experimental equipment at the remote laboratory

3 Software Programming

3.1 Description of the Server Application

The PC server is the main element in e-lab architecture. It is at the service of the learner customer to carry out all the tasks related to the practical activities. The server executes an M-file program developed under MATLAB, a flowchart of which is given in Fig. 5. It schematizes the principle of the operation of two applications that we intend to develop, here, as well as the different entrusted tasks to the server.

The developed functional organization is constructed in such a way that the model of the remote practical work is generic and reusable to implement different types of a practical work. The program at the server level is divided into two main parts: the first is the invariable and independent character of the practical activity. Its purpose is to establish a secure password connection between the client and the server via the network, as well as the modalities for

Fig. 3 Synoptic diagram of the communication between the server and the controlled process

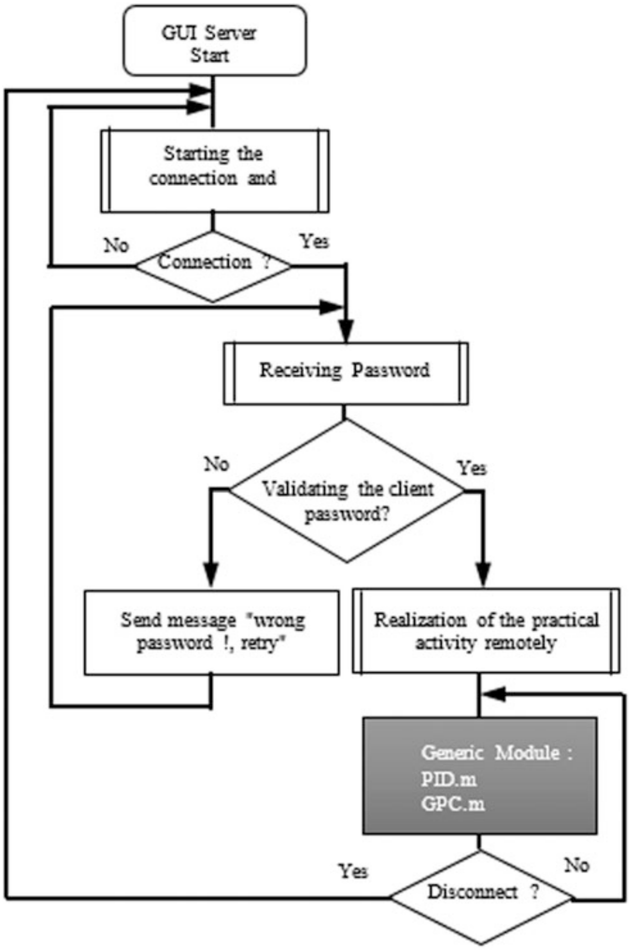

Fig. 5 Organizational chart of differences tasks implemented at the server level

the information exchange between client/server. This exchange mainly concerns the transmission, acquisition, processing, recording, and display of various data in real time. The second part of the server program offers the trainer, who is the pedagogical manager of the Practical Works, the possibility to modify the different themes without limits and to insert new experiments easily. Due to this organization, we have easily implemented two applications for Remote Practical Work in the Automation field. This generic aspect also allows for the setting up of a multiplicity of themes, particularly in the field of science and technology. This is why we consider this organization generic and open.

3.2 Description of the Client Application

Developed client interfaces for remote, hands-on activities are generated from the executable files of **.exe** extension. The next section will be devoted to a more detailed description of these graphical interfaces.

The client learner has the executable programs and documentation needed to install them on his personal computer as well as the Runtime version of Matlab. These programs can be provided with a physical medium (CD-ROM, USB flash memory) or downloaded from a remote training platform. In addition to these programs, the client learner will also have a teaching manual on the practical activity. In our case, the prototype applications of Remote Practical Work have been previously compiled in order to create two executable e-PIDMAT.exe and e-GPCMAT.exe relating, respectively, to the industrial regulation by the PID controller and the GPC predictive regulation. Indeed, according to the targeted practical activity, the client has two packages E-PIDMAT_pkg.exe and E-GPCMAT_pkg.exe, which it must run on Client's personal computer to generate, respectively, E-PIDMAT.exe and E-GPCMAT.exe. Each of these executions also generates MATLAB Compiler Runtime (MCR), necessary for the use of these interfaces.

The executable once installed on the client PC, generate HMI-like graphical interfaces for remote manipulation according to the teaching manual related to both hands-on and in-class activities.

The activity diagram of the client application is shown in Fig. 6. After executing GUI, the user sends to the server his/her choices relating to the experience he/she wishes to conduct. Following a pedagogical scenario, the learner can do: (i) the launch of the tests and the real-time visualization of the experimental results. This operation can be repeated as many times as desired by modifying the parameters of the experimentation according to its convenience; (ii) downloading the various experimental results such as the control and measurement signals. These results will be used to writing a report that will be evaluated later by the trainer.

4 Description of the E-PIDMAT and E-GPCMAT Applications

Although the techniques of process regulation are numerous, we have retained within the framework of these work two techniques that are known by their effectiveness and notoriety, exactly, the PID command implemented in the application named E-PIDMAT and the command GPC Implemented in the application named E-GPCMAT.

The functionalities of these interfaces are adapted according to the desired level of learning and the achievable pedagogical objective. Indeed, according to these criteria, each of these interfaces can be exploited partially or fully as soon as they are designed by blocks that operate independently of one another. The main functionalities of these interfaces include:

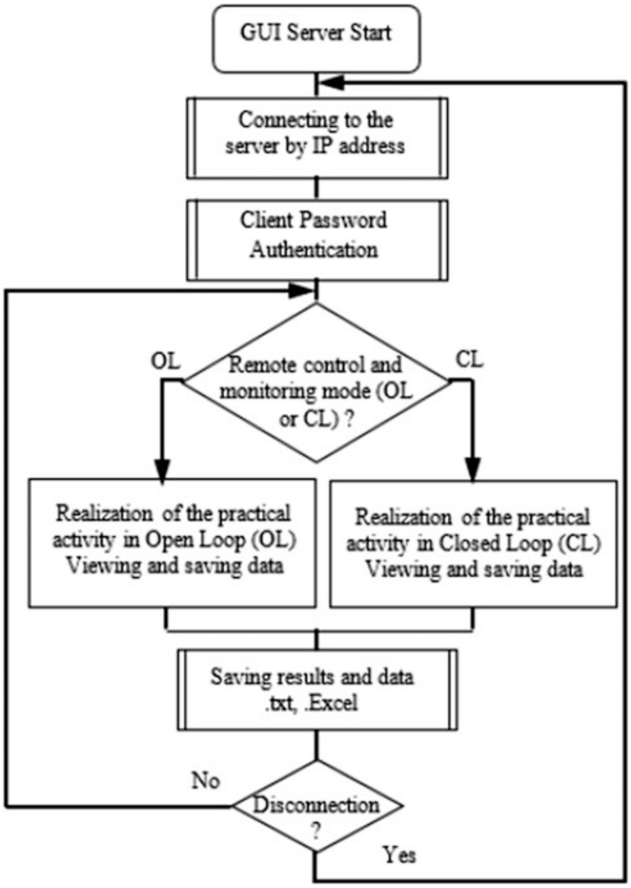

Fig. 6 An organizational chart of differences tasks implemented at the client level

- Exploit the open-loop control block to acquire the response of the process to a constant or variable command. This allows for a dynamic and permanent analysis of the process, as well as the identification of a parametric model;
- Use the closed-loop control block to acquire the closed-loop response according to the choice of the PID controller parameters in the application (E-PIDMAT) or the GPC controller synthesis parameters in the E-GPCMAT application.

In both operations, the learner has the option of saving the control and measurement signals for a later operation in .txt files.

4.1 E-PIDMAT Application

The graphical interface relating to E-PIDMAT generally deals with the operation of an open-loop and closed-loop process by the PID controller. Figure 7 shows screenshot of the **B1**: Connection block and experiment parameters. **B2**: Open-Loop Control block. **B3**: Closed-Loop Control block. **B4**: Display and backup block.

The interface is composed mainly of several blocks: (i) Block of connection to the server introducing its IP address and the common communication port. (ii) Authenticating the learning user with a password previously assigned to a client. (iii) Choice of whether to record input/output responses. (iv) Limitation of the control generated by the PID controller (1). (v) The selection of the P, PI, and PID regulator and their parameters with the option of adding or not a low-pass filter. (vi) Real-time display of the evolution of input/output signals.

$$R(p) = K(1 + \frac{K_i}{p})(1 + T_d p)(\frac{1}{1 + \tau p}) \qquad (1)$$

The graphical interface has a help menu so that the user can consult it at any time to know its different functionalities. The teacher or supervisor can follow the progress of the practical TP activity through a graphical interface generated by the PC server. Figure 8 shows an example of the server interface in which connection and authentication are valid and that the learner has performed a process test.

4.2 E-GPCMAT Application

The second type of envisaged control is the Generalized Predictive Control (GPC) (Clarket et al. 1987). It is recalled that the implementation of this command is based on a parametric model of the CARIMA type (Controlled Auto-Regressive Integrated Moving Average) as given below:

$$A(q^{-1})y(t) = q^{-d}B(q^{-1})u(t-1) + \frac{e(t)}{\Delta(q^{-1})} \qquad (2)$$

The E-GPCMAT application relates to the GPC command. Some of its features are similar to those of E-PIDMAT. It also allows for an easy entry of the various parameters of the GPC command. In addition to the block for open-loop control of the same process of the E-PIDMAT interface, E-GPCMAT offers full control possibility and remote monitoring of the closed-loop control systems. The learner entered the GPC controller parameters namely the minimum and maximum prediction horizon, the control horizon, and the weighting parameter on the command. Figure 9 shows a situation of the e-GPCMAT interface of a correctly established connection and the result of a closed-loop control temperature.

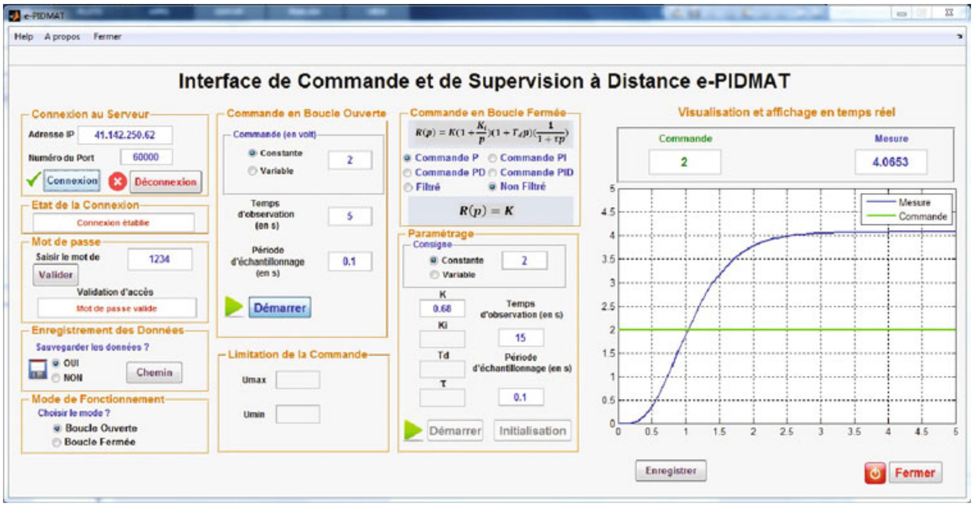

Fig. 7 Client application interface E-PIDMAT

Interface de Commande et de Supervision à Distance e-PIDMAT

Connexion au Serveur
Adresse IP: 41.142.250.62
Numéro du Port: 60000
Etat de la Connexion: Connexion établie
Mot de passe
Saisir le mot de: 1234
Validation d'accès: Mot de passe valide
Enregistrement des Données
Sauvegarder les données ? ● OUI ○ NON
Mode de Fonctionnement
Choisir le mode ? ● Boucle Ouverte ○ Boucle Fermée

Commande en Boucle Ouverte
Commande (en volt): ● Constante ○ Variable: 2
Temps d'observation (en s): 5
Période d'échantillonnage (en s): 0.1
Limitation de la Commande
Umax:
Umin:

Commande en Boucle Fermée
$R(p) = K(1 + \frac{K_i}{p})(1 + T_d p)(\frac{1}{1+\tau p})$
● Commande P ○ Commande PI ○ Commande PD ○ Commande PID ○ Filtré ● Non Filtré
$R(p) = K$
Paramétrage
Consigne: ● Constante ○ Variable: 2
K: 0.68
Ki:
Td:
T:
Temps d'observation (en s): 15
Période d'échantillonnage (en s): 0.1

Visualisation et affichage en temps réel
Commande: 2
Mesure: 4.0653

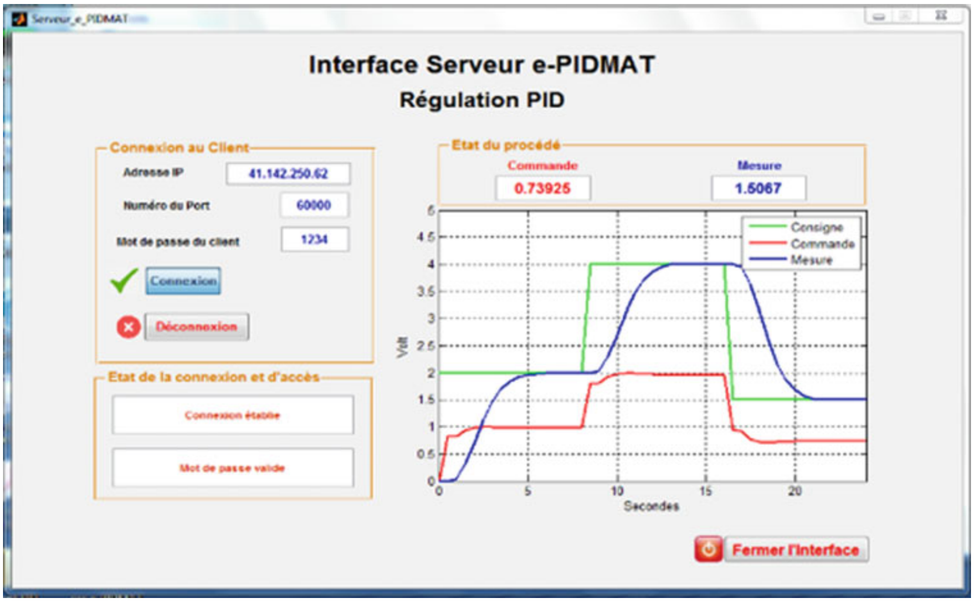

Fig. 8 Remote monitoring E-PIDMAT server interface

Interface Serveur e-PIDMAT
Régulation PID

Connexion au Client
Adresse IP: 41.142.250.62
Numéro du Port: 60000
Mot de passe du client: 1234
Etat de la connexion et d'accès: Connexion établie
Mot de passe valide

Etat du procédé
Commande: 0.73925
Mesure: 1.5067

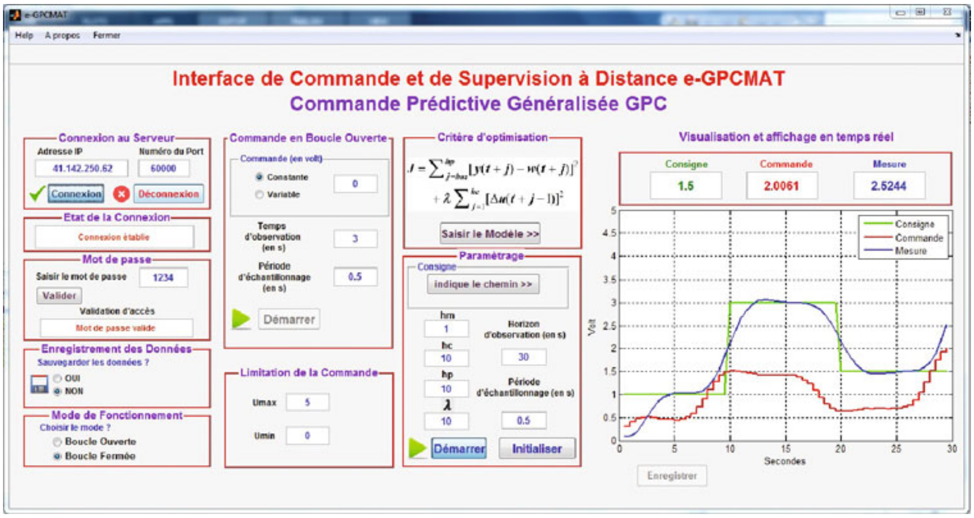

Fig. 9 Graphic Interface E-GPCMAT client side

Interface de Commande et de Supervision à Distance e-GPCMAT
Commande Prédictive Généralisée GPC

Connexion au Serveur
Adresse IP: 41.142.250.62
Numéro du Port: 60000
Etat de la Connexion: Connexion établie
Mot de passe
Saisir le mot de passe: 1234
Validation d'accès: Mot de passe valide
Enregistrement des Données
Sauvegarder les données ? ○ OUI ● NON
Mode de Fonctionnement
Choisir le mode ? ○ Boucle Ouverte ● Boucle Fermée

Commande en Boucle Ouverte
Commande (en volt): ● Constante ○ Variable: 0
Temps d'observation (en s): 3
Période d'échantillonnage (en s): 0.5
Limitation de la Commande
Umax: 5
Umin: 0

Critère d'optimisation
$$J = \sum_{j=hm}^{hp}[y(t+j) - w(t+j)]^2 + \lambda \sum_{j=1}^{hc}[\Delta u(t+j-1)]^2$$
Paramétrage
Consigne
hm: 1
hc: 10
hp: 10
λ: 10
Horizon d'observation (en s): 30
Période d'échantillonnage (en s): 0.5

Visualisation et affichage en temps réel
Consigne: 1.5
Commande: 2.0061
Mesure: 2.5244

To introduce the model's parameters (2), a secondary interface is generated by the main one. It allows the learner for capturing the parameters of the discrete model of the CARIMA process. It is specified that these parameters may be resulted either from prior identification of the method by using the "Open loop of E-GPCMAT" block or provided by the teacher. A remote monitoring E-GPCMAT server interface analog to E-PIDMAT server interface is available on the server side.

4.3 Teaching Scenario

The objective is to create through the network, sessions of relocated practical activities. The protagonists of remote practical activity are, on the one hand, the learner client who is equipped with installed application on his computer, and the trainer who is responsible for this activity on the other hand. The first one can be located anywhere connected to Internet; the second is located at the remote experimentation laboratory equipped also with Internet. In our case, the remote laboratory is the automation laboratory of ENSET (http://enset.um5.ac.ma/).

The client learner, provided with both the IP address of the server and the password that is provided with by the trainer, connects with the client application and performs at distance the practical activity according to a pedagogical scenario as well as in conventional situation. The student in remote situation has to follow the six phases cited below:

- Download the manual of the practical activity
- Installing the Client Application E-PIDMAT and/or E-GPCMAT
- Preparation of the theoretical part if requested by the trainer
- Connecting to remote laboratory
- Accomplishment of the practical activity
- Writing and online submission of the practical activity report.

As a perspective to this work, we plan to introduce the sound and the video to bring more reality to remote experiments.

5 Conclusion

In this work, we were interested in the design and realization of two graphical interfaces that allow enables students do real-time control experiments from a remote location (e.g., their homes, Campus) using internet. In our development, the Automatic Process Control has aroused our interest. Based on a generic and open architecture, other practical activities can be easily extended in other the field of Science and Technology.

They provide user-friendly accessibility for remote monitoring and control of various laboratory equipment. Tested in real and different situation, they have given a satisfactory feasibility. Virtually, all aspects that are related to automatic control are supported by the richness in their functionality. E-PIDMAT and E-GPCMAT graphical interfaces are implemented in MATLAB environment. This choice is largely justified by its user-friendliness and its adaptation to the automatic discipline.

The main contributions in e-Lab field can be summarized as follows:

- Client graphical interfaces provide complete real-time remote monitoring and control.
- No specific commercial equipment is suitable for remote control except a DAQ device and two computers, one of which acts as computer server and the other as computer client.
- Generic interfaces are independent of process control equipment, as long as it is assumed physically accessible by electrical input/output. They can be used to generate other client interfaces. In our development, we have easily switched from E-PIDMAT to E-GPCMAT interfaces by changing only the Closed-Loop Control part and its parameters.
- Applications do not require the installation of MATLAB software on the client computer. These applications are installed from executable files. No prerequisites for MATLAB are required to carry out the practical activities.
- Applications operate in both LAN and WAN network. This functionality gives of course a very wide dimension to the remote access equipment.

References

Petre, E. A., Luthon, F., Larroque, B., Dibon, P., & Fiton, J. M. (Nov 2010). LaboREM: Laboratoire flexible pour instrumentation déportée et travaux pratiques à distance. In: 7eme REAL Rencontre Europe Amérique Latine, Colombie.

Mucheta, D. (2011). Plate-forme pour travaux pratiques à distance sur le Web. Thèse de doctorat soutenue à l'Université de Ferhat Abbas de Sétif, Algérie.

Larroque, B., Luthon, F. (2016). LaboREM: de vrais TP d'électronique Oui mais à distance. Congrès National de la Recherche des IUT (CNRIUT'2016), Nantes, 8–9 Juin.

Iftode, L., Fosalau, C. (2013). Analysis of data transmitted between the server and the client through different types of communication. Publicat de Universitatea Tehnica Gheorghe Asachi din Iasi, Fasc. 1 (pp. 105–118). ISSN 1223-8139.

Matlab. https://ch.mathworks.com/fr/products/control.html.

Bisoyi, A., Pati, U. C. (March 2013). Implementation of ON/OFF and PID controller using TCP Protocol Based on Virtual instrumentation. *International Journal of Advanced Computer Research, 3*(8). ISSN No. 2249-7277

Uran, S., & Jezernik, K. (Feb 2008). Virtual laboratory for relative control design experiments. *IEEE Transactions on Education, 51* (1), 69–75.

Luthon, F., & Larroque, B. (2014). LaboREM: A remote laboratory for game-like training in electronics. *IEEE Transactions on Learning Technologies, Institute of Electrical and Electronics Engineers*, 1–13.

Abu-Aisheh, A., & Farahmand, F. (2010). LabVIEW-based integrated virtual learning platform. In*: 10th IEEE international conference on advanced learning technologies.* Sousse, Tunisia.

Garcia-Zubia, J. A. (2011). Using remote labs in education: Two little ducks in remote experimentation. University of Deusto, Bilbao, Spain. ISBN 978-84-9830-398-8.

Tepelea, L., Gavrilut, L., Neamtu, O., Gergely, E., & Gacsádi, A. (Oct 2011). A LabVIEW-based soundcard interface for e-laboratory. In: 17th building services mechanical and building industry days, International conference, Hungary.

Clarket, D. W., Mohtadit, C., & Tuffs, P. S. (1987). Generalized predictive control—Part I. The basic algorithm. *International Federation of Automatic Control, Automatic, 23*(2), 137–148.

Fillahi, D., Bennis, N., & El Hani, S. (2017*). International Conference on Electrical and Information Technologies (ICEIT)* (pp. 15–17). Rabat, Morocco.

ENSET of Rabat, University Mohammed V of Rabat, Morocco. http://enset.um5.ac.ma/.

Driss Filahi is a Ph.D. candidate at ENSET of Rabat of Mohammed V University, Morocco. He is attached to research team "**EODI**C: Energy Optimization, Diagnosis and control". He has received Master's degree in Electrical Engineering at ENSET in 2016. His research interests include Automation and Remote Control.

Najib Bennis received his "D.E.S" degree in Automatic control of distributed systems in 1986 from the University of Nantes, France in 1986. He received the "Doctorat en Science" degree in Automatic Control with honors in 2014 from Mohammed V University. Currently, he is the professor at Higher School of Technical Education (ENSET of Rabat, Morocco). His areas of interest include LMI optimization, large-scale systems control, identification systems, decentralized control, and their applications. He is attached to research team "**EODI**C: Energy Optimization, Diagnosis and control" attached to Research Center "**STIS**: Sciences et Technologies de l'Ingénieur et de la Santé". He is author and coauthor of several publications in the field of robust control applied to industrial and agricultural process. He is co-organizer of the International Conference on Electrical and Information Technologies ICEIT since 2015. He is a permanent member of the Scientific Committee of "Conférence Internationale en Automatique & Traitement de Signal" since 2018. He is also the member of "**AMARIST**: Association Marocaine de la Recherche et de l'Ingénierie en Sciences et Technologies". He has received several certificates for his contribution in reviewing of Elsevier's journals.

Soumia El Hani Prof. Dr. IEEE Senior Member, received Engineering Degree in 1992 from Higher school of Mines-Rabat. She received the "Doctorat en Science" degree and the "Habilitation Universitaire" degree in Electrical Engineering, Automatic with honors, respectively, in 2003 and 2006 from Mohammed V University, "EcoleMohammadiad'Ingénieurs" Morocco. Her research interests are in the area of Robust Control, Monitoring and Diagnosis of Electromechanical Systems. She in charge of the research team "Energy Optimization, Diagnosis and control" EODIC, Research Center in "Sciences et Technologies de l'Ingénieur et de la Santé". She is Author of several publications in the field of electrical engineering, including robust control systems, diagnosis, and control systems of Renewable Energy conversion.

She is the cofounder and the General Chair of the International Conference on Electrical and Information Technologies since 2015. She is the Scientific Committees member of IRSEC (Morocco), IEMDC 2017 Miami, ICSGCE since 2014 Malaysia. Soumia El Hani is a member of the Organizing and the Scientific Committees of several international conferences dealing with topics related to Renewable Energy, Electrical Machines and Drives. Professor Soumia El Hani is member of IEEE Power & Energy Society. Soumia El Hani is an Effective Member of the Moroccan Soroptimist Association, and Founding Member and chair of the association "l'AssociationMarocaine de la Recherche et de l'Ingénierie en Sciences et Technologies (AMARIST)".

She was the editor of the ICEIT 2017 Proceedings, the coeditor of the ICEIT 2016, ICEIT 2015 Proceedings. She is the author and coauthor of more than 50 papers which appeared in refereed specialized journals and symposia. She is the author of book chapters.

Moreover, she has supervised Ph.D. and Master's Theses dealing with different research topics concerned with her research interests. She has been the principal investigator and the project manager for research projects.

Toward a New Broadcasting Protocol to Disseminate Safety Messages in VANET

Assia Naja, Mohammed Boulmalf, and Mohamed Essaaidi

Abstract

VANETs are a kind of MANETs, where vehicles communicate among themselves via a vehicle-to-vehicle (V2V) communication, or with other devices located on the roadsides (RSU: Roadside Unit) via vehicle-to-infrastructure (V2I) communication. Some devices called on-board units (OBUs) are installed in each vehicle, and work in ad-hoc mode, being able to broadcast data through multiple hops to improve the driver's safety and the transportation efficiency. The fast actual trend of broadcasting protocols in VANET aims to provide additional comfort to the cars' drivers and be notified about a critical incident in the road. Therefore, the design of a good broadcasting protocol that performs well in all the previous criteria to avoid storm problem remains the most paramount task. The main issue is how to maximize the reachability while minimizing the rebroadcasting and the end-to-end delay. In most of the previous works, they either maximize the reachability or minimize the end-to-end delay, but they do not do both jointly. We present in this paper a novel method to calculate the waiting time of the counter-based and probability-based schemes, based on the speed of the vehicle, to assess the congestion level of the network. Simulation results through NS2 using 802.11P show that the new method performs better under different mobility scenarios (Grid and highway Map).

1 Introduction

Several unforeseen incidents can happen daily on the roads, which threaten people's lives. Many drivers or pedestrians may be injured due to an accident or may even lose their lives, or it can simply generate a traffic jam case. If the vehicles were informed before getting into the situation, they can improve the quality of driving by changing the direction or choosing alternative solution. A vehicular ad-hoc network (VANET) has been approved as effective solution to improve road safety. This is done by disseminating warning messages among vehicles of the network. VANET is a distributed system composed of a number of vehicular nodes. It forms an instant network to communicate with each other by the means of wireless links without the need of deploying any infrastructure. This is because of their self-organization. Vehicle nodes in VANET use dedicated short-range communications (DSRC) standard to communicate with each other (Mohammed et al. 2007). VANET is a key component of intelligent transportation systems (ITS) that aims to reduce the higher number of accidents. It is a class of MANET, and it has various different characteristics than MANET, such as dynamic topology, due to the frequent topology changes, high mobility of nodes due to high speed of vehicle nodes, and frequent data exchange. It is worth noting that the VANET is not energy constrained contrary to MANET.

Vehicles communicate with each other via vehicle-to-vehicle (V2V) and via vehicle-to-infrastructure (V2I) which are used for inter-vehicle communication (IVC) (Al-Sultan et al. 2014). This is to evolve traffic conditions and accident preventions, which are the primordial applications of VANETs. IVC becomes an interesting area of research that grew exponentially during the past few years. Several applications were proposed in this context such as local danger warning, intersection collision alarm, real-time traffic information, or emergency warning for public safety (Muthamizh et al. 2014). Another example is

A. Naja · M. Essaaidi
ENSIAS, Rabat, Morocco
e-mail: essaaidi@ieee.org

A. Naja (✉) · M. Boulmalf
UIR, Rabat, Morocco
e-mail: assia.naja@uir.ac.ma

M. Boulmalf
e-mail: mohammed.boulmalf@uir.ac.ma

S. El Hani and M. Essaaidi (eds.), *Recent Advances in Electrical and Information Technologies for Sustainable Development*, Advances in Science, Technology & Innovation, https://doi.org/10.1007/978-3-030-05276-8_18

when a vehicle informs other drivers of eventual accident or a car in a dangerous situation by means of sending messages, vehicles can proceed toward another destination, or more the system can calculate an alternate route if it possesses a navigation system to avoid congestion (Hartenstein and Laberteaux 2009). These kinds of applications help to improve safety and comfort to the drivers. Broadcasting is the suitable mode of communication for VANETs and has a primordial role in several applications in VANETs. For example, if an accident occurs, a message must be sent to all the vehicles in the surroundings to avoid an expected congestion or traffic jams. Each node in the network resends each received packet. However, a blindly broadcasting may result in frequent contentions and collisions, which leads to a serious problem, often known as the broadcast storm problem (Tseng et al. 2002). Thus, to well design a broadcasting protocol, it must meet some requirements, such as performing well in all areas which is the challenging chore (Rural, Urban, Sparse, and Dense areas). The broadcasting protocol should also ensure a good reachability, which means that all vehicles in the area can receive the transmitted messages. The storm problem caused by redundant broadcasts must be tackled in the same design taking into account that emergency messages have to be sent without any latency. So, we have to consider different parameters when evaluating the performance of a broadcasting protocol under realistic conditions of roads.

Taking into consideration all these facts, numerous papers and articles were interested in these issues. In the article (Hartenstein and Laberteaux 2009), the authors have studied broadcasting protocols for the VANETs technology and addressed an algorithm that supports the fast dynamic changes of the architecture of VANETs implying a variant threshold parameters. The main aim was to minimize the number of redundant received messages while maintaining good latency and reachability. In (Altayeb and Mahgoub 2013), authors focus on the general outlines and goals of routing protocols of VANETs, provide classifications of them, then give summarized comparisons between different classes schemes and some limitations of each one, and addressed finally different issues in this domain. In (Altayeb and Mahgoub 2013; Lin et al. 2010), authors have studied types of routing protocols in VANET.

This paper discusses how serious is the broadcast storm problem and presents a novel scheme that solves the problems of the probability-based and counter-based schemes. The scenarios of simulation were varied for the performances analysis: The number of nodes, the speed, and scenario of simulation (If it is a grid or a highway scenario).

This paper is structured as follows: Sect. 2 presents a general overview of VANET, and Sect. 3 tackles the related work. Section 4 introduces our proposed method. Section 5 presents and discusses the simulation results of the proposed methods, compared with the other schemes (Counter-based and Probability-based protocols). Section 6 concludes the paper.

2 Background

2.1 IEEE 802.11P Standard

IEEE 802.11 standard protocols are a big help for VANET, even though they are not designed to operate in highly dynamic outdoor environments such as ITS. So in Al-Holou et al. (2018) they have evaluated the performance of IEEE 802.11b/g standards in indoor and outdoor environments. In terms of communication range, time-to-login, throughput, jitter time, delay time, and SNR were measured under different conditions. And finally they conclude that IEEE 802.11g was more suitable than IEEE 802.11b for IVC environments because of its higher communication range. For the developing of suitable communication protocols for ITS, the dedicated short-range communication (DSRC) was first proposed, in the unlicensed 902–928 MHz frequency range, to support electronic toll collection systems (Al-Holou et al. 2018; Dedicated Short Range Communications (DSRC) Service 2016; IEEE Computer Society LAN/MAN Standards Committee 2007). Even so in 1999, a new frequency spectrum of IVC and RVC has been assigned by the federal communication commission FCC. A new physical layer and medium access layer (MAC) have been specified by IEEE under the 802.11p group with the transmission range of 250 m (Kamini and Kumar 2010). In 2003, the commission put up the service and license rules for dedicated short-range communications (DSRC) service, specified under IEEE standard 802.11p, which operates in 5.9GHz frequency band from 5850 to 5925 MHz. DSRC reduces the channel bandwidth to 10 MHz to reduce the impact of multipath propagation and Doppler shift effects; moreover, DSRC adds four maximum allowable effective isotropic radiated power EIRP levels to extend its communication range (Al-Holou et al. 2018; Dedicated Short Range Communications (DSRC) Service 2016). IEEE 802.11p was developed to specify a complete set of protocols for Wireless Access in Vehicular Environments (WAVE) (Krishnamachari et al. 2001; Uzcátegui et al. 2009), so different protocols have been proposed for both vehicle-to-vehicle (V2V) and vehicle-to-infrastructure (V2I) communications.

2.2 VANET Architecture

The inter-vehicular communication (IVC) is the main component of ITS, and it includes both V2V and V2I (Al-Sultan et al. 2014):

- V2V: Vehicle can communicate with other vehicles directly through a wireless medium called WAVE. V2V is classified into two types of communications: One-hop communication (Direct communication between vehicles) and Multi-hop communication (Vehicles relies on other vehicles)
- V2I: Communication between vehicles and fixed equipment located along the road. Figure 2 shows existing V2V and V2I communication and mixed mode (V2V and V2I), which can be achieved using different technologies.

2.3 Components of VANET

The main components to attain the targets of vehicle infrastructure integration (VII)—the vision of the future-generation transportation system in US—are as follows (Dedicated Short Range Communications (DSRC) Service 2016; About ITS 2018):

- On-board equipment (OBE) is the tool installed in the vehicle to permit wireless communication between vehicles (V2V) or with infrastructure (V2I).
- Roadside equipment (RSE) is the installed equipment on a roadside infrastructure. It allows communication with vehicles and with the network subsystem, they are usually connected to the Internet, and they could participate as a distribution point for vehicles (Altayeb and Mahgoub 2013; Karimi and Ithnin 2011).
- Network subsystem allows roadside equipment to communicate with each other and have access to Internet.

Figure 1 illustrates the main components to attain the targets of vehicle infrastructure Integration VII.

2.4 Applications of VANETS

It was developed in order to improve primarily safety and comfort of passengers, security, and efficiency of transportation systems, and also enable new mobile applications and services for the entertainment of traveling public (Hartenstein and Laberteaux 2008). The major types of applications are as follows:

- Safety applications: These applications assist the drivers in handling the surrounding road, by monitoring approaching vehicles, unpredictable events, or potential danger nearby traffic environment through the exchange of information among vehicles (Kamini and Kumar 2010; Paul and Islam 2012; Lee et al. 2010). Safety applications are intersection collision warning, post-crash warning, emergency electronics brake lights, road condition information, traffic signal violation, emergency warning signals, and location tracking (Kamini and Kumar 2010; Mittal and Vashist 2014).
- Comfort applications: Enhancing the degree of convenience of drivers, they are principally of traffic

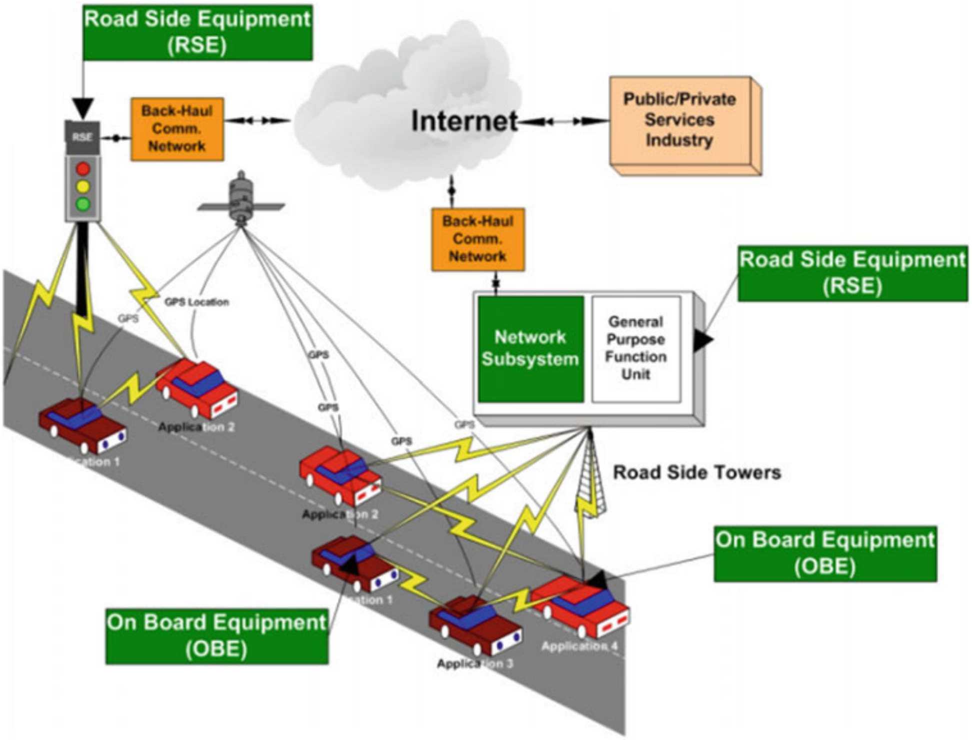

Fig. 1 VII consists of three interconnected components (Dedicated Short Range Communications (DSRC) Service 2016)

management type (Hartenstein and Laberteaux 2008; Kamini and Kumar 2010). Those applications improve the efficiency of the roads and to save drivers time and money (Mittal and Vashist 2014).

- Commercial applications help the driver to reach the maximum of satisfaction with providing the entertainment and various services as web access, streaming audio, and video (Hartenstein and Laberteaux 2008; Kamini and Kumar 2010).

2.5 Requirements of a Good Broadcasting Protocol

For any broadcasting techniques for VANET, it should satisfy some requirements like scalability (The broadcast protocol must be flexible with any increase in the traffic density), effectiveness (All nodes in the range receive the disseminated message), efficiency (The broadcast protocol needs to eliminate message redundancy due to limited bandwidth), delay (time of dissemination which must be negligible), delay-tolerant dissemination (It is desirable to cache information in frequent partitioning scenarios and propagate them later when new vehicles are available in the vicinity. Otherwise, important information can be lost when the network in the destination region is not fully connected), and robustness (The broadcast has to cope with packet losses in order to assure the correct function for vital safety applications) (Chitra and Sathya 2013).

3 Related Work

An improvement in the drivers' safety consists of disseminating notifications of any dangerous situation that can arise, in order to avoid any critical situation. There are many applications in this context which use data dissemination protocols to provide the state of the road and of the surrounding vehicles. Those protocols can be considered as infrastructureless broadcasting protocols. They can operate without any infrastructure (Costly infrastructure) to disseminate data. The main goal of those protocols is to inform all vehicles of the network while avoiding the storm broadcast problem. Indeed, several broadcast schemes were proposed in this context to cope with this problem. Noting that applications developed for VANET are different of those for MANET and aim to provide safe transportation systems. This includes probability-based protocols, counter-based, location-based, distance-based, and hybrid-based schemes. More details are presented in Mohammed et al. (2007).

Authors in Paula et al. (2014) propose a technique to avoid congestion using Volunteers Dilemma game; they modeled the problem and observed the effect of probability to volunteer in a Nash equilibrium stemmed from mixed strategies and the probability of volunteering in QRE equilibrium with additional parameter of aversion. The results showed that the involved concepts used in both equilibriums are goods and parameters to set the routing probability QRE equilibrium to contribute to this probability that decreases more slightly than in the Nash equilibrium. Prior work Tonguz et al. (2010) presents a distributed broadcast protocol that uses local connectivity information provided via periodic hello messages. It performs well in sparse areas, where network disconnections can occur mostly. This can be done by keeping a message by the node until it will be connected to other nodes. Authors Muthamizh et al. (2014) suggested a spanning tree-based broadcasting protocol which resends the emergency messages to all nearby vehicles in the location of the accident. This protocol reduces the redundant messages (that causes the storm problem) latency and evolves the packet delivery ratio. The source vehicle decides by executing prim's algorithm for finding the minimum cost spanning tree in which the vehicle is within its radio range. A vehicle density-based forwarding protocol was proposed for VANETs (Huang et al. 2014). It chooses adaptively the forwarder based on the nodes' density, gotten from the number of received hello messages in its transmission range, and with an optimal hop distance. Then, they assign several waiting times to decide whether to rebroadcast or to discard the message.

A Distance Defer Transmission (DDT) was proposed in Sun et al. (2000). They adopt the concept that the furthest vehicle will be treated as a gateway, which can relay the message using a brief waiting time. Thus, the waiting time is calculated in function of the distance between the receiver and transmitter nodes. It is inversely proportional to the same distance.

Sun et al. (2013) proposed an optimal ODAM-based broadcast protocol. It increases the packet delivery rate and thus reduces packet loss, based on two methods: the first one is by considering the angles between source nodes, forwarding nodes, and receiving nodes. The second one increases the redundancy of forwarding nodes which ensure a packet success delivery ratio.

Recent work presents an optimal multi-hop broadcast protocol Benaidja et al. (2013) which has the same concept of distance defer transmission. The only difference is the used equation to calculate the waiting time, to better cover a larger geographical area.

A cut-through rebroadcasting protocol was proposed in Akkhara et al. (2009) which accords a high relevance to the farthest vehicle from the source node in its transmission range. They assume that each vehicle has two transceivers which operate in different channels to avoid broadcast collision. To minimize the broadcast storm problem, authors in ALshaer and Horlait (2005) propose an optimistic adaptive probabilistic broadcast protocol that considers the previous broadcast probability and node density, gotten from beacon messages, to calculate its own forwarding probability. Thus, the node with high probability uses shorter waiting time. A reception estimation alarm routing protocol was suggested in Jiang et al. (2008). It uses the previous probability to calculate the broadcasting probability using the theoretical model of wireless channels. Thus, only vehicles in the propagation direction can calculate this reception probability. Then, relay vehicles are those with least contention delay. Compared to previous work, we suggest a function to set the waiting time value in terms of the speed of the received vehicle, trying to alleviate the network and focusing mainly on the broadcast storm. Then, we make a comparison of the probability-based and counter-based protocols with the mean of seven thresholds using the new delay formula against a random value of the same waiting time.

4 Our Proposed Broadcasting Protocol

The conventional technique to broadcast a packet in VANETs is flooding, where a vehicle simply rebroadcasts each received message once, which leads to the broadcast storm problem. This problem affects the resources utilization and degrades the bandwidth consumption. In this paper, we assume that all vehicles have the same transmission range. The underlying idea of our proposal is to change the waiting time from a random value to a value that depends on local parameters. It is worth mentioning that vehicles have slow speed in dense networks as compared to the sparse network. We modified the counter- and probability-based protocols by considering the relative speed of current vehicle to calculate the waiting time needed to initiate the broadcasting. Thus, the waiting time for each vehicle node can be calculated as follows:

$$\begin{cases} 0 < \tau < 0.4\,(\mathrm{s}) & 0 \leq speed < 30\,(\mathrm{kmph}) \\ 0.4 \leq \tau < 0.7\,(\mathrm{s}) & 30 \leq speed < 70\,(\mathrm{kmph}) \\ 0.7 \leq \tau < 1\,(\mathrm{s}) & speed \geq 70\,(\mathrm{kmph}) \end{cases} \tag{1}$$

where τ is the assessment delay given in seconds, while *speed* is the speed of the current vehicle given in Kmph. The assessment delay increases with the increase of vehicle local speed. We assume that the other vehicles around will have an average speed equal to the vehicle in question. Our proposed algorithm relies on only local parameters (Speed) to define the waiting time without complex computation.

Algorithm 1 *Probability-based with a new delay*

```
On hearing a broadcast message m for the first time
set a waiting time W(S)
Generate a random probability p
if p < P then
                                        ▷ (P: Probability threshold-value)
    Rebroadcast the message
else
    Stop waiting
    Drop the message
end if
```

Algorithm 2 *Counter-based with a new delay*

```
On hearing a broadcast message m for the first time
initialize the counter c = 1;
set a waiting time W(S);
For each new message, Increment c , c=c+1;
if c < C then
                                        ▷ (C: Counter threshold-value)
    Rebroadcast the message
else
    Stop waiting
    Drop the message
end if
```

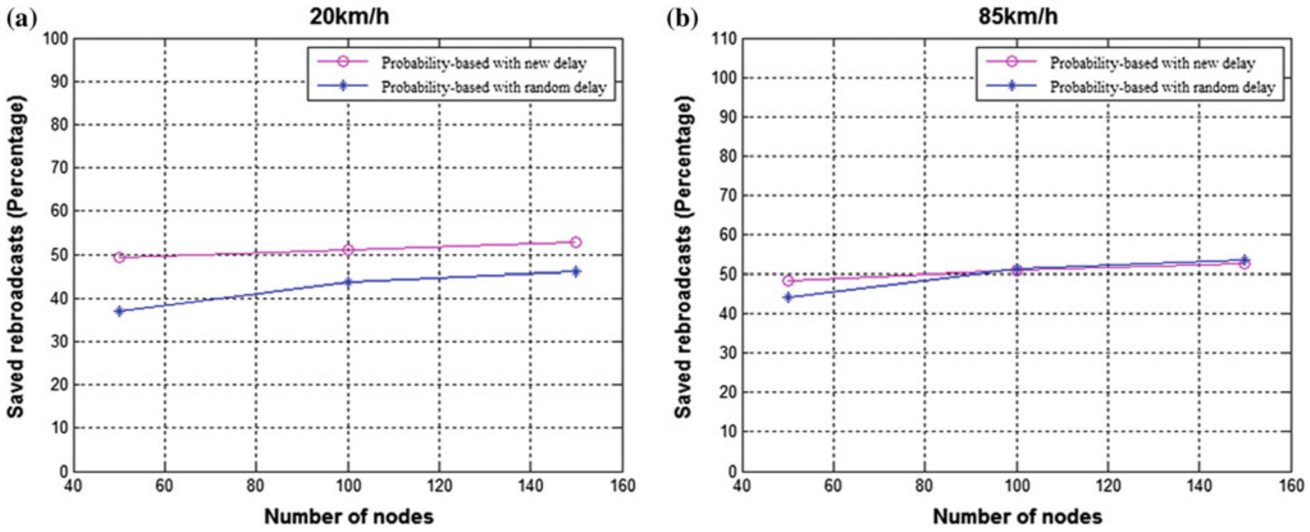

Fig. 2 SRB of probability-based schemes versus node density: **a** low speed (20 km/h), **b** high speed (85 km/h)

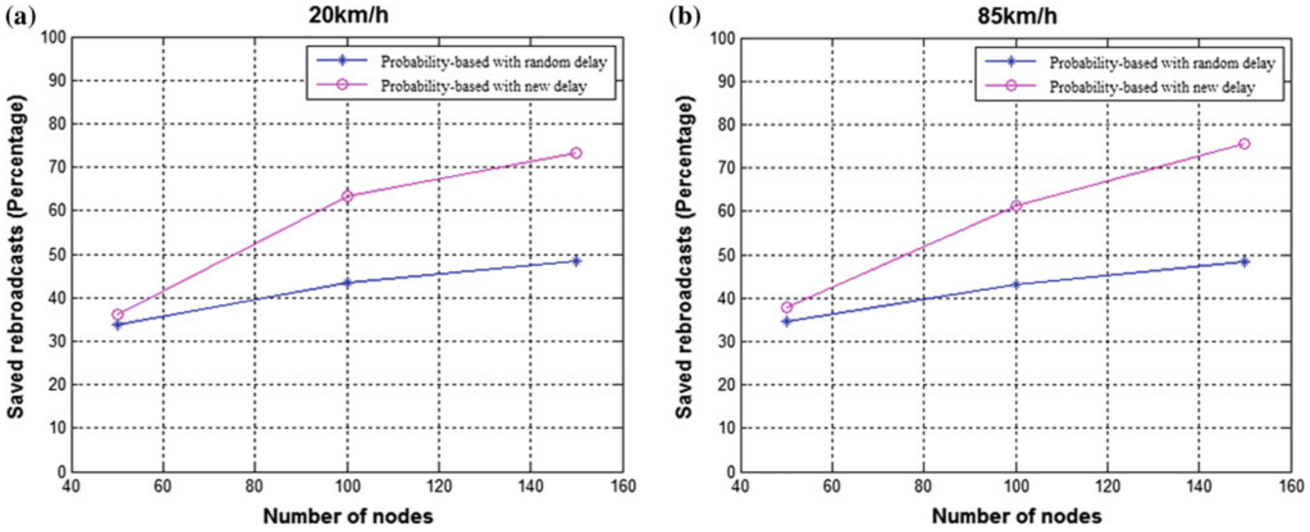

Fig. 3 SRB of counter-based schemes versus node density: **a** low speed (20 km/h), **b** high speed (85 km/h)

In the remainder, we test the probability-based and counter-based protocols with different fixed thresholds (But we will consider the mean value) for different scenarios, trying to mitigate the broadcast storm problem. The decision of whether or not to rebroadcast is made based on the waiting time and a probability or counter threshold. This solution will solve the problem of the generation of the waiting time in sparse and dense areas. Therefore, it will be suitable for safety warning messages which must be disseminated in short delays.

Although, for Algorithm 1, when a node receives a message for the first time, a waiting time is launched [calculated according to the previous formula (1)], when it expires, a random probability *p* is generated between 0 and 1, and if p is less than a threshold value P, the message is rebroadcast. Otherwise, the packet is discarded. Furthermore, for Algorithm 2, when a node receives a message for the first time, a counter c is initialized and incremented each time we receive the same message, and then a waiting time is calculated and launched. When it expires, if c is greater than

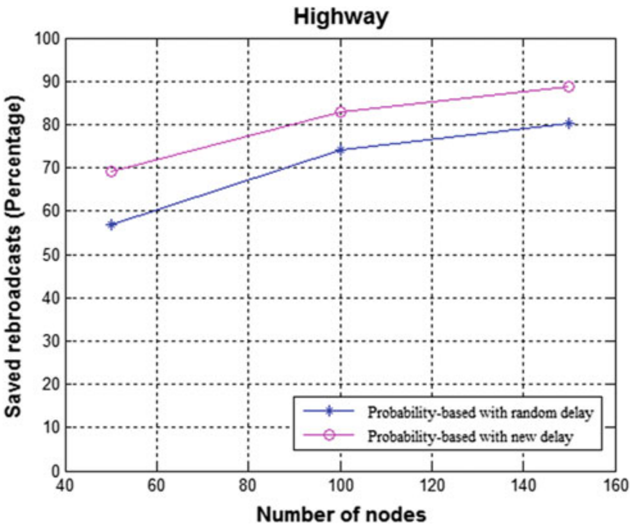

Fig. 4 SRB of counter-based schemes versus node density in a highway with high speed (120 km/h)

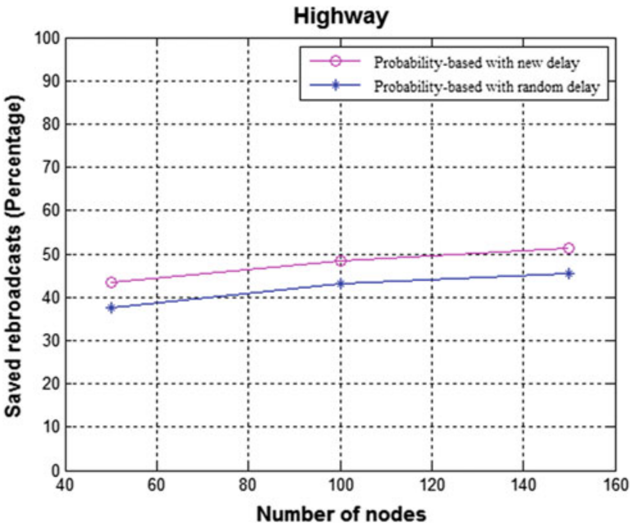

Fig. 5 SRB of probability-based schemes versus node density in a highway with high speed (120 km/h)

a threshold value C, the message is discarded. Otherwise, the packet is rebroadcast.

5 Simulation Environment and Performance Evaluations

This section contains details of performance metrics, simulation environment, simulation results, and their discussions.

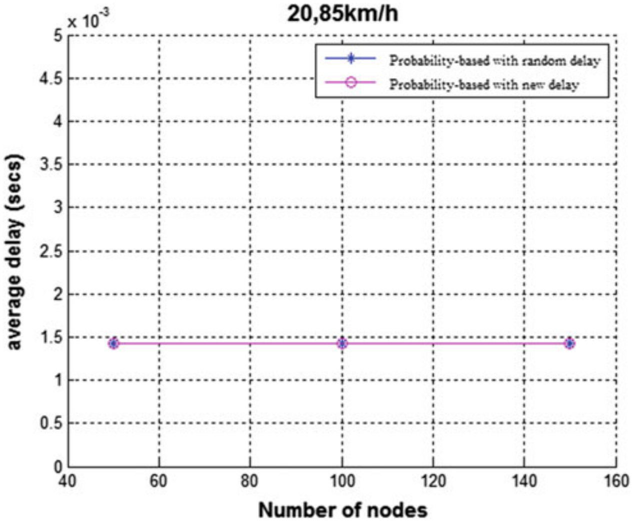

Fig. 6 Average delay of probability-based and counter-based schemes versus node density in a highway and grid map

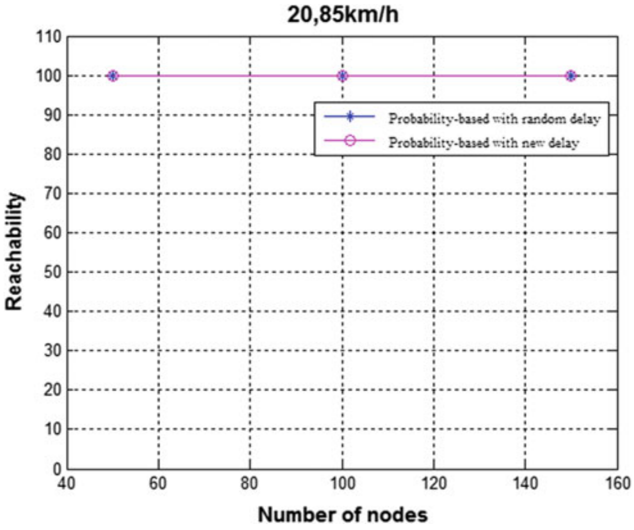

Fig. 7 Reachability of probability-based and counter-based schemes versus node density in a highway and grid map

5.1 Evaluation Metrics

The simulation evaluation is carried out through three metrics that have to be kept under consideration during the broadcasting mechanism (Mohammed et al. 2007; Tseng et al. 2002):

- **Reachability**: The amount of nodes that received the packet over the total number of the nodes in the network.
- **End-to-end delay**: The difference between the time when the packet is sent and the time is successfully received by the receiver.

- **Saved Rebroadcast**: The percentage of nodes that have received but not rebroadcast the message. Thus, SRB is defined as $((r - t)/r) * 100$, where r and t are the number of nodes that received the broadcast message and the number of nodes that transmitted the message, respectively.

5.2 Simulation Parameters

The network simulator ns2 (Issariyakul and Hossain 2011) is used to conduct simulations with different speeds (20, 85 km/h) and node densities (50, 100, and 150 nodes) that are randomly distributed in the area, and setting the transmission range to 250 m. Thus, we used the default propagation model of NS2, and a bit rate of 10 Mbps. A map of 800 * 800 m is used in this simulation with a block size of 200 * 200 m and a highway of 6000 m. In these scenarios, each node uses IEEE 802.11P MAC protocol for the transmission of messages. Therefore, a time simulation is set to 1000 s for the grid map and 3600 s for the highway. We repeated the simulation 20 times and took into consideration the mean value for every 20 outputs. Table 1 summarizes the used simulation parameters.

5.3 Simulation Results

Through all the simulations, the main goal is to improve saved rebroadcast, reduce latency, and increase the saved rebroadcast ratio, which leads to an important mitigation of the storm problem, and then reducing the packet collisions in the network. Afterward, we present a comparison of counter-based and probability-based schemes (Considering the mean of different thresholds) using a random assessment delay against the calculated waiting time. We evaluate the impact of the nodes' density, speed, and mobility scenario on the performance of the protocols.

The simulation was repeated 20 times and we chose several thresholds, but we have considered the mean output value. Figures 2 and 3 depict the results of the comparison of the probability-based and counter-based schemes, respectively, using a random delay against a new delay for different numbers of nodes and different nodes' speeds (20 and 85 km/h) in terms of saved rebroadcast ratio (SRB). The SRB increases as the nodes' density increases for the two speeds, 20 and 85 km/h, and for all scenarios. SRB is low for lower numbers of vehicles and increases as the number of vehicles increases. The results show that the modification of the waiting time gives better performances than the use of a random waiting time, which exhibits lower SRB. For a network of 50 nodes in Fig. 2 and for both speeds, the proposed method is 1.25 better than the probability-based schemes that use a random assessment delay. For a node density of 150 nodes, it is 1.66 better than the counter-based protocols. These results justify the effectiveness of the use of local information like the speed of the vehicles.

Figures 4 and 5 show also that SRB increases too as the nodes' density increases, and the proposed method outperforms the probability-based schemes by 1.27 for 50 nodes and the counter-based schemes by 1.18 for 50 nodes too.

Figure 6 presents the average delay of the probability-based and counter-based schemes, and we can remark that it stays constant and equals to 0.001425 s. It represents the time between needed for a node to send a message to another node in it is range. We remark that it is very small and near to 0.001 seconds because the use 802.11P that uses a dedicated channel to send data, and because we use one-hop communication; that is why, it stays as a constant for all the transmissions from a node to all the other nodes in its range, and for all nodes' densities and speeds.

Figure 7 presents a comparison of counter-based and probability-based algorithms with random delays against new delay for all network densities and sizes and all speeds. 802.11P offers a good reachability for all schemes. As a recapitulation, we can say that the proposed method outperforms the other schemes in terms of SRB, but the reachability and the average delay stay constant for all scenarios.

Table 1 Simulation parameters

Simulation parameter	Value
Simulator used	800 m × 800 m Grid, 6000 m highway
Transmission range	250 m
Speed of nodes (km/h)	20, 85 for grid; 120 for highway
Bandwidth	10 Mbps
Simulated of nodes	50, 100, 150
Packet size (bytes)	1000
Simulation time (s)	1000-grid map; 3600-highway
Trials	20

6 Conclusion

Congestion, in general, even if it is due to accidents or traffic jams, is a waste of time for car's drivers. Therefore, to avoid such situation, we have to use optimized broadcasting protocols to dispatch data without cluttering the network. A well-designed protocol must minimize the number of transmissions, whereas maximizing the number of receptions. In this paper, we tried to change the definition of the waiting time from a random generated number in a huge interval to a small random generated number in a specific interval, according to the local parameter (Speed of the current vehicle). The proposed method aims to get better performances for all requirements. Doing so, it lets us meet our goals, such as having a good reachability as well as a high saved rebroadcast and lower latency. Carried out experiments show that the proposed method helps to improve the performances better than the classical counter-based and probability-based schemes especially in terms of saved rebroadcasts. We plan in the future to realize extensive experiments while increasing the area size and use a real map. We expect also to use more realistic propagation models with a higher vehicular mobility.

References

About ITS|ITS Japan (English).

Akkhara, P., Sekiya, Y., & Wakahara, Y. (2009). Efficient alarm messaging by multi-channel cut-through rebroadcasting based on inter-vehicle communication. *IAENG International Journal of Computer Science*, *36*(2), 157–166.

Al-Holou, N., Mohammad, U., Alyusuf, B., Albarazi, K., Fallouh, S., Abdul-Hak, M., et al. (2018). *New approach evaluate the PERF vehicle-infrastructu and its communica*.

ALshaer, H., & Horlait, E. (2005). An optimized adaptive broadcast scheme for inter-vehicle communication. In *IEEE 61st Vehicular Technology Conference (VTC)* (Vol. 5, pp. 2840–2844).

Al-Sultan, S., Al-Doori, M. M., Al-Bayatti, A. H., & Zedan, H. (2014). A comprehensive survey on vehicular ad hoc network. *Journal of Network and Computer Applications,37*, 380–392.

Altayeb, M., & Mahgoub, I. (2013). A survey of vehicular ad hoc networks routing protocols. *International Journal of Innovation and Applied Studies*, *3*(3), 829–846.

Benaidja, A., Moussaoui, S., & Naït-Abdesselam, F. (2013). An optimal broadcast of warning messages in vehicular ad hoc networks. *International Journal of Computer and Information Technology (IJCIT)*, *2*(5), 986–992.

Chitra, M., & Siva Sathya, S. (2013). Efficient broadcasting mechanisms for data dissemination in vehicular ad hoc networks. *International Journal of Mobile Network Communications & Telematics (IJMNCT)*, *3*(3), 47–63.

Dedicated Short Range Communications (DSRC) Service. (2016) .

Hartenstein, H., & Laberteaux, K. (2009). *VANET: Vehicular applications and inter-networking technologies* (Vol. 1). Wiley.

Hartenstein, H., & Laberteaux, K. P. (2008). A tutorial survey on vehicular ad hoc networks. *IEEE Communications Magazine,46*(6), 164.

Huang, J., Huang, Y., & Wang, J. (2014). Vehicle density based forwarding protocol for safety message broadcast in VANET. *The Scientific World Journal*.

IEEE Computer Society LAN/MAN Standards Committee. (2007). IEEE standard for information technology-telecommunications and information exchange between systems-Local and metropolitan area networks-specific requirements part 11: Wireless LAN medium access control (MAC) and physical layer (PHY) specifications. *IEEE Std, 802.11*.

Issariyakul, T., & Hossain, E. (2011). *Introduction to network simulator NS2*. Springer Science & Business Media.

Jiang, H., Guo, H., & Chen, L. (2008). Reliable and efficient alarm message routing in VANET. In *28th International Conference on Distributed Computing Systems Workshops* (pp. 186–191).

Kamini, K., & Kumar, R. (2010). VANET parameters and applications: A review. *Global Journal of Computer Science and Technology*.

Karimi, R., Ithnin, N., Razak, S. A., & Najafzadeh, S. (2011). Non DTN geographic routing protocols for vehicular ad hoc networks. *International Journal of Computer Science Issues (IJCSI),8*(5), 86.

Krishnamachari, B., Wicker, S. B., & Bejar, R. (2001). Phase transition phenomena in wireless ad hoc networks. In: *GLOBECOM* (pp. 2921–2925).

Lee, K. C., Lee, U., & Gerla, M. (2010). Survey of routing protocols in vehicular ad hoc networks. In *Advances in vehicular ad-hoc networks: Developments and challenges* (pp. 149–170). IGI Global.

Lin, Y.-W., Chen, Y.-S., & Lee, S.-L. (2010). Routing protocols in vehicular ad hoc networks: A survey and future perspectives. *Journal of Information Science and Engineering*, *26*(3), 913–932.

Mittal, N. M., & Vashist, P. C. (2014). A detail survey on applications of vehicular ad hoc networks (VANETs). *International Journal of Computer Science and Mobile Computing,3*(6), 713–721.

Mohammed, A., Ould-Khaoua, M., Mackenzie, L. M., & Abdulai, J. (2007). Improving the performance of counter-based broadcast scheme for mobile ad hoc networks. In in *IEEE International Conference on Signal Processing and Communications* (pp. 1403–1406).

Muthamizh, B., Siva Sathya, S., & Chitra, M. (2014). Spanning tree based broadcasting for VANET. *International Journal of P2P Network Trands and Technology (IJPTT)*, *7*, 21–25.

Paula, M. R. P., Lima, D. S., Roberto, F. M., Cardoso, A. R., & Celestino, J., Jr. (2014). A technique to mitigate the broadcast storm problem in VANETs. *ICN 2014* (p. 253).

Paul, B., & Islam, M. J. (2012). Survey over VANET routing protocols for vehicle to vehicle communication. *IOSR Journal of Computer Engineering (IOSRJCE), ISSN*, 2278–0661.

Sun, M.-T., Feng, W.-C., Lai, T.-H., Yamada, K., Okada, H., & Fujimura, K. (2000). GPS-based message broadcast for adaptive inter-vehicle communications. In *52nd Vehicular Technology Conference, 2000. IEEE-VTS Fall VTC 2000* (Vol. 6, pp. 2685–2692). IEEE.

Sun, W., Xia, F., Ma, J., Fu, T., & Sun, Y. (2013). An optimal ODAM-based broadcast algorithm for vehicular ad-hoc networks. *arXiv preprint*. arXiv:1312.6827.

Tonguz, O .K., Wisitpongphan, N., & Bai, F. (2010). DV-CAST: A distributed vehicular broadcast protocol for vehicular ad hoc networks. *IEEE Wireless Communications,* 17(2).

Tseng, Y.-C., Ni, S.-Y., Chen, Y.-S., & Sheu, J.-P. (2002). The broadcast storm problem in a mobile ad hoc network. *Wireless Networks*, *8*(2/3), 153–167.

Uzcátegui, R. A., De Sucre, A. J., & Acosta-Marum, G. (2009). Wave: A tutorial. *IEEE Communications Magazine, 47*(5).

Assia Naja was born in Marrakech, Morocco, on September 15, 1988. She is currently a doctoral student in research laboratory SIME (AL JAZARI team) working under the supervision of Professor Mohamed Essaidi and Profesor Mohammed Boulmalf at National School of Computer Science and Systems Analysis (ENSIAS) in Rabat, Morocco. She received her engineering degree in Network and telecommunications from National School of Applied Sciences of Tangier (ENSAT), Morocco in summer 2012. Earlier in summer 2010, she got her Bachelor diploma in Network and Telecommunications at the University of Science Semlalia in Marrakech, Morocco. Her research is focused on Data dissemination in VANETs (modeling and simulation).

Mohammed Boulmalf received his B.E. in Telecommunications from the INPT in Rabat, Morocco, in 1987. He received his M.Sc. and Ph.D. degrees in Wireless Communications in 1994 and 2001, respectively. From September 1994 to December 1998, he served as an RF Research Engineer at INRS-Telecom. In January 1999, he joined ÉTS (École de Technologie Supérieure) at Quebec University where he was a lecturer. In September of the same year, he joined Microcell Telecommunications, GSM Operator in Canada, where he worked as a Senior Performance Network Engineer. From 2000 to 2002, he held the position of Principal Engineer in the Integration Department at Ericsson, in Montreal. In February 2002, he joined the Faculty of Information Technology at the United Arab Emirates University, Abu Dhabi, where he worked as an Assistant Professor until July 2007. In August 2007, he relocated to the School of Science & Engineering at Al Akhawayn University in Morocco where he worked as an Associate Professor of Computer Science until December 2010. Then, he was recruited by the International University of Rabat as a Professor of Networking/Security and the Dean of the Faculty of Computer Science. His research interests focus mainly on Wireless Networking and Communications, Wireless Sensor Networks, Mobile Computing, RFID Technologies, and Network Security.

Mohamed Essaaidi Prof. Dr. IEEE Senior Member, received the "Licence de Physique" degree, the "Doctorat de Troisième Cycle" degree, and the "Doctorat d'Etat" degree in Electrical Engineering and with honors, respectively, in 1988, 1992, and 1997 from Abdelmalek Essaadi University in Tetuan, Morocco. He is a Professor of Electrical Engineering in Abdelmalek Essaadi University since 1993. He is the Founder and the current Chair of the IEEE Morocco Section since November 2004. He was also a member of the Organizing and the Scientific Committees of several international symposia and conferences dealing with topics related to RF, microwaves and Information and Communication technologies, and their applications. Furthermore, he is a referee of the IEEE Transactions on Microwave Theory and Techniques, IEEE Transactions on Antennas and Propagation, Advanced Computational Electromagnetics Society Journal, European Microwave Association Proceedings, Serbian Journal of Electrical Engineering, and Korean Electronics and Telecommunications Research Institute Journal. His research interests focus mainly on RF and microwave passive and active circuits and antennas for wireless communications and medical systems.

Part V

Green Applications and Interdisciplinary Topics

Active Disturbance Rejection Control of Shunt Active Power Filter Based on P-Q Theory

Imad Aboudrar, Soumia El Hani, Hamza Mediouni,
and Ahmed Aghmadi

Abstract

Active filtering has been known as a promising solution for the compensation of reactive currents and harmonics in the grid energy quality. The present paper introduces a novel control algorithm for the detection of reference harmonic currents applied to a Shunt Active Power Filter (SAPF), where the calculation of the references currents is achieved by the instantaneous active and reactive power theories (p-q), and the control of the DC bus voltage is achieved using the active disturbance rejection control. The MATLAB–SIMULINK environment is used to evaluate the theoretical study and to compare the results of the new control strategy with the one obtained by the classical PI controller.

Keywords

SAPF • P-Q theory • PI control • ADRC • THD • Nonlinear load • ESO

1 Introduction

The semiconductor technology has suffered many improvements over the last three decades, resulting in the emergence of fast and powerful components, with a multitude of applications such as active filtering which has played a leading role in the provision of high clean and energy quality (Strzelecki 2008).

Since the implementation of their basics principle in 1971, active filters have constantly invested various axes of electrical engineering, from the harmonic depollution of the power grids to the compensation of voltage dips, and from imbalances to decentralized production from renewable energies (Carrasco et al. 2006). This is justified by the great flexibility of active filters, under their different structures with various conventional (PWM, hysteresis, etc.), optimized and intelligent (neural networks, fuzzy logic, and genetic algorithms) control strategies and to their good adaptation with the environments in which they are integrated, especially those devoted to renewable energy systems (Guerrero et al. 2013).

Several topologies of active filters have been proposed in literature (Pal et al. 2008). The first solution consists in connecting the active filter in parallel with the polluting system; the principle of the shunt active filter consists in generating harmonic currents in opposition of phase to those existing on the grid. A second approach consists in connecting the active filter in series with the grid; it then behaves as a source of voltage, which opposes the disturbing voltages coming from the source and those caused by circulation of the disturbing currents through the grid impedance (Pal et al. 2008).

At present, researchers are continuing to improve the control methods of the shunt active filters in order to obtain better results both from the point of view of better extraction of harmonics currents, improvement of dynamic regime, reduction of THD, etc, as well as the development of new control strategies for better adaptation and robustness of the latter to different types of nonlinear loads. In 1984, H. Akagi and Y. Kanazawa have introduced the concept of the instantaneous reactive power theory (Akagi et al. 1984) which is based on the measurement of the phase voltages and the load currents. However, this theory was conceptually limited to three-phase systems lacking zero sequence currents. A more generalized instantaneous reactive power theory, which is usable for sinusoidal or non-sinusoidal power systems, balanced or unbalanced, with or without zero sequence currents, was proposed later by Peng and Lai (1996). The active filters controlled based on this new generalized theory have provided better compensation characteristics for both transient and permanent regimes, another lack of this method is that it is based on PI controller which presents an overshoot while controlling the DC bus

---

I. Aboudrar (✉) · S. E. Hani · H. Mediouni · A. Aghmadi
Energy Optimization, Diagnosis and Control, STIS Center
ENSET, Mohammed V University, Rabat, Morocco
e-mail: imad.aboudrar@um5s.net.ma

S. E. Hani
e-mail: s.elhani@um5s.net.ma

S. El Hani and M. Essaaidi (eds.), *Recent Advances in Electrical and Information Technologies for Sustainable Development*,
Advances in Science, Technology & Innovation, https://doi.org/10.1007/978-3-030-05276-8_19

voltage and it is not robust to external and internal disturbances, so in order to mitigate this problems we propose a control strategy that combines the P-Q theory with the active disturbance rejection controller.

2 Shunt Active Power Filter

2.1 General Structure of SAPF

In this section, we briefly introduce the main parts of SAPF. Figure 1 shows the diagram of an active filter connected in parallel with the grid; it is most often controlled as a current generator. It injects into the grid disturbing currents equal to those absorbed by the polluting load, but in opposition of phase with them, in order to make the grid currents in the sinusoidal form (Prabhu et al. 2014).

The structure of a shunt active power filter decomposes into two units, the power and control units. The power unit consists of a voltage inverter based on power switches, controlled in priming and in blocking (GTO, IGBT, etc.), an output filter and of a passive element that works as an energy storage circuit, often it is a capacitor (Peng and Lai 1996). The control unit performs synthesis of the reference currents of the filter in a way to compensate the undesired harmonious current components. Since the currents synthesized by the filter depend on the average voltage of the storage element, it must be kept constant. The control algorithm of the shunt active power filter must provide this voltage control (Prabhu et al. 2014).

2.2 SAPF Parameters Estimation

The three main parameters to be estimated in the design of the power circuit in order to ensure adequate control and good filtering quality are (Aboudrar and El Hani 2017) as follows:

- Selection of the reference voltage value of the capacitor (V_{dcref}).
- Selection of the storage capacitor value C_{dc}.
- Selection of the inductance filter (L_f).

2.2.1 Reference Voltage V_{dcref}

In reference Lam et al. (2010, 2012), to ensure the current controllability of the shunt active power filter, the authors required that the DC link voltage V_{dcref} must be above the source peak phase voltage Vs.

The following equation can be applied:

$$V_{dcref} = \frac{2\sqrt{2}}{1.115} Vs \tag{1}$$

2.2.2 Storage Capacitor C_{dc}

For small and average powers, the most adapted energy storage element is a capacitor placed at the inverter DC side, which has two essential objectives:

- In permanent state, it maintains the average DC link voltage constant and with low oscillations.

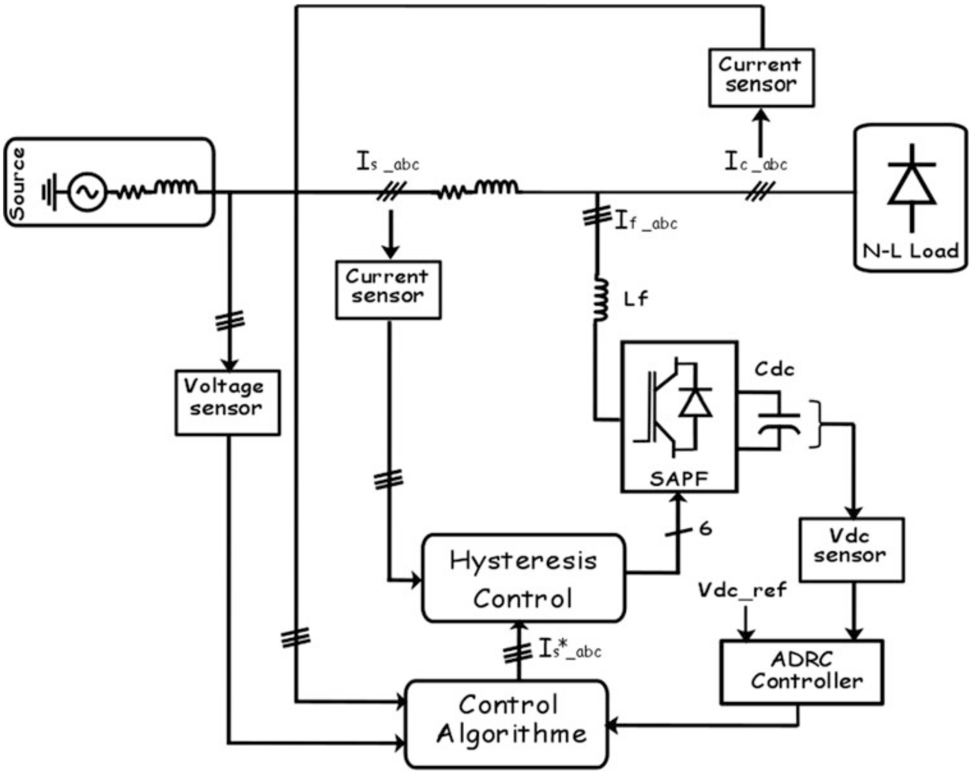

Fig. 1 General structure of a shunt active power filter

- During the transition state, it serves as an element of energy storage to compensate the real power difference between the load and the source.

The value of the capacitor C_{dc} is calculated with the following way (Chaoui 2010):

$$C_{dc} = \frac{I_h}{\varepsilon V_{dc}\omega_h} \tag{2}$$

ε: acceptable ripple, I_h: current harmonic order h, and ω_h: pulsation of the lowest harmonic rank.

2.2.3 Output Filter L_f

In order to connect the voltage inverter with the grid, it is necessary to have a connection filter between them. The purpose of this filter is, first, to convert the compensator into a current dipole from the grid point of view, and second to limit the current dynamics, to make it easier to control (Aboudrar and El Hani 2017).

The value of the coupling inductor Lf is calculated as follows (Chaoui 2010):

$$L_f = \frac{\Delta V}{I_f\omega} \tag{3}$$

where ΔV represents the potential difference between the source voltage and the inverter voltage, which depends on the DC bus voltage.

3 SAPF Control by ADRC and P-Q Theory

The control used in this paper is based on measurement of the N-L load current and then on the extraction of the harmonic components. In this way, the active filter estimates the fundamental component and compensates the harmonic current and the reactive power. For the identification of these harmonic components and the generation of references currents, the instantaneous power theory algorithm is used.

The diagram of Fig. 2 illustrates the various steps making it possible to obtain the harmonic current components of a nonlinear load.

3.1 Instantaneous Power Theory P-Q

The instantaneous power method also known as the P-Q theory was introduced by H. Akagi and al. This method is based on the measurement of the three-phase instantaneous variables presented on the grid (Akagi et al. 1984).

The P-Q theory implements a transformation from a stationary reference system in coordinates abc to a coordinate system (α, β). It corresponds to an algebraic transformation, known as the Clark transformation, which also produces a fixed reference system, where the coordinates (α-β) are orthogonal to one another. We notice the vectors of the single voltages at the connection point [Vs] and of the load currents [ic] of a three-phase system by (Imad et al. 2017)

$$[Vs] = \begin{bmatrix} v_{s1} \\ v_{s2} \\ v_{s3} \end{bmatrix} \text{ And } [i_c] = \begin{bmatrix} i_{c1} \\ i_{c2} \\ i_{c3} \end{bmatrix} \tag{4}$$

The transformation of the instantaneous three-phase voltage and current in the coordinate system α-β is given by the following expressions:

$$\begin{bmatrix} v_{s\alpha} \\ v_{s\beta} \end{bmatrix} = \sqrt{\frac{2}{3}} \begin{bmatrix} 1 & \frac{-1}{2} & \frac{-1}{2} \\ 0 & \frac{\sqrt{3}}{2} & \frac{-\sqrt{3}}{2} \end{bmatrix} \begin{bmatrix} v_{s1} \\ v_{s2} \\ v_{s3} \end{bmatrix} \tag{5}$$

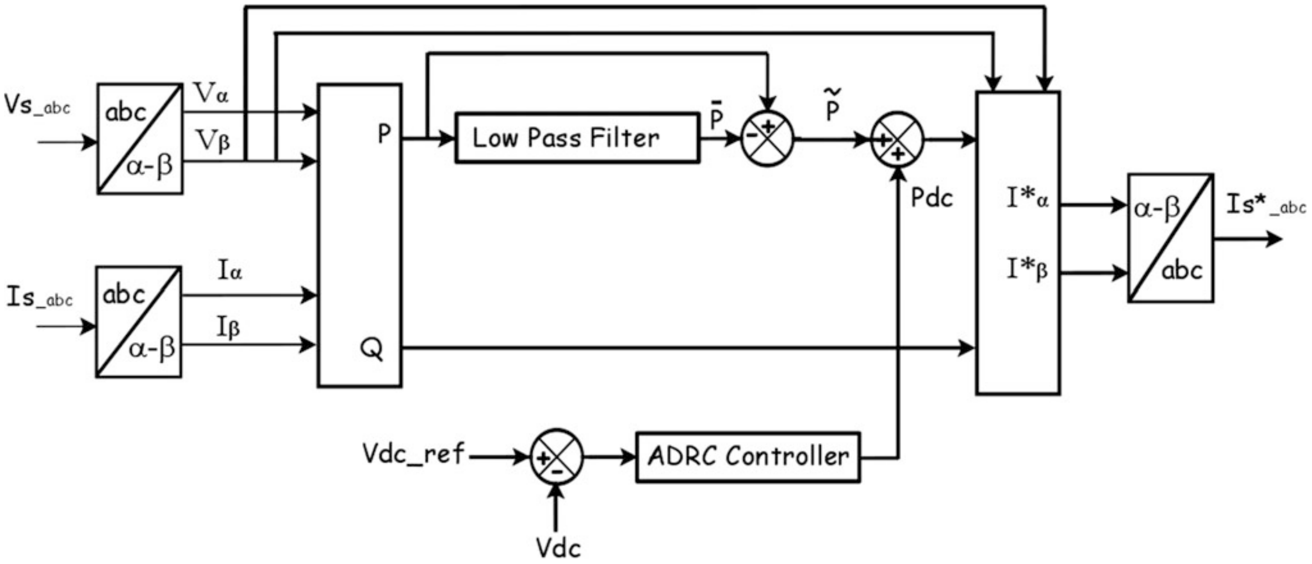

Fig. 2 Proposed control based on P-Q theory algorithm

$$\begin{bmatrix} i_{c\alpha} \\ i_{c\beta} \end{bmatrix} = \sqrt{\frac{2}{3}} \begin{bmatrix} 1 & \frac{-1}{2} & \frac{-1}{2} \\ 0 & \frac{\sqrt{3}}{2} & \frac{-\sqrt{3}}{2} \end{bmatrix} \begin{bmatrix} i_{c1} \\ i_{c2} \\ i_{c3} \end{bmatrix} \quad (6)$$

The vectors of voltages and currents are given by

$$\begin{aligned} \vec{v} &= v_{s\alpha} + j v_{s\beta} \\ \vec{i} &= i_{c\alpha} + j i_{c\beta} \end{aligned} \quad (7)$$

Thus, by defining the complex power $s = \vec{v}\vec{i}$, and taking into account the preceding transformations, we can define the active power p (the real part of the complex power), and the reactive power q (the imaginary part of the complex power) matrix as follows:

$$\begin{bmatrix} p \\ q \end{bmatrix} = \begin{bmatrix} v_{s\alpha} & v_{s\beta} \\ -v_{s\beta} & v_{s\alpha} \end{bmatrix} \begin{bmatrix} i_{c\alpha} \\ i_{c\beta} \end{bmatrix} \quad (8)$$

By replacing the α-β voltages and currents by their three-phase equivalents, we obtain

$$p = v_{s\alpha} i_{c\alpha} + v_{s\beta} i_{c\beta} = v_{s1} i_{c1} + v_{s2} i_{c2} + v_{s3} i_{c3} \quad (9)$$

Similarly, for the reactive power, we have

$$\begin{aligned} q &= v_{s\alpha} i_{c\beta} - v_{s\beta} i_{c\alpha} \\ &= -\frac{1}{\sqrt{3}} \left[(v_{s1} - v_{s2}) i_{c3} + (v_{s2} - v_{s3}) i_{c1} + (v_{s3} - v_{s1}) i_{c2} \right] \end{aligned} \quad (10)$$

From expression (8), we put

$$\Delta = v_{s\alpha}^2 + v_{s\beta}^2 \quad (11)$$

and we have

$$\begin{bmatrix} i_{c\alpha} \\ i_{c\beta} \end{bmatrix} = \frac{1}{\Delta} \begin{bmatrix} v_{s\alpha} & -v_{s\beta} \\ v_{s\beta} & v_{s\alpha} \end{bmatrix} \begin{bmatrix} p \\ q \end{bmatrix} \quad (12)$$

or

$$\begin{aligned} \begin{bmatrix} i_{c\alpha} \\ i_{c\beta} \end{bmatrix} &= \frac{1}{\Delta} \left\{ \begin{bmatrix} v_{s\alpha} & -v_{s\beta} \\ v_{s\beta} & v_{s\alpha} \end{bmatrix} \begin{bmatrix} p \\ 0 \end{bmatrix} + \begin{bmatrix} v_{s\alpha} & -v_{s\beta} \\ v_{s\beta} & v_{s\alpha} \end{bmatrix} \begin{bmatrix} 0 \\ q \end{bmatrix} \right\} \\ &= \begin{bmatrix} i_{c\alpha p} \\ i_{c\beta p} \end{bmatrix} + \begin{bmatrix} i_{c\alpha q} \\ i_{c\beta q} \end{bmatrix} \end{aligned} \quad (13)$$

with

$$i_{c\alpha p} = \frac{v_{s\alpha}}{\Delta} p; \; i_{c\alpha q} = -\frac{v_{s\beta}}{\Delta} q; i_{c\beta p} = \frac{v_{s\beta}}{\Delta} p; \; i_{c\beta q} = \frac{v_{s\alpha}}{\Delta} q \quad (14)$$

In case, where the voltages are sinusoidal and supply a nonlinear load (case of our system), the instantaneous powers p and q are expressed as

$$\begin{aligned} p &= \bar{p} + \tilde{p} \\ q &= \bar{q} + \tilde{q} \end{aligned} \quad (15)$$

with

$\bar{p}, \bar{q}$	continuous power linked to the active and reactive fundamental components of the current.
$\tilde{p}, \tilde{q}$	AC power related to the totality of the harmonic components of the current.

Considering Eqs. (12) and (13), we can separate the current in (α-β) frame into three active and reactive components at fundamental frequency and the summation of the harmonics. This leads to the following equation (Imad et al. 2017):

$$\begin{aligned} \begin{bmatrix} i_{c\alpha} \\ i_{c\beta} \end{bmatrix} &= \underbrace{\frac{1}{\Delta} \begin{bmatrix} v_{s\alpha} & -v_{s\beta} \\ v_{s\beta} & v_{s\alpha} \end{bmatrix} \begin{bmatrix} \bar{p} \\ 0 \end{bmatrix}}_{Active\_current} + \underbrace{\frac{1}{\Delta} \begin{bmatrix} v_{s\alpha} & -v_{s\beta} \\ v_{s\beta} & v_{s\alpha} \end{bmatrix} \begin{bmatrix} 0 \\ \bar{q} \end{bmatrix}}_{reactive\_current} \\ &+ \underbrace{\frac{1}{\Delta} \begin{bmatrix} v_{s\alpha} & -v_{s\beta} \\ v_{s\beta} & v_{s\alpha} \end{bmatrix} \begin{bmatrix} \tilde{p} \\ \tilde{q} \end{bmatrix}}_{Harmonic\_current} \end{aligned} \quad (16)$$

If we want to compensate the reactive power and harmonic currents generated by the nonlinear loads, the reference signal of the shunt active filter must include the reactive current and the harmonic current. In this case, the reference currents are calculated by

$$\begin{bmatrix} i_{c\alpha}^* \\ i_{c\beta}^* \end{bmatrix} = \frac{1}{\Delta} \begin{bmatrix} v_{s\alpha} & -v_{s\beta} \\ v_{s\beta} & v_{s\alpha} \end{bmatrix} \begin{bmatrix} \tilde{p} \\ \bar{q} + \tilde{q} \end{bmatrix} \quad (17)$$

The reference compensation currents are calculated by applying the inverse transformation of Clark:

$$\begin{bmatrix} i_{c1}^* \\ i_{c2}^* \\ i_{c3}^* \end{bmatrix} = \sqrt{\frac{2}{3}} \begin{bmatrix} 1 & 0 \\ -1/2 & \sqrt{3}/2 \\ -1/2 & -\sqrt{3}/2 \end{bmatrix} \begin{bmatrix} i_{c\alpha}^* \\ i_{c\beta}^* \end{bmatrix} \quad (18)$$

In order to identify one of the three components, for example, the harmonic currents, the AC parts of the active and reactive powers must be separated from the continuous parts (Akagi et al. 2017). This separation can be carried out using one of the two filtering devices illustrated in Fig. 3.

3.2 Mathematical Model of ADRC

ADRC is a robust control strategy proposed by Han on 2009. It mainly consists of three parts: tracking differentiator (TD), extended state observer (ESO), and nonlinear state error feedback (NLSEF). Figure 4 shows the block diagram of first-order standard ADRC (Han 2009).

In Fig. 4, $\boldsymbol{v}$ is the input signal of ADRC controller, $\boldsymbol{v_1}$ is the tracking signal of input signal, $\boldsymbol{y}$ is the feedback signal of the system, $\boldsymbol{z_1}$ is the tracking signal, $\boldsymbol{z_2}$ is the total

Fig. 3 Filters used for the extraction of the AC components

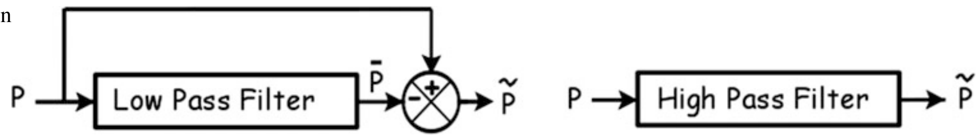

Fig. 4 The block diagram of first-order ADRC

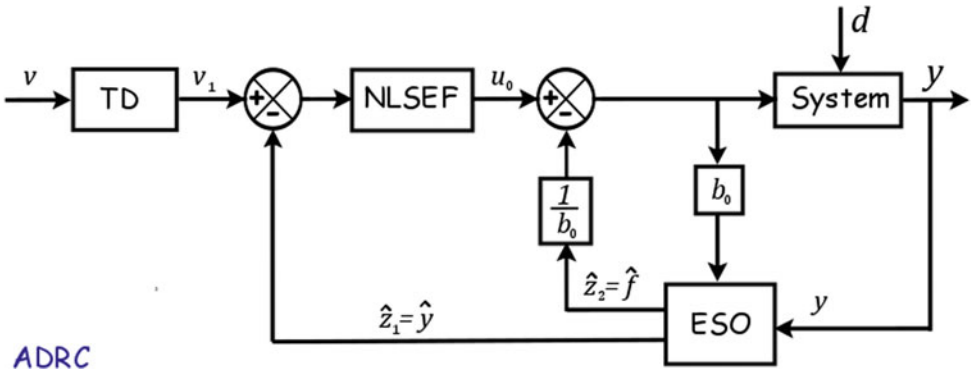

disturbance observation, $\boldsymbol{b_0}$ is the compensation factor, $\boldsymbol{z_2/b_0}$ is the compensation for internal and external disturbances, $\boldsymbol{u_0}$ is the initial signal of the controlled object by NLSEF, and $\boldsymbol{u}$ is the final control signal after compensating the disturbance.

For a first-order controlled object, its mathematical model of ADRC is

$$\begin{cases} \varepsilon_0 = v_1 - v \\ \frac{dv_1}{dt} = -rfal(\varepsilon_0, a_0, \delta_0) \end{cases} \tag{19}$$

$$\begin{cases} \varepsilon = z_1 - y \\ \frac{dz_1}{dt} = z_2 - \beta_{01} fal(\varepsilon, a, \delta) + bu(t) \\ \frac{dz_2}{dt} = -\beta_{02} fal(\varepsilon, a, \delta) \end{cases} \tag{20}$$

$$\begin{cases} \varepsilon = v_1 - z_1 \\ u_0 = \beta_1 fal(\varepsilon_1, a_1, \delta_1) \\ u = u_0 - \frac{z_2}{b_0} \end{cases} \tag{21}$$

$$fal(\varepsilon, a, \delta) = \begin{cases} |\varepsilon|^a \operatorname{sgn}(\varepsilon) & |\varepsilon| > \delta \\ \frac{\varepsilon}{\delta^{1-a}} & |\varepsilon| \le \delta \end{cases} \tag{22}$$

where Eq. (19) is the mathematical model of TD, (20) is ESO, (21) is NLSEF. And, $\beta_{01}, \beta_{02}, \beta_1$ are gains of output error, $fal(\varepsilon, a, \delta)$ is a best function which is defined as (22), δ is the filtering factor to ESO, and a is a nonlinear factor.

In practice, the ADRC controller needs to adjust a large number of parameters and adjusting these parameters is complicated. For so, in order to reduce the model complexity and the controller computational, a linear ADRC design method is proposed and applied to the shunt active power filter.

3.3 LADRC Design for DC Bus Voltage Control

The LADRC consists of a proportional controller and an ESO (Herbst 2013). The system uncertainties and external disturbance are taken as a generalized disturbance. The ESO is used to estimate the system states and the generalized disturbance. The proportional controller drives the tracking error between system's output and reference signal to zero (Ramírez-Neria et al. 2014; Yang et al. 2011).

The block diagram of a first-order LADRC is shown in Fig. 5.

Considering a first-order system, where the plant dynamics is given by

$$\frac{dy(t)}{dt} = -\frac{1}{T} y(t) + bu(t) \tag{23}$$

We add an external disturbance,$d(t)$ to the process and we replace $b = b_0 + \Delta b$, where b_0 will characterize the system known part and Δb, an (unknown) modeling errors part.

$$\begin{aligned} \frac{dy(t)}{dt} &= -\frac{1}{T} y(t) + \frac{1}{T} d(t) + \Delta bu(t) + b_0 u(t) \\ &= f(y, d, t) + b_0 u(t) \end{aligned} \tag{24}$$

where $f(y, d, t)$ represents the system general total disturbances.

Let $x_1 = \mathrm{y}$, $x_2 = f$ and $\dot{f} = h$.

The process state-space model is presented by

$$\begin{cases} \dot{x} = Ax + Bu + Eh \\ y = Cx \end{cases} \tag{25}$$

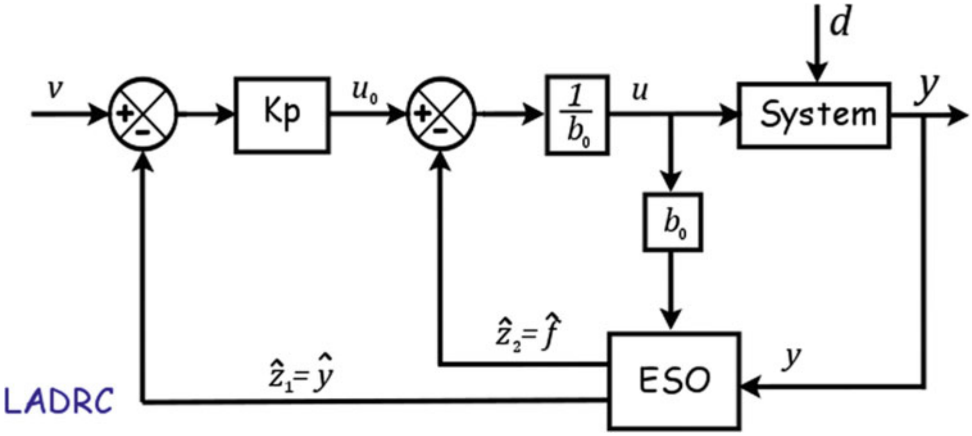

Fig. 5 Structure of the first-order linear ADRC

with

$$A=\begin{bmatrix}0 & 1\\ 0 & 0\end{bmatrix}, B=\begin{bmatrix}b\\ 0\end{bmatrix}, C=[1 \quad 0], E=\begin{bmatrix}0\\ 1\end{bmatrix}, x=\begin{bmatrix}x_1\\ x_2\end{bmatrix}$$

The linear extended state observer (LESO) used to estimate system state variables and total disturbances are represented by the following model:

$$\begin{cases}\dot{z}=Az+Bu+L(y-\hat{y})\\ \hat{y}=Cz\end{cases} \tag{26}$$

where z is the observed state vector, $z=[z_1 \quad z_2]^T$ (z_1 is estimation of x_1 and z_2 is estimation of x_2),$\hat{y}$ is the estimated output, and L is the observer gain vector.

The vector L is defined as $L=\left[2\omega_0 \quad \omega_0^2\right]^T$.

Where ω_0 is determined by the poles placement in closed loop to ensure both fast observer dynamics and minimal perturbations sensitivity.

The control law of the system is

$$y=\frac{(u_0-z_2)}{b} \tag{27}$$

where u_0 a virtual controller.

We suppose z_2 a correct estimation of f, ($z_2 \approx f$ By replacing (27) into (24), we have

$$\dot{y}=f+b_0\frac{(u_0-z_2)}{b_0}=f-z_2+u_0\approx u_0 \tag{28}$$

So the system (26) can be controlled by a proportional regulator (27), where K_P is the controller gain.

$$u_0=K_P(r-z_1)=K_P(r-\hat{y}) \tag{29}$$

where r is the input signal reference to track.

The tuning controller is chosen as $K_P =_c= \frac{4}{T_{settle}}$ where T_{settle} is the desired closed loop settling time. Generally is taken as $\omega_0=3{-}7\omega_c$,

The relationship between the active power absorbed by the capacitor and the terminal voltage is expressed by

$$P_{dc}=\frac{dW_{dc}}{dt}=\frac{d}{dt}\left(\frac{1}{2}C_{dc}V_{dc}^2\right) \tag{30}$$

This equation is adapted with LADRC canonical form.

$$\frac{dV_{dc}^2}{dt}=\frac{2}{C_{dc}}P_{dc} \tag{31}$$

We have,

$$\begin{cases}f(y,d,t)=\Delta b_0=\Delta\left(\frac{2}{C_{dc}}\right)\\ b_0=\frac{2}{C_{dc}}\\ u=P_{dc}\end{cases} \tag{32}$$

4 Simulations and Results

In this section, we will present the response of the active power filter controlled by hysteresis, for both PI and linear ADRC controllers.

The system parameters used in simulation are

$$f=50\,\text{Hz}, Vs=220\,\text{V}, Rs=1\,\text{m}\Omega, Ls=0.03\,\text{mH}, Rd=30\,\Omega$$
$$Ld=20\,\text{mH}, Cdc=550\,\mu\text{F}, Vdc_{ref}=600\,\text{V}, Lf=7\,\text{mH}$$

The following figure shows the spectral analysis of the source current while feeding a nonlinear load before putting into service the SAPF. As it can be seen in (Fig. 6), the current is polluted and its THD is equal to 18.14%.

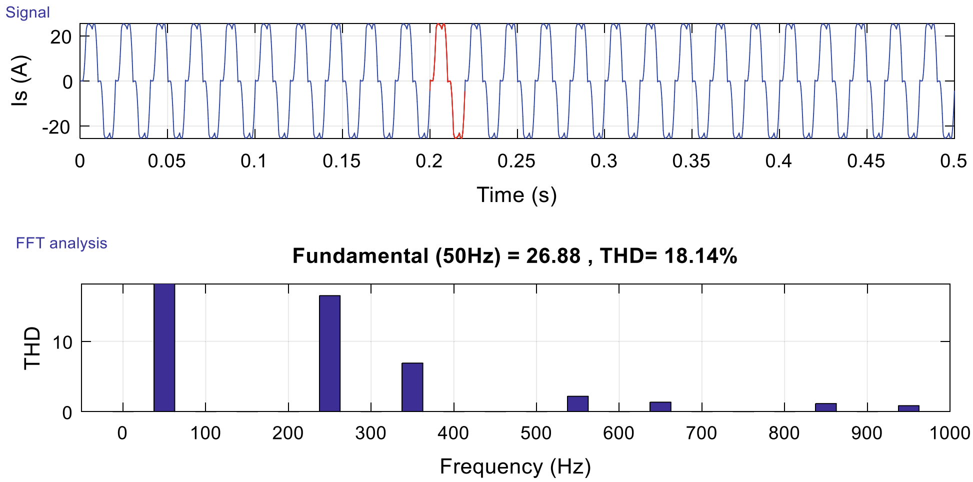

Fig. 6 Spectral analysis of source current Isa before active filtering

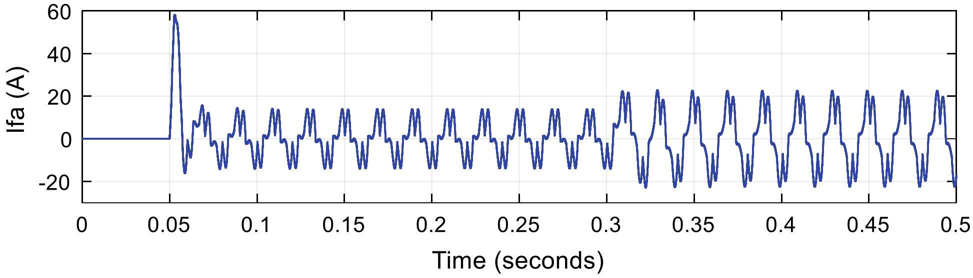

Fig. 7 Current injected by the SAPF with PI controller

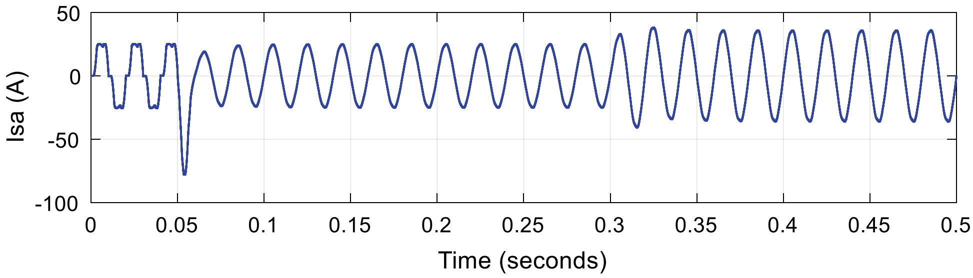

Fig. 8 Source current Isa after filtering with PI controller

4.1 Simulations with PI Controller

The simulations presented below were made with the PI controller, where the SAPF was put into service after a transitional of 0.05 s.

4.2 Simulations Results with Linear ADRC Controller

Here, we present the simulations of the SAPF while using the linear ADRC controller and the SAPF is put into service after a transitional of 0.05 s.

4.3 Results Interpretation

The figures above show the results obtained for the PI and LADRC controllers.

Figures 7, 8, 9, and 10 show that the source current takes the sinusoidal form after injecting the filter currents If and the THD has been reduced from 18.14 to 1.45% for the PI controller. While for the LADRC method, the THD has been improved to 1.05% (Figs. 11, 12, 13, and 14).

To test the robustness of the proposed control, we have changed the load value from Rd1 to Rd2. The voltage at the terminals of storage capacitor Vdc follows its reference with a response time of 0.15 s for the PI controller and 0.05 s for

Fig. 9 Control of DC bus voltage with PI controller

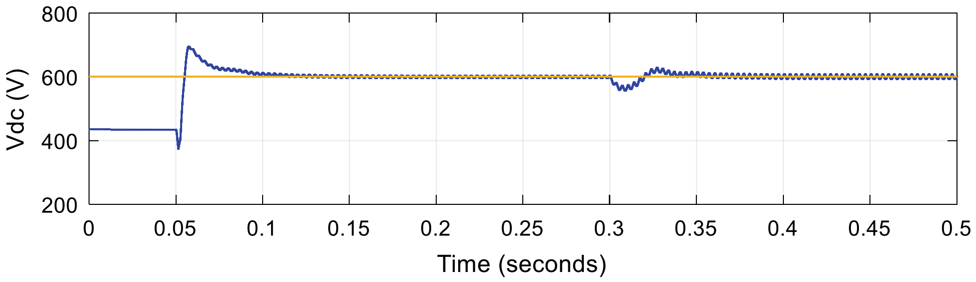

Fig. 10 THD of source current with PI controller

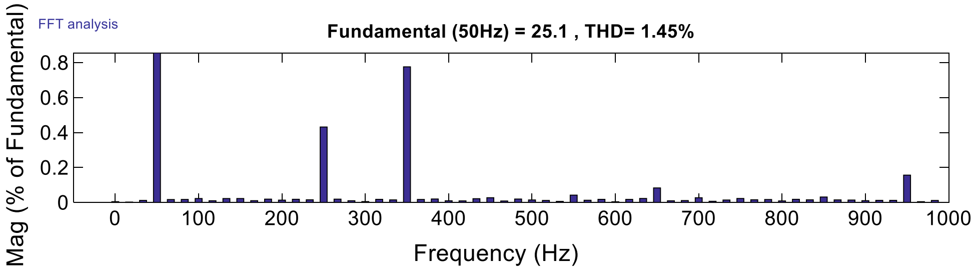

Fig. 11 Current injected by the SAPF with linear ADRC controller

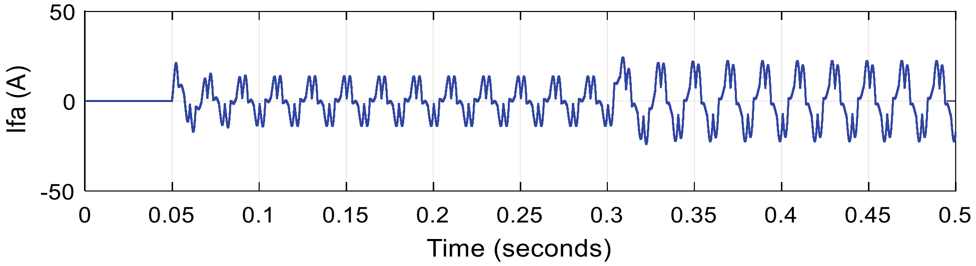

Fig. 12 Source current Isa after filtering with linear ADRC controller

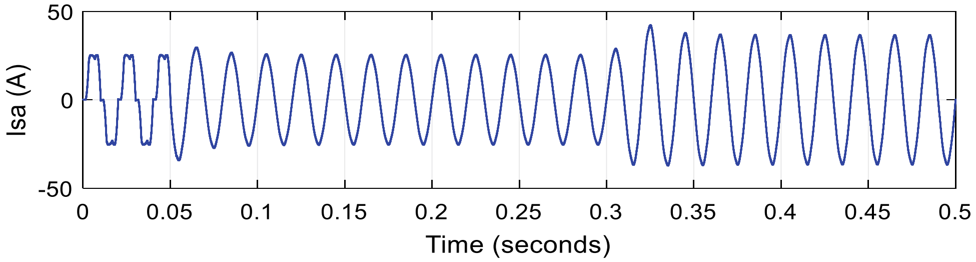

Fig. 13 Control of DC bus voltage with linear ADRC controller

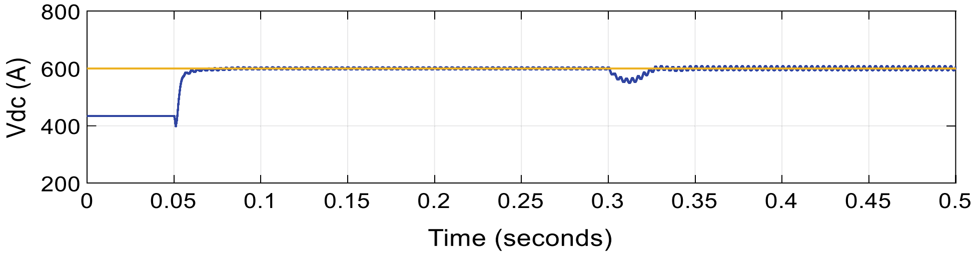

Fig. 14 THD of source current with linear ADRC controller

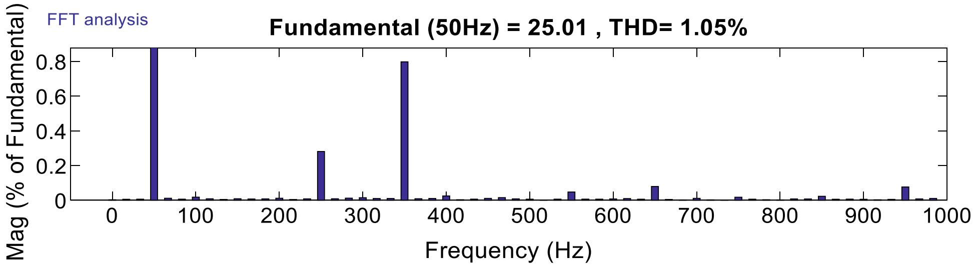

the linear ADRC. Also, we can see that the PI controller presents an overshoot which it is removed by linear ADRC.

Therefore, we can conclude that the linear ADRC controller is more efficient and robust than the PI controller.

5 Conclusion

We have presented, in this paper, two control strategies applied to the three-phase shunt active power filter based on the instantaneous power theory PQ: PI controller and linear ADRC controller, where we have introduced the mathematical model of ADRC and PQ theory.

From the simulation results, we have proved that these two methods compensate the harmonics caused by the nonlinear loads and make the source current on the sinusoidal form. However, it is have been proven that the linear ADRC controller is better in term of efficiency and robustness because it allows reducing the rate of THD and has a better response.

References

Aboudrar, I., & El Hani, S. (2017). Hybrid algorithm and active filtering dedicated to the optimization and the improvement of photovoltaic system connected to grid energy quality. *International Journal of Renewable Energy Research (IJRER), 7*(2), 894–900.

Akagi, H., Kanazawa, Y., & Nabae, A. (1984). Instantaneous reactive power compensators comprising switching devices without energy storage components. *IEEE Transactions on Industry Applications, 3,* 625–630.

Akagi, H., Watanabe, E. H., & Aredes, M. (2017). *Instantaneous power theory and applications to power conditioning* (Vol. 62). Wiley.

Carrasco, J. M., Franquelo, L. G., Bialasiewicz, J. T., Galván, E., PortilloGuisado, R. C., Prats, M. M., et al. (2006). Power-electronic systems for the grid integration of renewable energy sources: A survey. *IEEE Transactions on Industrial Electronics, 53*(4), 1002–1016.

Chaoui, A. (2010). Filtrage actif triphasé pour charges non linéaires. Thèse de doctorat. École nationale supérieure d'ingénieurs (Poitiers).

Guerrero, J. M., Loh, P. C., Lee, T. L., & Chandorkar, M. (2013). Advanced control architectures for intelligent microgrids—Part II: Power quality, energy storage, and AC/DC microgrids. *IEEE Transactions on Industrial Electronics, 60*(4), 1263–1270.

Han, J. (2009). From PID to active disturbance rejection control. *IEEE Transactions on Industrial Electronics, 56*(3), 900–906.

Herbst, G. (2013). A simulative study on active disturbance rejection control (ADRC) as a control tool for practitioners. *Electronics, 2*(3), 246–279.

Imad, A., El Hani, S., Mediouni, H., & Echchaachouai, A. (2017, November). Comparative analysis on current control methods of shunt active power filter for the improvement of grid energy quality. In *2017 International Conference on Electrical and Information Technologies (ICEIT)* (pp. 1–6). IEEE.

Lam, C. S., Choi, W. H., Wong, M. C., & Han, Y. D. (2012). Adaptive DC-link voltage-controlled hybrid active power filters for reactive power compensation. *IEEE Transactions on Power Electronics, 27* (4), 1758–1772.

Pal, Y., Swarup, A., & Singh, B. (2008, October). A review of compensating type custom power devices for power quality improvement. In *Joint International Conference on Power System Technology and IEEE Power India Conference, 2008. POWERCON 2008* (pp. 1–8). IEEE.

Peng, F. Z., & Lai, J. S. (1996). Generalized instantaneous reactive power theory for three-phase power systems. *IEEE Transactions on Instrumentation and Measurement, 45*(1), 293–297.

Prabhu, Y. S., Dharme, A. A., & Talange, D. B. (2014, December). A three phase shunt active power filter based on instantaneous reactive power theory. In *2014 Annual IEEE India Conference (INDICON)* (pp. 1–5). IEEE.

Ramírez-Neria, M., Sira-Ramírez, H., Garrido-Moctezuma, R., & Luviano-Juarez, A. (2014). Linear active disturbance rejection control of underactuated systems: The case of the Furuta pendulum. *ISA Transactions, 53*(4), 920–928.

Strzelecki, R. M. (Ed.). (2008). *Power electronics in smart electrical energy networks*. Springer Science & Business Media.

Yang, R., Sun, M., & Chen, Z. (2011). Active disturbance rejection control on first-order plant. *Journal of Systems Engineering and Electronics, 22*(1), 95–102.

Imad Aboudrar was born in Agadir, Morocco in 1993. He received the M. Sc. degree in electrical engineering in 2016 from the Mohammed V University, Rabat, Morocco—where he is currently working toward Ph.D. in the department of electrical engineering. Since 2016, his research interests are related to renewable energy, his current activities include the improvement of energy quality of an integrated PV and wind hybrid system connected to the grid.

Soumia El Hani, Prof. Dr. IEEE Senior Member received Engineering Degree in 1992 from Higher school of Mines-Rabat. She received the "Doctorat en Science" degree and the "Habilitation Universitaire" degree in Electrical Engineering, Automatic with honors, respectively, in 2003 and 2006 from Mohammed V University, "EcoleMohammadiad'Ingénieurs", Morocco. Her research interests are in the area of robust control, monitoring and diagnosis of electromechanical systems. She is in charge of the research team "Energy Optimization, Diagnosis and control" EODIC, Research Center in "Sciences et Technologies de l'Ingénieur et de la Santé." She is author of several publications in the field of electrical engineering, including robust control systems, diagnosis and control systems of renewable energy conversion.

She is the co-founder and the General Chair of the International Conference on Electrical and Information Technologies since 2015. She is the Scientific Committees member of IRSEC (Morocco), IEMDC 2017 Miami, ICSGCE since 2014 Malaysia. She is a member of the Organizing and the Scientific Committees of several international conferences dealing with topics related to renewable energy, electrical machines, and drives. Professor Soumia El Hani is member of IEEE Power and Energy Society. She is an Effective Member of the Moroccan Soroptimist Association, and Founding Member and chair of the Association l'AssociationMarocaine de la Recherche et de l'Ingénierie en Sciences et Technologies (AMARIST).

She was the editor of the ICEIT2017 Proceedings, the co-editor of the ICEIT2016, ICEIT 2015 Proceedings. She is the author and coauthor of more than 50 papers which appeared in refereed specialized journals and symposia. She is the author of book chapters.

Moreover, she has supervised Ph.D. and Masters Theses dealing with different research topics concerned with her research interests. She has been the principal investigator and the project manager for research projects.

Hamza Mediouni was born in Khourigba, Morocco, in 1993. He received the M.S. degree in electrical engineering in 2016 from the Mohammed V University in Rabat–Morocco. Where he is currently working toward Ph.D.

in the department of electrical engineering. Since 2017, his research interests are related to electrical machines and drives control.

Ahmed Aghmadi was born in Jeddah, Saudi Arabia. He received his B.Sc. degree from the Superior School of Technology, Hassan 1st University, Settat, Morocco in 2015 and M.Sc. degree in Electrical Engineering from Mohamed 5th University, Morocco in 2017. He is currently a Ph.D. candidate at The Energy Optimization, Diagnosis and Control Research Laboratory at Electrical Engineering Department, Ecole Normale Suprieure de l'Enseignement Technique, Mohamed 5th University, Rabat, Morocco. His current research interests are smart grids, renewable energy systems, optimization and management of hybrid energy systems and hybrid AC/DC power systems.

Sliding Mode Control of a Cascade Boost Converter for Fuel Cell Energy Generation System

Fatima Zahra Belhaj, Hassan El Fadil, Abdelouahad Tahri, Khawla Gaouzi, Aziz Rachid, and Fouad Giri

Abstract

In recent years, the renewable energy sources are used as an electric source to reduce energy demand and environmental pollution which occurred using fossil fuels. Fuel cell which is one of the renewable energy sources, and especially Proton Exchange Membrane fuel cell (PEMFC) is a good candidate to solve this problem because it has low emission, high efficiency, perfect part-load performance, and wide size range. This paper deals with the problem of controlling a DC–DC cascade boost converter which is used as a power block for energy conversion system of fuel cell electric vehicle. Using a sliding mode technique, the power converter is controlled in order to achieve two objectives: (i) tight regulation of DC voltage and (ii) asymptotic stability of the closed-loop system. It is worth noting that the nonlinearity of the PEMFC characteristic is taken into account in this work by considering a polynomial approximation of the V–I curve. Moreover, the dynamic model of DC–DC cascade boost converter is analyzed and simulated. It is shown using theoretical analysis and simulations that the controlled system satisfies all the objectives.

Keywords

PEMFC • DC–DC cascade boost converter • Sliding mode controller • Average model

Nomenclature

Parameter	Designation
E^{Cell}	Reversible cell potential (V)
E_0^{Cell}	Reference potential at standard operating conditions (V)
R	Universal gas constant [J/(mol K)]
T	Stack temperature (K)
F	Faraday's constant (C/mol)
P_{H_2O}	Partial pressure of water (atm)
P_{O_2}	Pressure of hydrogen (atm)
a, b	Constant in Tafel equation (V/K)
a_0	Constant in Tafel equation (V/K)
I	Stack current (A)
I_l	Limiting current (A)
n_s	Number of PEM fuel cell stacks
$V_{O,FC}$	Open-circuit output voltage of the PEM fuel cell (V)
V_{fc}	Output voltage of PEM fuel cell (V)

1 Introduction

Today fossil fuels are the principal energy source that is being used by most industrialized and developing countries. But their overconsumption can cause serious environmental problems and since they are derived from prehistoric fossils, fossil fuels would not be available once they are fully used. Their sources are limited and they are depleting at a faster rate. As of today, fossil fuels are being extracted at an exorbitant rate to meet the gap between demand and supply and it is estimated that they will be finished in next 30–40 years. Since they are nonrenewable, it is obvious that fuel expenses will face a steep hike in near future. It would take

---

F. Z. Belhaj (✉) · H. El Fadil · A. Tahri · K. Gaouzi · A. Rachid
ESIT Team, LGS Laboratory ENSA, Ibn Tofail University,
14000 Kénitra, Morocco
e-mail: fz.blhj@gmail.com

H. El Fadil
e-mail: elfadilhassan@yahoo.fr

A. Tahri
e-mail: abd.tahri@gmail.com

K. Gaouzi
e-mail: khawla.gaouzi@gmail.com

A. Rachid
e-mail: rachidaziz03@gmail.com

F. Giri
Laboratoire D'Automatique de Caen, Université de Caen,
Bd Marechal Juin, B.P. 8156, 14032 Caen, France
e-mail: fouad.giri@unicaen.fr

S. El Hani and M. Essaaidi (eds.), *Recent Advances in Electrical and Information Technologies for Sustainable Development*,
Advances in Science, Technology & Innovation, https://doi.org/10.1007/978-3-030-05276-8_20

millions of years to replace coal, and oil, and this means that we will not be able to drive cars anymore unless we switch to electric cars that use energy from renewable energy sources. This means once these nonrenewable sources are completely used up, there is nothing more left.

In the other hand, the renewable energy sources such as solar, wind, and hydrogen are good candidates to be alternative of fossil fuel due to their efficiency which is continuously improved and their cost which is continuously reduced. Hydrogen technology is strongly related to fuel cells, since hydrogen is the crucial energy carrier in fuel cells. The FCs are electrochemical converter that can convert chemical energy to electric energy and heat with high efficiency without using mechanical energy (Mert et al. 2007). The FCs produce electrical energy by chemical reaction of hydrogen and oxygen. Nowadays, FCs attractive owing to their high efficiencies, perfect part-load performance, low emissions, and wide size range (Eberle et al. 2012). The FCs can be used as a stationary or mobile power source ignore climatic condition. For high efficiency, the FCs do not need high operating temperature and FCs become an appealing option for applications that include transportation system applications, electricity for house, producing heat, and mobile and portable systems by means of its high efficiency (Clerk Maxwell 1892). There are many types of FCs such as Proton Exchange (polymer electrolyte) Membrane Fuel Cell (PEMFC). Although there are various FC technologies available for use in vehicular systems, according to scientists and vehicle developers, a prime candidate is the Proton Exchange Membrane FC (PEMFC), because the PEMFC has higher power density and lower operating temperatures than other types of FC systems (Garraín et al. 2011). A stand-alone FC system integrated into an automotive power train is not always sufficient to provide the load demands of a vehicle. To provide the initial peak power during transients such as start-up, acceleration, or sudden changes in load and also to take advantage of the regenerative power of an electric vehicle at braking, a supercapacitor (SC) bank is needed in addition to the FC (Uzunoglu et al. 2007; Tahri et al. 2014a, b, 2018; El Fadil et al. 2012, 2014). The general system topology is represented in Fig. 1 which is usually called Hybrid Energy Storage System (HESS).

The FCs have nonlinear and non-regulated DC output power so they need interfaces systems to make suitable the levels of input and output voltage, by this way the FCs and the load are both kept safe. The interface system is a DC–DC cascade boost converter that steps up the low output voltage (Merin George et al.). Conventional DC–DC cascade boost converters which consist of two or more conventional DC–DC boost converters have wider voltage ratio but power losses increase by connecting more conventional DC–DC boost converter in cascade form (Dawidziuk 2011). The DC–DC cascade boost converters, which have different topologies, use only a switch and have quadratic duty cycle. The control method used for DC–DC cascade boost converter must overcome its nonlinearity, the variation of voltage, and provide stability for all conditions with fast response.

In this paper, the focus is made on modeling and nonlinear control strategy of cascade boost converter used to interface the FC. Using a sliding mode technique, a controller is designed taking into account the nonlinear characteristic of the PEMFC. Moreover, the dynamic equations describing the DC–DC cascade boost converter are derived for continuous conduction mode useful to start the system analysis and develop a Sliding Mode Controller (SM). It is shown using theoretical formalism and simulations that the controlled system satisfies all the objectives, mainly: (i) tight regulation of DC voltage and (ii) asymptotic stability of the closed-loop system.

The paper is organized as follows. In Sect. 2, the PEMFC and the DC–DC cascade boost converter are described and modeled. Section 3 is devoted to the controller design and

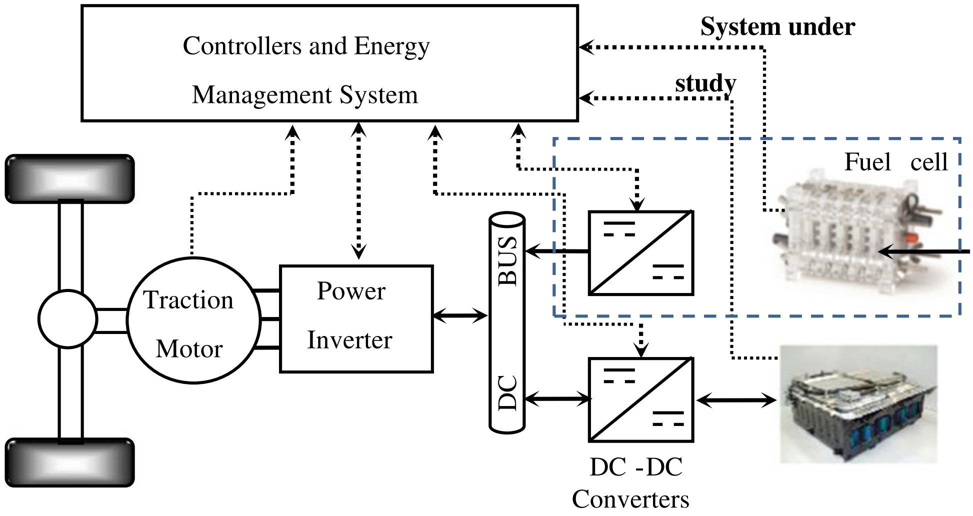

Fig. 1 Circuit of typical hybrid vehicle

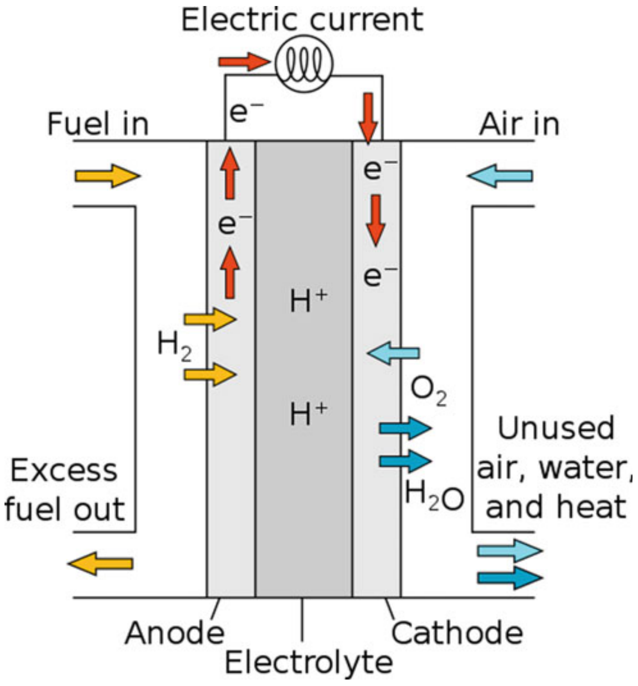

Fig. 2 Proton exchange membrane fuel cell diagram

closed-loop theoretical analysis. The controller tracking performances are illustrated through numerical simulations in Sect. 4. A conclusion ends the paper.

2 System Modeling and Analysis

2.1 Energy Source Model

FC is an energy conversion device that directly converts the chemical energy of a fuel into electricity (Fig. 2).

This energy is released whenever a fuel (hydrogen) reacts chemically with the oxygen of air. The reaction occurs electrochemically and the energy is released as a combination of low-voltage DC electrical energy and heat. In the literature, we find alkaline FC, polymer electrolyte membrane FC, direct methanol FC, phosphoric acid FC, molten carbonate FC, and solid oxide FC (Alloui et al. 2014). The Proton Exchange Membrane (or "solid polymer") Fuel Cells (PEMFCs) are nowadays the most promising type of FC for automotive use and have been used in most current prototypes. Hydrogen oxidation and oxygen reduction are given by the following formulas:

$$H_2 \Rightarrow 2H^+ + 2e^- \tag{1a}$$

$$2H^+ + 2e^- + \frac{1}{2}O_2 \Rightarrow H_2O \tag{1b}$$

and occur in two different places separated by the membrane which carries protons from the anode to the cathode and is impermeable to electrons. The static V–I polarization curve for a single-cell fuel cell is shown in Fig. 3, where the drop of the fuel cell voltage with load current density can be observed. This voltage reduction is caused by three major losses: activation losses, ohmic losses, and transport losses. The reversible single cell potential E^{Cell} generated by a single cell is governed by the Nernst equation.

$$E^{Cell} = E_0^{Cell} + \frac{RT}{2F}\ln\left[\frac{P_{H_2}(P_{O_2})^{0.5}}{P_{H_2O}}\right] \tag{2}$$

E_0^{Cell} is standard cell potential obtained in ideal conditions without considering the losses occurring during the load. The losses are given by the following equations:

Fig. 3 V–I characteristic of elementary single cell of the PEMFC made by Ballard

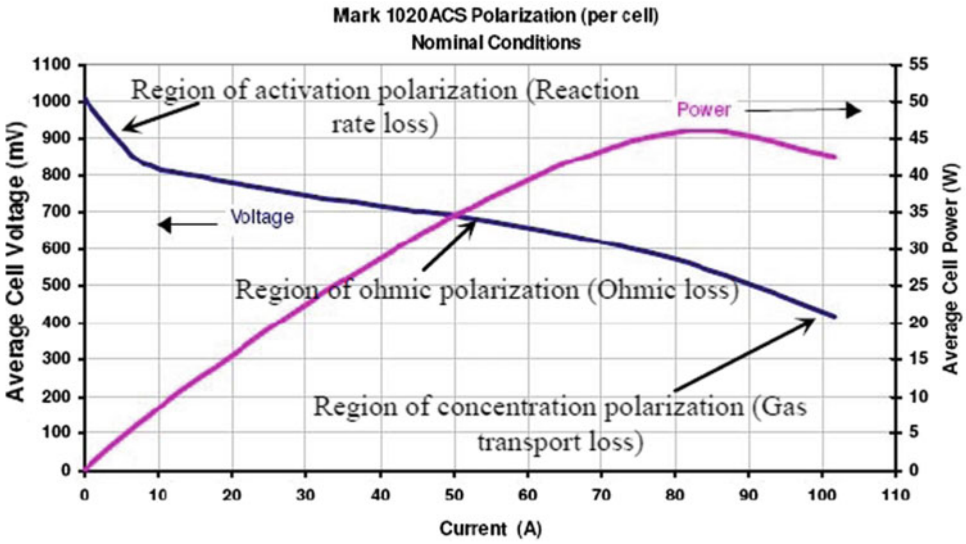

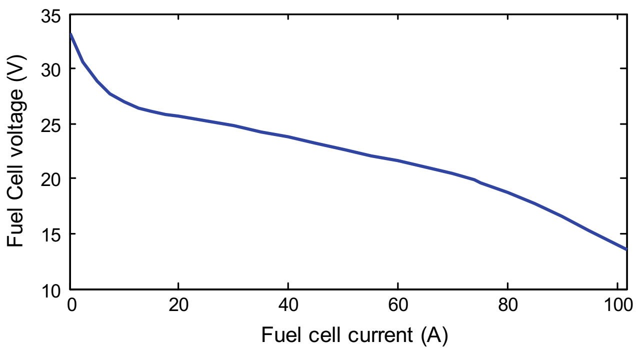

Fig. 4 FC V–I polynomial approximation

- Activation losses (V_{act})

$$V^{act} = a_0 + T[a + b\ \ln((I))] \quad (3)$$

- Ohmic losses (V_{ohm})

$$V^o = V_A^O + V_C^O + V_M^O \quad (4)$$

- Concentration losses (V_{conc})

$$V_{conc} = \frac{RT}{2F}\ln[1 - I_l] \quad (5)$$

E^{Cell} is the individual open-circuit output voltage of one cell. It can be assumed that parameters of an individual cell can be assembled to from PEM fuel cell stack. Then the open-circuit output voltage of the PEM fuel cell can be given as follows:

$$V_{O,FC} = n_s E^{Cell} \quad (6)$$

Hence, the actual output voltage of the PEM fuel cell at normal operation conditions is given by subtracting voltage losses from the open-circuit output voltage of the PEM fuel cell as follows (Puranik et al. 2010):

$$V_{fc} = V_{O,FC} - ns\left(V^{Act} + V^o + V^{Conc}\right) \quad (7)$$

It is very important to take into account the nonlinearity of this characteristic for control design purposes. With this aim, a polynomial approximation of the V–I curve in Fig. 3 is used in this paper (El Fadil et al. 2014; Salhi et al. 2015; Tahri et al. 2016). Thus, the approximated function, illustrated by Fig. 4, will be used for the control design which will be addressed in Sect. 3.

2.2 DC–DC Cascade Boost Converter Model

The DC–DC cascade boost converter circuit has high boost rate with low duty cycle, low voltage stress on components, and high efficiency and these features make it more favorable than the conventional DC–DC boost converters. As it is shown in Fig. 5, the DC–DC cascade boost converter consists of one switch, two boost inductors L_1 and L_2, three diodes D_0, D_1, and D_2; and capacitors C_1 and C_0.

The DC–DC cascade boost converter used to interface the PEMFC is derived from the conventional DC–DC boost converter topology by adding L_2, D_0, D_2, and C_0. The input voltage of the converter is denoted V_{in} (which is the fuel cell voltage) while its output voltage is V_0 and its control signal input is the duty ratio denoted by μ (El Fadil and Giri 2012). The converter consists of two cascaded conventional boost converters. The first conventional DC–DC boost converter circuit consists of L_1, D_1, D_2, C_1, and M (switch). The transfer gain of this circuit is given by

Fig. 5 DC–DC cascade boost converter

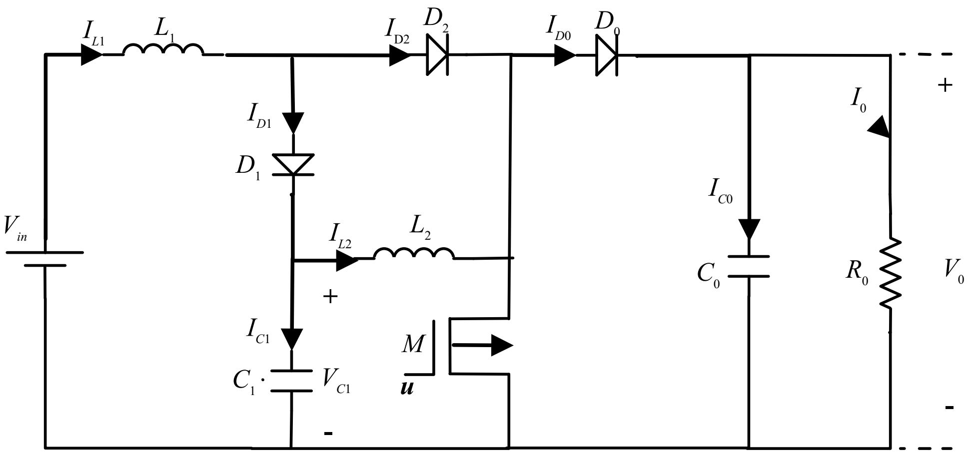

$$\frac{V_{C1}}{V_{in}} = \frac{1}{1-\mu} \tag{8}$$

The second conventional DC–DC boost converter consists of C_1, L_2, M, D_0, and C_0. Its voltage transfer gain is

$$\frac{V_0}{V_{C1}} = \frac{1}{1-\mu} \tag{9}$$

The total voltage transfer gain of DC–DC cascade boost converter is then obtained, using (8) and (9), as follows:

$$\frac{V_0}{V_{in}} = \frac{1}{(1-\mu)^2} \tag{10}$$

Using Kirchhoff's laws and taking into account that u can take the binary values 1 or 0 (depending on the M switch's ON and OFF positions), the averaged model of the studied system is given by the following equations:

$$\frac{dx_1}{dt} = -\frac{(1-\mu)}{L_1}x_3 + \frac{1}{L_1}V_{in} \tag{11a}$$

$$\frac{dx_2}{dt} = -\frac{(1-\mu)}{L_2}x_4 + \frac{1}{L_2}x_3 \tag{11b}$$

$$\frac{dx_3}{dt} = \frac{(1-\mu)}{C_1}x_1 - \frac{1}{C_1}x_2 \tag{11c}$$

$$\frac{dx_4}{dt} = \frac{(1-\mu)}{C_0}x_2 - \frac{1}{C_0R_0}x_4 \tag{11d}$$

where $x_1 = \ <i_{L1}>$; $x_2 = \ <i_{L2}>$; $x_3 = \ <V_{C1}>$; $x_4 = \ <V_0>$; and $\mu = \ <u>$.

Equations (11a–11d) can be rewritten in the following compact form:

$$\dot{x} = Ax + g(x)\cdot\mu + f_0 \tag{12a}$$

where

$$A = \begin{pmatrix} 0 & 0 & -\frac{1}{L_1} & 0 \\ 0 & 0 & \frac{1}{L_2} & -\frac{1}{L_2} \\ \frac{1}{C_1} & -\frac{1}{C_1} & 0 & 0 \\ 0 & \frac{1}{C_0} & 0 & -\frac{1}{C_0R_0} \end{pmatrix}, \; g(x) = \begin{pmatrix} \frac{x_3}{L_1} \\ \frac{x_4}{L_2} \\ -\frac{x_1}{C_1} \\ -\frac{x_2}{C_0} \end{pmatrix}, \; f_0 = \begin{pmatrix} \frac{V_{in}}{L_1} \\ 0 \\ 0 \\ 0 \end{pmatrix} \tag{12b}$$

3 Sliding Mode Controller

The control objective is to regulate the output capacitor voltage V_0 of the DC–DC cascade boost converter associated with the fuel cell source to its desired positive value V_d. To this end, the Sliding Mode Control (SMC) approach is used (Belhaj et al. 2016; El Fadil et al. 2013; El Fadil and Giri 2012; El Fadil et al. 2011). First, the equilibrium points of the system, using (11a–11d), are obtained as follows:

$$x_{10} = \frac{V_d^2}{V_{in}R_0} \tag{12}$$

$$x_{20} = \frac{V_d}{R_0}\sqrt{\frac{V_d}{V_{in}}} \tag{13}$$

$$x_{30} = \sqrt{V_{in}V_d} \tag{14}$$

$$x_{40} = V_d \tag{15}$$

It is well known that the SMC provides a method to design a system in such a way that the controlled system is to be insensitive to parameter variations and external load disturbances. The main objective of the SMC is to make the system evolve on a surface containing the desired equilibrium point. Such an equilibrium point must be an asymptotically stable point of the system's trajectory restricted to the surface. Several sliding surfaces are presented and studied, however, by taking into account the control objective and the fact that the cascade boost converter has a non-minimum phase feature, the following sliding surface is chosen:

$$S = k^T e \tag{16}$$

where the components of the vector error $e = [e_1 \quad e_2 \quad e_3 \quad e_4]^T$ are given as follows:

$$e_1 = x_1 - x_{10} \tag{17a}$$

$$e_2 = x_2 - x_{20} \tag{17b}$$

$$e_3 = x_3 - x_{30} \tag{17c}$$

$$e_4 = x_4 - x_{40} \tag{17d}$$

And, $k = [k_1 \quad k_2 \quad k_3 \quad k_4]^T$ is a vector of design parameters.

The derivative of the sliding surface along the trajectories (17a–17d) can be obtained as follows:

$$\dot{S} = \frac{dS}{dt} = \frac{\partial S}{\partial x}\left(\frac{\partial x}{\partial t}\right) \tag{18}$$

This can be rewritten, using (12a), in the following form:

$$\dot{S} = \frac{\partial S}{\partial x}(Ax + g(x).\mu + f_0) \tag{19}$$

Let us consider that the control law is μ that is composed of two components: an equivalent component μ_{eq} and a nonlinear component μ_N.

$$\mu = \mu_{eq} + \mu_N \tag{20}$$

The equivalent control component constitutes a control input, which, when exciting the system, produces the motion of the system on the sliding surface whenever the system is on the surface. However, the second component μ_N is to ensure the equilibrium $S = 0$ to be globally asymptotically stable.

First, the equivalent control is obtained as the solution of the following equation:

$$\dot{S} = \frac{\partial S}{\partial x}\left(Ax + g(x)\cdot\mu_{eq} + f_0\right) = 0 \tag{21}$$

This gives

$$\mu_{eq} = -\left[\frac{\partial S}{\partial x}g(x)\right]^{-1}\left\{\frac{\partial S}{\partial x}(Ax + f_0)\right\} \tag{22a}$$

where

$$\frac{\partial S}{\partial x}g(x) = \frac{k_1}{L_1}x_3 + \frac{k_2}{L_2}x_4 - \frac{k_3}{C_1}x_1 - \frac{k_4 x_2}{C_0} \tag{22b}$$

$$\frac{\partial S}{\partial x}g(x) \neq 0, \forall t > 0 \tag{22c}$$

$$\begin{aligned}\frac{\partial S}{\partial x}(Ax + f_0) = {} & k_1\left(-\frac{1}{L_1}x_3 + \frac{1}{L_1}V_{in}\right) + k_2\left(\frac{1}{L_2}x_3 - \frac{1}{L_2}x_4\right)\\ & + k_3\left(\frac{1}{C_1}x_1 - \frac{1}{C_1}x_2\right) + k_4\left(\frac{1}{C_0}x_2 - \frac{1}{C_0 R_0}x_4\right)\end{aligned} \tag{22d}$$

The nonlinear component μ_N will be determined to ensure the attractiveness of the controlled trajectory toward the sliding surface. It can be chosen as follows:

$$\mu_N = \left[\frac{\partial S}{\partial x}g(x)\right]^{-1}\hat{\mu}_N \tag{23}$$

For a sliding mode to exist, the state $x = [x_1, x_2, x_3, x_4]^T$ should be driven to reach the sliding surface and afterward be constrained to this surface. That is, the surface must be rendered attractive and invariant by an appropriate switching of the control μ. To this end, let us consider the following Lyapunov function:

$$V(x) = \frac{1}{2}S^2 \tag{24}$$

Its time derivative is

$$\dot{V} = S\dot{S} \tag{25}$$

The derivative of the sliding surface can be written, using (16), (18), and (19), as follows:

$$\dot{S} = \frac{\partial S}{\partial x}Ax + \left(\frac{\partial S}{\partial x}g(x)\right)\left[\mu_{eq} + \left(\frac{\partial S}{\partial x}g(x)\right)^{-1}\hat{\mu}_N\right] + f_0 \tag{26}$$

which, using (20), (22a) and (23), yields

$$\dot{S} = \hat{\mu}_N \tag{27}$$

which in turn, using (25), gives

$$\dot{V} = S\hat{\mu}_N \tag{28}$$

The latest suggests the following choice of $\hat{\mu}_N$

$$\hat{\mu}_N = -\lambda S \tag{29}$$

Indeed, with this choice, one has

$$\dot{V} = -\lambda S^2 \tag{30}$$

which is negative definite. This clearly ensures that the equilibrium $S = 0$ is globally asymptotically stable.

Finally, combining (20), (22a–22d), (23), and (29) the following SMC law is obtained:

$$\begin{aligned}\mu = -\frac{1}{\frac{k_1}{L_1}x_3 + \frac{k_2}{L_2}x_4 - \frac{k_3}{C_1}x_1 - \frac{k_4}{C_0}x_2} & \left[k_1\left(-\frac{1}{L_1}x_3 + \frac{1}{L_1}V_{in}\right)\right.\\ & + k_2\left(\frac{1}{L_2}x_3 - \frac{1}{L_2}x_4\right) + k_3\left(\frac{1}{C_1}x_1 - \frac{1}{C_1}x_2\right)\\ & \left. + k_4\left(\frac{1}{C_0}x_2 - \frac{1}{C_0 R_0}x_4\right) + \lambda S\right]\end{aligned} \tag{31}$$

The main results of the paper are now summarized in the following theorem.

Theorem Consider the closed-loop system consisting of the fuel cell source and DC–DC cascade boost converter represented by (11a–11d), and the controller composed of the control laws (30). Then, one has

(i) The closed-loop system is globally asymptotically stable (GAS).
(ii) The tracking error e_4 converges to zero implying tight output voltage regulation.

4 Simulation Results

The dynamic behaviors of DC–DC cascade boost converter that is controlled with SMC under variable input voltages are examined.

The performances of the proposed nonlinear controller are now illustrated by simulations using the MATLAB/SIMULINK software. The converter is modeled according to parameters given in Table 1. The design control parameters are chosen as follows which proved to be convenient $k_1 = 1000$,

Table 1 Parameters of the controlled system

Parameter	Value
Inductance L_1	470 μH
Inductance L_1	550 μH
Capacitor C_0	470 μF
Capacitor C_1	220 μF
Resistance R_0	50 Ω

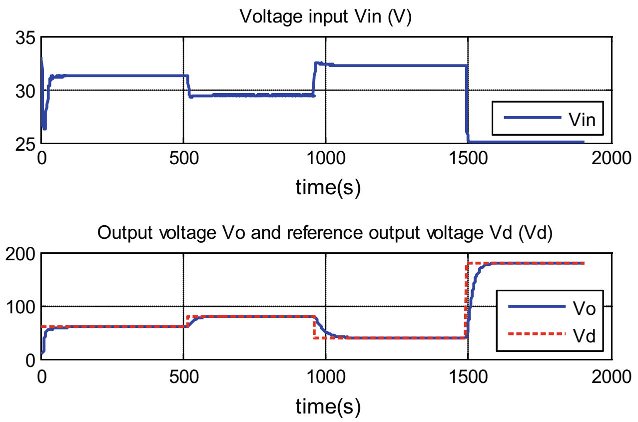

Fig. 6 Output voltage V_o and fuel cell voltage V_{in} in presence of step changes of the output voltage reference signal

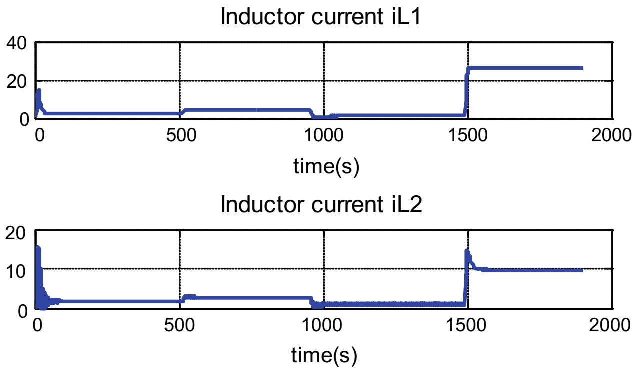

Fig. 7 Inductor current i_{L1} and i_{L2} in presence of step changes of the output voltage reference signal

$k_2 = 100$, $k_3 = 10$, $k_4 = 10$, $\lambda = 10^4$. The resulting control performances are shown in Figs. 6, 7, and 8.

Figure 6 illustrates the behavior of the controller in presence of step changes of the output voltage reference signal between 60 and 180 V and a constant load resistance $R_0 = 50\,\Omega$. As can be seen from the figure, the output voltage perfectly tracks its reference. The figure also illustrates the fuel cell voltage which varies according to its V–I characteristic illustrated by Fig. 4. Figure 7 shows the resulting inductor currents i_{L1} and i_{L2}, while Fig. 8 illustrates the duty ratio μ and the sliding surface.

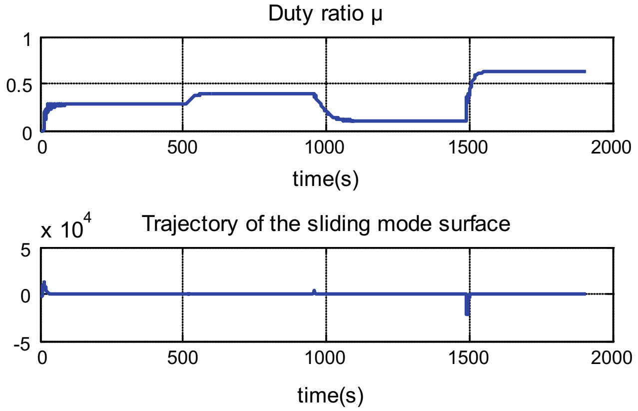

Fig. 8 Duty ratio μ in presence of step changes of the output voltage reference signal and the trajectory of the SM surface

5 Conclusion

The problem of controlling a DC–DC cascaded boost converter associated with the Fuel Cell (FC) has been considered. Using sliding mode technique, a nonlinear controller is elaborated taking into account the nonlinear V–I characteristic of the FC and the nonlinear model of the cascade boost converter. It is formally shown using both formal analysis and simulations that the proposed controller achieves the objectives, mainly: tight output voltage regulation and asymptotic stability of the closed-loop system.

Acknowledgements The authors gratefully acknowledge the support of the Moroccan Ministry of Higher Education (MESRSFC) and the CNRST under grant number PPR/2015/36.

References

Alloui, H., Marouani, K., Becherif, M., Sid, M. N., & Benbouzid, M. H. (2014). A control strategy scheme for fuel cell-vehicle based on frequency separation in green energy. *International Conference on*, 170–175.

Belhaj, F. Z., El Fadil, H., & El Idrissi, Z. (2016, April 21–22). Sliding mode control of DC–DC boost converter for electric vehicle applications. In *Proceeding of the 3rd International Conference on Wireless Technologies embedded and intelligent Systems, WITS 2016* (pp. 309–313). Kénitra, Morocco.

Clerk Maxwell, J., (1892). A treatise on electricity and magnetism (3rd ed., Vol. 2, pp. 68–73). Oxford: Clarendon.

Dawidziuk, J. (2011). Review and comparison of high efficiency high power boost DC/DC converters for photovoltaic applications. *Bulletin of the Polish Academy of Sciences: Technical Sciences, 59*(4), 499–506.

Eberle, U., Müller, B., & von Helmolt, R. (2012). Fuel cell electric vehicles and hydrogen infrastructure. *Energy & Environmental Science, 5*(10), 8780.

El Fadil, H., Giri, F., Guerrero, J. M., & Tahri, A. (2014). Modeling and nonlinear control of a fuel cell/supercapacitor hybrid energy storage system for electric vehicles. *IEEE Transactions on Vehicular Technology, 63*(7), 3011–3018.

El Fadil, H. & Giri, F. (2012, September 2–5). Sliding mode control of fuel cell and supercapacitor hybrid energy storage system. In *Proceeding of the IFAC Symposium on Power Plants and Power Systems control (PPPSC'12)* (pp. 669–674). Toulouse, France.

El Fadil, H., Giri, F., & Guerrero, J. M. (2011, June 6–8). Adaptive sliding mode control of interleaved parallel boost converter for fuel cell energy sources. In *Proceeding of ELECTRIMACS Conference*, Cergy-Pontoise, France.

El Fadil, H., Giri, F., & Guerrero, J. M. (2013). Adaptive sliding mode control of interleaved parallel boost converter for fuel cell energy generation system. In *IMACS transactions on Mathematics and Computers in Simulation (ELSEVIER), 91,* 193–210.

Garraín, D., Lechón, Y., & de la Rúa, C. (2011). Polymer electrolyte membrane fuel cells (PEMFC) in automotive applications: Environmental relevance of the manufacturing stage. *Smart Grid and Renewable Energy, 2*(2), 68–74.

MerinGeorge P. P., George, S., Eldo, S., & Raina, A. *Cascaded boost converter for PV applications*.

Mert, S. O., Dincer, I., & Ozcelik, Z. (2007). Exergoeconomic analysis of a vehicular PEM fuel cell system. *Journal of Power Sources, 165* (1), 244–252.

Puranik, S. V., Keyhani, A., & Khorrami, F. (2010). State-space modeling of proton exchange membrane fuel cell. *IEEE Transactions on Energy Conversion, 25*(3), 804–813.

Salhi, B., El Fadil, H., Magarotto, E., Ahmed Ali, T., & Giri, F. (2015). Adaptive output feedback control of interleaved parallel boost converters associated with fuel-cell. *Electric Power Components and Systems, 43*(8–10), 1141–1158.

Tahri, A., El Fadil, H. E., Guerrero, J. M, Giri, F. & Chaoui, F. Z. (2014a). Modeling and nonlinear control of electric power stage in hybrid electric vehicle. *2014 IEEE Conference on Control Applications (CCA)* (pp. 641–646). Juan Les Antibes.

Tahri, A., Fadil, H., Giri, F., Chaoui, F. Z. (2014b, August 24–29). Nonlinear control and observation of a boost converter associated with a fuel-cell source in presence of model uncertainty. In *Proceeding of the 19th IFAC World Congress* (pp. 575–580). Cape Town, South Africa.

Tahri, A., El Fadil, H., Belhaj, F. Z., Gaouzi, K., Rachid, A., Giri, F., et al. (2018). Management of fuel cell power and supercapacitor state-of-charge for electric vehicles. *Electric Power Systems Research, 160,* 89–98.

Tahri, A., El Fadil, H., Giri, F., & Chaoui, F.-Z. (2016). Nonlinear adaptive control of a hybrid fuel cell power system for electric vehicles—A Lyapunov stability based approach. *Asian Journal of Control, 18,* 166–177.

Uzunoglu, M., & Alam, M. S. (2007). Dynamic modeling, design and simulation of a PEM fuel cell/ultra-capacitor hybrid system for vehicular applications. *Energy Conversion and Management, 48*(5), 1544–1553.

Fatima Zahrae Belhaj was born in Kenitra, Morocco in 1991. She received an electrical engineering degree from the National School of Applied Sciences, Mohammed Premier University, Oujda, in 2014.

She is currently pursuing Ph.D. in the optimization of the energy of an electrical system combining a fuel cell and a supercapacitor used in electric vehicles, in the LGS Laboratory in the National School of Applied Sciences, Ibn Tofail University, Kénitra, under the supervision of Prof. H. El Fadil. Her research interests include optimization and nonlinear control systems of energy in electric vehicles. She is author or coauthor of several papers on these topics.

Hassan El Fadil was born in Maghnia, Alnif, Morocco in 1970. He received the B.S. degree in Electronics, the Agrégation degree in Electrical Engineering, the M.S. degree in Automatic Control and Ph.D. in Automatic Control from Mohammadia School of Engineers, Mohammed V University, Rabat, Morocco, in 1994, 1999, 2003, and 2008, respectively.

Since 2011 he has been successively Assistant Professor and Habilitated Professor in the National School of Applied Sciences, Ibn Tofail University, Kénitra, Morocco. He is currently with the LGS Laboratory, and his research interest includes nonlinear and adaptive control, power converters and electric motors control, renewable energy, distributed energy resources, smart grid, and electric vehicles. He has published over 70 journal/conference papers.

Abdelouahad Tahri was born in 1964. He received Aggregation of Electrical Engineering from Ecole Normale Supérieure de l'Enseignement Technique, (ENSET), Rabat, Morocco, in 2009, the Master degree in Autmatique, Signal Processing and Industrial Computing from Faculty of Science and Technology of Settat, Morocco, in 2012, He is currently pursuing Ph.D. in modeling and nonlinear control of electric vehicles fed by renewable sources of energy, at ENSET, under the supervision of Prof. H. Elfadil, Prof. F. Giri, Prof. F.Z. Chaoui. Currently, he is a Professeur-Agrégé with the technical school in BTS classes, Sidi Kacem-Morocco. His research interests include optimization, observation, and nonlinear control systems of energy in electric vehicles. He has coauthored several papers on these topics.

Khawla Gaouzi was born in 1992. She received electrical engineering degree from the National School of Applied Sciences, Ibn Tofail University, Kénitra, in 2015.

Since 2016, she is preparing her Ph.D. in the nonlinear control of power converters, in the LGS Laboratory in ENSA Kenitra, under the supervision of Prof. H. El Fadil. Her research focuses on nonlinear and sampled data system, power converter control, and adaptive observer of nonlinear system. She is author or coauthor of several conference papers.

Aziz Rachid received the B.S. degree in Electrotechnics, the Aggregation degree in Electrical Engineering, the M.S degree in Electrical Engineering from the Higher School of Technical teaching (ENSET), Mohammed V University, Rabat, Morocco, in 1991, 1997, and 2016, respectively. From 1991 to 1997, he was an Electrical Engineering Professor in technical school, Agadir, Morocco. Since 1997 he has been an Associate Professor in BTS department in technical school Al Farabi, Salé, Morocco. Since 2004 he is a Cisco Instructor and he is teaching computer networks. He is currently pursuing Ph. D. in Electrical Engineering at LGS laboratory, Ibn Tofail University, Kénitra, Morocco. His main research area includes electric vehicles, V2X technology, and nonlinear control of power converters. He has coauthored several journal and conference papers.

Fouad Giri received a Ph.D. from the Institut National Polytechnique of Grenoble, France, in 1988 and is now Distinguished Professor at the University of Caen Basse-Normandie, Caen, France. He is currently serving as the General Chair of the IFAC Int. Workshops ALCOSP 2013 and PSYCO 2013. He is the Vice-Chair of the IFAC TC "Adaptive and Learning Systems" and is holding membership positions in the IFAC TCs on "Modelling, Identification and Signal Processing" and "Power Plants and Power Systems," and the IEEE CSS TC "System Identification and Adaptive Control." He is Associate Editor of the IFAC Journal Control Engineering Practice of the IEEE Transactions on Control Systems Technology and of the Editorial Board of IEEE CSS conferences. His research interests include nonlinear system identification, adaptive nonlinear control, constrained control, and control applications to power converters, electric machines, and power systems. He has supervised 20 PhDs and has coauthored three books and over 250 journal and conference papers on these topics.

Improvement of Power Quality Using Backstepping Control Strategy for a Transformerless Dual-Stage Grid-Connected Photovoltaic System

K. Chigane and M. Ouassaid

Abstract

A nonlinear control of the active and reactive power for a photovoltaic system is presented in this paper. The generated power is injected into the electrical grid via transformerless single-phase voltage source inverter. The conception of the proposed controller is based on the backstepping approach to develop the inverter control laws. Additionally, the global asymptotic stability of the system is guaranteed using the Lyapunov stability approach. In order to examine the performance of the proposed controller, a comparative study has been established between the obtained results and those of the conventional linear controller under irradiance variation. As a result, the proposed controller presents better reference tracking and provides unity power factor. Moreover, the harmonic analysis demonstrates that the injected power into the electrical grid has an improved quality using the backstepping control approach.

Keywords

Grid-connected inverter • Backstepping control • Active and reactive power control • Total harmonic distortion

1 Introduction

The growing demand for energy and the depletion of fossil energies makes renewable ones the only way to avoid an energy crisis. In the last years, photovoltaic (PV) power which is characterized by their direct conversion of sunlight to electricity, drew a great attention due to their increasing efficiency, simple exploitation and reducing costs (Rekioua and Matagne 2012; Kousksou et al. 2015).

The grid-tied form is one of the most gainful ways to exploit the PV energy. Very often, the injection of PV power into the network is made through a voltage source inverter (VSI), and sometimes includes a DC link converter in double stage structure, a transformer, or even both. According to (Kerekes et al. 2011; Schimpf and Norum 2008; González et al. 2008; Carrasco et al. 2006), the transformerless VSI are typified by their small size, lightweight, high efficiency, low cost and simple topology compared with their counterparts with galvanic insulation. The control of the injected active and reactive power can be achieved directly by controlling the current components of the VSI (Dhar and Dash 2016).

In fact, diverse current control methods have been proposed for the grid-connected PV systems. For instance, Proportional Resonant (PR), Proportional Integral (PI), Current Hysteresis Control (CHC) and Voltage-Oriented Control (VOC) can be cited as the significant ones (Timbus et al. 2009; Monfared and Golestan 2012; Teodorescu et al. 2006). At the electrical network frequency, the PR controller inserts a high gain allowing the removal of the steady-state error. Unfortunately, it has a bad transient response and high sensibility to the system parameter fluctuation. Similarly and despite its simplicity of design, the PI controller shows vulnerability to instability in the case of parameters disturbances and bad performances when the operating point varies (Blaabjerg et al. 2006). Likewise, the CHC is characterized by its fast dynamic response and ease of design and realize. However, the main drawback of this controller is its inconsistent switching frequency. The supremacy of the VOC is that the switching losses and the current harmonics can be reduced, but, the downside of this controller is its dependency on the applied current control method for the connected grid conditions and performance (Kadri et al. 2011; Chatterjee et al. 2017).

K. Chigane (✉) · M. Ouassaid
Ecole Mohammadia d'Ingénieurs, Mohammed V University in Rabat, Rabat, Morocco
e-mail: khalidchigane@research.emi.ac.ma

M. Ouassaid
e-mail: ouassaid@emi.ac.ma

S. El Hani and M. Essaaidi (eds.), *Recent Advances in Electrical and Information Technologies for Sustainable Development*, Advances in Science, Technology & Innovation, https://doi.org/10.1007/978-3-030-05276-8_21

It is worth noting that in addition to the mentioned control methods, some new techniques based on fuzzy logic (Premrudeepreechacharn and Poapornsawan 2000), sliding mode (Song Kim 2007; Song Kim et al. 2006), predictive control (Kojabadi et al. 2006; Yu and Chang 2005), artificial neural networks (Viola et al. 2007) and digital repetitive control (Guofei et al. 2012; Xuesong et al. 2010; Bojoi et al. 2011) are presented and implemented in the literature. The main objective of all these strategies of control is to maintain the benefits of conventional control techniques, notably specific control with low harmonic noises and distortion at the detriment of complicated design and implementation, more mathematical development and good identification of the system parameters (Monfared and Golestan 2012).

Thanks to its recursive and systematic design methodology for nonlinear feedback control, the Backstepping control has received significant attention these last years (Wang et al. 2013; Abouobaida et al. 2011; Ouassaid et al. 2005). In this work, the Backstepping approach is adopted to control the VSI of the grid-tied PV system. The aim is to ensure high performance in terms of harmonic distortion and dynamic response even under low solar irradiance. To this end, a single phase double stage inverter without transformer is used to minimize the injected PV power cost.

This chapter was structured according to these sequencing sections. After introduction in Sect 1, Mathematical model of grid-connected voltage source inverter and PV cell are described in Sect 2. Nonlinear control laws of voltage source inverter using backstepping approach are elaborated in Sect 3. Section 4 proposes MATLAB/Simulink simulations in order to verify the performance of the proposed control strategy. Finally, Sect 5 provides conclusion related to this work.

2 Mathematical Model of Grid-Connected Voltage Source Inverter and PV Cell

2.1 Modeling of the Photovoltaic Cell

A solar cell is a nonlinear device and can be represented as a current source model as shown in Fig. 1 (Rekioua and Matagne 2012; Messalti et al. 2015). It consists of a light generated current source, a single diode representing p-n junction cell, a shunt resistance R_p and a series resistance R_s describing an internal resistance of cell to the current flow. The solar cell terminal current can be expressed as follows:

$$I = I_{ph} - I_d - I_p \tag{1}$$

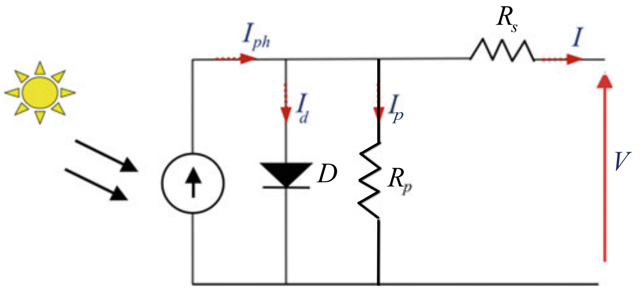

Fig. 1 Simplified equivalent circuit of a photovoltaic cell

where:

I_d	is the current through the diode,
I_{ph}	is the current generated by the incident light,
I_p	is the current through the parallel resistor R_p.

The current–voltage characteristic of a PV array is described by the following equation:

$$I = N_p I_{ph} - N_p I_{rs}\left[e^{\frac{q(V+R_sI)}{nkTN_s}} - 1\right] - N_p \frac{q(V+R_sI)}{N_s R_p} \tag{2}$$

where

V	is the cell output voltage (V),
I_{rs}	is the cell reverse saturation current,
T	is the reference cell operating temperature,
n	is the diode ideality constant,
q	is the electron charge ($1.60217646 \times 10^{-19}$ C),
k	is the Boltzmann constant ($1.3806503 \times 10^{-23}$ J/K),
R_p and R_s	are the shunt and series resistors of the cell, respectively.
N_p and N_s	are the number of parallel and series cells, respectively.

The generated photocurrent I_{ph} is related to the solar irradiation by the following equation:

$$I_{ph} = \frac{G}{1000}\left(I_{sc} + k_i(T - T_a)\right) \tag{3}$$

where:

I_{sc}	Cell short circuit current at reference temperature and irradiation,
k_i	Short-circuit current temperature coefficient,
T_a	Cell reference temperature,
G	Solar irradiation in W/m^2.

Fig. 2 Block diagram of the proposed control method of the VSI

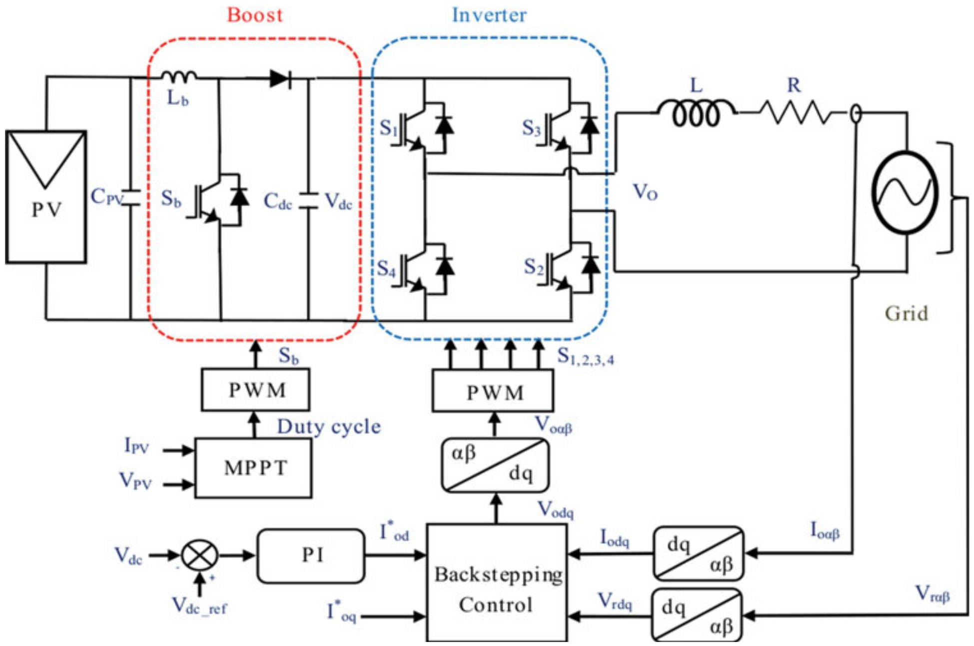

2.2 Modeling of the Grid-Connected VSI

The complete photovoltaic energy conversion system consists of the photovoltaic generator, the PWM converters (Boost and Inverter) and the electrical grid filter. The system considered is shown in Fig. 2.

The relationship between the supply, inverter, and line currents in the stationary reference frame α–β with Kirchhoff's voltage law according to Fig. 2, is given as follows (Samerchur et al. 2011):

$$\begin{bmatrix} V_{o\alpha} \\ V_{o\beta} \end{bmatrix} = L\frac{d}{dt}\begin{bmatrix} I_{o\alpha} \\ I_{o\beta} \end{bmatrix} + R\begin{bmatrix} I_{o\alpha} \\ I_{o\beta} \end{bmatrix} + \begin{bmatrix} V_{r\alpha} \\ V_{r\beta} \end{bmatrix} \tag{4}$$

where ($I_{o\alpha}$, $I_{o\beta}$), ($V_{o\alpha}$, $V_{o\beta}$) and ($V_{r\alpha}$, $V_{r\beta}$) are the outputs current and voltage of the inverter and the supply voltage components in the stationary reference frame α–β, respectively. L is the inductance and R is the parasitic resistance of inductance.

Presenting the voltage Eq. (4) in the rotating reference frame using d–q transformation at the supply frequency gives:

$$\begin{cases} \frac{dI_{od}}{dt} = \frac{1}{L}\left(L\omega I_{oq} - RI_{od} + V_{od} - V_{rd}\right) \\ \frac{dI_{oq}}{dt} = \frac{1}{L}\left(-L\omega I_{od} - RI_{oq} + V_{oq} - V_{rq}\right) \end{cases} \tag{5}$$

where ω is the angular frequency of the grid voltage. For a single-phase system, the active and reactive powers outputs, seen from the grid side, can be defined as:

$$\begin{cases} P = \frac{V_{r\max}}{\sqrt{2}} \cdot \frac{I_{o\max}}{\sqrt{2}}\cos(\varphi) \\ Q = -\frac{V_{r\max}}{\sqrt{2}} \cdot \frac{I_{o\max}}{\sqrt{2}}\sin(\varphi) \end{cases} \tag{6}$$

Here, $I_{o\max}$ and $V_{r\max}$ are the maximum output current of inverter and supply voltage respectively, and φ is the phase difference between the grid voltage V_r and the output current I_o.

Furthermore, the initial angle of the phase 1 is set to 0 and the initial angle of the d–q reference frame is set to π/2, this leads the V_{rq} component to be zero. The above P and Q equations in this reference frame will become:

$$\begin{cases} P = \frac{1}{2}V_{rd}I_{od} \\ Q = -\frac{1}{2}V_{rd}I_{oq} \end{cases} \tag{7}$$

Hence, the active and reactive power can be controlled by the I_{od} and I_{oq} respectively. It is worth to notice that, the DC-bus voltage has been controlled using a conventional PI controller to eliminate the instantaneous error.

3 Nonlinear Control of Voltage Source Inverter Using Backstepping Approach

In order to control the active and reactive power using Backstepping approach, we define the tracking error signals involving the desired variables I_{od}^{*} and I_{oq}^{*} ,respectively:

$$\begin{cases} e_{od} = I_{od}^{*} - I_{od} \\ e_{oq} = I_{oq}^{*} - I_{oq} \end{cases} \tag{8}$$

where I_{od}^{*} is the desired value of I_{od} which is given by the PI controller of the DC-bus voltage, and I_{oq}^{*} is the reference value of I_{oq} which is forced to be equal zero in order to obtain a unity power factor.

The differentiation of the error signals e_{od} and e_{oq} can be expressed as:

$$\begin{cases} \dfrac{de_{od}}{dt} = \dfrac{dI_{od}^{*}}{dt} - \dfrac{dI_{od}}{dt} = \dfrac{dI_{od}^{*}}{dt} - (a_2 I_{oq} - a_3 I_{od} + a_1(V_{od} - V_{rd})) \\ \dfrac{de_{oq}}{dt} = \dfrac{dI_{oq}^{*}}{dt} - \dfrac{dI_{oq}}{dt} = \dfrac{dI_{oq}^{*}}{dt} - (a_1 V_{oq} - a_2 I_{od} - a_3 I_{oq}) \end{cases} \tag{9}$$

where $a_1 = 1/L$, $a_2 = \omega$, and $a_3 = R/L$. Consider the Lyapunov function candidate as:

$$V_L = \frac{1}{2}(e_{od}^2 + e_{oq}^2) \tag{10}$$

Then its derivative is given as:

$$\frac{dV_L}{dt} = e_{od}\frac{de_{od}}{dt} + e_{oq}\frac{de_{oq}}{dt} \tag{11}$$

This yields the following:

$$\begin{aligned} \frac{dV_L}{dt} = {} & e_{od}\left(\frac{dI_{od}^{*}}{dt} - a_2 I_{oq} + a_3 I_{od} - a_1(V_{od} - V_{rd})\right) \\ & + e_{oq}\left(\frac{dI_{oq}^{*}}{dt} - (a_1 V_{oq} - a_2 I_{od} - a_3 I_{oq})\right) \end{aligned} \tag{12}$$

The Eq. (12) can be written as

$$\begin{aligned} \frac{dV_L}{dt} = {} & e_{od}\left(K_{od}e_{od} + \frac{dI_{od}^{*}}{dt} - a_2 I_{oq} + a_3 I_{od} - a_1(V_{od} - V_{rd})\right) \\ & + e_{oq}\left(K_{oq}e_{oq} + \frac{dI_{oq}^{*}}{dt} - (a_1 V_{oq} - a_2 I_{od} - a_3 I_{oq})\right) \\ & - K_{od}e_{od}^2 - K_{oq}e_{oq}^2 \end{aligned} \tag{13}$$

where K_{od} and K_{oq} are positive design constants that determine the closed loop dynamics. To ensure the Lyapunov stability criteria i.e., $\frac{dV_L}{dt} \leq 0$ (Pervej et al. 2016), the nonlinear controls inputs V_{oq}^{*} *and* V_{od}^{*} are defined as:

$$\begin{cases} V_{od}^{*} = L\dfrac{dI_{od}^{*}}{dt} - \omega L I_{oq} + V_{rd} + LK_{od}e_{od} + RI_{od} \\ V_{oq}^{*} = L\dfrac{dI_{oq}^{*}}{dt} + I_{oq}R + LK_{oq}e_{oq} + \omega L I_{od} \end{cases} \tag{14}$$

Theorem 1 *The global asymptotic stability of* (9) *is guaranteed, if the control laws are given by* (14). *Therefore, the asymptotic convergence of the current components* I_{od} *and* I_{oq} *to their desired values* I_{od}^{*} *and* I_{oq}^{*}, *respectively is achieved.*

Proof By replacing (14) in (13), the derivative of the Lyapunov function can be derived as follows:

$$\frac{dV_L}{dt} = -K_{od}e_{od}^2 - K_{oq}e_{oq}^2 \leq 0 \tag{15}$$

Consequently, the global asymptotic stability of the Backstepping controller is guaranteed.

4 Simulation Results

In order to verify the performance of the proposed nonlinear Backstepping control, a comparative computer simulation study between the conventional control using PI controllers and the proposed nonlinear controller has been carried out in MATLAB/Simulink environment. The simulation has been executed under temperature of 25 °C and variation of solar irradiance.

4.1 Performance of the Proposed Control Method

A switching frequency of 10 kHz was used in the simulations for the both methods of control. The control parameters of the Backstepping control are $K_{od} = 34$ and $K_{oq} = 140$.

As can be seen in Fig. 3a, the current injected into the grid is in phase agreement with the supply voltage and it has the sinusoidal waveform. Also, it can be noticed that the power factor, of proposed controller, is unitary. In addition,

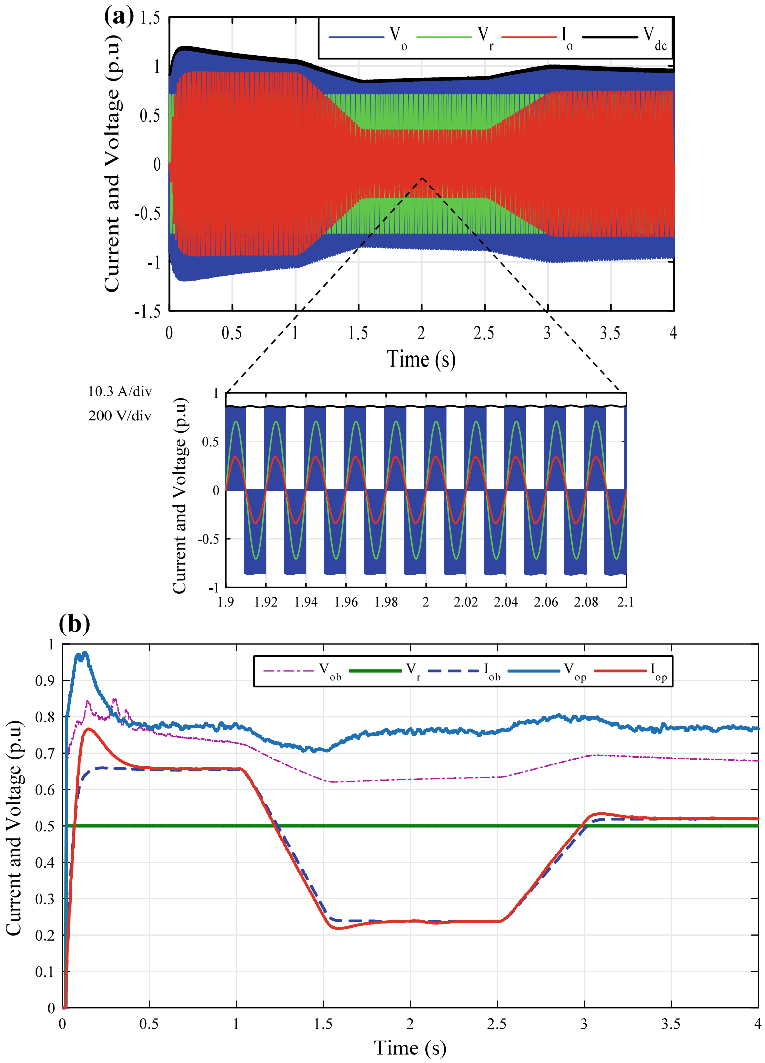

Fig. 3 Current and voltage at the grid connection point, **a** Backstepping control technique, **b** Root mean square values for Backstepping control (**b**) and linear control (p)

the root mean square values of current and voltage with Backstepping control present a good performance and fast response as shown in Fig. 3b.

Figure 4 shows that the frequency is less disturbed around 50 Hz in the nonlinear control than the conventional control method. Moreover, the reactive power of the proposed control is equal to 0 VAr, even under the solar irradiation variation, while the linear controller shows instability around the reference value of the reactive power.

The active power of both control methods is presented in Fig. 5. It is clear that the Backstepping control has a better dynamic response reflected in time response of 0.45 s and overshot of 0.73% compared with a PI controller method which has 0.7 s and 17.2% respectively.

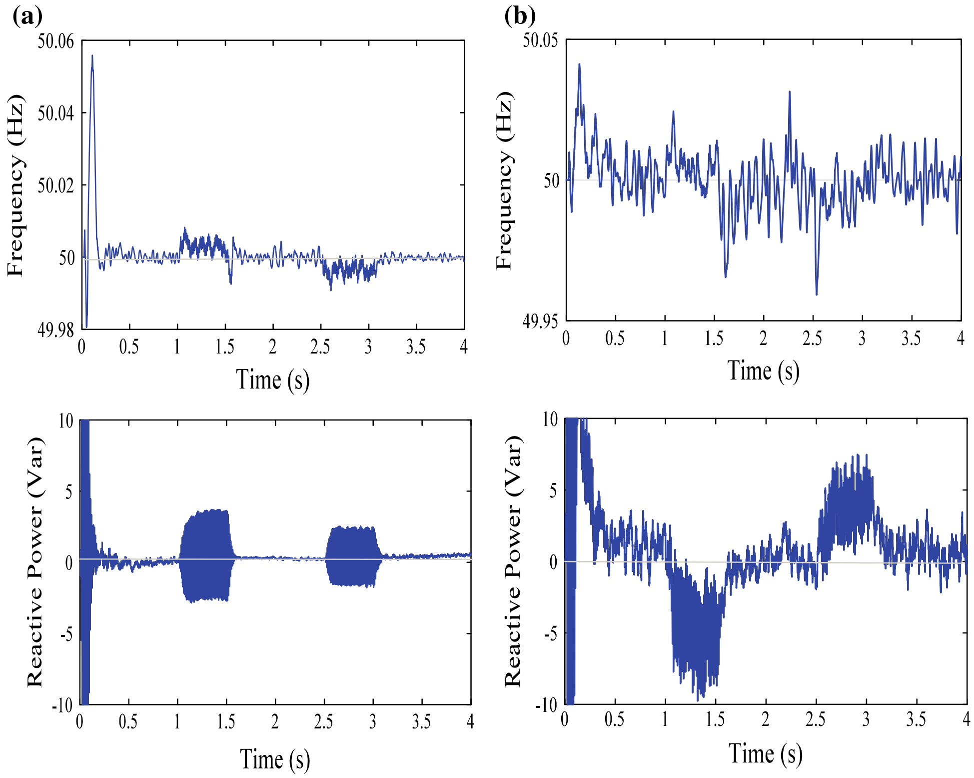

Fig. 4 Power PWM inverter performances. **a** Backstepping control method. **b** Conventional method PI control

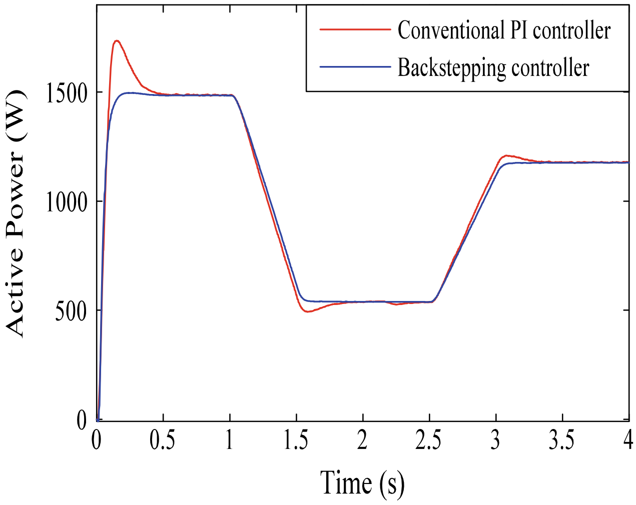

Fig. 5 Active power injected

4.2 Impact of the Solar Irradiance on the THD

The third harmonic and the fifth harmonic of the current injected into the electrical grid, computed by the discrete Fourier transform (DFT) for both methods of control is shown in Table 1. The THD of the output current for the VSI control system for the two strategies of control is shown in Fig. 6.

As it can be seen from this figure, the injected current decrease and its THD increase when the solar irradiance decreases. Table 1 demonstrates that the third and the fifth harmonics have not an order of increasing or decreasing while the THD still rises when the solar irradiance decreases, due to the respective decrease in the current generated by the PV panel. The analysis of Table 1 yields to conclude that the THD of the current with the proposed controller is smaller than THD induced by the PI controller for any solar irradiance.

Table 1 Third harmonic and fifth harmonic of the current injected into the grid

Solar irradiance (W/m^2)	Backstepping control		PI control	
	Third harmonic (%)	Fifth harmonic (%)	Third harmonic (%)	Fifth harmonic (%)
1000	1.47	0.87	1.22	1.02
900	1.47	0.86	1.31	0.9
800	1.46	0.85	1.46	0.73
700	1.58	0.89	1.6	0.52
600	1.62	0.92	1.65	0.49
500	1.71	0.97	2.02	0.46
400	1.62	0.89	2.22	0.48
300	1.33	0.73	2.66	1.09
200	2.95	1.6	3.78	1.62
100	1.81	0.84	1.87	4.85

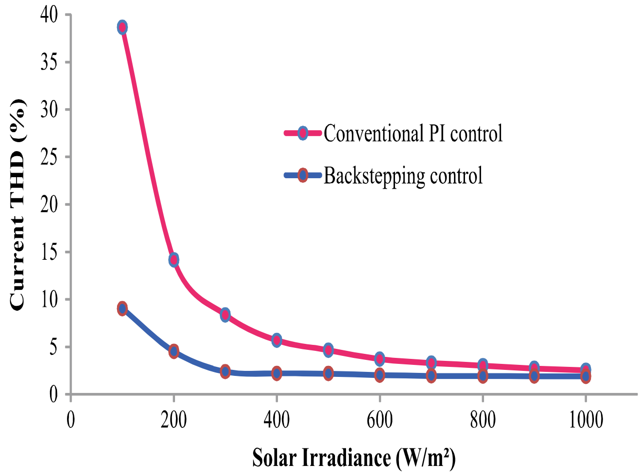

Fig. 6 THD of the current injected into the electrical grid

As expected, the proposed control is capable of providing accurate tracking of reactive and active power references and keeping good decoupling of reactive and active power control. Moreover, a good power factor correction is reached.

5 Conclusion

In this paper, a nonlinear Backstepping control approach has been developed and applied to the transformerless grid-connected VSI. The aim is to guarantee high power quality of the solar energy converted and injected into the grid. To this end, the detailed establishment of the inverter control laws has been given and proven using Lyapunov stability theory. Hence, independent and stable control of the active and reactive power is achieved employing the proposed technique.

Through a comparative study with the classical PI controller, the validity of the proposed controller is confirmed for the PV system. In other terms, the Backstepping controller provides a good synchronization with the network, higher quality of dynamic performances and great references tracking with minimum THD than the linear PI controller.

In short, the proposed control strategy owns a good decoupling of active and reactive power to deal with solar irradiance variation.

References

Abouobaida, H., Cherkaoui, M., & Ouassaid, M. (2011). Robust maximum power point tracking for photovoltaic cells: A backstepping mode control approach. In *International Conference on Multimedia Computing and Systems* (pp. 1–4). https://doi.org/10.1109/icmcs.2011.5945706.

Blaabjerg, F., Teodorescu, R., Liserre, M., & Timbus, A. V. (2006). Overview of control and grid synchronization for distributed power generation systems. *IEEE Transactions on Industrial Electronics, 53,* 1398–1409. https://doi.org/10.1109/tie.2006.881997.

Bojoi, R. I., Limongi, L. R., Roiu, D., & Tenconi, A. (2011). Enhanced power quality control strategy for single-phase inverters in distributed generation systems. *IEEE Transactions on Power Electronics, 26,* 798–806. https://doi.org/10.1109/tpel.2010.2103572.

Carrasco, J. M., Bialasiewicz, J. T., Guisado, R. C. P., & León, J. I. (2006). Power-electronic systems for the grid integration of renewable energy sources: A survey. *IEEE Transactions on Industrial Electronics, 53,* 1002–1017. https://doi.org/10.1109/TIE.2006.878356.

Chatterjee, A., Mohanty, K., Kommukuri, V. S., & Thakre, K. (2017). Design and experimental investigation of digital model predictive current controller for single phase grid integrated photovoltaic systems. *Renewable Energy, 108,* 438–448. https://doi.org/10.1016/j.renene.2017.02.057.

Dhar, S., & Dash, P. K. (2016). A new backstepping finite time sliding mode control of grid connected PV system using multivariable dynamic VSC model. *International Journal of Electrical Power and Energy Systems, 82,* 314–330. https://doi.org/10.1016/j.ijepes.2016.03.034.

Gonzàlez, R., Gubia, E., Lopez, J., & Marroyo, L. (2008). Transformerless single-phase multilevel-based photovoltaic inverter. *IEEE Transactions on Industrial Electronics, 55,* 2694–2702. https://doi.org/10.1109/tie.2008.924015.

Guofei, T., Guochun, X., Zhibo, Z., & Yong, L. (2012). A control method with grid disturbances suppression for a single-phase LCL-filter-based. In *Twenty-Seventh Annual IEEE Applied Power Electronics Conference and Exposition (APEC)* (pp. 1489–1493). https://doi.org/10.1109/apec.2012.6166017.

Kadri, R., Gaubert, J. P., & Champenois, G. (2011). An improved maximum power point tracking for photovoltaic grid-connected inverter based on voltage-oriented control. *IEEE Transactions on Industrial Electronics, 58,* 66–75. https://doi.org/10.1109/tie.2010.2044733.

Kerekes, T., Teodorescu, R., Rodriguez, P., Vazquez, G., & Aldabas, E. (2011). A new high-efficiency single-phase transformerless PV inverter topology. *IEEE Transactions on Industrial Electronics, 58,* 184–191. https://doi.org/10.1109/tie.2009.2024092.

Kim, I.-S. (2007). Robust maximum power point tracker using sliding mode controller for the three-phase grid-connected photovoltaic system. *Solar Energy, 81,* 405–414. https://doi.org/10.1016/j.solener.2006.04.005.

Kim, I.-S., Kim, M. B., & Youn, M. J. (2006). New maximum power point tracker using sliding-mode observer for estimation of solar array current in the grid-connected photovoltaic system. *IEEE Transactions on Industrial Electronics, 53,* 1027–1035. https://doi.org/10.1109/tie.2006.878331.

Kojabadi, H. M., Yu, B., Gadoura, I. A., Chang, L., & Ghribi, M. (2006). A novel DSP-based current-controlled PWM strategy for single phase grid connected inverters. *IEEE Transactions on Power Electronics, 21,* 985–993. https://doi.org/10.1109/tpel.2006.876851.

Kousksou, T., Allouhi, A., Belattar, M., Jamil, A., El Rhafiki, T., Arid, A., & Zeraouli, Y. (2015). Renewable energy potential and national policy directions for sustainable development in Morocco. *Renewable and Sustainable Energy Reviews, 47,* 46–57. https://doi.org/10.1016/j.rser.2015.02.056.

Messalti, S., Harrag, A., & Loukriz, A. (2015). A new neural networks MPPT controller for PV systems. In *6th International Renewable Energy Congress (IREC)* (pp. 1–6). https://doi.org/10.1109/irec.2015.7110907.

Monfared, M., & Golestan, S. (2012). Control strategies for single-phase grid integration of small-scale renewable energy sources: A review. *Renewable and Sustainable Energy Reviews, 16,* 4982–4993. https://doi.org/10.1016/j.rser.2012.04.017.

Ouassaid, M., Cherkaoui, M., & Maaroufi, M. (2005). Improved nonlinear velocity tracking control for synchronous motor drive using backstepping design strategy. In *IEEE Russia Power Tech, St. Petersburg* (pp. 1–6). https://doi.org/10.1109/ptc.2005.4524565.

Pervej, M. F., Roy, T. K., Tumpa, F. K., & Sarkar, M. I. (2016). Nonlinear backstepping controller design for a three-phase grid-connected photovoltaic system using DPC approach. In *9th International Conference on Electrical and Computer Engineering* (pp. 407–410). https://doi.org/10.1109/icece.2016.7853943.

Premrudeepreechacharn, S., & Poapornsawan, T. (2000). Fuzzy logic control of predictive current control for grid-connected single phase inverter. In *Conference Record of the Twenty-Eighth IEEE Photovoltaic Specialists Conference* (pp. 1715–1718). https://doi.org/10.1109/PVSC.2000.916234.

Rekioua, D., & Matagne, E. (2012). *Optimization of photovoltaic power systems: Modelization, simulation and control*. London: Springer Verlag.

Samerchur, S., Premrudeepreechacharn, S., Kumsuwun, Y., & Higuchi, K. (2011). Power control of single-phase voltage source inverter for grid-connected photovoltaic systems. In *IEEE/PES Power Systems Conference and Exposition* (pp. 1–6). https://doi.org/10.1109/psce.2011.5772504.

Schimpf, F., & Norum, L. E. (2008). Grid connected converters for photovoltaic, state of the art, ideas for improvement of transformerless inverters. In *Nordic Workshop on Power and Industrial Electronics*.

Teodorescu, R., Blaabjerg, F., Liserre, M., & Loh, P. C. (2006). Proportional-resonant controllers and filters for grid-connected voltage-source converters. *IEE Proceedings Electrical Power Application, 153,* 750–762. https://doi.org/10.1049/ip-epa:20060008.

Timbus, A., Liserre, M., Teodorescu, R., Rodriguez, P., & Blaabjerg, F. (2009). Evaluation of current controllers for distributed power generation systems. *IEEE Transactions on Power Electronics, 24,* 654–664. https://doi.org/10.1109/tpel.2009.2012527.

Viola, J., Restrepo, J., Aller, J. M., Diaz, M., Harley, R., & Habetler, T. (2007) Simplified control structure for current control of single phase rectifiers using COT-ANN-PWM. In *Proceedings of International Joint Conference on Neural Networks* (pp. 1370–1374). https://doi.org/10.1109/ijcnn.2007.4371158.

Wang, G., Wai, R., & Liao, Y. (2013). Design of backstepping power control for grid-side converter of voltage source converter-based high-voltage dc wind power generation system. *IET Renewable Power Generation, 7,* 118–133. https://doi.org/10.1049/iet-rpg.2012.0358.

Xuesong, Z., Daichun, S., Youjie, M., & Deshu, C. (2010). Grid-connected control and simulation of single-phase two-level photovoltaic power generation system based on repetitive control. In *International Conference on Measuring Technology and Mechatronics Automation* (pp. 366–369). https://doi.org/10.1109/icmtma.2010.307.

Yu, B., & Chang, L. (2005). Improved predictive current controlled PWM for single-phase grid-connected voltage source inverters. In *PESC Record—IEEE Annual Power Electronics Specialists Conference* (pp. 231–236). https://doi.org/10.1109/pesc.2005.1581629.

Khalid Chigane was born in Morocco in 1993. He received the Bachelor's degree in Engineering Sciences from the Faculty of Sciences and Techniques, Moulay Ismaïl University, Errachidia, Morocco, in 2014 and the Master degree in Renewable Energies and Storage from the Faculty of Sciences, Mohammed V University, Rabat, Morocco, in 2016. He is currently working toward the Ph.D. degree in the Department of Electrical Engineering, Mohammadia School of Engineering (EMI), Mohamed V University, Rabat, Morocco, his research interests include control and optimization of grid-connected PV systems.

Mohammed Ouassaid received his Diploma of Agrégation degree in Electrical Engineering from Ecole Normale Supérieur de l'Enseignement Technique, Rabat, in 1999, and MScA and Ph.D. degrees in Electrical Engineering from Mohammadia School of Engineering (EMI), Mohamed V University, Rabat, Morocco, in 2002 and 2006, respectively. In 2012, he received the diploma of University's Habilitation.

During 2008–2015, he was a Professor at National School of Applied Sciences (ENSA-Safi) Cadi Ayyad University, Morocco. In 2015, he joined the Department of Electrical Engineering, Mohammadia School of Engineering, Rabat, Morocco, where he is currently a Professor. His main research interests include electrical drives, power systems, control, and optimization of renewable energy, integration of wind power and photovoltaic system, and smart grid. He is the author or coauthor of numerous book chapters and papers in refereed journals and international conference proceedings. Dr. Ouassaid is also involved in a number of research and teaching projects. He is a member of the IEEE Power & Energy Society.

A Multi-Modelling Approach and Optimal Control of Greenhouse Climate

Ayoub Moufid and Najib Bennis

Abstract

The objective of greenhouse climate control is to improve the cultural development and to minimize the production costs. In this paper, we propose a comparison between two approaches to modelling and control greenhouse's inside climate. This one is defined by internal temperature and hygrometry. The classical approach is based on a single linear model to describe the dynamic of greenhouse internal climate and using a strategy control to regulate the microclimate inside the greenhouse. The multi-modelling approach aims to reduce the complexity of the system in terms of variables to take into account in modelling and controllers design. Therefore, we have developed two linear models for representing the greenhouse inside climate in two different durations. Those diurnal and nocturnal phases. For the control of greenhouse inside climate based on finite-horizon optimal control, we present two methods. The first one is a classical method and consists of controlling the internal climate by using a single controller for all days. The other one is based on two models and two controllers for nocturnal and diurnal phases. For the needs of simulation purpose, we have used a nonlinear model to describe more effectively the behaviour of greenhouse dynamic climate. A successful feasibility study of the proposed controller is presented and simulation results show good performances despite the high interaction between the process internal and external variables. The comparison results confirm the superiority of a multi-modelling approach.

Keywords

Greenhouse • Climate control • Multi-modelling • Diurnal and nocturnal phases • Identification • Finite-horizon optimal control

1 Introduction

The agricultural greenhouse is a multi-function system of protecting and controlling the development of plantation. Its role consists of reducing the effect of outside climate in order to ensure a safe space for plants growing. However, the demanding needs of growers have remarkably changed in term of quality and quantity of production. Actually, the problem is not limited to protection of plantations, but it treats the control and improvement of plantation evolution. That is why several researchers have interested to control greenhouse inside climate. The objective is to maintain de internal temperature and hygrometry near to the suitable values.

Principally, the aim of inside climate control is to respect the following constraints:

(1) To profit more from the growing season in term of improving the quantity of production, and the duration of cultivation.
(2) To ensure a perfect control of inside climate which permits to obtain a high quality of products.
(3) Permit to growers a low-cost production system, with minimal natural resources.

Achieving these objectives requires more clarifying the physical interaction between all components of agricultural greenhouses. The internal state depends on the effects of actuators and strongly influenced by the outside weather. The difficulty to modelling and to control inside climate lies on the diversity of phenomena that affect its evolution. Essentially dictated by the day/night cycle, the growth season, the local climate and the nature of the culture.

A. Moufid (✉) · N. Bennis
ENSET of Rabat, University Mohamed V of Rabat, Rabat, Morocco
e-mail: ayoub.moufid@um5s.net.ma

N. Bennis
e-mail: n.bennis@um5s.net.ma

S. El Hani and M. Essaaidi (eds.), *Recent Advances in Electrical and Information Technologies for Sustainable Development*, Advances in Science, Technology & Innovation, https://doi.org/10.1007/978-3-030-05276-8_22

Therefore, the greenhouse system is considered as a nonlinear, multivariable, no stationary system and open to the exterior environment (Bennis et al. 2008).

In recent years, many researchers have been considerably interested in the subject of modelling and control greenhouse inside climate and have contributed to the elaboration of diverse technics of control. Thus, different types of algorithms have been submitted like robust control (Bennis et al. 2008), multi-model and neural modelling (Laribi et al. 2006), model-free control (Lafont et al. 2015), fuzzy control (Lafont and Balmat 2002), optimal control (Straten and Henten 2010), PID and Intelligent PI (El Afou et al. 2014), Genetic algorithm (Herrero et al. 2008).

Several intelligent controllers have been applied to control inside climate: Dynamic decoupling controllers (Paraforos and Griepentrog 2013), Multiple neural control (Fourati 2014), feedforward and recurrent neural networks (Fourati and Chtourou 2007), smart frost control in greenhouses (Castañeda-Miranda and Castaño 2017). In this work, we propose a special regulator profiting the high performances of multi-modelling approach and the robustness of finite-horizon optimal control. The modelling of the greenhouse is based on the splitting of the day into diurnal and nocturnal phases for which optimal controllers are designed.

This paper is organized into five sections. Section 2 is dedicated to greenhouse modelling and parametric identification. Section 3 focuses on a finite-horizon optimal control applied to a single and multi-modelling approaches. Section 4 is dedicated to present the simulation results, which show the feasibility of the proposed approach. Finally, a conclusion is given in the last section.

2 Greenhouse Climate Modelling and Identification

2.1 Introduction to Greenhouse Climate Modelling

The main objective of modelling agricultural greenhouse inside climate is to present a mathematical description of internal variables evolution. In our case, we consider the temperature and the hygrometry as relevant variables to describe the inside climate. In several researches (Bennis et al. 2008; Laribi et al. 2006), we found two approaches to modelling internal climate. The first one is based on physical laws to describe the interactions between different variables. This one is an efficient way to simulate the behaviour of internal climate in a different meteorological situations. In addition, it permits to compare different methods of control in the same conditions as the disturbance phenomena. Such a comparison is only possible through the numerical simulation as meteorological disturbances are not repetitive phenomena. For the need of simulation, we propose to develop a nonlinear model as benchmark to describe a realistic greenhouse behaviour and two linear models for control design.

In the case of the greenhouse system, a single model does not seem able to describe the dynamic at any time of the days and the years.

For improving the performances of inside climate modelling, we propose the multi-modelling approach as detailed in Sect. 3. This method is interesting as it describes a complex process by a set of linear models, which constitute a library of models (Laribi et al. 2006).

2.2 Inputs/Outputs of Greenhouse Process

The block diagram of the greenhouse system is presented in Fig. 1.

All variables that influence the internal climate of the process are mentioned and classified into three categories:

The control inputs:

- *Ch*: Heating manipulated by on–off control.
- *Ov* (°): Roofing.
- *Om* (m): Shadiness.
- *Br*: Moistening manipulated by on–off control.

The controlled outputs:

- *Ti* (°C): Internal temperature.
- *Hi* (%): Internal hygrometry.

The meteorological disturbances:

- *Rg* (W/m^2): Global radiation.
- *Te* (°C): External temperature.
- *He* (%): External hygrometry.
- *Vv* (m/s): Wind spend.

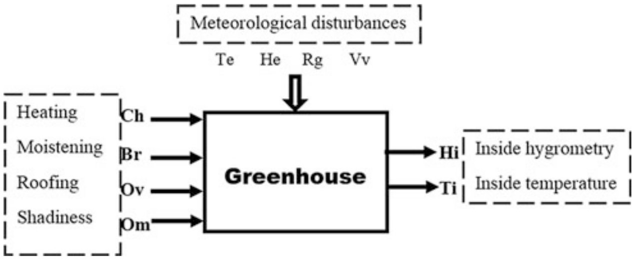

Fig. 1 Block diagram of the greenhouse

2.3 A Nonlinear Model Development

For the needs of simulation, we first adopt a nonlinear model basing on physical laws to describe the real evolution of internal climate. This one has elaborated by (Bennis et al. 2008). This model is derived from energy balance for the temperature and water mass balance for the hygrometry. The idea is to extend the physical model established in (Gaudin 1981) by taking in account an important number of relevant variables conditioning the behaviour of the greenhouse. This model can be written as the following form:

$$\begin{cases} T_i(k+1) = f(Ti(k), Hi(k), U(k), D(k), \lambda) \\ H_i(k+1) = g(Ti(k), Hi(k), U(k), D(k), \theta) \end{cases} \tag{1}$$

where f and g are two nonlinear functions, (λ, θ) are a set of parameters to be identified, and

$$\begin{cases} D(k) = [Te(k)\, He(k)\, Rg(k)\, Vv(k)]^T \\ U(k) = [Ch(k)\, Br(k)\, Ov(k)\, Om(k)]^T \end{cases} \tag{2}$$

As this model is linear with regard to general parameters, (λ, θ), we have applied the off-line least squares method as presented in Fig. 2.

The nonlinear model obtained have been validated successfully for the data collected during the day used for identification and for three successive days as shown in Fig. 3. This model is considered as a benchmark model and it will be used to represent in realistic conditions the greenhouse behaviour during successive days.

2.4 A Linear Models Control Development and Identification

2.4.1 Single Model Approach

The objective is the design of linear controller to regulate greenhouse inside climate. The previous model is nonlinear and permits to predict the dynamic evolution of internal climate in the greenhouse. However, it is so complex to use the linearization notion around a steady state operating point to obtain a linear model. In the case of the greenhouse, we do not have only one operating point. Indeed, this one can be defined according to periods given of the day, or according to seasons given of the year.

In this work, we have adopted an approach that consists in considering the greenhouse system as a black box model and to identify the parameters of proposed model. Therefore, we propose the following simple linear stationary and discrete-time model of the process permitting to elaborate a linear regulator:

$$\begin{cases} Ti(k+1) = a_1Ti(k) + a_2Hi(k) + a_3Te(k) + a_4He(k) + a_5Ov(k) \\ \qquad + a_6Rg(k) + a_7Vv(k) + a_8Om(k) + a_9Br(k) + a_{10}Ch(k) \\ Hi(k+1) = b_1Ti(k) + b_2Hi(k) + b_3Te(k) + b_4He(k) + b_5Ov(k) \\ \qquad + b_6Rg(k) + b_7Vv(k) + b_8Om(k) + b_9Br(k) + b_{10}Ch(k) \end{cases} \tag{3}$$

The parameters identification is based on the off-line least squares method as presented in Fig. 2 basing on the input/output data measured during 24 hours.

2.4.2 Multi-Model Approach

It appears that a single model is not able to describe the dynamic behaviour of internal climate. So a better modelling

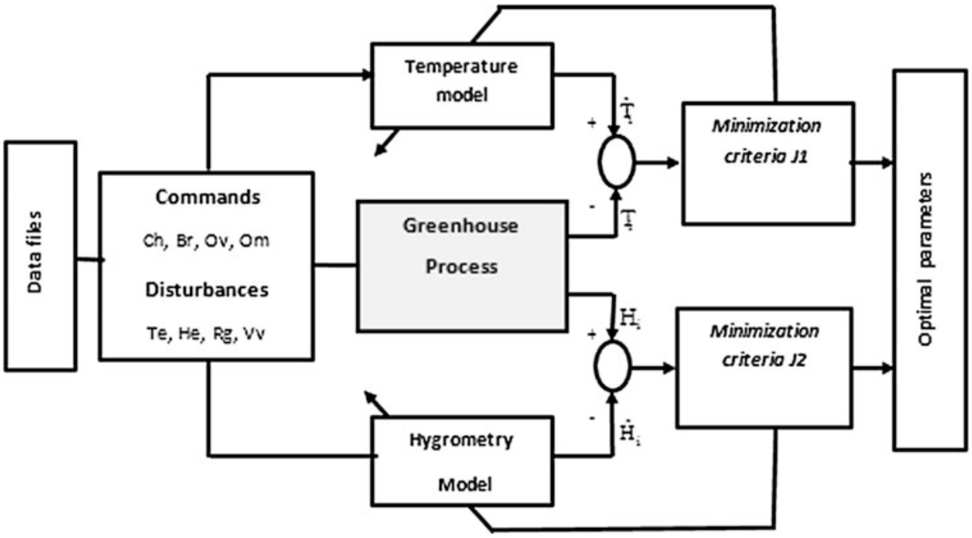

Fig. 2 Block diagram of the off-line parameters identification

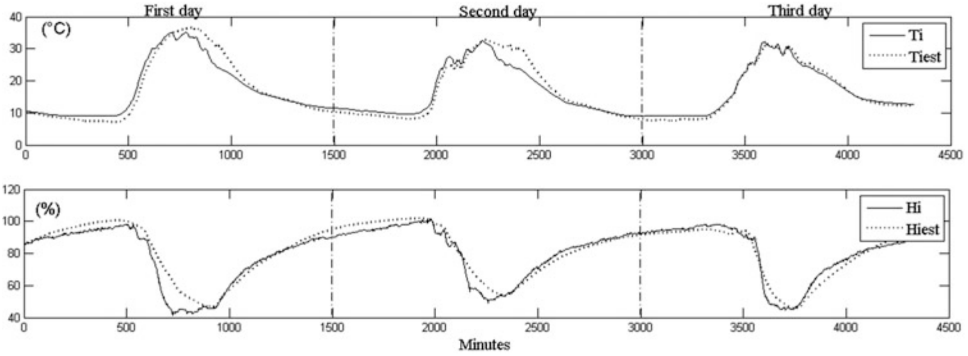

Fig. 3 Nonlinear model identification: estimated (*Tiest*; *Hiest*) and measured (*Ti; Hi*) inside temperature and hygrometry during three successive days

must be considered. The multi-modelling approach consists of modelling the greenhouse system by a set of models (Laribi et al. 2006; Ksouri et al. 2001). Each one is specified to describe the process in a domain of validity. Generally, the ranges of validity are defined using a human expertise. In (Laribi et al. 2006), the multi-model approach has applied to model the internal temperature of a greenhouse. The authors have presented a library of five models cover the range of temperature from 5 to 18 °C but some relevant characteristics are neglected. Indeed, the proposed model is single-input/single-output and insufficient to describe the temperature control. The number of models used here requires a significant time in the real-time control situation.

In our case, we present a realistic multi-modelling approach that permits to describe the internal climate state by using two models taking into account relevant variables that influence the internal climate. This approach consists of dividing a period of 24 hours into diurnal and nocturnal periods. We have based on a human expertise to determine two temporal domains profiting the knowledge of the greenhouse system in order to propose two models.

Figure 4 and Fig. 5 present respectively the synoptic schema of diurnal and nocturnal models.

$$\begin{cases} Ti(k+1) = \alpha 1Ti(k) + \alpha 2Hi(k) + \alpha 3Te(k) + \alpha 4He(k) + \alpha_5 Ov(k) \\ \qquad + \alpha_6 Rg(k) + \alpha 7Vv(k) + \alpha 8Om(k) + \alpha 9Br(k) \\ Hi(k+1) = \beta 1Ti(k) + \beta 2Hi(k) + \beta 3Te(k) + \beta 4He(k) + \beta_5 Ov(k) \\ \qquad + \beta_6 Rg(k) + \beta 7Vv(k) + \beta 8Om(k) + \beta 9Br(k) \end{cases} \tag{4}$$

$$\begin{cases} Ti(k+1) = \alpha 1Ti(k) + \alpha 2Hi(k) + \alpha 3Ch(k) + \alpha 4Om(k) + \alpha 5Te(k) \\ \qquad + \alpha 6He(k) + \alpha 7Vv(k) \\ Hi(k+1) = \beta 1Ti(k) + \beta 2Hi(k) + \beta 3Ch(k) + \beta 4Om(k) + \beta_5 Te(k) \\ \qquad + \beta_6 He(k) + \beta 7Vv(k) \end{cases} \tag{5}$$

Therefore, we propose the simple linear stationary and discrete-time model (4) and (5), respectively, for the diurnal and nocturnal period of the day.

After the data measured during 24 hours has been divided into two phases, we have used the off-line least squares method to determine multi-model parameters.

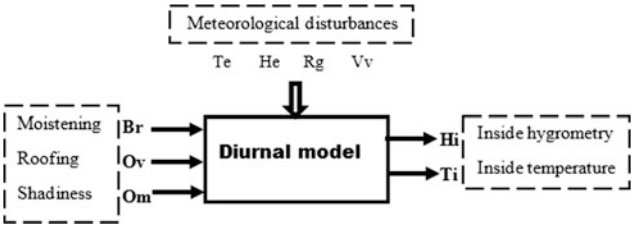

Fig. 4 Synoptic schema of diurnal model

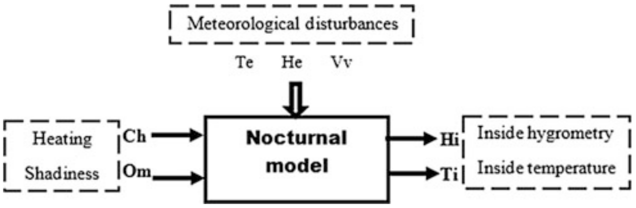

Fig. 5 Synoptic schema of nocturnal model

Figure 6 represents a different models responses and data measure during three successive days. A comparison between measured and estimated values of inside air temperature and hygrometry shows a satisfactory result for the day that has been used for the parameters identification (third day), but a clear mismatch can be seen for others days.

It appears that a single model is not able to describe the dynamic behaviour of internal climate. So a better modelling must be considered.

For comparing a single model (3) and a multi-model (4), (5), the modelling and identification results presented in Fig. 6 shows an improvement of the hygrometry modelling quality by using a multi-model linear approach. However, the quality of temperature modelling remain similar for both approaches.

Table 1 confirms all remarks and conclusions about the comparison steady between the estimated and measured variables for one day and successive days. The criterion performance used is the root mean least squared errors.

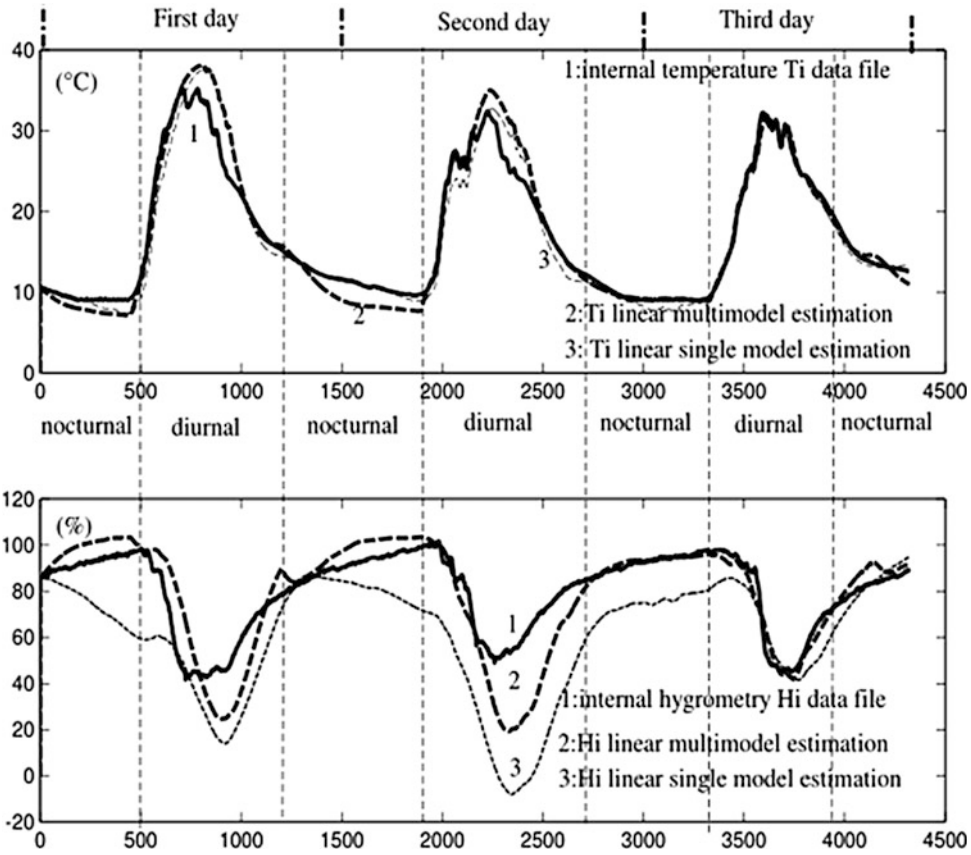

Fig. 6 Linear single and multi-modelling identification. Estimation of internal temperature and hygrometry

Table 1 Inside greenhouse temperature and hygrometry models validation over several days

Day(s)	One day		Three consecutive days	
N: samples	1440		1440 * 3	
	Single model	Multi-model	Single model	Multi-model
$\frac{\sum_{k=1}^{N} \vert Tiest(k)-Ti(k) \vert}{N}$	0.49	0.40	0.23	1.26
$\frac{\sum_{k=1}^{N} \vert Hiest(k)-Hi(k) \vert}{N}$	6.20	2.97	19.89	7.89
Ti, Hi: measured values	Tiest, Hiest: estimated values		N: size of the data samples	

3 Optimal Control of the Greenhouse

The second part of this work deals with the conception of two optimal controllers able to give a suitable environment for growing. The control law synthesis to regulate the microclimate of a greenhouse passes by a control model that represents imperfectly the reality. The sources of uncertainties on the model of the greenhouse are numerous: badly known or neglected dynamic, effect of the linearization, stationary hypothesis. From the moment that we use an imperfect model, it becomes necessary to consider the robustness of this control law, that is, in a qualitative way, the aptness to use imperfect models to regulate the internal environment of the greenhouse.

For both models, we propose herein to apply a finite-horizon optimal control as strategy control adapted for multivariable systems. In the case of multi-modelling approach, we have elaborated two controllers, respectively, for the nocturnal and diurnal periods. Switching protocol permits to commute from nocturnal to diurnal controllers and reciprocally at the beginning of each phase. The objective is to generate control laws permit to follow nearly the desired trajectory of inside temperature and hygrometry despite the strong meteorological disturbances.

3.1 Optimal Controller Design

For synthesis optimal linear controller and without loss of generality, we consider a discrete-time system obtained from the linear model (3) or multi-model (4), (5):

$$\begin{cases} X(k+1) = AX(k) + BU(k) + BpD(k) \\ Y(k+1) = X(k+1) \end{cases} \tag{6}$$

The approach consists of minimizing the criterion J (7) that permits to determine the optimal control law defined by U (8). R and Q are the weighting matrices, respectively, symmetric, positive definite and symmetric, positive semi-definite.

$$J = \sum_{k=1}^{k=N} \left(\left(U^T(K)RU(k) + (Y_r(k) - Y(k)) \right)^T Q(Y_r(k) - Y(k)) \right) \tag{7}$$

The optimal control law *U(k)* is defined by

$$U(k) = -F(k)X(k) + T(k) \tag{8}$$

were *F(k)* is a state feedback gain, *T(k)* is a matrix of anticipation:

$$\begin{cases} F(k) = (R + B^T K(k+1)B)^{-1} B^T K(k+1)A \\ T(k) = (R + B^T K(k+1)B)^{-1} B^T (M(k+1) + K(k+1)B_P D(k)) \end{cases} \tag{9}$$

K(k) is the solution of Riccati equation:

$$\begin{cases} K(k) = A^T K(k+1)A - H(k) + Q \\ H(k) = A^T K(k+1)B(R + B^T K(k+1)B)^{-1} B^T K(k+1)A \\ M(k) = W(k)(M(k+1) + K(k+1)B_P D(k)) - QY_R(k) \\ W(k) = \left(A - B(R + B^T K(k+1)B)^{-1} B^T K(k+1)A \right)^T \end{cases} \tag{10}$$

To generate the optimal control law *U(k),* we fix in the first step the desired trajectory *Yr(k)* to be followed and we choose the weighting matrices R and Q adequately. The relative magnitudes of Q and R may be selected to trade off requirements on the smallness of the state against requirements on the smallness of the input.

For simplicity reason, these matrices are chosen block-diagonal as following:

$$Q = \begin{bmatrix} q_1 & 0 \\ 0 & q_2 \end{bmatrix}; R = \begin{bmatrix} r_1 & 0 & 0 & 0 \\ 0 & r_2 & 0 & 0 \\ 0 & 0 & r_3 & 0 \\ 0 & 0 & 0 & r_4 \end{bmatrix} \tag{11}$$

We recall that our objective is to show the feasibility of multi-model approach comparing with a single model approach. In this condition, it is necessary to make a comparative study using the same disturbances measured *D(k)* along the horizon of control.

3.2 Simulation Block Diagram

For the need of the simulation of the real-time situation, we have introduced the normalization functions and taking into account the actuators characteristics. Figure 7 represents the simulation diagram implanted on Simulink/Matlab.

The set points for the temperature and the hygrometry are fixed respectively to *Tic* = 11 °C and *Hic* = 70%. Switching protocol permits to commute from nocturnal to diurnal controllers and reciprocally at the beginning of each phase.

4 Optimal Control Evaluation and Simulation Results

Figure 8 shows the evolution of the internal temperature and hygrometry and the applied commands during three successive days.

It illustrates the good behaviour of the heating and the moistening, as they are activated instantly when the temperature and the hygrometry cross their respective set points.

We give a comparative performance between the approaches based on single model and multi-model (see Table 2) by using the mean value of deviation (12) in temperature and in hygrometry over one day and then three days:

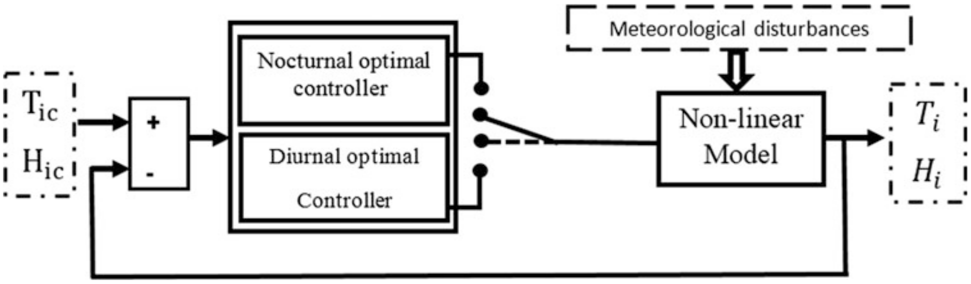

Fig. 7 Block diagram simulation of the optimal multi-model controller

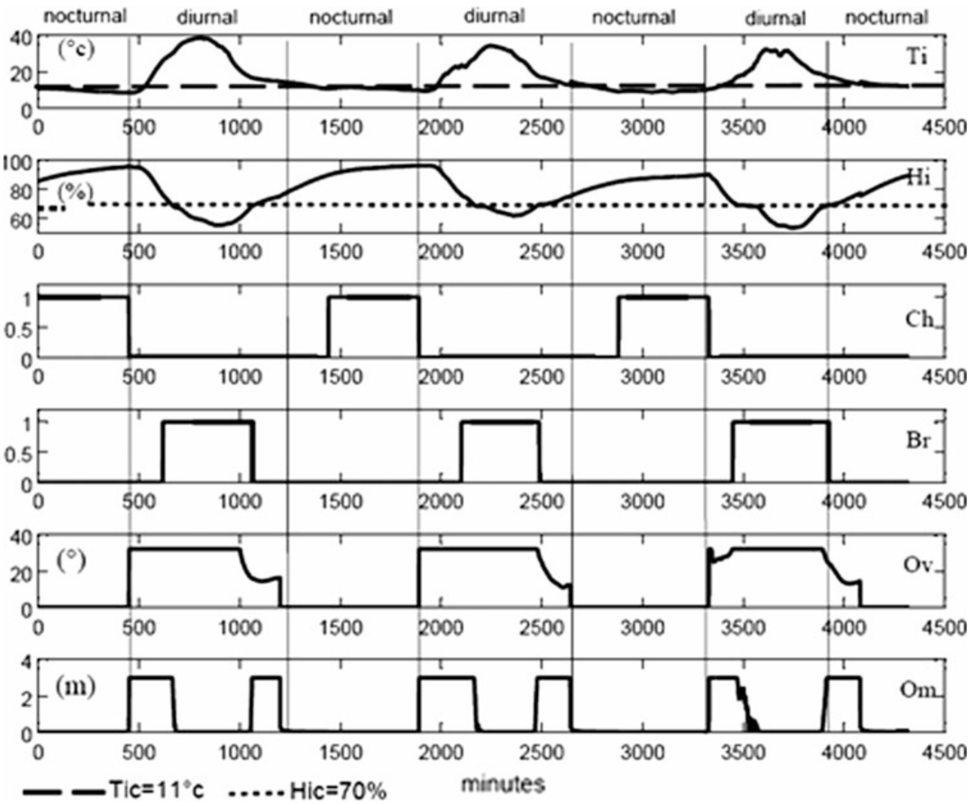

Fig. 8 Multi-model optimal control actions and the internal temperature and hygrometry evolution

Table 2 Comparison between single and multi-model approaches to control inside climate

Day(s)	One day		Three consecutive days	
N: samples	1440		1440 * 3	
	SMC	MMC	SMC	MMC
J_{Ti}	5.34	6.09	6.25	7.09
J_{Hi}	15.99	12.63	15.69	13.27
SMC: single model control				
MMC: multi-model control				

$$J_{Ti} = \frac{\sum_{k=1}^{N} |Ti(k) - Tic(k)|}{N}; J_{Hi} = \frac{\sum_{k=1}^{N} |Hi(k) - Hic(k)|}{N} \quad (12)$$

For the hygrometry case, the multi-model control is performing slightly better than the single model control under similar meteorological situation and operating conditions. However, for temperature control, the performances remain substantially the same.

Due to the complexity of the greenhouse system, it is impossible to attain exactly suitable performances. The greenhouse considered in this work is a pilot plant with insufficient equipment power, yielding the large bias in the set points values due to strong perturbations.

It is worth to mention that if we discard the limits on the control signals, then the controllers achieve better performance.

5 Conclusion

This paper deals with the modelling and control of the inside climate of an agricultural greenhouse. The internal state of the plant has been defined by two variables, namely, the internal temperature and hygrometry ones. These two variables are correlated and strongly sensitive to the external meteorological conditions to the greenhouse. The challenge is to maintain the temperature and the hygrometry nearly of their set points despite the strong meteorological disturbances. To improve this objective, we have proposed a multi-model approach instead of a single model approach. The idea consists to develop two linear models, respectively, for the diurnal and nocturnal phases. This temporal separation is based on human expertise. A comparison study has shown a superiority of multi-model approach in term of modelling and control performance of greenhouse. The results performances have confirmed clearly the robustness of multi-modelling approach comparing with the classical method of modelling.

The advantage of multi-model approach is also to reduce the complexity of control design. For the control strategy of the inside climate, we have adopted a finite-horizon optimal control taking into account the performance specifications. This strategy is adapted to the greenhouse control and the simulations results show a good performance of the proposed controller using a multi-approach despite the high interaction between the process variables and the external meteorological conditions.

References

Bennis, N., Duplaix, J., & Enéa, G. (2008). Greenhouse climate modelling and robust control. *Computers and Electronics in Agriculture, 6I*, 96–107.

Castañeda-Miranda, A., Castaño, V.-M. (May 2017). Smart frost control in greenhouses by neural networks models. *Computers and Electronics in Agriculture, 137*, 102–114.

El Afou, Y., Belkoura, L., Outanoute, M., Guerbaoui, M., Rahali, A., Ed-Dahhak, A., Lachhab, A., Join, C., & Bouchikhi, B. (June 2014). Feedback techniques using PID and PI intelligent for greenhouse temperature control. *International Journal of Advanced Research in Electrical, Electronics and Instrumentation Engineering, 3*(6).

Fourati, F. (2014). Multiple neural control of a greenhouse. *Neurocomputing, 139,* 138–144.

Fourati, F., & Chtourou, M. (2007). A greenhouse control with feed-forward and recurrent neural networks. *Simulation Modelling Practice and Theory, 15,* 1016–1028.

Gaudin. (1981). Simulation et commande auto-adaptative d'une serre agricole. Thesis, University of Nantes, France.

Herrero, J. M, Blasco, X, Martinez, M. R., & Sanchis, C. J. (2008). Robust identification of non-linear greenhouse model using evolutionary algorithms. *Control Engineering Practice, 16*, 515–530.

Ksouri, M., Mhiri, R., Feki, E. (June 2001). Modelling of the temperature under greenhouse by multi-model approach. *IFAC Proceedings Volumes, 34*(26), 113–118.

Lafont, F., & Balmat, J.-F. (2002). Optimized fuzzy control of a greenhouse. *Fuzzy Sets and Systems, 128,* 47–59.

Lafont, F., Balmat, J.-F., Pessel, N., & Fliess, M. (2015). A model-free control strategy for an experimental greenhouse with an application to fault accommodation. *Computers and Electronics in Agriculture, 110,* 139–149.

Laribi, I., Homri, H., & Mhiri, R. (2006). *Modeling of a Greenhouse Temperature: Comparison Between Multimodel and Neural Approaches*. Montreal, Quebec, Canada: IEEE ISIE.

Paraforos, D. S, & Griepentrog, H. W. (August 27–30, 2013). Multivariable greenhouse climate control using dynamic decoupling controllers. In *4th IFAC Conference on Modelling and Control in Agriculture, Horticulture and Post-Harvest Industry*. Espoo, Finland.

Van Straten, G., & Van Henten, E. J. (2010). Optimal greenhouse cultivation control: Survey and perspectives. *FAC Proceedings Volumes, 43,* 18–33.

Ayoub Moufid is a Ph.D. candidate at ENSET of Rabat of Mohammed V University, Morocco. He is attached to research team '**EODIC**: Energy Optimization, Diagnosis and control'. He has received master's degree in electrical engineering at ENSET in 2016. His research interests include modelling and control systems applied to agricultural process. Currently, he is working on the development of advanced control algorithms: Neural, PSO and MPC technics to control the greenhouse inside climate.

Najib Bennis received his 'D.E.S' degree in Automatic control of distributed systems in 1986 from the University of Nantes, France in 1986. He received the 'Doctorat en Science' degree in Automatic Control with honours in 2014 from Mohammed V University. Currently, he is professor at Higher School of Technical Education (ENSET of Rabat, Morocco). His areas of interest include LMI optimization, large-scale systems control, identification systems, decentralized control, and their applications. He is attached to research team '**EODIC**: Energy Optimization, Diagnosis and control' attached to Research Center '**STIS**: Sciences et Technologies de l'Ingénieur et de la Santé'. He is author and co-author of several publications in the field of robust control applied to industrial and agricultural process. He is co-organizer of the International Conference on Electrical and Information Technologies ICEIT since 2015. He is a permanent member of the Scientific Committee of 'Conférence Internationale en Automatique & Traitement de Signal' since 2018. He is also member of '**AMARIST**: Association Marocaine de la Recherche et de l'Ingénierie en Sciences et Technologies'. He has received several certificates for his contribution in reviewing of Elsevier's journals.